

Sheet Metal Forming

Processes
and
Applications

Edited by
Taylan Altan and A. Erman Tekkaya



Sheet Metal Forming

PROCESSES
AND
APPLICATIONS

Edited
by
Taylan Altan and A. Erman Tekkaya



ASM International®
Materials Park, Ohio 44073-0002
www.asminternational.org

Copyright © 2012
by
ASM International®
All rights reserved

No part of this book may be reproduced, stored in a retrieval system, or transmitted, in any form or by any means, electronic, mechanical, photocopying, recording, or otherwise, without the written permission of the copyright owner.

First printing, August 2012

Great care is taken in the compilation and production of this book, but it should be made clear that NO WARRANTIES, EXPRESS OR IMPLIED, INCLUDING, WITHOUT LIMITATION, WARRANTIES OF MERCHANTABILITY OR FITNESS FOR A PARTICULAR PURPOSE, ARE GIVEN IN CONNECTION WITH THIS PUBLICATION. Although this information is believed to be accurate by ASM, ASM cannot guarantee that favorable results will be obtained from the use of this publication alone. This publication is intended for use by persons having technical skill, at their sole discretion and risk. Since the conditions of product or material use are outside of ASM's control, ASM assumes no liability or obligation in connection with any use of this information. No claim of any kind, whether as to products or information in this publication, and whether or not based on negligence, shall be greater in amount than the purchase price of this product or publication in respect of which damages are claimed. THE REMEDY HEREBY PROVIDED SHALL BE THE EXCLUSIVE AND SOLE REMEDY OF BUYER, AND IN NO EVENT SHALL EITHER PARTY BE LIABLE FOR SPECIAL, INDIRECT OR CONSEQUENTIAL DAMAGES WHETHER OR NOT CAUSED BY OR RESULTING FROM THE NEGLIGENCE OF SUCH PARTY. As with any material, evaluation of the material under end-use conditions prior to specification is essential. Therefore, specific testing under actual conditions is recommended.

Nothing contained in this book shall be construed as a grant of any right of manufacture, sale, use, or reproduction, in connection with any method, process, apparatus, product, composition, or system, whether or not covered by letters patent, copyright, or trademark, and nothing contained in this book shall be construed as a defense against any alleged infringement of letters patent, copyright, or trademark, or as a defense against liability for such infringement.

Comments, criticisms, and suggestions are invited, and should be forwarded to ASM International.

Prepared under the direction of the ASM International Technical Book Committee (2011–2012), Bradley J. Diak, Chair.

ASM International staff who worked on this project include Scott Henry, Senior Manager, Content Development and Publishing; Karen Marken, Senior Managing Editor; Steven L. Lampman, Content Developer; Victoria Burt, Content Developer; Sue Sellers, Editorial Assistant; Bonnie Sanders, Manager of Production; Madrid Tramble, Senior Production Coordinator; and Diane Whitelaw, Production Coordinator.

Library of Congress Control Number: 2012938493
ISBN-13: 978-1-61503-844-2
ISBN-10: 0-61503-844-2
SAN: 204-7586

ASM International®
Materials Park, OH 44073-0002
www.asminternational.org

Printed in the United States of America

Contents

Preface	vii
Abbreviations and Symbols	ix
Chapter 1 Blanking	1
1.1 Blanking Process.....	1
1.2 Forces and Stresses	2
1.3 Part Edge Characteristics	3
1.4 Effects of Tooling and Presses.....	6
1.5 Tool Materials	11
1.6 Ultra-High-Speed Blanking	12
1.7 Fine Blanking.....	12
1.8 Shearing.....	14
1.9 Finite-Element Simulations.....	15
Chapter 2 Bending, Flanging, and Hemming	19
2.1 Mechanics of Bending	19
2.2 Air Bending.....	27
2.3 Stretch Bending	33
2.4 Other Industrial Bending Processes.....	34
2.5 Contour and Hole Flanging	37
2.6 Hemming.....	39
2.7 Bending Machines	42
2.8 Other Bending Machines	48
Chapter 3 Process Simulation	51
3.1 Advantages of Process Simulation	51
3.2 Commercial Codes for Forming Simulations	51
3.3 Steps Involved in FEM Simulations	52
3.4 Case Studies in Sheet Metal Forming	54
3.5 Factors Affecting the Accuracy of FEM Simulations	67
Chapter 4 Progressive and Transfer Die Forming	73
4.1 Process Design Using Finite-Element Analysis	73
4.2 Application of FEA in Progressive Die Design.....	81

Chapter 5	Warm Forming of Magnesium and Aluminum Alloys.....	83
	5.1 Mechanical Behavior and Testing Methods	83
	5.2 Warm Forming Process	90
	5.3 Applications of Warm Forming	96
	5.4 Deep Drawing	98
Chapter 6	Forming of Advanced High-Strength Steels (AHSS)	107
	6.1 Mechanical Behavior of AHSS	108
	6.2 Forming of AHSS	114
	6.3 Tribology in Forming AHSS	119
	6.4 Presses and Tooling.....	122
	6.5 Springback.....	126
Chapter 7	Hot Stamping.....	133
	7.1 Significant Process Variables	134
	7.2 Material Flow and Process Simulation	139
	7.3 Finite-Element Simulation of Hot Stamping.....	143
	7.4 Heating Methods	147
	7.5 Tools (Dies) for Hot Stamping	149
	7.6 Coatings for Oxidation Prevention.....	153
	7.7 Other Areas of Importance.....	154
Chapter 8	Sheet Hydroforming	157
	8.1 The Room-Temperature Sheet Hydroforming System.....	157
	8.2 Process Description, Advantages, and Disadvantages	158
	8.3 Advantages and Disadvantages	158
	8.4 Sheet Hydroforming—Process Variations	160
	8.5 Sheet Hydroforming Presses.....	162
	8.6 Tool Design.....	164
	8.7 Process Limits, Defects, and Process Window in SHF-P.....	167
	8.8 Process Simulation: Room-Temperature Sheet Hydroforming.....	169
	8.9 Elevated-Temperature Sheet Hydroforming	170
	8.10 Industrial Applications of Sheet Hydroforming	173
	8.11 Sheet Hydroforming Process Economics.....	173
Chapter 9	Tube Hydroforming	179
	9.1 Applications.....	179
	9.2 Tube Hydroforming as a System.....	181
	9.3 Materials for Tube Hydroforming	181
	9.4 Tube Bending.....	185
	9.5 Mechanics of Tube Hydroforming	189
	9.6 Friction and Lubrication in Tube Hydroforming	192
	9.7 Presses and Tooling.....	193
	9.8 Tube Hydroforming Process Design and Design Guidelines.....	202
Chapter 10	Roll Forming	211
	10.1 Roll Forming Lines.....	212
	10.2 Roll Design.....	215
	10.3 Recent Developments and the Future of Roll Forming Technology ...	221

10.4	Future of Roll Forming.....	224
Chapter 11	High-Velocity Forming.....	227
11.1	High-Velocity Hydroforming.....	228
11.2	High-Velocity Mechanical Forming.....	233
11.3	Electromagnetic Forming	234
Chapter 12	Spinning, Shear Forming, and Flow Forming	249
12.1	Spinning	249
12.2	Flow Forming.....	259
12.3	Shear Spinning.....	266
Chapter 13	Incremental Sheet Forming.....	273
13.1	Process Variations of ISF	274
13.2	Equipment and Basic Process Parameters.....	275
13.3	Process Mechanics and Process Limits.....	277
13.4	Multistage Forming Strategies.....	282
13.5	Process Modeling	283
13.6	Hybrid Process Variations	285
Chapter 14	Mechanical Joining by Forming	289
14.1	Riveting	289
14.2	Clinching.....	293
14.3	Future Trends	296
14.4	Fatigue Behavior of Clinched Joints.....	298
14.5	Crimping.....	299
Chapter 15	Sensors for Sheet Metal Forming	301
15.1	Measurement of Forces	301
15.2	Displacement Sensors.....	304
15.3	Detection of Tool Breakage and Flaws in Parts.....	307
15.4	Measurement of Material Flow during Forming	308
15.5	Machine Vision Systems.....	309
15.6	Online Material Property Evaluation.....	311
15.7	Sensors for Lubrication	314
15.8	Summary	314
Chapter 16	Tool Materials, Treatments, and Coatings	317
16.1	Background	317
16.2	Tool Materials	318
16.3	Treatments to Harden the Tools.....	320
16.4	Plating and Coating	324
16.5	Galling/Wear Tests	329
16.6	Guidelines for Selecting Tool Materials, Treatments, and Coatings....	332
Index.....		339

Preface

In sheet metal forming, a sheet blank that has a simple shape is plastically formed between tools (or dies) to obtain a part with relatively complex geometry with desired tolerances and properties. Sheet metal forming processes usually produce little scrap and generate the final part geometry in a very short time, usually in one stroke or a few strokes of a press. As a result, sheet forming offers potential savings in energy and material, especially in medium and large production quantities, where tool costs can be easily amortized.

The ever-increasing costs of material, energy and manpower require that sheet metal forming processes and tooling be designed and developed with minimum amount of trial and error with shortest possible lead times. Therefore, to remain competitive, the cost-effective application of computer-aided technologies, i.e. CAD, CAM, CAE, and especially finite element analysis (FEA), computer-based simulation is an absolute necessity. Thus, process modeling using FEA has been discussed in all appropriate chapters.

The practical and efficient use of these technologies requires a thorough knowledge of the principle variables of the sheet metal forming processes and their interactions. These variables include:

1. the flow behavior and formability of the formed sheet material under processing conditions;
2. die geometry, materials and coatings;
3. friction and lubrication;
4. the mechanics of deformation, i.e. strains, stresses and forces;
5. characteristics of the sheet metal forming presses and tooling;
6. geometry, tolerances, surface finish and mechanical properties of the formed parts, and
7. the effects of the process on the environment.

These topics are addressed in two companion volumes *Sheet Metal Forming—Fundamentals* and *Sheet Metal Forming—Processes and Applications*. Principles are described, and major emphasis is placed on the latest developments on the design of sheet forming operations, equipment and tooling.

In *Sheet Metal Forming—Fundamentals*, the role of sheet metal forming in manufacturing has been introduced in Chapter 1. Chapter 2 gives the classification and description of sheet metal forming operations. The fundamentals of plastic deformation, i.e. metal flow, flow stress of materials, testing methods to determine flow stress and formability are discussed in Chapters 3, 4, and 5. Chapters 6 and 7 cover the significant process variables materials and friction. The introduction to deep drawing is discussed in Chapter 8. Chapters 9, 10, 11, and 12 discuss the characteristics and operations of various sheet metal forming presses (hydraulic, mechanical, servo-drive) and cushion systems.

In *Sheet Metal Forming—Processes and Applications*, Chapters 1 and 2 cover blanking, and bending. Process modeling and its applications are discussed in Chapter 3 as well as in several other chapters, where appropriate. Chapter 4 reviews progressive and transfer die forming. Relatively new technologies, i.e. warm forming, forming of advanced high strength steels (AHSS) and hot stamping are discussed in Chapters 5, 6, and 7, respectively. Processes that are related to sheet forming such as sheet and tube hydroforming, roll forming, and high velocity forming are covered in Chapters 8, 9, 10, and 11. Special sheet forming operations spinning, incremental forming and mechanical joining are discussed in Chapters 12, 13, and 14. Sensors and die materials are critical for practical application of sheet forming technology and they are discussed in Chapters 15 and 16.

The preparation of this book was possible through extensive efforts by many friends, associates and students of the editors who authored and co-authored many of the chapters. We would like to thank them all for their very valuable contributions.

We would like to thank Ms. Linda Anastasi, Administrative Assistant of the Center for Precision Forming (CPF – www.cpforming.org), who revised the chapters several times, Mr. Xi Yang and Manan Shah at CPF who assisted in the editing of some chapters and Mr. Doug Dragoo of Cincinnati Inc. who reviewed Chapter 15 on Bending and made valuable suggestions. We would also like to thank our families, who offered us enormous support and encouragement throughout the preparation of this book.

Finally, we would like to gratefully acknowledge the financial support from member companies of CPF and especially from the National Science Foundation (NSF) that helped us summarize the results of sheet metal forming research, conducted over the years at The Ohio State University.

Taylan Altan
Center for Precision Forming (CPF)
The Ohio State University

A. Erman Tekkaya
Institut für Umformtechnik und Leichtbau
(IUL)
Technische Universität Dortmund, Germany

Abbreviations and Symbols

a_d	die angle	CDV	critical damage value
a_p	punch tip angle	C.L.	curvilinear length
A	area, geometric contact area, instantaneous cross-sectional area	CMM	coordinate measuring machine
A_a	apparent contact area	CNC	computer numerical controlled
A_{BH}	area of the blank under the blankholder	COF	coefficient of friction
A_f	cross-sectional area at fracture	CP	complex-phase, commercially pure
A_p	cross-sectional area of the punch	CPF	Center for Precision Forming
A_{piston}	area of piston	CQ	commercial quality
A_r, A_r	area reduction, real contact area	CR	cold rolled
A_s	area of the cut surface	CVD	chemical vapor deposition
A_0	original cross-sectional area	d	punch stroke, diameter, diameter of mandrel, vertical deflection, dimpling
ac	alternating current	d_b	blank diameter, diameter of blankholder
AHSS	advanced high-strength steel	d_c	diameter of die cavity
AISI	American Iron and Steel Institute	d_d, D_d	die diameter, punch-die clearance
AKDQ	aluminum-killed drawing quality	d_f	diameter of flanged hole after flanging
AS	adaptive simulation	$d_{F,max}$	outside diameter of flange when drawing load is maximum
ASAME	Automated Strain Analysis and Measurement Environment	d_h	diameter of pierced hole
b	width of die opening	d_m	diameter of the cup wall at max- imum drawing force
BA	bend allowance	d_p, D_p	punch diameter, external cup diameter at maximum drawing force
bcc	body-centered cubic	d_s	punch stroke
BD	bend deduction	d_0	initial diameter, blank diameter
BDC	bottom dead center	d_1	inner cup diameter
BEF	Bauschinger effect factor	de	infinitesimal engineering strain
BH	bake hardening, bake hardenable	dl	differential change of length
BHF	blankholder force	dt	infinitesimal time
BHP	blankholder pressure	$d\epsilon$	infinitesimal natural strain
c	Cowper-Symonds coefficient	$d\epsilon_{xy}$	infinitesimal shear angle change
c	empirical factor, width of warp	D	diameter, sag
c_d	speed of sound	D_{cp}	depth of crack penetration
c_p	heat capacity	D_F	mandrel diameter
C	die clearance, stiffness		
C_F	compression force, stiffness of the fluid column		
C_θ	angular stiffness		
CAD	computer-aided design		
CAM	computer-aided manufacturing		

D_p	punch diameter	F_R	ring force, radial force
D_0	diameter of initial blank	F_S	blanking force
dc	direct current	F_T	tangential force
DCV	directional control valve	F_V	vertical force
DDS	deep-drawing steel	fcc	face-centered cubic
DIN	German Industry Standard	F	index to define material flow
DP	dual phase	FE	finite element
DQ	drawing quality	FEA	finite-element analysis
DQSK	drawing quality, special killed	FEM	finite-element method, finite-element modeling
DR	dent resistant, draw ratio	FLC	forming limit curve
DS	drawing steel	FLD	forming limit diagram
e	engineering strain, endpoint of tool motion, eccentricity of the load	FRF	flexible roll forming
e_t	total elongation	h	clearance, depth of cup, slide position
e_u	uniform elongation	h_{conv}	convective heat-transfer coefficient
E	Young's modulus, elastic modulus, energy of deformation	h_d	bulge or dome height
E'	Young's modulus in plane strain	h_{eff}	effective heat-transfer coefficient
$E_{cushion}$	cushion energy	h_o	original height
E_D	elastic deflection	$h(P)$	contact heat-transfer coefficient
E_{EM}	electric motor energy	h_{rad}	radiation heat-transfer coefficient
E_F	friction energy	H	height, surface hardness
$E_{forming}$	forming energy	H_c	heat-transfer coefficient with air
E_M	machine energy	H_t	heat-transfer coefficient
E_p	process energy	HCO	hem curved outboard
E_{slide}	slide energy	HDGA	hot dip galvanized
E_T	total energy	HDGI	hot dip galvanized
EA	evolutionary algorithm	HE	hole expansion
E-coating	electrocathodic coating	HER	hole expansion ratio
EDDS	extra-deep-drawing steel	HF	hot forming
EDDS+	extra-deep-drawing steel plus	HR	hot rolled
EL	elongation	HRB	Rockwell B hardness
EMF	electromagnetic forming	HRC	Rockwell C hardness
EP	extreme pressure	HSLA	high-strength, low-alloy
ERC/NSM	Engineering Research Center for Net Shape Manufacturing	HSPR	hydro-self-pierce riveting
ET	extreme temperature	HSS	high-strength steel
f	friction factor	HV	Vickers hardness
f^c	modified friction factor	I	moment of inertia, angular inertia, identity sensor
f_b, F_b	blankholder force	IE	Erichsen index
f_f	feed rate	IF	interstitial free
F	force, applied load	IFU	Institut für Umformtechnik (Institute of Forming Technology)
F_b	bending force	ISF	incremental sheet forming
F_{BH}	blankholder force	ISM	inside of metal
F_c	clamping force, clamping load	ISO	International Organization for Standardization
F_d	deformation force	IUL	Institut für Umformtechnik und Leichtbau (Institute of Forming Technology and Lightweight Construction)
$F_{d,max}$	maximum punch force	J	deviatoric stress invariant
$F_{draw,max}$	maximum drawing force	k	empirical constant
F_f	friction force		
F_G	counterforce		
F_H	horizontal force		
F_N	normal force		
F_p	punch force		

k	stripping constant, heat conductivity, shear strength, bend allowance	p_i	internal pressure
k_f	flow stress	p_{\max}	maximum pressure
K	springback ratio, strength coefficient, wear coefficient, shear flow stress	P	penetration, pressure, compression load, normal load, deformation power
K-B	Keeler-Breizer equation	P_b	blankholder pressure
KSIF	kinematic incremental sheet forming	P_c	interface pressure
l	distance, length, roll spacing	P_f	fluid pressure
l_f	total elongation at fracture	P_i	instantaneous pressure
l_o, l_0	original length	PPG	pulsed power generator
l_U	uniform elongation	PTFE	polytetrafluoroethylene
l_1	final length	PVD	physical vapor deposition
L	length, sliding distance, load	\dot{Q}	flow rate
L_d	draw-in length	QPF	quick plastic forming
L_{hem}	hem length	r	bending radius, tube radius, mean radius, instantaneous radius, plastic or normal anisotropy, plastic strain ratio or Lankford coefficient, eccentricity of the crank
L_M	machine load	r_{avg}	average strain ratio
L_{min}	dimensions of smallest element	r_c	die cavity radius
L_o, L_0	initial length	r_d, r_D	die radius, die corner radius
L_p	process load	r_f	die fillet radius
L_{st}	stripping force	r_m	weighted average of strain ratios
LDH	limiting dome height	r_o	outer radius
LDR	limiting draw ratio	r_p	punch corner radius
LED	light-emitting diode	r_R	die corner radius
LVDT	linear variable differential transformer	r_z	radius of curvature in the longitudinal direction
m	friction factor	r_0	parallel to the rolling direction
m	friction shear factor, strain-rate sensitivity	r_{45}	diagonal to the rolling direction
m_r	modified shear factor	r_{90}	transverse to the rolling direction
M	index describing the shape of the yield loci	r_0	bulge radius, radius of curvature in the hoop direction
M	bending moment, tilting moment, torque	r_{0o}	tube radius prior to deformation
MPC	multipoint cushion	\bar{r}, \bar{R}	normal anisotropy
MS	martensitic steels	Δr	planar anisotropy
n	strain-hardening coefficient, strain exponent, speed of crank in revolutions per minute, number of strokes per minute	R	rake, radius, bending radius, bend die radius, instantaneous outside radius, stress ratio, total eccentricity
n_p	number of strokes per minute under load	R_c	radius of die ring
n_0	number of strokes per minute when idle	R_d	die radius, bulge radius
OBI	open-back inclinable press	R_i	initial radius, inner bending radius
OD	outside diameter	R_m	mean bending radius, tensile strength
OEM	original equipment manufacturer	R_{min}	minimum bend radius
OSM	outside of metal	R_n	neutral radius
p	Cowper-Symonds coefficient	R_o	outer bending radius
p	pressure, normal pressure, hydraulic pressure, magnetic pressure	R_p	punch radius, punch tip radius
p_{BH}	blankholder pressure	RD	rolling direction
		RT	room temperature

s	instantaneous sheet flange thickness, stroke, recoil	TRIP	transformation-induced plasticity
s_h	flange height	TS	tensile strength
s_{ij}	deviatoric stress state	TSA	thickness strain analysis
s_{max}	maximum stroke	TW	tendency of wrinkling
s_0	initial sheet thickness, wall thickness, blank thickness	TWIP	twinning-induced plasticity
s_1	instantaneous sheet wall thickness	u	instantaneous material point velocity in the x -direction
S	strength, arc length of inner curve, yield stress, microstructure, stroke length, slide	u_D	punch-die clearance
S_r	pressure release displacement time	U_d	constant speed
S_s	shear strength	U_D	die clearance
S_{th}	theoretical displacement time	UHS	ultra-high speed
S_u	ultimate tensile strength	UHSS	ultrahigh-strength steel
SB	stretch bend	UTS	ultimate tensile strength
SDT	strip drawing test	v	distribution of tool motion, sliding velocity
SF	self-feeding	\dot{v}	instantaneous material point velocity in the y -direction
SHF-D	sheet hydroforming with die	v_p	punch velocity
SHF-P	sheet hydroforming with punch	V	velocity, volume
SMA	simplified modeling approach	V_p	slide velocity under pressure
SPIF	single-point incremental forming	V_p^{punch}	punch velocity
spm, SPM	strokes per minute	V_ϕ	angle distribution
SPR	self-piercing riveting	VPB	viscous pressure bulge
SQ	surface quality, structural quality	w	width, depth of warp
SS	structural steel	\dot{w}	instantaneous material point velocity in the z -direction
t	thickness, sheet thickness, time	W	width, V-die opening, worn volume
t_d	thickness at apex of bulge	W_{d^0}, W_D	die opening width
t_0, t_0	initial thickness	W_0	original width
t_p	time under pressure	y	distance
t_γ	austenitization time	Y	yield strength
T	thickness, sheet thickness, tension stress, temperature, applied torque	YS	yield strength
T_e	temperature of environment	z_b, Z_b	burr zone
T_f	temperature at forming	z_f, Z_f	fracture/rupture zone
T_F	tension load, tension force, final thickness	z_r, Z_r	roll-over zone
T_1	initial temperature	z_s, Z_s	shear zone
T_0	original thickness	α	angle, measured angle, bending angle, crank angle, angular deflection, thermal expansion, heat-transfer coefficient, stress ratio, cone angle, real contact area ratio
T_{punch}	punch temperature	α_d	die angle
T_t	tool temperature	α_N	design angle
T_u	temperature of contact plates	α_p	punch tip angle
T_y	tension required for yield	β	camera angle, spinning ratio, depressor angle
T_γ	austenitization temperature	γ	clearance angle
T_0	initial temperature	Δr	planar anisotropy
TCT	twist compression test	ϵ	strain, true or natural strain
TD	transverse direction, thermal diffusion	$\dot{\epsilon}$	strain rate
TDC	top dead center	ϵ_b	bending strain
THF	tube hydroforming	ϵ_e	elastic strain
TPIF	two-point incremental forming	ϵ_{el}	elastic strain
TRB	tailored rolled blanks		

$\varepsilon_{e,0}$	elastic limit	ρ_e	elastic radius of curvature
ε_o	initial strain	ρ_0	radius of curvature
ε_{pl}	plastic strain	σ	stress, flow stress, true normal stress
ε_r	strain in radial direction	σ_b	yield stress in balanced biaxial state
ε_t	total strain, strain in thickness direction, strain in tangential direction	σ_{CY}	compressive yield strength
ε_w	width strain	σ_e	engineering stress
ε_z	strain in axial direction	σ_f	flow stress
ε_0	prestrain	σ_m	stress quantity, mean stress
ε_θ	strain in the hoop direction	σ_n	normal stress
ε_ϕ	strain in the longitudinal direction	σ_{oc}	compression yield stress
$\bar{\varepsilon}$	equivalent strain, effective strain	σ_r	rupture stress, stress in radial direction
$\bar{\varepsilon}^p$	plastic strain	σ_t	stress in tangential direction
$\bar{\dot{\varepsilon}}$	equivalent strain rate, effective strain rate, von Mises equivalent plastic strain	σ_{UTS}	ultimate tensile strength
η	lubricant viscosity, deformation efficiency, efficiency factor	σ_Y	yield strength
θ	bending angle, punch angle, crankshaft rotation, temperature	σ_z	longitudinal stress, stress in axial direction
θ'	final bend angle	σ_0	initial yield stress
θ_p	half bending angle	σ	hoop stress
θ_s	springback angle	$\bar{\sigma}$	flow stress, instantaneous yield stress
θ_1	half angle (under load)	τ	shear stress, frictional shear stress
θ_2	half angle (unloaded)	τ_a	average shear stress at contacting asperity peaks
$\theta\theta$	hoop stress	τ_b	average shear stress at lubricant pockets
$\theta\phi$	axial stress	τ_f, τ_r	frictional shear stress
$\Delta\theta$	springback angle	τ_s	shear stress
κ	bulk modulus	ϕ	bend angle, logarithmic strain
λ	hole expansion ratio, roughness parameter	ω	angular speed or velocity
μ	coefficient of friction	2-D	two-dimensional
μ_m	mean coefficient of friction	3-D	three-dimensional
ν	Poisson's ratio		

CHAPTER 1

Blanking

Soumya Subramonian, The Ohio State University

BLANKING AND PIERCING are metal-shearing processes in which the incoming sheet material is sheared to a desired shape. In blanking, the removed piece of material is the product, whereas in piercing, the material that is removed is scrap, while the remaining part of the strip is the product (Fig. 1.1). Blanking or piercing is used in almost all sheet-forming operations. The size of holes punched can vary from less than 1 to 100 mm (0.05 to 4.0 in.) or more.

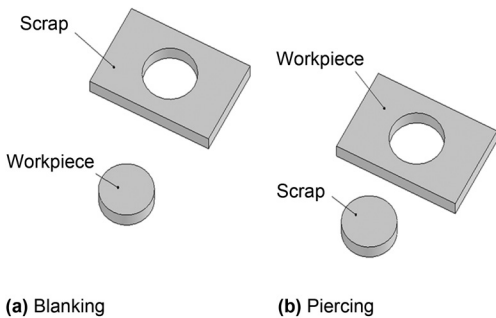


Fig. 1.1 Schematic of blanking and piercing

This chapter gives an overview of the phases in blanking, forces and stresses involved, factors affecting part quality and tool life, as well as tooling and press requirements. Fine blanking is also briefly explained.

1.1 Blanking Process

The blanking process can be considered to include a series of phases in which the sheet metal undergoes deformation and separation, as seen in Fig. 1.2.

Contact of the Punch. The punch first touches the fixed sheet. At impact, a compressive stress rapidly builds on the punch and sends a shock wave through it.

Elastic and Plastic Deformation. The punch penetrates into the sheet, first causing an elastic and then plastic deformation.

Shearing and Crack Formation. When the stresses increase, shearing occurs followed by fracture. Fracture begins from both the punch end and die end of the sheet. They usually meet, and complete fracture of the material takes place.

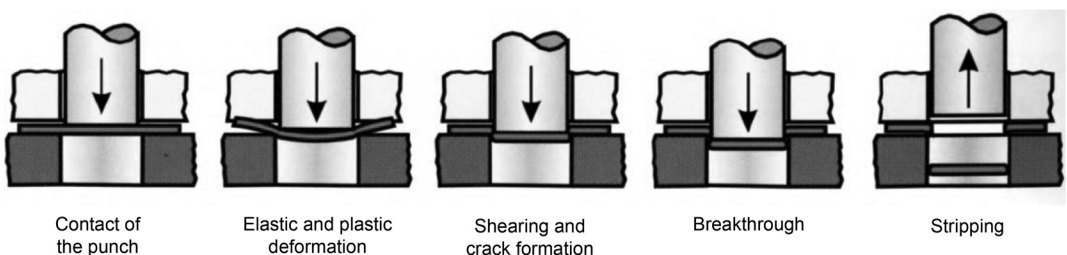


Fig. 1.2 Phases of the blanking process. Source: Ref 1.1

Breakthrough. If the sheet material has a high strength or is thick, a large force is required for the blanking process. During fracture, compressive forces are stored in the tool. When complete fracture occurs, there is an instant release of these compressive forces. These generate shock, which can lead to breakage of the punch in some cases.

Stripping. The punch moves down to the bottom dead center and ejects the part. At the bottom dead center, the direction of punch motion is reversed. Due to the friction between the stock and the surface of the punch, the surface pressure intensifies. A stripper or blank holder strips the blank from the punch.

1.2 Forces and Stresses

The cutting forces do not act linearly along the cutting edge. Instead, the vertical force, F_v , and horizontal force, F_H , act in a small area near the cutting edge, as shown in Fig. 1.3 (Ref 1.2).

The distribution of those compressive forces is nonuniform. The distance, l , between the forces F_v and F_v' causes a bending moment that either bends or tilts the workpiece. This moment must be compensated for by a counterbending moment that is created by bending stresses and horizontal normal stresses between the workpiece and tool. Figure 1.3 also shows the resulting frictional forces, $\mu \cdot F_H$ and $\mu \cdot F_v$. These frictional forces increase the total blanking force. When the punch and die surfaces are flat and the motion of the punch is at right angles to the die, the force required in a blanking process can be determined using the following formula:

$$F = LtS_s \tag{Eq 1.1}$$

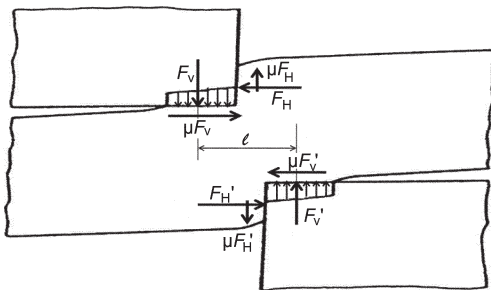


Fig. 1.3 Force distribution in the workpiece during blanking. Source: Ref 1.2

The compressive stress in the punch can be calculated using the following formula:

$$S_p = F/A_p \tag{Eq 1.2}$$

where F is the force required for blanking, L is the total length (perimeter) of the cut, t is the sheet material thickness, S_s is the shear strength of the material, and A_p is the cross-sectional area of the punch.

Stripping force is the force needed to free the blank from the die or the strip from the punch when they stick or jam because of springback and friction. Stripping force can be calculated using:

$$L_{st} = kA_s \tag{Eq 1.3}$$

where L_{st} is the stripping force (in pounds), k is a stripping constant (in pounds per square inch), and A_s is the area of the cut surface (in square inches) (stock thickness, t , multiplied by length or perimeter of cut, l). Approximate values for the constant k (as determined by experiment for low-carbon steel) are (Ref 1.2):

- 1500 for sheet metal thinner than 1.57 mm (0.060 in.) when the cut is near an edge or near a preceding cut
- 2100 for other cuts in sheet thinner than 1.57 mm
- 3000 for sheet more than 1.57 mm thick

The blanking process can be investigated by monitoring the changes in the blanking force during the cutting process. The force varies with punch displacement, punch entry time, or crank angle. Because part quality is evaluated in terms of regions formed along the part edge, it is preferred to present the load versus punch displacement. In addition, the cutting work can be calculated by integrating the force over the stroke. The theoretical load-stroke curve in a blanking process can be described schematically as seen in Fig. 1.4:

- *Step 1:* The sheet metal deforms elastically.
- *Step 2:* The limit of elastic deformation is reached, and the material starts to deform plastically. The material flows along the cutting edges in the direction of the punch penetration and into the gap between punch and die (comparable to deep drawing). The material flow causes strain hardening, which

results in an increase of the cutting force up to the maximum load. At this time, the cross section is not reduced and shearing has not started.

- *Step 3:* The increased pressure at the cutting edges prevents the material from flowing, and shearing starts. Due to a decreasing cross section, the blanking force decreases despite the strain hardening of the material.
- *Step 4:* Fracture starts after the formability limit of the material is exceeded. As soon as

the initial cracks meet each other, slug and skeleton are completely separated. The cutting force decreases rapidly during this phase.

A way to reduce the maximum force on the tool would be to change the design of the punch such that it is stepped or has an angle on the punch edge. This would lower the maximum force by spreading the work over a larger depth, as seen in Fig. 1.5 and 1.6.

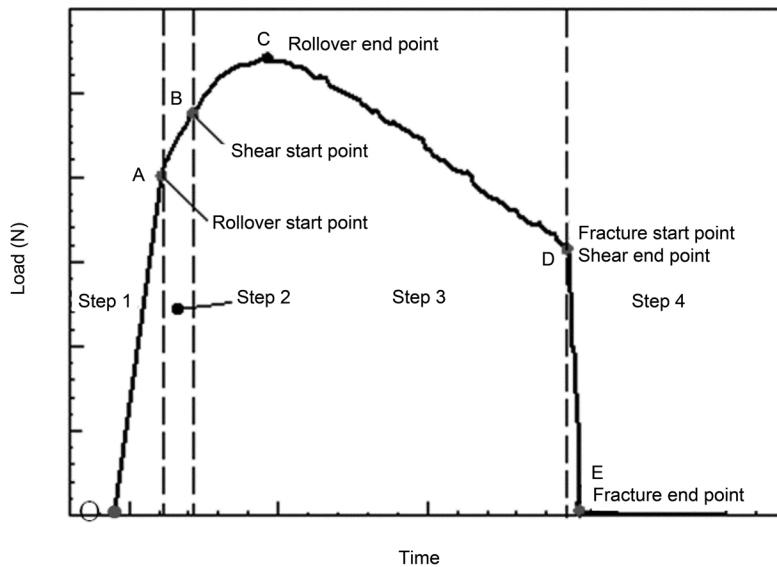


Fig. 1.4 Load-stroke curve of a blanking/piercing operation

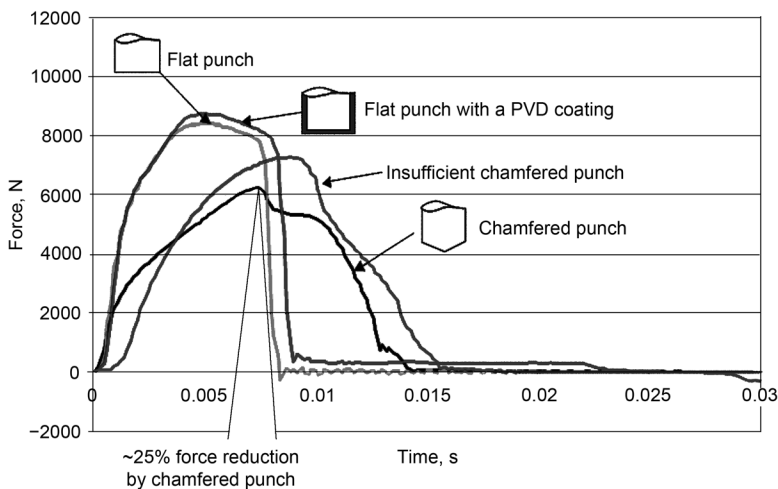


Fig. 1.5 Punch force profiles for different tip geometries. PVD, physical vapor deposition. Adapted from Ref 1.7

1.3 Part Edge Characteristics

Different Zones of a Part Edge

The shear edge is made of different zones based on the method of material deformation that has occurred. The ratio of the different zones is influenced by different parameters, such as the punch-die clearance, material properties, and punch corner radius, to name a few. In general, it is preferred to have a large shear zone and smaller burr.

The zones and deformation modes of a blanked part edge are given as follows and in Fig. 1.7:

- *Rollover zone (Z_r):* Caused by plastic material deformation
- *Shear zone (Z_s):* Smooth and shiny area, created during material shearing
- *Fracture/rupture zone (Z_f):* Rough surface, results after the material cracks
- *Burr zone (Z_b):* Caused by plastic deformation
- *Depth of crack penetration (D_{cp}):* Angle of fracture zone, depends mainly on clearance
- *Secondary shear:* Created if cracks do not run toward each other and material is sheared again

Factors Influencing Part Edge Characteristics

Effect of Blanking Clearance on Part Edge Quality. In general, as the clearance between punch and die increases, the shear zone, roll-

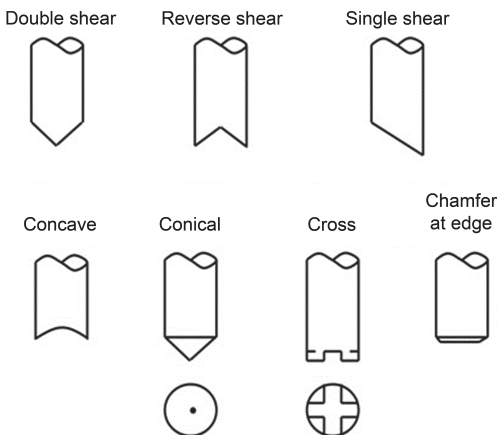


Fig. 1.6 Punch geometries used in blanking. Adapted from Ref 1.3

over zone, fracture angle, and burr increase while the fracture zone decreases. Insufficient clearance produces secondary shear; that is, the cracks originating at the punch and die do not meet. Hence, a ring of material is further stressed to its shear limit, expending more energy. Excessive clearance causes large plastic deformation, large burr, and high fracture angle. Furthermore, tool life is also lowered by improper clearance. Many applications demand a certain shear zone and fracture zone limit in the hole/blank for good assembly/alignment. Based on the demands required by the specific application and tool life consideration, a specific clearance can be set between the punch and die. Advanced high-strength steels require greater clearances of approximately 10 to 14% compared to mild steels, which give good part edges at clearances of approximately 6% of sheet thickness (Ref 1.3).

The effect of punch-die clearances in the range of approximately 5 to 20% in blanking 1.4 mm (0.06 in.) DP590 steel is shown in Fig. 1.8 (Ref 1.4).

The effect of tool wear on part edge quality is significant. Tool wear leads to the formation of burrs and increases burr length. Burr length is generally an important criterion in the industry to evaluate part quality. Burr length indicates when the tool should be reground to obtain the sharp die-and-punch radius. It has also been observed that the effect of tool wear is more pronounced at higher blanking clearances. This has also been shown experimentally by Makich et al. (Ref 1.5) (Fig. 1.9).

Tool wear can be estimated using finite-element simulations by theoretically increasing the punch and die corner radii in simulations.

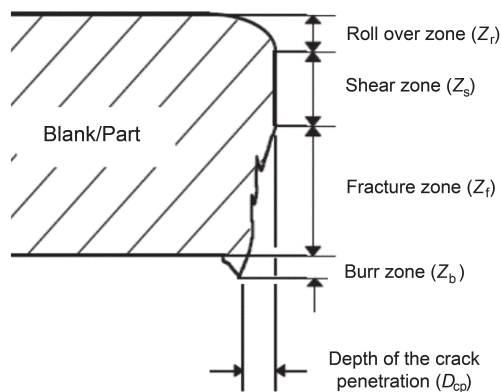


Fig. 1.7 Different zones of a blanked part edge

The effect of tool wear on part edge quality is significant. Tool wear leads to the formation of burrs and increases burr length, as shown in Fig. 1.10 in the work done by Husson et al. (Ref 1.6), where the effect of tool wear was simulated by assuming different punch corner radii in simulations. It has also been observed that the effect of tool wear is more pronounced at higher blanking clearances (Fig. 1.10).

Effect of Material on Part Edge Quality. The part edge quality also depends on the mate-

rial being blanked. Materials with large ductility, low yield strength, and homogeneity will have better blanked edge quality, dimensional tolerances, and longer tool life. Makich et al. performed blanking experiments on different materials and observed burr formation on each of them (Ref 1.5). The burr volume was calculated for each material. It can be observed from this study that the burr volume depends significantly on the type of material blanked (Fig. 1.11).

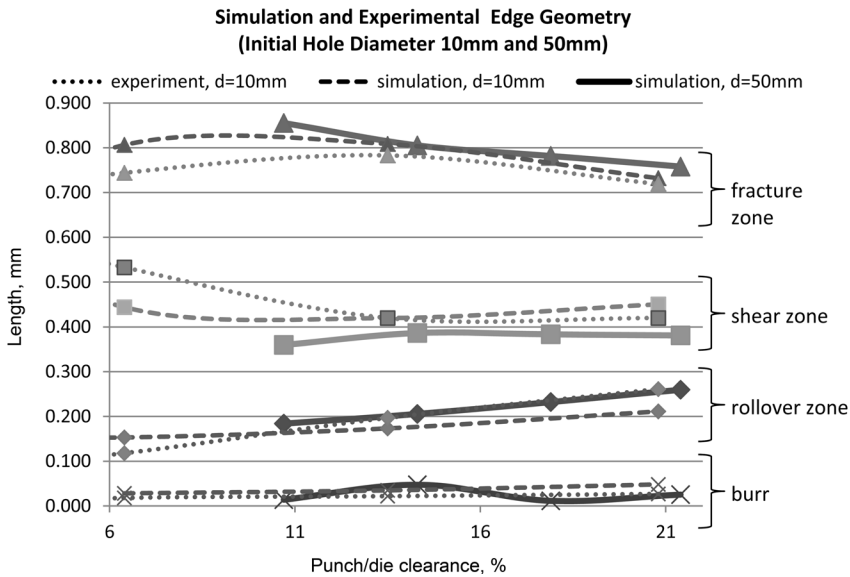


Fig. 1.8 Effect of punch-die clearance on part edge quality in blanking DP590 steel of 1.4 mm (0.06 in.) thickness. Source: Ref 1.4

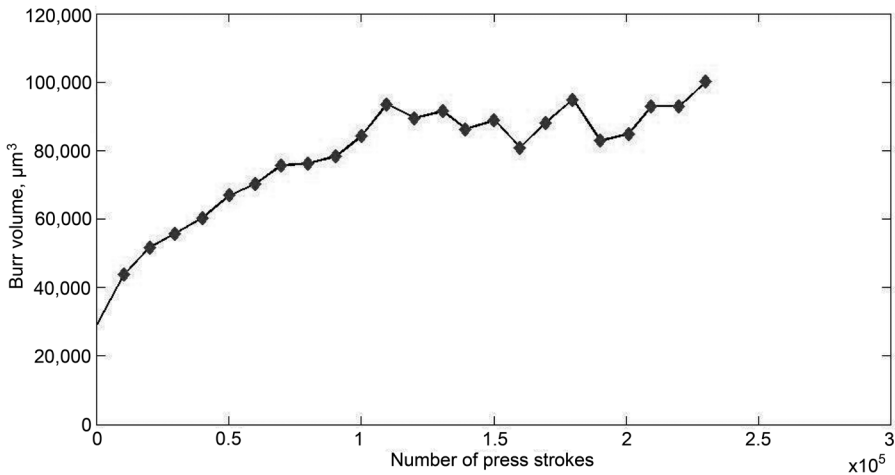


Fig. 1.9 Increase in burr volume with increasing press strokes because of tool wear. Source: Ref 1.5

1.4 Effects of Tooling and Presses

Punch Geometry

Punch geometry affects the punch stresses and temperatures as well as punch life. Figure 1.5 shows the maximum forces while using different punch shapes when blanking a round part. The punch forces differ because the area of contact with the sheet at a given instant in the penetration length is not the same. Shear angles/

chamfers on punches are also used for easy stackup of the slugs. The slugs, when bent, become neatly stacked over one another. Figure 1.6 shows the various punch shapes, and Table 1.1 lists the advantages and disadvantages of the different shapes.

Die Geometry (Ref 1.3)

Minimal die land length allows the slug to fall away. Fewer slugs in the die matrix can

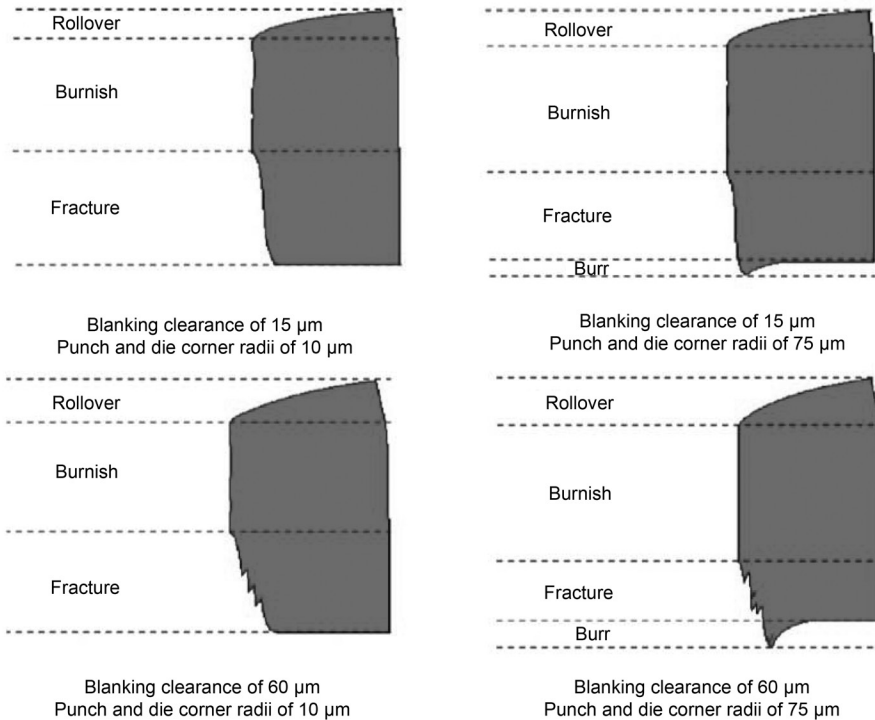


Fig. 1.10 Effect of tool wear and blanking clearance on part edge quality as predicted by simulations on 0.58 mm (0.02 in.) thick copper alloy. Source: Ref 1.6

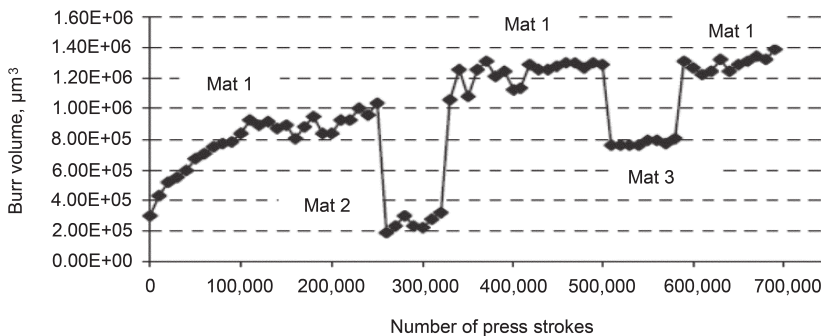


Fig. 1.11 Burr depends on material blanked; Mat 2 and Mat 3 are more ductile and homogeneous than Mat 1. Source: Ref 1.5

prevent slug jamming and pulling. Land length should not exceed four times material thickness for effective slug removal. When full tapers are sharpened, the dimensions of the die change a little; in terms of slug removal, they perform the best. Increased taper is designed to prevent soft part material from sticking in the relief area, which minimizes slug stacking. Figure 1.12 shows the various die geometries with respect to die length and taper. The figure on the right in Fig. 1.12 shows the shear angles on the die (instead of having the shear angle on the punch) to achieve lower forces. This would enable the part to be flat instead of bent, which occurs when the shear angle is on the punch.

Punch Stagger (Ref 1.3)

It is a common practice to stagger punches to minimize impact and snap-thru shock. Punch

staggering (Fig. 1.13) reduces the initial shock but does not reduce the total shock. Staggering punches implies that different groups of punches come in contact with the blank material at different instants of time by having different punch lengths. If the shear zone length of the blanked part is used as stagger, it allows the next group of punches to contact the blank material prior to the first group snapping through. Hence, the snap-thru energy from the first group of punches is absorbed to drive the next group of punches. This is particularly important in high-speed stamping.

Factors Affecting Punch Life

Punch materials and coatings play an important role in influencing punch life. Punch material and coatings are selected depending on the blank material, forces involved, and the expected tool life.

Table 1.1 Properties of various blanking punch shapes (Fig. 1.11 and 1.12)

Punch and die end shapes	Advantages	Disadvantages
Flat	...	Large punch force generated
Single shear	Lower punch force because shear is local instead of entire tool periphery Reduce reverse tonnage	Unilateral displacement of punch due to asymmetry
Double shear, reverse shear, conical	Lower punch force Unilateral displacement of punch is avoided Can control negative tonnage/snap-thru	Deformed slug Chipping can occur in reverse shear
Conical, chamfer at edge	Used when deformed slug is required; easy for slug stacking	Punch forces may not be reduced because entire periphery of the punch comes in contact with the blank at the same instant
Convex and concave dies	Lower punch forces Slug remains flat, important when it is the useful part	...

Source: Ref 1.3

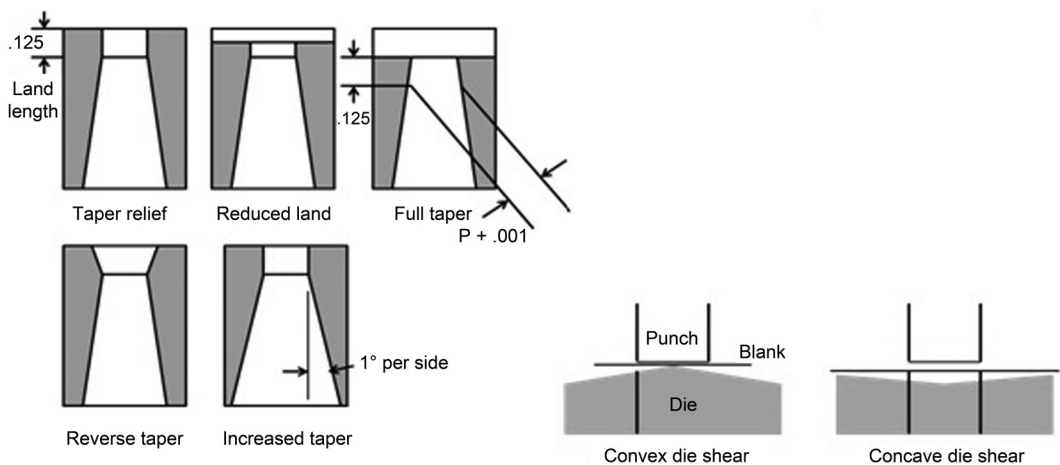


Fig. 1.12 Die geometries and sheared dies used in blanking. Adapted from Ref 1.3, 1.8

Clearance. Punch wear is greatly influenced by the clearance between punch and die. Smaller clearances induce greater punch forces. There is an optimum clearance for which punch forces are the minimum, based on the properties and thickness of the material blanked.

Effect of Punch-Die Clearance in High-Speed Stamping (Ref 1.3)

Traditionally, clearance of approximately 5% material thickness per side is used as punch-die clearance. However, a clearance of approximately 10 to 12% instead of 5% has many advantages. During impact, when the punch first touches the sheet, the part material bulges from under the punch point and compresses into the die. Using greater clearances produces the opposite effect; that is, the part stretches under tensile stress. This is predominant in materials thinner than 0.5 mm (0.02 in.). Hole characteristics differ with different clearances. Lower clearances achieve lower burr. The burr length increases with increase in clearance but starts to decrease and reaches a minimum value at a higher clearance close to the engineering clearance. Using a higher clearance also gives a higher tool life. While using engineered clearance, there should be a means of slug control. Otherwise, there would be a problem of slug at withdrawal of the punch. Some of the solutions for slug pulling are Jektole punches with side vent holes, air blowoff, or different punch point configuration and die designs. Jektole punches have a hole along the length of the punch for air to pass through, which would enable easy slug removal (Fig. 1.14). The slug becomes stuck to the punch because of the vacuum formed between the punch and slug, and Jektole punches prevent that from occurring. Jektole punches may not be effective for heavily applied lubri-

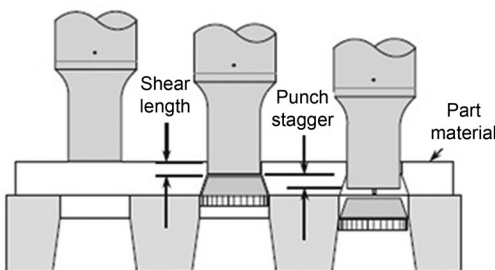


Fig. 1.13 Punch stagger method to reduce instantaneous shock. Adapted from Ref 1.3

cant and lightweight slugs. Overentry of the punch into the die may cause excessive wear and slug pulling.

Punch Misalignment (Ref 1.1)

The punch and die assembly can align well on the bench during die set-up. But when the press is up and running, the deflective forces in the press and tooling can cause the punch to drift and misalign. Punch vibrations also cause misalignments and greater stresses in the tool. These vibrations must be dampened for a longer punch life. An effective guiding system for the press and tooling can help reduce both the problems.

Punch Rigidity during Impact

Long, slender punches are more prone to damage during impact. The shock waves under impact must be transmitted vertically to the punch body instead of laterally within the more fragile points. If the punch is long enough and is not guided well, this may lead to buckling/bending or even breakage.

Punch Point Geometry

Some point geometries experience lower stresses than others, as discussed earlier. The lower the tool stress, the lower the wear and the longer the tool life. This results in better part quality and longer periods before resharpener.

Effect of Lubrication on Punch Wear (Ref 1.9)

Punch wear changes with the amount of lubrication during blanking. Results of a test conducted with varying amounts of lubricants and measuring the punch wear volume are shown in Fig. 1.15. Copper alloy of 0.254 mm (0.010 in.) thickness was blanked with a cylindrical punch of 3.7 μm diameter. Wear volume of the punch was measured by subjecting a blanking tool to selective activation (on a particular area of the punch) by a beam of irradiating particles and calibrating the energy output to wear volume.



Fig. 1.14 Jektole punch with side vent hole. Source: Ref 1.3

Figure 1.15 shows that the wear volume of the punch does not increase much when lubrication is increased by 40% of the standard lubrication condition.

Stripper Plate (Ref 1.3)

Stripper plate plays three important roles in blanking:

- The part is held firmly during the blanking operation by the stripper.
- The punch is guided to the blank through the clearance hole in the stripper.
- The part is stripped off the end of the punch after blanking at withdrawal.

There are three basic kinds of strippers: fixed, urethane, and spring strippers (Fig. 1.16). Fixed strippers do not hold the material during blanking because a clearance is required for material movement. Hence, the part material tends to buckle. Fixed strippers also do not absorb impact and snap-thru, which are important for blanking, depending on the material and thickness of the part.

Urethane strippers are simple to use and are inexpensive. They slide over the end of the

punch with a slight press fit. Urethane strippers deform easily under load and do not form a flat surface for holding the part material. They fatigue through use and become loose on the punches. Spring strippers perform all three functions mentioned previously. Spring strippers are much more effective in holding the part during blanking. They also prevent the part from lifting or hanging up on punch withdrawal. A spring stripper hangs below the ends of the perforating punches. As one of the first components to contact the part material, it holds the part in a fixed position throughout the cycle of the press.

Stripping force depends on the part material and thickness and the punch-die clearance. Strippers with the right design and force can have an effect on part quality. They also help in absorbing shock at snap-thru and reducing the shock felt by the tooling.

Pilots

Pilots, as the name suggests, locate the part in the blanking tool (Fig. 1.17). They have nosed or tapered ends and usually enter an existing hole for guidance and move the stock strip into

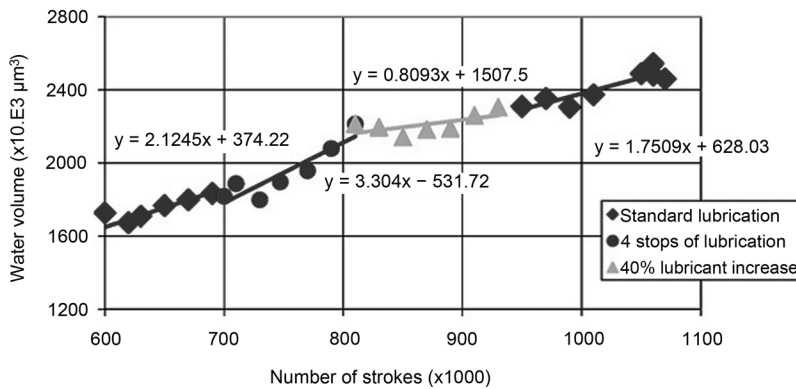


Fig. 1.15 Influence of lubrication on punch wear. Source: Ref 1.9

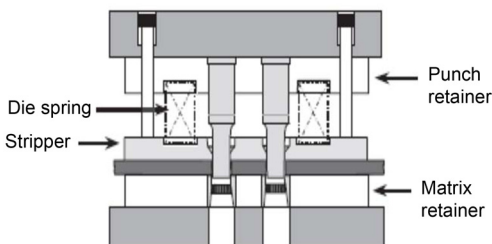


Fig. 1.16 Spring stripper plate. Adapted from Ref 1.3

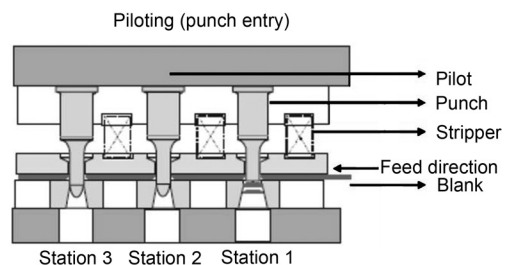


Fig. 1.17 Pilots used to locate the part

a proper location before the stripper makes contact. They do not deform the part material. The pilots first enter the part, followed by the stripper and finally the punch. The pilot working length is longer than the punch length and fully extended stripper. Pilot diameters are generally 0.025 mm (0.001 in.) smaller than the punch diameters.

Gibs

Precision in slide gib columns is important while using high-quality blanking dies and producing parts with high accuracy. The gibs are made of steel, and the bushings are made of bronze. An eight-track roller gib system, with 16 roller elements, is generally used. The rollers run along hardened gib rails, backlash-free (Ref 1.1).

Blanking Presses (Ref 1.1)

Blanking presses are high-speed eccentric or link-drive presses. They feature a high degree of rigidity as well as small bearing and gib clearances. The slide generally has a maximum stroke of 300 to 450 mm (12.0 to 18.0 in.) and is mounted using eight guide gibs. Blanking presses must be equipped for noise reduction. There are a number of factors that influence noise, including the impact speed of the punch on sheet metal and the slide velocity in the work area. A link-drive system generates less noise than an eccentric press because of lower impact speed. Further noise is generated during material breakthrough. Secondary measures such as providing closures are applied to reduce the noise emission.

High performance, high-speed blanking presses run at speeds of 2000 or more strokes per minute (spm), and they are equipped with counter-balance systems. Forces in the press change very rapidly during material breakthrough. These forces can cause dynamic displacement in the dies, which in turn can affect the service life of dies and part quality. Vertical vibrations are caused because of play existing in the force flow of the press and elastic properties of the press. They increase the blanking depth of the punch in the die. This results in punch wear. Eccentric shafts in roller bearings and hydraulic slide adjustment clamps reduce vertical play. A control device is often used in high-speed presses to detect increase in blanking depth and provide automatic correction. The horizontal vi-

brations on the press also exist but are overcome with the use of accurate slide guidance and special configurations on the press body and very good tool guidance. Considerable research is being conducted to investigate the dynamics of high-speed blanking presses and to reduce vibrations due to dynamic forces (Ref 1.10). High-speed presses are used in applications where large numbers of high-precision micro-sized parts must be stamped. The electronics industry has been a major driver for high-speed precision requirement in stamping presses. The materials to be stamped have become thinner, the speed pitches shorter, and the required precision and repeatability higher. Press capacity as low as 200 kN would be sufficient for these applications. The stroke length would be approximately 30 mm (1.0 in.), and a press can run at a speed of approximately 2000 spm or higher. To prevent deflection of the punches due to eccentric loading, the ram guide elements are placed in strip level.

Snap-Thru and Damping Systems

Snap-thru forces, also called reverse tonnage, are evident while blanking thick or very strong materials such as advanced high-strength steels. During blanking, some portion of the material is sheared and the rest is fractured. The fracturing happens much faster than shearing, and there is a significant reverse tonnage at the end of fracture on the press. The press components reach their maximum deflection just before fracture. After fracture, they spring back to their original shape and beyond, unopposed at a very high velocity, and there is a sudden release of energy. The ram is accelerated to a high speed. The drivetrain of the press has clearances around every moving component. When the clearances have reversed, the ram stops suddenly, expending all the energy and sending a shockwave. The press deflects in the opposite direction, as when the forward tonnage was developed, and generates the snap-thru forces. The reverse tonnage or snap-thru forces can be as high as 50% or more of the regular blanking tonnage in the case of very strong materials (Fig. 1.18).

There are different ways to resolve the problem of snap-thru forces. When possible, staggering punches would minimize the reverse load. Punch stagger is explained in an earlier section. Nitrogen cylinder cushions can be built

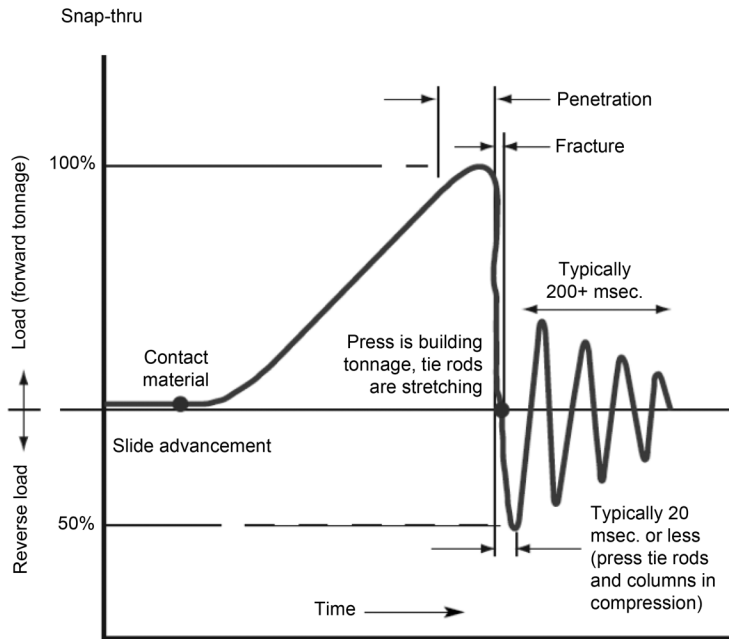


Fig. 1.18 Schematic of forces during snap-thru. Source: Ref 1.11

to absorb the shock energy during snap-thru. However, this would require additional forward tonnage equivalent to the cushion capacity. Hydraulic shock dampers are the most widely used solution for combating snap-thru shocks (Ref 1.12). They do not require additional forward tonnage and do not lower the press capacity. They are large-capacity shock absorbers with a short stroke. Springs hold up cylinders in their raised position, and when the ram moves downward, the cylinder is forced to close and hydraulic oil is forced to escape through small orifices. During fracture, the energy released is used to force more oil to escape through the orifices, thus generating a lot of heat. These are hydraulic dampers. Properly sized and adjusted shock dampers will eliminate or at least lower reverse tonnage to a large extent.

1.5 Tool Materials (Ref 1.13)

Tool material is selected based on the number of parts to be blanked before regrinding the tool. Commonly used tool materials include different tool steels, cemented carbides, steel-bonded carbides, or powder metallurgy tools. Tool coatings are also instrumental in increasing tool life.

Cast irons hardenable to ~60 HRC are used to blank softer materials and at slower speeds. Among tool steels, A2, M2, and D2 are used. A2 is used for producing parts on the order of thousands, while M2 is used for larger quantities on the order of 100,000. High-speed tool steels have been shown to produce smaller burrs than D2 steels. Carbides clearly give a longer tool life than tool steels. Steel-bonded carbides and high-vanadium carbide powder metallurgy tools, such as CPM 10V, are considered for critical applications. Cemented tungsten carbide tooling is considered when long tool life between regrinding or high-volume blanking is required. The composition of cobalt and tungsten is varied to obtain the required toughness and wear resistance.

Coatings and surface treatments include nitriding, hard facing with nickel-base alloys, boronizing, vapor deposition coating, and hard-chromium coating. Tool life at least doubles with coatings and treatments. Chemical vapor deposition (CVD) coating with TiC is well known. Tools coated with TiC also greatly improve the surface roughness of fine-blanked parts. Physical vapor deposition of hard coatings is also useful, with better dimensional control and lower treatment temperature but less resistance to abrasive wear than CVD coatings.

1.6 Ultra-High-Speed Blanking

Ultra-high-speed (UHS) blanking refers to punch velocities greater than 5 m/s (16 ft/s). Ultra-high-speed blanking can provide sheared edge quality almost similar to fine blanking at a lower cost. Typical punching operations undergo three phases: elastic, plastic, and fracture. At very high speeds, the material bypasses the elastic and plastic phases, and rolled edges and burrs do not have the time to be formed.

Adiabatic Phenomenon. During UHS blanking, the punch hits the blank with high velocity that produces an adiabatic band in the punch line of the sheet material. The result is a strong temperature increase in the adiabatic zone during a very short time (100 μ s) (Ref 1.14). During this process, the heat produced has no time to dissipate as quickly as it is being generated. The material softens instantly (known as adiabatic softening), and the produced adiabatic shear bands can split both soft and hard materials. During adiabatic blanking, because the part is strongly accelerated by the punch impact, its own inertia force contributes to the blanking process. The adiabatic blanking process requires high acceleration and deceleration values (10,000 to 100,000 m/s², or 32,800 to 328,000 ft/s²) because of high velocity and small stroke length. The design also must take into account the kinetic energy of the moving parts as well as potential rebounds and vibration.

Advantages and Applications of UHS Blanking. The advantages of UHS blanking over conventional blanking in terms of part quality include:

- Reduced or nonexistent burr height
- Decreased rollover
- Lesser distortion

Further advantages of the technology include:

- Dry, oil-free cutting process
- Reduction of finishing processes

High-speed blanking has been used to manufacture blanks for coins or circular blanks for aluminum packaging applications. Product material applications include aluminum and relatively soft alloyed materials, such as brass or bronze, up to very hard materials, such as nickel or special/stainless steels. The process is now also extended to harder materials, wider strips, higher production rates, and even the manufacture of bimetal rings—all of which require higher press capacities.

Ultra-high-speed blanking presses operating at punch velocities greater than 5 m/s (16 ft/s) are pneumatically, electromagnetically, or even hydraulically driven. Pneumatic presses can operate at velocities up to 20 m/s (65 ft/s), giving excellent edge quality of the blanked part by using compressed air as the pressure source to operate the ram. LMC Inc. offers a series of blanking press systems based on the adiabatic technology, with one of their presses, LMC SIP-15B, running up to 1000 parts per minute (Ref 1.15). AIRAM Press Co. Ltd. (Ref 1.16) also manufactures pneumatically-driven presses that can run at velocities up to 8 m/s (25 ft/s). Although hydraulic presses traditionally were used only for low-speed blanking, Hydropulsor, a Swedish company, produces hydraulic presses for high-velocity adiabatic blanking operations (Ref 1.17). The hydraulically-operated ram can move at speeds of approximately 10 m/s (32 ft/s). Electromagnetic presses are also a recent development in the area of high-velocity forming and are used for adiabatic blanking as well. WinSets Technologies, LLC (Lourdes Systems Inc.) and Netronics offer electromagnetic presses for adiabatic blanking (Ref 1.18).

1.7 Fine Blanking

Fine blanking is also known as precision blanking or fine stamping. The basic purpose of fine blanking is to manufacture parts with a smooth sheared surface. The difference between standard blanking and fine blanking is that the material is blanked only by shear and no fracture after being clamped on all sides. There is no snap-thru force in fine blanking, and consequently, there is less noise and vibration. The tooling costs are higher than that for conventional blanking, and the process cannot be carried out at very high speeds.

Three forces—V-ring force (F_R), counterforce (F_G), and blanking force (F_S)—act on the blank. These forces are generated, as shown in Fig. 1.19, by the V-ring (2), the ejector (4), the punch (3), and the die plate (1). In general, this operation is carried out on triple-action hydraulic presses on which the punch, guide plate, and die movements are controlled individually. Forces in fine blanking have great influence on part quality. During the beginning of the process, F_R and F_G are applied. These forces provide a firm clamp on the material before blanking begins. F_S acts when the press moves down

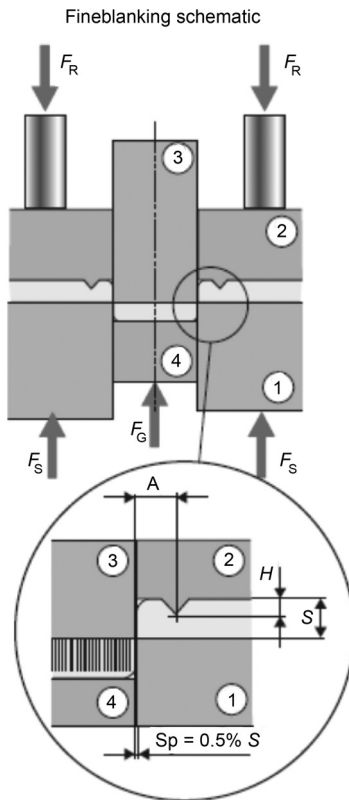


Fig. 1.19 Schematic of fine blanking process. Source: Ref 1.19

and completes the blanking operation (Ref 1.20).

Figure 1.20 illustrates a complete fine blanking cycle. In (A), the tool is open and the blank is pushed into position. At (B), the main piston is activated, and cutting begins at (C). After cutting ends (D), hydraulic pressures are released and the tool opens (E). At stages (F), (G), and (H), the strip moves forward. The part and scrap are removed from the tool. Suggested die clearance in fine blanking is approximately 0.5% of the blank thickness. In fine blanking presses, the slide always works from the bottom upward. The slide stroke is divided into a rapid closing, touching, blanking, and rapid return travel.

Fine-blanked parts are usually produced in a single stroke of the slide, using complete blanking dies or compound dies. Parts manufactured this way have a high degree of flatness. Progressive dies are also used in fine blanking when forming operations such as bending, drawing, and coining are to be done. Compared to complete blanking, the part produced using progres-

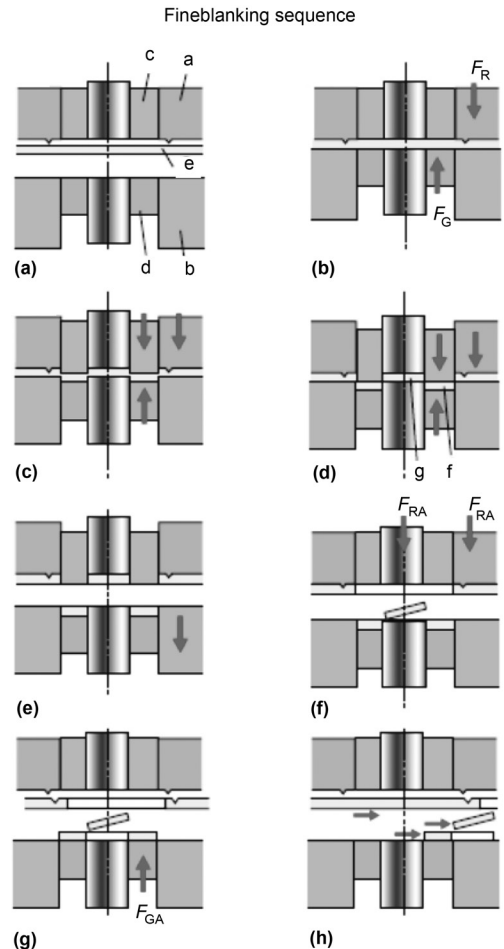


Fig. 1.20 Stages in the fine blanking process. Source: Ref 1.19

sive blanking has larger tolerances and lower flatness.

The dies are subdivided into moving punch and fixed punch systems, as seen in Fig. 1.21. Moving punch systems are used mainly for complete blanking dies and in the production of small- to medium-sized parts. Fixed punch systems are used for the blanking of thick and large parts. Moving punch systems are not as rigid as fixed punch systems. The fixed punch system also can be used for progressive blanking dies, compound progressive dies, and transfer dies.

Because blanking force, V-ring force, and counterforce are required in fine blanking, triple-action mechanical or hydraulic presses are used. The narrow blanking clearances should not change even under dynamic conditions and high stresses. Precision slide gibs, high frame

rigidity, and parallelism of die clamps are of high importance (Ref 1.1).

1.8 Shearing

Shearing is a metal-cutting operation very similar to blanking. Blanking is cutting a closed contour out of the blank, whereas shearing refers to cutting an open contour out of the blank. During shearing, the material goes through the same phases as explained for the blanking process.

Tooling consists of an upper blade, a lower blade, and a holder that holds the stock rigidly during shearing. The upper shear is slanted at an angle between 0.5 and 2.5°, as shown in Fig.

1.22 (left). The lower blade is stationary, while the upper blade moves vertically to shear the part. The upper blade has a rake angle (Fig. 1.22, right) that lowers the instantaneous cutting force:

$$F = \left(\frac{S \times P \times T^2 \times 12}{R} \right) \left(1 - \frac{P}{2} \right) \tag{Eq 1.4}$$

where F is shear force (lb), S is shear strength of the blank (psi), T is thickness (in.) of the material, R is rake (in./ft) of the knife blade (vertical rise of the upper blade per unit length of horizontal measurement), and P is penetration (%) of the knife into the material, which is equivalent to the percentage of shear zone of the blank. Figure 1.23 shows penetration during shearing.

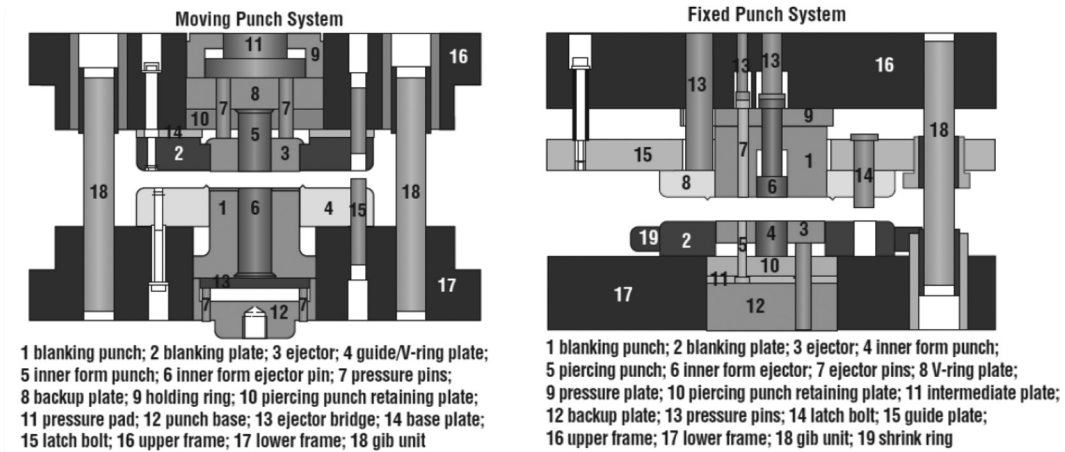


Fig. 1.21 Moving and fixed punch systems in fine blanking. Source: Ref 1.1

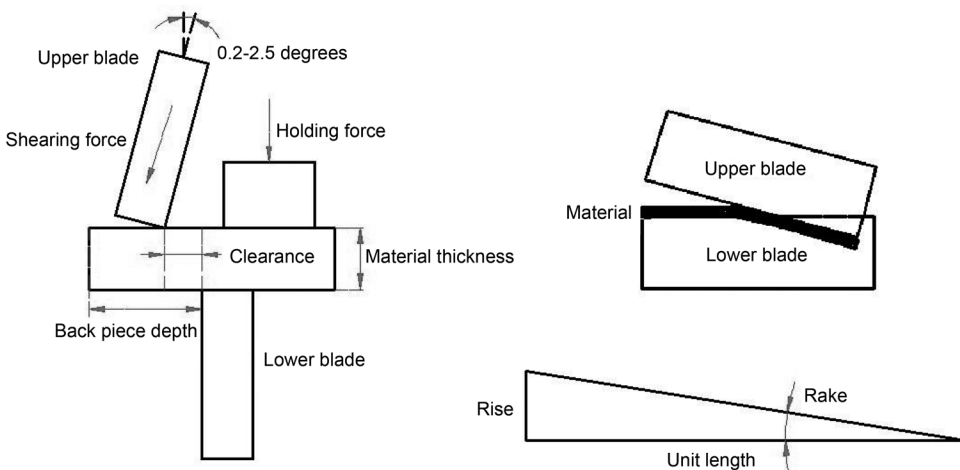


Fig. 1.22 Schematic of shearing

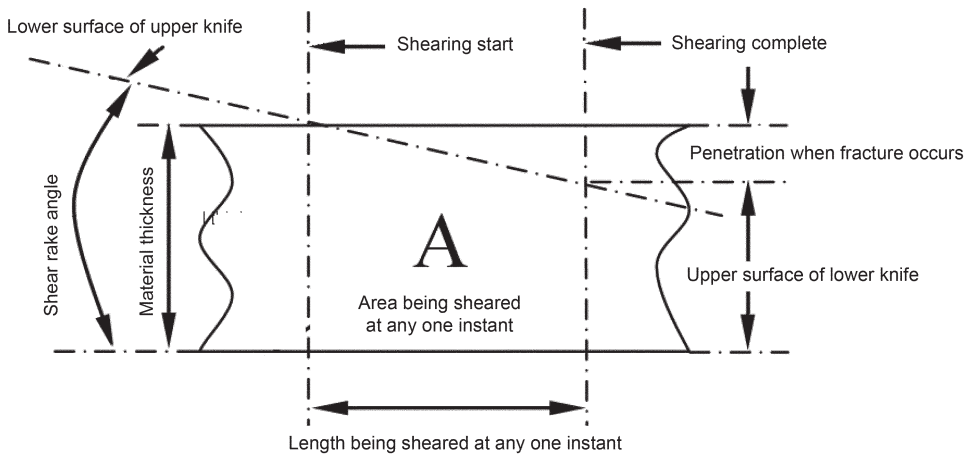


Fig. 1.23 Penetration during shearing. Adapted from Ref 1.21

Generally, values for the percent penetration and shear strength of various materials can be estimated approximately, as suggested in Ref 1.13.

Factors Influencing Part Edge Characteristics and Shearing Force

Material Properties. Ductile materials show more plastic deformation and hence more shear zone than brittle materials. The force required to shear the material also depends on the shear strength of the material and the material thickness, as suggested by Eq 1.4.

Hold-down force ensures that the material remains on the table and does not lift during shearing. There must be a uniform and sufficient pressure exerted along the material to resist the forces during shearing.

Rake is usually expressed as the ratio of the amount of rise to a given linear measurement. This slope of the upper die permits progressive shearing of work metal along the length of the knife. As the rake decreases, a larger surface of the upper die is in contact with the blank, which results in a greater shearing force. A higher rake reduces the required shearing force, allowing a smaller shearing machine to shear the material. However, a higher rake increases the distortion of material (Ref 1.22). Thus, rake is a trade-off between shearing force, distortion, and other factors.

Blade clearance is the distance between upper blade and lower blade, as indicated in Fig. 1.22 (left). The major effects of knife clearance are the appearance of the sheared edge and

squareness of the cut (Ref 1.22). An excessive blade clearance usually will cause an edge that appears like a tear rather than a clean cut, and the cutting surface will not be perpendicular with the sheet metal. Too little blade clearance will result in double shears, characterized by a burnished/sheared area at the top and bottom with a rough area between the burnished areas. Blade clearance depends on the type of material being sheared and is generally expressed as a percentage of material thickness.

Shearing Velocity. As in the case of blanking, shearing velocity has an influence on the quality of the sheared edge. Higher shearing velocity gives a better sheared edge.

Ram incline is the angle of the upper blade, as shown in Fig. 1.22 (left). During shearing, as the ram and upper blade descend at an angle into the material, the blade moves down and away from the lower blade, ensuring that the material falls away without binding between the back gage and the blade. It also can prevent the blades from rubbing against each other. The incline of the ram varies from 0.5 to 2.5°. A 0.5° incline angle provides greater edge squareness than a 2.5° incline angle.

1.9 Finite-Element Simulations

Finite-element (FE) simulations of blanking have been carried out to predict the part edge quality, that is, the ratios of the various zones (similar to the schematic shown in Fig. 1.24). Conditions such as punch and die corner radii, punch shape, and blank material affect the part

edge quality; these can be predicted by simulations. Punch force and stresses on the tool can be predicted by modeling elastic tools.

An example of an FE simulation model for blanking a circular part is shown in Fig. 1.24. Part at fracture and the various zones, such as the rolover, shear, fracture, and burr, are shown in Fig. 1.25. When the tools are modeled as elastic, the stresses on them can be predicted

using FE, as shown in Fig. 1.26. Finite-element predictions have been found to give reasonably accurate estimations (Ref 1.23).

Finite-element analysis has also been used to study the influence of various parameters, such as punch-die clearance, tool wear, stripper pressure, and blanking speed, on part edge quality and tool life. However, FE modeling of blanking alone is not sufficient to predict the part quality and dimensional and geometric accuracy of the parts. There are several other factors that affect the dimensional accuracy of the part, such as the dynamics of the tooling and press, misalignment of tooling due to deflections, and elastic deflections of the tooling and press. These factors are not incorporated in blanking simulations. Ongoing studies in incorporating the effect of these factors in forming simulations show improved accuracy of results during blanking. Finite-element simulations can also be used to estimate the forces and tool stresses in shearing.

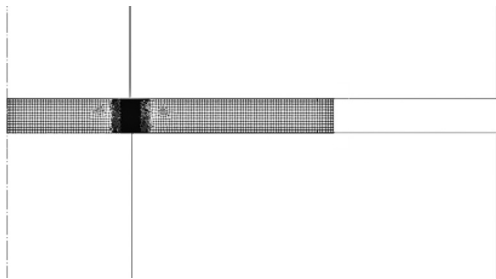


Fig. 1.24 Finite-element model for blanking a circular part

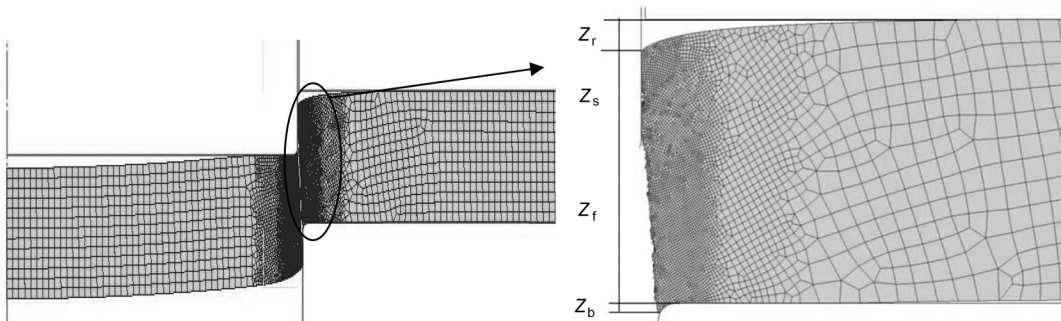


Fig. 1.25 Part at fracture (left) and part edge with different zones indicated (right) (similar to the schematic in Fig. 1.5)

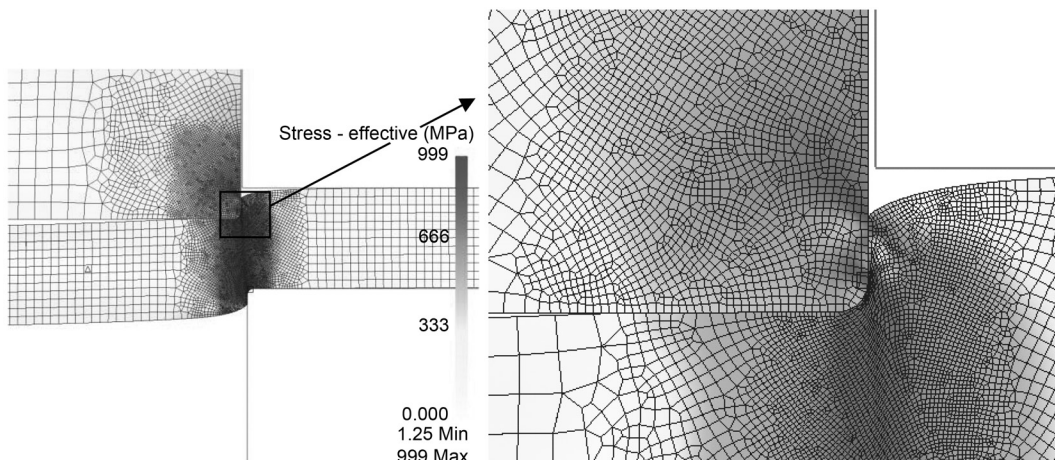


Fig. 1.26 Finite-element model showing elastic stresses in punch

REFERENCES

- 1.1 Schuler, GmbH, *Metal Forming Handbook*, Springer, 1998
- 1.2 K. Lange, *Handbook of Metal Forming*, McGraw-Hill, 1985
- 1.3 Dayton Progress Corporation, <http://www.daytonprogress.com>
- 1.4 R. Wiedenmann, P. Sartkulvanich, and T. Altan, "Finite Element Analysis on the Effect of Sheared Edge Quality in Blanking upon Hole Expansion of Advanced High Strength Steel," IDDRG 2009 International Conference, June 2009
- 1.5 H. Makich, L. Carpentier, G. Monteil, X. Roizard, J. Chambert, and P. Picart, Metrology of the Burr and the Punch Wear in Blanking Process of Copper Alloy Thin Sheet, *Proceedings of the 12th International Conference on Metal Forming*, 2008, p 1–2
- 1.6 C. Husson, J.P.M. Correia, L. Daridon, and S. Ahzi, Finite Elements Simulations of Thin Copper Sheets Blanking: Study of Blanking Parameters on Sheared Edge Quality, *J. Mater. Process. Technol.*, Vol 199 (No. 1–3), 2008, p 74–83
- 1.7 Böhler-Uddeholm Corporation, <http://www.uddeholm.com>
- 1.8 Y. Seo, "Improving Blank Edge Conditions," TheFabricator.com, Fabricators & Manufacturers Association, Intl., July 24, 2003, <http://www.thefabricator.com/article/toolanddie/improving-blank-edge-conditions>
- 1.9 G. Monteil, F. Greban, and X. Roizard, In Situ Punch Wear Measurement in a Blanking Tool, by Means of Thin Layer Activation, *Wear*, Vol 265, 2008, p 626–633
- 1.10 M. Hirsch, P. Demmel, R. Golle, and H. Hoffmann, Light Metal in High Speed Stamping Tools, *Key Eng. Mater.*, Vol 473, 2011, p 259–266
- 1.11 R. Miles, Combating Snapthrough, *Met. Form. Mag.*, March 2004
- 1.12 R. Wonsetler and M. White, "The Use of Hydraulic Shock Dampers to Arrest the Reverse Load of Blanking in Presses," Crane Production Systems Corp., 2002, www.craneprosys.com
- 1.13 Selection of Materials for Shearing, Blanking, and Piercing Tools, *Metalworking: Sheet Forming*, Vol 14B, *ASM Handbook*, ASM International, 2006, p 57–68
- 1.14 L. Lazzarotto and R. Michon, "Adiabatic Blanking of Metal Sheets: Technological Positioning and Industrial Developments for Production," Fifth Car Body Colloquium (Chemnitz, Germany), 2008
- 1.15 "HVAI Blanking: Adiabatic Blanking Capabilities and Benefits," LMC, Inc., <http://www.lmcpress.com/adiabatic/blanking.php>
- 1.16 AIRAM Press Co. Ltd., <http://www.airam.com>
- 1.17 Hydropulsor, <http://www.hydropulsor.com>
- 1.18 WinSet Technologies, LLC, <http://www.winset.net>
- 1.19 F. Birzer, *Forming and Blanking*, 2nd ed., Feintool, 1999
- 1.20 T. Altan, Blanking Developments—Part 1: Fine Blanking Process and Tool Design, *Stamp. J.*, July 2007
- 1.21 Cincinnati Incorporated, <http://www.e-ci.com>
- 1.22 S.L. Semiatin, Ed., *Metalworking: Sheet Forming*, Vol 14B, *ASM Handbook*, ASM International, 2006, p 39–45
- 1.23 P. Sartkulvanich, B. Kroenauer, R. Golle, A. Konieczny, and T. Altan, Finite Element Analysis of the Effect of Blanked Edge Quality upon Stretch Flanging of AHSS, *CIRP Ann., Manuf. Technol.*, Vol 59 (No. 1), 2010, p 279–282

SELECTED REFERENCE

- E. Taupin, J. Breitling, W. Wei-Tsu, and T. Altan, Material Fracture and Burr Formation in Blanking Results of FEM Simulations and Comparison with Experiments, *J. Mater. Process. Technol.*, Vol 59 (No. 1–2), 1996, p 68–78

CHAPTER 2

Bending, Flanging, and Hemming

H. Kim, Edison Welding Institute
S. Chatti, Technische Universität Dortmund, Germany
N. Kardes, The Ohio State University

BENDING, FLANGING, AND HEMMING are widely used in sheet metal fabrication where the parts require simple or complex bent profiles (Fig. 2.1). Bending is usually defined as the forming of sheet or plate to produce angled parts or sheet profiles.

After bending, elastic springback occurs and residual stresses may result. If the bend radius is too small, excessive tensile strain on the outside surface may cause fracture. A sheet is bent by an imposed moment, by stretching over a cylindrical form, or by a combination of both moment and tension. In practice, bending angles up to 90° can be obtained easily. For larger bend angles, additional tooling including a cam mechanism may be required. There are different types of bending operations, such as air bending, wiping die bending, U-die bending, V-die bending, and rotary bending. For industrial applications, the following predictions are crucial during process design (Ref 2.1):

- Bendability assessment (determining minimum bending radius without fracture)
- Prediction of bending forces
- Control of the dimensions, shape, and quality of the bent part (dimensional tolerances, springback, residual stresses, wrinkling, and splitting)

2.1 Mechanics of Bending

To understand the mechanics and variables of bending operations, it is useful to consider bending as a system that includes the following:

- Sheet material (thickness, properties, and surface finish)
- Equipment/machine used (control and capacity)
- Tools (material and coating)
- Tool-sheet interface (friction)
- Deformation work zone (strains, stresses, and forces)
- Product (dimensions and quality)
- Environment (handling and safety)

The common terminology used in practice for air bending is shown in Fig. 2.2.

The sheet metal can be bent without failure to a very small radius, depending on the ductility of the material, sheet thickness, bending angle, and loading conditions. Bending severity is usually expressed as the R/t ratio, where R is the bending radius (also referred as R_b) and t is the original sheet thickness. For example, the cold-rolled draw-quality low-carbon steel sheets (e.g., aluminum-killed drawing-quality steel) can be

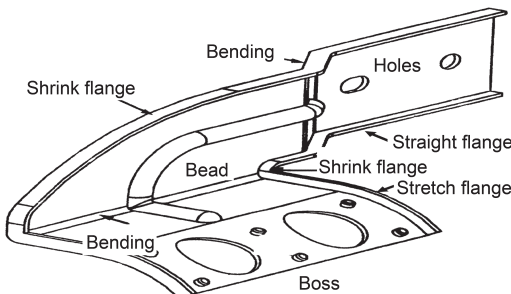


Fig. 2.1 Sample part made by various sheet bending operations. Courtesy of Eaton Corp.

bent to an R/t ratio of nearly zero as in automotive hemming applications, whereas the less formable aluminum and advanced high-strength steels (AHSS) will be subject to failure either by fracture or necking at relatively low R/t ratios. Estimation of the bending force is important in selecting the press capacity and designing the tooling. More important than load predictions is the dimensional quality of the part after bending. Springback and cracking are common problems in terms of quality. All bent parts exhibit springback after unloading, and the amount of springback depends on die geometry, friction, bending angle, punch radius, and material properties. In the case of air bending, for example, the prediction of punch stroke becomes crucial for compensation of springback.

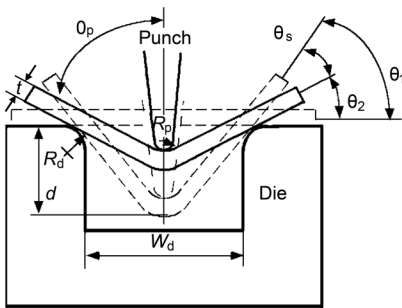
The variables used in the analysis of bending mechanics are shown in Fig. 2.3, where M is the constant bending moment, t is the sheet thickness, θ is the bending angle, R_i is the inner bending radius, w is the width of the sheet, R_o is the outer bending radius, R_m is the mean bend-

ing radius ($R_m = R_i + t/2$), R_n is the neutral radius (where the elongation is zero), and R is the radius of an arbitrary layer, used in analysis.

During a bending operation, the outer fibers of the sheet metal are stretched while the inner fibers are compressed. Furthermore, during bending additional deformation mechanisms, such as tension and shear, may occur. Simplified bending theory (or pure bending with a constant bending moment, M) can be used as a reasonable initial approximation to predict strains, stresses, and springback. Primary mechanics and assumptions in bending theory are introduced in the following sections (Ref 2.1).

Prediction of Strain. The cross section of a specimen under pure bending moment, M , is shown in Fig. 2.4. The bending strain on a fiber at y distance away from the neutral axis in this loading condition can be expressed approximately as:

$$\epsilon_b = \ln\left(\frac{l}{l_o}\right) = \ln\left(\frac{R}{R_n}\right) \tag{Eq 2.1}$$



- R_p = punch radius
- R_d = die radius
- W_d = die opening
- θ_s = springback angle = $2\theta_1 - 2\theta_2$
- θ_p = half bending angle (after springback)
- t = sheet thickness
- d = punch stroke
- θ_1 = half angle (under load)
- θ_2 = half angle (unloaded)

Fig. 2.2 Schematic of air bending and the commonly used terminology. Source: Ref 2.1

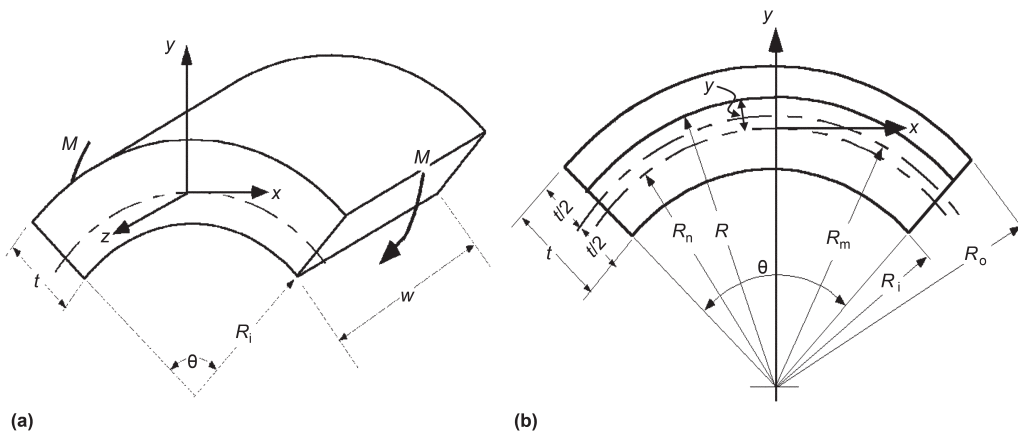


Fig. 2.3 Geometric variables used in the analysis of sheet bending. (a) Overall dimensions. (b) Dimensions used in bending analysis

where ϵ_b is the bending strain, l is the length of the fiber at y distance away from the neutral axis, with length l_0 , R is the radius of that fiber, and R_n is the radius of the neutral axis where there is no change in length of the fiber. If R is expressed in terms of y , the bending strain becomes:

$$\epsilon_b = \ln\left(1 \pm \frac{y}{R_n}\right) \tag{Eq 2.2}$$

For a large bending ratio (e.g., R/t), R_n is approximately equal to R_m :

$$R_n \approx R_m = R_i + \frac{t}{2} \tag{Eq 2.3}$$

Using Taylor's expansion for Eq 2.2, the higher-order terms can be neglected:

$$\epsilon_b = \frac{y}{R_m} - \frac{1}{2}\left(\frac{y}{R_m}\right)^2 + \frac{1}{3}\left(\frac{y}{R_m}\right)^3 - \dots = \frac{y}{R_n}\left[1 - \frac{y}{2R_m}\right] \tag{Eq 2.4}$$

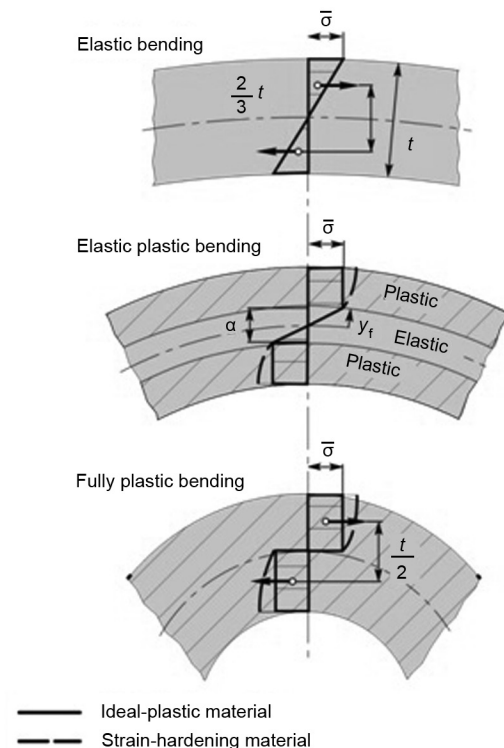


Fig. 2.4 Stress-strain distributions in elementary bending theory

For a large bending radius, true strain is very close to engineering strain, and it becomes linearly proportional to the radial distance y . Therefore, Eq 2.4 can be simplified to Eq 2.5:

$$\epsilon_b \approx e_b = \frac{y}{R_m} \tag{Eq 2.5}$$

Thus, the maximum strain at the outer fiber can be expressed as in Eq 2.6:

$$\epsilon_b^{\max} = \ln\left(1 \pm \frac{t/2}{R_m}\right) = \ln\left(1 \pm \frac{t}{2R_i + t}\right) \text{ or } \epsilon_b^{\max} \approx e_b^{\max} = \pm \frac{t}{2R_i + t} \tag{Eq 2.6}$$

State of Stress. The state of stress is determined by the ratio of the sheet width to thickness. In a part with a short width compared to its thickness (such as a bar), no transverse stresses are developed during bending ($\sigma_2 = \sigma_3 = 0$), and thus, uniaxial deformation conditions exist. Hence, the transverse and longitudinal strains are related ($\epsilon_2 = -1/2\epsilon_1$), which causes an increase in width in the compression area and a decrease in width in the tension area.

If the sheet is sufficiently wide, then the plane-stress condition occurs only at the edges, and a transverse curvature of these regions takes place. At the center of wide parts or at other locations far from the free edges, the transverse curvature is zero, and thus, $\epsilon_2 = 0$. This is called the plane-strain condition.

To express the state of stress and anisotropy, Hill (Ref 2.2) proposed the use of an index F to define the material flow (Table 2.1). Several yield criteria can be employed, depending on the availability of material properties. According to the distortion energy criterion originally

Table 2.1 List of yield indices (F) for some material and stress/strain-state configurations

F (Hill's yield index)	Anisotropy and stress/strain state
1	Isotropic and uniaxial stress
$2/\sqrt{3}$	Isotropic and plane strain
$\frac{1+\bar{R}}{\sqrt{1+2\bar{R}}}$	Normally anisotropic and plane strain (Ref 2.2)
$\frac{[2(1+\bar{R})]^{1/M} - [1+(1+2\bar{R})^{1/(1-M)}]^{(M-1)/M}}{2}$	Normally anisotropic and plane strain (Ref 2.3)

Note: \bar{R} is the normal anisotropy, and M is an index describing the shape of the yield loci. $\bar{R} = 1.0$, and $M = 2.0$ for the isotropic material.

proposed by von Mises, yield can be described as follows:

$$\bar{\varepsilon} = F\varepsilon_1 \tag{Eq 2.7}$$

$$\sigma_1 = F\bar{\sigma} \tag{Eq 2.8}$$

where $\bar{\sigma}$ and $\bar{\varepsilon} = F\varepsilon$ are the flow stress and strain, respectively. For isotropic material and plane-strain conditions:

$$\bar{\varepsilon} = \frac{2}{\sqrt{3}}\varepsilon_1 \text{ and } \sigma_1 = \frac{2}{\sqrt{3}}\bar{\sigma} \tag{Eq 2.9}$$

Prediction of Stress. Figure 2.4 shows the stress distribution in the elementary bending theory. Under plane-strain condition, the stress component causing elastic deformation, $\sigma_{b,e}$, is found using Hooke’s law:

$$\sigma_{b,e} = \frac{E}{(1-\nu^2)}\varepsilon_b = \pm \frac{E}{(1-\nu^2)}\frac{y}{R_n} \quad 0 < \varepsilon_b \leq \varepsilon_{e,o} \tag{Eq 2.10}$$

where E is Young’s modulus, ν is Poisson’s ratio, and $\varepsilon_{e,o}$ is the elastic limit.

The plastic stress component depends on the complexity of the material-hardening model. For rigid perfectly plastic material (Fig. 2.5a), using Hill’s yield index F , the bending (tangential) stress is:

$$\sigma_{b,p} = F\bar{\sigma} \text{ for } \varepsilon_{e,o} < \varepsilon_b \tag{Eq 2.11}$$

When the generalized power law (Swift’s law, Fig. 2.5c) is used, the bending stress becomes:

$$\sigma_{b,p} = KF^{n+1} \left[\frac{\varepsilon_o - \varepsilon_{e,o}}{F} + \varepsilon_b \right]^n = KF^{n+1} \left[\frac{\varepsilon_o - \varepsilon_{e,o}}{F} + \ln \left(1 \pm \frac{y}{R_n} \right) \right]^n \text{ for } \varepsilon_{e,o} < \varepsilon_b \tag{Eq 2.12}$$

Bending Moment. Internal bending moment is the integration of bending stress over sheet thickness. In the elementary bending theory, for rigid plastic material, thinning of the material is zero. Then, bending moment per unit width is calculated as (Ref 2.1):

$$M = M_p = \int_0^t \sigma_x y dy = \int_{-t/2}^{t/2} F\bar{\sigma} y dy = F\bar{\sigma} \frac{t^2}{4} \tag{Eq 2.13}$$

Springback is defined as the elastic recovery of the material after unloading of the tools. It results in a dimensional change in the bent part; after springback, the bend radius and angle become larger (Fig. 2.6).

The springback angle ($\Delta\theta = 2(\theta_1 - \theta_2)$) depends mainly on material and process variables. It tends to increase with increasing material yield strength, strength coefficient, strain-hardening coefficient, minimum bending ratio (R/t), and anisotropy of the material. However, springback tends to decrease with increasing Young’s modulus. In air bending, a longer flange arm and a larger bend angle are the main causes of increased springback. On the other hand, in wiping die bending, springback is known to increase with a reduced pad force, a larger punch-die clearance, and a longer flange arm (Table 2.2).

Under plane-strain condition, springback angle is expressed as:

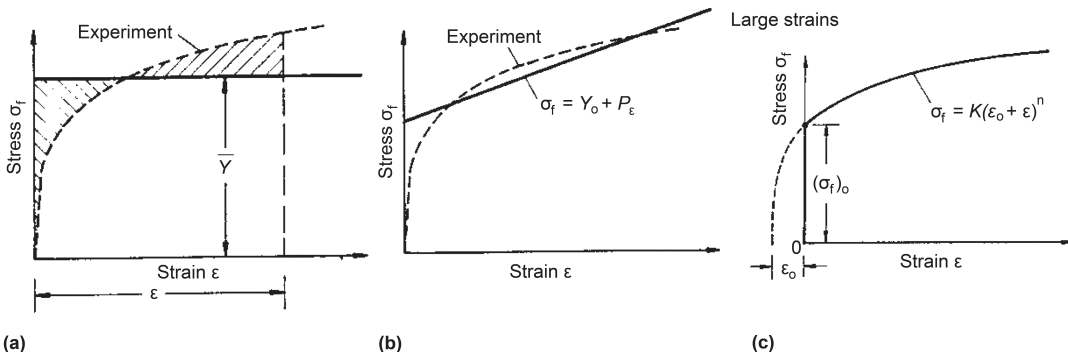


Fig. 2.5 Different material-hardening models used in bending approximations. (a) Rigid perfectly plastic. (b) Rigid linear strain-hardening plastic. (c) Power law according to Swift. Source: Ref 2.4

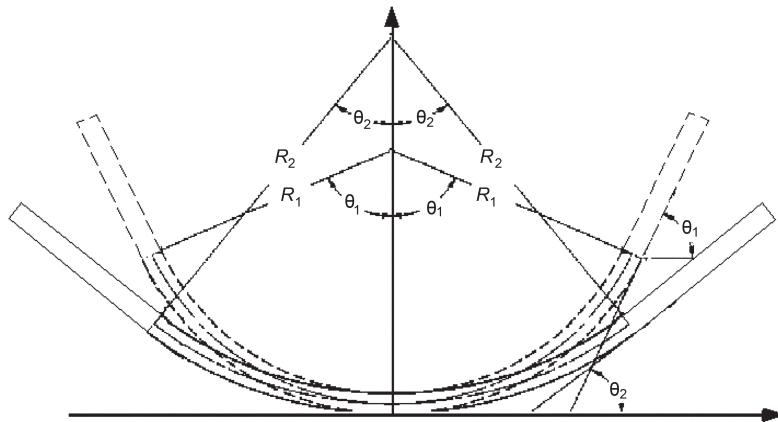


Fig. 2.6 Illustration of springback in air bending. Source: Ref 2.5

Table 2.2 Trends in springback as a function of major material and geometric variables

Springback angle, $\Delta\theta$	Parameter	
	Bending angle, θ	↗
	R_1/t	↗
	E	↘
	σ_y or Y	↗
	K	↗
	n	↘
	Anisotropy	↗

$$\Delta\theta = S \left(\frac{1}{R_1} - \frac{1}{R_2} \right) \tag{Eq 2.14}$$

where $\Delta\theta$ is springback angle, S is the arc length of the inner curve, R_1 is the inner bend radius under load, and R_2 is the inner bend radius after unloading (Fig. 2.6). In this equation, $\frac{1}{R_1} - \frac{1}{R_2}$ can be calculated as:

$$\frac{1}{R_1} - \frac{1}{R_2} = \frac{M(1-\nu^2)}{IE} \tag{Eq 2.15}$$

where M is the (internal) bending moment, ν is the Poisson's ratio, I is the moment of inertia, and E is the Young's (elastic) modulus (Ref 2.6).

Another representation of springback is in the form of a ratio known as the springback ratio. For relatively small bending angles and under pure bending, the springback ratio, K , is defined as:

$$K = \frac{\theta'}{\theta} = \frac{R_1 + t/2}{R_2 + t/2} \quad (K \leq 1.0) \tag{Eq 2.16}$$

An example graph illustrating the springback ratio (K) for various materials is shown in Fig. 2.7 (Ref 2.7).

Factors Affecting Springback in Bending.

For a given bending process, the material properties (flow stress, Young's modulus, and strain-hardening coefficient) determine the magnitude of the springback, as illustrated in Fig. 2.8. Furthermore, the springback amount depends on the process data such as total strain, sheet metal thickness, bending radius, and bending angle.

When keeping all other parameters of the stress-strain curve constant, an increase in total strain, ϵ_t , leads to a bigger springback because the elastic part of the strain, ϵ_e , increases (Fig. 2.8a). Over the total strain, the influence of the bending radius on the springback magnitude can be explained. Sheet metals with small bending radius and correspondingly large total strain spring back much less than sheet metals with large bending radius or smaller strain, respectively. Under smaller total strains, thinner sheet metals spring back more than thicker ones. The material properties have a wide influence on the springback amount. A higher flow stress results, at the same total strain, in larger elastic strains and therefore higher springback magnitude (Fig. 2.8b). Furthermore, the springback depends on the Young's modulus. At the same total strain, ϵ_t , a bigger Young's modulus, E (higher inclination), leads to a smaller elastic part, ϵ_e , of the total strain and therefore to a weaker springback (Fig. 2.8c). For materials with the same flow stress, an increase of the strain-hardening coefficient, n , increases the elastic strain, ϵ_e , and, accordingly, the amount of springback (Fig.

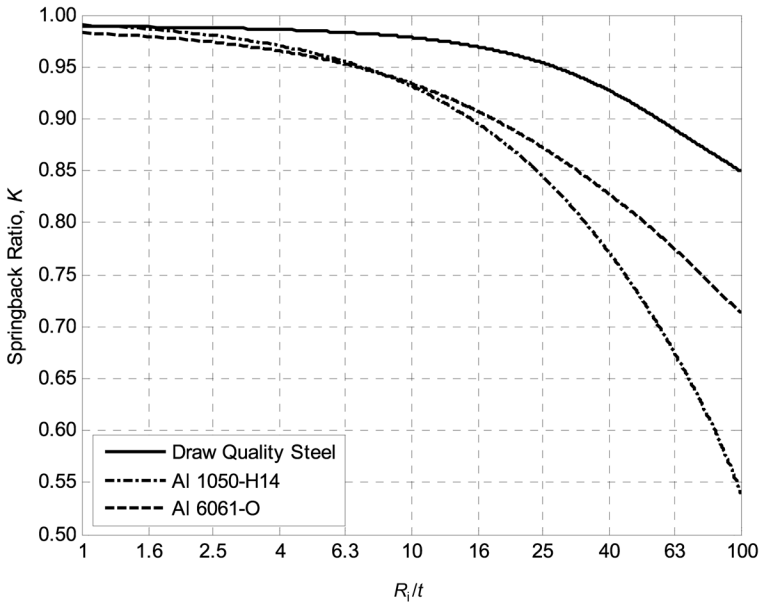


Fig. 2.7 Springback ratio (K) versus minimum bending ratio (R_1/t) for various materials. Source: Ref 2.7

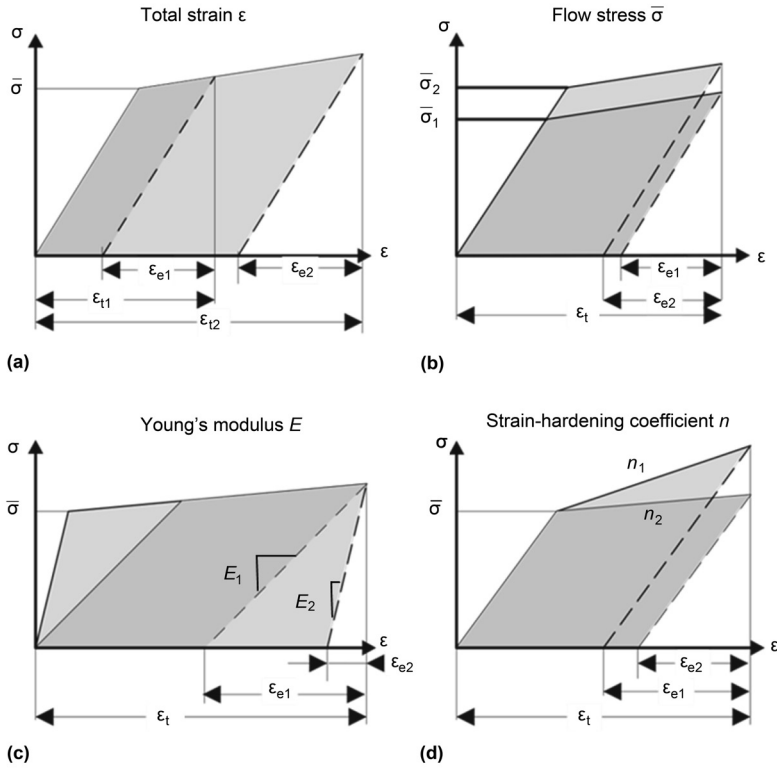


Fig. 2.8 Schematic illustrating the influences of various properties on elastic recovery in forming materials

2.8d). Hence, when computing the elastic springback, the material model plays a decisive role, because different models with different strain-hardening behaviors are available.

The difference in springback for various steel grades is illustrated in Fig. 2.9 in forming a U-channel. It is seen that the springback increases with increasing ultimate tensile strength of the sheet material (Ref 2.8).

In wipe bending, for example, the springback factor, K (Eq 2.16), decreases with increasing die-radius-to-sheet-thickness ratio (R/t), as shown in Fig. 2.10 (Ref 2.9).

In wipe bending, the ratio of die clearance between die and punch, C , versus sheet thickness, t , also affects springback, as shown in Fig. 2.11 (Ref 2.9) for various die radii.

Bending Under Tension. In most bending operations, the deformation is achieved by both bending and tension. Initially, when the bending moment is applied without any tension, the stress distribution will be as shown in Fig. 2.12(a). When tension is applied, the stress at the outer fiber will increase, as shown in Fig. 2.12(b). At some point, the stress will reach the yield stress, S , as shown in Fig. 2.12(c). With further tension, a zone of plastic deformation increases from the outside (Fig. 2.12d), until the whole section is plastic (Fig. 2.12e).

When the outer fiber stress reaches the yield stress, the tension stress, T , has the value:

$$T = St - E' \left(\frac{1}{\rho_0} \right) \frac{t^2}{2} = T_y \left(1 - \frac{\rho_c}{\rho_0} \right) \quad (\text{Eq 2.17})$$

where t is the thickness of the sheet metal, E' is Young's modulus in plane strain, $T_y (= St)$ is the tension required to yield the sheet in the absence of any moment, and ρ_0 is the radius of curvature of the former. The limiting elastic radius of curvature, ρ_e , is calculated as:

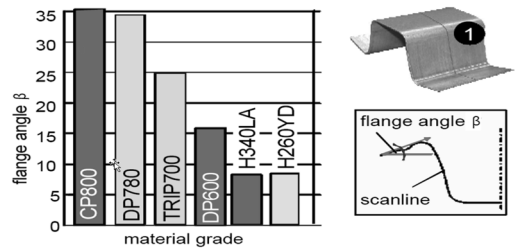


Fig. 2.9 Comparison of springback in U-channel part from high-strength and advanced high-strength steels. Source: Ref 2.8

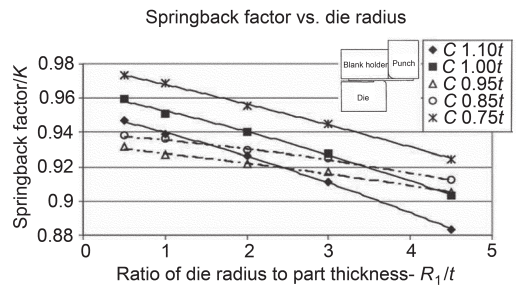


Fig. 2.10 Springback factor (K , Eq 2.16) versus ratio of die radius to thickness (R/t) for aluminum. Source: Ref 2.9

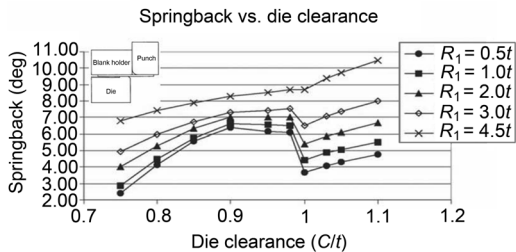


Fig. 2.11 Springback with change of materials and die clearance versus sheet thickness ratio (C/t) for an aluminum alloy for different die radii in wipe bending. Source: Ref 2.9

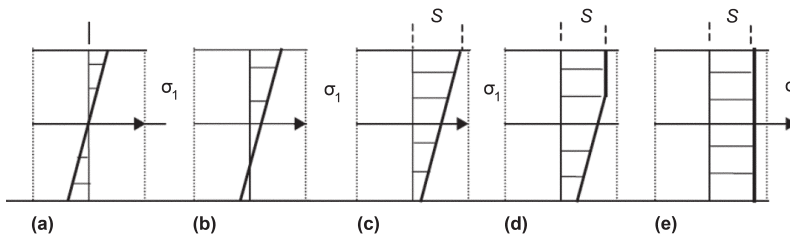


Fig. 2.12 Development of stress distribution as tension in the sheet increases. Source: Ref 2.10

$$\left(\frac{1}{\rho_c}\right) = \frac{2S}{E't} \tag{Eq 2.18}$$

The initial moment, when $T = 0$, is:

$$M = \frac{E't^3}{12} \left(\frac{1}{\rho_0}\right) = M_0 \tag{Eq 2.19}$$

When the tension exceeds the value obtained from Eq 2.17, the moment will start to decrease. At some point, the elastic/plastic interface is at a distance $mt/2$ from the middle surface, as shown in Fig. 2.13, where $-1 < m < 1$. The moment will then reduce to:

$$M = \frac{E't^3}{12\rho_0} \left(\frac{2+3m-m^3}{4}\right) = M_0 \left(\frac{2+3m-m^3}{4}\right) \tag{Eq 2.20}$$

The tension at this moment reduces to:

$$T = T_y \left[1 - \frac{\rho_c}{4\rho_0} (m+1)^2\right] \tag{Eq 2.21}$$

Finite-Element Analysis of Bending and Springback. Although the analytical approach to sheet metal bending and springback gives quick predictions, it involves some large assumptions, which, in return, reduce the resulting accuracy. For instance, the inner radius of the sheet is usually assumed to be known and constant over the bending area, but in practice, it varies over the bend, and the sheet may not have full contact with the tool. The finite-element method can give results that are much more accurate if used carefully in cases in which sheet, tool geometry, and loading conditions are difficult to model analytically. However, selec-

tion of the appropriate element and solver type and definition of the tool model and boundary conditions are crucial to obtaining an accurate solution in a reasonable amount of computation time.

All commercial codes are capable of simulating bending operations. The selection of element types (shell or brick) affects the accuracy of the results. Brick-type elements model the variations of stress and strain in the thickness direction more accurately, so they are more appropriate to use with small bending radii. Depending on bending geometry, a choice between two-dimensional (2-D) and three-dimensional (3-D) simulations must be made. In most practical bending operations, however, when no flanging around a curved line is involved, 2-D simulations give reasonably accurate results. Furthermore, it is very important to input correct material data, such as hardening model, hardening law, and E -modulus, into finite-element codes in order to obtain accurate results. Studies conducted on AHSS steels indicated that E -modulus decreases with strain (Ref 2.11).

At the Engineering Research Center for Net Shape Manufacturing (ERC/NSM) of The Ohio State University, finite-element analysis (FEA) was conducted to predict springback for V-die bending tests performed at Cincinnati Incorporated. A schematic of V-die bending is given in Fig. 2.14. The testing parameters, simulation parameters, and flow stress data that were used for the tests and FEAs are given in Tables 2.3 and 2.4 and Fig. 2.15. The E -modulus was assumed to be constant. The flow stress data were obtained by a viscous pressure bulge (balanced biaxial) test. The springback angle is the difference between the inner bending angles under load and after unloading.

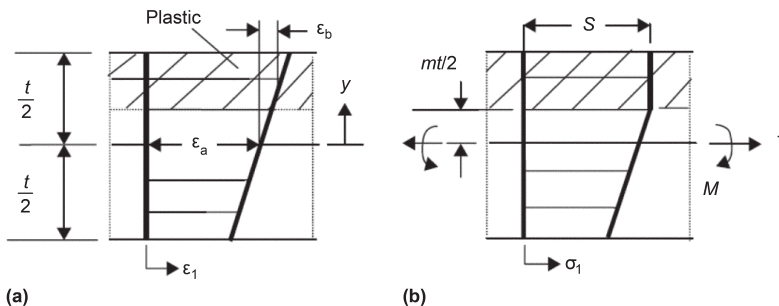


Fig. 2.13 Distribution of (a) strain and (b) stress in an elastic, perfectly plastic sheet bent to a gentle curvature and stretched. Source: Ref 2.10

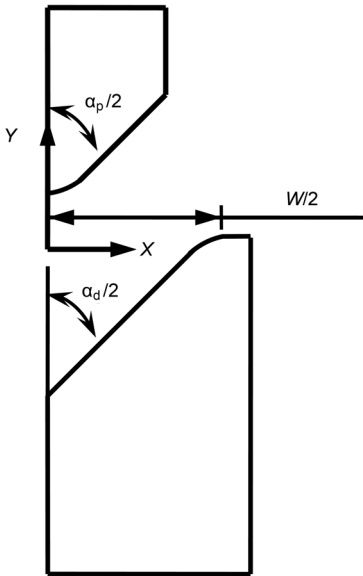


Fig. 2.14 Tool geometry of V-die bending used in studies conducted at the Engineering Research Center for Net Shape Manufacturing (in cooperation with Cincinnati Inc.)

The 2-D and 3-D FEAs of V-die bending were done using DEFORM to investigate the differences between 2-D and 3-D simulation results. The 3-D FEA of the V-die bending process was also done using PAMSTAMP to investigate the effect of element type (brick versus shell). Comparison of springback angles obtained by DEFORM, PAMSTAMP, and experiments are given in Fig. 2.16. Finite-element simulations performed with DEFORM-2D and PAMSTAMP had a better agreement with experimental results than those performed with DEFORM-3D.

2.2 Air Bending

Air bending, also called three-point bending or free bending, is the simplest bending process commonly used in fabrication industries for automotive and aerospace structural parts. It has an advantage over other bending processes in that there is no need to change the dies to obtain different bend angles (Fig. 2.2, 2.17). For a

Table 2.3 Test conditions for V-die bending tests (geometry in Fig. 2.14)

Testing parameters	Description
Sheet material	DP780
Sheet thickness, width and length, mm (in.)	1 × 60 × 210 (0.04 × 2.4 × 8.3)
Sheet orientation	Rolling and transverse direction
V-die angle (α_d) and punch tip angle (α_p), degrees	75
Punch tip radius (R_p), mm (in.)	4.75 (0.20)
V-die opening (W), mm (in.)	38.1 (1.5)
Approximate inner bending angles, degrees	170, 160, 150, 140, 120, 90
Number of samples/condition	3
Dwell time in press brake	10 s max

Table 2.4 Finite-element simulation parameters (geometry in Fig. 2.14)

Simulation parameters	Description
Sheet material	DP780 (1 mm)
Material type	Sheet: elastic-plastic V-die and punch: rigid
V-die angle (α_d), degrees	75
V-die opening (W), mm (in.)	38.1 (1.5)
Punch tip angle (α_p), degrees	75
Punch tip radius (R_p), mm (in.)	4.75 (0.20)
Maximum punch stroke, mm (in.)	15 (0.60)
Coefficient of friction (μ)	0.12
Maximum E -modulus (constant), GPa (10^3 ksi)	207 (30)

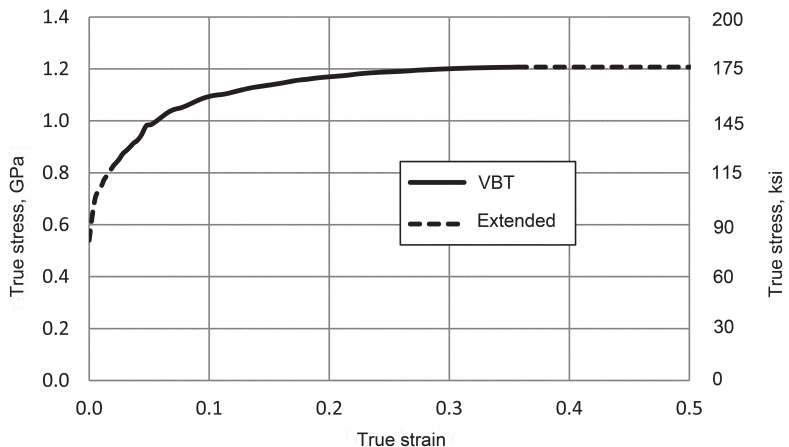


Fig. 2.15 Flow curve of DP780 material, obtained from a viscous pressure bulge test (VBT). Source: Ref 2.12

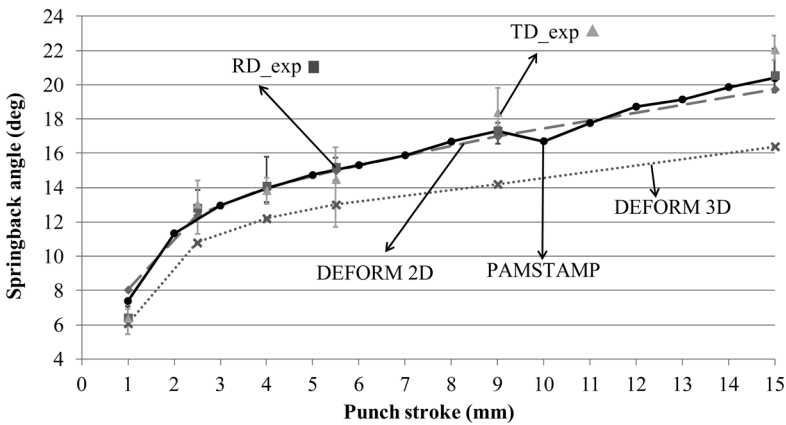


Fig. 2.16 Comparison of springback angles obtained by DEFORM-2D, DEFORM-3D, PAMSTAMP, and experiments (constant *E*-modulus). Source: Ref 2.12

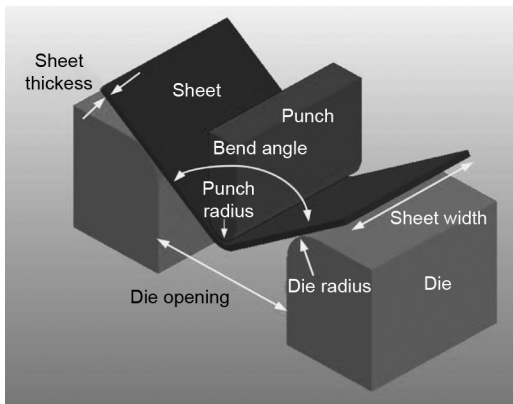


Fig. 2.17 Schematic of air bending

given die opening and blank, the bend angle is determined by the punch stroke (Ref 2.13).

An important challenge in air bending is to maintain geometric tolerances of the finished part. Thus, assembly or subassembly operations can be carried out without additional adjustments or corrections of the part geometry. This problem is related to springback and elongation/compression of the sheet as it undergoes deformation. Springback refers to the elastic recovery of the nonuniformly distributed stresses in a deformed part after the forming load is removed.

With the increasing use of high-strength materials, prediction and correction of springback becomes critical, particularly when tight toler-

ances must be met. Ultimately, this springback must be predicted in advance so that the punch stroke can be controlled to obtain the desired bending angle after springback and thus maintain the required tolerances in the finished part.

Another challenge in maintaining geometric tolerances is the prediction of bend allowance (or bend deduction) (Fig. 2.18). Bend allowance is a parameter that compensates for the elongation of the sheet in bending.

Bend allowance or bend deduction is necessary to determine the original length of the blank. One or the other value is used, depending on how the length of the bent sheet is measured (Fig. 2.18). It is easy to calculate the lengths of the bent sheet when bend deduction is considered.

A simple empirical equation was proposed by Sachs (Ref 2.14) to calculate the bend allowance (BA) as:

$$BA = (R_p + kt) \theta \tag{Eq 2.22}$$

where *k* is an empirical constant that depends on material, bending type, and sheet thickness; *t* is sheet thickness; θ is bending angle; and R_p is the inner bending (punch) radius.

The limitation of this empirical equation is that it is based on experimental results and does not consider the properties of the sheet material. Several studies have been conducted to predict various parameters of the air bending operation (bend allowance, springback, punch stroke position, etc.). These are summarized in a recent

publication that also discusses the development of a computer program, BEND, which predicts bending variables (Ref 2.13).

Mathematical Model for Air Bending

In designing air bending operations (tool design, control of punch stroke), it is necessary to predict both of the following:

- Bend allowance, so that for a given final bent product the initial length of the flat sheet can be determined
- Bending force and springback, so that the appropriate bending machine (usually a press brake) and the exact punch stroke can be selected

These predictions are best made using a computerized analytical model. For this purpose, the deformation zones in the bent sheet can be divided into two categories: those along the sheet length and those along the sheet thickness. In a study conducted at the ERC/NSM (The Ohio State University) during air bending, depending on the amount of strain, the sheet can be divided into four zones along the length (as shown in Fig. 2.19): plastic zone, elasto-plastic zone, elastic zone, and rigid zone (Ref 2.1).

In the plastic zone (region O-A), the sheet is in contact with the punch. This region can be assumed to be circular because it conforms to the shape of the punch nose. Most of the plastic

deformation (i.e., length elongation and thickness reduction) takes place in this zone. Therefore, accurate prediction of strains in this region is essential for calculating bend allowance.

In the elasto-plastic zone (region A-E), a part of the sheet undergoes elastic deformation while the remaining part undergoes plastic deformation. The elastic recovery after unloading (after the punch is withdrawn) causes redistribution of the stresses and the springback phenomenon. The profile of the sheet in this region is neither circular as in the plastic zone nor straight as in the elastic zone (after unloading). The profile of this zone depends on several factors: die opening width (W_D), punch stroke (d_s), punch tip radius (R_p), sheet thickness (t), and sheet material properties. The noncircular profile and the elongation of the sheet due to plastic deformation in this region are taken into account for bend allowance calculation. The elastic recovery of the material in the elasto-plastic zone is also considered for springback calculation.

In the elastic zone (region E-B), the sheet deforms elastically during bending but recovers on unloading, because the sheet undergoes purely elastic deformation. This region is important for springback calculations. The sheet profile in this region is assumed to be straight, with no elongation in the unloaded stage. Therefore, this region does not contribute to the bend allowance calculation.

In the rigid zone (region B-C), the sheet is beyond the die-sheet contact. This is the overhanging region of the sheet, and it does not experience any deformation. The profile of the sheet is also assumed to be straight, because there is no elongation. This zone is not consid-

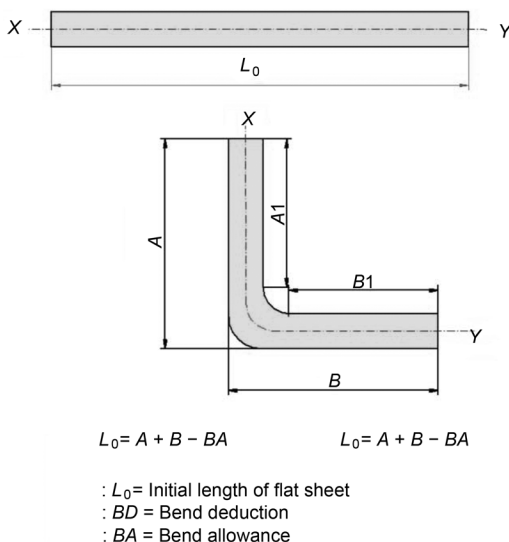


Fig. 2.18 Bend allowance and bend deduction

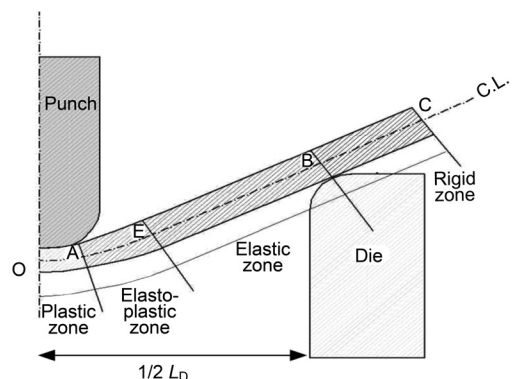


Fig. 2.19 Deformation zone along the sheet length

ered in calculating the bend allowance and the springback angle.

In a bending process, the sheet undergoes tension (on the outer fiber, R_o) and compression (on the inner fiber, R_i) simultaneously. All the fibers except the neutral fiber are under stress and strain. There is also thickness reduction of the sheet in the plastic and elasto-plastic zones. As a result, the absolute positions of all the fibers before and after bending are not the same.

To develop a practical analytical model that was computerized for rapid use, the following assumptions were made (Ref 2.13):

- The bent sheet can be divided into four zones: the plastic zone, the elasto-plastic zone, the elastic zone, and the rigid zone.
- The contact region between punch and sheet is circular and in purely plastic deformation.
- The thickness reduction of the sheet in the elasto-plastic zone is linearly extrapolated based on the thickness reduction in the plastic zone and the original thickness of the sheet.
- The bending moment is linearly distributed between the elasto-plastic zone and the elastic zone.
- Swift’s model ($\bar{\sigma} = K(\epsilon_0 + \bar{\epsilon})^n$) was selected to express the sheet material property.
- Hill’s nonquadratic yield criterion (Ref. 2.2) was used to define the plastic yielding behavior of normal anisotropic material.

Computer Program BEND

The mathematical model briefly described previously has been coded into a computer software, called BEND, and used to make practical predictions (Ref 2.13). The latest version of BEND v 5.0 includes the influence of the Young’s modulus variation and nonconstant K and n values of advanced high-strength steel. The predictions made by BEND have been compared with results available in the literature as well as experimental measurements (Ref 2.13). The good agreement illustrates that the predictions are accurate.

Prediction of Bend Allowance. Using experimental data provided by an air bending company for sheet/plate, BEND programs were verified for three different sheet materials: ASTM A36; a high-strength, low-alloy steel; and a stainless steel. The main parameter of comparison was the initial flat length of the bent

sheet, L_0 , with the flat length obtained from the BEND program (Fig. 2.20). The parameter L_0 was selected for comparing the predictions with experimental data because experimental L_0 values were available and are important in practice. The initial flat length was predicted by BEND within an error of 1.5% compared with the experimental measurements.

Prediction of Springback. The results obtained from the BEND program were also compared to the experimental results found in the literature (Ref 2.5). The sheet material properties of Al-2024 as determined by experiment are given in Table 2.5. Table 2.6 shows the comparison of the measured punch stroke to the predicted punch stroke from the BEND program for given values of bend angle, punch radius, die radius, and die opening. The punch stroke values predicted were observed to be within an acceptable accuracy of 1.3%. The springback angle as a function of punch stroke is given in Fig. 2.21. The BEND program predicts satisfac-

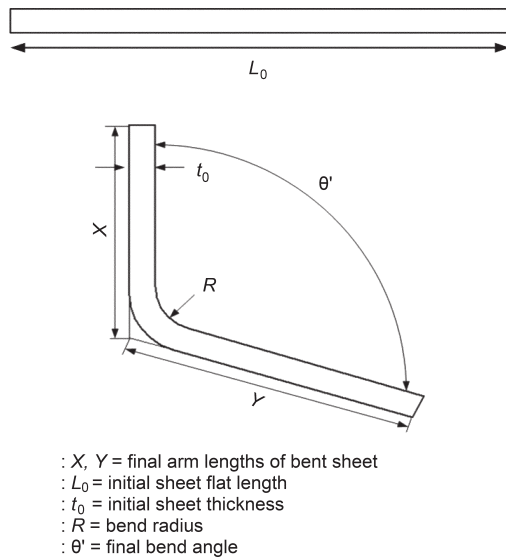


Fig. 2.20 Final dimensions of the bent sheet

Table 2.5 Aluminum 2024 material properties, sheet geometry, and friction condition

Strain-hardening exponent (n)	0.242
Strength coefficient (K), MPa (ksi)	339 (50)
Initial yield stress (σ_0), MPa (ksi)	90 (13)
Young’s modulus (E), GPa (10^3 ksi)	73 (10)
Initial sheet thickness (t_0), mm (in.)	1.27 (0.05)
Sheet width (w), mm (in.)	51 (2)
Friction coefficient (m)	0.1

tory results in comparison with experiments using low-carbon steels (Ref 2.5). The program is now being further developed for application to bending of AHSS.

Control of Springback Using a Tractrix Die

In tractrix die bending (Fig. 2.22a), the die contour has the shape of a tractrix curve instead of a radius (Ref 2.1). As a result, a more con-

stant springback angle can be achieved regardless of the punch stroke. The bending arc length is constant ($L_1 = L_2$) as the sheet is bent by adopting the tractrix curve as the die profile. Springback at a specific punch stroke can be compensated by overbending. Figure 2.22(b) gives the prediction of springback at different bending angles in tractrix die bending.

Minimum Bend Radius

The smallest inner bend radius, R_i , at which cracking occurs on the outer surface of the bend is called the minimum bend radius, R_{min} ; it determines the bendability of a given sheet material and is usually expressed as a multiple of sheet thickness, that is, $2t$, $3t$, and so on. The R_{min} is usually affected by the ductility of the sheet material and is usually determined by conducting air bending experiments close to plane-strain conditions, as shown in Fig. 2.23 (Ref 2.15).

There are no generally accepted standards for conducting the air bending tests to determine the minimum bend radius of materials. However, various investigators attempt to use the same test fixture parameters (given in Fig. 2.23 and Table 2.7) to compare the results generated by various researchers.

In this test, the sample is bent until a crack occurs on the outer bent surface. The start of a crack is identified by a measured load drop, and cracks are later confirmed visually under a microscope. The maximum bending angle (α) is measured after removal of the sample from the fixture, that is, after springback. It is limited by the fixture geometry and sheet sample thickness.

Table 2.6 Comparison of predicted and measured (experiments) punch stroke values

	Case 1	Case 2
Punch radius (R_p), mm (in.)	2.286 (0.09)	1.524 (0.06)
Die radius (R_d), mm (in.)	1.83 (0.07)	1.52 (0.06)
Die opening (W_d), mm (in.)	9.53 (0.38)	6.35 (0.25)
Bend angle, degrees	90	90
Punch stroke (experiment), mm (in.)	4.39 (0.17)	3.07 (0.12)
Punch stroke (BEND), mm (in.)	4.45 (0.18)	3.06 (0.12)
Error, %	+1.32	-0.162

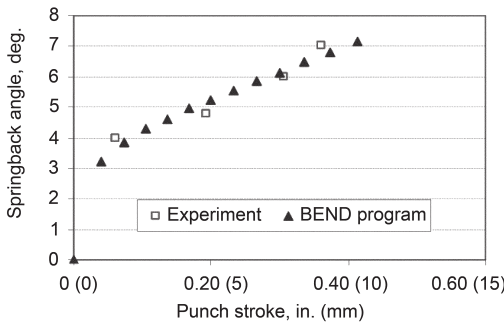
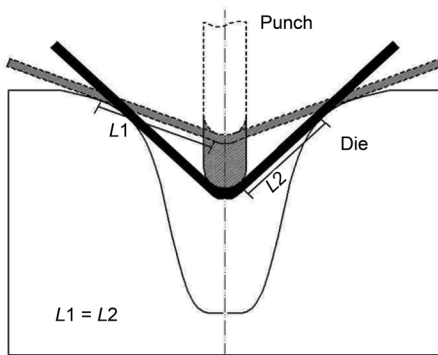
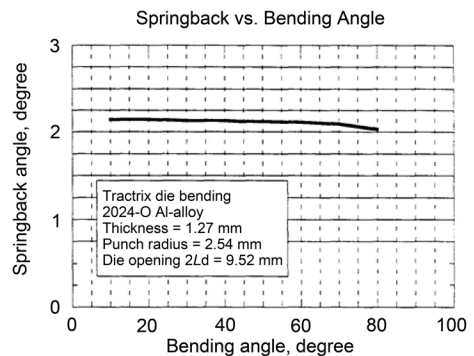


Fig. 2.21 Comparison of predictions with experiments for required punch stroke versus springback angle



(a)



(b)

Fig. 2.22 (a) Tractrix die bending. (b) Bending angle versus springback angle in tractrix bending. Source: Ref 2.1

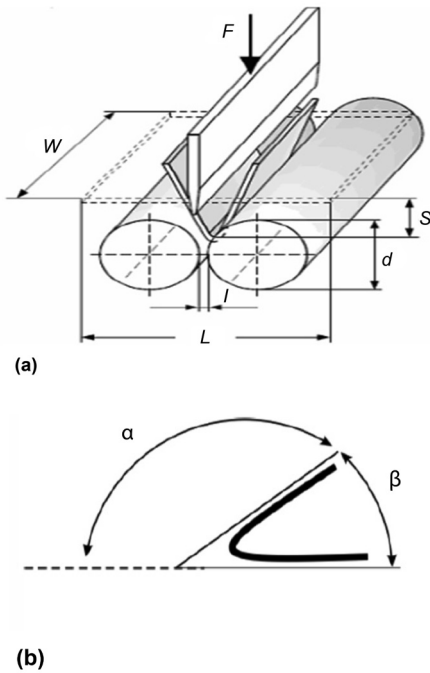


Fig. 2.23 Schematics of (a) an air bending test fixture, used to determine bendability, and (b) the bending angle measurement. Source: Ref 2.15

Figure 2.24 summarizes the results of extensive air bending tests conducted for various sheet materials and thicknesses. This figure illustrates how the minimum bending radius divided by the sheet thickness varies with sheet material ductility, as expressed by percent reduction in area, A_r , in a tensile test (Ref 2.16).

2.3 Stretch Bending

In many practical stamping operations, especially in forming automotive parts, sheet material is stretched and bent simultaneously.

Table 2.7 Parameters of the bending fixture seen in Fig. 2.23

Parameter name	Value
Sample thickness (t)	# mm
Sample width (W), mm (in.)	60 (2.4)
Sample length (L), mm (in.)	60 (2.4)
Roll diameter (d), mm (in.)	30 (1.2)
Roll spacing (l), mm	$2 * t$
Punch radius, mm (in.)	0.2 (0.01)

Source: Ref 2.15

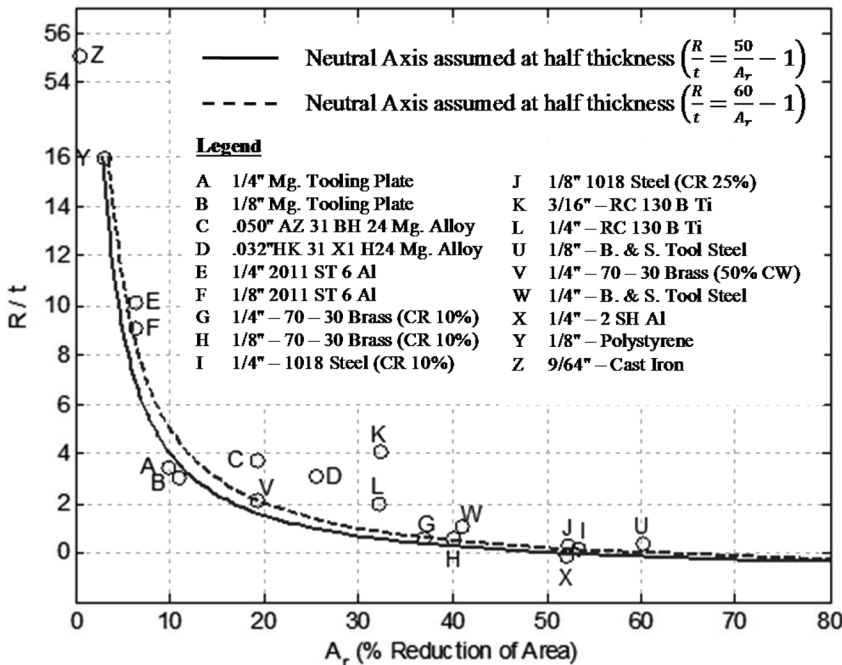


Fig. 2.24 Experimental data superimposed on analytical curves of bending radius/sheet thickness (R/t) versus percentage reduction in area (A_r). Source: Ref 2.16

Thus, prediction of minimum bend radius and potential fracture under stretch bending conditions is an important and challenging task. This task is especially important in stretch bending of AHSS because potential fracture can be predicted by finite-element simulation but not by using forming limit curves that are routinely used for predicting failure in stamping.

The understanding of fracture under stretch bending conditions has been investigated by various research groups. Commonly used stretch bending tests are illustrated in Fig. 2.25. In these tests (Fig. 2.25a), a strip specimen is clamped

with lock beads and bent by a moving punch (with different radii between 1 and 10 mm) at a selected speed until fracture occurs (Ref 2.17). For a given sheet material, the ratio of punch radius and sheet thickness (R_p/t) determines the punch stroke at fracture. Thus, from the results of the stretch bending tests, it is possible to determine how to compare the bendability of various materials.

It is desirable to predict the stretch bendability of sheet material, that is, punch stroke at fracture for a given R_p/t value, using tensile properties of the material. Toward this goal, finite-element simulations of the stretch form-

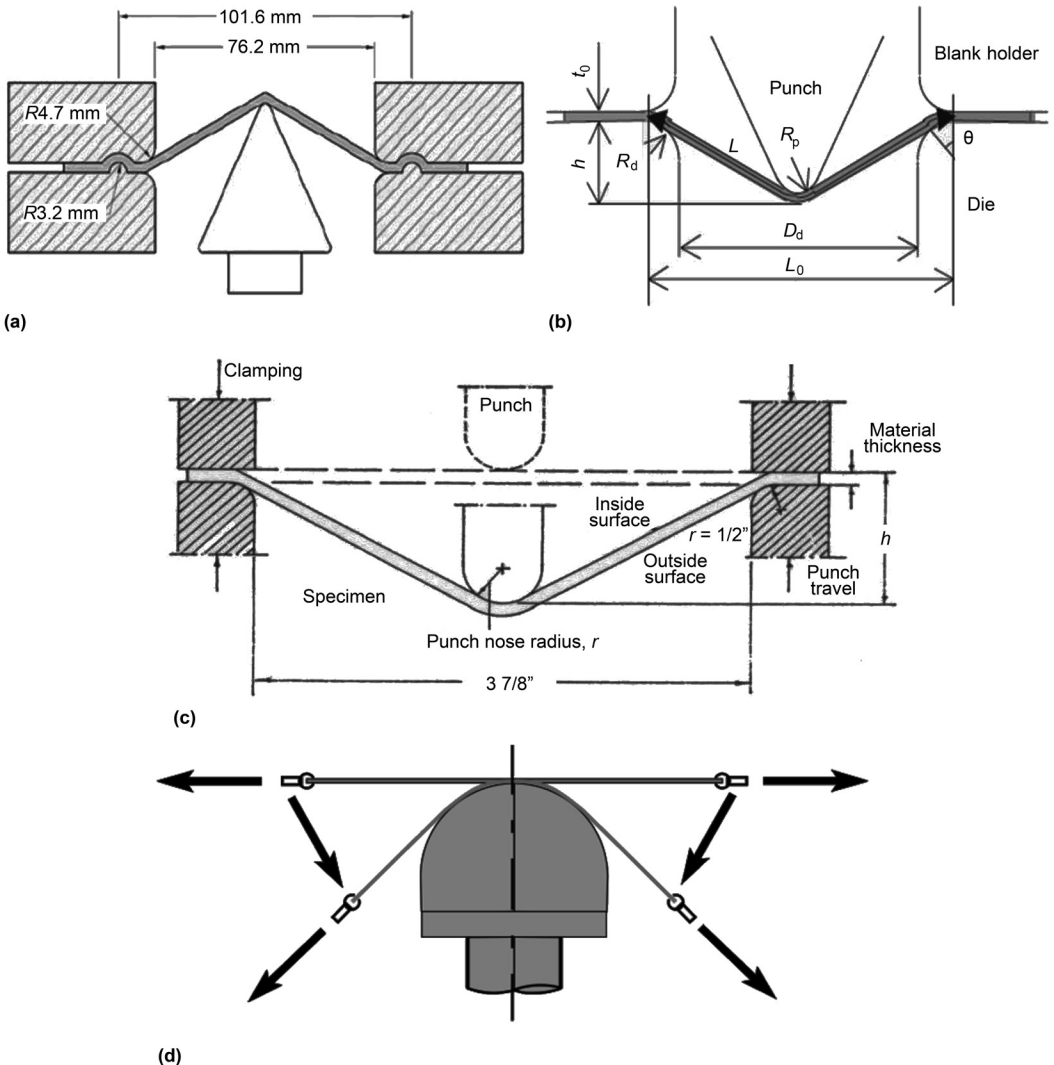


Fig. 2.25 Schematics of stretch bending tests. (a) Stretch forming test. Source: Ref 2.17. (b) Stretch bending test. Source: Ref 2.18. (c) Stretch bend test. Source: Ref 2.19. (d) Tangential stretch bending

ing test were conducted using DEFORM-2D at the ERC/NSM. Predictions of the punch stroke at fracture, made with and without a fracture criterion, were compared with experimental results from the literature for DP600 steel (Ref 2.17). The Cockcroft-Latham fracture model was used to predict the fracture in finite-element simulations. The results indicate that it may be possible to predict fracture conditions in stretch bending, using material properties and finite-element simulations (Ref 2.20).

2.4 Other Industrial Bending Processes

V-Die Bending. In V-die bending, both the bending die and the bending punch are V-shaped with a specified angle (Fig 2.17). The clearance between punch and die is constant and equal to the thickness of the sheet blank. The thickness of the sheet ranges from approximately 0.5 to 25 mm. The bending force, F_b , without coining at the end of the process is the same as in the case of air bending, that is, approximately (Ref 2.21):

$$F_b = 1.2Wt^2S_u/W_d \tag{Eq 2.23}$$

where F_b is the bending force, W is the width of the sheet, t is the sheet thickness, S_u is the ultimate tensile strength of the sheet material, and W_d is the total die opening width.

Bottoming and coining are typical methods to reduce springback in die bending by applying compressive stress in the bending zone (Fig. 2.26). In some cases, the punch tip can be also shaped (Fig. 2.26b) to increase the amount of plastic deformation and to further reduce springback. Parts made by bottoming and coining have more consistent dimensional tolerances.

However, in this case, the maximum bending force would be 3 to 5 times larger than the free bending force, F_b , of Eq 2.23.

Bending force increases suddenly when the punch begins bottoming or coining the part (Fig. 2.27). In these cases, the press tonnage needed to produce a given part may be three to five times larger than that needed for air bending. Therefore, bottoming is used only when it is necessary, for example, for parts requiring high accuracy and sharp corners (Ref 2.22).

U-Die Bending. In U-die bending (Fig. 2.28), two parallel bends are produced in the same operation. A backing pad is often used under the punch to force the sheet web to maintain contact with the punch bottom during bending. A backing pad force of approximately 25% of the bending force is required to keep the sheet in contact with the bottom of the punch. Thus, the bending force, F_b , can be calculated approximately for bending with or without the pressure pad by using Eq 2.24 or 2.25, respectively (Ref 2.21):

$$F_b = 0.4btS_u, \text{ without pressure pad} \tag{Eq 2.24}$$

$$F_b = 0.5bW_dS_u, \text{ with pressure pad} \tag{Eq 2.25}$$

where W is the width of the sheet, t is the thickness of the sheet, b is the width of the die opening, and S_u is the ultimate tensile strength of the sheet material. Figure 2.29 shows bending force versus punch displacement. The pad pressure and die gap are two important process variables in controlling springback. Springback is reduced by increasing the backing pressure and decreasing the clearance between the punch and die. A comparison of Fig. 2.28(a) and (b) shows that the pad prevents the bending of the flat portion of the U-shape and helps to control the dimensional tolerances of the part.

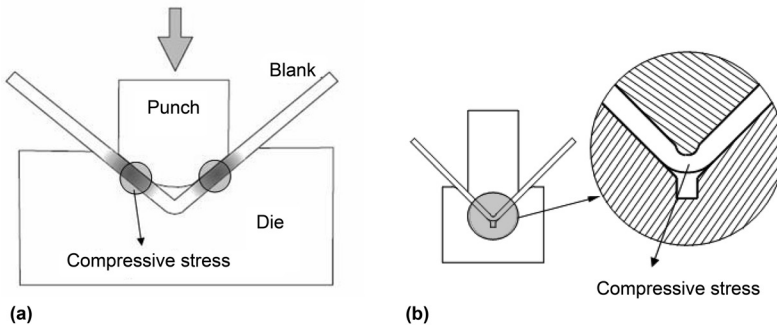


Fig. 2.26 (a) Bottoming and (b) coining in V-die bending

Rotary Bending. In rotary bending, a rocker or rotating die is used to simultaneously hold, bend, and overbend the sheet (Fig. 2.30). The edges of the rocker are filleted to reduce scratch marks on the surface of the workpiece. The sheet is bent between the edges of the rocker and the corner of the die. Rotary bending can be used to obtain angles larger than 90°. The springback is controlled by overbending instead of coining (Ref 2.25).

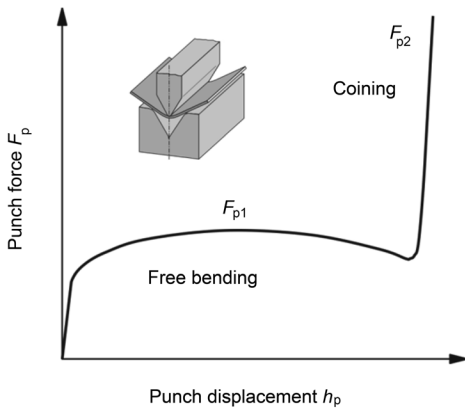


Fig. 2.27 Schematic of punch force/punch displacement curve during V-die bending

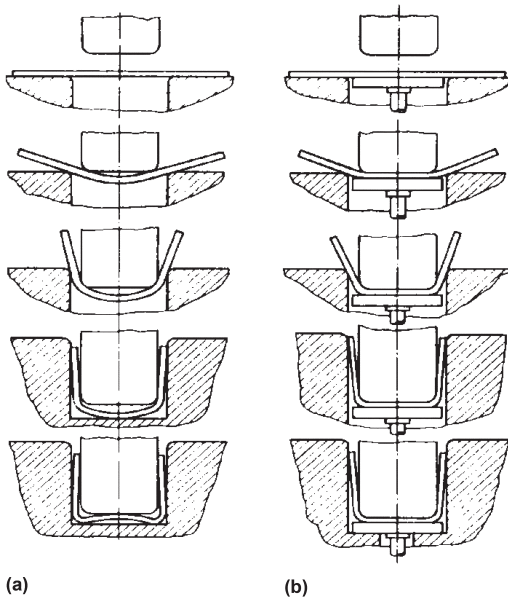


Fig. 2.28 U-die bending (a) without pressure pad and (b) with pressure pad. Source: Ref 2.23

The advantages of rotary bending compared to straight flanging or wipe bending are as follows:

- It eliminates the blank holder.
- It compensates for springback by overbending.
- It reduces the amount of bending force needed.

Wipe Die Bending and Straight Flanging.

In wipe die bending, or straight flanging, a narrow strip at the edge of a sheet is bent along a straight line (Fig. 2.31). Compared to other bending processes, flanging is applied on the edges of parts, and the flange length is relatively small. In this operation, a blank holder (pressure pad) loaded by a spring, nitrogen, or hydraulic cylinder is used to clamp the sheet to the die. Then, the punch wipes one side of the sheet with the press stroke.

The blank holder force, F_{BH} , is approximately half of the bending force given by Eq 2.24:

$$F_{BH} = 0.2W_d t S_u \tag{Eq 2.26}$$

where W is the width of the sheet, t is the thickness of the sheet, and S_u is the ultimate tensile strength of the sheet material.

The punch stroke is usually enough to bend all of the edge down over the die, so that the punch stroke position does not matter compared to other types of bending operations. There are different ways of controlling springback by overbending, double bending, bottoming the wiper (Fig. 2.32), or flanging with counterpressure (Fig.

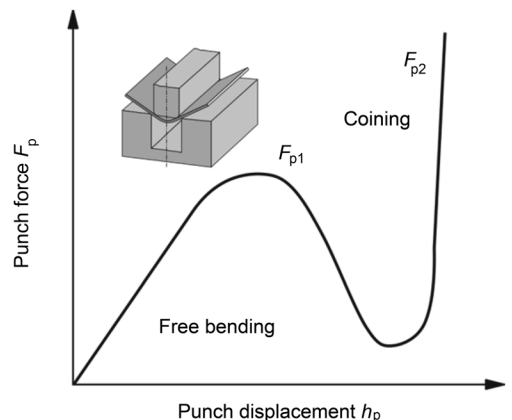


Fig. 2.29 Schematic of punch force/punch displacement curve during U-die bending

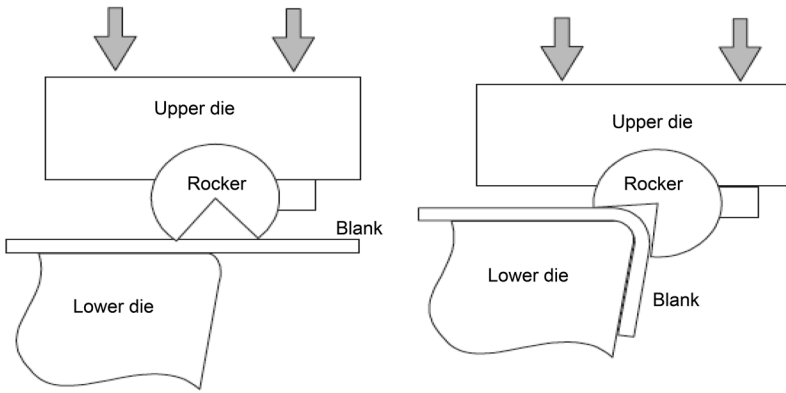


Fig. 2.30 Schematic and operation of rotary bending. Source: Ref 2.24

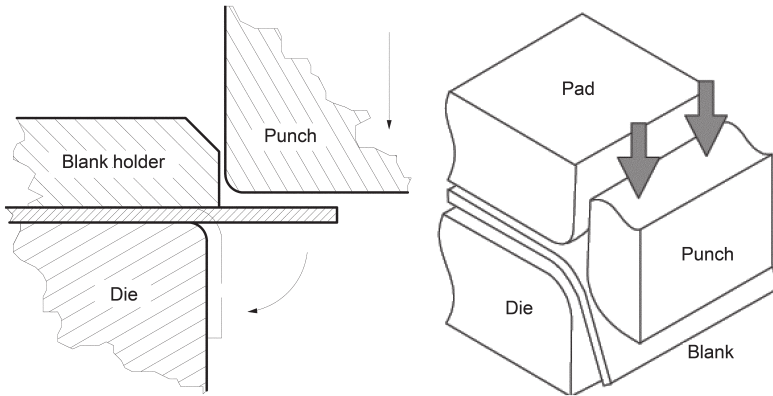


Fig. 2.31 Schematics of straight flanging (wipe die) bending

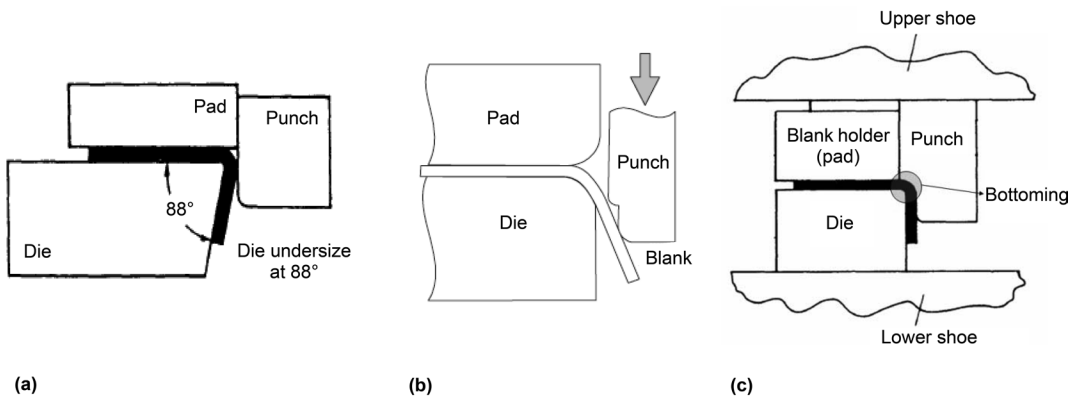


Fig. 2.32 Springback-compensating methods in flanging. (a) Overbending. (b) Double bending. (c) Bottoming. Source: Ref 2.26

2.33). Overbending (Fig. 2.32a) allows compensating for springback. Double bending (Fig. 2.32b) reduces springback because the punch applies tensile stresses to the bent portion of the sheet by ironing and friction. Bottoming (Fig. 2.32c) applies additional compressive coining stresses at the curvature, similar to coining in V-bending. Flanging (Fig. 2.33) applies tensile stresses to the flange.

Roll bending is used to form sheet into cylindrical or conical parts for manufacturing pressure vessels or containers, using three or four rollers (Fig. 2.34). Roll bending is essentially an air bending process with bending of both ends of the sheet. In the stages, as shown in Fig. 2.34, bending of the ends of the sheet can be conducted separately in a die. Whereas small cylindrical parts can be formed from a single sheet, larger cylinders may be made in several sections. Figure 2.34 shows the individual phases of the process on a three-roll bending machine. The bending of the ends can be made either at the

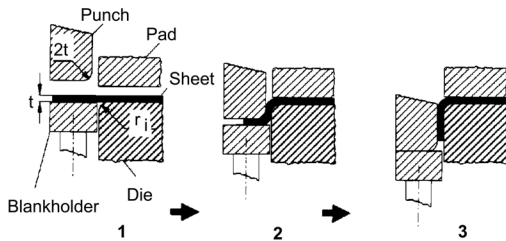


Fig. 2.33 Flanging with counterpressure. Source: Ref 2.26

beginning of the process, as shown in Fig. 2.34, or at the end. The bending of the ends in a die before roll bending is a further alternative. The middle part of the workpiece is then bent, with increasing roll adjustment after each bending step, until the sheet metal ends meet.

2.5 Contour and Hole Flanging

Contour Flanging. Figure 2.35 shows examples of contour flanging. Because of the nature of the curvature, the process is called either stretch flanging (concave edge curvature) or shrink flanging (convex edge curvature). In contour flanging operations, because of the curvature of the bending line, the deformation is not plane strain but three-dimensional. The tension or compression is zero at the bending radius and achieves its maximum at the flange edge (the bent part of the sheet). The tangential strain component increases from the bending line to the flange edge, limiting the maximum flange height that can be formed without defects. Wrinkling (localized buckling) is the common failure mode in shrink flanging, whereas tearing and splitting are typical failure modes in stretch flanging (Fig. 2.36). To eliminate wrinkling and splitting, the flange width must be reduced with decreasing contour radius, as shown in Fig. 2.36.

Hole flanging is essentially stretch flanging around a circular contour. Therefore, this pro-

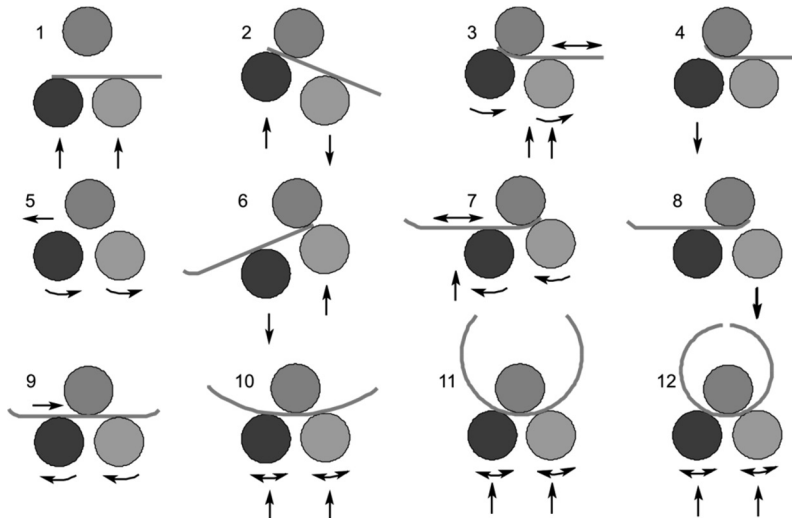


Fig. 2.34 Working stages in three-roll bending. Source: Ref 2.7

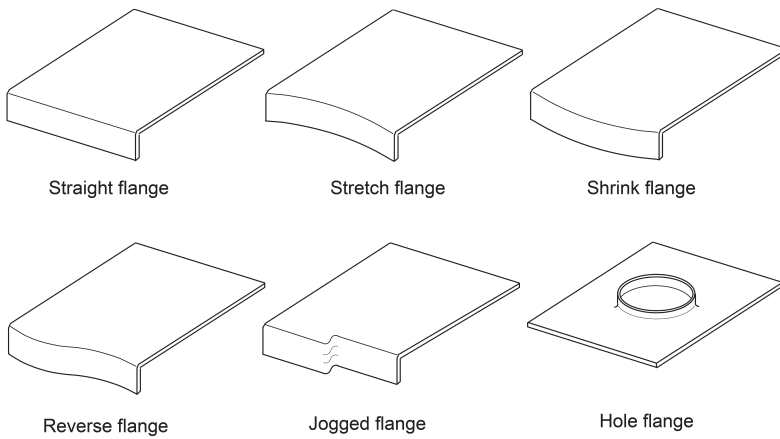


Fig. 2.35 Types of contoured flanges

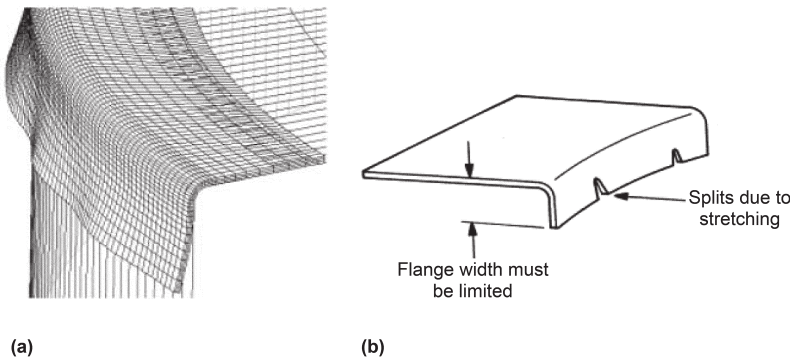


Fig. 2.36 Defects in contour flanging. (a) Wrinkling in shrink flanging. (b) Fracture in stretch flanging

cess can be used to evaluate the formability in flanging, that is, edge cracking, of various materials, especially of AHSS, which is increasingly used in the automotive industry.

Factors such as edge condition of the punched hole before flanging, punch shape, shearing operations, and the microstructure (volume fractions of the different phases) affect the ability of the hole flange to stretch. The forming limit curve (FLC) traditionally used to evaluate formability is not sufficient to predict edge cracking because the FLC represents the limit of stretching but not bending.

Therefore, the edge stretchability is studied using a hole expansion test that can emulate the stress/strain conditions that exist during hole flanging. In the hole expansion test, a pierced hole is expanded to fracture using a conical, hemispherical, or flat-bottomed punch. A blank holder clamps the sheet to restrict the material

movement in the flange (Fig. 2.37). The edge of the hole is under stretching and bending conditions. Therefore, the circumferential strain/stress along the edge leads to cracking. It is most probable, however, that a complex stress/strain history, and the edge quality of the pierced hole, can determine when edge cracking occurs.

The hole expansion ratio (HER) is used as a criterion to evaluate the hole flange stretchability:

$$HER(\lambda) = \frac{d_f - d_0}{d_0} \times 100 \tag{Eq 2.27}$$

where d_f and d_0 are the diameters of the flanged hole after and before flanging, respectively. The higher the HER (λ), the better the stretchability of the hole flange.

Various shearing operations that are used to form the prehole, as well as the tool condition,

directly influence sheared edge quality. Tests show that, as expected, the HER of AHSS decreases as the punch wears out during production (Ref 2.27).

Other studies show that the edge quality of the hole has a significant influence on hole flange stretchability (Ref 2.28). Also, the level of martensite in the material and the homogeneity of its microstructure have considerable influence on hole flange stretchability. Even the location of the burr at the blanked edge affects HER; studies have shown that HER is larger if the burr is placed down.

It is desirable to predict and eliminate the edge cracking in hole flanging. Some studies have used FEA together with thickness distribution and damage value as a fracture criterion (Ref 2.25). In a preliminary study, the FEA commercial code DEFORM-2D was used to establish a relationship between the stress/strain states in hole flanging, material properties, and the edge quality of the prehole. The FEA predictions were

compared for mild steel and high-strength steel with experimental data obtained from literature (Ref 2.29). The simulation results showed agreement with experimental data obtained using a conical punch. Similar results were obtained when comparing the finite-element predictions with hole flanging using a spherical punch.

2.6 Hemming

Hemming is the process whereby the edge of the sheet is folded to 180° or more. In addition to increasing the stiffness of the part, hemming also eliminates acute edges, improves appearance, and joins parts. A number of automotive interior and exterior panels are formed by bending and flanging and are then joined by hemming.

There are several different types of hems (Fig. 2.38). Flattened, open, and teardrop hems are used for edge finish and appearance pur-

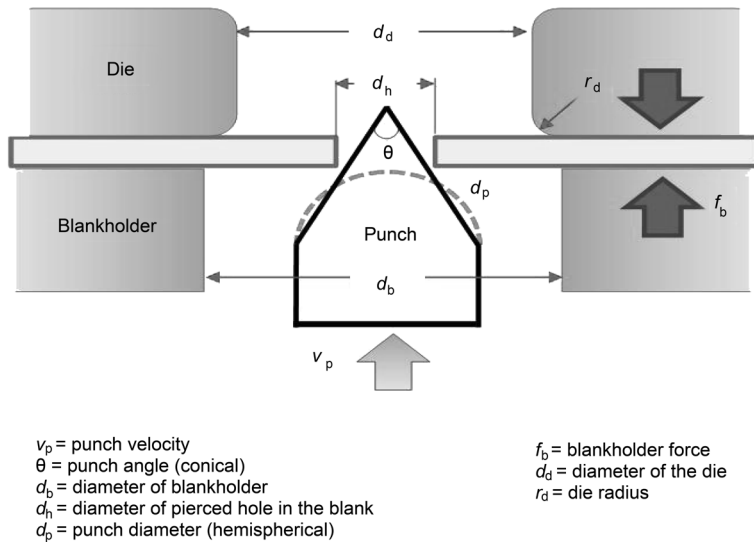


Fig. 2.37 Schematic of a hole expansion test with a conical punch used to evaluate how far a sheet sample can be flanged without fracture. Source: Ref 2.25

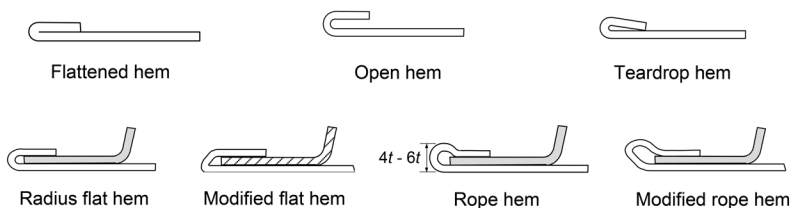


Fig. 2.38 Most common types of hems

poses, whereas the radius flat, modified flat, rope, and modified rope hems are used for seaming two sheet metal parts. Compared to radius hems, modified flat hems have better fitting behavior and shape fixation. Rope hems are used for brittle materials.

Hemming operations are usually performed in three stages: bending or flanging to 90°, prehemming to approximately 135°, and hemming to 180° or more, called flattening (Fig. 2.39).

A **prehemming operation** using a vertical (downward) path is illustrated in Fig. 2.40. Prehem steel, usually with a constant face angle and flat surface, approaches the flange, and the flange is bent further while the flange tip slides on the prehem steel face. Because the fillet region of the flange is strain hardened during the flanging operation, it has more resistance to bending than the neighboring flat sections. Therefore, while the flange gets a curved shape under loading, the bottom of the sheet is slightly lifted upward and the edge rolls in. When the flange angle becomes parallel to the prehem steel, the contact point moves to the bottom of

the flange, while bending the flange further and causing severe creep (roll-in, inward movement of the bend edge).

In common practice, the prehem steel stroke is usually down to the point at which the flange is bent to the same angle as the prehem steel surface. Geometry control of the sheet during prehemming is complicated, because the sheet is not supported by any other tool while being formed by the prehem steel. Thus, it is indirectly controlled by the following factors:

- Sheet material properties and thickness
- Hem edge geometry (straight, contoured, etc.)
- Previous deformation transferred from stamping and flanging phases
- Prehem steel path
- Prehem steel displacement (stroke)
- Prehem steel geometry (profile, face angle, etc.)
- Frictional conditions
- Influence of the additional support by the inner panel

Flattening. Final hemming, or flattening, is conducted using a flat horizontal die (in the case of radius flat hem) commonly called the hemming steel (or upper die) (Fig. 2.41). The approach path of the hemming steel is usually vertical or circular. The final position of the hemming steel is crucial because it determines the final hemming pressure and thus the final hem geometry.

Defects. The failure modes in hemming are determined by the geometric configuration of

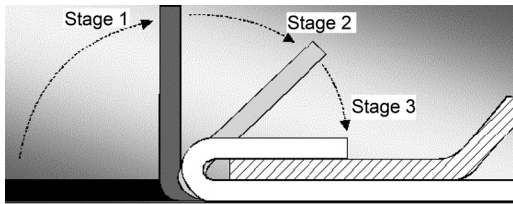


Fig. 2.39 Three stages of the hemming operation

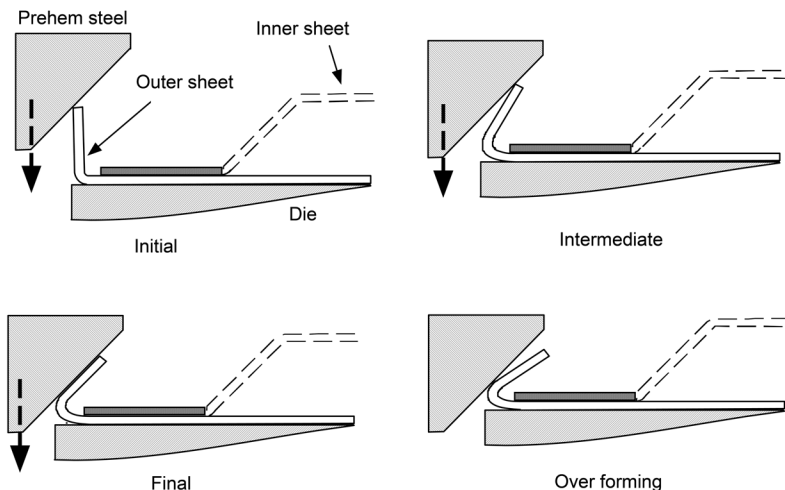


Fig. 2.40 Illustration of prehemming operation with a vertical tool path

surface and edge curvature. Figure 2.42 shows the most typical geometric configurations of hems used by the automobile industry. The flat surface/straight edge configuration (the plane-strain case) is the simplest of all. Complexity of deformation increases with the addition of edge and/or surface curvatures.

The most common hemming defects are shown in Fig. 2.43 (Ref 2.30) and include fracturing (cracking or splitting) and wrinkling, which are the most common defects in all stamping operations. Creep and grow are the in-

ward and outward shift of the hem edge, causing a change in outer panel size, respectively (Fig. 2.43a). Recoil (hemming deflection, sag) is the out-of-plane displacement of the outer panel hem edge after final hemming (Fig. 2.43b), and warp is the indentation in the outside of the outer panel after final hemming (Fig. 2.43c). Wind is outward and localized waviness on the outer panel edge on the panel plane (Fig. 2.43d). Hem-out is a localized and exaggerated combination of recoil and grows where the flange is subjected to excessive compression,

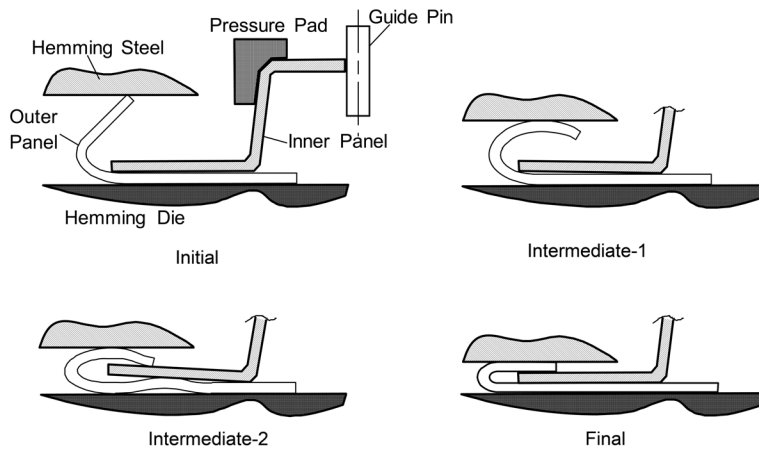


Fig. 2.41 Illustration of the final hemming operation

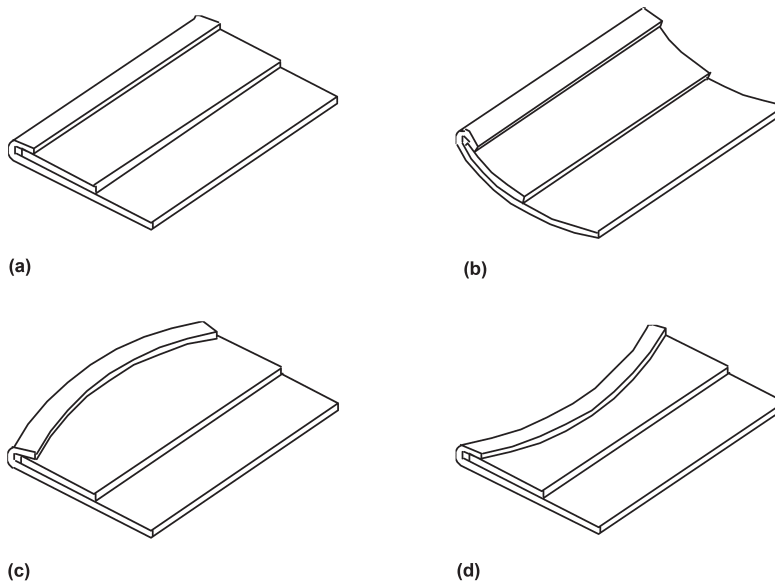


Fig. 2.42 Some important geometric configurations in hemming. (a) Straight-flat. (b) Straight-curved. (c) Convex-flat. (d) Concave-flat

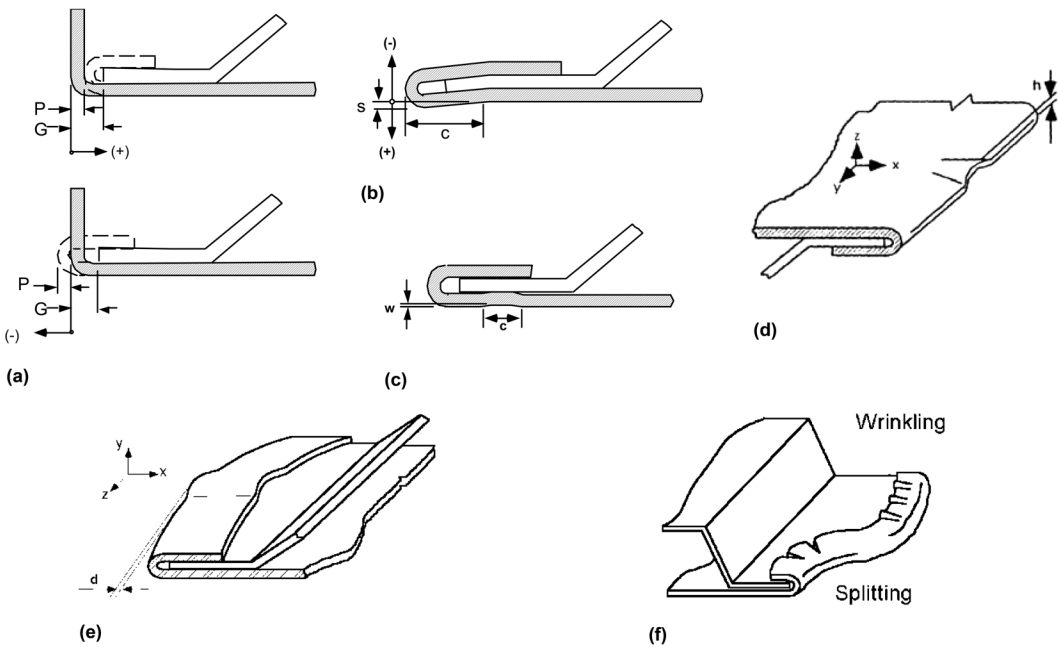


Fig. 2.43 The most common hemming defects. (a) Creep/grow. (b) Recoil. (c) Warp. (d) Wind. (e) Hem-out. (f) Wrinkling and splitting. Source: Ref 2.30

exhibits instability, and bends in the opposite direction (Fig. 2.43e).

2.7 Bending Machines

Press Brakes

Bending with vertical tool motion is primarily performed on press brakes whenever the bending length exceeds a specified amount, or when production runs are so small that making a tool for a conventional press is uneconomical. Press brake bending is used extensively in the fabrication industry because it offers flexibility in forming different alloys, sheet thicknesses, and bending angles, and it also affords easy setup and relatively low tooling costs. Both air and die bending processes can be conducted in press brakes.

Drive Types in Press Brakes

To select the drive type for a press brake, a user must consider many important factors, including required tonnage (striking force), stroke length, length of bed, and the range of available drive and control systems for the sheet material type, the gage, and the required production rate.

Four types of press brake drives are commonly used: mechanical, hydraulic, hydraulic-servo, and alternating current electric servo. Each of these designs has its own special features and applications.

Mechanical Drive. A mechanical press brake uses a motor, flywheel, and crankshaft to convert the rotary motion of the motor and flywheel into a vertical or reciprocating motion of the punch and ram (Fig. 2.44).

High-speed flywheel rotation in these presses allows a large number of cycles per minute, which is suitable for high-volume production. At the bottom dead center (BDC), the theoretical tonnage capability of the press reaches infinity. Thus, the applied force is limited only by the load-carrying capacity of the press frame. Therefore, if the press is not set up properly, high-tonnage coining techniques may cause tool damage or locking of the press at the BDC.

Hydraulic Drive. A hydraulic press uses a motor and a pump to move hydraulic oil into the top of the cylinders that move the punch and ram (Fig. 2.45). The tonnage of a hydraulic press brake is directly proportional to the oil pressure and the area of the pistons under pressure. The punch speed can be controlled easily by adjusting the oil flow. However, in general,

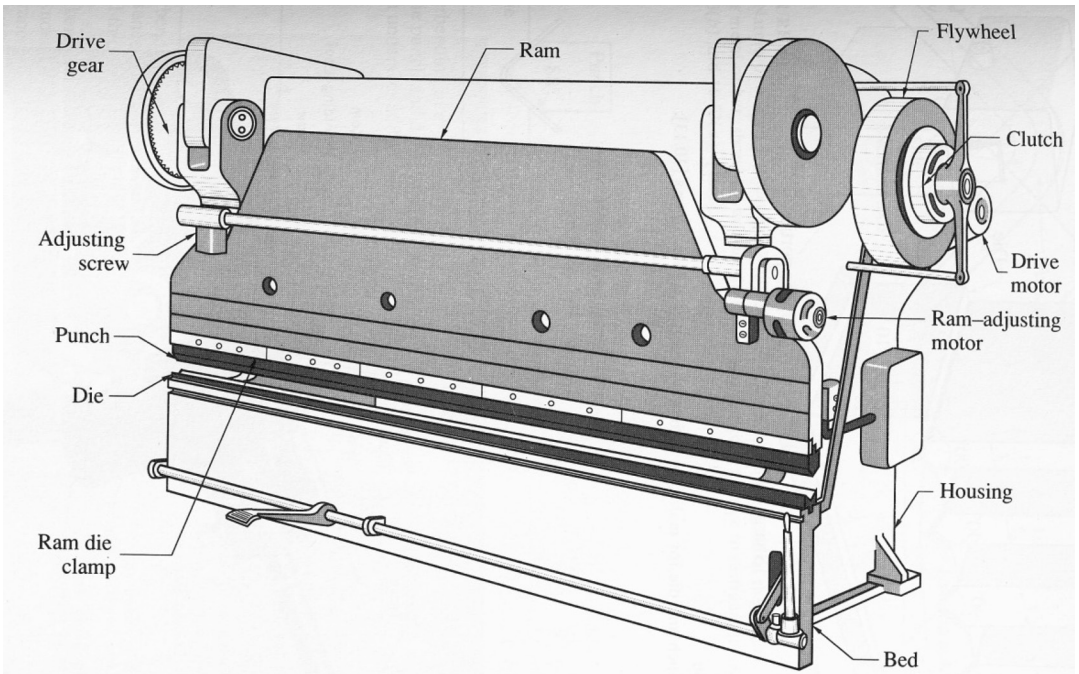


Fig. 2.44 Principal components of a mechanical press brake. Source: Ref 2.31

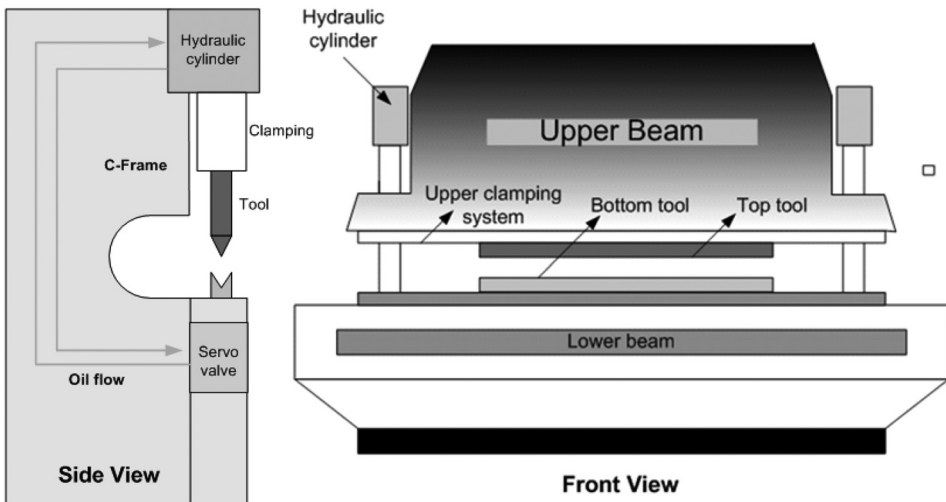


Fig. 2.45 Schematic of hydraulic press brake

the hydraulic press does not allow the higher number of strokes per minute that can be obtained with a mechanical drive.

Hydraulic-Servo Drive. In a hydromechanical-servo drive press brake, a single hydraulic cylinder powers a mechanical linkage system to bend, punch, or form material. This unique de-

sign provides full tonnage at any point across the bed, assures parallel movement of the ram regardless of off-center loading, and yields excellent punch position repeatability (± 0.025 mm, or 0.001 in.).

The design of the hydromechanical-servo press brake is similar to that of the mechanical

press brake. A major difference from the mechanical drive is that a hydraulic pump, rather than a flywheel, generates the necessary force to drive the ram. The resulting hydraulic pressure causes a hydraulic motor to turn an eccentric shaft, producing the up-and-down action of the ram and the necessary power for bending. Unlike mechanical press brakes, which must complete a full stroke of the ram every time, the hydromechanical press brake has the ability to limit the ram stroke. The full tonnage can be built at any stroke position, and the open height can be set at any point above the BDC.

Alternating Current-Servo Drive. The energy of rotating servo motors is transmitted to the ball screw by the timing belt, and the upper tool is moved up and down by the reciprocating motion of the ball screw. The operation of an alternating current (ac)-servo press brake is similar to other mechanical servo-drive presses. It can be programmed to control slide speed and position during the press stroke and can provide BDC accuracy in the range of micrometers. An ac-servo motor maintains constant torque and energy even at reduced speed. The ac-servo press brake is gaining popularity because of the trend toward using increasingly thin sheet materials.

Measurement of Bending Angle

The most important requirement in modern press brakes is the accuracy of the bending angle. Variations in mechanical properties or thickness of the workpiece may cause errors in bending angles due to springback. Precise measurement and control of springback is the key to

obtain close tolerances in bent parts. There are different methods for measuring the bending angle.

Bending Angle Measurement Using Non-contact Method with Optical/Laser Sensors. This contact-free angle measurement method uses laser beams projected on the contour of the sheet being bent. The charge-coupled device cameras, which are positioned at “A” and “B” in Fig. 2.46, look up diagonally and measure the positions of the laser projection line on both sides of the bent sheet. Considering the measured angle (α) between laser projection lines and fixed camera angle (β), the bend angle (ϕ) can be calculated. Bending accuracies within $\pm 0.2^\circ$ can be achieved. Easy-Form Laser, developed by Strippit/LVD, employs a similar technique (Ref 2.32).

Similar noncontact methods based on image-processing techniques have been developed for research (Ref 2.33) and production (Ref 2.34).

Bending Angle Measurement Using a Contact Method with Mechanical Disk Sensors. In this method, two sensor disks with different diameters are embedded into a punch (Fig. 2.47). These disks contact the sheet at four different points. The bending angle is measured from the distance between the two centers of the disks and is used to modify the ram position of the press. The use of disk sensors is limited to a range of bending angles. Therefore, this technique is not very flexible.

In the bending of long workpieces, three sensors are used (Fig. 2.48a). The two outer sensors regulate angle accuracy and parallelism; the middle sensor controls crowning. Accuracies

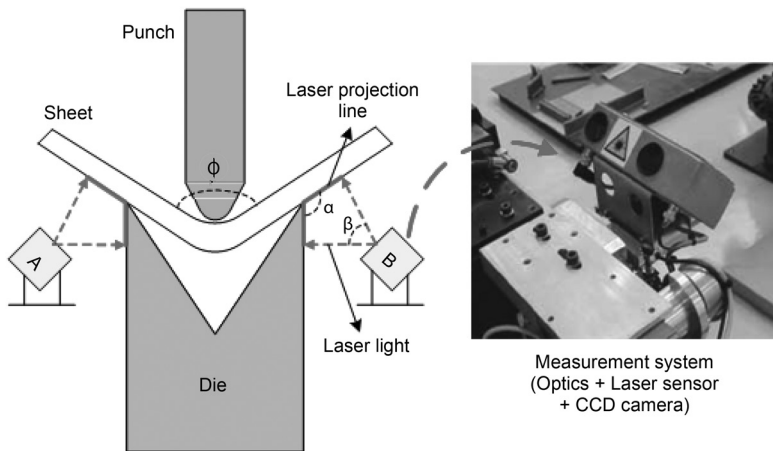


Fig. 2.46 Schematic of bending angle measurement using the COPRA LaserCheck (data M Corp.). CCD, charge-coupled device. Source: Ref 2.32

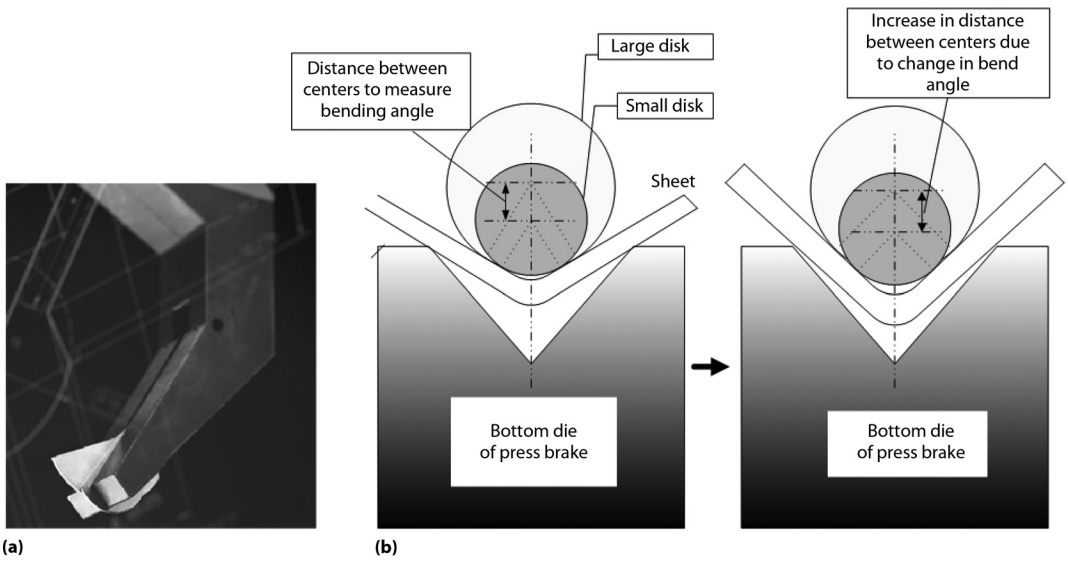


Fig. 2.47 Schematic of (a) sensor tool and (b) four-point measurement with sensor disks. Source: Ref 2.35

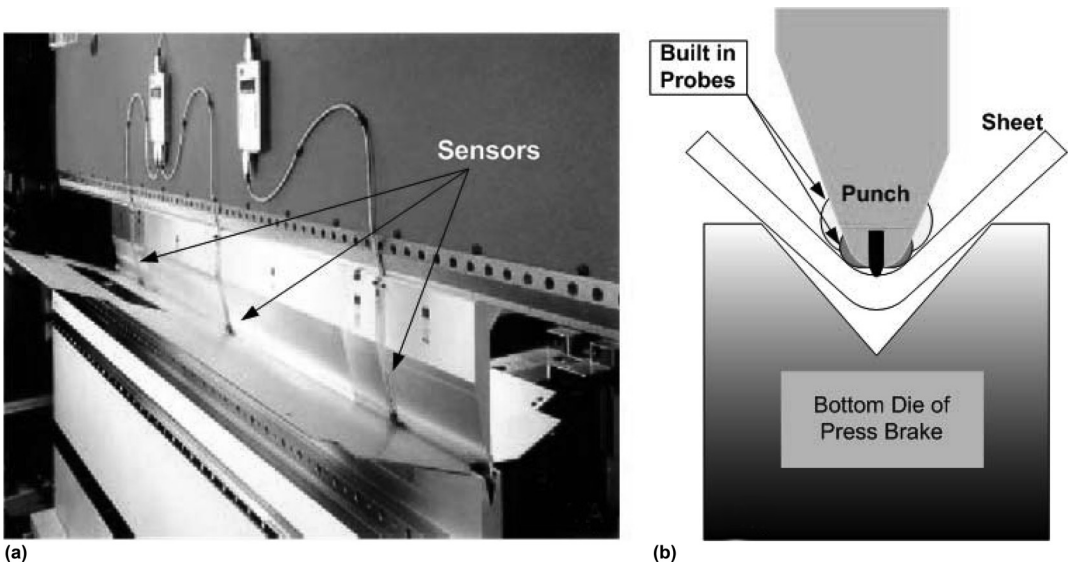


Fig. 2.48 (a) Bending with three sensors. Source: Ref 2.35. (b) Schematic of angle measurement using four probes. Source: Ref 2.36

within $\pm 0.3^\circ$ can be achieved. A similar method uses four probes built into the punch (Fig. 2.48b). The four probes measure the material thickness and springback and modify the punch penetration accordingly.

Press Brake Tooling and Accessories

Press Brake Tooling and Clamping. Depending on the final part geometry required and

the type of operation performed (such as hemming, wiping, and bending), various bending tools can be used in a press brake (Fig. 2.49). For instance, a gooseneck punch is used in bending box-type parts in order to avoid interruption between the tool and workpiece.

To hold the upper tool in a press brake, there are mechanical and hydraulic clamping systems, such as from Wila USA, that provide manual or automatic clamping capability.

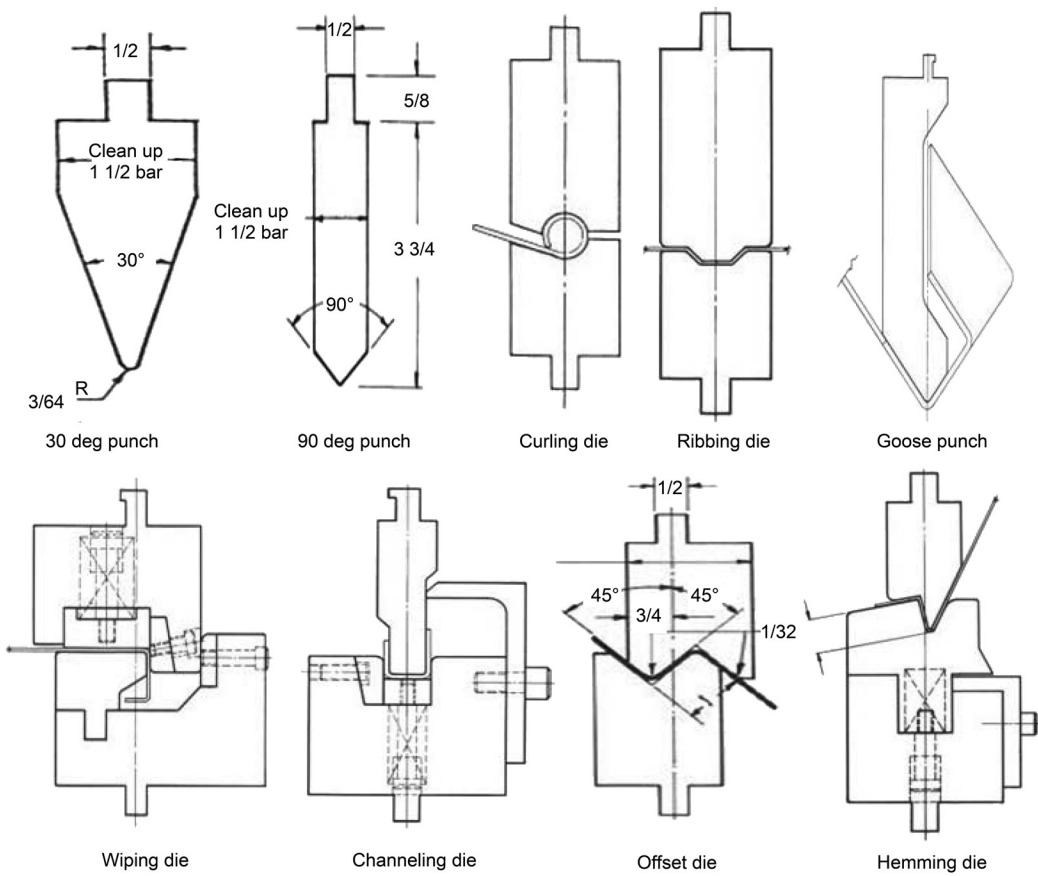


Fig. 2.49 Various tools used for a press brake. Source: Ref 2.37

Crowning System. When the press brake experiences elastic deflections during bending long and thick plates/sheets, the top tool does not penetrate to the same depth into the bottom tool across the working length. As a result, the bending angle is not constant over the entire product length. To compensate for this elastic deflection, which is called crowning, the bottom die can be elastically deformed using wedges that are moved manually by computer numerical control, such as from Enutron, or by optional hydraulic crowning systems, such as Auto Crown from Cincinnati Inc. (Ref 2.38).

Online Process Control Strategies for Air Bending

The demands for accuracy in both shape and dimension of bent sheet metal parts have continuously increased and the batch sizes have become smaller. The air bending process, which is

one of the most widely used processes for the manufacturing of sheet metal bending parts, is an excellent way to provide the flexibility needed for production under such conditions. This process allows the manufacturing of a great variety of bend angles with just one tool. However, the accuracy that can be achieved with air bending depends on a large number of variables, such as the springback of the material, variations of material properties (including variations within a single batch), and the deflection of the bending machine and tools. These variables must be either taken into account during the generation of the numerical control data or counterbalanced later in the manufacturing process by automatic process control (Ref 2.39).

A basic precondition for obtaining an accurate bend angle under automatic process control is the in-process measurement of relevant process data. Using these data, the final bend angle can be predicted and deviations from the de-

sired values can be corrected. The most common methods of achieving this objective are:

- Direct process control by in-process measurement of the bend angle and compensation of potential errors
- Indirect process control by deduction of relevant material data from such parameters as punch force and punch position, for which the measurement is more straightforward than for the bend angle. The recorded information is then used in connection with a process simulation program to control the bending process.

These two different methods can also be combined to some extent.

Direct Process Control. Control strategies that rely on direct recording of the bend angle are based on the determination of the springback angle or unloaded bend angle after punch unloading. This so-called intermediary unloading may, in principle, be carried out either partly or completely. Complete unloading is the simplest method for direct control of air bending. In this method, the bending-unloading sequence is repeated until the desired bend angle after unloading, α_2 , is reached. Another frequently followed approach is the online recording of the springback angle over a partial unloading and the use of the amount of the measured springback for overbending.

The advantage of direct process control is that it provides relatively high accuracy through direct recording of the target parameter. The disadvantages are the higher hardware expenses, the comparatively more complex handling, and the higher expenditure of time when an unloading of the punch is required to determine the sheet metal springback (Ref 2.40).

Indirect Process Control. An example of this approach is the use of a measured force-displacement curve. Through mathematical modeling of the bending process (process simulation), the target parameter (bend angle) can be calculated from measured values (Ref 2.13, 2.41). However, through the in-process calculation of the unknown bend angle from other process parameters, additional errors may occur and affect the process. The computation can be optimized by means of an adaptive adjustment of the model parameters on the basis of the actual bend angle for a sufficiently high number of pieces. The relationship between bend angle under load and punch displacement can be generated on the

basis of a reference bending for a combination of tool, material, and sheet thickness (Ref 2.42).

The main advantage of the indirect recording of the process data is the relatively low expense associated with hardware and handling, because the press brakes are usually equipped with pressure or bending force sensors. In addition, less time will be consumed if the intermediary unloading is omitted, for instance, through estimation of springback using process simulation.

Comparison of Different Process Control Strategies. Existing control methods based almost exclusively on direct and only infrequently on indirect strategies can deliver satisfactory results in bend angle accuracy.

Direct process control with intermediary unloading is characterized by high accuracy and process reliability but difficult handling. It is mostly applied for narrow-tolerance components. However, the determination of springback by an intermediate unloading and the related tool-bound angle sensors requires additional time and cost expenditure. If no close tolerances but rather high process velocities are required in the day-to-day operations, indirect process control without intermediary unloading is favored. Both control strategies are used in industry, although for different applications.

2.8 Other Bending Machines

In a leaf bending machine, a leaf bar indirectly bends a sheet instead of the movement of a punch, as shown in Fig. 2.50. The leaf brake is mostly used for prototype work, because of its slow production rate.

In a three-roll bending machine, all three rolls are hydraulically driven independently. A top roll can be adjusted to obtain the desired bent shape.

REFERENCES

- 2.1 C.T. Wang, G.L. Kinzel, and T. Altan, Mathematical Modeling of Plane-Strain Bending of Sheet and Plate, *J. Mater. Process. Technol.*, Vol 39, 1993, p 279–304
- 2.2 R. Hill, *The Mathematical Theory of Plasticity*, Oxford, London, 1950, p 288–294
- 2.3 R. Hill, Theoretical Plasticity of Textured Aggregates, *Mat. Proc. Cambridge Philos. Soc.*, Vol 85, 1979, p 179–181

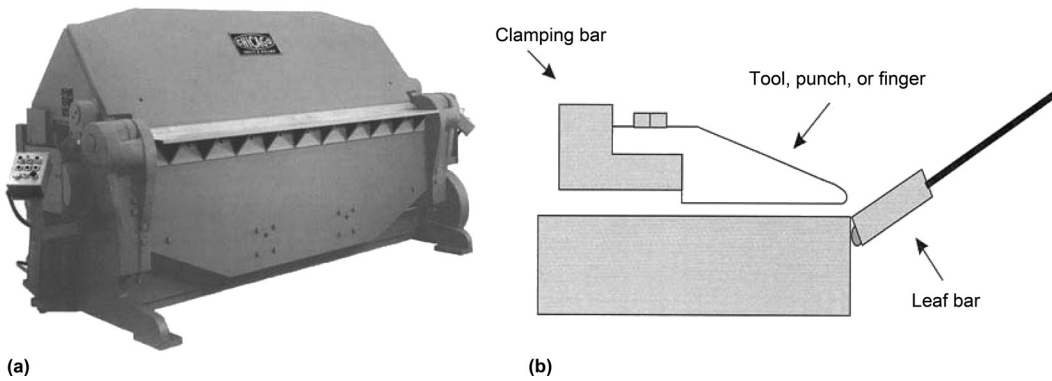


Fig. 2.50 (a) Leaf bending machine. Source: Ref 2.43. (b) Principle of leaf bending. Source: Ref 2.4

2.4 S. Kalpakjian, *Manufacturing Processes for Engineering Materials*, Addison Wesley, 1997

2.5 P. Raghupathi, M. Karima, N. Akgerman, and T. Altan, A Simplified Approach to Calculate Springback in Brake Bending, *Proc. NAMRC XI*, May 1983, p 165–171

2.6 Z.T. Zhang and D. Lee, Development of a New Model for Plane Strain Bending and Springback Analysis, *J. Mater. Eng. Perform.*, Vol 4, 1995, p 291–300

2.7 K. Lange, Chap. 19, *Handbook of Metal Forming*, McGraw-Hill Book Company, 1986

2.8 T. Hallfeldt and C. Greisert, Formability and Mechanical Properties of Advanced High Strength Steel Sheets for Automotive Applications, *Proc. of Recent Advances in Manufacture and Use of Tools and Dies and Stamping of Steel Sheets*, Oct 5–6, 2004 (Olofström, Sweden), p 96–100

2.9 Y.E. Ling, H.P. Lee, and B.T. Cheok, Finite Element Analysis of Springback in L-Bending of Sheet Metal, *J. Mater. Process. Technol.*, Vol 168, 2005, p 296–302

2.10 Z. Marciniak, J. Duncan, and S.J. Hu, *Mechanics of Sheet Metal Forming*, Butterworth-Heinemann, Linacre House, Jordan Hill, Oxford, 2002

2.11 R. Cobo, M. Pla, R. Hernandez, and J.A. Benito, “Analysis of the Decrease of the Apparent Young’s Modulus of Advanced High Strength Steels and Its Effect in Bending Simulations,” IDDRG, June 1–3, 2009 (Golden, CO)

2.12 N. Kardes, Y. Demiralp, G. Sukumaran, C. Choi, H. Kim, J. Gonzalez-Mendez, N. Agarwal, M. Deshpande, and T. Altan, “Control of Springback and Dimensional Tolerances in Forming of Advanced High Strength Steel (AHSS) Parts, Part I: Load-Unload Tensile Test and V-Die Bending,” Report CPF/1.4/10/01, Center for Precision Forming, The Ohio State University, 2010

2.13 H. Kim, N. Nargundkar, and T. Altan, Prediction of Bending Allowance and Springback in Air Bending, *J. Manuf. Sci. Eng.*, Vol 129, 2007, p 1–10

2.14 G. Sachs, *Principles and Methods of Sheet Metal Fabrication*, Van Nostrand Reinhold, New York, 1976, p 95–115

2.15 M.S. Walp, “Impact Dependent Properties of A/UHSS,” SAE Paper 2007-01-0312, 2007

2.16 J. Datsko and C.T. Yang, Correlation and Bendability of Materials with Their Tensile Properties, *J. Eng. Ind.*, Vol 82, 1960, p 309

2.17 A. Hudgins, D. Matlock, J. Speer, J. Fekete, and M. Walp, The Susceptibility to Shear Fracture in Bending of AHSS, *Materials Science and Technology (MS&T) Conference* (Detroit, Michigan), 2007, p 145–157

2.18 M. Yoshida, F. Yoshida, H. Konishi, and K. Fukumoto, Fracture Limits of Sheet Metals under Stretch Bending, *Int. J. Mech. Sci.*, Vol 47, 2005, p 1885–1896

2.19 D. Uko, R. Sowerby, and J.L. Duncan, Strain Distribution in the Bending under Tension Test, *CIM Bull.*, May 1977, p 127

- 2.20 K. Kim and T. Altan, Shear Fracture in Bending Advance High-Strength Steel Sharp Die Radii Make AHSS Vulnerable, *Stamp. J.*, Dec 2008, p 14–15
- 2.21 H.E. Theis, *Handbook of Metal Forming Processes*, Marcel Dekker, Inc., 1999
- 2.22 C. Wick, J.T. Benedict, and R.F. Veilleux, Chap. 10, *Forming*, Vol 2, *Tool and Manufacturing Engineers Handbook*, 4th ed., SME, Dearborn, MI, 1984
- 2.23 G. Oehler, *Bending*, München, Hanser, 1963
- 2.24 P. Sartkulvanich and T. Altan, Investigation of Springback in Rotary Bending, *Stamp. J.*, Sept/Oct 2009, p 10–11
- 2.25 P. Sartkulvanich, B. Kroenauer, R. Golle, A. Konieczny, and T. Altan, FEA of the Effect of Blanked Edge Quality upon Stretch Flanging of AHSS, *Ann. CIRP*, Vol 59 (No. 1), 2010, p 279–282
- 2.26 O.D. Lascoe, *Handbook of Fabrication Process*, ASM International, 1988, p 181–190
- 2.27 B. Carlsson, P. Bustard, and D. Eriksson, “Formability of High Strength Steel Dual Phase Steels,” Paper F2004F454, SSAB, Tunnsplatt AB, Borlange, Sweden, 2004
- 2.28 A. Konieczny and T. Henderson, “On Formability Limitations in Stamping Involving Sheared Edge Stretching,” SAE Paper 2007-01-0340, 2007
- 2.29 H. Takuda, K. Mori, H. Fujimoto, and N. Hatta, Prediction of Forming Limit in Bore Expanding of Sheet Metals Using Fracture Criterion, *J. Mater. Process. Technol.*, Vol 92–93, 1999, p 433–438
- 2.30 MAG, The Global Machine Tool Manufacturer, www.mag-ias.com/en.html
- 2.31 E.M. Mielnik, *Metalworking Science and Engineering*, McGraw-Hill, Inc., 1991, p 700–742
- 2.32 A. Klein, Get a Better Angle on Press Brake Bending, *Form. Fabric.*, May 2003
- 2.33 S.K. Kwok and W.B. Lee, The Development of a Machine Vision System for Adaptive Bending of Sheet Metals, *J. Mater. Process. Technol.*, Vol 48, 1995, p 43–49
- 2.34 T. Oenoki and T. Otani, Development of Highly Accurate Bending System with the Bend Angle Sensor, *Adv. Technol. Plast.*, Vol 2, 1996, p 590–582
- 2.35 Trumpf Inc., Farmington, CT, www.trumpf.com
- 2.36 Enutron International, Pennsburg, PA, www.enutron.com
- 2.37 Wila USA, Hanover, MD, www.wilausa.com
- 2.38 Cincinnati Inc., Harrison, OH, www.e-ci.com
- 2.39 S. Chatti, “Production of Profiles for Lightweight Structures,” Habilitation Thesis, Books on Demand GmbH, Nordstedt, Germany, 2005
- 2.40 B. Heller, “Halbanalytische Prozess-Simulation des Freibiegens von Fein- und Grobblechen,” Ph.D. thesis, University of Dortmund, Verlag Shaker, Aachen, Germany, 2002
- 2.41 J. Reissner, M. Meier, and H.J. Renker, Computer Aided Three Point Bending of Multiple Bend Profiles, *Ann. CIRP*, Vol 34 (No. 1), 1985, p 259–264
- 2.42 N. Ridane, “FEM-Gestützte Prozessregelung des Freibiegens,” Ph.D. thesis, University of Dortmund, Verlag Shaker, Aachen, Germany, 2008
- 2.43 American Machine Tool Corp., Chicago, IL, www.americanmachinetools.com
- 2.44 S.D. Benson, V-Die Selection for Press Brakes, *The Fabricator*, March 2006, p 40–41

CHAPTER 3

Process Simulation

Manan Shah, The Ohio State University
Partchapol Sartkulvanich, RTI International Metals Inc.

UNTIL RECENTLY, the design of metal forming tools was based mainly on knowledge gained through experience and expensive trial-and-error processes. However, today the metal forming industry is making use of finite-element methods even in the early stages of die and process design. The emerging role of modeling and simulation can be explained by the growing competition in the world market that requires shorter lead times and cost-effective solutions while developing a new design of process and product.

3.1 Advantages of Process Simulation

The lead time for designing and manufacturing sheet metal parts can be shortened considerably. In several cases, by using simulation the tool development and die try-out time has been reduced by approximately 50% and can be expected to be reduced even further over the next few years. The development of simulation techniques reached a stage where the results can be fed directly into the press (Ref 3.1).

Currently, the practical objectives of forming simulation can be summarized into three main groups (Ref 3.2):

- Time reduction
 - a. Early evaluation of producibility
 - b. Reduction in the development times
 - c. Reduction of the try-out times
 - d. Quick response to needed modifications
- Cost reduction
 - a. Lower product costs
 - b. Reduction of the die costs

- c. Press downsizing
- d. Increase of reliability
- Increase of product quality
 - a. Optimal selection of the workpiece material
 - b. Production of more complicated parts
 - c. Know-how accumulation for new materials
 - d. Press repeatability

In sheet metal forming, modeling can be used for many purposes, such as predicting material flow, stress, strain, and temperature distribution; estimating forces; predicting potential sources of failures; and improving part quality. Simulations can be effectively performed at various stages of design to support decision-making.

3.2 Commercial Codes for Forming Simulations

The basic concept of the finite-element method (FEM) is one of discretization. The model is constructed by the number of finite points, called nodes, and elements systematically divided within the object. The assembly of elements is connected together appropriately on their boundaries. The function is approximated locally within each element by continuous functions that describe their node values associated with that particular element (Ref. 3.3). Finite-element analysis consists of five major steps (Ref 3.3):

1. Problem identification
2. Element definition

3. Derivation of the equations for one element
4. Combining all individual element equations to a global equation
5. Numerical solution of the global equations

Table 3.1 lists some of the commercially available software packages that are used by the industry for the simulation of sheet metal forming processes.

The basic code features, such as static implicit, dynamic explicit, and inverse (one-step) methods indicated in Table 3.1, are summarized as follows.

The quasi-static implicit approach enables a full static solution of the deformation problem with a convergence control. However, this approach is limited by determining the contact conditions. Another drawback of this approach is that the computational time of a simulation increases quadratically with an increase in element number. This numerical discretization is recommended mainly for bulk metal forming processes. For sheet metal forming, explicit (dynamic) models are appropriate.

Dynamic Explicit. A notable advantage of using the dynamic explicit approach is its robustness along with a higher computational speed and a lower memory requirement as compared to the static implicit method. The explicit approach also predicts wrinkles along the workpiece, which are initiated through numerical inaccuracies. The region where these wrinkles occur is quite accurately determined, but the number and amplitude of wrinkles may be inaccurate.

Inverse (One-Step) Method. The so-called one-step simulation codes are suited for use in the design stage, where the geometry of the part

is not fully described and the tooling data do not exist. Combining the functions of the computer-aided design (CAD) software and the automatic meshing ability, this one-step method may give some valuable information about the feasibility of the new concept at the first stages of the design process. In certain cases, the accuracy of these results can be low (Ref 3.2).

3.3 Steps Involved in FEM Simulations

A user primarily wants to know whether it is feasible to form a part without any defects, such as fracture or wrinkling. From a practical perspective, finite-element simulations include an input to simulations, a solution, and an output/predictions from simulations (Ref 3.4).

Input to Simulations

To conduct reliable process simulations, it is necessary to have accurate information on the geometry of the tooling, the sheet metal/blank dimensions and properties, and the coefficient of friction at the tool/die and sheet interface. The input preparation is often called preprocessing. Reliable input parameters are needed to model the sheet material for the successful modeling of a stamping simulation at room and elevated temperatures. Introduction of multiphase steels (advanced high-strength steels, transformation-induced plasticity steels, commercially pure steels) makes the modeling of a material even more difficult. Thus, in addition to the simulation capability, it is necessary to have standard test methods for determining the important input parameters, such as mechanical properties of the material and interface friction conditions (Ref 3.5).

Geometry (CAD Model) for the Tooling. Creating the geometry is the first step of preprocessing. The tooling geometry with dimensions is created using a CAD program. Depending on the geometric complexity, the part can be simulated as two-dimensional, axisymmetric, or even three-dimensional for certain cases. To reduce the complexity and improve the efficiency of the simulation, the user may remove some minor geometric features that will not have a significant effect on the material flow. In cases where the meshing capability of the finite-element codes is not able to create a customized mesh, these CAD models could be exported to a mesh generator, for example, Altair Hypermesh software, to create a finer customized mesh.

Table 3.1 Commercial software used for sheet metal forming simulations

Software	Origin and company	Code type
ABAQUS-Standard	HKS, USA	Static
MARC	MSC, USA	implicit
NIKE3D	LSTC, USA	
AUTOFORM-Explicit	Autoform, Switzerland	Static implicit (special)
DYNA3D	LSTC, USA	Dynamic
PAMSTAMP	ESI, France	explicit
OPTRIS	Dynamic Software, France	
AUTOFORM-one step	Autoform, Switzerland	Inverse
ISO PUNCH	Sollac, France	methods
SIMEX2	SimTech, France	

Source: Ref 3.2

Material Properties. It is necessary to have accurate material data to predict the material flow. In the past, the material properties were determined by uniaxial tensile test, but these data may be insufficient for conducting sheet metal forming simulations. The data obtained from tensile tests are for relatively low strains and must be extrapolated to use under higher strains. Thus, the applicability of tensile test data must be used with caution in sheet forming simulations, where higher strains may occur. A circular viscous pressure bulge test was developed by the Engineering Research Center at The Ohio State University to estimate the flow stress of the material in a biaxial state through inverse analysis. Using the bulge test would give more reliable stress-strain data that are applicable at higher strains than the tensile test and could eliminate the need for extrapolation (Ref 3.6).

The coefficient of friction is required as another input parameter while conducting sheet metal forming simulations. In most cases, the friction coefficient is considered a constant throughout the stamping process. In reality, the frictional behavior depends on the surface roughness of the sheet and tool material, contact pressure, sliding speed, lubrication, and temperature in the sliding surface (Ref 3.1, 3.7). For room-temperature conditions, usually the strip drawing test, modified limiting dome height test, deep drawing test, or the stamping lubricant tester can be used to determine the friction coefficients. For elevated-temperature conditions, the coefficient of friction can be calculated by several other methods, such as by using the tribosimulator (Ref 3.8), modified cup drawing test (Ref 3.9), and pin-on-disc test (Ref 3.10).

Influence of Temperature and Heat-Transfer Coefficients. Because the material at elevated temperatures is strain-rate sensitive, the material properties must be considered as a function of temperature and strain rate simultaneously. This capability is included with the latest version of commercial codes; for example, PAMSTAMP-2G (2011) and LS-DYNA are particularly useful in the simulation of warm forming of lightweight alloys.

The hot forming and quenching processes of high-strength steels are widely used in the automotive industry for improving part strength as well as reducing part weight. The simulation of this process requires a thermomechanically coupled simulation, because the user would like to have an accurate idea about the temperature dis-

tribution across the sheet metal part. The heat-transfer coefficients between the sheet metal and the tooling must be known accurately to be able to predict the temperature gradient. Some codes, such as LS-DYNA and PAMSTAMP-2G (2011), have the capability to input a variable surface heat-transfer coefficient as a function of pressure or gap.

Output/Predictions from Simulations

After the user inputs all of the process conditions (tooling geometry, boundary conditions, and friction coefficients) and the appropriate material properties, the finite-element solver checks for any errors and may give warnings. In this step, the user can check if all the input parameters were correctly inserted in the finite-element code. After performing the check, the simulations are run and the results are examined in the postprocessing step. The output data obtained from the finite-element simulations give an idea about the defects that occurred in the part. They also predict the material flow and calculate the forces required in forming and strains developed in the part during deformation.

Summarized as follows is the list of outputs that can be obtained through finite-element simulations that will help the user understand whether the part can be formed without any defect:

- Part formed (thickness along the curvilinear length of a section)
- Temperature distribution (in the workpiece and the tooling)
- Pressure distribution on the tooling
- Punch force and blank holder force versus punch stroke
- Stress (von Mises) and strain (maximum plastic strain) distribution along the workpiece
- Formed part contour (during loading and unloading to obtain a measure of springback)

To validate these finite-element predictions/outputs, experiments are conducted using the same process parameters, and a comparison is made. These studies, comprising their objectives, input parameters, finite-element model, and output/predictions, are explained in Section 3.4, “Case Studies in Sheet Metal Forming” in this chapter.

Prediction of Stamping Defects

Defects such as tearing and wrinkling are commonly observed during the stamping and

hydroforming processes. Tearing mostly occurs due to excessive thinning along the part and must be corrected to avoid failure of the part during production (Ref 3.11).

To predict the defect of tearing during finite-element simulation, percentage thinning, or the forming limit diagram (FLD), is commonly used. Percentage thinning calculates the change in thickness over the initial thickness at every time step or punch progression. The FLD shows the limiting in-plane strain beyond which failure would occur. If the strain calculated at any point in the formed part lies above the forming limit curve, the part is expected to fail, as shown in Fig. 3.1.

The other common defect observed in stamping is wrinkling, which occurs due to excessive compressive stresses. Researchers (Ref 3.12, 3.13) used Timoshenko's buckling theory in the explicit finite-element code to calculate the critical stresses. These critical stresses were compared with the stresses in the sheet material at every step to check for the potential failure of wrinkling. Note that the assumptions of the boundary conditions are very critical in determining the stresses, because they cause a huge difference in the calculation of the stresses. Thus, this method may not be entirely reliable to predict the defect of wrinkling in the stamping and sheet hydroforming processes (Ref 3.11).

In predicting deformation and springback when forming advanced high-strength steels (dual-phase alloys), the conventional model of

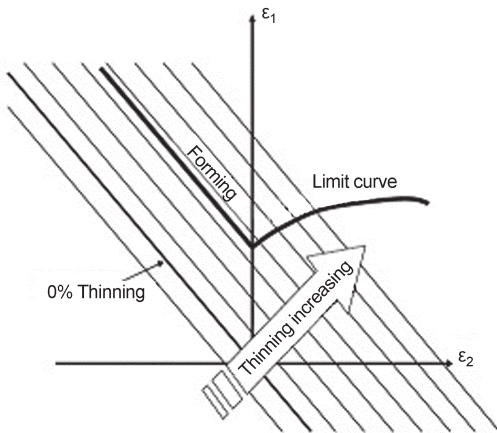


Fig. 3.1 Schematic of forming limit diagram curves and constant thinning to illustrate the choice of indicator for failure in the part during the stamping/sheet hydroforming process. Source: Ref 3.11

FLD commonly used for mild steels may not be a reliable criterion for predicting fracture, because the dual-phase alloys have unusual characteristics, such as E modulus that varies with strain, and the strain-hardening coefficient (n) that is not constant with varying strain.

3.4 Case Studies in Sheet Metal Forming

These case studies/practical examples of applications of finite-element simulations are presented for the improvement of existing or for designing new forming processes for manufacturing sheet metal parts. Included in each of these cases is the list of required inputs to conduct a successful simulation, and the outputs/predictions give the user an idea of the appropriate changes to make, if necessary, in the design phase.

Blanking/piercing is demonstrated by the following case study (Ref 3.14).

Objective. To evaluate different ductile fracture criteria and determine the critical damage value for blanking simulations of DP590

In this study, all objects were set to be rigid except for the sheet, which is modeled as plastic. The simulations were considered to be non-isothermal because local temperature increases may soften the work material and affect the shearing conditions. The Johnson-Cook constitutive model was used to represent the material data to be used in the FEM simulations. This constitutive model captures the strain-rate and temperature dependency of the material, which is necessary for the nonisothermal simulation.

To emulate material separation in the finite-element simulation, ductile fracture criteria and the element deletion routine were used. Ductile fracture criteria can be represented as a function of stress and strain history. The critical damage value (CDV) is the maximum damage value that indicates crack initiation in the simulation. Once the fracture values at any mesh elements reach the CDV, those elements will be deleted to emulate material separation. Eight ductile fracture criteria were evaluated. Four CDVs were obtained by matching the length of the shear zone to that of experiments for four punch/die clearances. Theoretically, one material should exhibit one CDV. Therefore, a smaller deviation of the CDVs should reflect a better applicability of the criterion.

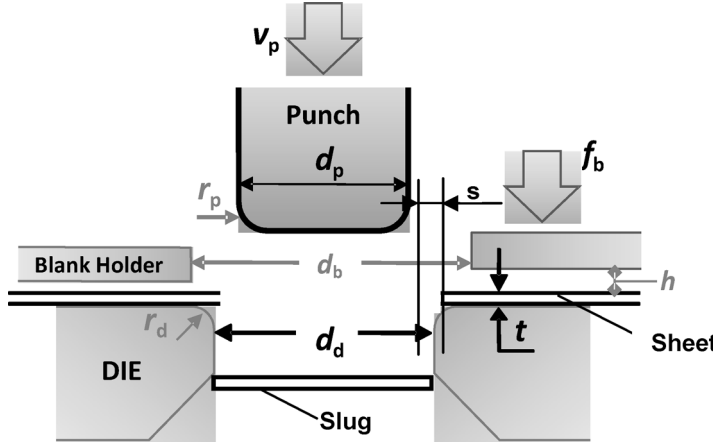
Table 3.2 gives the tooling geometry dimensions and the friction coefficients that are used to conduct finite-element simulations in blanking.

Output. The adapted Rice and Tracey criterion seems to be the most applicable fracture criterion in FEM simulations of blanking of

DP590 because of the lowest deviation of CDV over the mean CDV, as shown in Fig. 3.2.

Figure 3.3 shows a comparison of the length of the shear zone obtained in experiments (Ref 3.15) and from FEM simulation using the mean CDV of the fracture criteria from the normal-

Table 3.2 Schematic of the blanking process and experimental and simulation settings



Punch velocity (assumed according to conventional blanking)	$v_p = 150 \text{ mm/s (5.9 in./s)}$
Model assumption	Nonisothermal and axisymmetric
Shear friction coefficient	$\mu = 0.1$
Punch diameter	$d_p = 10 \text{ mm (0.4 in.)}$
Die diameters (punch/die clearance) (using different die diameters for different punch/die clearances)	$d_{d1} = 10.031 \text{ mm (0.39492 in.)} \quad (s = 1.1\%)$ $d_{d2} = 10.179 \text{ mm (0.40075 in.)} \quad (s = 6.4\%)$ $d_{d3} = 10.378 \text{ mm (0.40858 in.)} \quad (s = 13.5\%)$ $d_{d4} = 10.582 \text{ mm (0.41661 in.)} \quad (s = 20.8\%)$
Sheet thickness	$t = 1.4 \text{ mm (0.06 in.)}$
Blank holder force	$f_b = 6.7 \text{ kN (1.5 kip)}$
Die corner radius (assumed)	$r_d = 0.05 \text{ mm (0.002 in.)}$
Punch corner radius (assumed)	$r_p = 0.05 \text{ mm}$
Diameter of the blank holder	$d_b = 15 \text{ mm (0.59 in.)}$
Clearance between blank and stripper plate	$h = \sim 0$

Source: Ref 3.15

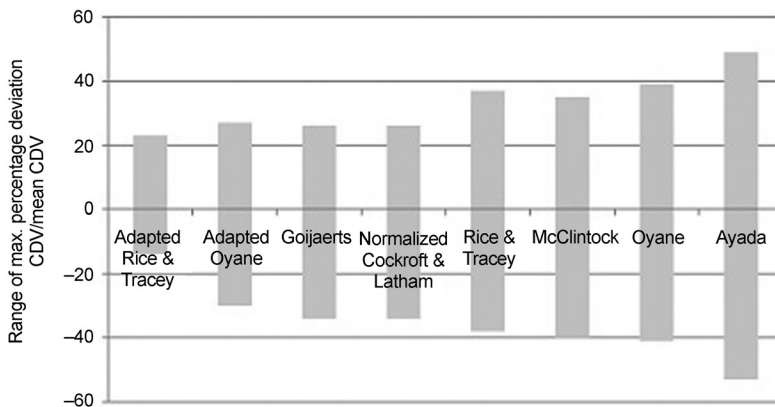


Fig. 3.2 Range of maximum percentage deviation (critical damage value, or CDV, divided by mean CDV) of different fracture criteria used in the blanking simulation of DP590. Source: Ref 3.14

ized Cockroft and Latham, adapted Rice and Tracey, and adapted Oyane. This figure shows that the implementation of the adapted Rice and Tracey criterion results in the lowest deviation from experimental results. A comparison of the predictions obtained using the adapted Rice and Tracey criterion with the experimental results is shown in Table 3.3. The lengths of the shear and fracture zone are in good agreement with the experimental results. The error of the length of the rollover zone increases significantly with decreasing punch/die clearance. Figure 3.4 shows the predicted sheared edge from a blanking simulation with a punch/die clearance of 20.8%.

Deep drawing of round and rectangular cups is demonstrated by the following case study (Ref 3.16).

Objective. To check the formability of round cup drawing and understand the effects of various input parameters using the finite-element code PAMSTAMP-2G

ASTM A1011 DS type B material was used in the deep drawing experiments of round and rectangular cups (Ref 3.16). A finite-element simulation model was established according to an experimental setting. Shell elements were used to define the mesh of the blank sheet. Punch, die, and blank holder were assumed to be rigid, and the sheet was assumed to be elastic-plastic. Biaxial and elliptical bulge tests were conducted to obtain material flow stress properties. Material properties included the strength coefficient (K) and strain-hardening coefficient (n) for $\bar{\sigma} = K\bar{\epsilon}^n$. The tool dimensions used in the simulations and experiments are listed as follows and are schematically shown in Fig. 3.5.

The influences of the following process variables (input parameters, see Table 3.4) on the finite-element simulation results were analyzed:

- Blank diameter
- Blank thickness

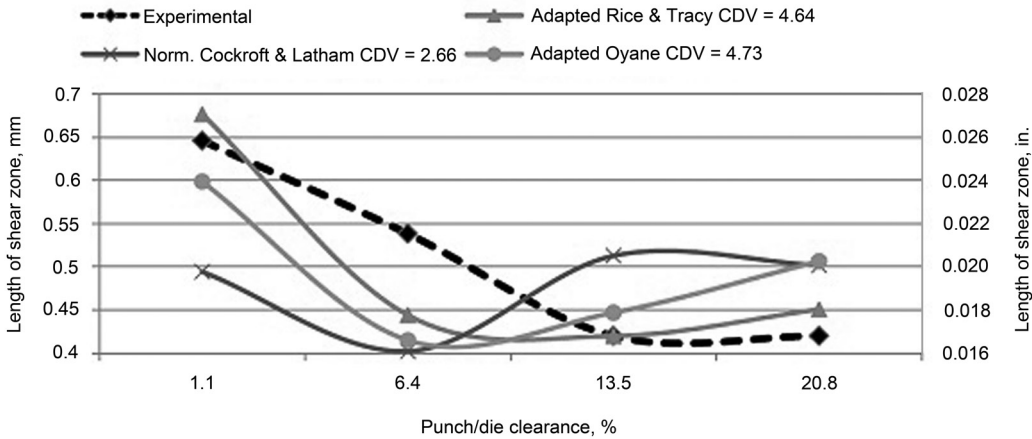


Fig. 3.3 Comparison of obtained length of shear zone using different fracture criteria. CDV, critical damage value. Source: Ref 3.14

Table 3.3 Comparison of experimental results with finite-element method (FEM) results using adapted Rice and Tracey criterion in blanking DP590

Punch/die clearance, %		1.1	Error	6.4	Error	13.5	Error	20.8	Error
Shear zone (z_s), mm	FEM	0.677	5%	0.444	21%	0.420	0%	0.451	7%
	Exp.	0.646		0.538		0.420		0.420	
Fracture zone (z_f), mm	FEM	0.574	18%	0.806	8%	0.809	3%	0.732	2%
	Exp.	0.678		0.744		0.783		0.719	
Rollover zone (z_r), mm	FEM	0.158	52%	0.153	23%	0.173	14%	0.211	23%
	Exp.	0.076		0.118		0.197		0.261	
Burr height (z_b), mm	FEM	0.033	96%	0.028	36%	0.035	24%	0.048	45%
	Exp.	0.001		0.018		0.022		0.027	

Source: Ref 3.14

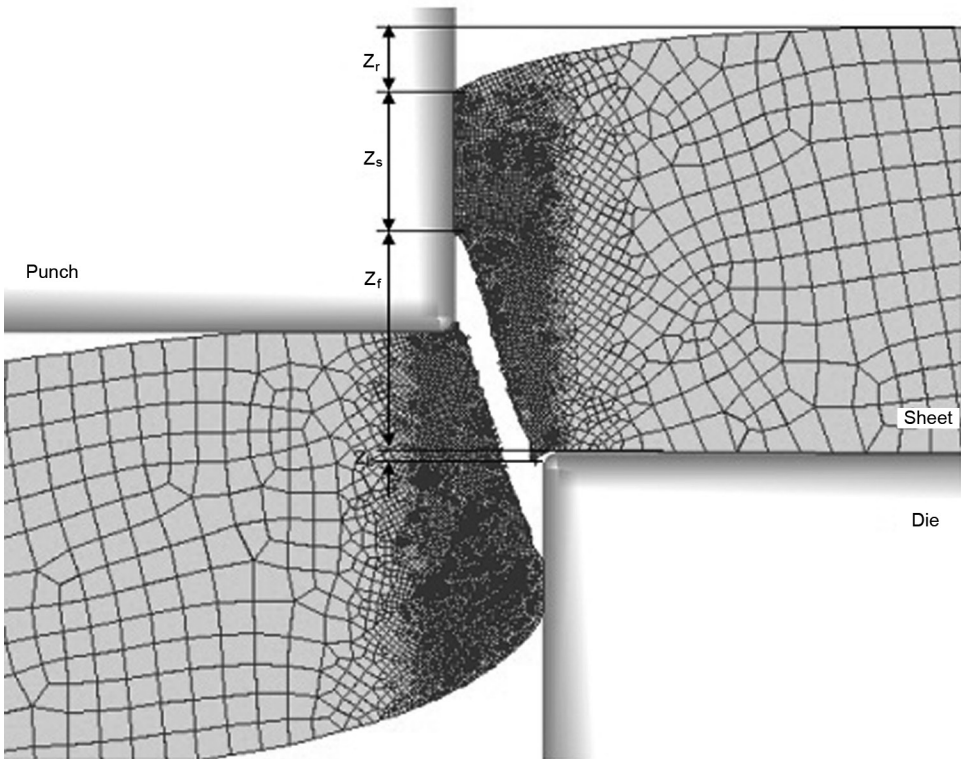


Fig. 3.4 Sheared edge obtained in simulation (punch/die clearance = 20.8%, z_r = rollover zone, z_s = shear zone, z_f = fracture zone, z_b = burr height). Source: Ref 3.14

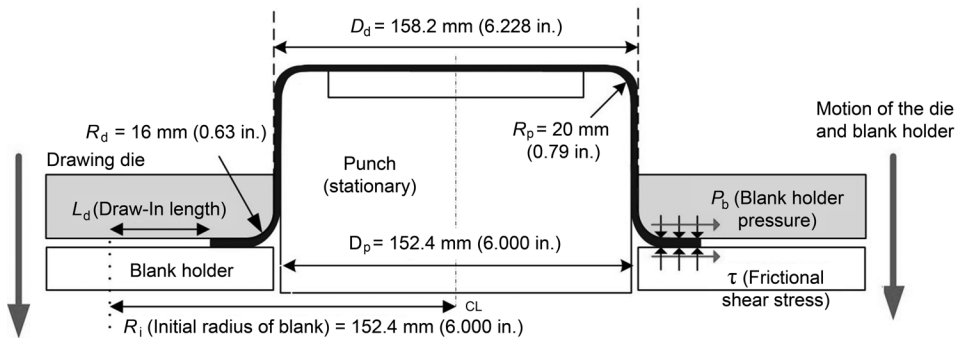


Fig. 3.5 Tool geometry used in deep drawing of a round cup

- Coefficient of friction (μ)
- Blank holder force (BHF)

Several simulations were conducted and the effects were investigated by varying only one process parameter at a time and keeping all the others constant in the simulations to eliminate the interaction between various process parameters and to study the individual effects. The

predictions were then compared with experimental results. The finite-element model is shown in Fig. 3.6.

Output. To see the effect of the various process variables (input parameters), the following output variables were studied:

- Equivalent stress and strain distribution along the part

- Punch force versus stroke curve
- Draw-in of the sheet (flange draw and cup depth)
- Maximum thinning (percentage) along the curvilinear length of the part, showing the point where maximum thinning occurs on the part formed

In deep drawing of rectangular cups, the prediction of the blank shape and BHF is critical for achieving a successful forming operation.

A **progressive die sequence** is demonstrated by the following case study (Ref 3.17).

Objective. The Engineering Research Center for Net Shape Manufacturing (ERC/NSM), in cooperation with a commercial stamping company, designed a progressive die sequence whose

main objective was to estimate the number of forming stages, the tool geometry for each stage (punch/die diameter, and punch corner and die corner radii), and the process parameters for each stage.

The ERC/NSM improved the existing design through analysis using finite-element simulation to reduce the potential for failure in the formed part (excessive thinning and wrinkling). The estimated final sequence to form the part without final trimming is shown in Fig. 3.7, and the input parameters are in Table 3.5. In addition, the blank shape was estimated to reduce thinning and excessive scrap material. The predicted thinning distribution at the final step is shown in Fig. 3.8; the maximum thinning was less than 30%, and no wrinkling was observed (Ref 3.18).

It could be observed that for the sequence predicted by finite-element analysis (FEA) and using the optimal blank shape, maximum thinning in all the critical locations is less than 30%

Table 3.4 Input parameters

Material properties of ASTM A1011 DS type B	
Young's modulus (E), GPa (10^6 psi)	210 (30)
Poisson's ratio (ν)	0.3
Strength coefficient (K), MPa (ksi)	498.8 (72.35)
Strain-hardening coefficient (n)	0.131
Normal anisotropy	1.5
Process parameters	
Coefficient of friction (μ)	0.07–0.09
Blank holder force, kN (kip)	445 (100)
Ram speed, mm/s (in./s)	15 (0.59)

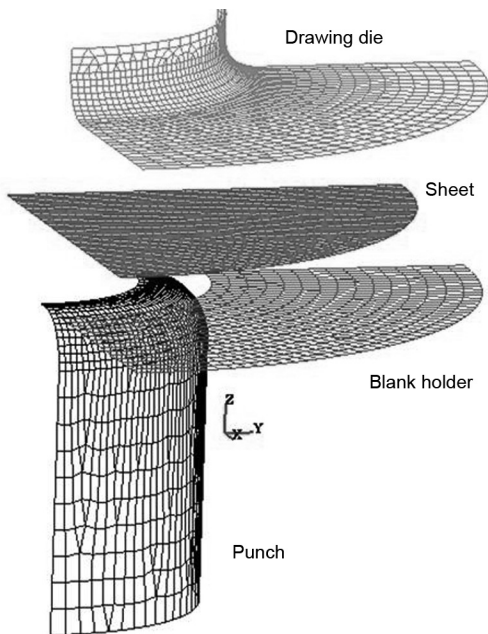


Fig. 3.6 One-fourth finite-element model of round cup drawing

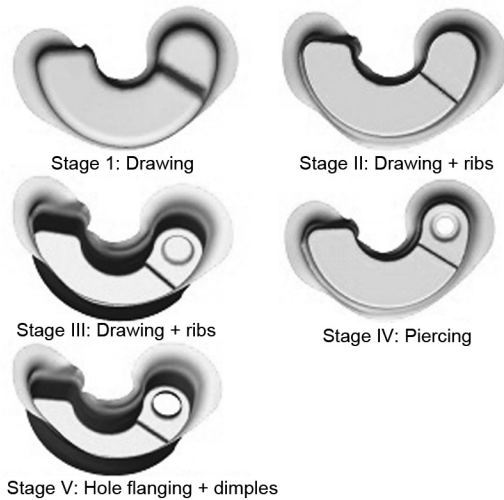


Fig. 3.7 Schematic of the designed progressive die sequence by the Engineering Research Center for Net Shape Manufacturing. Source: Ref 3.17

Table 3.5 Input parameters for the finite-element simulation of stamping with progressive dies

Sheet material	AKDQ-1006, thickness = 0.5 mm (0.020 in.)
Flow stress (material 1008)	Obtained from viscous pressure bulge test
Anisotropy constants	$r_0 = 1.92, r_{45} = 1.83, r_{90} = 2.14$
Force on draw pad, kN (lb)	12 (2800)
Force on knockout, kN (lb)	0.9 (200)
Interface friction condition (μ)	0.1
Punch stroke, mm (in.)	15.1 (0.594)

except at location “E,” which would be trimmed. This indicates that the sequence estimated by FEA along with optimal initial blank geometry would result in minimum thinning and reduce the risk of failure (Ref 3.17).

Blank holder force optimization is demonstrated by the following case study (Ref 3.19).

Objective. To develop an optimization technique coupled with finite-element simulation to estimate the BHF variable in location/space and constant with punch stroke in order to form a full-sized automotive panel (liftgate-inner) from aluminum alloy A6111-T4 and from bake-hardened steel BH210

A recent multipoint cushion control system allows variable BHF setting in the stamping process, which provides the flexibility to control various amounts of stretching for different

regions of the formed part. The finite-element model of the liftgate tooling in finite-element code PAMSTAMP (2000) is shown in Fig. 3.9, and the simulation parameters are listed in Table 3.6. One-half of the tool was modeled due to symmetry in the tool geometry and boundary conditions. The segmented elastic blank holder was modeled as an elastic object to account for its elastic deflection and to accurately consider the variation of the BHF in space. The material properties of the workpiece material (A6111-T4 thickness = 1.0 mm, or 0.04 in.; BH210 thickness = 0.815 mm, or 0.032 in.) were obtained from a viscous pressure bulge test.

With the BHF variable in space/location and constant in time/stroke, each cushion pin applies a different force. Hence, the design variables were individual pin forces, and the num-

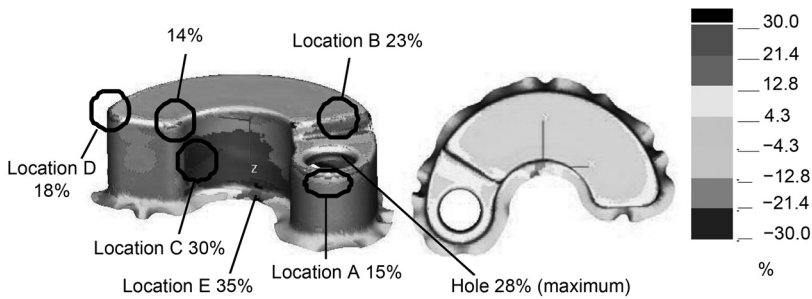


Fig. 3.8 Thinning distribution in the final part predicted by finite-element simulation using optimum initial blank geometry. Source: Ref 3.17

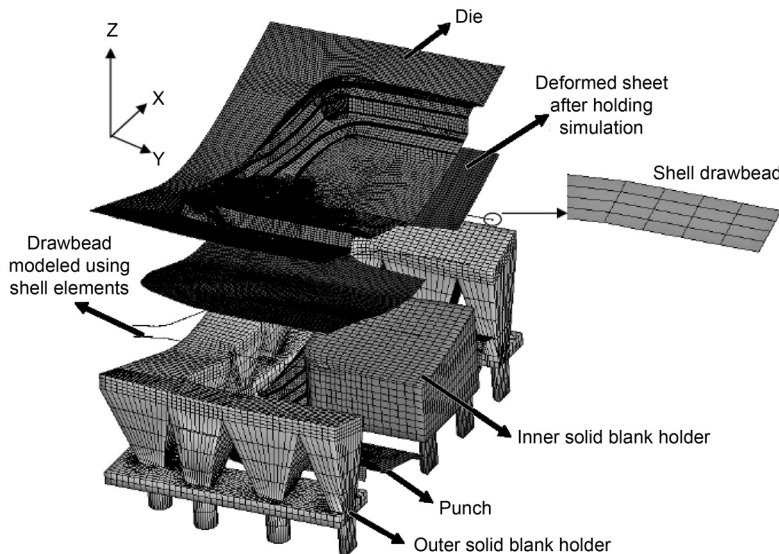


Fig. 3.9 Schematic of the finite-element model for the forming simulation of a liftgate part. Source: Ref 3.19

ber of design variables for the liftgate-inner tooling was 15, due to symmetric conditions.

Output. The finite-element results in Fig. 3.10 show that the forces at pins 2, 3, and 4 were in the range of 45 to 50 kN (10 to 11 kip) to allow easy material flow in the two corners close to pins 2, 3, and 4 and to avoid the formation of wrinkles. Among the pins on the sides (pins 5 through 8), pin 6 applied higher BHF because the flange region close to pin 6 is subjected to compressive stress and resulted in thickening of the sheet due to the inherent shape of the die compared to flange regions in pins 5, 7, and 8. In the inner blank holder pins, pin 12 applied lower BHF to reduce thinning; however, pin 13

applied high BHF to reduce material flow and avoid thinning due to excessive opening of the inside cutout.

Sheet hydroforming with punch (SHF-P) is demonstrated by the following case study (Ref 3.20).

Objective. To establish a finite-element simulation model to determine the process parameters (BHF versus punch stroke, and pot pressure versus stroke) to form the part by the SHF-P process at room and elevated temperatures

The material properties of aluminum alloy 5754-0 at room temperature up to 260 °C (500 °F) were obtained from tensile tests (Ref 3.21). Advantages of the SHF-P process are tool cost reduction, because only one side of the die is used, and the capability to form parts that are difficult to form by conventional stamping operations. A two-dimensional axisymmetric finite-element model of the tool geometry is shown in Fig. 3.11, and the input parameters used in the SHF-P room-temperature simulation are listed in Table 3.7.

The experimental measured pot pressure (reaches a steady-state pressure of 2 MPa, or 300 psi) is used as an input for the fluid pressure into finite-element simulations for SHF-P simulations. If extra fluid pressure was exerted on the sheet, it may cause the sheet to bulge unexpectedly, and there may be a probability that the blank holder would lift up.

Output. The thinning profile obtained from the finite-element results for the SHF-P process for a punch stroke of 34.3 mm (1.35 in.) is shown in Fig. 3.12. This figure also shows the maximum thinning location along the curvilinear

Table 3.6 Input parameters for the liftgate-inner forming finite-element simulation

Sheet material	BH210	A6111-T4
Sheet thickness, mm (in.)	0.815 (0.032)	1 (0.04)
Material properties	Flow stress obtained from bulge test	
	$r_0 = 1.475, r_{45} = 1.308,$ $r_{90} = 1.878$	$r_0 = 0.677, r_{45} = 0.534,$ $r_{90} = 0.562$
Friction coefficient (μ)	0.08	
Inner blank holder material	Zinc alloy cast (KirkSITE)	
Elastic material properties	Young's modulus = 83 GPa (12×10^6 psi), Poisson's ratio = 0.32, shear modulus = 0.25 GPa (0.04×10^6 psi)	
Outer blank holder material	Gray cast iron (SAE G4000)	
Elastic material properties	Young's modulus = 150 GPa (22×10^6 psi), Poisson's ratio = 0.29, shear modulus = 48 GPa (7×10^6 psi)	

Source: Ref 3.19

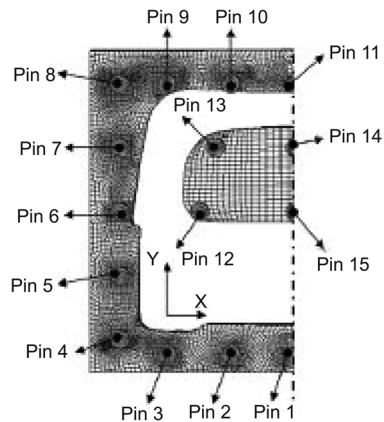
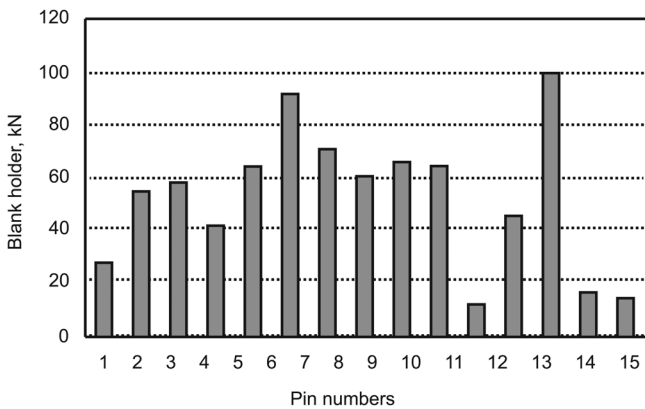


Fig. 3.10 Optimized blank holder force variable in space and constant in time (predicted by optimization for forming the liftgate part from aluminum alloy A6111-T4 of 1 mm, or 0.04 in., thickness). Source: Ref 3.19

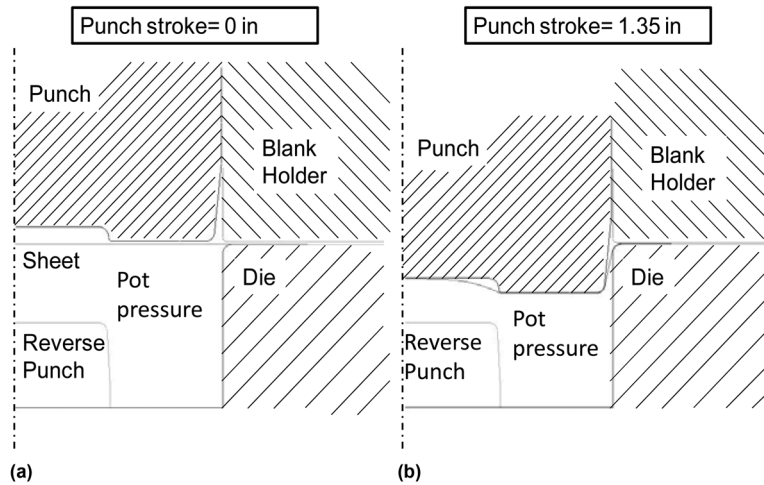


Fig. 3.11 Finite-element model of sheet hydroforming with punch at (a) initial position and (b) final stroke position (34.3 mm, or 1.35 in., downward). Prepared using PAMSTAMP-2G 2009. Source: Ref 3.20

Table 3.7 Input parameters for sheet hydroforming with punch process for AA5754 material

Blank diameter = 430 mm (17 in.); thickness = 1 mm (0.04 in.)

Mechanical properties

Blank material	AA5754-O
Flow stress	Ref 3.21
Young's modulus (E), GPa (10 ⁶ psi)	69 (10)
Poisson's ratio (ν)	0.3
r_{0° , r_{45° , r_{90°	1 (material assumed isotropic)

Interface condition

Friction coefficient (μ) (blank/tools)	0.12
--	------

Mesh

Element type	Shell (Belytschko-Tsay)
--------------	-------------------------

Object type

Blank	Elastic, plastic
Tools	Rigid

Process conditions

Aquadraw	Activate
Bulk modulus (K), GPa (10 ⁶ psi)	50 (7)
Pot pressure	Up to 2 MPa (300 psi) at room temperature; up to 5.8 MPa (840 psi) at elevated temperature
Blank holder force, kN (kip)	4–31 (1–7)
Punch stroke, mm (in.)	34.3 (1.35)
Punch velocity, mm/s (in./s)	1.9 (0.074)

Source: Ref 3.20

ear length of the SHF-P drawn part. From the finite-element results, the maximum thinning is located at point A, which is near the punch corner radius. From the experimental results, it was

found that many parts failed around this punch corner radius when the BHF was higher than 25 kN (6 kip).

Figure 3.13 shows a comparison of the part profiles measured by a coordinate measuring machine (CMM) and obtained from finite-element results. In Fig. 3.13, points A and B are the starting points of the CMM profile and the finite-element profile for the punch stroke of 34.3 mm (1.35 in.), respectively. For the CMM measurement of the experimental sample, a slight reverse bulge is observed at the blank holder portion of the part.

Another interesting output is the final flange perimeter of the drawn part, which can be used to validate the finite-element prediction of the material flow. The predicted final flange perimeter (finite-element results) for the SHF-P process was within ± 13 mm (0.5 in.) of the experimental results.

Figure 3.14 illustrates the comparison of the thickness profile of the sample formed at elevated temperature. The thickness profile for the finite-element simulation matches fairly well with the measurements. Finite-element results predict that maximum thinning occurred near the reverse bulge region (position 8) along the curvilinear length. Both finite-element simulations and experiments show that SHF-P at elevated temperature can form a cup with larger cup height and better reverse bulge profile than SHF-P at room temperature.

Hot stamping is demonstrated by the following case study (Ref 3.22).

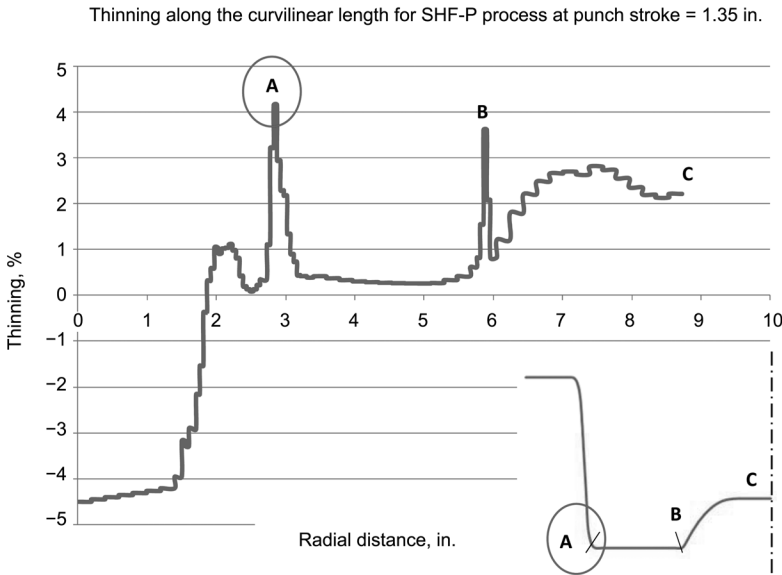


Fig. 3.12 Predicted thinning percentage along the curvilinear length for sheet hydroforming with punch process at a punch stroke = 34.3 mm (1.35 in.). Source: Ref 3.20

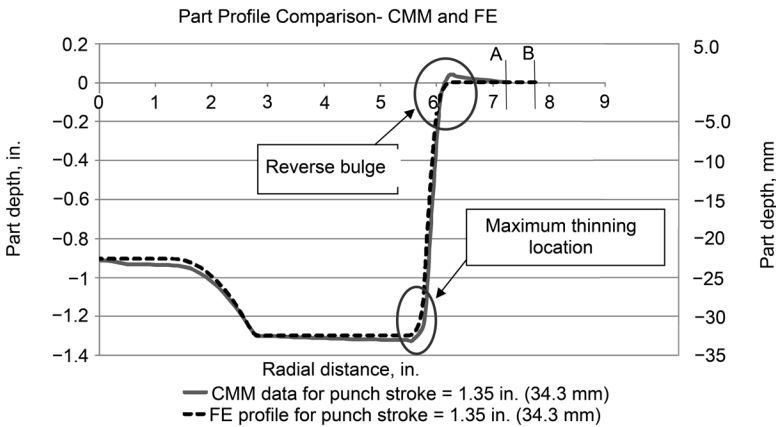


Fig. 3.13 Part profile comparison between experimental part measured using a coordinate measuring machine (CMM) and finite-element (FE) result (for part drawn by the sheet hydroforming with punch process). Source: Ref 3.20

Objective. To establish a coupled thermomechanical finite-element simulation model of the hot stamping process for 22MnB5 material

Commercial finite-element codes DEFORM and PAMSTAMP were used to analyze hot stamping of a B-pillar. Part geometries, material, and process information were taken from Ref 3.23, in the benchmark problem number 3. A two-dimensional section was initially chosen to study closely such effects as thermal expansion and shrinkage of the part, varying contact

conditions between die and tool, and heat transfer between tool and part. Simulation of hot stamping was modeled according to process sequence, which included blank heating and blank transfer, blank forming at elevated temperature, heat transfer during quenching, and air cooling.

Figure 3.15 shows the selected two-dimensional section of the B-pillar and the finite-element model used for plane-strain simulation of hot stamping. Table 3.8 shows the input parameters for the sheet material 22MnB5. The process pa-

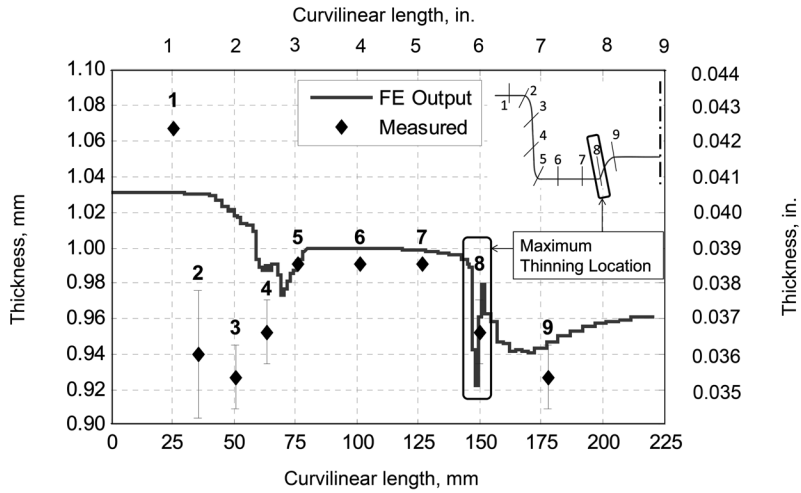


Fig. 3.14 Thickness profile along the curvilinear length measured by the mechanical indicator and compared with finite-element (FE) results for sheet hydroforming with punch using punch stroke = 38.1 mm (1.50 in.), average temperature = 150 °C (300 °F), pot pressure = 5.8 MPa (840 psi)

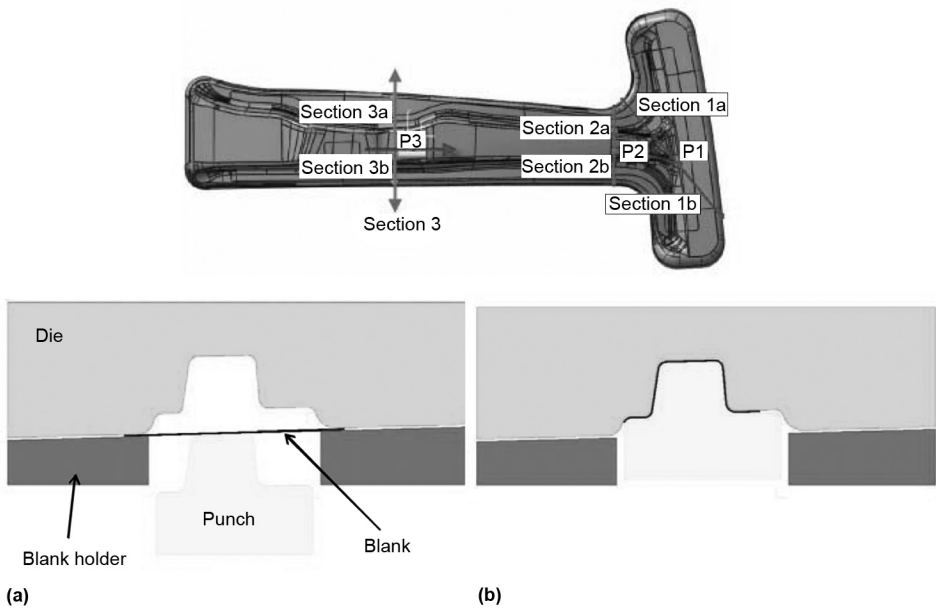


Fig. 3.15 Section 3 of a B-pillar was selected for conducting a two-dimensional plane-strain simulation. (a) Initial punch position. (b) Final punch position (punch moves up by 83.3 mm, or 3.28 in.). Source: Ref 3.24

rameters are listed in Table 3.9, showing the initial temperature of the blank and the tooling along with the heat-transfer coefficient. The material data corresponding to two temperature values of 650 and 800 °C (1200 and 1470 °F) were used for the sheet material, with each one provided for three different strain rates (0.01, 0.1, and 1 s⁻¹).

Figure 3.16 shows the heat-transfer coefficient between sheet and die (H_t) as a function of contact pressure (P), as provided in Ref 3.23. The parts are modeled using four-node quadrilateral elements. The blank has four elements in the thickness direction, which enables the calculation of through-thickness temperature gradients and thinning distribution.

Table 3.8 Input parameters for sheet material (22MnB5)

Young’s modulus (E), constant, GPa (10^6 psi)	100 (14.5)
Poisson’s ratio (ν), constant	0.3
Thermal expansion (α), constant, $10^{-6}/K$ ($10^{-6}/^{\circ}F$)	13 (7.2)
Heat conductivity (k), constant, W/m-K (Btu/h-ft- $^{\circ}F$)	32 (18)
Heat capacity (c_p), constant, J/kgK	650
Initial sheet thickness (t_0) (Ref 3.23), mm (in.)	1.95 (0.076)
Sheet length (L), assumed, mm (in.)	250 (9.8)

Table 3.9 Process parameters

Initial temperature of blank at the beginning of forming process (T_i), $^{\circ}C$ ($^{\circ}F$)	810 (1490)
Initial temperature of tools (T_t), $^{\circ}C$ ($^{\circ}F$)	75 (165)
Temperature of the environment (T_c), $^{\circ}C$ ($^{\circ}F$)	20 (70)
Coefficient of friction (μ), constant	0.4
Heat-transfer coefficient with air (H_c), constant, W/ m^2K	160

Source: Ref 3.23

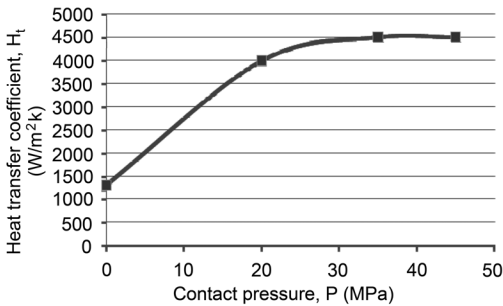


Fig. 3.16 Heat-transfer coefficient as a function of pressure. Source: Ref 3.23

Output. The thickness distribution along the curvilinear length of the final part was also obtained and is shown in Fig. 3.17. Simulations also provide other useful information, that is, contact regions, temperature distributions, and contact pressure distributions over time. Accurate prediction of regions of contact between the tool and the blank during the deformation stage and quenching process is one of the key outputs from the simulations, as they can have a huge effect on the final properties of the part because the cooling at these points controls the martensitic transformation, as discussed in detail in Chapter 7, “Hot Stamping,” in this book.

At the selected two-dimensional section, thermal analysis inside the die can be conducted for various cooling channel configurations, as shown in Fig. 3.18. Cooling channel diameters of 8 and 10 mm (0.3 and 0.4 in.) distance from the die surface are considered. The cooling channels were assumed to have a constant surface temperature. Quenching simulation was conducted for 20 s under a constant closing pressure of 35 MPa (5100 psi) with rigid dies. Figure 3.18 shows the temperature distribution on the die and the punch after ten forming cycles. Temperatures at the selected critical points in the formed part over time were evaluated to check whether the cooling rates at various regions of the blank were sufficient for quenching condition (>25 $^{\circ}C/s$, or 45 $^{\circ}F/s$).

With finite-element code DEFORM, hot stamping of a simple part geometry (e.g., hat shape) can be simulated. This code is currently

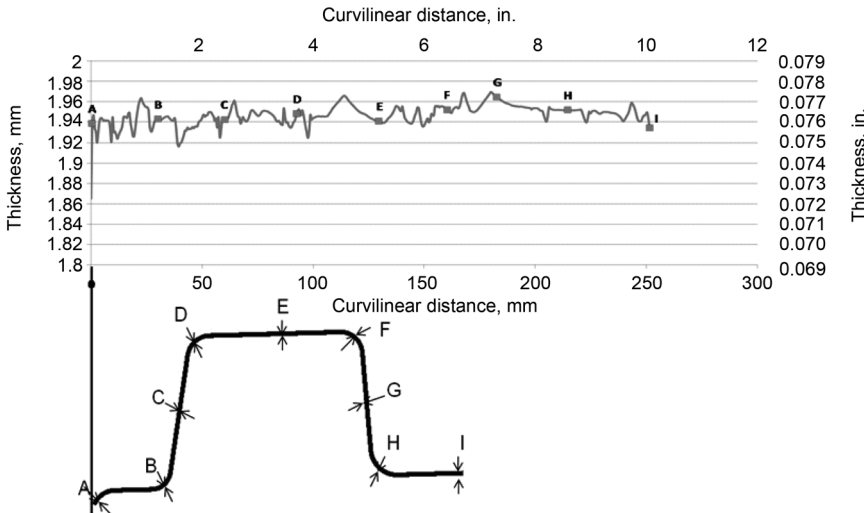


Fig. 3.17 Thickness distribution along the curvilinear length. Source: Ref 3.22

suitable for simulating simple laboratory experiments for hot stamping. For industrial complex geometries, forming simulation can be conducted faster and more robust by using other commercial finite-element codes specially developed for sheet metal forming (e.g., PAMSTAMP, LS-DYNA, etc). Figure 3.19 shows a hot stamping simulation of a B-pillar using PAMSTAMP. However, almost all finite-element codes for sheet metal forming model the blank using shell elements and the dies as surface objects (not solid). Thus, in the current version of this finite-element code, there is no calculation of temperatures within the dies.

Springback and bending of advanced high-strength steels (AHSS) is demonstrated by the following case study (Ref 3.25).

Objective. To predict springback for V-die bending tests of AHSS. One of the objectives of the FEA simulation of the bending process by using DEFORM was to determine the tool geometry for V-die bending tests to avoid cracks and rubbing of sheet to V-die side walls during the test.

The flow stress data were obtained by viscous pressure bulge test. Springback angle is the difference between the inner bending angles under load and after unloading. Figure 3.20 shows the

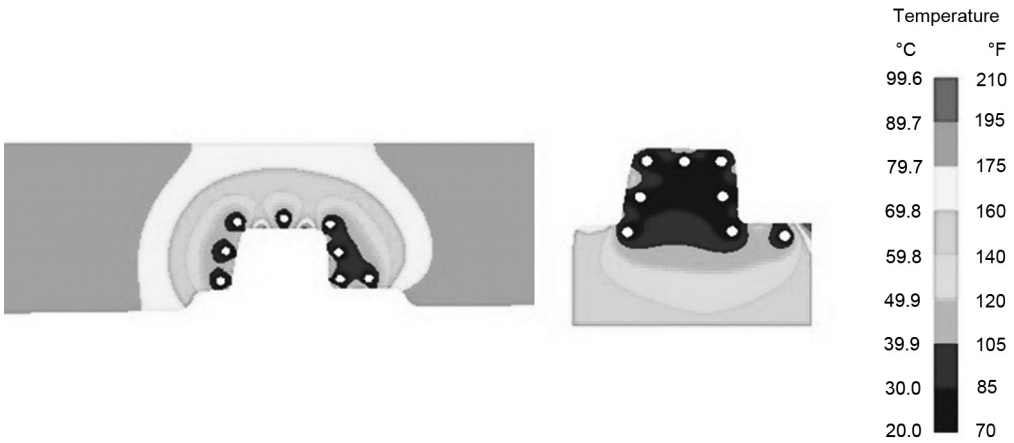


Fig. 3.18 Temperature distribution in the die (left) and punch (right) at the end of ten forming cycles. Source: Ref 3.24

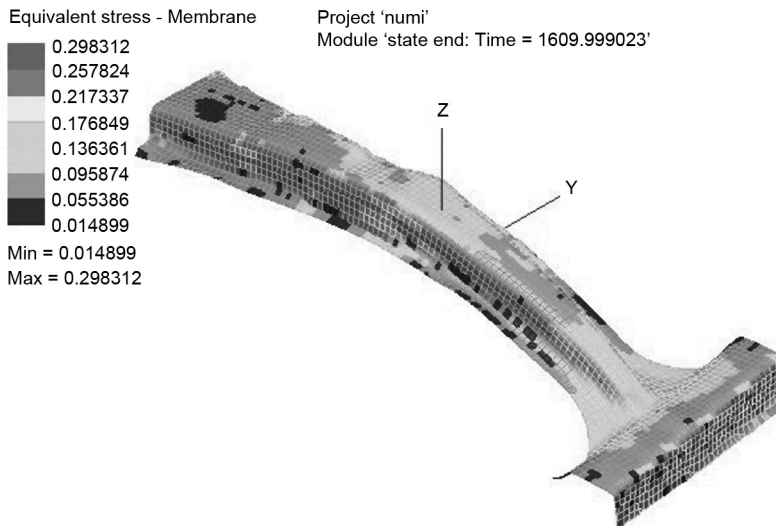


Fig. 3.19 Forming simulation of a B-pillar using PAMSTAMP. Input data were taken from Ref 3.23

tooling geometry used to model the V-bending test, and Table 3.10 shows the input parameters used in the finite-element software DEFORM 2D and PAMSTAMP-2G.

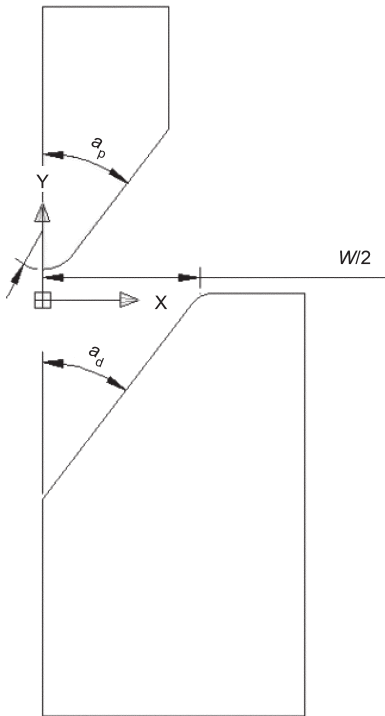


Fig. 3.20 Tool geometry of V-die bending (a_p = punch tip angle, a_d = V-die angle). Source: Ref 3.25

Output. Comparisons of inner bending angles under load and springback angles obtained by DEFORM and experiments are given in Fig. 3.21. In actual experiments, it was found that anisotropy has a small effect on springback. The difference between springback angles for samples cut in the rolling direction and transverse direction increased with an increase in punch stroke.

Comparisons of springback angles obtained by PAMSTAMP-2G and experiments are compared in Fig. 3.22. The maximum difference in springback angles was 1.51° , which corresponds to a 15 mm (0.59 in.) punch stroke (Fig. 3.22).

Further studies can be conducted to predict springback considering apparent modulus variation. From Fig. 3.23, it was found that the elasticity modulus decreased approximately 28% as

Table 3.10 Finite-element simulation input parameters for DEFORM 2D and PAMSTAMP

Simulation parameters	Description
Sheet material	DP780
Initial thickness, mm (in.)	1 (0.04)
Material type	Sheet: elastic, plastic V-die and punch: rigid
V-die angle (a_d)	75°
V-die opening (W), mm (in.)	38.1 (1.50)
Punch tip angle (a_p)	75°
Punch tip radius (R_p), mm (in.)	4.75 (0.187)
Maximum punch stroke, mm (in.)	15 (0.59)
Coefficient of friction	0.12
Elastic modulus (constant), GPa (10^6 psi)	207.27 (30.054)

Source: Ref 3.25

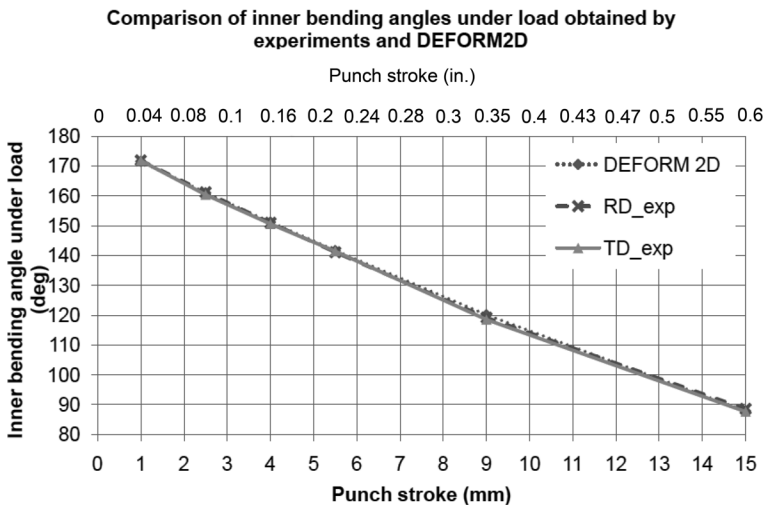


Fig. 3.21 Comparison of inner bending angles under load obtained by DEFORM 2D and experiments (constant E modulus). RD, rolling direction; TD, transverse direction. Source: Ref 3.25

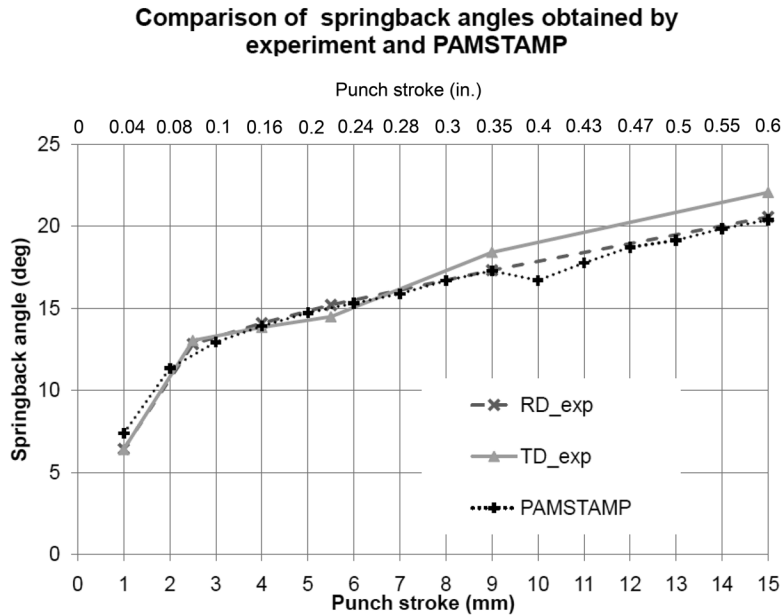


Fig. 3.22 Comparison of springback angles obtained by PAMSTAMP (ram velocity: 0.05 mm/ms, or 0.002 in./ms) and experiments (constant E modulus). RD, rolling direction; TD, transverse direction. Source: Ref 3.25

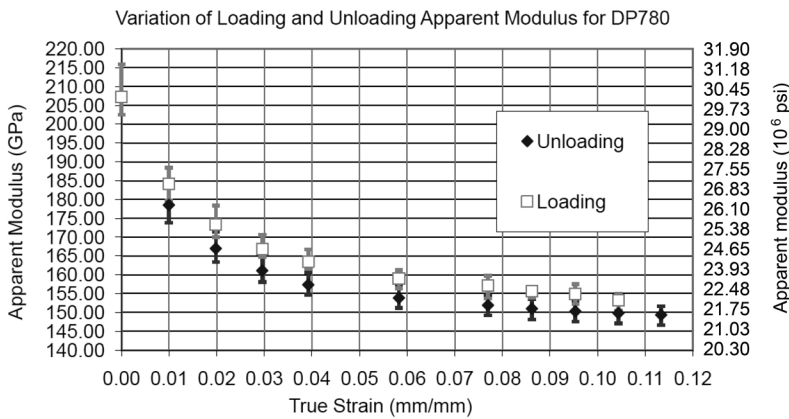


Fig. 3.23 Variation of loading and unloading apparent modulus with strain for DP780 sheet material in a tensile test. Source: Ref 3.25

strain increased up to 0.11 from tensile tests of DP780. This large reduction of apparent modulus is expected to significantly impact the prediction of springback from the finite-element code. For springback simulations, the unloading apparent modulus is more relevant, and this nonlinear curve can be used in data form or in equation form to describe the elastic properties of DP780 in finite-element simulations.

3.5 Factors Affecting the Accuracy of FEM Simulations

Despite recent improvements to enhance the application of finite-element simulation for process modeling, the successful application of FEM depends mainly on the reliability of the input parameters, such as material properties, friction conditions, and the user's ability to

transform the physical problem to the finite-element model accurately and to interpret the finite-element results/predictions. Industrial users emphasize that in the production environment the simulation codes must be reliable, easy to use, and should give out fast solutions. Conferences such as NUMISHEET and NUMIFORM are a great resource for learning the work done by researchers, mainly from the universities. However, in many cases, the research presented in papers cannot be easily reproduced in production.

Table 3.11 shows a comparison of the sheet metal forming process characteristics in produc-

Table 3.11 Comparison of reality and the simulation model

Factor	Reality	Simulation
Production stroke rate	Not constant	Not in the model
Machine	Elastic	Not in the model
Tool	Elastic	Rigid
Characteristics in the direction of draw	Not constant	Not mapped
Coefficient of friction	Not constant	Constant
Topology of the blank holder force	Not constant	Not in the model
Material	Complex	Simple models

Source: Ref 3.1

tion (or in reality) and in finite-element simulations. Table 3.11 gives a general idea about the comparison of physical reality of the sheet metal forming process to the finite-element simulations. In addition to these examples, there could be many other significant factors in the finite-element simulations that could also be incorrectly predicted. Some of the factors that affect the accuracy of finite-element predictions are as follows.

Springback Issues—Influence of Elastic Modulus. The input of elastic modulus remains a constant in a finite-element model, but in the case of springback, it may not remain constant. For example, for a high-strength steel, as yield stress increases, springback increases, and for the case of aluminum, as the elastic modulus decreases, springback increases. Thus, elastic modulus and yield stress have a clear effect on the springback of the material (Ref 3.1).

Thickness Variation of the Incoming Material. In the case study presented earlier on SHF-P, one of the outputs that could be examined is the thickness profile of the part along its curvilinear length. Figure 3.24 shows the comparison of the finite-element thickness profile for the part drawn to a depth of 34.3 mm (1.35 in.), with the thickness measurements taken by

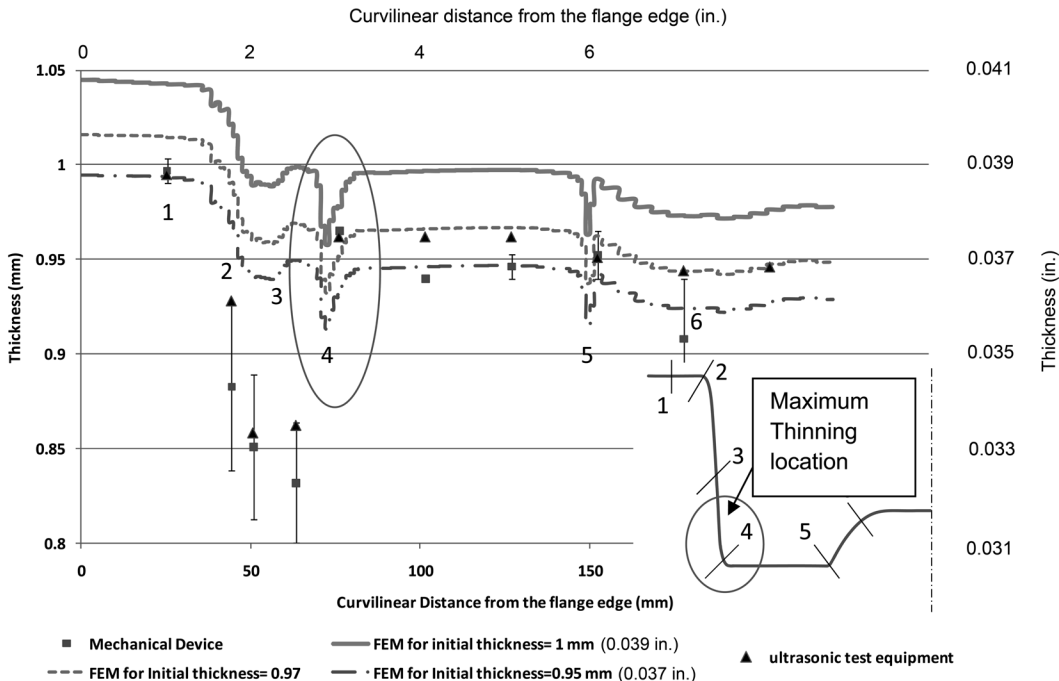


Fig. 3.24 Comparison of thickness profile using mechanical indicator and ultrasonic test equipment with finite-element output results (punch stroke = 34.3 mm, or 1.35 in.). Source: Ref 3.20

using a mechanical indicator and ultrasonic test equipment. The maximum thinning occurs at the punch corner region (position number 4) along the part profile.

The initial assumption was that the initial thickness of the blank would be according to the specification, 1 mm (0.04 in.). However, from the results of the mechanical indicator and the ultrasonic test equipment, the thickness along the flange region appeared to be lower than 1 mm (near the position number 1). There may be a possibility that the initial thickness of the blank may not be exactly 1 mm but slightly lower, so variable initial blank thickness values of 0.95 and 0.97 mm (0.037 and 0.038 in.) were input to the finite-element simulations to compare the thickness profile for lower initial thickness values. The results shown in Fig. 3.24 illustrate that the finite-element results for an initial thickness of 0.97 mm match well with the ultrasonic test equipment measurements. The thickness results shown at positions 2, 3, and 4 (side wall region of the part), measured using mechanical and ultrasonic devices, show a much smaller value of thickness as compared to the finite-element results for the three initial thickness inputs (0.95, 0.97, and 1 mm). This study shows the importance of the initial thickness of the blank and the influence of variation of initial thickness on final thickness profiles of the formed parts.

Shell Elements. In FEM, the sheet metal can be represented by shell elements, where the sheet metal is discretized into elements and the variation of the displacement, strain, and stress within the element is assumed. The dimension of the sheet along the thickness direction is negligible as compared to the other two dimensions but is thick enough to support bending loads. The shell element represents the sheet mid-plane, and each node of the element has five degrees of freedom that include displacement in the X -, Y -, and Z -direction and rotation about the X - and Y -axis. The shell element accounts for both the stretching and bending strain in the deformation of the sheet (Ref 3.11).

Bending causes plastic stress in the extreme fibers of the sheet, thereby resulting in nonlinear variation of the stress along the thickness direction. Therefore, numerical integration must be performed along the thickness direction as well as with more integration points to accurately calculate the nonlinear bending stresses (Ref 3.4). For the simulations conducted by PAMSTAMP-2G, the required number of inte-

gration points is set to five by default along the thickness direction (Ref 3.26). Note that the accuracy of the stamping operations may be affected by simply changing the number of integration points along the thickness direction. In studies (Ref 3.27), the number of integration points required to ensure accuracies within 1% was up to 51. Several researchers have since reported that between 5 and 11 integration points are adequate.

Nonisothermal Simulations (Heat-Transfer Coefficients). During the deformation and quenching stages in hot stamping or in the non-isothermal warm forming process, conduction is the most dominant form of heat transfer, and so the heat-transfer coefficient for conduction becomes paramount. Using the correct value of the heat-transfer coefficient can be very crucial in predicting accurate thermal gradients and forces over the workpiece.

Experiments were conducted to calculate the contact heat-transfer coefficient between the sheet materials and the die (Ref 3.9). From the experimental results, the heat-transfer coefficient between the die and the sheet material is almost constant (100 W/m²K) until the contact distance between die and sheet reaches 0.5 mm (0.02 in.), and the value increases steeply to 1200 W/m²K when the die touches the material. The value of the heat-transfer coefficient with an environment for hot stamping simulation can be between 125 W/m²K (Ref 3.9) and 160 W/m²K (Ref 3.23) and as estimated by Ref 3.28.

In the hot stamping case study, martensitic transformation, which gives the final part its high strength, necessitates a minimum cooling rate of 27 K/s (49 °F/s). Thus, the heat-transfer coefficient plays an important role in conducting finite-element simulations and obtaining accurate prediction of the thermal gradient over time and thickness distribution along the workpiece.

REFERENCES

- 3.1 K. Roll, "Simulation of Sheet Metal Forming—Necessary Developments in the Future," NUMISHEET 2008
- 3.2 E. Tekkaya, State-of-the-Art of Simulation of Sheet Metal Forming, *J. Mater. Process. Technol.*, Vol 103, 2000, p 14–22
- 3.3 S. Kobayashi, S. Oh, and T. Altan, *Metal Forming and the Finite-Element Method*, Oxford University Press, 1989

- 3.4 O.C. Zienkiewicz, R.L. Taylor, J.Z. Zhu, and P. Nithiarasu, *The Finite Element Method: Its Basis and Fundamentals*, Butterworth-Heinemann, 2000
- 3.5 T. Altan and H. Palaniswamy, Process Modeling and Optimization in Sheet Metal Forming—Selected Applications and Challenges, *Steel Res. Int.*, Vol 78, 2007
- 3.6 A. Al-Nasser et al., Determination of Flow Stress of Five AHSS Sheet Materials (DP600, DP780, DP780-CR, DP780-HY and TRIP780) Using Uniaxial Tensile and Biaxial Viscous Pressure Bulge (VPB) Tests, *J. Mater. Process. Technol.*, Vol 210 (No. 3), 2010, p 429–436
- 3.7 B.H. Lee, Y.T. Keum, and R.H. Wagoner, Modeling of Friction Caused by Lubrication and Surface Roughness in Sheet Metal Forming, *J. Mater. Process. Technol.*, Vol 130–131, 2002, p 60–63
- 3.8 A. Yanagida and A. Azushima, “Evaluation of Coefficients of Friction for Hot Stamping by Newly Developed Tribosimulator,” International Deep Drawing Research Group Conference (Golden, CO), 2009
- 3.9 M. Geiger, M. Merklein, and J. Lechler, *Determination of Tribological Conditions within Hot Stamping*, German Academic Society for Production Engineering, 2008
- 3.10 J. Hardell, E. Kassfeldt, and B. Prakash, Friction and Wear Behavior of High Strength Boron Steel at Elevated Temperature up to 800C, *Wear*, Vol 264, 2008, p 788–799
- 3.11 H. Palaniswamy, “Determination of Process Parameters for Stamping and Sheet Hydroforming of Sheet Metal Parts Using Finite Element Method,” The Ohio State University, 2007
- 3.12 J. Cao and X. Wang, On the Prediction of Side Wall Wrinkling in Sheet Metal Forming Processes, *Int. J. Mech. Sci.*, Vol 42, 2000, p 2369–2394
- 3.13 L.S. Xie and Z.Q. Xiong, Study on the Theory and Application of the Energy Method and Application of Energy Method for Analyzing Compressive Instability in Sheet Forming, *J. Mater. Process. Technol.*, Vol 129, 2002, p 255–260
- 3.14 R. Wiedenmann, P. Sartkulvanich, and T. Altan, “Finite Element Analysis on the Effect of Sheared Edge Quality in Blanking upon Hole Expansion of Advanced High Strength Steels,” International Deep Drawing Research Group Conference (Golden, CO), 2009
- 3.15 A. Konieczny and T. Henderson, “On Formability Limitations in Stamping Involving Sheared Edge Stretching,” SAE technical paper 2007-01-0340, 2007
- 3.16 H. Kim, J. Sung, R. Sivakumar, and T. Altan, Evaluation of Stamping Lubricants Using the Deep Drawing Test, *Int. J. Mach. Tools Manuf.*, Vol 47 (No. 11), 2007, p 2120–2132
- 3.17 J. Hoffmann, P. Bartot, H. Palaniswamy, and T. Altan, “Analysis and Design of Progressive Die Stamping Process for Airbag Part,” ERC/NSM-05-R-18, 2005
- 3.18 M. Ahmetoglu, T.R. Brock, G. Kinzel, and T. Altan, Blank Holder Force to Eliminate Wrinkling and Fracture in Deep Drawing Rectangular Parts, *Ann. CIRP*, Vol 44 (No. 1), 1995, p 247–250
- 3.19 H. Palaniswamy, M. Braedel, A. Thandapani, and T. Altan, Optimal Programming of Multi-Point Cushion Systems for Sheet Metal Forming, *Ann. CIRP*, Vol 55, 2006
- 3.20 M. Shah, E. Billur, P. Sartkulvanich, J. Carsley, and T. Altan, “Cold and Warm Hydroforming of AA5754-O Sheet—FE Simulations and Experiments,” NUMISHEET 2011 (Seoul, Korea)
- 3.21 N. Abedrabbo, F. Pourboghra, and J. Carsley, Forming of AA5182-O and AA5754-O at Elevated Temperatures Using Coupled Thermo-Mechanical Finite Element Models, *Int. J. Plast.*, Vol 23, 2007, p 841–875
- 3.22 D. Ravindran, A. Naganathan, C. Choi, and T. Altan, “Finite Element Simulation of Hot Stamping—Examples,” CPF-5.5/10/03, 2010
- 3.23 “The NUMISHEET Benchmark Study,” NUMISHEET, 2008
- 3.24 A. Naganathan, P. Sartkulvanich, D. Ravindran, N. Pierschel, and T. Altan, “Progress on FE Simulation of the Hot Stamping Process,” The Third International Conference on Hot Sheet Metal Forming of High Performance Steel-CHS, June 13–16, 2011 (Kassel, Germany)
- 3.25 N. Kardes, Y. Demiralp, G. Sukumaran, C. Choi, H. Kim, L. Gonzalez-Mendez,

- et al., "Control of Springback and Dimensional Tolerances in Forming of AHSS Steel Parts," CPF-1.4/10/01, 2010
- 3.26 *PAMSTAMP-2G Manual*, ESI Group, 2009
- 3.27 R.H. Wagoner and M. Li, Simulation of Springback: Through-Thickness Integration, *Int. J. Plast.*, Vol 23, 2007, p 345–360
- 3.28 B.S. Arthur, "Using LS-DYNA for Hot Stamping," Seventh European LS-DYNA Conference, 2009

CHAPTER 4

Progressive and Transfer Die Forming

Parth Pathak, Cameron
Ajay Yadav, Caterpillar Technical Center

IN PROGRESSIVE DIE FORMING, a series of fundamental forming operations are carried out at two or more stations during each press stroke as the strip of material moves through the die (Fig. 4.1). There could be one or more idle stations where no forming operation is performed. These idle stations help the strip travel or simplify the die design. At a given station, each partially formed part is attached to a portion of the strip material, called carrier, as it moves from one station to the next. With every stroke of the press, one or more parts are produced.

The distance between two adjacent stations is equal to the travel of the strip at each stroke of the press and is called progression, advance, or pitch. The feeding of the strip is automatic and depends on the pitch. Pilot pins are provided for positioning the strip, making the process less time-consuming and more accurate than if it were carried out using conventional single dies as forming stations. Progressive die forming is considered for large production volumes and for relatively small parts that can be transported by the strip carrier.

Transfer die forming is similar to progressive die forming except that the parts are formed from individual blanks and transferred from one

die station to the next by means of a mechanical transfer mechanism in the press, as seen in the example in Fig. 4.2 (Ref 4.2). Every process sequence design used in progressive or transfer die forming must include the number of forming stations, tool geometry for each station (punch and die diameter, punch corner, and die corner radii), draw depth for each forming station, and blank holder force (if needed) at each station. The challenging tasks in designing a process sequence are how to determine the minimum number of required forming stations and the corresponding tool geometry to satisfy specifications of the produced part concerning overall dimensions, tolerances, residual stresses, and surface finish.

Process sequence design for a new part generally is based on experience and knowledge gained from producing similar parts and necessary prototype runs. This experience-based methodology requires extensive resources and increases the design lead time. There are several articles and books that summarize the basic practical principles involved in designing progressive and transfer dies, such as part orientation, part transport, piloting, die alignment and clamping, the setting of feed line height, and scrap removal as well as lubrication (Ref 4.3–4.5).

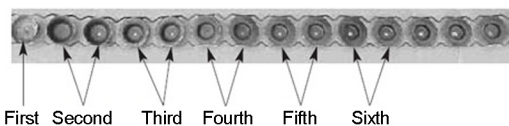


Fig. 4.1 Typical progressive die strip. Source: Ref 4.1

4.1 Process Design Using Finite-Element Analysis

Finite-element analysis (FEA), coupled with knowledge-based design, can reduce lead times and enhance the robustness of the progressive

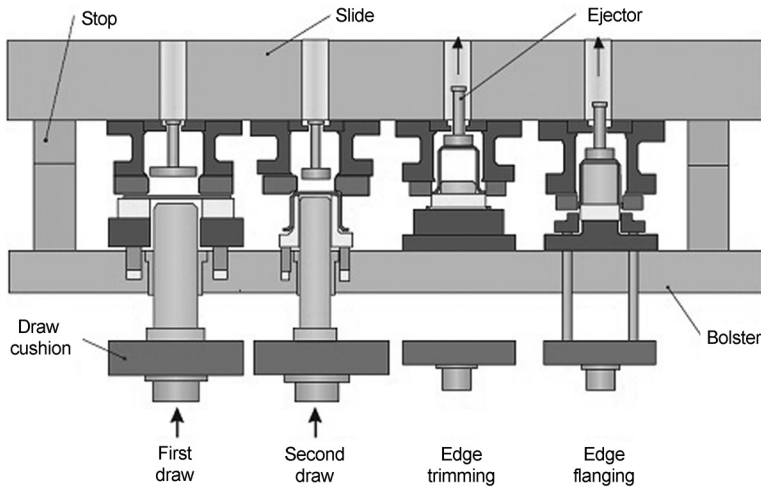


Fig. 4.2 Transfer die set for a press with draw cushion and positive stops. Source: Ref 4.2

die sequence (Ref 4.6). A robust process accounts for variability during production, such as variations in incoming stock material properties and variations in process conditions (forming speed and forces) and interface conditions (lubrication and frictional forces).

Knowledge-based systems have been explored to determine required forming stages in deep drawing and two-dimensional forging problems. Knowledge for these systems is derived from plasticity theory, experimental results, and the empirical know-how of field engineers. This approach has shown some success. However, it cannot consider the process conditions that are not already stored in the knowledge base. In earlier studies, Cao et al. (Ref 4.7) used numerical simulations and sensitivity analysis to optimize the number of forming stages in a multistep deep drawing problem. Kim et al. (Ref 4.8) carried out tool design analysis for multistep drawing using the finite-element method (FEM). In these studies, only design improvements in existing multistep tooling were carried out.

Case Study I: Progressive Die Design

To develop die sequence design guidelines for a new part, it is often useful to conduct FEA on an existing part (part A), as seen in Fig. 4.3 (Ref 4.1). Material parameters, process conditions, and tool geometry data were available for this part in six forming stages. Design rules developed from this study were meant to assist in process sequence design for new parts.

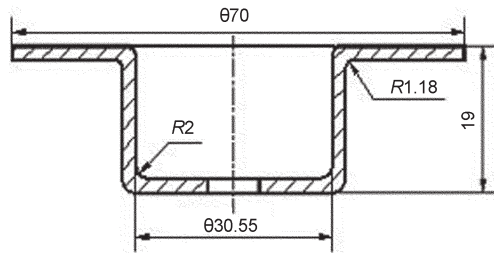


Fig. 4.3 Dimensions of an existing automotive part (part A), used to develop die design guidelines. Source: Ref 4.1

Each stage of the sequence for the selected part (part A, Fig. 4.3) was simulated for the given process conditions using the commercial finite-element code DEFORM-2D (Ref 4.9). Results such as thickness distributions and strain hardening were predicted for each stage and carried over to the successive stages to account for work hardening. At each stage, the FEA accurately predicted strain distribution, part geometry, and punch forces. Figure 4.4 shows the part geometries predicted for all six forming stages.

The FEA experience gained in designing the forming stages for the part seen in Fig. 4.3 (part A) was applied to designing the progressive dies for a new part (part B) shown in Fig. 4.5, using the following design guidelines (Ref 4.6):

- Higher draw ratios are used in the initial forming stages. Figure 4.6 shows the trends for the variation of punch diameters and

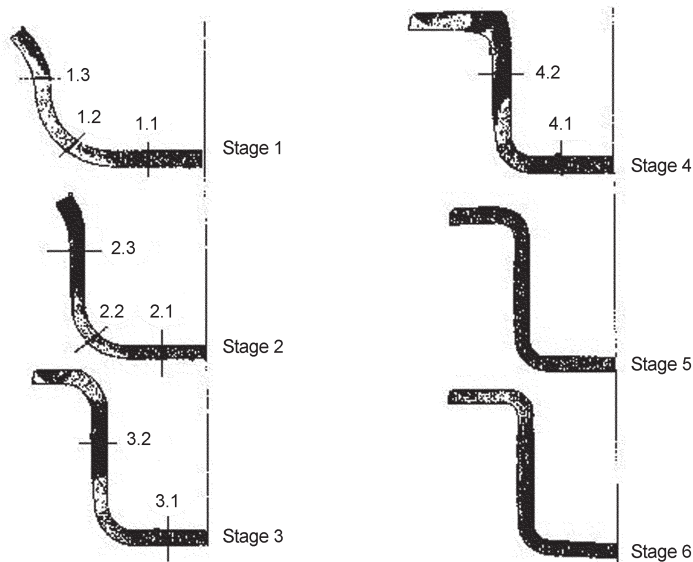


Fig. 4.4 Finite-element-analysis-predicted geometry and thickness distribution in the part after each deformation stage. Source: Ref 4.1

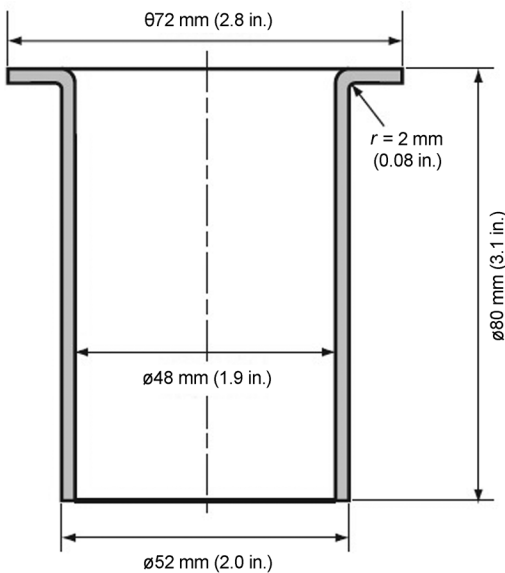


Fig. 4.5 Geometry of the new part (part B) used in the finite-element analysis study (blank thickness: 2.15 mm, or 0.085 in.). Source: Ref 4.6

maximum wall thinning. The punch diameter is reduced rapidly during the initial stages of deformation and relatively little in the later stages. Based on this trend, the maximum wall thinning was decided to be constrained to below 4% in the first forming

stage of part B. In the example part A, the ratio of the punch corner radius to die corner radius was kept to less than 1 in all the forming stages, that is, the ratio varied from 0.75 to 0.95. This condition was taken into account in determining the punch corner and die corner radii for various forming stages of part B.

- The example part A, with a height of 19 mm (0.75 in.), was manufactured using six forming stages. Because the height of part B is 80 mm (3.1 in.), it was assumed that this part would require more than six forming stages.

Process Sequence Design. The design guidelines discussed previously, and others obtained from die design handbooks (Ref 4.10), were applied in the design of a progressive die sequence for part B. Figure 4.7 shows the flow chart of the steps conducted to determine the parameters of the first forming stage for part B using FEM.

The simulation model used is shown in Fig. 4.8. The geometry was modeled over a unit radian about the Z-axis due to the axisymmetric deformation mode. The sheet was meshed with an axisymmetric quadrilateral element, with eight elements along the thickness to capture thickness distribution. The dies were modeled to be rigid, and the stress-strain relation for the deforming material was $\sigma = 657(\epsilon)^{0.24}$ MPa. A

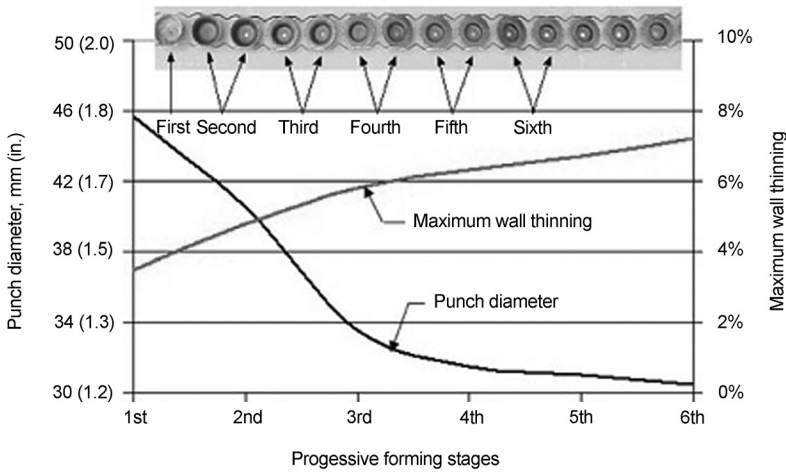


Fig. 4.6 Variation of punch diameter and wall thinning in progressive forming stages (part A). Source: Ref 4.6

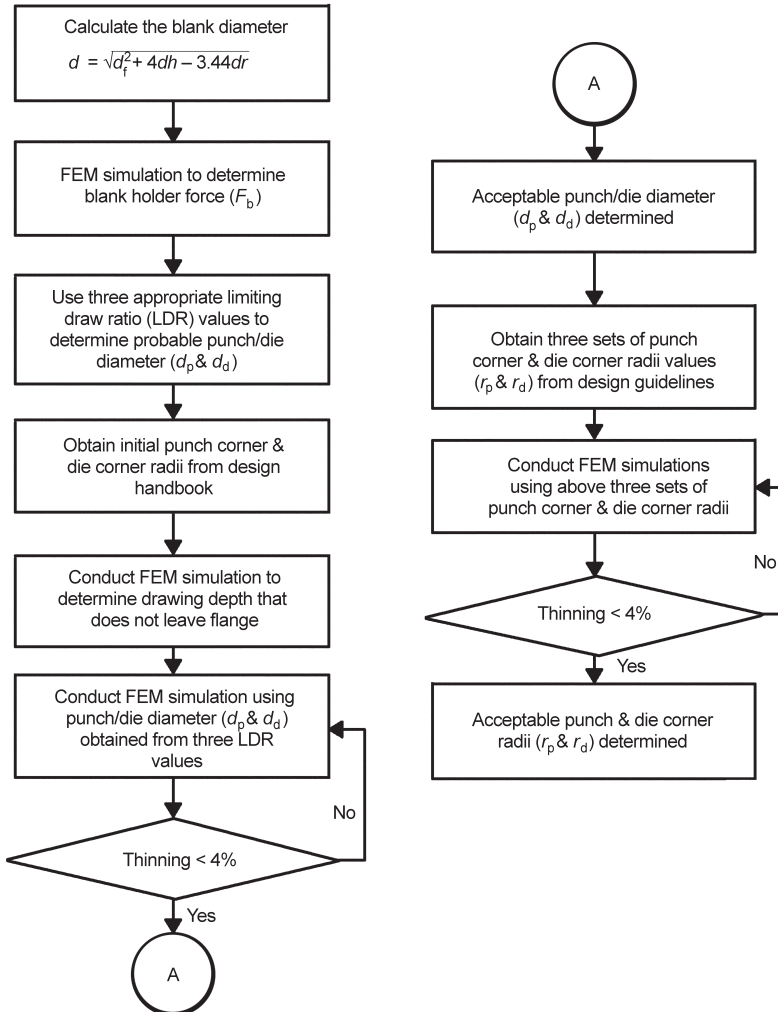


Fig. 4.7 Flow chart to determine the design parameters of the first forming stage for part B. FEM, finite-element method. Source: Ref 4.6

Coulomb friction coefficient, $\mu = 0.1$, was selected as the thinning distribution from FEM simulation; using this value matched experimental results for the example part A. The initial blank diameter, d_b , was determined to be 165 mm (6.50 in.) through volume constancy using the part dimensions given in Fig. 4.5. The punch velocity of 150 mm/s (5.9 in./s) was used in the simulations.

The blank holder force for the first stage was determined by performing simulations with different blank holder forces. If the blank holder force is insufficient, the FEM simulation shows that the blank holder will move upward (Fig. 4.8), resulting in flange wrinkling. In the first forming stage, the minimum blank holder force of 50 kN (11 kip) was selected to prevent wrinkling, that is, the upward movement of the blank holder. A similar strategy was used to determine the blank holder forces in subsequent forming stages.

The punch diameter, die diameter, and drawing depth for the first stage have maximum influence on wall thinning. The maximum wall thinning was constrained to be less than 4% in the first stage. Moreover, in the first stage, the cup is drawn completely without flange to put more material into the die cavity. Table 4.1 shows the simulation matrix used to determine the optimum (dimensions to constrain the wall

thinning below 4% and minimize the number of forming stages) punch diameter for the first stage. The draw ratios of 1.65, 1.6, and 1.55 were obtained from a die design handbook (Ref 4.10) for the initial determination of punch diameters. The punch diameters of 100, 97, and 95 mm (3.9, 3.8, and 3.7 in.) were calculated from these ratios. The die clearance was taken as $1.1 t_0$, while t_0 is the initial sheet thickness. The last column in Table 4.1 shows the maximum wall thinning obtained from FEM. The maximum wall thinning is less than 4% for punch diameters of 97 and 100 mm. To reduce the number of forming stages, the punch diameter of 97 mm was selected.

The most important output from FEM simulations is the location of the maximum thinning in the part. Design engineers can use this information to select the punch diameters for subsequent stages. The punch radius for the first stage was selected to be 48.5 mm (1.91 in.). After the first-stage drawing, the maximum wall thinning of 3.72% is observed in the part at a distance of 43.7 mm (1.72 in.) from the center line (Fig. 4.9). Hence, any punch radius equal to or more than 43.7 mm in the second stage will hit the maximum thinning area, which would result in significant wall thinning. Therefore, the second-stage punch radius should be smaller than 43.7 mm. The FEM simulations thus gave the upper

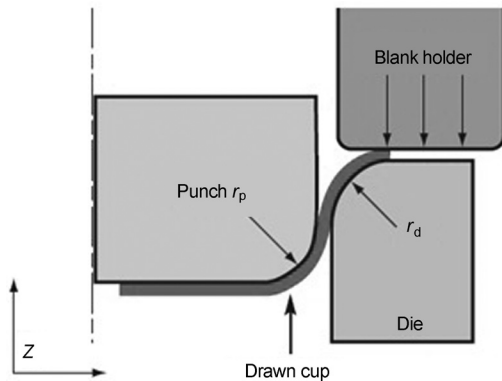


Fig. 4.8 Simulation model

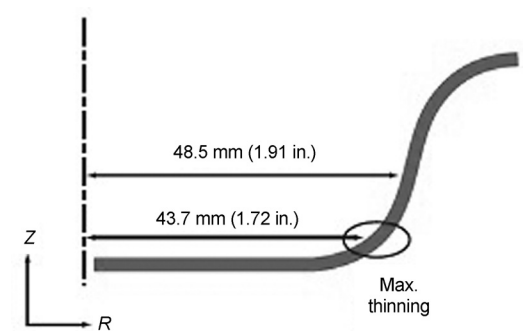


Fig. 4.9 Location of maximum thinning at the first stage (determines the upper limit of the punch diameter for the next stage)

Table 4.1 Simulation matrix for determining the optimum punch diameter

Case No.	Diameter				Corner radii				Blank holder force		Max. wall thinning from finite-element modeling, %
	Punch (d_p)		Die (d_d)		Punch (r_p)		Die (r_d)		kN	kip	
	mm	in.	mm	in.	mm	in.	mm	in.			
1	100	3.9	104	4.1	19.5	0.768	21.5	0.846	50	11	3.3
2	97	3.8	101.5	4.0	19.5	0.768	21.5	0.846	50	11	3.7
3	95	3.7	99.5	3.9	19.5	0.768	21.5	0.846	50	11	4.1

limit for the next-stage punch diameter. Simulations were then carried out to determine the optimum punch diameter for the subsequent stages. Cups were completely drawn for the first four stages, and the maximum thinning was restricted below 6%.

Punch Corner and Die Corner Radii for the First Stage. After determining the optimum punch diameter, it is necessary to determine the punch corner and die corner radii. Table 4.2 shows the simulation matrix used for this purpose. Initial values of punch corner and die corner radii were taken from a design handbook (Ref 4.7). Also, the ratio of punch corner radius to die corner radius was kept to less than 1 based on the guidelines obtained from the investigation of the die design of the example part A. The last column in Table 4.2 shows wall thinning values for different punch and die corner radii at the first stage. Punch and die corner radii of 19.5 and 21.5 mm (0.768 and 0.846 in.), respectively, were selected to meet the thinning criterion (i.e., to keep wall thinning below 4%) and reduce the number of forming stages. A similar approach was adopted to determine the

optimum set of punch and die corner radii for the subsequent stages.

Final Progressive Die Sequence. The progressive sequence design using FEM simulation consisted of ten forming stages and a final piercing/wall ironing stage. Figure 4.10 shows the progressive die sequence and the corresponding maximum thinning in percentage for each stage.

Progressive Die Design—Comparison between FEM and Experience-Based Methods. Figure 4.11 shows the comparison of punch diameters obtained from finite-element-assisted and experience-based methods. The FEM predicted ten forming stages, while the experience-based method predicted nine forming stages. As observed from the slope of two curves, punch diameter change in the FEM-assisted method is gradual. However, larger draw ratios were used for the first five stages in the experience-based method. Figure 4.12 shows the comparison of thickness distributions obtained from the FEM-assisted method and the experience-based method. Thickness distributions obtained from these two designs show that gradual change in punch

Table 4.2 Simulation matrix for determining the optimum punch corner and die corner radii

Case No.	Diameter				Corner radii				Ratio r_p/r_d	Blank holder force		Max. wall thinning from finite-element method, %
	Punch (d_p)		Die (d_d)		Punch (r_p)		Die (r_d)			kN	kip	
	mm	in.	mm	in.	mm	in.	mm	in.				
1	97	3.8	101.5	4.0	18	0.71	20	0.79	0.9	50	11	4.3
2	97	3.8	101.5	4.0	19.5	0.768	21.5	0.846	0.9	50	11	3.7
3	97	3.8	101.5	4.0	22	0.87	25	0.98	0.88	50	11	3.5

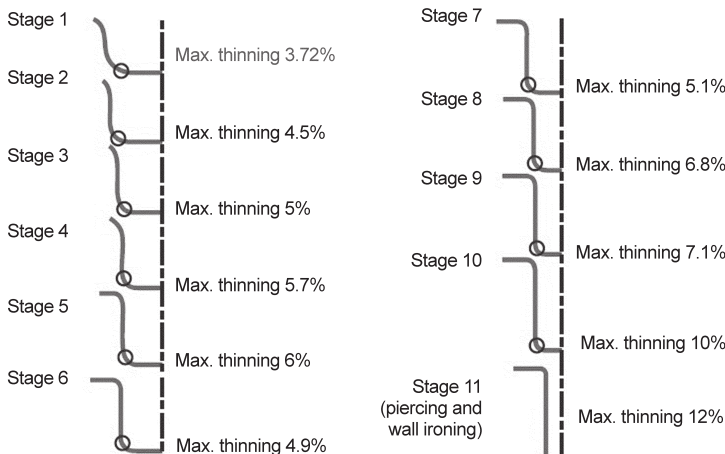


Fig. 4.10 Shape of deformed part at each stage for progressive die sequence design

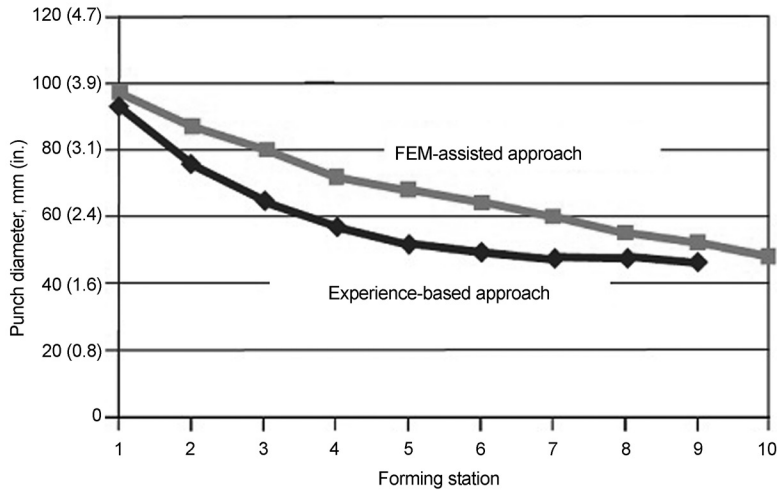


Fig. 4.11 Comparison of punch diameters predicted by experience-based and finite-element method (FEM)-assisted methods

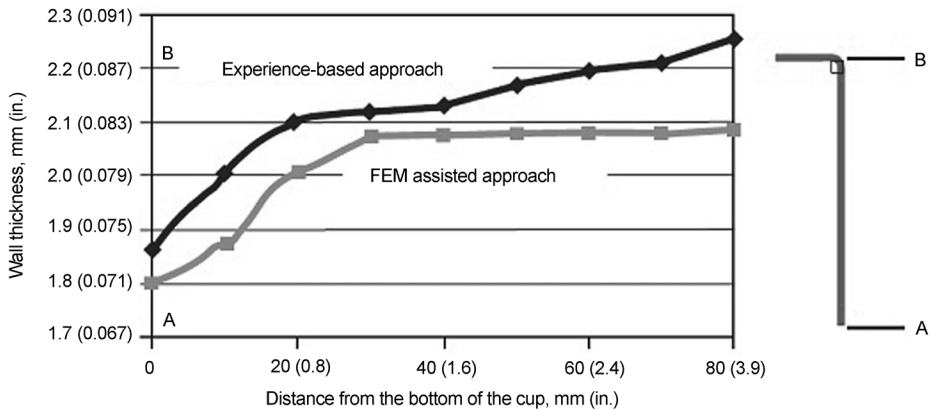


Fig. 4.12 Thickness distribution in the final part predicted by experienced-based and finite-element method (FEM)-assisted methods

diameter would result in a more uniform wall thickness distribution in the final part. Figure 4.13 shows the comparison of punch corners for FEM-assisted and experience-based methods. Similar trends were observed for corner radii as well.

Case Study II: Transfer Die Forming of a Clutch Hub

The clutch hub investigated in this study had a diameter of approximately 48 mm (1.9 in.) and was formed in three steps, as shown in Fig. 4.14 (Ref 4.11). After the flanging operation, it was

necessary to upset the flange wall to obtain a sharp external radius. Flanging alone results in relatively large radii and sometimes in excessive thinning at the bend, as seen in Fig. 4.15. Upsetting of the flanged wall is necessary to have a flat surface near the flanged corner where fastening bolts are located.

During the upsetting operation, there is no support on either side of the flanged wall. This operation, while resulting in a sharper radius than that obtained by flanging alone, causes shear stresses at the base of the flange. Thus, in some cases, cracks develop at the inner bend corner, as seen in Fig. 4.15.

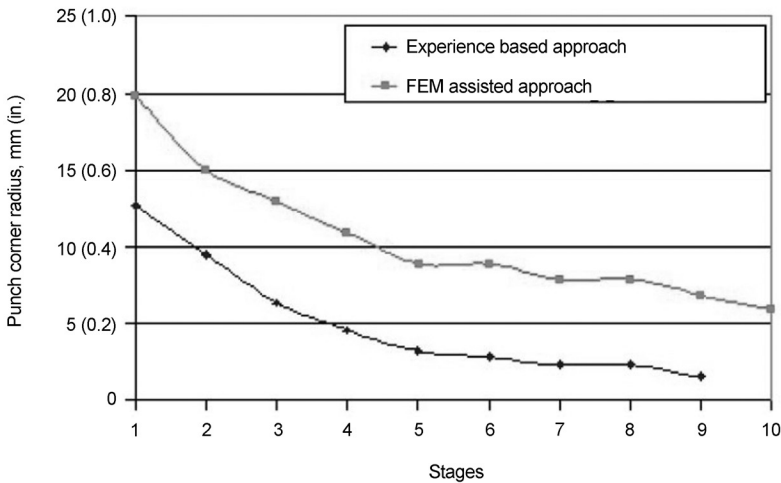


Fig. 4.13 Comparison of punch corner radii predicted by experience-based and finite-element method (FEM)-assisted methods

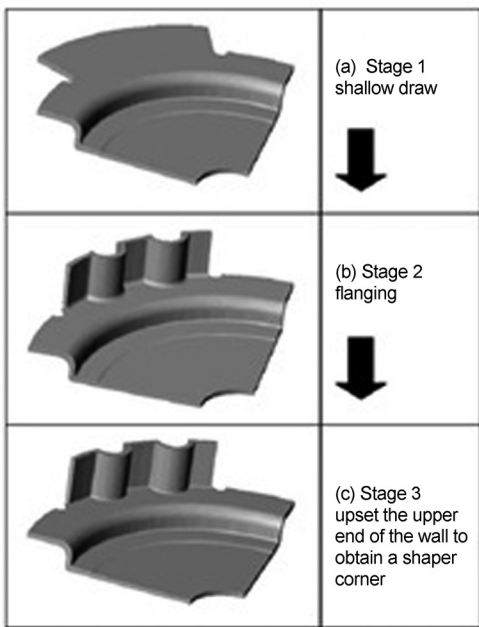


Fig. 4.14 Three stages in the process

To understand the process, it was necessary to:

- Simulate the flanging operation by assuming a noncorrugated flange wall
- Simulate the upsetting of the flanged wall (Fig. 4.16)

To eliminate the formation of the cracks, discussed earlier, the following improvements of the flanging operation were considered:

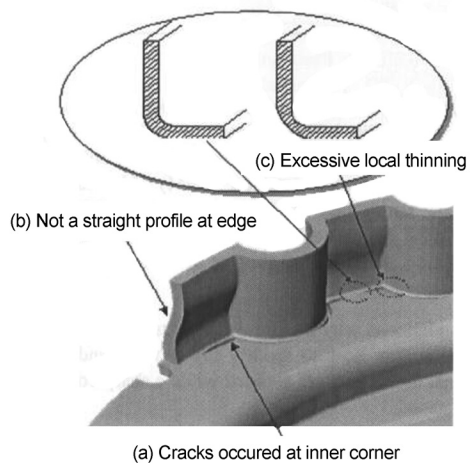


Fig. 4.15 Three defects observed in the present forming operation

- Coin (offset) the plate edge before flanging, as shown in Fig. 4.17. It was expected that this coining will lead to a sharper bend. It is necessary to determine the clearance in the tooling and the geometry of the coined surface. As seen in Fig. 4.17, it is expected that the top coining radius (upper plate surface) will be smaller than the bottom coining radius (lower plate surface).
- Coin the outside radius of the corner after flanging, as shown in Fig. 4.18. This is done in some cases to reduce springback and to achieve a sharper radius, and can be achieved during the flanging.

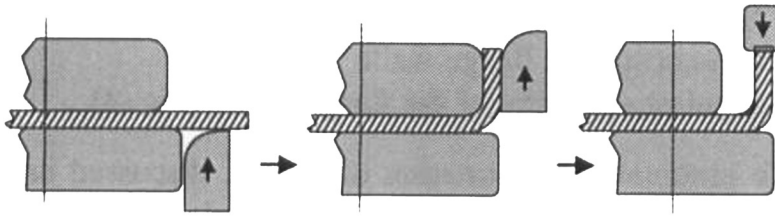


Fig. 4.16 Current process—flanging and upsetting

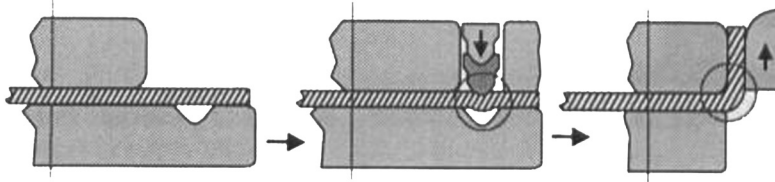


Fig. 4.17 Coin the plate before flanging

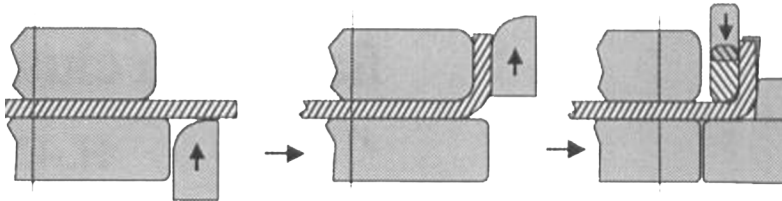


Fig. 4.18 Coin the inside corner after flanging

Simulations were conducted to investigate how these potential improvements could lead to the formation of a sharper corner and outside radius. The results of these simulations were evaluated, and, based on these results, the best alternative was selected for investigation during flange coining or upsetting. Using a tapered punch to coin the inner corner (Fig. 4.18) helped to reach both the inner and outer dimensions without fracture. However, this required a higher punch load if coining was done in one stroke. The solution was to coin regions A and C in one die station and regions B and D in another die station, as illustrated in Fig. 4.19 (Ref 4.11).

4.2 Application of FEA in Progressive Die Design

Process simulation using FEA and commercial software, such as PAMSTAMP, LS-DYNA, and AUTOFORM, is a commonly accepted die and process design tool in the automotive indus-

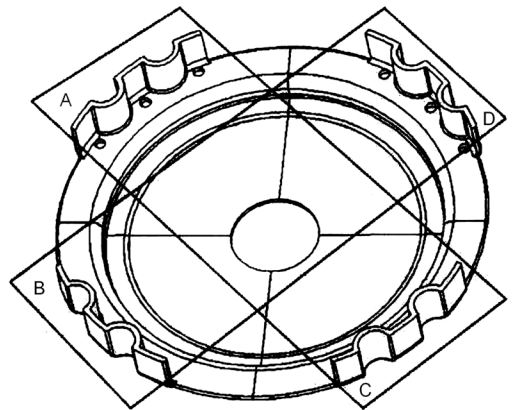


Fig. 4.19 Clutch hub investigated in this study, illustrating the coining of the inside corners by two steps (A and C; B and D)

try. Nearly all outer and inner panel dies are manufactured only after extensive process simulation and verification of metal flow to ensure no defects have been caused by wrinkling or splitting. Therefore, it is possible to select the

optimum geometry and location of draw beads, blank size and shape, and blank holder pressure.

Commercial software packages are also available for progressive die design. Most of these packages use solid modeling software, such as Solidworks or similar types. Thus, it is possible to achieve strip layout, draw reductions, unbending/flattening, as well as interference and collision detection. In addition to these geometry-related design considerations, it is also possible to apply FEA to predict metal flow, wall thinning, and to optimize the punch and die geometries, as discussed earlier.

Some die development studies that use finite-element simulation are available in the literature. For example, the optimum design of multiple-stage deep drawing of a molybdenum cup was conducted using a nonlinear optimization algorithm (Ref 4.12). A similar study for process and die design of multiple-step forming of round parts was carried out by other researchers (Ref 4.13–4.15). In summary, the review of literature and industrial state of technology indicated that the use of FEA, widely accepted for process and die design of large automotive panels, is gradually being employed for design and manufacturing of progressive and transfer dies.

REFERENCES

- 4.1 T. Altan et al., Sequence for Progressive Dies—Parts I and II, *Stamp. J.*, Jan 2005, p 32; Feb 2005, p 30
- 4.2 Schuler, GmbH, *Metal Forming Handbook*, Springer, 1998
- 4.3 M. Korneli, Designing Progressive Dies, *Stamp. J.*, Sept 17, 2001
- 4.4 D.B. Dallas, “Progressive Dies—Principles and Practices of Design and Construction,” SME, Dearborn, MI, 1994
- 4.5 A. Hedrick, Setting Up Progressive Dies—Parts I and II, *Stamp. J.*, Oct 2, 2006; Oct 10, 2006
- 4.6 N. Jain et al., Progressive Die Sequence Design for Deep Drawing of Cups Using FEA, *J. Manuf. Sci. Eng. (Trans. ASME)*, Vol 128, Feb 2006, p 366
- 4.7 J. Cao et al., Analysis of an Axisymmetric Deep Drawn Part Forming Using Reduced Forming Steps, *J. Mater. Process. Technol.*, Vol 117, 2001, p 193
- 4.8 S.H. Kim et al., Tool Design in Multi-Stage Drawing and Ironing Process of a Rectangular Cup with a Large Aspect Ratio Using FEA, *Int. J. Mach. Tools Manuf.*, Vol 42, 2002, p 863
- 4.9 DEFORM Simulation Software, Scientific Forming Technologies Corporation, www.deform.com
- 4.10 K. Lange, *Handbook of Metal Forming*, McGraw-Hill, New York, 1985
- 4.11 H.C. Wu and T. Altan, Process Optimization in Stamping—A Case Study for Flanging a Clutch Hub from Steel Plate, *J. Mater. Process. Technol.*, Vol 146, 2004, p 8
- 4.12 H.K. Kim and S. Hong, FEM-Based Optimum Design of Multi-Stage Deep Drawing Process of Molybdenum Sheet, *J. Mater. Process. Technol.*, 2007, p 354
- 4.13 S. Khamitkar et al., Process and Die Design for Multistep Forming of Round Parts from Sheet Metal, *J. Mater. Process. Technol.*, 1996, p 24
- 4.14 S.H. Kim, S.H. Kim, and H. Huh, Tool Design in a Multi-Stage Drawing and Ironing Process of a Rectangular Cup with a Large Aspect Ratio Using Finite Element Analysis, *Int. J. Mach. Tools Manuf.*, Vol 42, 2002, p 863–875
- 4.15 T.W. Ku and B.K. Ha, Finite Element Analysis of Multi-Stage Deep Drawing Process for High-Precision Rectangular Case with Extreme Aspect Ratio, *J. Mater. Process. Technol.*, Vol 130–131, 2002, p 128–134

CHAPTER 5

Warm Forming of Magnesium and Aluminum Alloys

Serhat Kaya, The Ohio State University

ONE OF THE MAJOR GOALS of engineering design and manufacturing is weight reduction to save energy. One way to achieve energy savings without jeopardizing the structural integrity of the product is to use lightweight metals, such as aluminum, magnesium, titanium, and their alloys. Although aluminum and magnesium alloys have great potential for producing sheet metal parts with reduced weight, these alloys have limited formability at room temperature and require special processing techniques. One way of improving the formability limits of these materials is to conduct the forming operation at elevated temperatures. In this chapter, material testing methods, data, and the warm forming processes for forming aluminum and magnesium sheet are discussed.

Among all metals, magnesium stands out with its lower density (1.7 g/cm^3) compared to aluminum (2.7 g/cm^3) and titanium (4.7 g/cm^3),

and with its high strength-to-weight ratio. Magnesium alloy AZ31B has the lowest E -modulus (48 GPa, or 6960 ksi) and yield stress (170 MPa, or 24 ksi) at room temperature (Fig. 5.1). However, magnesium has the highest specific strength (strength/density) of all metals. Figure 5.2 shows that it has approximately the same specific stiffness (elastic modulus/density) as other common metals, such as 1006 low-carbon steel, ASTM A572 high-carbon steel, and 5086 aluminum alloy.

5.1 Mechanical Behavior and Testing Methods

At elevated temperatures (~ 200 to $350 \text{ }^\circ\text{C}$, or 390 to $660 \text{ }^\circ\text{F}$), the magnesium and aluminum alloys exhibit a significant increase in formability. This feature is especially important in stamp-

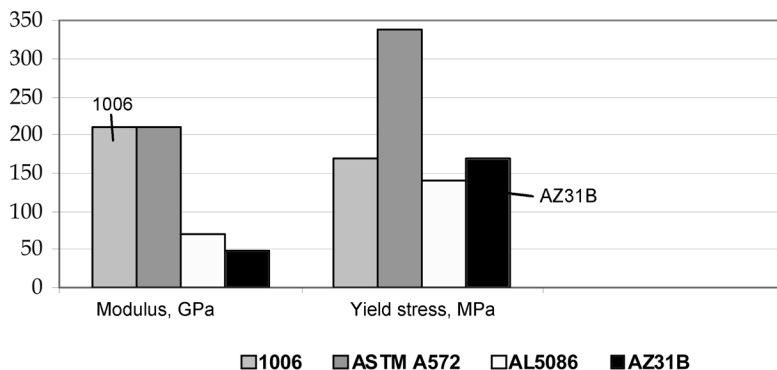


Fig. 5.1 E -modulus and yield stress comparison of various metals. Source: Ref 5.1

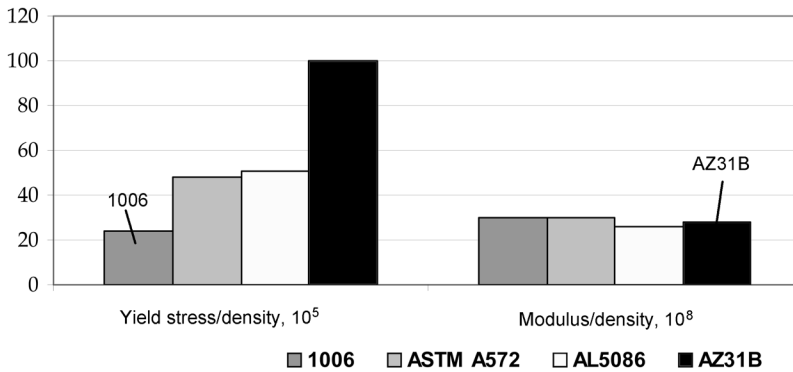


Fig. 5.2 Specific strength and specific stiffness comparison of various metals. Source: Ref 5.1

ing and drawing operations. This phenomenon becomes more obvious when relatively complex parts are desired, because the forming limits are reached at very early stages of the forming operation. Also, the tendency toward galling increases at elevated temperatures.

Tensile (Uniaxial) and Bulge (Biaxial) Tests

In testing materials at elevated temperatures to determine material behavior, uniform temperature distribution in the specimen is an important requirement. If this condition is not met, sections of the specimen with higher temperature will yield first and cause an unbalanced metal flow, which may lead to premature fracture.

The uniaxial tensile test (Fig. 5.3) is probably the most commonly used sheet metal formability test. The specimen is locked at each end and stretched until it fractures. The elevated-temperature tensile testing procedure is standardized in ASTM E 21 09. ASTM B 557M-94 describes the standard test methods for tensile testing of wrought and cast aluminum and magnesium alloys. The majority of the mechanical properties available in the literature are obtained by uniaxial tensile testing.

In an actual deformation process, the state of stress is mostly multiaxial rather than uniaxial. Therefore, a test that represents the actual deformation, such as bulging of a sheet, provides data closer to reality. In recent years, bulging of sheets at elevated temperatures has been in the focus of researchers.

In a bulge test, equi-biaxial state of stress is achieved. In this test, the sheet is clamped between the lower and upper dies (Fig. 5.4). When the medium in the lower chamber is pressur-

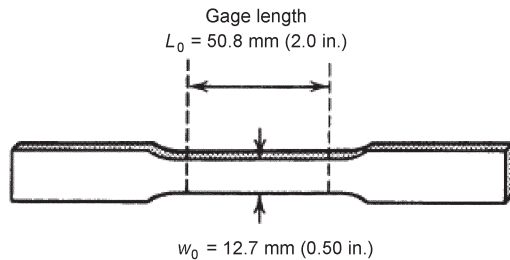


Fig. 5.3 Tensile test specimen

ized, the sheet is bulged into the cavity of the upper die. The clamping force between the lower and upper die must be high enough to prevent sliding of the sheet to the die cavity. Sometimes, a lockbead is used to prevent the movement of the sheet in the clamped region, so that the sheet will only be stretched and no draw-in will occur. When the deformation of the material exceeds its formability limit, the sheet ruptures. In this test, the deformation is not affected by friction; therefore, the reproducibility of the test results is good. Figure 5.5 shows a slab from the apex of the dome of the bulged sheet. Due to equi-biaxial deformation, σ_1 and R_1 are assumed to be equal to σ_2 and R_2 , respectively.

By using membrane theory and calculating the hoop and transverse stresses (Fig. 5.5), it is possible to obtain the effective stress values for determining the flow-stress curves.

Definitions of the parameters shown in Fig. 5.4 are:

- t_0 = initial thickness of the sheet
- t_d = thickness at the apex of the bulge

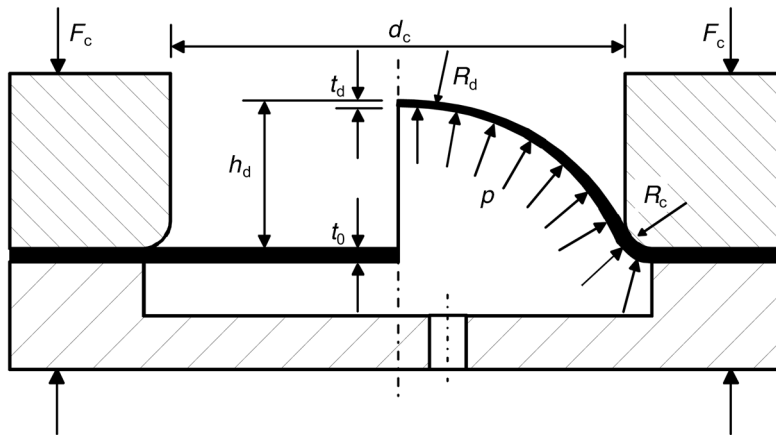


Fig. 5.4 Initial (left) and pressurized (right) sheet in the hydraulic bulge test and geometrical/process-related parameters

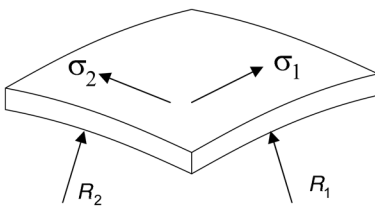


Fig. 5.5 Hoop (σ_1) and transverse (σ_2) stresses and dome radii shown in a slab from the apex of the dome

h_d = bulge height
 R_d = bulge radius
 d_c = diameter of the die cavity
 R_c = radius of the die ring
 F_c = clamping force
 p = hydraulic pressure

There are various methods of heating the sheet in hydraulic bulge testing. The most common method is holding the sheet between heated tools and applying air or gas pressure to bulge the damaged sheet. Another approach is to conduct the test under a heated liquid bath to obtain uniform temperature in the sheet. This method is explained later in this chapter.

Aluminum Alloys. Table 5.1 and Fig. 5.6 and 5.7 provide the details of tensile testing of 3003-H aluminum alloy, engineering stress-strain curves, and true stress-true strain curves, respectively. Similar data are provided in Table 5.2 and Fig. 5.8 for aluminum 5182-O for a higher strain range and temperature. Variation of strain-rate sensitivity index (m) and strain-hardening index (n) with temperature and strain

Table 5.1 Aluminum 3003-H111 tensile test data

Material	AA3003-H111 (Mn, 1.10%; Fe, 0.5%; Si, 0.21%; Zn, 0.01%; Ti, 0.02%; Cu, 0.07%; Mg, 0.02%)
Test procedure	Uniaxial tension tests, Instron Model 1127
Dimensions/standards	ASTM E 8 and E 517; G = 50 mm, W = 12.5 mm
Range of strain	0–0.5
Range of strain rate	0.0083/s
Range of temperature	25–260 °C (75–500 °F)
Heating method	Convection heating

Source: Ref 5.2

rate for aluminum alloys 5182, 5754, and 6111 are given in Fig. 5.9 and 5.10. Tensile and bulge tests of 3003-H alloy show that while 0.2 maximum strain is obtained in a tensile test, 0.8 maximum strain is obtained in the bulge test. Balanced biaxial testing of 3003-H aluminum sheet (Table 5.3 and Fig. 5.11) clearly shows the higher strain levels of 0.8 that are obtained. Figure 5.12 shows another comparison between uniaxial and balanced biaxial testing of AlMg0.4Si1.2 (German designation; 60XX is the corresponding alloy group in U.S. designation). At 200 °C (390 °F), effective strain values of 0.22 and 0.67 are obtained from the tensile and the hydraulic bulge tests, respectively (Fig. 5.12).

Magnesium Alloys. The most important group of magnesium alloys that can be formed is the Mg-Al-Zn (AZ alloy) group, with alloying elements of aluminum and zinc. The most common AZ alloys are AZ31 (3% Al, 1% Zn), AZ61 (6% Al, 1% Zn), and AZ80 (8% Al, 0.5%

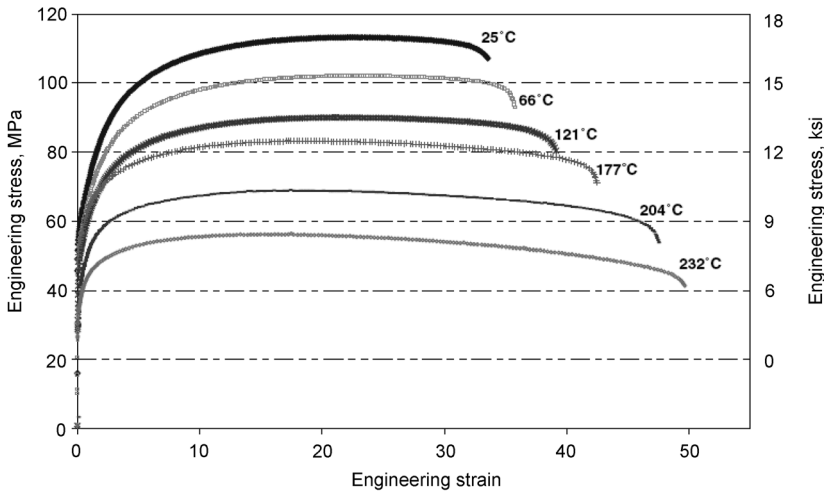


Fig. 5.6 Engineering stress versus engineering strain curves at various temperatures. Source: Ref 5.2

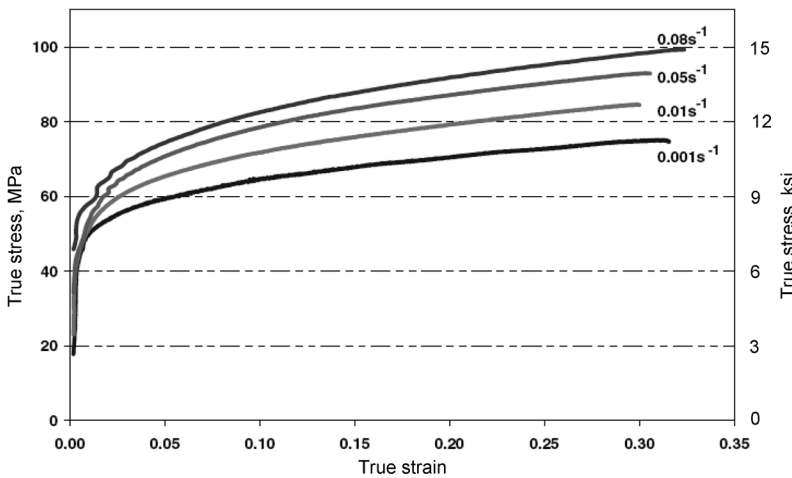


Fig. 5.7 True stress versus true strain curves at various strain rates at $T = 240\text{ }^{\circ}\text{C}$ ($464\text{ }^{\circ}\text{F}$). Source: Ref 5.2

Table 5.2 Aluminum 5182-O tensile test data

Material	Al 5182-O (Mg, 4.51%; Fe, 0.2%; Mn, 0.3%; Si, 0.1%; Cu, 0.04%; Cr, 0.04%; Zn, 0.01%)
Test procedure	Uniaxial tension tests
Range of strain	0–0.9
Range of strain rate	Negative
Range of temperature	20–320 °C (75–610 °F)
Source: Ref 5.3	

Zn). Doege et al. (Ref 5.6) have conducted investigations on the mechanical properties of magnesium alloy sheet AZ31B at room temperature by conducting uniaxial tensile tests in which the alloy showed an elongation of 17%

and a strain-hardening coefficient of 0.17. Takuda et al. (Ref 5.7) have conducted uniaxial tensile tests at constant crosshead velocities (0.02, 0.2, 2, and 20 mm/s) between 150 and 300 °C (300 and 570 °F).

Above 200 °C (390 °F), magnesium alloy sheet (AZ31B) shows a remarkable increase in formability, as shown in Fig. 5.13. The effect of strain rate on the flow stress of AZ31B at 200 °C is also investigated by conducting uniaxial tensile tests at various strain rates from 0.002 to 2 s⁻¹. As the strain rate increased, the flow stress of AZ31B increased, as shown in Fig. 5.14 (Ref 5.6).

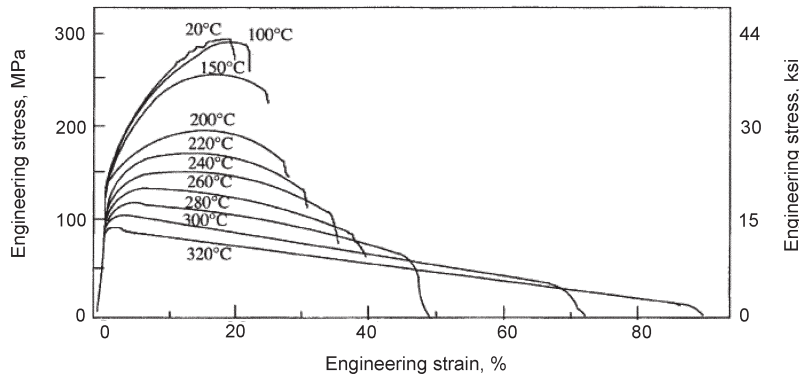


Fig. 5.8 Engineering stress-strain curves of 5182-O at various temperatures. Source: Ref 5.3

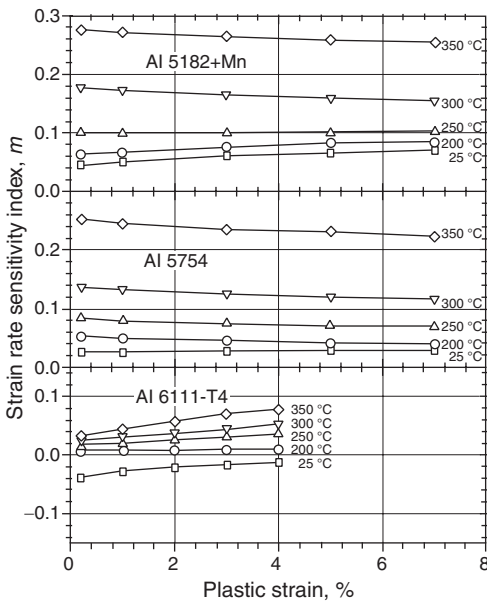


Fig. 5.9 Variation of strain-rate sensitivity exponent with plastic strain at various temperatures for various aluminum alloys. Source: Ref 5.4

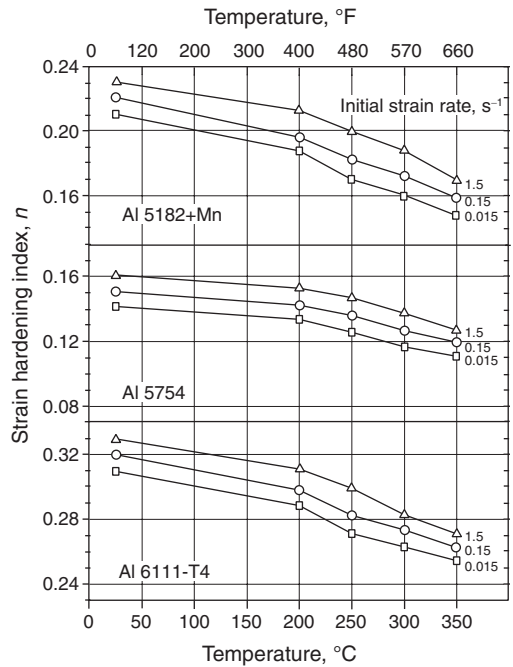


Fig. 5.10 Variation of strain-hardening rate with temperature at various strain rates for various alloys. Source: Ref 5.4

Kaya et al. (Ref 5.8) have performed hydraulic bulge testing of magnesium sheets using the submerged testing method (Fig. 5.15). The objective of this method is to minimize or eliminate the temperature gradient in the sheet. Figure 5.16 shows room- and elevated-temperature forming behavior of magnesium AZ31-O sheet. Figure 5.17 shows the calculated true stress and true strain curves at approximate strain-rate values of 0.025 s^{-1} at various temperatures. A maximum strain value of 0.7 s^{-1} is reached, whereas

Table 5.3 Aluminum 3003-H111 bulge test data

Material	AA3003-H111(Mn, 1.10%; Fe, 0.5%; Si, 0.21%; Zn, 0.01%; Ti, 0.02%; Cu, 0.07%; Mg, 0.02%)
Test procedure	Balanced biaxial tension (bulge) test
Range of strain	0–0.5
Range of strain rate	0.001–0.08 s^{-1}
Range of temperature	25–232 °C (75–450 °F)

Source: Ref 5.2

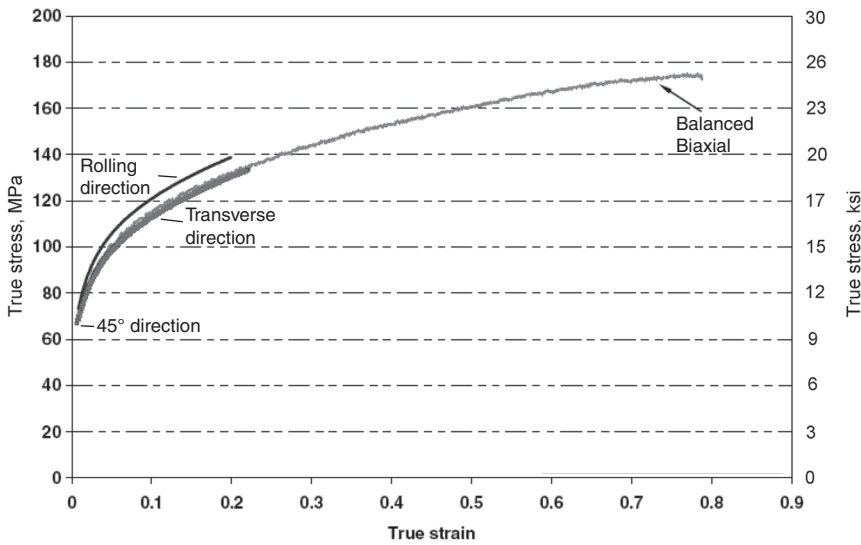


Fig. 5.11 Comparison of true stress versus true strain curves conducted by tensile tests in different directions and bulge tests. Source: Ref 5.2

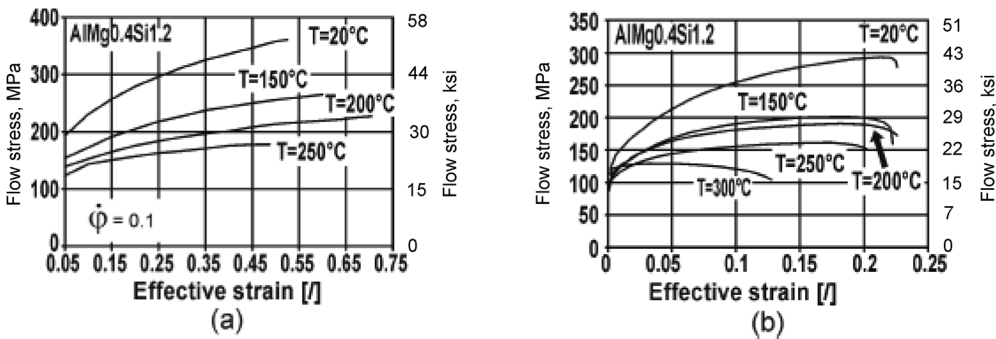


Fig. 5.12 Aluminum flow-stress curves determined by (a) bulge and (b) tensile tests. Source: Ref 5.5

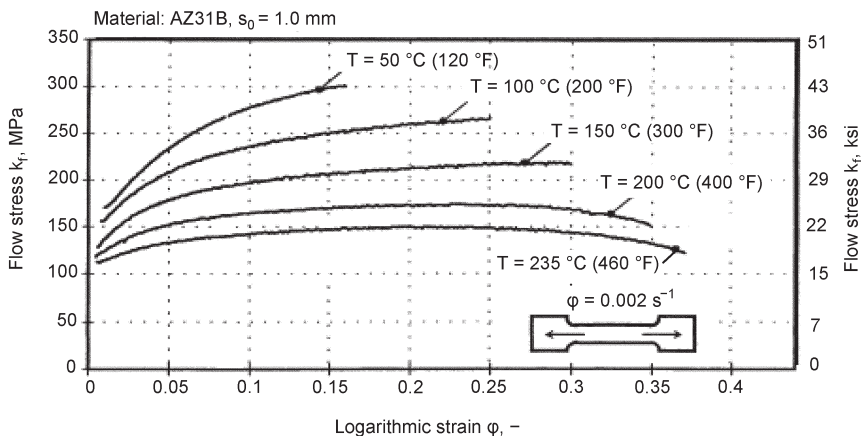


Fig. 5.13 Temperature-dependent flow stress of magnesium AZ31B alloy determined by tensile test. Source: Ref 5.6

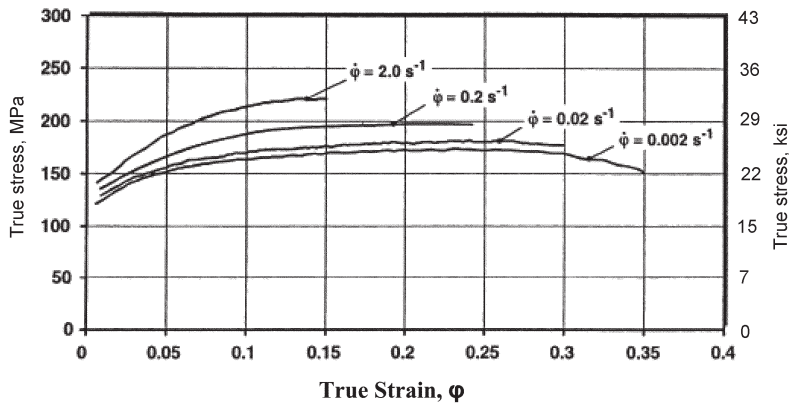


Fig. 5.14 Effect of strain rate on flow stress ($t_0 = 1 \text{ mm}$; $T = 200 \text{ }^\circ\text{C}$, or $390 \text{ }^\circ\text{F}$). Source: Ref 5.6

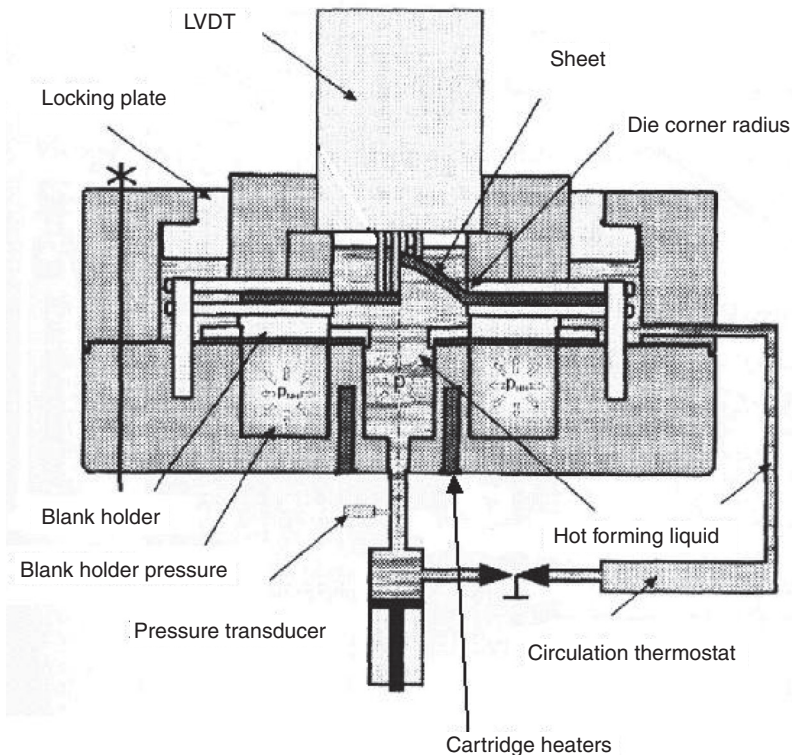


Fig. 5.15 Submerged bulge test tooling. LVDT, linear variable differential transformer. Source: Ref 5.8

the achievable strains using the tensile test are approximately 0.3 at the same strain-rate values.

Strength Asymmetry in Magnesium Alloy Sheet

Magnesium alloy sheets tend to exhibit asymmetric behavior in yielding (much higher yield stress during in-plane tension than compression)

because of different metallurgical mechanisms that operate under different loading conditions. Early studies conducted using magnesium alloys HM21A-T8, HK31A-H24, and HM31A-T5 show that tensile yield strengths are considerably higher than compressive yield strengths at room temperature. However, at approximately $200 \text{ }^\circ\text{C}$ ($390 \text{ }^\circ\text{F}$), the difference between tensile and compressive yield strengths decreases to an

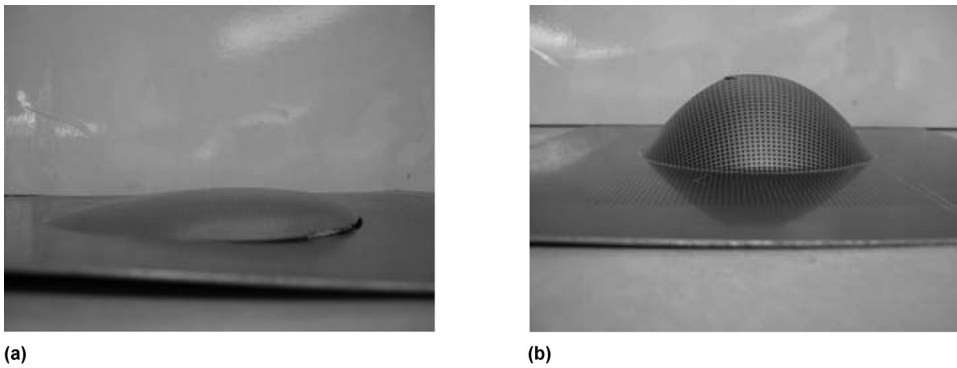


Fig. 15.16 Variation in formability at room and elevated temperatures. (a) Bulge height: 12 mm (0.5 in.); room temperature. (b) Bulge height: 38 mm (1.5 in.); 225 °C (435 °F). Source: Ref 5.8

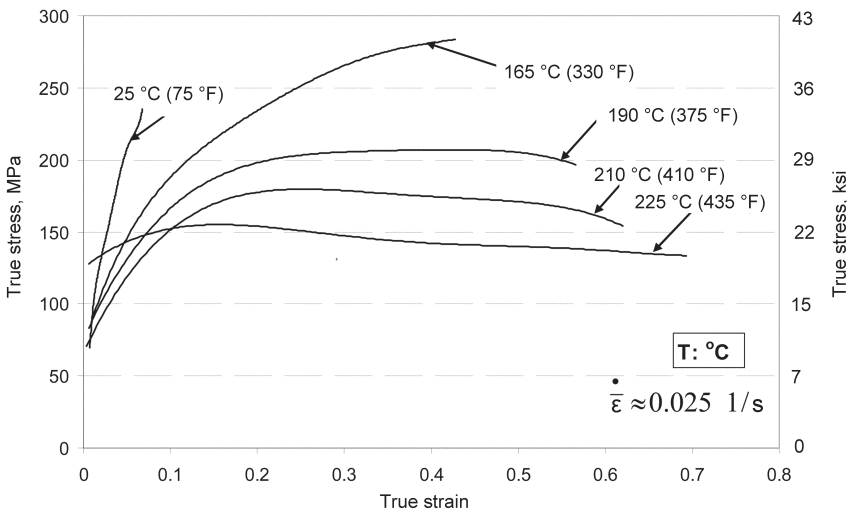


Fig. 5.17 Magnesium AZ31-O flow-stress curve obtained from the hydraulic bulge test. Source: Ref 5.8

average value of 7.5 MPa (1.1 ksi). Above 315 °C (600 °F), the tensile and compressive yield strengths become equal (Ref 5.9). Figure 5.18 shows the flow curves obtained from rolling direction and transverse direction compression tests at different temperatures in which test samples were strained to a strain of 1.0 or failure, whichever occurred first. The transverse direction samples are stronger at every temperature, as observed by Duygulu et al. (Ref 5.11).

5.2 Warm Forming Process

Warm Forming as a System

Compared to room-temperature forming, elevated-temperature forming brings many complexities and requires a systematic approach.

The incoming material dimensional tolerances and properties, the forming temperature, the interface condition (lubricant/friction and heat transfer), the tool temperature, the forming speed (or strain rate), and the forming equipment strongly influence the final product shape and properties as well as the economics of the process. A fundamental understanding of the relationship between the input and output variables of the system is essential for developing a robust, productive, and economical manufacturing process.

Isothermal and Nonisothermal Warm Forming

Warm forming can be conducted under isothermal or nonisothermal conditions. For forming under isothermal conditions, all tooling

components (die, blank holder, and punch) are heated, but for nonisothermal conditions, only the die and blank holder are heated and the punch is cooled. The effect of cooling the punch on the enhancement of the formability is quite significant and is discussed later.

The selection of isothermal or nonisothermal warm forming depends on the desired increase in formability. Especially in deep drawing, nonisothermal tooling can provide more formability compared to isothermal tooling but will be more expensive because of the extra equipment and controls needed to cool the punch.

In warm forming, various heating methods can be used to heat the sheet. These are as follows:

- *Heating the sheet in a furnace that is outside the tool and forming in a nonheated tool:* This method poses a risk of causing inhomogeneous temperature in the sheet. Also, any heating outside the tooling will require additional equipment to transfer the sheet from the furnace to the tool. It should be kept in mind that the objective is faster and homogeneous heating of the sheet.
- *Using a heated medium to heat the sheet in a hydraulic bulging or pressure forming process:* This method was described in the introduction to this chapter, and an industrial application of this type of process is provided later in the chapter.

- *Heating the sheet between heated tools:* This method requires a press that would allow the press ram to stop and dwell before forming.

Mechanics of Deformation

One way to enhance formability in warm forming (deep drawing) is to cool and heat different portions of the sheet at the same time. In Fig. 5.19, a schematic of a deep-drawn sheet divided into five deformation zones (A-B, B-C, C-D, D-E, E-F) shows heating and cooling of various zones.

The portion of the blank that is between the blank holder and the die (E-F) must be heated in order to reduce the compressive stresses at the flange area and facilitate the metal flow. Therefore, the blank holder and the die must be heated. However, once the sheet enters the die corner (E-D) and starts contacting the punch wall (D-C) and the punch corner area (C-B), the sheet temperature drops through the transfer of heat to the (cooled) punch. Therefore, the sheet in contact with the punch will be cooler than the rest of the sheet. This means that it can withstand more drawing stress and therefore will stretch less. Since the deformation is continuous, the portion of the drawn cup in contact with the punch continues to cool. However, the sheet that is under the heated dies has a higher temperature, which is necessary for forming around the die corner. This drop in sheet tem-

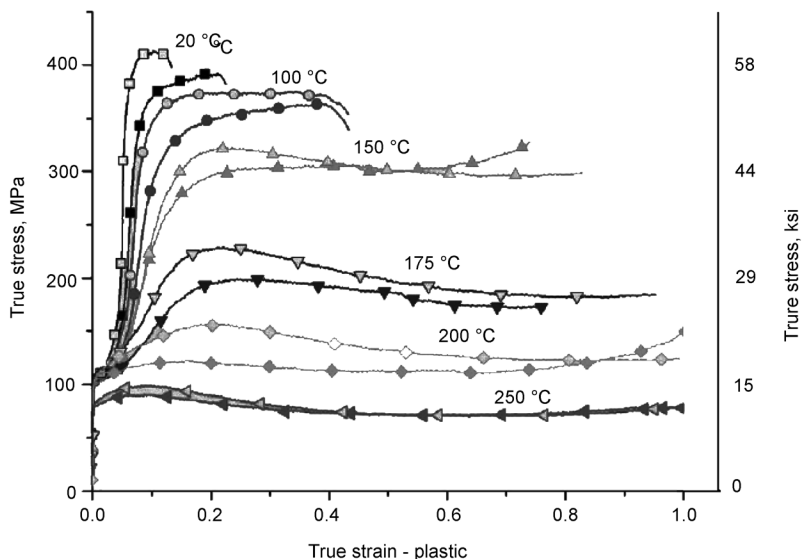


Fig. 5.18 Flow curves as a function of testing temperature. The transverse direction samples (open symbol) are stronger than the rolling direction samples (closed symbols) at all temperatures. Source: Ref 5.10

perature prevents premature fracture and allows the sheet to be drawn into the die cavity successfully. As the punch temperature decreases, formability increases. The effect of punch temperature on the limiting draw ratio is shown in Fig. 5.20.

Lubrication and Heat Transfer

Heat transfer at the tool/blank interface is affected by the surface roughness of the blank/tool, the lubricant, and the amount of interface pressure. Among these, lubrication becomes more important in warm forming than in room-temperature forming, because temperature changes the property of the lubricant, and the tendency toward galling increases. Lubricant performance depends primarily on the forming temperature. For temperatures up to 120 °C (250 °F), oil, grease, tallow, soap, and wax are

generally used in warm forming of metals. A soap solution is acceptable for temperatures of up to 230 °C (450 °F). When the forming temperature exceeds 230 °C, the choice of lubrication is generally restricted to molybdenum disulfide, a colloidal solution of graphite, and polytetrafluoroethylene (PTFE). These lubricants should be cleaned from magnesium parts as soon as possible to avoid corrosion and permanent sticking to the part (Ref 5.12, 5.13). Kaya et al. (Ref 5.14) have used a PTFE film (327 °C, or 620 °F, melting temperature and 600% elongation) and obtained satisfactory results (Fig. 5.21). The main advantages of this lubricant are that it is lower cost, hazard-free, environmentally friendly, easy to apply and peel off, and not productive of fumes and smoke when exposed to heat.

Tool and Process Design

In the design of warm forming tooling, temperature distribution and control at different locations of the die, blank holder, and punch are very critical for obtaining defect-free parts. A uniform temperature distribution in the sheet will ensure proper deformation of the sheet. Because of the temperature, thermal expansion plays a significant role in tool design. For example, the difference in coefficient of thermal expansion between mild steel and magnesium makes it necessary to provide dimensional allowances on the punch and die, which will affect the part geometry (Ref 5.13).

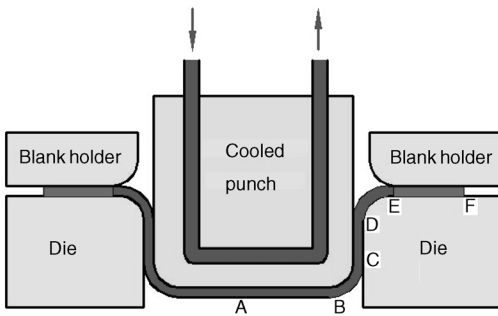


Fig. 5.19 In nonisothermal warm forming, cooling the die corner and the punch increases drawability.

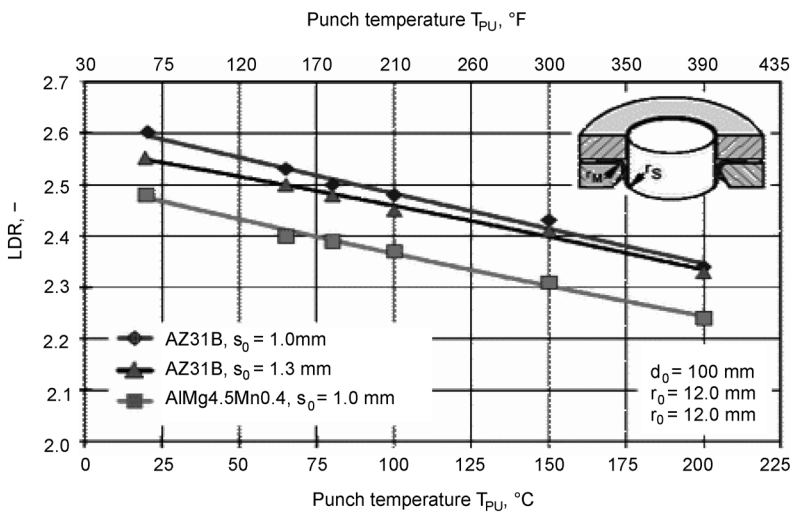


Fig. 5.20 Limiting draw ratio (LDR) decreases with increasing punch temperature. Source: Ref 5.1

The minimum bending radius noticeably decreases with increasing forming temperature. Table 5.4 provides design guidelines for the minimum bending radii of AZ31-O/H24 alloy sheets (thickness: 0.51 to 6.3 mm, or 0.02 to 0.249 in.). These minimum bend radii are based on bending a 152 mm (6 in.) wide specimen through 90°. It is clearly seen that bendability of an annealed (-O) magnesium alloy is higher ($5.5t_0$) than a hardened alloy (-H) ($8t_0$) at room temperature. However, at elevated temperatures of approximately 260 °C (500 °F), the minimum bending radius becomes $2t_0$ for both annealed and hardened alloys.

In case of higher strain requirements at lower temperatures, the use of soft-annealed (-O temper) magnesium sheets provides higher formability than cold-worked alloys (-H temper).

The recommended draw ring radius is from 4 to 7 times the initial sheet thickness (t_0). A draw ring radius in this range is found to provide the maximum drawability. Recommended punch-die clearance is 0.13 to 0.25 mm (0.005 to 0.01 in.) in addition to the sheet thickness. Draw ring



Fig. 5.21 Polytetrafluoroethylene film used in warm forming. Source: Ref 5.14

Table 5.4 Minimum bending radii for magnesium sheets

Temperature		Minimum bending radius as multiple of initial sheet thickness, mm	
°C	°F	AZ31B-O	AZ31B/H24
21	70	5.5	8.0
149	300	4.0	6.0
204	400	3.3	3.0
260	500	2.0	2.0

Source: Ref 5.15

radii larger than $7t_0$ may increase the tendency for puckering. Unparallel upper and lower tooling will have an amplified effect in the drawing of the sheet due to the temperature in the sheet (Ref 5.15).

Die Heating Techniques and Press Selection

Heating elements (cable heaters, cartridge heaters, etc.), insulation, temperature sensors, and temperature-control devices are part of the tooling used for warm forming. While designing the heated die system for the forming of aluminum and magnesium alloys, consideration must be given to the high thermal conductivity and low specific heat capacity of these alloys, because they can lose and gain heat rapidly when they come in contact with the dies.

Many methods are used for heating sheet and tools before and during forming operations, depending on the production volume, the type of forming process, and the equipment. Either gas or electricity can be used as the primary heat source. Actual heating may be done by ovens, platen heaters, ring burners, electric heating elements, heat-transfer liquids, or induction heaters. Among the methods available for heating the dies, resistance heating using cartridge heaters appears to be most appropriate for deep drawing. A schematic view of a tooling with cartridge heaters (up to 450 °C, or 840 °F) in a round cup tooling is given in Fig. 5.22. Another example of a tooling (up to 250 °C, or 480 °F) used by General Motors is given in Fig. 5.23.

Figure 5.24 shows a schematic view of a rectangular warm forming tool (die cavity size is 110 by 50 mm, or 4.3 by 2 in.; punch size is 100 by 40 mm, or 3.9 by 1.6 in.) with heated dies and punch. All radii in this tool were designed to be 5 mm (0.2 in.). Li et al. (Ref 5.18) have reported part depths of 8 and 20 mm (0.3 and 0.8 in.) with this tooling when the punch and the die were set at 200 and 350 °C (390 and 660 °F) (isothermal conditions), respectively. However, they also observed that the formability of the aluminum alloy was higher when the punch temperature was set at least 50 °C (90 °F) lower than the dies.

A deep drawing tooling that is heated with cartridge heaters (up to 310 °C, or 590 °F) while the punch is cooled (~65 °C, or 150 °F) by water circulation was built by Aida (Ref 5.19) and used by Kaya et al. (Ref 5.14). The die and blank holder temperatures were measured and controlled through a temperature controller

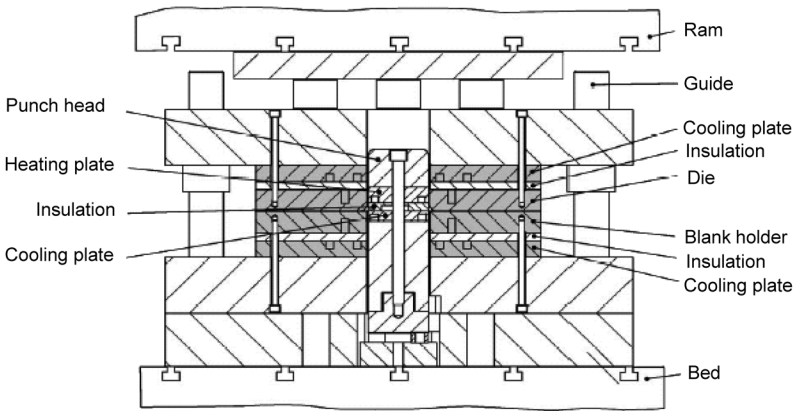


Fig. 5.22 Heating system for round cup tooling. Source: Ref 5.16

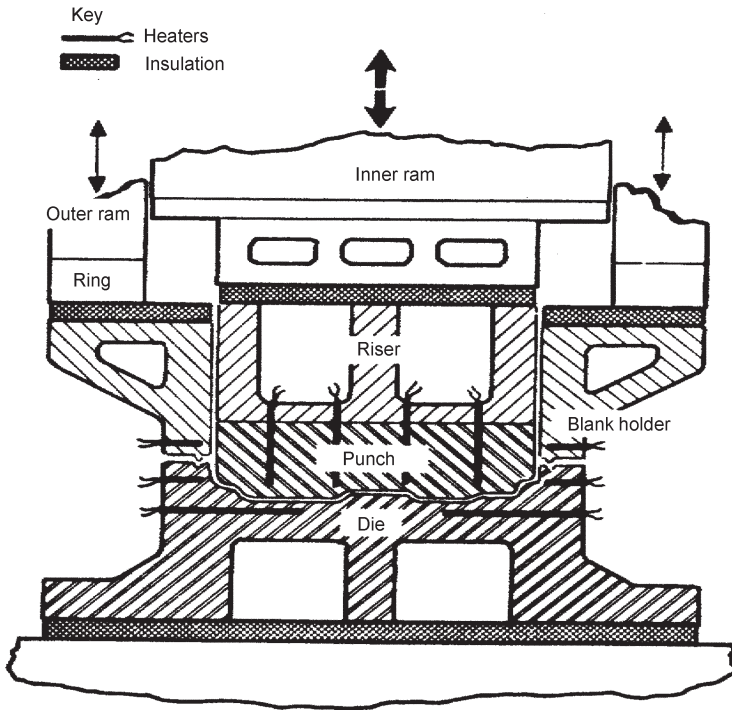


Fig. 5.23 Heating systems for industrial stamping tooling. Source: Ref 5.17

within $\pm 1\text{ }^\circ\text{C}$ ($2\text{ }^\circ\text{F}$) accuracy. Glass fiber insulators were used between the tool plates and the die ring holder to prevent heat transfer to the upper and lower press beds and to minimize thermal expansion. Figures 5.25 and 5.26 show the tool geometry and the upper and lower dies, respectively. The tool was placed in a servomotor-controlled press to obtain maximum flexibility in the press motion.

Figure 5.27 shows a tooling setup for deep drawing of magnesium in a hydraulic press. In this setup, ring burners provide gas heat to the blank holder, draw ring, bottoming die, and punch when necessary. Figure 5.28 shows a different tool setup with electric heaters used in a mechanical press.

One of the main advantages of warm forming is that, because the sheet is heated and the form-

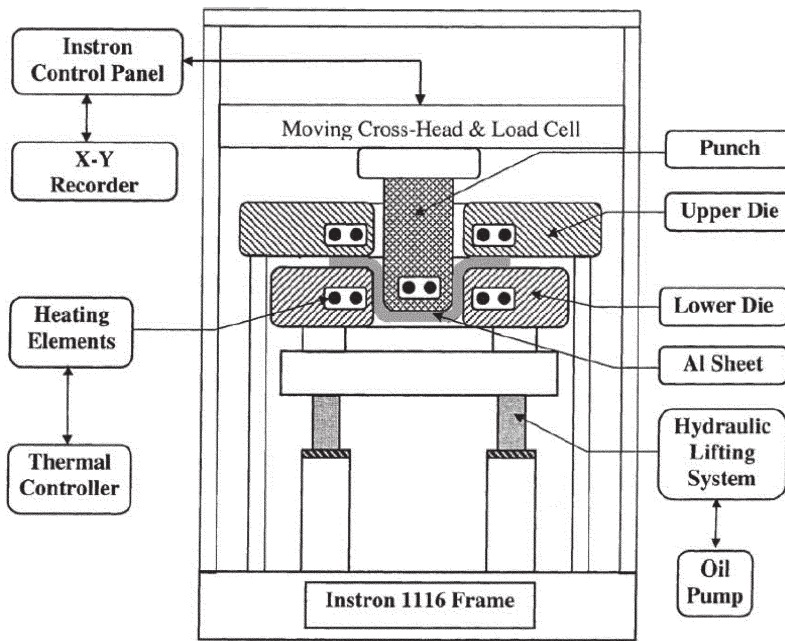


Fig. 5.24 Schematic view of a tooling in which dies and punch are heated. Source: Ref 5.18

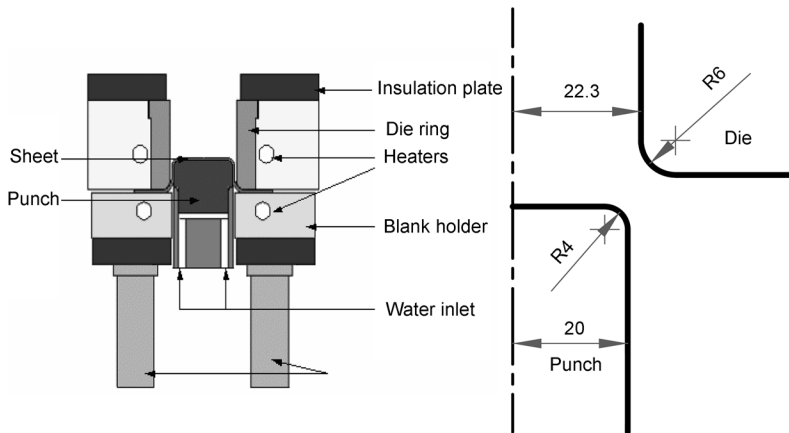


Fig. 5.25 Schematic view/dimensions of the round tool. Courtesy of Aida-America Corporation

ing load requirement is therefore reduced, less press tonnage is required. Selection of the press (mechanical, hydraulic, servo) is important because the process speed determines the amount of heat transfer that takes place in the sheet before and during forming. Therefore, press selection should be based on careful calculation of the allowable heat transfer for a successful part. This becomes especially important in nonisothermal forming because of the contact of the heated sheet with the cold punch.

Hydraulic and servo-driven presses are preferred when more accurate press control is needed for forming an intricate part. Mechanical presses are preferred when higher production rates are needed in parts with moderate depth of draw.

Servo-motor-driven presses are the newest press technology; they provide extreme accuracy and flexibility in press motion. The schematic drive system of a 110 ton AIDA servo press is seen in Fig. 5.29. Unlike conventional

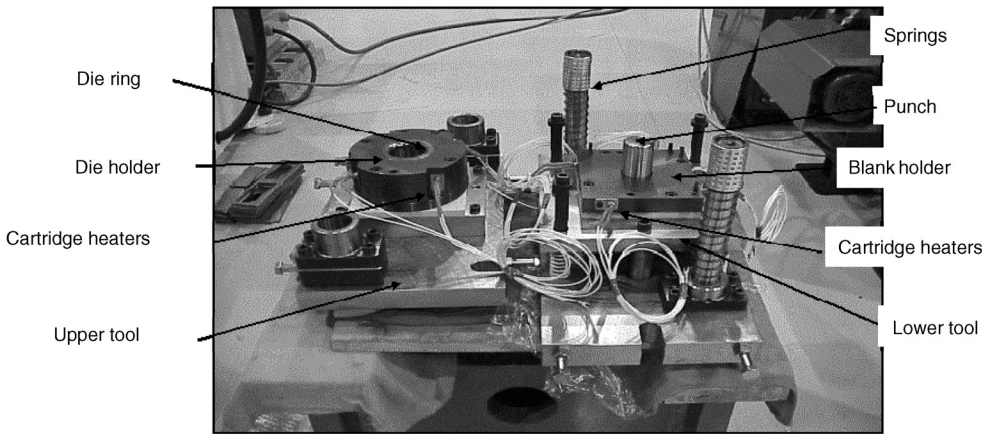


Fig. 5.26 Open warm forming tooling (top die set on the left, bottom die set on the right). Courtesy of Aida-America Corporation

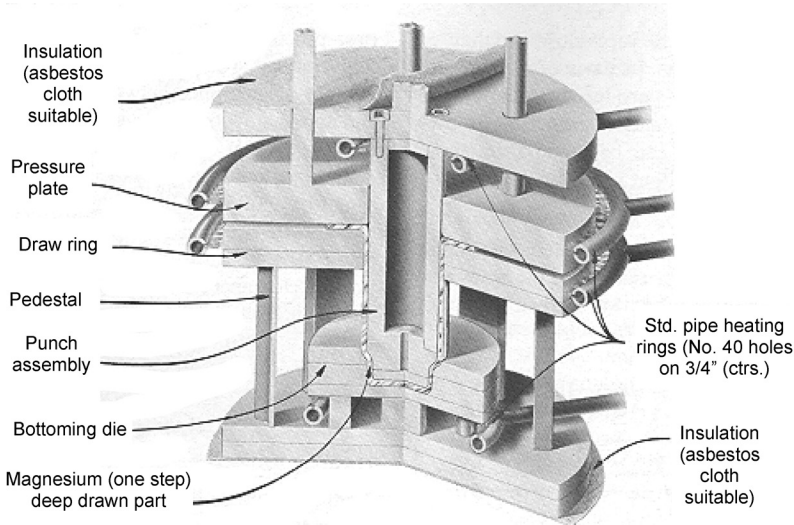


Fig. 5.27 Tooling design for warm forming in a hydraulic press using gas ring burners. Source: Ref 5.13

mechanical and hydraulic presses, the servo drive allows programming the press slide stroke position and velocity in infinite ways, as illustrated in Fig. 5.30 for warm forming processes. Additionally, the press slide provides constant load throughout the stroke at any speed. The press can be stopped prior to deformation, and the sheet can be heated between the heated upper and lower tools under a certain load for a certain amount of time. This stage is called the dwelling stage. With a servo-motor-controlled press, the need for an outside heating furnace is eliminated, and an accurate sheet temperature

can be obtained because the dwelling time can be changed as needed.

5.3 Applications of Warm Forming

The basis for selecting any material for producing a part should be that the part will offer the best compromise between cost and functionality. The main reasons for using aluminum and/or magnesium alloys are their light weight and their potential applications in the automotive, electronics, and appliance industries. Addition-

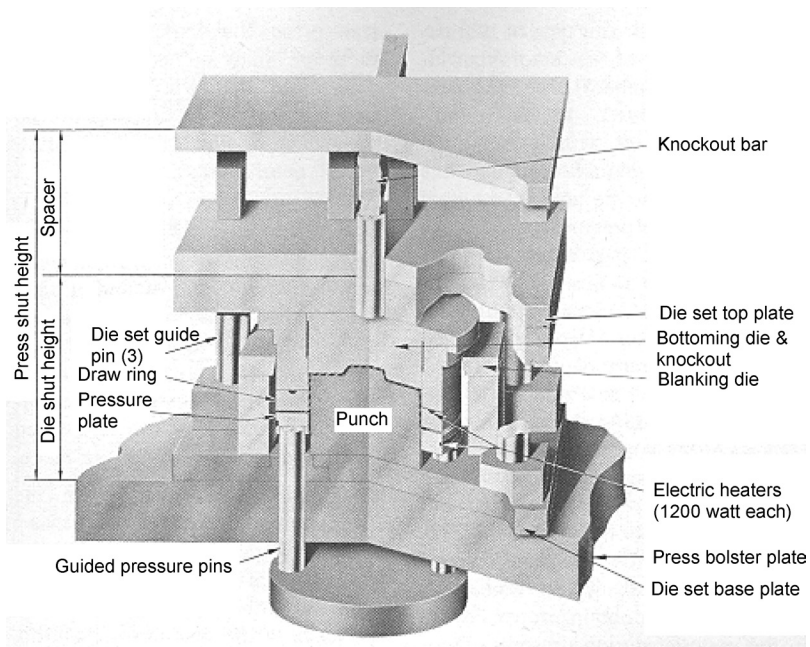


Fig. 5.28 Tooling design for warm forming in a mechanical press using electric heating elements. Source: Ref 5.13

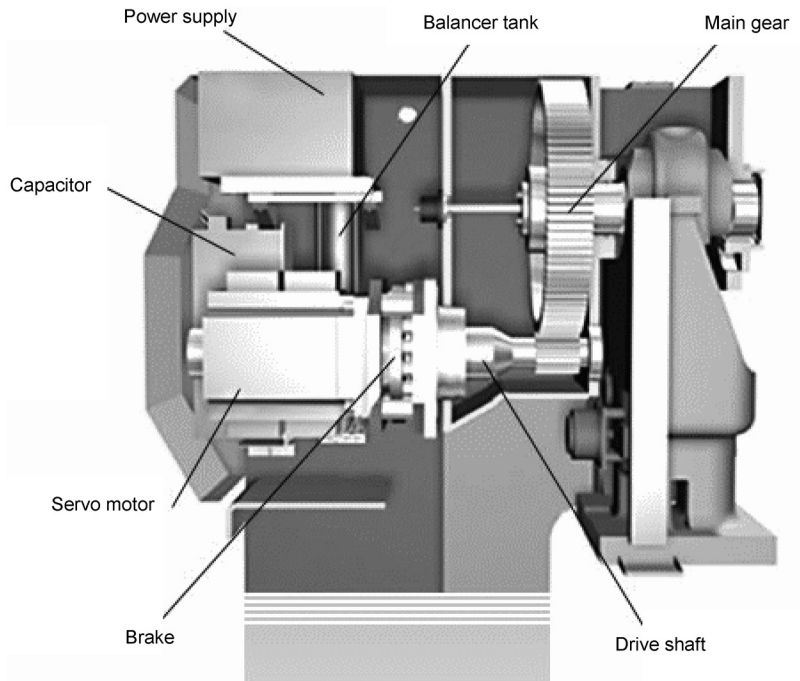
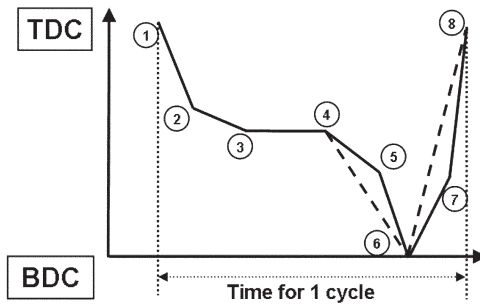


Fig. 5.29 Schematic view of the servo motor drive system. Courtesy of Aida-America Corporation



1-2	Fast approach
2-3	Slower approach reduces impact and vibrations. Both tools are in contact at 3.
3-4	Dwell (heating of the blank)
4-5	Slower punch velocity for forming sharp corner radii
5-6	Higher velocity for faster forming
6-7	Slower exit from the tool
7-8	Faster return to TDC

Fig. 5.30 Slide motion of the servo press in warm forming. TDC, top dead center; BDC, bottom dead center

ally, some advantages and cost-savings may be realized through reduced forming loads (and therefore reduced press capacity requirements), reduced wear, and the use of lower-grade tool steels with lower hardness.

5.4 Deep Drawing

In warm deep drawing, as the forming temperature increases and punch velocity decreases, formability (drawability) increases. Among the earliest studies on deep drawing aluminum alloys, in both annealed and hardened tempers, are those reported in Ref 5.20 and 5.21. In these studies, elevated-temperature drawability of several aluminum alloys for drawing both rectangular and circular cups was investigated. Even the precipitation-hardened alloys 24S-T (2024-T4), 24S-T86 (2024-T86), and 75S-T (7075-T6) showed significant improvement in their drawability (indicated by cup height) at a relatively moderate temperature of 150 °C (423 K), for both rectangular and circular cups. Typical results of improved drawability with increasing temperature are shown in Fig. 5.31. Bolt et al. (Ref 5.22) performed cup drawing tests using 1050-, 5754-, and 6016-series alumi-

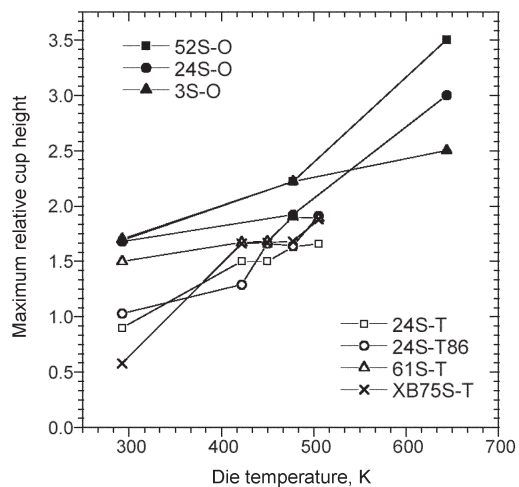


Fig. 5.31 Effect of die temperature on the maximum relative height (height of cup/punch radius) of cups for various aluminum alloys. Source: Ref 5.20

num sheets, and the product height was increased 50% in the range 175 to 250 °C (350 to 480 °F). Li et al. (Ref 5.18) investigated warm forming of rectangular parts using internally heated punch and die in both isothermal and nonisothermal conditions.

Additional information for warm forming technology for aluminum alloys can be found in Ref 5.17 and 5.22 to 5.29.

Experimental Investigations

Kaya et al. (Ref 5.14) conducted experiments to determine the operating window (forming velocity, tool temperature, and blank size/limiting draw ratio, or LDR) for the warm deep drawing process. Figures 5.32 and 5.33 show the variation of LDR with punch velocity at various temperatures for aluminum 5754-O and magnesium AZ31-O, respectively. The tool geometry is given in Fig. 5.25. The numbers in boxes at each point in Fig. 5.32 and 5.33 show the maximum thinning (in percent) obtained in the fully drawn cups.

Blank size influences the attainable punch velocity significantly. Punch velocities up to 300 mm/s (11.8 in./s) are obtained for the magne-

sium alloy sheet, whereas the best punch velocity for the aluminum alloy uses 35 mm/s (1.4 in./s). Significant variation in properties of magnesium alloy sheets obtained from various suppliers has been reported (Ref 5.14).

Possible forming defects (early fracture, wrinkling, unequal flow of the sheet) in warm forming are shown in Fig. 5.34 for an aluminum alloy (Ref 5.30). Figure 5.34(a) shows early fracture caused by insufficiently high flange temperature and/or excessive blank holder force. This means that the sheet temperature at the flange was not high enough to facilitate the draw into the die cavity. Also, in deep drawing, blank holder force should be just high enough to prevent wrinkling (Fig. 5.34b). Insufficient punch cooling causes fracture (Fig. 5.34c), because the drawing stress that the cup wall can withstand decreases with temperature. This problem can sometimes be eliminated by drawing at a slower punch speed so that the sheet cools down through contact with the punch. A higher LDR is obtained with warm deep drawing than with conventional deep drawing at room temperature (Fig. 5.34d).

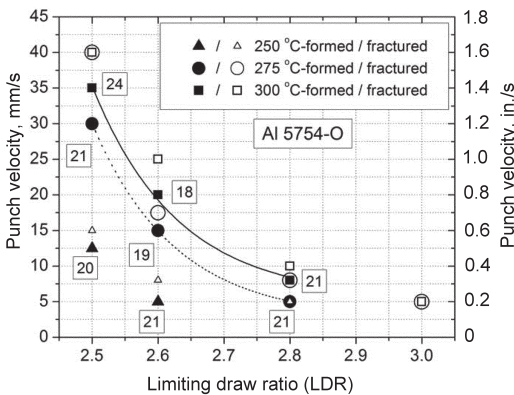


Fig. 5.32 Process window for aluminum 5754-O alloy

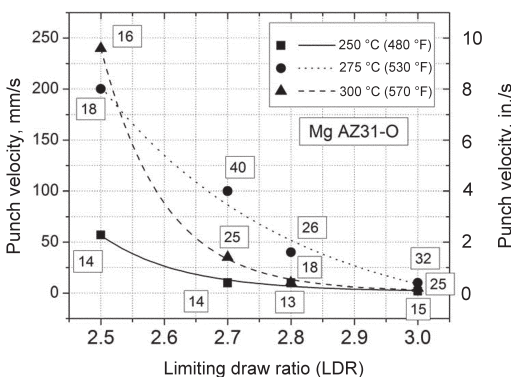


Fig. 5.33 Process window for magnesium AZ31-O alloy (only successfully drawn cups)

Finite-Element Analysis of Warm Forming of Aluminum 5754-O Alloy

To investigate the effect of the heat-transfer coefficients on the deep drawing process and to check the accuracy and applicability of those coefficients, an experimental case was selected to simulate the warm forming of an aluminum 5754-O sheet alloy. Experimentally measured thickness distributions and punch loads were compared with the predicted values by using finite-element analysis code DEFORM-2D. Table 5.5 provides related tool geometry and process data.

Flow-stress data for the aluminum 5754-O alloy sheet used in this study were obtained from Ref 5.25. Thermal data such as thermal conductivity and heat capacity were obtained from Ref 5.32. For the finite-element analysis, selection of the friction coefficient is based on previous experimental experience on testing PTFE lubricants and comparison of predicted and measured punch load and thickness distributions using this lubricant.

Various heat-transfer coefficients were used to investigate their effect on the punch load and the thickness distribution of the cup. It was found that when heat-transfer coefficients of 2 and 3 kW/m² · C were used, the cup showed

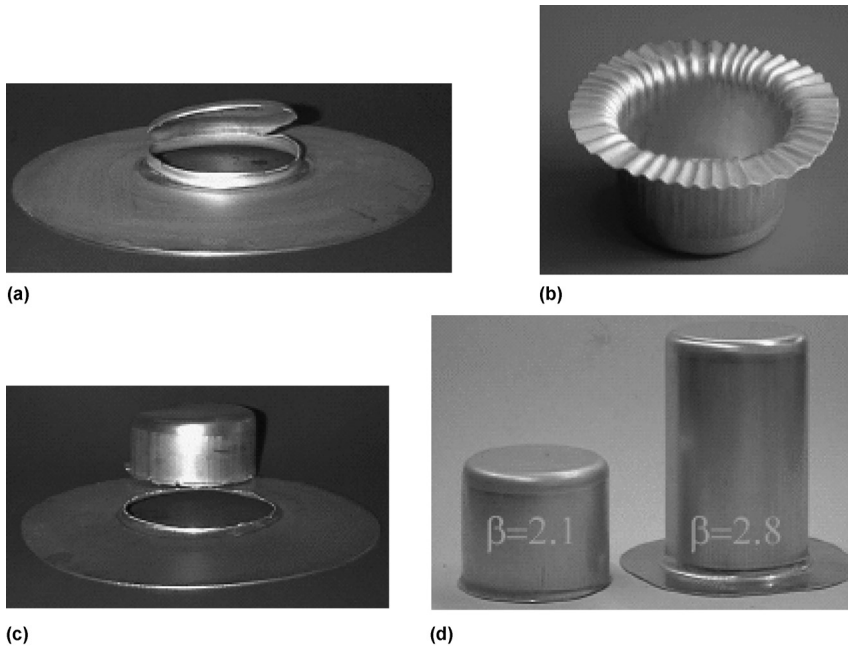


Fig. 5.34 Possible defects and successfully drawn cups in warm deep drawing. (a) Fracture due to insufficient flange temperature and/or excessive blank holder force. (b) Wrinkling due to low blank holder force. (c) Fracture due to insufficient punch cooling. (d) Cold deep drawing: limiting draw ratio (LDR) = 2.1. Warm deep drawing with partial cooling: LDR = 2.8. Source: Ref 5.30

Table 5.5 List of geometric data and input parameters to the finite-element model

Punch shoulder radius (r_p), mm (in.)	4 (0.16)
Punch diameter (D_p), mm (in.)	40 (1.6)
Die shoulder radius (r_d), mm (in.)	6 (0.24)
Punch-die clearance (D_d), mm (in.)	2.3 (0.09)
Initial sheet thickness (s_0), mm (in.)	1.3 (0.05)
Initial sheet temperature, °C (°F)	250 (480)
Initial punch temperature, °C (°F)	60 (140)
Friction coefficient (μ)	0.04
Heat-transfer coefficients, kW/m ² · °C	4/6/11

Source: Ref 5.31

excessive thinning at the first 15 mm (0.6 in.) of the stroke. This result showed that such lower coefficients of heat transfer did not allow the sheet to cool down enough (through contact with the cold punch) and withstand the stresses generated in the cup wall. Punch load and thickness distribution curves are shown in Fig. 5.35 and 5.36, with every parameter held constant except the heat-transfer coefficients. The results show that the effect of the heat-transfer coefficients on punch load is negligible. However, the difference in the thickness distribution of the cup between 0 and 30 mm (1.2 in.) curvilinear length (this is the punch/sheet interface in which there is considerable contact pressure) is af-

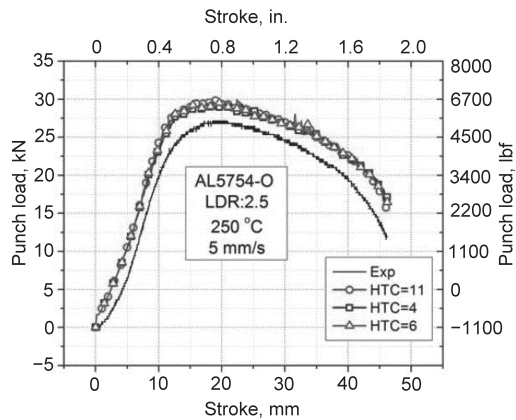


Fig. 5.35 Comparison of punch load predictions using various heat-transfer coefficients (HTC = kW/m² · °C) with experiments (5 mm/s at 250 °C). LDR, limiting draw ratio. Source: Ref 5.31

ected by the heat-transfer coefficient. A higher coefficient provides a better match than the lower ones. Beyond 30 mm (1.2 in.) (this is the cup wall/punch interface, and there is no contact pressure), the effect of the heat-transfer coefficient is not seen, because the sheet is not touching the punch.

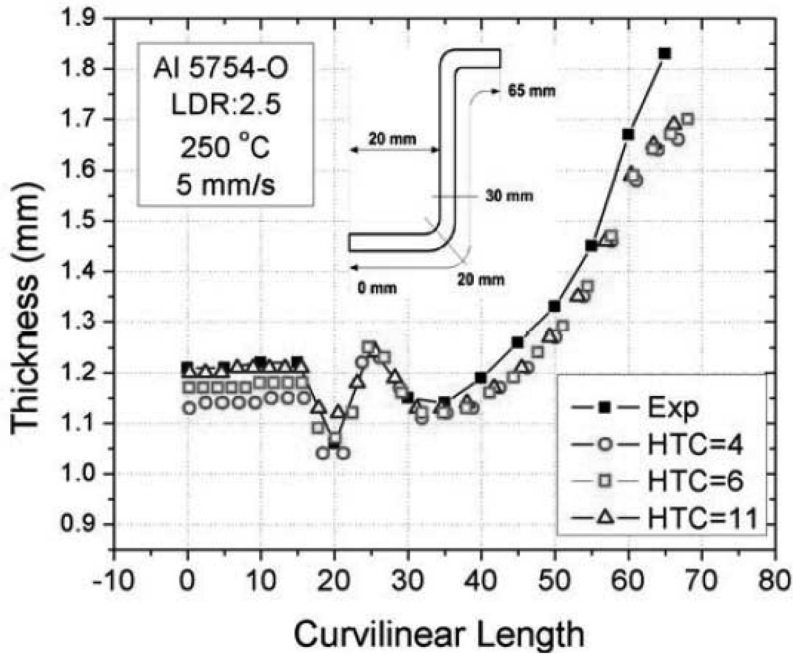


Fig. 5.36 Predicted thickness distribution comparison with various heat-transfer coefficients (HTC) (5 mm/s at 250 °C). LDR, limiting draw ratio. Source: Ref 5.31

Generally, it is difficult to obtain heat-transfer coefficients from tests that are closer to the actual forming conditions. The heat-transfer coefficients in warm forming seem to be within 2 and 11 $\text{kW/m}^2 \cdot ^\circ\text{C}$ for contact pressures of 1.5 and 26 MPa (0.2 and 3.8 ksi), based on the comparison of predicted and experimentally measured temperature curves with a servo press. Different values within this range can be used as input to finite-element analysis. Thus, by validating the punch load, sheet temperature, and thickness, acceptable results can be obtained.

Industrial Processes and Components

Currently, aluminum and magnesium alloys that are used in automobiles, aircraft, and space vehicles are processed primarily by forming (aluminum) and die casting (aluminum and magnesium). The automotive industry, a major consumer, uses magnesium alloy castings in numerous interior parts, such as steering wheel frames, steering column housings, shifter levers, and dash panel substrates. In addition, drive train components, including engine blocks, gear-box housings, and valve covers, among others, are made using magnesium alloy castings. The drive train unit constitutes approximately 25%

and the chassis and the body constitute nearly 50% of the total weight of a compact car (Ref 5.33). Applications of die-cast components in chassis and body parts are limited, mainly because the mechanical properties of castings often do not meet safety and flexural/bending stiffness requirements. A promising alternative can be found in the use of aluminum and magnesium parts manufactured by forming processes.

Cases for cell phones, medical devices, and personal computers/laptops made of magnesium alloys are potential replacements for plastics. Currently-available magnesium alloy sheets are not capable of meeting the corrosion-resistance and surface-finish requirements for outer panels. Therefore, a hybrid body panel with exterior aluminum sections and interior magnesium sections is an attractive solution to the lightweight design of vehicles. Currently, formed aluminum alloy components find applications only as shallow parts in automobile body panels and the chassis area. Two of the main disadvantages of aluminum sheets are higher cost and slower forming speeds. The biggest successes have been in producing door panels, hoods, and lift gates for sport utility vehicles.

The Institute for Metal Forming Technology at the University of Stuttgart has developed a pneumatic bulge tooling (Fig. 5.37) that allows the performance of forming operations at elevated temperatures. The tooling consists of an upper and lower die, both heated. The upper die that contains the inlet for the internal pressure is heated by cartridge heaters. To ensure that no metal flows into the die cavity during deformation, lockbeads are used. These lockbeads also provide sealing. The lower die is heated by a band heater and has the pressure inlet that allows forming parts when using counterpressure.

General Motors Lift Gate. General Motors Corp. has developed a process called quick plastic forming (QPF) as a hot sheet blow forming process for forming complex aluminum shapes to be manufactured at automotive vol-

umes of up to 100,000 parts/year. In QPF, a heated aluminum sheet is subjected to high-pressure air that makes it conform to the shape of a heated tool. The high temperature improves the formability so that even complex shapes can be manufactured. Dimensionally correct panels are possible because springback is nearly eliminated. A simpler one-sided tooling also reduces development time and aids in shortening the vehicle development process (Fig. 5.38). Strain rates in QPF are between 10^{-3} and 10^{-1} , and temperature is approximately 450 °C (840 °F).

This technology has been successfully used on four production closures, including the Oldsmobile Envoy lift gate, the Oldsmobile Aurora deck lid, the Chevrolet Malibu Maxx lift gate, and the Cadillac STS deck lid, with over 300,000 panels produced through 2005 using

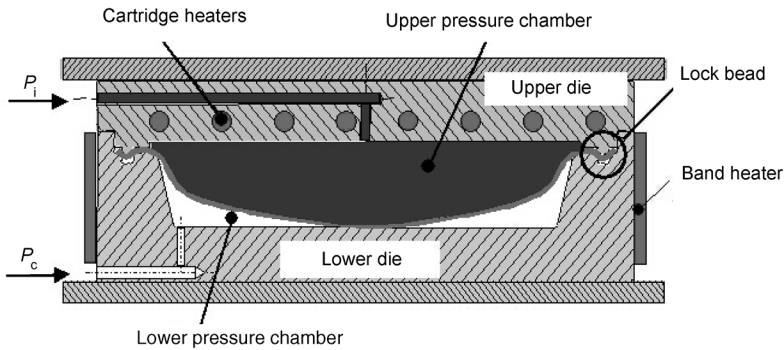


Fig. 5.37 Tool setup for pneumatic forming tooling developed at the Institute for Metal Forming Technology at the University of Stuttgart. Source: Ref 5.34

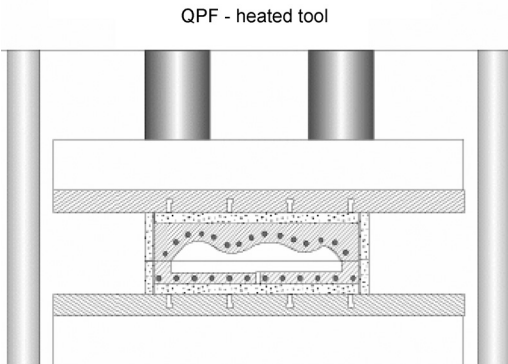


Fig. 5.38 Heated tool used in quick plastic forming (QPF). Source: Ref 5.35



Fig. 5.39 Chevrolet Malibu Maxx lift gate manufactured by using quick plastic forming. Source: Ref 5.35

aluminum 5083 alloy (Fig. 5.39). In this application, aluminum material cost is comparable to that of stamping-grade sheet. However, initial investment and tooling costs are relatively higher compared to superplastic forming.

Business Card Holder and Laptop Cover.

Figure 5.40 shows a production line developed by Aida Engineering Ltd., Japan. This line consists of coil material straightening, blanking of the sheet, forming, cooling, and finally blanking

and trimming. The top part of the figure shows the heating stage of the blank. The bottom part of the figure shows the press ram at the bottom dead center. This operation is conducted using a servo-motor-driven press because the press velocity must be adjusted for the forming/heating and cooling stages.

Figure 5.41 shows a business card holder that is formed by using magnesium AZ31-O alloy sheet at 300 °C (570 °F). The deformation in the

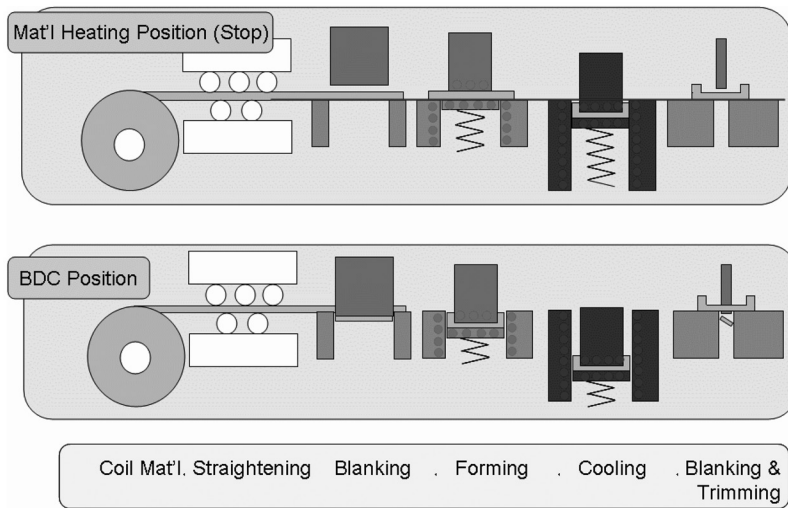


Fig. 5.40 Magnesium forming production line. BDC, bottom dead center. Courtesy of Aida Engineering Ltd., Japan

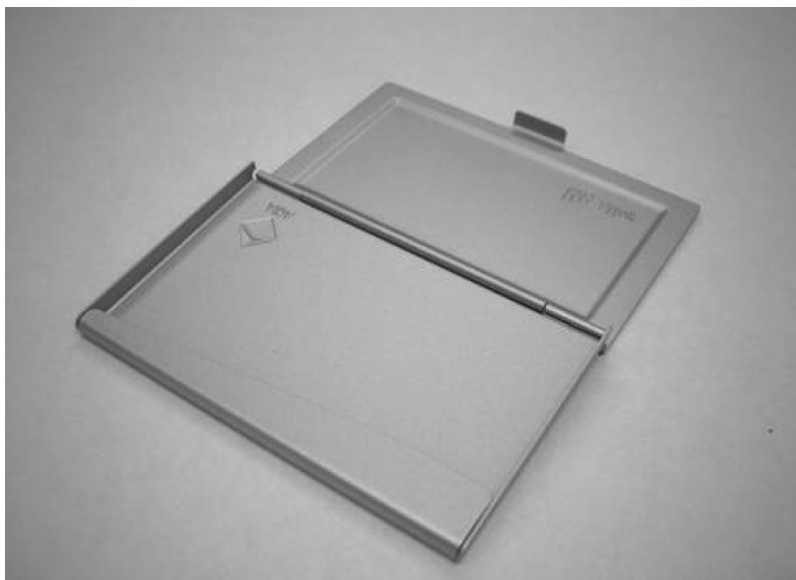


Fig. 5.41 Business card holder made by using magnesium AZ31-O. Courtesy of Aida Engineering Ltd.



Fig. 5.42 Cover of an electrical device. Courtesy of Aida Engineering Ltd.

production of this part is mostly bending, and it is possible to form parts with relatively smaller bending radii at elevated temperatures.

Magnesium has been used in producing laptop covers formed at 300 °C by using a programmed servo-motor-controlled press (Fig. 5.42).

Mercedes Inner Door Panel. Multimaterial manufacture, sometimes known as hybrid construction, that incorporates various materials, including steel, aluminum, and magnesium as well as plastic moldings for application in the vehicle body structure, is gaining ground over single-metal body systems in either steel or aluminum. For example, the latest Mercedes CL body-in-white has been constructed by using steel in regions under high load in the frontal and side impact sites, such as the roof pillars and longitudinal and body cross members. Aluminum has been used for large surface panels for the roof, hood, rear panels, and rear wings. Magnesium has been employed for the inner door panels and seat frames, and plastic moldings have been used for secondary components such as the trunk lid, spare wheel well, and front wings. A weight savings of 50 kg (110 lb) over the previous version of the model was achieved, and the whole vehicle is 340 kg (750 lb) lighter than its predecessor.

REFERENCES

- 5.1 K.G. Droeder, “Untersuchungen zum Umformen von Feinblechen aus Magnesiumknetlegierungen,” Dr.-Ing. dissertation, Hannover, Dec 1999
- 5.2 N. Abedrabbo, F. Pourbhograt, and J. Carsley, Forming of Aluminum Alloys at Elevated Temperatures, Parts 1 and 2, *Int. J. Plastic.*, 2006
- 5.3 H. Takuda, K. Mori, I. Masuda, Y. Abe, and M. Matsuo, Finite Element Simulation of Warm Deep Drawing of Aluminum Alloy Sheet when Accounting for Heat Conduction, *J. Mater. Process. Technol.*, Vol 146, 2002, p 52–60
- 5.4 D. Li and A. Ghosh, Tensile Deformation Behaviour of Aluminum Alloys at Warm Forming Temperature, *Mater. Sci. Eng. A*, Vol 352, 2003, p 279–286
- 5.5 P. Groche, R. Huber, J. Doerr, and D. Schmoeckel, Hydromechanical Deep-Drawing of Aluminum-Alloys at Elevated Temperatures, *CIRP Ann.*, Vol 51 (No. 1), 2002, p 215
- 5.6 E. Doege and K. Droeder, Sheet Metal Formability of Magnesium Wrought Alloys—Formability and Process Technology, *J. Mater. Process. Technol.*, Vol 115, 2001, p 14–19

- 5.7 H. Takuda, T. Morishita, T. Kinoshita, and N. Shirakawa, Modelling of Formula for Flow Stress of a Magnesium Alloy AZ31 Sheet at Elevated Temperatures, *J. Mater. Process. Technol.*, Vol 164–165, 2005, p 1258–1262
- 5.8 S. Kaya, T. Altan, P. Groche, and C. Kloepsch, Determination of Flow Stress of Magnesium AZ31-O Sheet at Elevated Temperatures Using the Hydraulic Bulge Test, *Int. J. Mach. Tools Manuf.*, Special issue, *Advances in Sheet Metal Forming Applications*, Vol 48 (No. 5), 2008, p 550–557
- 5.9 R.W. Fenn, “Evaluation of Test Variables in Determination of Elevated-Temperature Compressive Yield Strength of Magnesium Alloy Sheet,” Symposium on Elevated-Temperature Compression Testing of Sheet Materials, ASTM Special Technical Publication No. 303, 64th Annual Meeting (Atlantic City, NJ), June 29, 1961
- 5.10 A. Jain, M.S. thesis, University of Virginia, 2005
- 5.11 O. Duygulu and S. Agnew, Plastic Anisotropy and Role of Non-Basal Slip in Magnesium Alloy AZ31B, *Int. J. Plastic.*, Vol 21, 2005, p 1161–1193
- 5.12 M. Avedesian and H. Baker, *Magnesium and Magnesium Alloys*, ASM International, 1999
- 5.13 *Forming Magnesium*, The Dow Chemical Company, 1962
- 5.14 S. Kaya, G. Spampinato, and T. Altan, An Experimental Study on Non-Isothermal Deep Drawing Process Using Aluminum and Magnesium Alloys, *J. Manuf. Sci. Eng. (Trans. ASME)*, Vol 130, 2008
- 5.15 M. Baucchio et al., Ed., *ASM Metals Reference Book*, 3rd ed., ASM International, 1993
- 5.16 E. Doege, L.E. Elend, and F. Meiners, Comparative Study of Massive and Sheet Light Weight Components Formed of Different Light Weight Alloys for Automobile Applications, *Proc. ISATA*, 2000, p 87–94
- 5.17 B. Taylor and H.W. Lanning, Warm Forming of Aluminum—Production Systems, *25th National SAMPE Symposium and Exhibition*, 1980, p 471–480
- 5.18 D. Li and A.K. Ghosh, Biaxial Warm Forming Behavior of Aluminum Sheet Alloys, *J. Mater. Process. Technol.*, Vol 145, 2004, p 281–293
- 5.19 AIDA-America Corporation, www.aida-global.com
- 5.20 D.M. Finch, S.P. Wilson, and J.E. Dorn, Deep Drawing Aluminum Alloys at Elevated Temperatures, Part I: Deep Drawing Cylindrical Cups, *Trans. ASM*, Vol 36, 1946, p 254–289
- 5.21 D.M. Finch, S.P. Wilson, and J.E. Dorn, Deep Drawing Aluminum Alloys at Elevated Temperatures, Part II: Deep Drawing Boxes, *Trans. ASM*, Vol 36, 1946, p 290–310
- 5.22 P.J. Bolt, N.A.P.M. Lamboo, and P.J.C.M. Rozier, Feasibility of Warm Drawing of Aluminum Products, *J. Mater. Process. Technol.*, Vol 115, 2001, p 118–121
- 5.23 P.J. Bolt, R.J. Werkhoven, and A.H. van de Boogaard, Effect of Elevated Temperatures on the Drawability of Aluminum Sheet Components, *Proc. ESAFORM*, 2001, p 769–772
- 5.24 A.H. van de Boogaard, P.J. Bolt, and R.J. Werkhoven, Aluminum Sheet Forming at Elevated Temperatures, *Simulation of Materials Processing: Theory, Methods and Applications*, 2001, p 819–824
- 5.25 A.H. van de Boogaard, P.J. Bolt, and R.J. Werkhoven, A Material Model for Aluminum Sheet Forming at Elevated Temperatures, *Proc. ESAFORM*, 2001, p 309–312
- 5.26 X. Wu, Y. Liu, and S. Wang, Superplastic Deformation and Forming of Commercial Magnesium and Aluminum Alloys with Initial Coarse Grains, *Proceedings of the 2002 NSF Design, Service and Manufacturing Grantees and Research Conference*, p 2072–2080
- 5.27 T. Naka, G. Torikai, R. Hino, and F. Yoshida, The Effects of Temperature and Forming Speed on the Forming Limit Diagram for Type 5083 Aluminum-Magnesium Alloy Sheet, *J. Mater. Process. Technol.*, Vol 113, 2001, p 648–653
- 5.28 F. Shehta, M.J. Painter, and R. Pearce, Warm Forming of Aluminum/Magnesium Alloy Sheet, *J. Mech. Work. Technol.*, Vol 2, 1978, p 279–290
- 5.29 D. Li, P. Ripson, and A.K. Ghosh, “Warm Forming of Aluminum Alloys,” DoE-LEMS Project Quarterly Reports, 2000
- 5.30 M. Kleiner, M. Geiger, and A. Klaus, “Manufacturing of Lightweight Compo-

- nents by Metal Forming,” CIRP 2003 General Assembly (Paris), 2003
- 5.31 S. Kaya and T. Altan, “Non-Isothermal Deep Drawing of Aluminum and Magnesium Alloys Using Servo Presses,” ASME, 2010
- 5.32 F.P. Incropera and P.D. Dewitt, *Fundamentals of Heat and Mass Transfer*, 5th ed., John Wiley & Sons, Inc., 2002
- 5.33 H. Friedrich and S. Schumann, Research for a “New Age of Magnesium” in the Automotive Industry, *J. Mater. Process. Technol.*, Vol 117, 2001, p 276–281
- 5.34 K. Siegert, S. Jaeger, and M. Vulcan, Pneumatic Bulging of Magnesium AZ31 Sheet Metals at Elevated Temperatures, *CIRP Ann.*, 2003, p 241–244
- 5.35 J. Carsley, P. Krajewski, J. Schroth, and T. Lee, “Aluminum Forming Technologies: Status and Research Opportunities,” Presentation made at IFU, University of Stuttgart, 2006

CHAPTER 6

Forming of Advanced High-Strength Steels (AHSS)

Hari Palaniswamy, Altair Engineering Inc.
 Amin Al-Nasser, The Ohio State University

INCREASED REQUIREMENTS for vehicle safety and weight reduction in automotive design led to the increased use of advanced high-strength steels (AHSS) in the automotive industry. The AHSS are characterized by yield strength higher than 550 MPa (80 ksi). Figure 6.1 illustrates the percent usage of AHSS for manufacturing of an example body-in-white in the past and in the present, reflecting the increased application of AHSS.

According to Ref 6.2, “Advanced High Strength Steels (AHSS) are multi-phase steels which contain martensite, bainite, and/or retained austenite in quantities sufficient to produce unique mechanical properties.” Different

types of AHSS exist. These include dual-phase (DP) steels, transformation-induced plasticity (TRIP) steels, martensitic steels (MS), complex-phase (CP) steels, hot forming (HF) steels, and twinning-induced plasticity (TWIP) steels. This chapter focuses on DP and TRIP steels because of their importance and extensive use in sheet forming of automotive parts. Table 6.1 gives a brief description of the microstructure and general characteristics of different types of AHSS (Ref 6.3).

The increased formability of AHSS is the main advantage over conventional high-strength steels. Nevertheless, compared to draw-quality steels, AHSS have relatively low ductility. Fig-

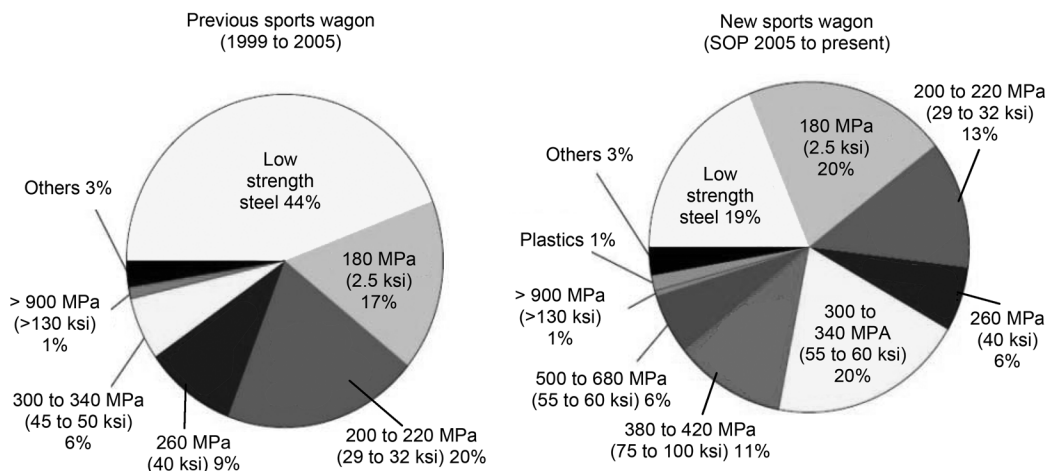


Fig. 6.1 Change in usage of materials for body-in-white parts. Source: Ref 6.1

ure 6.2 shows the relation between the total elongation (EL) and ultimate tensile strength (UTS) for different AHSS. This curve is usually referred to as the “banana curve.” This chart shows how a dramatic drop in the EL happens with increasing strength of the material.

The AHSS are basically multiphase steels, where microstructure plays important roles in the behavior and performance of these materials (Ref 6.4). These steels have higher strength, lower ductility, limited formability, and they exhibit limited postnecking deformation; that is, fracture can occur with minimal necking. Consequently, practical forming of AHSS presents a number of challenges in terms of:

- Inconsistency of the incoming material characteristics
- Determination of forming limits

- Higher tool stresses, tool wear, and press load
- Higher contact pressure and temperature rise during deformation
- Lubrication
- Higher forming load and required press capacity
- Large springback leading to dimensional inaccuracy in the formed part

6.1 Mechanical Behavior of AHSS

Flow Stress. Dual-phase steels that represent the majority of AHSS used in the automotive industry have high initial strain hardening and a high tensile-to-yield strength ratio, which accounts for the relatively high ductility, compared to conventional high-strength steels (Ref

Table 6.1 Metallurgy and general characteristic of each type of advanced high-strength steel (AHSS)

AHSS type(a)	Metallurgy/microstructure	Characteristics
DP	Ferrite matrix + martensite	Combined strength and ductility
TRIP	Ferrite matrix + martensite + bainite + ≥5% retained austenite	Higher ductility than DP steels
CP	Fine ferrite + martensite + bainite + microalloying precipitates of Nb, Ti, or V	High energy absorption
MS	Martensite matrix + ferrite + bainite	Very high strength, very low ductility
HF	Boron steels (high-strength steels with high amount of manganese and boron)	Formable, very low springback, very high strength after forming (ultimate tensile strength: 1400–1500 MPa, or 205–215 ksi; yield strength: 1000–1200 MPa, or 145–175 ksi)
TWIP	Fully austenite (include 15–25% Mn, Ni, Si, Al)	High strength, very high strain hardening, very high ductility, high energy absorption, very expensive

(a) DP, dual phase; TRIP, transformation-induced plasticity; CP, complex phase; MS, martensitic steels; HF, hot forming; TWIP, twinning-induced plasticity. Source: Ref 6.3

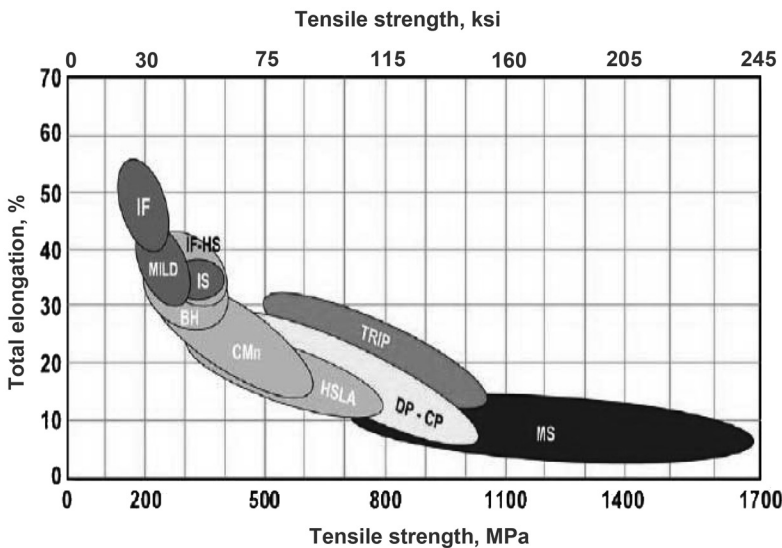


Fig. 6.2 Total elongation versus ultimate tensile strength “banana curve” of automotive steels. Source: Ref 6.3

6.5, 6.6). During deformation, the soft ferrite flows plastically before the hard martensite. The ferrite at the phase boundary encounters a high stress concentration, resulting in more plastic deformation. This explains the high initial strain hardening of DP steels. When the martensite starts to deform plastically, the strain-hardening rate decreases. The TRIP steel retains its strain hardening as high strain values. This is due to the retained austenite-to-martensite phase transformation that takes place during plastic deformation. The formation of the hard martensite, and the stress concentration resulting from the volume expansion during phase transformation, increases the strain hardening of the material and thus both the uniform and total elongation (Ref 6.3).

The variation of the strain-hardening characteristic of a material with strain can be illustrated by plotting the instantaneous n -value ($d \ln \sigma / d \ln \epsilon$) versus strain. Figure 6.3 shows how

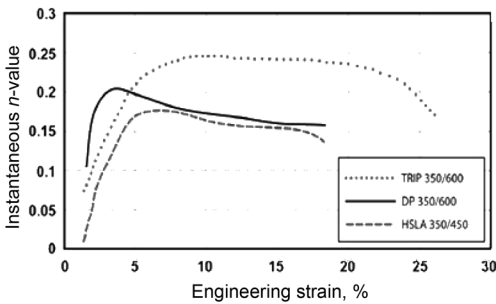


Fig. 6.3 Variation of the instantaneous n -value with engineering strain for HSLA 350/450, DP 350/600, and TRIP 350/600 steels. Source: Ref 6.3

the instantaneous n -value changes for a DP steel and a TRIP steel, as compared to a conventional, high-strength, low-alloy (HSLA) steel. The decrease in the n -value for DP 350/600 is explained by the martensite starting to plastically deform. The constant n -value of TRIP 350/600 is explained by the strain-induced phase transformation. These observations indicate that the power law ($\sigma = K\epsilon^n$), which is used extensively to describe the behavior of many materials, may not be valid for AHSS because of the variation of the instantaneous n -value. Furthermore, because the hardening behavior of AHSS changes with strain, the finite-element simulations with extrapolated flow stress data may not be accurate.

Figure 6.4 compares the engineering stress-strain curve of four different DP steels and one TRIP steel. Again, the higher initial strain hardening of DP steels compared to TRIP steel is clear. Moreover, compared to conventional steels, the flow curves of AHSS are almost flat around the UTS. It can also be noticed that TRIP 780 is more formable compared to other DP steels with the same UTS (780 MPa, or 113 ksi).

Elastic modulus includes both loading (Young's) and unloading moduli. It is conventionally assumed that the elastic modulus for loading and unloading is the same and is a constant value regardless of the plastic strain. Recent studies (Ref 6.8–6.12) indicated that the loading modulus and unloading modulus are different for AHSS, and the unloading modulus decreases with the plastic strain (Fig. 6.5). Perez et al. (Ref 6.10) also observed that in TRIP steels, the loading modulus did not change with

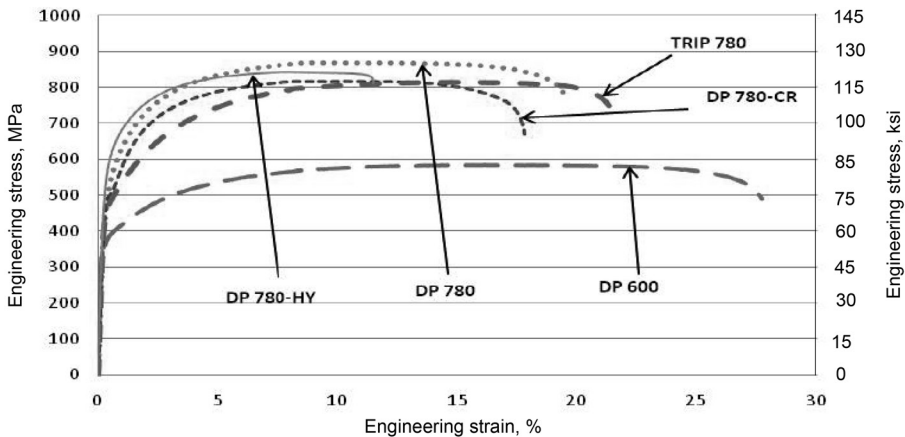
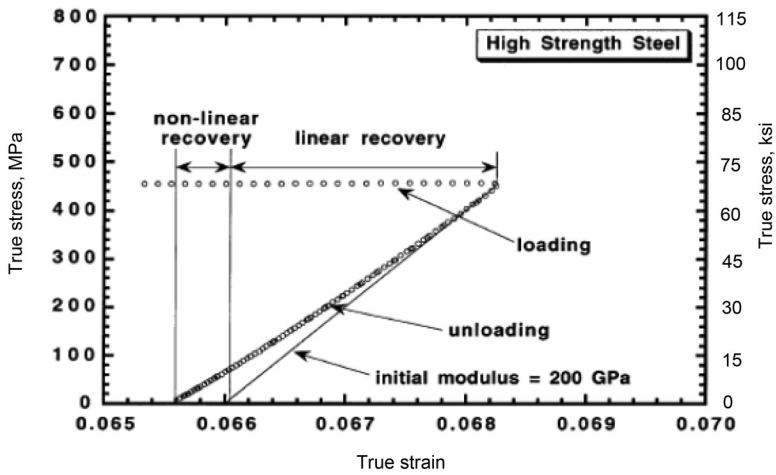
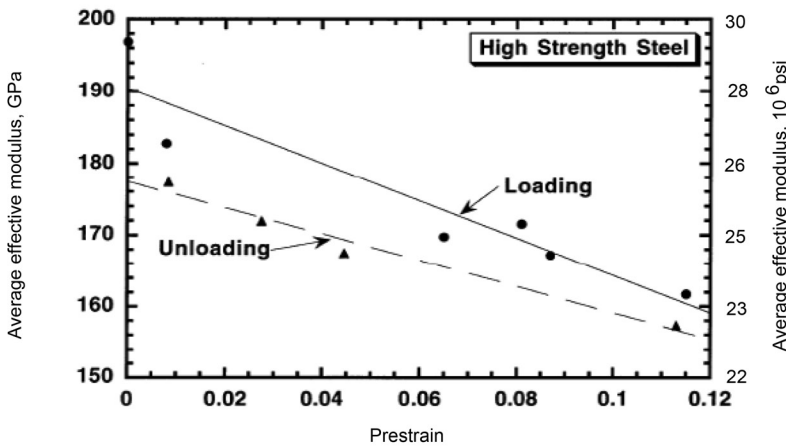


Fig. 6.4 Engineering stress-strain curves of five advanced high-strength steel sheet materials. Source: Ref 6.7



(a)



(b)

Fig. 6.5 Variation in Young’s modulus with plastic strain. (a) Nonlinear unloading behavior leading to change in Young’s modulus. (b) Decrease in Young’s modulus with plastic strain. Source: Ref 6.8

plastic strain, while the unloading modulus decreased with plastic strain.

Recent studies conducted at the Engineering Research Center for Net Shape Manufacturing (ERC/NSM) also illustrated that the elastic modulus changes with increasing strain, as seen in Fig. 6.6 for DP 780.

These results indicate that it is necessary to consider the Young’s modulus variation with strain for accurate prediction of springback, particularly in parts manufactured from DP and TRIP steel. The data on the variation of Young’s modulus are available for a smaller range of strain due to limitation in the tensile test. However, strains in stamped parts, especially in load-

bearing members, are higher than strains in tensile tests. Therefore, there is need for a method to estimate the variation of unloading modulus over a larger strain range.

Bake Hardening. The bake-hardening effect is the increase in the yield strength of the pre-strained material in the formed parts during the paint/bake cycle of heating to 170 °C (340 °F) for 30 min, associated with automotive painting. Bake hardening is highly dependent on the degree of deformation and the type of steel (composition, especially the interstitial carbon and nitrogen levels, and microstructure), and the bake-hardening effect can be varied by initial strain, baking temperature, and baking time.

Figure 6.7 shows how the initial strain, baking temperature, and baking time affect the increase in yield strength due to bake hardening. Bake hardening (BH) steels are low-carbon steels developed with a higher bake-hardening effect to increase the strength. The DP steels show similar or more bake hardening compared to that of BH steel. Also, it is observed that bake hardening is higher for TRIP and DP steels compared

to HSLA steels that are subjected to the same prestrain (Ref 6.3).

Bauschinger Effect. In a typical sheet metal forming process, the material may experience cyclic loads, for example, bending-unbending at the die shoulder and reverse bending-unbending at the punch corner. The Bauschinger effect is the softening in the material observed when a reverse load is applied after forward loading. As

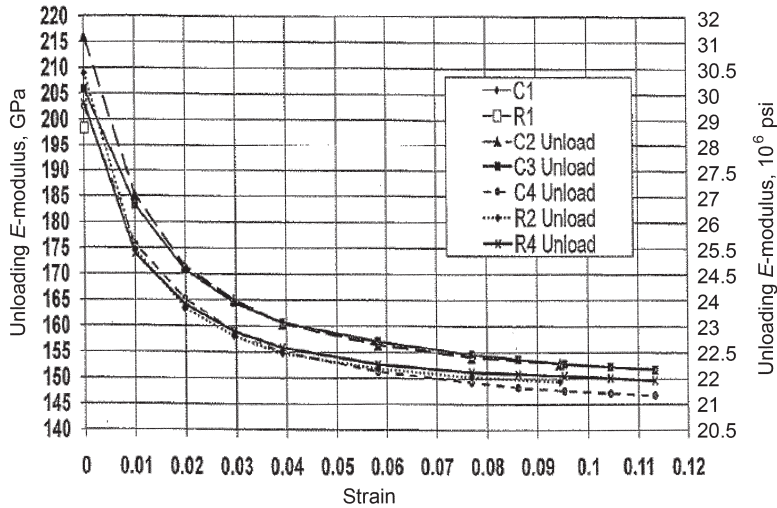


Fig. 6.6 Variation of unloading E -modulus with true strain. Tensile tests with DP 780

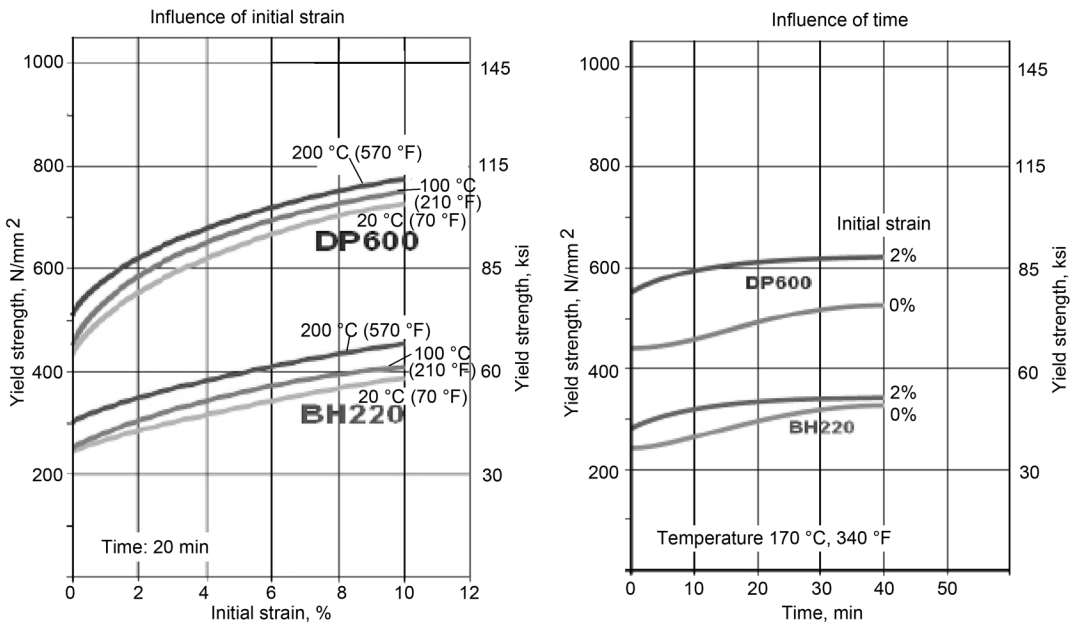


Fig. 6.7 Comparison of the effect of initial prestrain, baking temperature, and baking time on the bake-hardening (BH) effect for dual-phase (DP) and BH steels. Source: Ref 6.3

a result, not only there is lowering of yield stress, but also the whole shape of the hardening curve is modified after reverse loading. Modeling of this phenomenon is important to accurately predict the stresses and later predict the shape and mechanical properties of the formed parts after springback.

Sadagopan et al. (Ref 6.13) investigated the Bauschinger effect in several AHSS using tensile and compression tests for a maximum plastic strain of 0.05, as shown in Fig. 6.8. In this figure, the Bauschinger effect factor (BEF) is defined as the ratio of the value of reverse yield stress divided by maximum forward flow stress at a given plastic strain. A lower value of BEF represents a higher Bauschinger effect, which increases with increase in plastic strain. This indicates that hardening models used to describe the material in analyzing the deformation process should account for the Bauschinger effect varying with strain observed for AHSS, to accurately predict the stress-strain history and the springback in the part after forming. Additionally, new test methods must be developed to measure the Bauschinger effect in AHSS at higher strains relevant to sheet metal forming.

Anisotropy. The normal anisotropy (\bar{r}) describes the difference in the property between the in-plane direction to along the thickness direction in the sheet material. Normal anisotropy greater than 1 indicates that the material has high resistance to thinning during forming; therefore, it is better for deep drawing compared to a normal anisotropy value of less than 1.0. The anisotropy values for AHSS are approximately close to 1 compared to aluminum-killed

drawing-quality and HSLA steels that have normal anisotropy values greater than 1.0, as seen in Fig. 6.9. Thus, AHSS show less deep drawability compared to high-strength and low-carbon steels.

Effect of Strain Rate. Grassel et al. (Ref 6.14) observed that for both TRIP and TWIP steels, the increase in the strain rate from 1 to ~800/s results in an increase of approximately 15% in the flow stress but in no significant difference in the total elongation and strain-hardening behavior of both materials. Studies conducted by the Ultralight Steel Auto Body Programme on AHSS also indicated that flow stress obtained from tensile tests increases with strain rate, but the uniform elongation and strain-hardening behavior of AHSS were not very sensitive to strain rate. It should be noted that strain rates in stamping are approximately 10/s. The change in yield stress and tensile stress around a strain rate of 10/s is small compared to the change in yield stress and tensile stress between the different coils, heats, and suppliers. Thus, strain-rate effects in forming AHSS can be neglected for all practical purposes. However, this is not the case in considering crash analysis, where strain rates are much higher.

Effect of Temperature. With the exception of boron steels used in hot stamping, the practical applications of warm or hot forming AHSS are extremely limited. The tensile strength of DP 980 remains approximately constant for temperatures up to 400 °C (750 °F), while the total elongation decreases (Ref 6.15). However, beyond 400 °C, the total elongation increases while the tensile strength decreases, as observed

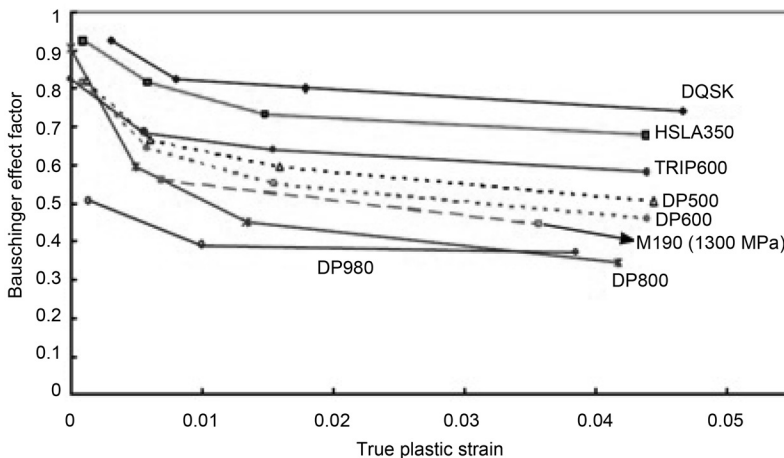


Fig. 6.8 Variation of Bauschinger effect factor with plastic strain. Source: Ref 6.13

for conventional steels at elevated temperature. The behavior of TRIP and TWIP steels at elevated temperature is different (Ref. 6.14). For TRIP steel, in the range of 200 to 400 °C (390 to 750 °F), the properties are not affected by temperature. In the range of 70 to 200 °C (160 to 390 °F), the tensile strength, uniform elongation, total elongation, and yield strength decrease with increasing temperature. Similar effects were observed by Khaleel et al. and Berrahmaune et al. (Ref 6.16, 6.17). In the case of TWIP steel, all tensile properties (yield strength, uniform elongation, total elongation, and tensile strength) decrease with increasing temperature (Ref 6.14).

During the forming process, the deformation energy is released as heat into the workpiece, and through the workpiece to the tools, resulting in heating of the tools. In forming of AHSS, die temperatures may reach 70 to 100 °C (160 to 210 °F), depending on the stroking rate of the press. Increase in temperature may result in decrease in the toughness of the tool and breakdown in lubrication, causing galling and wear. Additionally, in forming TRIP steels an increase in temperature beyond 80 °C (175 °F) results in a decrease in strain hardening and formability; in TWIP steels, an increase in temperature beyond room temperature decreases the formability. Hence, tools used in forming AHSS, especially TRIP and TWIP steel, may be cooled to enhance formability and improve lubrication and die life (Ref 6.18).

Inconsistency of Material Properties. One of the biggest problems in application of AHSS is the inconsistency of incoming material. Figure 6.10 shows example variations in the strain-hardening behavior of DP 600 sheet material of different thicknesses. There are many examples where essentially the same materials, but from different suppliers, exhibit considerable variations in total elongation and/or in yield strengths. For example, Khaleel et al. (Ref 6.16) reported on three batches of TRIP 800 where all three materials had approximately the same yield strength, while the strain-hardening behaviors were different. As a result, the ultimate tensile strengths had approximately the same value, while the uniform and total elongations were quite different. A large number of alloying elements and complex cooling cycles are required to obtain the multiphase structure in AHSS. Any small change in alloying elements or cooling cycle could result in different proportions of ferrite, retained austenite, bainite, and martensite in the sheet, leading to different mechanical properties. This poses a considerable challenge for process control in steel mills to produce different grades and different thicknesses of AHSS.

AHSS Compared to Conventional Steels.

The behavior of AHSS under loading is different compared to conventional steels:

- The strain hardening of the AHSS material changes considerably with strain, depending on the type of AHSS, while in conventional

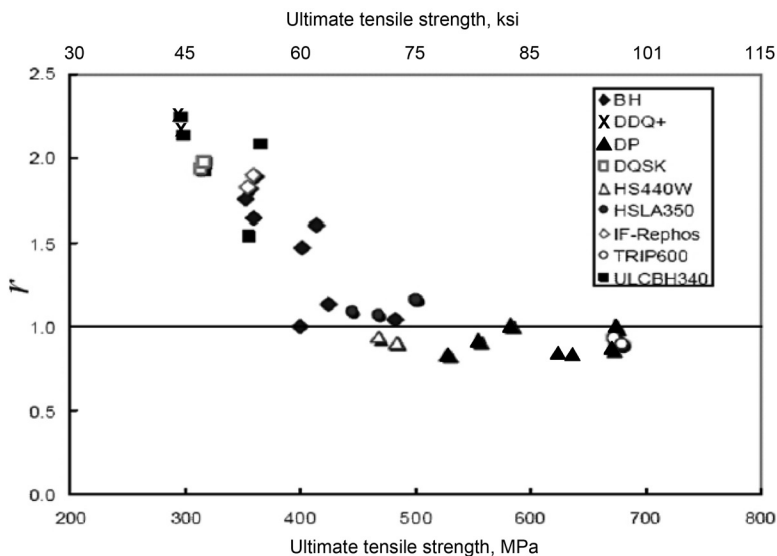


Fig. 6.9 Comparison of anisotropy (r) of various steels. Source: Ref 6.13

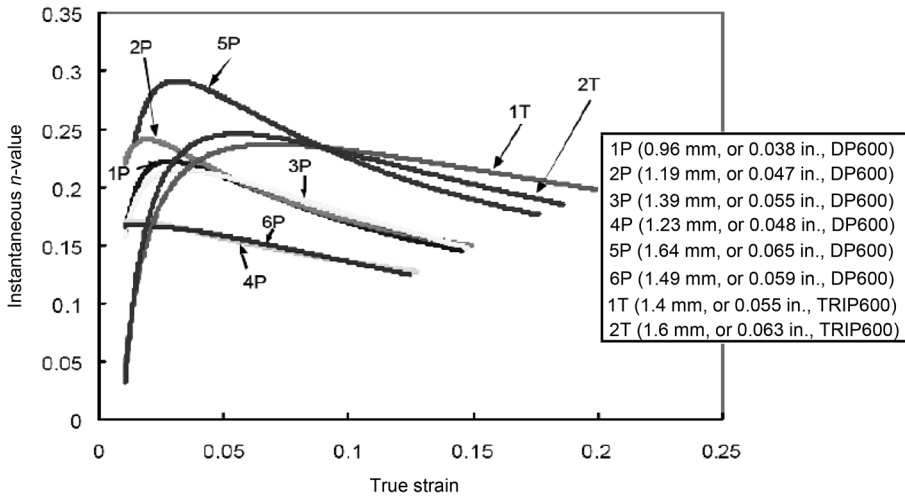


Fig. 6.10 Variation in the instantaneous *n*-value between DP 600 and TRIP 600 sheet materials of different thicknesses. Source: Ref 6.13

steel, the strain hardening remains approximately constant with increasing strain.

- The elastic modulus of AHSS decreases with plastic strain, while it is assumed to be constant for conventional steels. Additionally, the unloading behavior of AHSS in tensile test is nonlinear, leading to large springback in the formed parts compared to conventional steels.
- The AHSS show higher bake-hardening effect compared to conventional BH steels.
- Reverse loading in AHSS results in higher softening (Bauschinger effect) compared to conventional steels. Also, the strain hardening in reverse loading is different compared to proportional loading.
- The anisotropy of AHSS is approximately equal to 1, and therefore, they show less deep drawability compared to low-carbon and high-strength steels with anisotropy values greater than 1.
- The yield strength and tensile strength of AHSS sheet material increase with strain rate, while uniform elongation remains approximately the same, indicating that AHSS properties are not very sensitive to strain rate in the range of 0.1 to 100/s.
- The effect of temperature on the forming properties depends on the type of AHSS. In tensile test, DP steels show improvement in formability beyond 400 °C (750 °F). The optimum temperature for forming TRIP steels is approximately 60 to 80 °C (140 to 175 °F) in tensile test, while TWIP steels show bet-

ter formability in tensile test at room temperature.

- Due to a significant difference in behavior of AHSS compared to high-strength steel, material models developed for high-strength steels must be modified to account for variation in strain hardening with strain, variation of elastic modulus with plastic strain, and the Bauschinger effect to accurately model the materials.
- Due to large variation in the properties of AHSS between coils/heats/suppliers, the stamping process for AHSS must be designed with a larger operating window to accommodate these variations in material properties. Furthermore, it is questionable whether the uniaxial tensile test is sufficient to determine the variations that are present between AHSS produced from different heats and/or different suppliers.

6.2 Forming of AHSS

For practical use of AHSS, it is essential to understand how these materials behave under various stress and strain conditions that exist in various basic deformation processes, for example, stretching, bending, flanging, deep drawing, and blanking.

Stretching. Stretchability is the ability of the material to be stretched without failure, and it is commonly elevated by the hydraulic bulge and the limiting dome height (LDH) tests. In both

tests, the sheet material is clamped at the edges and bulged against the die with a circular cavity. The height of the bulge/dome before burst and the maximum strain at the apex indicates the stretchability of the material. While both tests are not standardized, the hydraulic bulge test is more reliable because it does not include the influence of the friction that exists between the sheet and the hemispherical punch in LDH tests. Nevertheless, both tests are used to evaluate stretchability. Figure 6.11 shows a comparison of the stretchability of DP and martensitic steels with conventional mild steel. The H/d is the ratio of the maximum dome height (H) of the sheet before fracture to the diameter (d) of the hemispherical punch used in the tests. Steels that have a higher and more uniform strain-hardening behavior show better stretchability. Similar studies, conducted by Dykeman et al. (Ref 6.19) using the LDH test, showed varia-

tions between three different 1.2 mm (0.047 in.) thick types of DP 780, while TRIP 780 had the best stretchability.

Bending. During bending, the outer fiber of the material is subjected to tensile stress, while the inner fiber is subjected to compressive stress. Fracture starts when the maximum tensile stress at the outer fiber exceeds a critical value. The stress in the outer fiber depends on the bend radius, bending angle, and the sheet thickness. Three-point bending tests were conducted to determine the bendability of the AHSS in comparison with high-strength steel (Fig. 6.12). The bendability is defined as the minimum r/t ratio, where r is the minimum bending radius at the bending angle of 90, and t is the thickness of the sheet material. A smaller value of r/t implies better bendability, because the sheet material can be bent over a very small corner radius.

Similar tests were conducted by Dykeman et al. (Ref 6.19) with 1.2 mm (0.047 in.) sheet from various DP 780 and TRIP 780 materials (Fig. 6.13).

Deep Drawing. Drawability is defined by the limiting draw ratio (LDR). The LDR is determined by using a specific tool set, that is, punch and die radii and diameters, and is the ratio of the largest blank diameter that can be drawn to a circular cup. Drawability of AHSS is compared with conventional mild steel in Fig. 6.14. A similar study by Cugy et al. (Ref 6.20) showed that AHSS DP 590, TRIP 800, and DP 980 show less drawability compared to conventional steel DC04. However, X-IP steel, due to

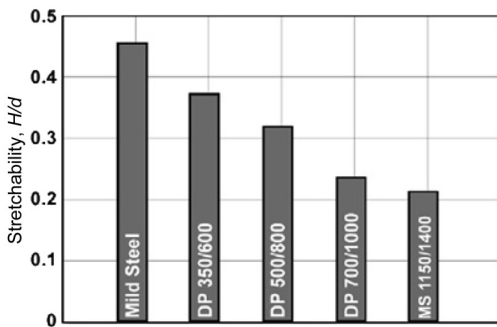


Fig. 6.11 Comparison of the stretchability of mild steel and advanced high-strength steels. Source: Ref 6.3

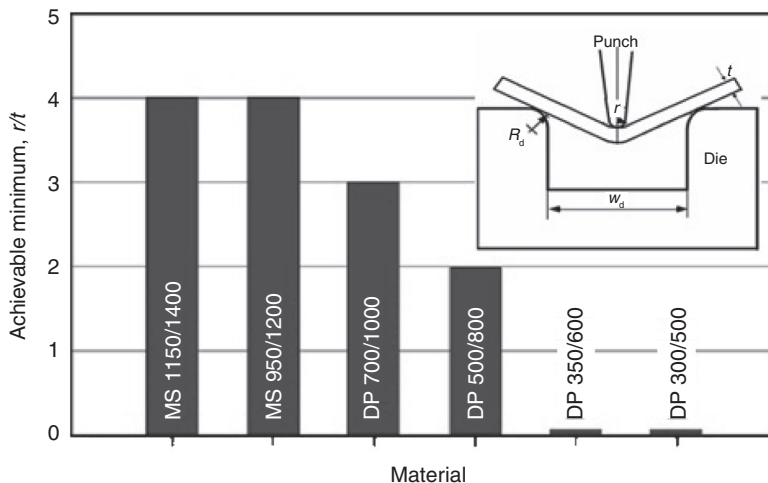
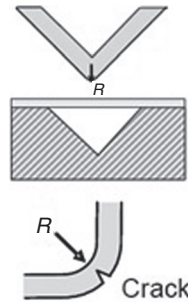


Fig. 6.12 Bendability of advanced high-strength steels in three-point bending test. Source: Ref 6.3



Material	Direction(a)	Bend radius(b), mm (in.)			
		2.0 (0.08)	1.5 (0.06)	1.0 (0.04)	0.5 (0.02)
DP 780 A	L	O	X	X	X
	T	O	O	X	X
DP 780 B	L	O	O	O	X
	T	O	O	O	O
DP 780 C	L	O	O	O	O
	T	O	O	O	O
TRIP 780	L	O	O	O	O
	T	O	O	O	O

(a) L, longitudinal; T, transverse. (b) O, no crack; X, crack

Fig. 6.13 Evaluation of bendability of various advanced high-strength steels using the 90° V-bend test (sheet thickness 1.2 mm, or 0.05 in.). Source: Ref 6.19

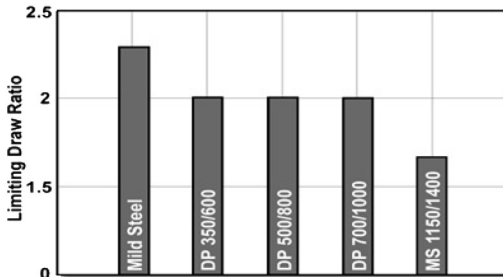


Fig. 6.14 Comparison of limiting draw ratio of mild steel and advanced high-strength steels. Source: Ref 6.3

its twinning mechanism that results in higher strain hardening with increase in strain, distributes the strain more uniformly, leading to higher drawability.

Combined Bending and Stretching. The AHSS are more susceptible to shear fracture when the sheet material is stretched and bent simultaneously at a sharp die radius, as occurs in practical stamping operations (Fig. 6.15). The conventional forming limit curve, used routinely for predicting fracture, is not always reliable in predicting fracture in bending.

The angular stretch bend test (Fig. 6.16a) is widely used for evaluating the bendability of various steels under stretching conditions. The sheet locked by the draw beads is stretched and bent continuously along a straight line by the

moving punch until it fractures. The limit of bending under tension is represented by the punch stroke (height) at which failure occurs in the test for different radius/thickness (R/t) ratios. Figure 6.16(b) shows the height at which failure occurred for different AHSS and mild steel.

It is desirable to predict when cracks may occur in bending AHSS so that the dies and the stamping process can be designed to avoid fracture in the part. In a preliminary study, finite-element analysis (FEA), together with various fracture criteria, was used to correlate the state of strain and stress in bending with the basic properties (yield stress, tensile strength, elongation) and the flow stress of AHSS. The FEA predictions, made by the commercial code DEFORM-2D, were compared with experimental data given in the literature (Ref 6.21). The preliminary investigation showed that, using the appropriate fracture criterion, it is possible to estimate when fracture occurs and to predict the effect of punch radius on fracture in bending (Fig. 6.17) (Ref 6.22).

Flanging/Edge Stretching. During stretch flanging of AHSS, edge cracking may occur. The tendency of a steel to edge crack is usually determined by using hole flanging experiments, as seen in Fig. 6.18. In general, the hole expansion ratio (D/d , where d is the initial hold diameter, and D is the hole diameter after the hole expansion test) decreases with increasing UTS

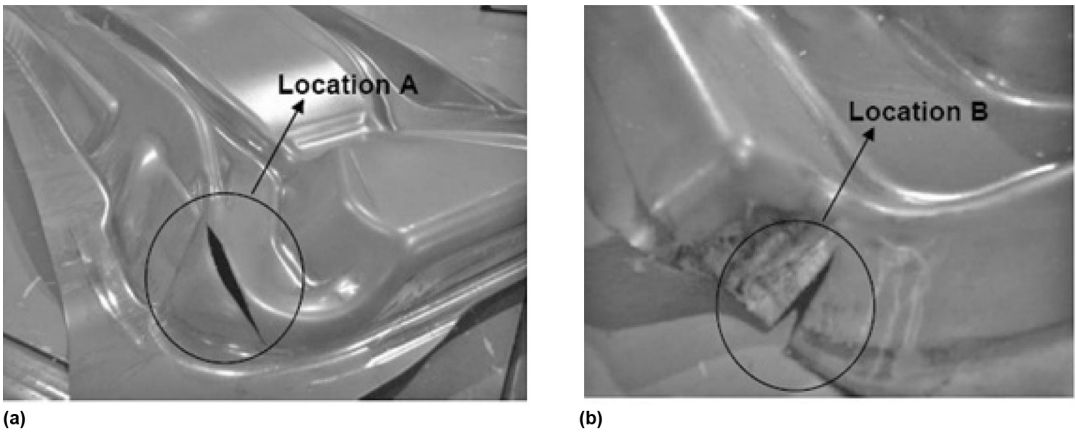


Fig. 6.15 Examples of DP 600 sheet fractured during (a) bending and (b) bending and stretching

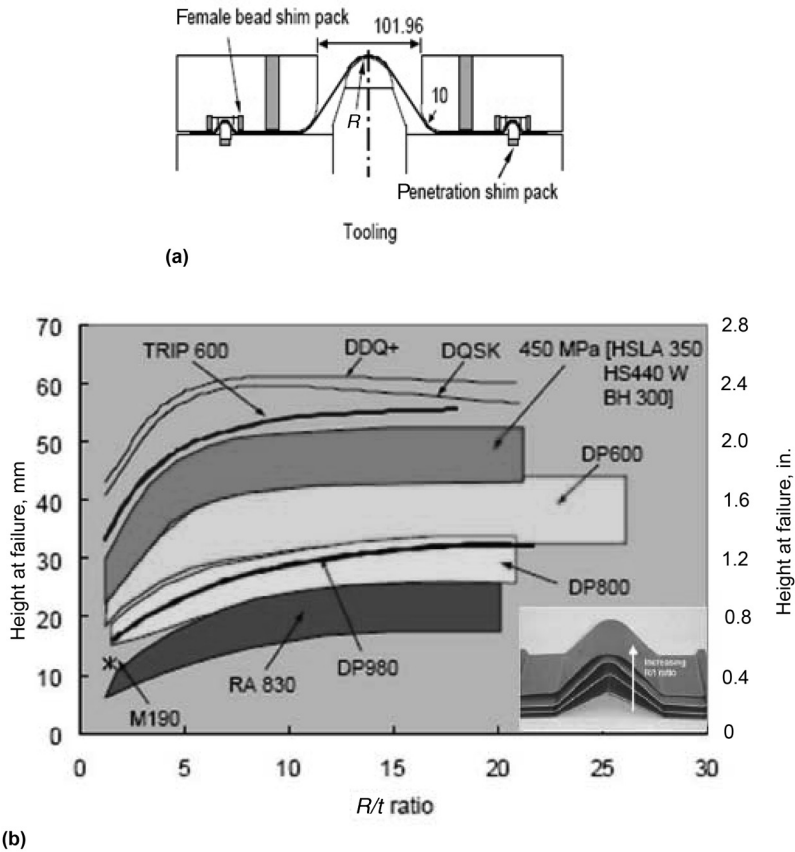


Fig. 6.16 Comparison of achievable height/punch stroke of advanced high-strength steels with mild steels in the angular stretch bend test. Source: Ref 6.13

(Ref 6.13). However, for a given material, this ratio also depends upon the quality of the initial hole (laser cut, punched with new-ground tools, punched with worn-out tools), as illustrated in Fig. 6.19.

Forming Limit Curve. Various studies conducted on generating forming limit curves (FLCs) for AHSS indicate that FLCs are valid for predicting fracture in stamping AHSS (Ref 6.3, 6.4, 6.13, 6.24).

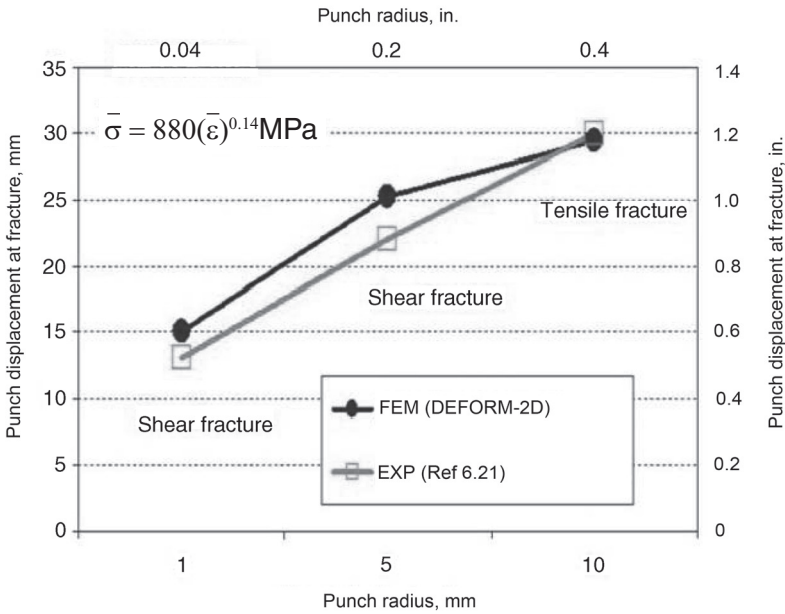
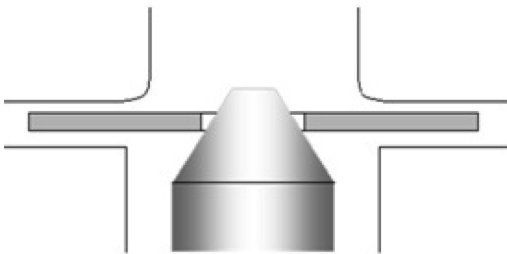
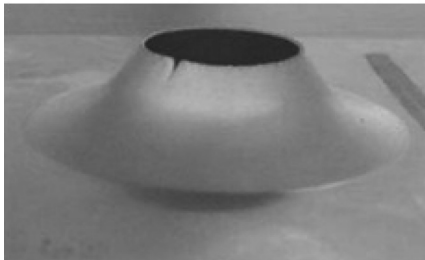


Fig. 6.17 Comparison of finite-element model (FEM)-predicted punch displacement at fracture with experimental results in stretch bending DP 600 with different punch radii. Source: Ref 6.22



(a)



(b)

Fig. 6.18 Hole expansion test using a conical punch. Source: Ref 6.13

In North America, FLCs for mild steel, high-strength steel, and selective AHSS have been studied, and the FLC curve for the sheet material is approximated by the Keeler-Breizer (K-B) equation based on the initial sheet thickness (t) and the strain exponent (n) of the material:

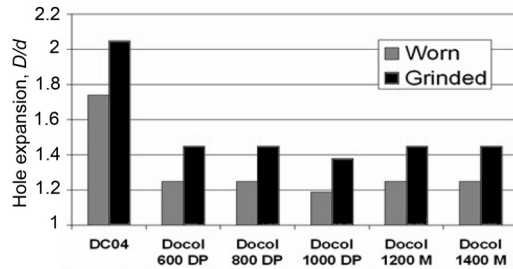


Fig. 6.19 Effect of piercing punch conditions on hole expansion test results. D , hole diameter after hole expansion test; d , initial hole diameter. Source: Ref 6.23

$$FLD_0^{true} = \ln \left[1 + (23.3 + 14.13f) \frac{n}{0.21} \right]; \quad n \leq 0.21 \tag{Eq 6.1}$$

$$\epsilon_1 = FLD_0^{true} - \epsilon_2; \quad \epsilon_2 \leq 0 \tag{Eq 6.2}$$

$$\epsilon_1 = \ln \left[0.6(\exp(\epsilon_2) - 1) \right] + \exp(FLD_0^{true}); \quad \epsilon_2 > 0 \tag{Eq 6.3}$$

where FLD is the forming limit diagram, and ϵ_1 and ϵ_2 are the true major and minor strains, respectively (Ref 6.13).

Sadagopan et al. and Konieczny (Ref 6.13, 6.24) investigated the validity of the K-B

equation for DP and TRIP steels. Their work indicates that the FLC obtained from the K-B equation matches well with experimental measurements, but it is more conservative in predicting the limits for both DP and TRIP steels.

It should be noted that FLCs represent the limit of forming for different strain ratios considering only stretching (membrane strains). However, the FLC may not be adequate enough to predict failure in AHSS under bending, stretch bending, and flanging conditions. Therefore, for these conditions, different tests are used to characterize AHSS, as discussed previously.

6.3 Tribology in Forming AHSS

Forming of AHSS involves higher contact pressures and temperatures at the tool-sheet interface compared to forming mild steel, due to the higher strength and higher strain-hardening behavior of AHSS. These conditions lead to galling, abrasive and adhesive wear in the tool, and significantly reduce tool life. Figure 6.20 illustrates the complex tribological interactions that occur in forming AHSS to minimize/eliminate tribological failures.

Workpiece—Sheet Metal. Draw bead tests conducted by Dalton et al. (Ref 6.25) showed that galvanized material resulted in less interface friction and less tendency to gall compared to ungalvanized steel. Among the different sur-

face treatments, galvannealing resulted in less galling and lower friction. Sakare et al. (Ref 6.26) conducted U-bend tests to evaluate friction and galling in forming DP 600 with and without hot dip galvanized coating and different tool materials (Calmax, Rigor, Sleipner, Sverker, cast iron 0731, cast iron 0741, Vanadis). In the experiments, hot dip galvanized material did not result in galling even after 10,000 strokes for all the tool coatings, while uncoated DP 600 resulted in galling after approximately 1000 strokes for most die coatings.

Similarly, twist compression tests conducted with bare (no coating) and hot dip galvanized (HDGI) DP 600 by the ERC/NSM illustrated that DP 600-HDGI showed the best results in reducing galling. Furthermore, hot dip galvanized (HDGA) coating resulted in less galling than the HDGI. This was explained by the fact that HDGA hardness value is approximately five times higher than that of HDGI (Ref 6.27).

Lubrication. Forming high-strength steels generates high contact pressure and temperature due to higher strength and higher strain hardening compared to the conventional steels. Higher interface temperature and interface pressure are detrimental to both liquid lubricants and dry film lubricants, leading to failure of commonly used lubricants for forming AHSS. Hence, the lubricants used for AHSS forming should have high-pressure and high-temperature additives that are activated at extreme forming conditions

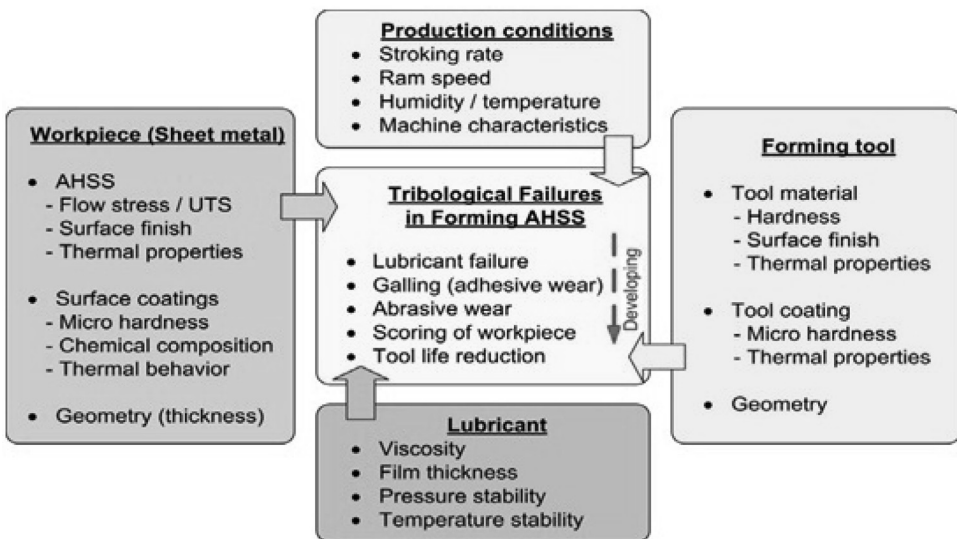


Fig. 6.20 Factors influencing tribological failures in forming advanced high-strength steel (AHSS)/ultrahigh-strength steel. UTS, ultimate tensile strength

to enhance their performances. Also, the lubricant must act as a cooling agent to take the heat generated due to cold working and friction at the interface and act as a thermal barrier to avoid excessive heat transfer to the tools from forming.

Wet Lubricants. A recent study indicated that, while forming AHSS on automotive suspension parts, the average temperature in the die reaches 115 °C (240 °F) under production conditions (Ref 6.28). At such elevated-temperature condition, a high-solids polymer lubricant was found to give consistent tool protection and friction control, while straight oil with extreme-pressure (EP) additives lost its performance (Ref 6.28, 6.29). To endure this elevated tool temperature, several liquid lubricants such as some petroleum-based and water-based synthetic lubricants with EP additives are recommended by lubricant manufacturers (Ref 6.30).

Dry film lubricants applied on sheet metal act as a thin film separating the sheet from contact with the die. Carlsson et al. (Ref 6.31) used organic dry film lubricants (mixed acrylic/polyurethane/polyester resin) to evaluate their performance against galling and tool wear for 55% Al-Zn-coated steel sheet and hot dip galvanized steel using several laboratory tests (scratching test and pin-on-disk test). Organic coatings were found to have lower friction and low galling tendency for both materials. Mori et al. (Ref 6.32) suggested a patented film made from urethane resin-containing silanol that could withstand the high temperature of ~200 °C (390 °F) involved in forming AHSS, compared to other

resin-based films that fail at elevated temperature.

In a recent study (Ref 6.27), deep drawing and ironing tests at 70 mm/s (3 in./s) ram speed were conducted using uncoated D2 (59 to 61 HRC) and uncoated A2 (58 to 60 HRC), DP 590 GA sheet material, and six stamping lubricants (two polymer-based with EP additive, two straight oil-based, one chlorinated water emulsion, and one synthetic water emulsion lubricant). The results indicate that most investigated lubricants were effective for use at deep drawing operations, with moderate blank holder pressures. However, the polymer-based lubricants with EP additives (IRMCO 146-492 and IRMCO 136-292) performed best under the most severe conditions, that is, in deep drawing tests with high blank holder pressure.

Tooling considerations include tool materials and coatings.

Tool Materials. Tool wear is often concentrated at the draw radii or draw beads that encounter higher contact pressure compared to other surfaces. Tool wear was investigated while forming U-channels from AHSS with different tool materials (Fig. 6.21). The conventional tooling material GGG70L with flame hardening resulted in a significant amount of wear. Uddeholm developed several tool materials manufactured by conventional ingot casting with or without electroslag melting, spray forming, or powder metallurgy for use in forming AHSS (Ref 6.33). These tool materials were tested in forming various sheet materials used in the automotive industry. Guidelines for selecting the tool materials

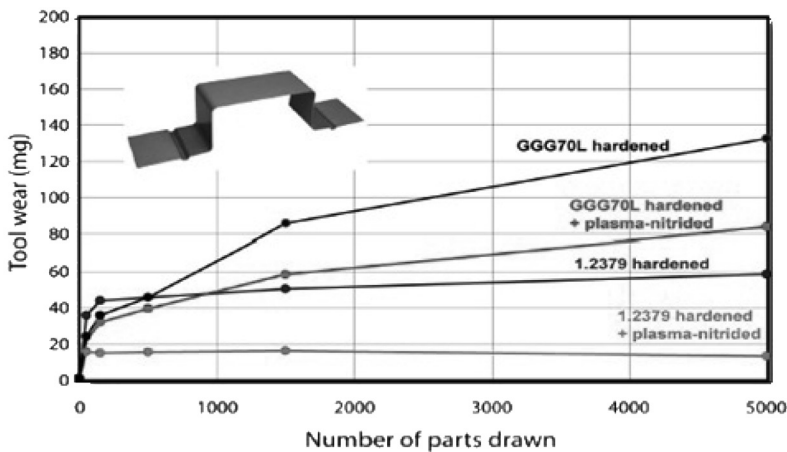


Fig. 6.21 Surface treatment effects on tool wear in U-channel drawing of dual-phase steels, thickness 1 mm (0.04 in.). GGG70L, spheroid graphite-bearing cast iron, flame hardened; 1.2379, tool steel (X155CrMo12/1; U.S. D2; Japan SKD 11). Source: Ref 6.3

for use in forming various sheet materials are given in Table 6.2.

New tool steels were tested by Volvo in forming U-channels and in production tools for structural parts. Based on the test results, preferred tool materials as inserts for punch, blank holder, and die for forming DP 600, DP 800, and DP 1000 are as given in Table 6.3 (Ref 6.34). An example for forming AHSS with inserts from tool steel materials is shown in Fig. 6.22 (Ref 6.34, 6.35).

A recent ERC/NSM study focused on the evaluation of tool materials using different lubricants and DP 590-GA, DP 600-GI, and TRIP 780-GA sheet materials. Tool inserts and coatings were from uncoated D2 (900 VHN), K340-PVD (2000 VHN), Vancron 40 (850 VHN), and spheroidal graphite cast iron (500 VHN). The results showed that:

- Physical vapor deposition (PVD)- coated tools (Caldie-PIN/PVD and K340-PVD) showed high coefficient of friction in the twist compression test at 170 MPa (25 ksi) interface pressure.
- Through-hardened tools (Vancron 40, D2, and K340-PIN) showed slightly better anti-galling performance than the cast iron tool.
- The case-hardened tool (K340-PIN) did not

reduce galling compared to Vancron 40 and D2 (Ref 6.36).

Tool coatings. Production results at Volvo indicate that additional and adequate lubricant is required to reduce wear and galling when forming AHSS using PVD- or chemical vapor deposition (CVD)-coated tools (Ref 6.34). Duplex treatment of tools that involve plasma nitriding followed by PVD coating could reduce the required lubrication by 75% compared to conventional CVD and offer better antigalling and wear resistance properties (Ref 6.34). Recent studies indicate that several amorphous hard carbon coatings such as diamondlike carbon and hard amorphous hydrogenated carbon with regular lubricants are promising die coating materials for use with zinc-plated AHSS sheets, stainless steel, and aluminum alloys that are prone to galling (Ref 6.37, 6.38).

The ERC/NSM investigated the galling properties of DP 980-GI with various lubricants and coated DC 53 (HRC 62) die inserts (Ref 6.27). The results showed that TiCN gave superior anti-galling properties compared to PVD coatings. These results were explained by the higher hardness of TiCN (2500 VHN) compared to the hardness of other coatings (in the range of 1300 VHN).

Table 6.2 Tool steel materials selection (Uddeholm grades) for forming various sheet materials

Type of sheet	Yield strength of sheet material		Tool steel grade	Base die		Inserts		Surface treatment(a)
	MPa	ksi		Bar	Cast	Bar	Cast	
Soft/mild	<350	<50	Carmo	X	X	X	...	Not needed
			Calmax	X	X	X	...	
			Sleipner	X	X	X	X	
High strength	330–570	48–85	Carmo	X	X	X	...	Optional/needed
			Calmax	X	X	X	...	
			Caldie	X	X	X	X	Optional
			Sleipner	X	X	X	X	
			Vanadis 4 Extra	X	...	X	...	
			Vanadis 6	X	...	X	...	
Extrahigh strength	570–800	85–115	Carmo	X	X	X	...	Nitriding + PVD needed
			Calmax	X	X	X	...	
			Caldie	X	X	X	X	PVD/CVD needed
			Sleipner	X	X	X	X	
			Vanadis 4 Extra	X	...	X	...	
			Vanadis 6	X	...	X	...	
			Vanadis 40	X	...	X	...	
			Roltec	X	...	X	...	
Ultrahigh strength	>800	>115	Sleipner	X	X	X	X	PVD/CVD needed
			Caldie	X	X	X	X	
			Roltec	X	...	X	...	
			Weartec	X	...	X	...	
			Vanadis 4 Extra	X	...	X	...	
			Vanadis 6	X	...	X	...	
			Vanadis 10	X	...	X	...	
			Vanadis 40	X	...	X	...	

(a) PVD, physical vapor deposition; CVD, chemical vapor deposition. Source: Ref 6.33

Table 6.3 Selection of tool material for forming DP 600, DP 800, and DP 1000 sheet material

Tool	Sheet thickness (t), <1.2 mm (0.05 in.)		Sheet thickness (t), >1.2 mm (0.05 in.)		Comments
	Coated	Uncoated	Coated	Uncoated	
Sheet material: DP 600					
Punch	GGG70L	GGG70L	GGG70L	GGG70L	Steel inserts at expected wear areas
Lower die	GG25	GG25	GG25	GG25	...
Inserts	Calmax + nitriding	Calmax + nitriding + PVD	Calmax + nitriding	Calmax + nitriding + PVD	All inserts are through hardened
	Sleipner	Sleipner + PVD	Sleipner + nitriding	Sleipner + PVD	All inserts are through hardened
Blank holder	GGG70L	GGG70L	GGG70L	GGG70L	Without draw beads
Inserts	...	Calmax + nitriding + PVD	Calmax + nitriding	Calmax + nitriding + PVD	With draw beads
	...	Sleipner + PVD	Sleipner	Sleipner + PVD	With draw beads
Sheet material: DP 800					
Punch	Sleipner	Sleipner	Sleipner	Sleipner	Wrought and through hardened
	Calmax	Calmax	Calmax	Calmax	Through hardened
Lower die	GG25	GG25	GG25	GG25	...
Inserts	Sleipner + PVD	Sleipner + PVD	Sleipner + PVD	Sleipner + PVD	Wrought and through hardened
	Sleipner 21 + PVD	Sleipner 21 + PVD	Sleipner 21 + PVD	Sleipner 21 + PVD	Through hardened
Blank holder	Sleipner + PVD	Sleipner + PVD	Sleipner + PVD	Sleipner + PVD	Wrought and through hardened
	Sleipner 21 + PVD	Sleipner 21 + PVD	Sleipner 21 + PVD	Sleipner 21 + PVD	Through hardened
Sheet material: DP 1000					
Punch	Sleipner	Sleipner	Sleipner	Sleipner	Wrought and through hardened
Lower die	GG25	GG25	GG25	GG25	...
Inserts	Sleipner + PVD	Sleipner + PVD	Sleipner + PVD	Sleipner + PVD	Wrought and through hardened
	Sleipner 21 + PVD	Sleipner 21 + PVD	Sleipner 21 + PVD	Sleipner 21 + PVD	Through hardened
Blank holder	Sleipner + PVD	Sleipner + PVD	Sleipner + PVD	Sleipner + PVD	Wrought and through hardened
	Sleipner 21 + PVD	Sleipner 21 + PVD	Sleipner 21 + PVD	Sleipner 21 + PVD	Through hardened

Note: PVD, physical vapor deposition. Source: Ref 6.34

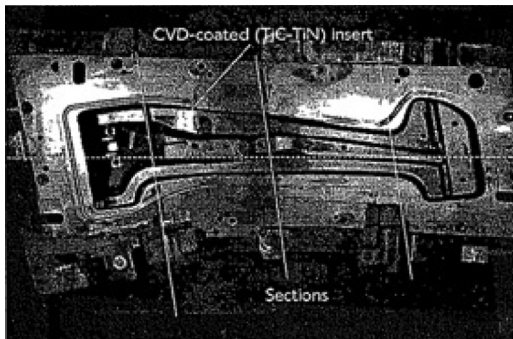


Fig. 6.22 Tooling construction with tool steels as inserts in cast iron die for forming advanced high-strength steels at Volvo. CVD, chemical vapor deposition. Source: Ref 6.34

Young et al. (Ref 6.39) used a progressive die for forming uncoated DP 980 to emulate several stamping operations, such as forming, piercing, flanging, and trimming. This study showed that, compared to other die steels and coatings (D2, Vanadis 4E, D2 + PVD/AlTiN, M2, and M4 with and without coatings), D2 + CVD/TiC and Carmo + plasma nitride + PVD CrN showed the longest die life (50,000+ hits) without galling.

Janoss (Ref 6.40) recommends certain coatings without giving details about the base tool materials and sheet materials used in the tests (Table 6.4).

6.4 Presses and Tooling

Forming Force and Energy. Due to their high strength (flow stress, UTS, and yield strength), forming of AHSS requires high tool stresses and consequently high press load and energy. This requirement is illustrated in Fig. 6.23 by comparing the true stress (or flow stress) of DP 600 with that of HSLA 450 (Ref 6.41).

While the flow-stress curve of the sheet material determines the magnitude of tool stresses and forming forces, the area under the flow-stress curve determines the forming energy, that is, ram force and ram displacement, needed to perform the forming operation. During the forming process, the sheet metal is drawn into the cavity, and the corners are embossed against the die toward the very end of the forming process. The corners that are strain hardened during drawing require higher force during embossing,

resulting in significant increases in the force requirement to form the part (Fig. 6.24).

The best way to estimate forming force and energy is to use finite-element simulation of the process. This simulation takes into account the flow stress of the sheet material, the friction, and the part geometry. Thus, FEA becomes more useful for estimating not only the material flow (thinning, wrinkling, fracture) but also the

forming forces and energy. Table 6.5 shows an example comparison of the maximum force predicted by FEA and the actual maximum force required to form parts from AHSS using a hydraulic press. It could be observed that finite-element predictions are within $\pm 20\%$ of the load measured in production.

Often it is required to switch from one material (for example, an HSLA steel) to an AHSS while the part geometry is essentially the same. In this case, it is necessary to investigate whether corner billet and flange radii can be made larger to facilitate deformation. Furthermore, the force and energy required in forming the new material must be increased by considering the flow-stress curves of the HSLA and the AHSS material, namely, the magnitudes of the flow-stress curves as well as the specific energy used for forming the materials, that is, the area under the flow curve, as illustrated in Fig. 6.23.

Generally, AHSS are preferred for structural parts, which are smaller in size compared to the

Table 6.4 Tool coatings for stamping advanced high-strength steel

Application	Good	Better	Best
Piercing	PVD TiCN	PVD AlTiN PVD TiCrN	CVD TiC PVD solid film lubricant
Blanking/ trimming	PVD TiCN	PVD TiCrN	PVD AlTiN
Forming/ drawing	PVD CrN	PVD TiCrN PVD AlTiN	CVD TiC TD PVD solid film lubricant

Note: PVD, physical vapor deposition; CVD, chemical vapor deposition; TD, thermal diffusion. Source: Ref 6.40

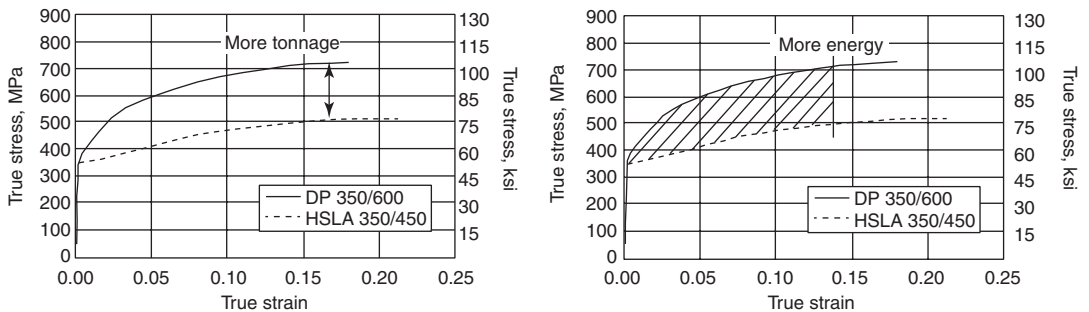


Fig. 6.23 Flow-stress curves of DP 699 and HSLA 450 steels illustrating the required additional forming force (load) and energy in forming DP 600

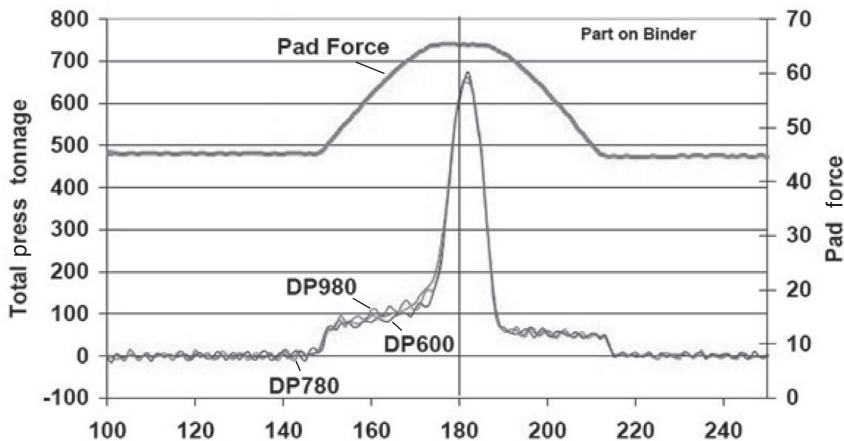


Fig. 6.24 Schematic of the press force and pad force required to form a part from dual-phase steels. Source: Ref 6.42

skin panels. Existing press lines used for smaller parts may not have sufficient tonnage to form the parts from the AHSS. An option would be to use a large press that has higher capacity and larger bed size. This option is feasible; however, the larger bed-size presses are usually not designed to take load over a small area where the die is attached and could lead to failure. Therefore, care should be taken before using large bed-size presses to form small parts of high-strength steel.

Similar considerations are valid for the binder (or blank holder) force. In forming AHSS, the binder force will also be larger, as determined by the flow stress of the sheet material. Furthermore, the initial binder force at impact before the forming operation starts will be considerably larger than in forming conventional steels. Thus, the press vibrations and resulting wear and tear of the press cushion are also larger. Consequently, the conventional cushion systems may not be adequate for forming AHSS.

Therefore, the use of hydraulic cushions with multiple-point control provides considerable advantages.

Transfer Presses. A transfer press consists of a single large slide that carries the dies for several forming stages (Fig. 6.25).

In most cases, the first stage/die in the transfer press is for deep drawing or stretching, where the sheet is deformed nearly to its desired form. Secondary operations such as trimming, piercing, and bending are carried out in successive operations to obtain the final product. Among the various operations performed in one stroke of the slide in a transfer press, the drawing stage and the trimming stage require maximum forces at a certain instant during the stroke. The drawing process requires higher force at the very end of the forming process, where corners/radii are coined to obtain the desired contour, while in blanking/trimming, the maximum force is required just before the end of the stroke of the slide. Hence, during a single stroke of the slide, the peak load requirements change from one location to another, resulting in localized tilting and reverse tilting due to the off-center loading. This tilting and reverse tilting induces a deformation wave in the slide that affects the adjacent stages and the press life (Fig. 6.25). Considering the large off-center loads that may occur in forming AHSS, press builders introduced transfer presses with independent slides (Ref 6.44, 6.45). The first slide moves independently of the adjacent slide and is used specifically for the drawing operation. The second slide is the blanking slide, where the secondary operations such as blanking, trimming, punching, and flanging are performed.

Tandem Press Lines. In tandem-line arrangement, presses are placed adjacent to each other to perform a series of operations, starting from

Table 6.5 Comparison of forming force predicted by finite element (FE) and actual measurement

Part name	Material	FE prediction		Actual measurement	
		tons	kN	tons	kN
Reinforcement A pillar front upper	DP 600-GA, 1.7 mm (0.07 in.) thick	740	6580	800	7115
Reinforcement A pillar rear upper	DP 600-GA, 1.7 mm (0.07 in.) thick	740	6580	702	6245
Reinforcement central body pillar	DP 600-GI, 1.65 mm (0.065 in.) thick	800	7115	900	8005
Reinforcement central pillar outer	DP 590-GI, 2.00 mm (0.08 in.) thick	1014	9020	922	8200

Source: Ref 6.43

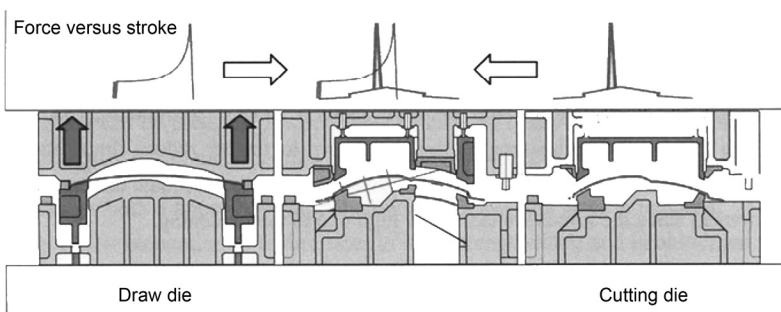


Fig. 6.25 Schematic illustrating the die setup in a transfer press and the effect of variation of peak load during stroke and of location on slide tilting. Source: Ref 6.44

deep drawing/stretching followed by trimming, flanging, and so on, using transfer dies to obtain the final part. The part is transferred from one press to another with a special part-handling mechanism or a robot. To provide the higher force and energy required in forming AHSS, hybrid press lines are introduced where the lead press in the press lines is replaced with a hydraulic triple-action press. The triple action consists of a cushion in the bottom and two slides in the top, such that the press is able to accommodate both single-action as well as double-action dies. Structurally separating two slides allows the press to use just the inner slide for smaller dies that require a higher force for forming. Also, large single-action dies can be used in the press by attaching the two slides and synchronizing the motion, which is always possible in a hydraulic press. Due to advances in the hydraulics, the production rate of the hydraulic press is very close to that of the mechanical press, and hence, it can be synchronized with other mechanical presses in the line for continuous production (Ref 6.44, 6.45).

Blanking Presses. Blanking presses are usually eccentric-driven mechanical presses to achieve high stroking rate (rpm) and short stroke. These presses are designed to counteract the impact of the snap-through force that occurs during blanking and introduces large downward acceleration of the upper die half (Ref 6.41). The snap-through force depends on the blanking speed and the shear strength of the blank material. Thus, blanking of AHSS results in very high impact snap-through forces that cause higher die wear and reduced press life because the press is subjected to very high fatigue loading. To reduce the high impact forces at the start of the blanking operation, and the snap-through forces after blanking, hydraulic presses, linkage presses, and servo-drive presses are preferred for blanking AHSS. Furthermore, hydraulic and pneumatic cushion systems are available to reduce the snap-through forces and vibrations in order to protect the dies and the press.

The large shearing stresses that occur during blanking and piercing of AHSS require larger clearances between punch and die compared to those required for mild steel (Ref 6.41). Table 6.6 gives suggested blanking clearances for several AHSS. Selection of tool materials (a balance between toughness and hardness) and coatings is especially important to achieve an acceptable tool life in blanking AHSS.

Tooling construction includes the monoblock design for cast iron as well as cast or tool steel.

Monoblock Design. The dies for deep drawing/stretch forming of automobile panels are usually from cast iron based on the monoblock design (Fig. 6.26). They are flame hardened at high-pressure locations for increased wear resistance. The conventional cast die material does not have sufficient toughness and wear resistance for forming AHSS. Therefore, dies from cast steel offer the next best alternative to withstand high forces involved in forming AHSS, as given in Table 6.7. The monoblock cast steels are supplied in hardened and tempered condition for better hardness and toughness. In certain cases, cast steel can be surface hardened and offers much better dimensional stability (Ref 6.18, 6.46).

Tools with Cast or Tool Steel. Cast steels offer higher toughness and wear resistance compared to cast iron (GGG70L) and are the next alternative as a tooling material for monoblock design. However, the maximum weight of the

Table 6.6 Suggested punch-die clearances for blanking several advanced high-strength steels

Thickness		Suggested cutting clearances (punch-to-die clearance per side), %			
mm	in.				
2.0	0.08	14–16	14–16	14	12–14
1.5	0.06	14	12–14	12–14	12
1.0	0.04	12–14	12	10–12	10–12
0.5	0.02	12	10–12	10	10
Material grade →		DP 800	DP 1000	MS 1200	MS 1400

Source: Ref 6.41

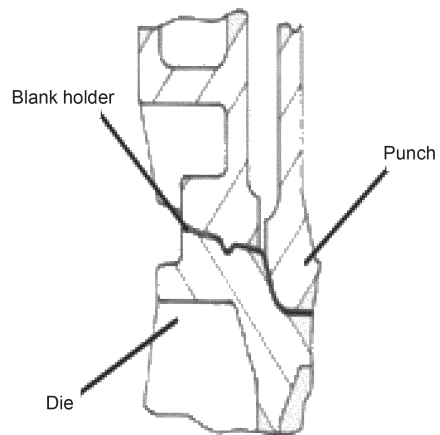


Fig. 6.26 Schematic illustrating monoblock design made from casting for stamping tooling construction. Source: Ref 6.18

Table 6.7 Cast steel materials for stamping tools to form advanced high-strength steel

Material			Usual delivery condition	Recommended production weight
DE-brand	Code	W. No.		
GPCNP(S)	G-45CrNiMo4-2	1.2769	Annealed max. 250 HB Hardened + tempered 850–1050 N/mm ² (125–150 ksi)	Max. 7000 kg (7.7 tons)
GMF	G-47CrMn6	1.7140	Annealed max. 230 HB Hardened + tempered 800–950 N/mm ² (115–135 ksi)	Max. 7000 kg (7.7 tons)
Cast cut	Special material	...	Annealed max. 240 HB Hardened + tempered 800–950 N/mm ² (115–135 ksi)	Max. 7000 kg (7.7 tons)
GP3M	G-60CrMoV10-7	1.2320	Annealed max. 250 HB Hardened + tempered 800–950 N/mm ² (115–135 ksi)	Max. 5000 kg (5.5 tons)
G-AMO	G-59CrMoV18-5	1.2333	Annealed max. 250 HB Hardened + tempered 800–950 N/mm ² (115–135 ksi)	Max. 4000 kg (4.4 tons)
GP4M	Special material	...	Annealed max. 250 HB Hardened + tempered 900–1250 N/mm ² (130–180 ksi)	Max. 1500 kg (1.7 tons)
GP5M	G-X100CrMoV5-1	1.2370	Annealed max. 275 HB	Max. 1000 kg (1.1 tons)
GCPPU	G-X155CrVMo12-1	1.2382	Annealed max. 285 HB	Max. 250 kg (550 lb)

Source: Ref. 6.46

material that can be cast is limited depending on the cast steel (Table 6.7). Hence, monoblock tools made from cast steel are limited to small die size. In large tools, cast steel or tool steel is used as inserts for locations that are at high contact pressure, as discussed earlier (Fig. 6.23). Cast steel inserts can be much larger than tool steel inserts and significantly reduce the necessary number of inserts and the assembly time. Cast steels also show better dimensional stability during heat treatment (Ref 6.18, 6.46).

Tool steels offer much higher toughness and wear resistance than cast steel. Hence, they are preferred over cast steel as insert material in the monoblock design tool when the contact pressure and the loads are very high.

6.5 Springback

Springback is a common phenomenon that causes shape deviation from the design-intended geometry (Ref 6.4) and that occurs after elastic-plastic deformation of the part during stamping.

Springback increases with the magnitude of the flow stress, that is, local strains, and decreases with the magnitude of the geometric restraint resulting from the shape of the formed part. When the forming load is released, or when the part is trimmed, the elastic stresses in various locations of the part are relaxed. The geometry of the part, however, does not allow all the strains to become zero, as schematically shown in Fig. 6.27. Thus, the part relaxes or springs back only partially, while some residual stresses still remain in the part after springback.

There are four types of springback behavior in sheet metal forming: bending (angle change), membrane (wall curl), hybrid, and twisting (Ref 6.47). A pure bending springback occurs only in plane-strain bending. The membrane springback is the elastic recovery of the in-plane tension/compression stresses. This type of springback may occur in pure stretch forming with dies having large die and punch radii. Shrinkages in panels are the result of the membrane springback. The hybrid springback is common to most automotive stampings made through draw die forming and contour flanging. Twisting is an elastic instability resulting from uneven springback in different directions and magnitudes. Twisting is more prone to occur in a thin sheet metal component with large differences in sectional dimensions, such as rails and shallow panels with nearly flat surfaces.

Due to their higher strength and strain hardening compared to mild steels, AHSS that are work hardened to the same level of strain as mild steel exhibit larger springback. As a result, prediction and compensation of springback represent a very significant effort in die engineering for forming AHSS parts.

Predicting Springback in AHSS. Finite-element simulation of the forming process is widely used in the industry for predicting springback in the formed part. Springback predicted by finite-element codes depends on:

- Parameters used to describe the sheet material behavior during deformation (flow stress, hardening model that accurately predicts hardening behavior in cyclic loading,

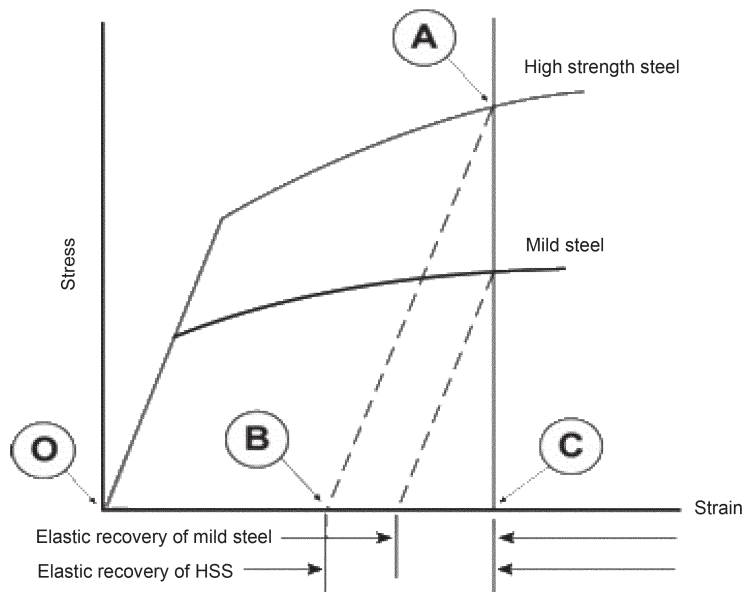


Fig. 6.27 Schematic illustrating elastic recovery of end springback in the formed sheet material. HSS, high-strength steel

anisotropy, and the Young's modulus variation with plastic strain)

- Type of elements to describe the sheet material (element type, number of integration points along the thickness direction)
- Mesh used to describe the corner radius in the tools
- Type of contact used to describe the contact between the sheet and the tools

The springback prediction using finite-element simulation for conventional mild steel and high-strength steel are approximately 70 to 80% accurate and are usually underestimated by using conventional material models (Ref 6.47). However, AHSS show much more Bauschinger effect compared to mild steel. Furthermore, the hardening behavior in reverse loading changes and may not be accurately modeled using the existing hardening laws in finite-element simulation. In addition, experimental investigation indicates that the unloading modulus of AHSS decreases with increase in plastic strain, as discussed in an earlier section. This behavior is generally not considered in finite-element simulation. Hence, the current state-of-the-art to predict springback accurately is not adequate. Research is being conducted by various companies and research institutes to improve the accuracy in predicting springback (Ref 6.4, 6.12, 6.42).

Compensation for Springback. Springback can be compensated for by changing the die surface (overbending/overforming), locally deforming (bottoming), or stretching by a high restraining force at the binder drawbead. These springback compensation procedures are classified as geometry-based compensation, which involves change in the tool geometry, and mechanics-based compensation, which compensates/reduces springback by controlling the factors affecting forming mechanism and springback.

Overbending/Overforming. In overbending/overforming, the sheet metal is deformed more in the forward direction such that after it springs back, it comes back to the desired position (Fig. 6.28). Figure 6.29 shows the overforming technique in forming channels. The top of the punch has a negative crown and the die has a corresponding positive crown such that after springback, the part comes back to the desired position. Often, this technique results in undercuts and cannot be used. Therefore, part design with large included angles greater than 90° is suggested to facilitate ease of manufacturing and compensation for springback (Fig. 6.30).

Bottoming. This is the most common practice to reduce springback in the flanging and bending process, where the sheet metal at the bending radius is intentionally subjected to compressive stress (squeezed, thinned) between the punch and die (Fig. 6.28), so that the material at

the bend radius is plastically deformed and there is little elastic recovery after unloading.

Part or Process Modification. Part designs for AHSS may be modified to have additional features that increase the stiffness of the part and reduce springback (Ref 6.42). The AHSS are widely used for producing channellike sections used in structural parts, as seen in Fig. 6.31.

In conventional drawing, the sheet is subject to cyclic bending and unbending, using springback due to curl. In crash forming, the sheet material is formed against the die by the punch in the absence of a blank holder. Crash forming, depending on the part geometry, could result in wrinkles in the formed part. Form drawing is similar to crash forming; however, there is a blank holder that comes in contact with the sheet toward the end of the forming process to iron out any wrinkles in the flange and to stretch the walls by applying restraining force. Form

drawing results in reduced springback because the cyclic bending and unbending stresses are avoided/minimized due to the absence of a blank holder during the initial stages of forming. Also, toward the end of the forming process, the presence of the blank holder with restraining force stretches the sheet material at the die corner radius, thereby avoiding the opening of the flange as well.

Modification of Forming Velocity. Servo-motor-driven presses offer flexibility in slide motion variations that can be used to reduce springback. Mori et al. (Ref 6.48) investigated the effect of forming speed, dwelling time at bottom dead center, and sheet thickness of the finished part (position) on the springback in V-bending of ultrahigh-strength steel sheets using a servo-drive press. As seen in Fig. 6.32, the forming velocity and the dwell time did not have an effect on the springback in the formed part. However, reduction in finishing sheet thickness induces more plastic strain in the deformation zone, resulting in reduction of springback.

A recent study conducted by Aida (Ref 6.49) in forming a curved hot section from DP 590 material illustrated that by reducing the forming speed and by carrying out two dwells at bottom dead center, it is possible to reduce springback considerably. Research is in progress to determine how best to use servo-drive presses for reducing springback in stamping.

Warm Forming. Mori et al. (Ref 6.15) investigated the possibility of reducing springback in the part formed from AHSS by forming a U-channel from DP 980, DP 780, DP 590, DP 440, and mild steel at elevated temperature. This

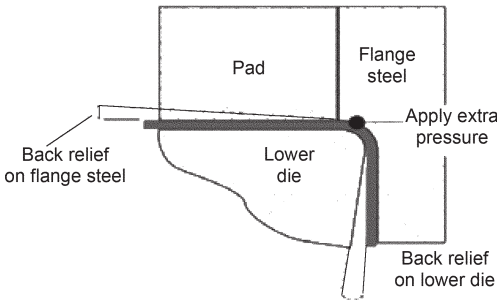


Fig. 6.28 Schematic of overbending to compensate for springback in bending. Source: Ref 6.3

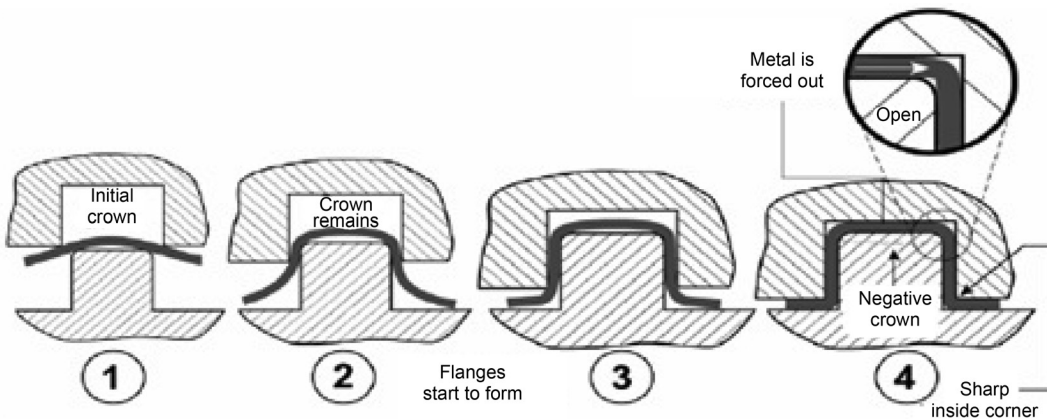


Fig. 6.29 Schematic of overforming to compensate for springback in the bottom of the channel. Source: Ref 6.3

study showed that, as expected, springback was reduced with increasing temperature. At 800 °C (1470 °F), almost no springback was observed in all formed parts. However, a large reduction in springback was still present when forming at 400 °C (750 °F). Also, the measured hardness in the part after forming was higher than the hardness of the initial sheet, so that the part strength was not reduced.



Fig. 6.30 Channel cross-sectional design for advanced high-strength steel with larger included angles to facilitate manufacturing. Source: 6.3

Thyssen Krupp investigated warm forming of complex-phase (CP) steels to reduce springback. The CP steels show significant reduction in flow stress (40 to 60%) at a temperature range of 500 to 700 °C (930 to 1290 °F). This process, conducted near 600 °C (1110 °F), does not require controlled cooling at the end of forming, thereby resulting in a much higher production rate than in hot stamping. The yield strength in the semi-hot formed part was in the range of 800 to 1220 MPa (115 to 175 ksi), as in cold forming of CP steels, but warm forming increases the geometric complexity of the parts that can be achieved from CP steels. Also, the springback in the semi-hot stamped parts was found to be even lower than hot stamping and much lower than the values obtained in room-temperature forming (Ref 6.50).

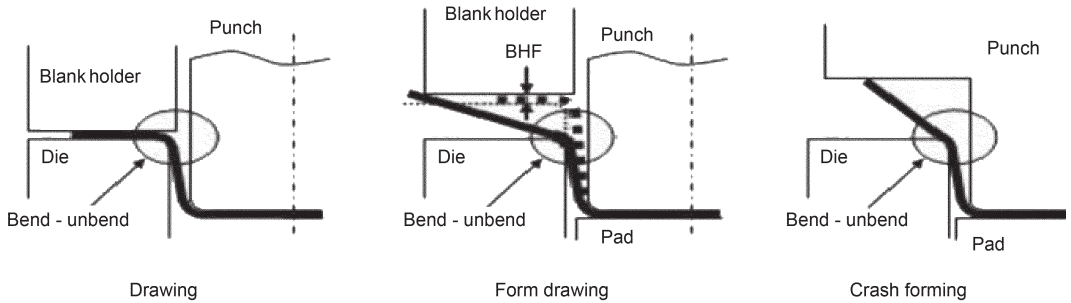


Fig. 6.31 Schematic of the drawing, form drawing, and crash forming process investigated to reduce springback in forming advanced high-strength steel. BHF, blank holder force. Source: Ref 6.3

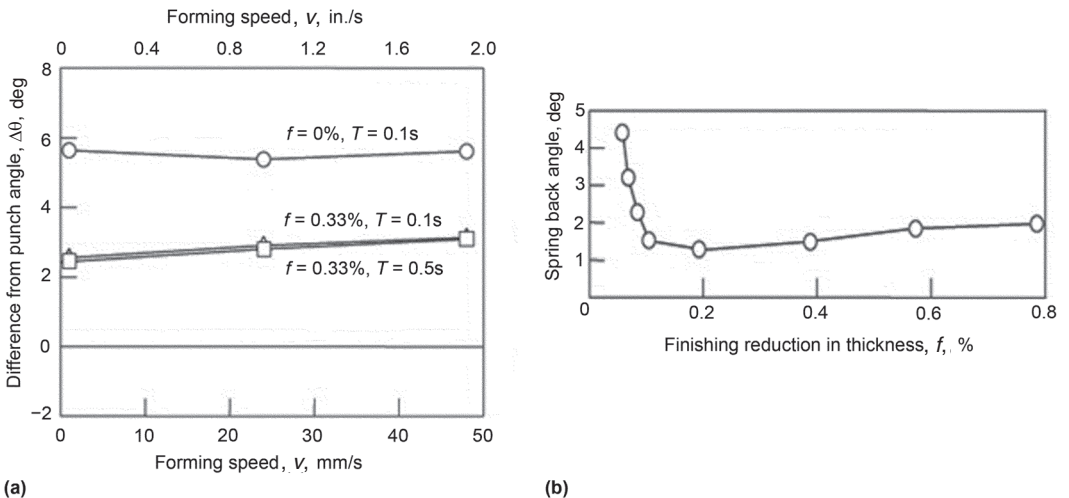


Fig. 6.32 Effects of punch velocity, dwell time, and sheet thickness reduction on reducing springback. Source: Ref 6.48

REFERENCES

- 6.1 M. Pfestdorf, "The Need for Multi-Phase Steel for the Body-in-White of a Passenger Car," Great Designs in Steel Seminar 2005, American Iron and Steel Institute, 2005, www.autosteel.org
- 6.2 J. Shaw and B. Zuidema, "New High Strength Steels Help Automakers Reach Future Goals for Safety, Affordability, Fuel Efficiency and Environmental Responsibility," SAE 2001-01-3041, 2001
- 6.3 "Advanced High Strength Steels (AHSS) Application Guidelines," Version 4.1, World Steel Association, June 2009, www.worldautosteel.org
- 6.4 B. Yan, "Progress and Challenges in Forming of AHSS," Presentation at the Workshop on AHSS, The Ohio State University, April 29, 2009
- 6.5 X.M. Chen, M.F. Shi, G. Chen, M. Kamura, K. Watanabe, and Y. Omiya, "Crash Performances of Advanced High Strength," SAE 2005-01-0354, 2005
- 6.6 J. Shaw, K. Watanabe, and M. Chen, "Metal Forming Characterization and Simulation of Advanced High Strength Steel," SAE 2001-01-1139, 2001
- 6.7 A. Al-Nasser, P. Pathak, A. Yadav, and T. Altan, Determination of Flow Stress of Five AHSS Sheet Materials (DP600, DP780, DP780CR, DP780HY and TRIP 780) Using the Uniaxial Tensile Test and Biaxial Viscous Pressure Bulge Test, *JMPT*, Feb 2010, p 429–436
- 6.8 R. Cleveland and A. Ghosh, Inelastic Effects on Springback in Metals, *Int. J. Plast.*, Vol 18, 2002, p 769–785
- 6.9 H. Zhu, L. Huang, and C. Wong, "Unloading Modulus on Springback in Steels," Society of Automotive Engineering, 2004
- 6.10 R. Perez, A. Benito, and J.M. Prado, Study of the Inelastic Response of TRIP Steels after Plastic Deformation, *ISIJ Int.*, Vol 45, 2005, p 1925–1933
- 6.11 D. Fei and P. Hodgson, Experimental and Numerical Studies of Springback in Air V-Bending Process for Cold Rolled TRIP Steels, *Nucl. Eng. Des.*, Vol 236, 2006, p 1847–1851
- 6.12 T. Stoughton, C. Xia, C. Du, and M. Shi, "Challenges for Constitutive Models for Forming of Advanced Steels," Advanced High Strength Steel Workshop, Oct 22–23, 2006 (Virginia)
- 6.13 S. Sadagopan and D. Urban, "Formability Characterization of a New Generation of High Strength Steels," AISI/DOE Road Map Program, 2003, www.autosteel.org
- 6.14 O. Graessel, L. Krueger, G. Frommeyer, and L.W. Meyer, High Strength Fe±Mn±(Al, Si) TRIP/TWIP Steels Development—Properties—Application, *Int. J. Plast.*, Vol 16, 2000, p 1391–1409
- 6.15 K. Mori, S. Maki, and Y. Tanaka, Warm and Hot Stamping of Ultra High Tensile Strength Steel Sheets Using Resistance Heating, *CIRP Ann.*, Vol 54 (No. 1), 2005, p 209–212
- 6.16 M. Khaleel, J. Carpenter, and P. Sklad, Evaluations of the Effects of Manufacturing Processes and In-Service Temperature Variations on the Properties of TRIP Steels, *Automotive Light Weighting Materials 2005 Annual Report*, 2005, p 179–186
- 6.17 M.R. Berrahmoune, S. Berveiller, K. Inal, A. Moulin, and E. Patoor, Analysis of the Martensitic Transformation at Various Scales in TRIP Steel, *Mater. Sci. Eng. A*, Vol 378 (No. 1–2, special issue), 2004, p 304–307
- 6.18 G. Haller, Tool Concepts and Materials for the Forming of High Strength Steels, *New Developments in Sheet Metal Forming*, K. Siegert, Ed., IFU, Stuttgart, 2004, p 317–326
- 6.19 J. Dykeman, D. Hoychick, T. Link, and H. Mitsuji, "Material Property and Formability Characterization of Various Types of High Strength Dual Phase Steel," SAE Paper 2009-01-0794, 2009
- 6.20 P. Cugy, A. Hildenbrand, M. Bouzekri, D. Cornette, S. Goklu, and H. Hofmann, "A Super High Strength Fe-Mn-C Austenitic Steel with Excellent Formability for Automobile Applications," Correspondence from Audi, 2006
- 6.21 A. Hudgins, D. Matlock, J. Speer, J. Fekete, and M. Walp, "The Susceptibility to Shear Fracture in Bending of Advanced High Strength Sheet Steels," *Materials Science and Technology (MS&T)*, Sept 16–20, 2007
- 6.22 K. Kim and T. Altan, Shear Fracture in Bending AHSS, *Stamp. J.*, Dec 2008, p 14

- 6.23 “Tooling Solutions for Advanced High Strength Steels,” Product Guide, SSAB, 2008
- 6.24 A. Konieczny, “Advanced High Strength Steels—Formability,” Great Designs in Steel Seminar 2003, American Iron and Steel Institute, Feb 2003, www.auto-steel.org
- 6.25 G.M. Dalton and J.A. Schey, Effect of Bead Finish Orientation on Friction and Galling in Drawbead Test, *SAE Trans.*, Vol 101 (No. 5), 1992, p 509–519
- 6.26 T. Skare and F. Krantz, Wear and Frictional Behavior of High Strength Steel in Stamping Monitored by Acoustic Emission Technique, *Wear*, Vol 255, 2003, p 1471–1479
- 6.27 H. Kim, S. Han, F.E. Goodwin, K. Kim, and T. Altan, “Evaluation of Die Coatings and Stamping Lubricants in Forming Galvanized A/UHSS Using the Strip Drawing Test,” IDDRG Int. Conference, June 2009 (Golden, CO)
- 6.28 B. Jeffery, Advanced Lubricant Technology for High-Strength Steel, *Stamp. J.*, June 8, 2004, p 107
- 6.29 B. Jeffery, AHSS Tooling Requires Greater Protection, *Stamp. J.*, Sept 13, 2005
- 6.30 M. Brown and P. Bosler, Jr., Selecting Stamping Lubricants for Advanced High-Strength Steels, *Met. Form.*, Feb 2006
- 6.31 P. Carlsson, U. Bexell, and M. Olson, Tribological Performance of Thin Organic Permanent Coating Deposited on 55% Al-Zn Coated Steel—Influence of Coating Composition and Thickness on Friction and Wear, *Wear*, Vol 251, 2001, p 1075–1084
- 6.32 Y. Mori, M. Yamazaki, and H. Shindo, Film Designed for Lubricative Coated Steel Sheets, *Prog. Org. Coatings*, Vol 40, 2000, p 119–120
- 6.33 O. Sanderberg and B. Johansson, Tool Steels for Blanking and Forming—New Developments, *International Conference on Recent Developments in Manufacture and Use of Tools and Dies and Stamping of Steel Sheets*, 2004, p 77–94
- 6.34 M. Liljengren, K. Kjellsson, N. Asnafi, and T. Johansson, Die Materials, Hardening Methods and Surface Coatings for Forming High, Extra High and Ultra High Strength Steel Sheets (HSS/EHSS/UHSS), *Proc. of IDDRG 2006*, 2006, p 597–604
- 6.35 N. Asnafi, K. Kjellsson, and T. Johansson, Blanking, Stamping and Trimming Die Experiences at Volvo Cars, *International Conference on Recent Developments in Manufacture and Use of Tools and Dies and Stamping of Steel Sheets*, 2004, p 263–274
- 6.36 H. Kim, J. Sung, F.E. Goodwin, and T. Altan, Investigation of Galling in Forming Galvanized AHSS Using TCT, *JMPT*, Vol 205, 2008, p 459
- 6.37 M. Murakawa, N. Koga, S. Watanabe, and S. Takeuchi, Tribological Behavior of Amorphous Hard Carbon Films against Zinc-Plated Steel Sheets, *Surf. Coat. Technol.*, Vol 184, 1998, p 425–430
- 6.38 T. Sato, T. Besshi, I. Tsutsui, and T. Morimoto, Anti-Galling Property of a Diamond-Like Carbon Coated Tool in Aluminum Sheet Forming, *J. Mater. Process. Technol.*, Vol 104, 2000, p 21–24
- 6.39 D. Young, T. Mulholand, and M. Klein, “Investigation of Tooling Durability for AHSS,” Presented at the Seminar on Great Designs in Steel (Livonia, MI), 2009
- 6.40 B. Janoss, Selecting, Using Tool Coatings to Stamp AHSS, *The Fabricator*, July 2008
- 6.41 S. Keeler and P. Ulintz, Forming High Strength Steels, *Met. Form.*, April 2009, p 18
- 6.42 J. Fekete, “Product and Process Effects on Stamping Performance of Advanced High Strength Steels,” Great Designs Seminar 2006, www.autosteel.org
- 6.43 B.K. Zuidema, “Advanced High Strength Steel Application Guidelines,” Great Designs Seminar 2007, www.autosteel.org
- 6.44 D. Haller, Requirements of New Materials in the Press Shop of Tomorrow, *New Developments in Sheet Metal Forming*, M. Liewald, Ed., IFU, Germany, 2006, p 75–96
- 6.45 “TECTRENDS,” Schuler, Feb 2006, www.schulergroup.com
- 6.46 C. Escher and T. Henke, Tool Materials for the Processing of High Strength Steels, *New Developments in Sheet Metal Forming*, K. Siegert, Ed., IFU, Stuttgart, 2004, p 103–122

- 6.47 C.T. Wang, An Industrial Outlook for Springback Predictability, Measurement Reliability and Compensation Technology, *Proc. of NUMISHEET 2002*, p 597–604
- 6.48 K. Mori, K. Akita, and Y. Abe, Springback Behavior in Bending of Ultra-High Strength Steel Sheets Using CNC Servo Press, *Int. J. Mach. Tools Manuf.*, Vol 47 (No. 2), 2007, p 321–325
- 6.49 Aida, private communication with T. Altan, Sept 16, 2009
- 6.50 R. Kolleck, D. Steinhofner, J.A. Feindt, T. Heller, and F.J. Lenze, Hot Forming and Cold Forming—Two Complementary Processes for Light Weight Auto Bodies, *New Developments in Sheet Metal Forming*, K. Siegert, Ed., IFU, Stuttgart, 2004, p 235–244

CHAPTER 7

Hot Stamping

A. Naganathan, Cummins Engine Company
L. Penter, University of Dresden, Germany

IN THE AUTOMOTIVE INDUSTRY, to improve vehicle safety and reduce fuel consumption, manufacturing of lightweight body parts from ultrahigh-strength steels (UHSS) is rapidly increasing. Forming of UHSS at room temperature is limited by low formability and considerable springback. Therefore, hot stamping is accepted as a viable alternative solution and widely used (Fig. 7.1). “Hot stamping is a non-isothermal forming process for sheet metals, where forming and quenching take place in the same forming step” (Ref 7.2). This process takes advantage of low flow stress of boron-alloyed steel (22MnB5) in austenitic phase at elevated temperature and allows the manufacturing of parts with ultrahigh strength, minimum springback, and reduced sheet thickness.

Hot stamping was developed and patented in 1977 by a Swedish company (Plannja), which used the process for saw blades and lawn mower blades (Ref 7.3). In 1984, Saab Automobile AB was the first vehicle manufacturer who adopted a hardened boron steel component for the Saab 9000 (Ref 7.4). The number of produced parts increased from 3 million parts per year in 1987 to 8 million parts per year in 1997, which further increased to approximately 107 million parts per year in 2007 (Ref 7.5).

There are two different methods of hot stamping: direct and indirect.

Direct Method. In the direct method (Fig. 7.2), the blanks are austenitized at temperatures between 900 and 950 °C (1650 and 1740 °F) for 4 to 10 min inside a continuous-feed furnace

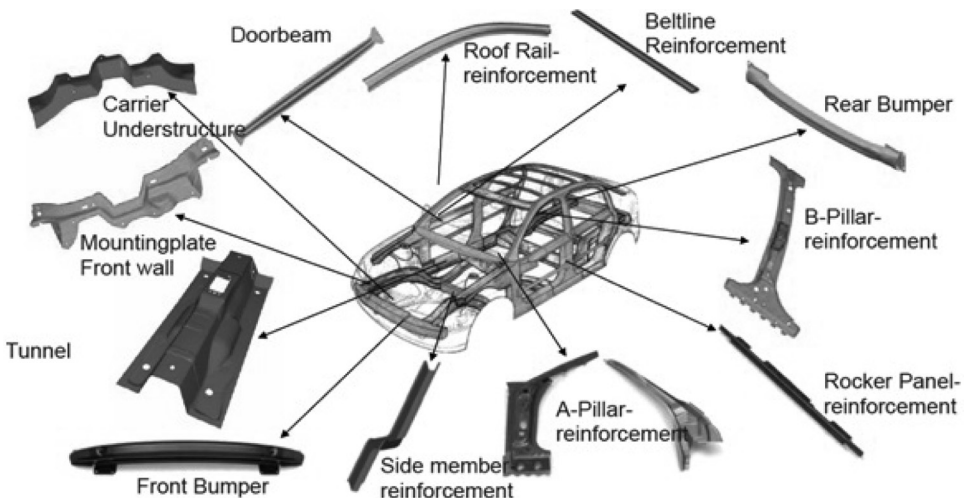


Fig. 7.1 Components manufactured using hot stamping. Source: Ref 7.1

and subsequently transferred to an internally cooled die set via a transfer unit. The transfer usually takes less than 3 s. At high temperature (650 to 850 °C, or 1200 to 1560 °F), the material has high formability, and complex shapes can be formed in a single stroke. The blanks are stamped and cooled down under pressure for a specific amount of time according to the sheet thickness after drawing depth is reached. During this period, the formed part is quenched in the closed die set that is internally cooled by water circulation at a cooling rate of 50 to 100 °C/s (90 to 180 °F/s), completing the quenching (martensitic transformation) process. The total cycle time for transferring, stamping, and cooling in the die is 15 to 25 s. The part leaves the hot stamping line at approximately 150 °C (300 °F) and with high mechanical properties of 1400 to 1600 MPa (200 and 230 ksi) and a yield

strength between 1000 and 1200 MPa (145 and 175 ksi).

Indirect Method. Unlike the direct process, indirect hot stamping (Fig. 7.3) provides a part to be drawn, unheated, to approximately 90 to 95% of its final shape in a conventional die, followed by a partial trimming operation, depending on edge tolerance. Then, the preforms are heated in a continuous furnace and quenched in the die. The reason for the additional step is to extend the forming limits for very complex shapes by hot forming and quenching the cold-formed parts.

7.1 Significant Process Variables

Temperature Transformation Curve. The continuous time-temperature transformation curve

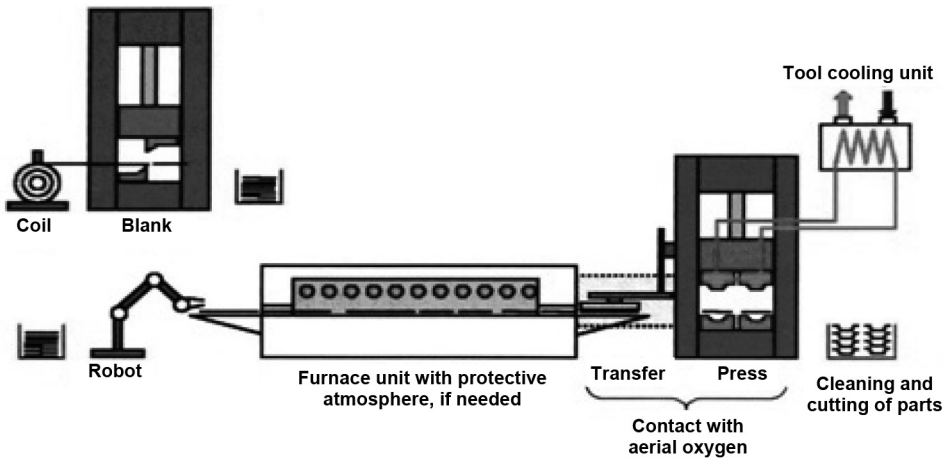


Fig. 7.2 Direct method of hot stamping. Source: Ref 7.6

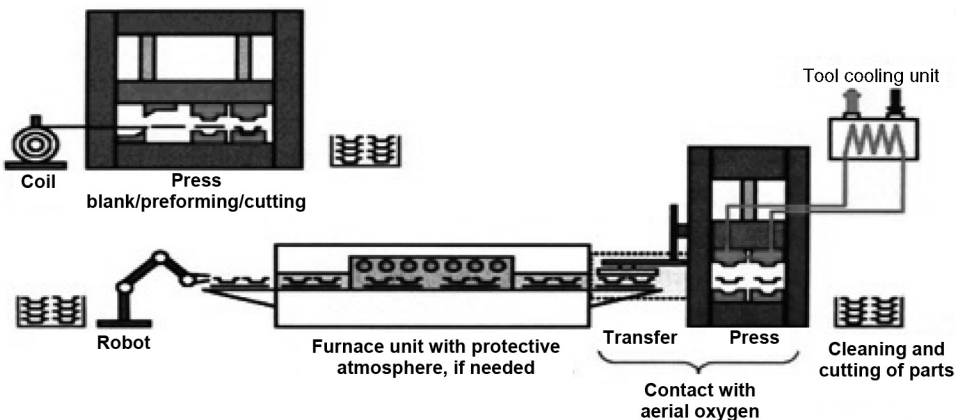


Fig. 7.3 Indirect method of hot stamping. Source: Ref 7.6

illustrates the microstructural evolution of a particular material, depending on the cooling rate. To reach tensile strength up to 1600 MPa (230 ksi) of the final part, a complete transformation of the austenitic to martensitic microstructure is required. Therefore, cooling rates faster than 27 K/s (49 °F/s) in the part must be achieved to avoid bainitic or even ferritic-pearlitic transformation, as shown in Fig. 7.4.

Chemical Composition of 22MnB5. The addition of boron into the steel alloy lowers the critical cooling rate and therefore extends the process window (Table 7.1). Furthermore, alloying boron reduces the carbon equivalent and therefore increases the weldability. Chrome and manganese increase the tensile strength of the quenched material.

Flow-Stress Data for 22MnB5. Reliable finite-element simulation of the hot stamping process requires accurate flow-stress data. For 22MnB5 steel, flow-stress data were obtained as a function of temperature, strain, and strain rate using a modified Gleeble system (Fig. 7.5) (Ref 7.2, 7.8, 7.9).

The rolling direction does not have any influence on the flow-stress data. Temperature has strong influence on the flow stress, as given by the experimental values in Fig. 7.6.

With increase in temperature, there is a decrease in the flow-stress values and the work-hardening exponent. Furthermore, the curve shows an asymptotic trend around 700 to 800 °C (1290 to 1470 °F). This behavior is due to the temperature-induced dynamic, microstruc-

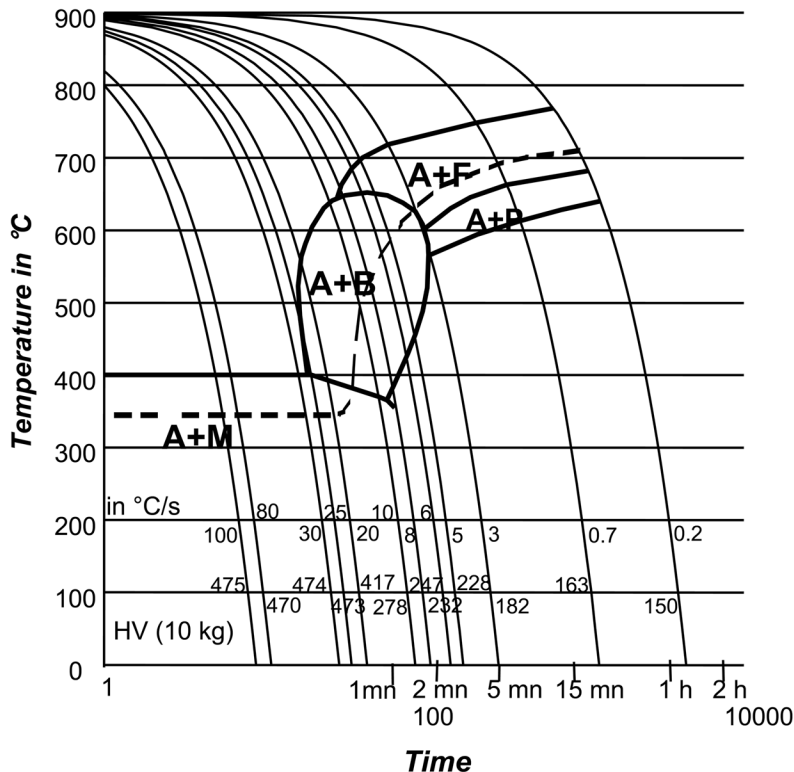


Fig. 7.4 Continuous cooling transformation diagram of 22MnB5 from Arcelor. A, austenite; B, bainite; F, ferrite; P, pearlite; M, martensite. Source: Ref 7.2

Table 7.1 Chemical composition of USIBOR 1500 (1.2 mm, or 0.047 in., thick)

Material	Composition, wt%											
	C	Mn	Si	Ni	Cr	Cu	S	P	Al	V	Ti	B
USIBOR	0.221	1.29	0.28	0.013	0.193	0.01	0.001	0.018	0.032	0.005	0.039	0.0038

Source: Ref 7.7

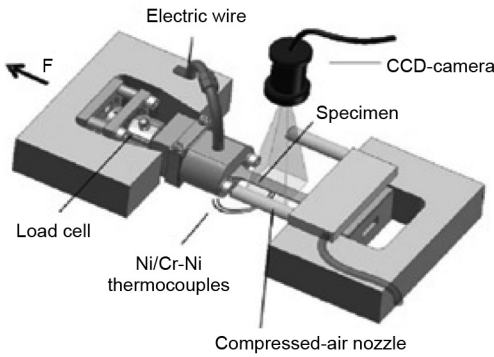


Fig. 7.5 Modified Gleeble 1500 system. CCD, charge-coupled device. Source: Ref 7.2

tural recovery process balancing the strain-hardening effect.

Increase in strain rate increases the flow-stress level and strain-hardening exponent (Fig. 7.7). Increase in the strain-hardening exponent is due to the short annihilation or recovery time available during the test.

At 500 °C (930 °F), the lowest strain rate, 0.01 s⁻¹, leads to higher flow-stress values, as shown in Fig. 7.8.

The reason for significant increase of flow stress at strain rate 0.01 s⁻¹ is due to the sudden initiation of the microstructural transformation from austenite to bainite. For higher strain rates, deformation takes place in the austenitic phase, and the flow-stress values show conventional behavior (Ref 7.9).

To study the effect of cooling rate, tests were conducted at an air cooling rate of 15 K/s (25 °F/s) and a rapid cooling rate of 80 K/s (145 °F/s); the results are shown in Fig. 7.9. At 650 and 800 °C (1200 and 1470 °F), the flow-stress values have no effect on the cooling rate. At 500 °C (930 °F), bainite formation caused an increase of flow stress at the lower cooling rate of 15 K/s.

Friction Coefficient. The friction coefficient is an important parameter for calculating accurate material flow and heat transfer during hot stamping simulation. The friction coefficient under relevant conditions of hot stamping is calculated using a tribosimulator (Ref 7.10) and the modified cup drawing test (Ref 7.11). Figure 7.10 represents a schematic of the testing machine used for determining friction in hot stamping (Ref 7.10).

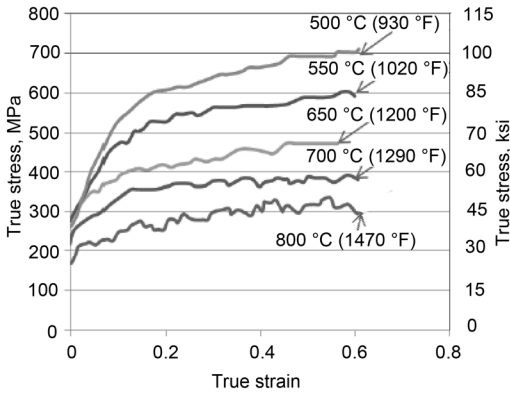


Fig. 7.6 Influence of temperature on flow-stress data. Cooling rate = 80 K/s (145 °F/s); strain rate = 0.1 s⁻¹. Source: Ref 7.9

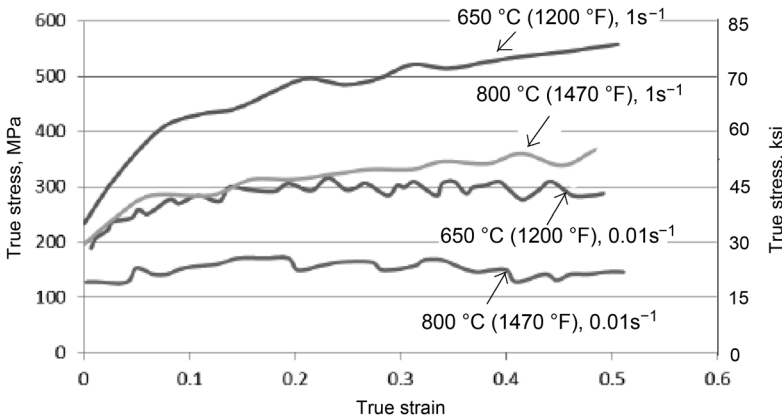


Fig. 7.7 Influence of strain rate. Cooling rate = 80 K/s (145 °F/s). Source: Ref 7.9

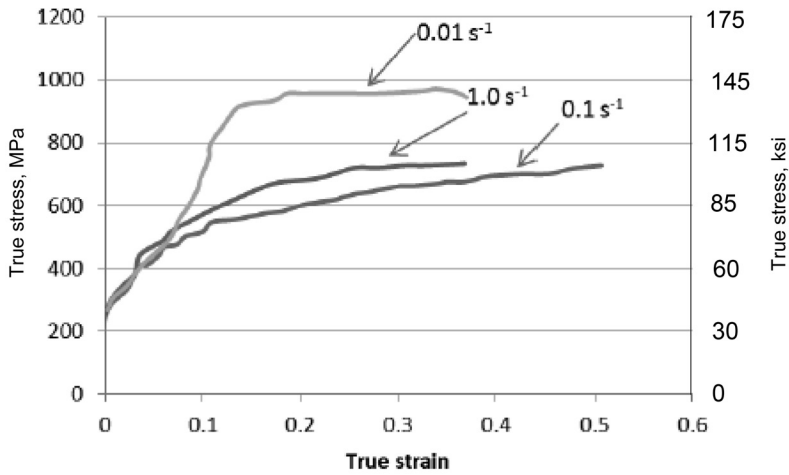


Fig. 7.8 Influence of strain rate at 500 °C (930 °F). Cooling rate = 80 K/s (145 °F/s). Source: Ref 7.9

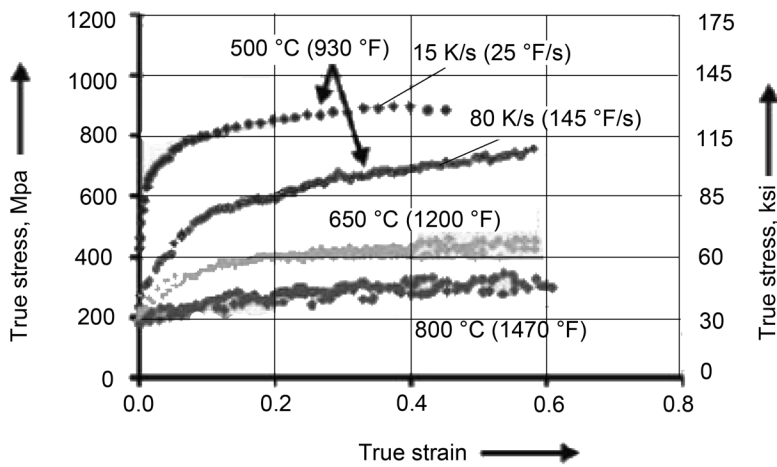


Fig. 7.9 Influence of cooling rate. Source: Ref 7.9

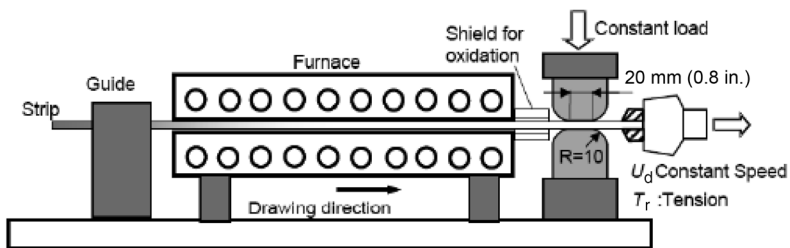


Fig. 7.10 Schematic of testing machine used to determine friction in hot stamping. Source: Ref 7.10

The 22MnB5 sheet material is heated in the infrared furnace to its austenitization temperature under inert gas atmosphere. One end of the strip is clamped with the chuck of the tension device and is pulled at constant speed. Once the heated zone of the strip reaches the entrance of the die, a constant compression load, P , is applied. The coefficient of friction, μ , is calculated from the constant compression load, P , and tension load, T_F , using:

$$\mu = T_F/2P \tag{Eq 7.1}$$

The experiments were conducted under dry condition without lubricants.

Figure 7.11 shows that with an increase in temperature, there is an increase in the friction coefficient for 22MnB5 steel, and the effect is small for SPHC steel. This effect is due to the scale thickness generated during preheating.

Figure 7.12 represents a schematic of the modified cup drawing test, which is also suggested for determining the coefficient of friction

(Ref 7.11). The tool is connected to a hydraulic press equipped with load cells for measuring the punch force, F_p , and the blank holder force, F_{BH} , during the test. The sheet samples are heated in a furnace. The tests were conducted without applying blank holder force in the flange area of the sheet to avoid unnecessary heat transfer. The tests were conducted with a punch velocity (V_{punch}) of 10 mm/s (0.4 in./s). The temperature of the punch (T_{punch}) was kept constant at room temperature (RT). Each parameter combination was tested at least five times ($n = 5$). The coefficient of friction is calculated using the equation by Siebel (Ref 7.12) that estimates the maximum deep drawing force.

From Fig. 7.13 and 7.14, it is seen that the friction coefficient decreases with an increase in the temperature of the die and the blank holder. The significant temperature-dependent plastic softening of the material 22MnB5 leads to reduced normal forces transferred from the bulk sheet material to the interacting surfaces at the die. This causes reduction in the friction coefficient with an increase in temperature.

Heat-Transfer Coefficient. The heat transfer between sheet material and die with integrated cooling channels determines the martensite formation and final part properties. The experimental setup for calculating the contact heat-transfer coefficient between sheet materials and die is shown in Fig. 7.15.

The setup contains two water-cooled rectangular plates for quenching the specimen under pressure. The specimen is heated in a furnace to the austenitization temperature of 850 to 950 °C (1560 to 1740 °F) and placed manually on four spring-seated pins. With this experimental setup, the specimens can be loaded during quenching up to a pressure of 40 MPa (6 ksi). The heat-transfer coefficient is calculated using Newton’s cooling law, given by:

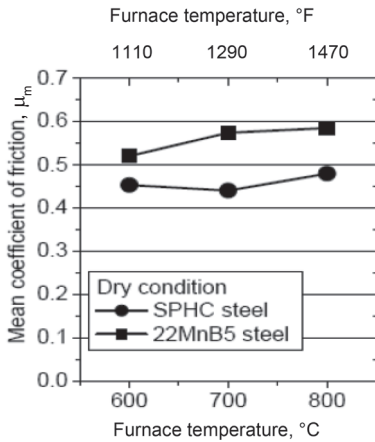


Fig. 7.11 Effect of temperature on mean friction coefficients under dry conditions. Source: Ref 7.10

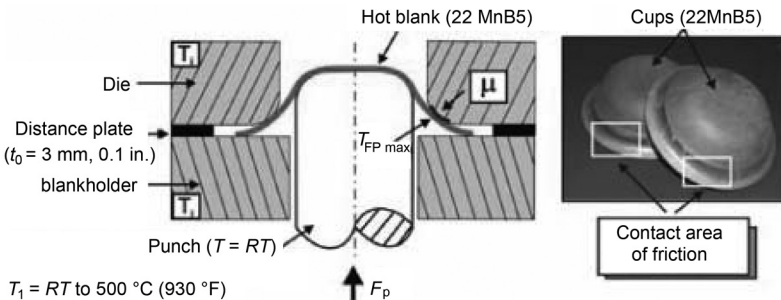


Fig. 7.12 Schematic of experimental setup of the cup deep drawing test (left) and two drawn cups at elevated temperatures (right). Source: Ref 7.11

$$T(t) = (T_0 - T_u) \cdot e^{-\frac{\alpha A}{c_p} t} + T_u \quad (\text{Eq 7.2})$$

where T_0 and $T(t)$ are the initial and current temperature of the specimen during the cooling experiment, T_u is the temperature of the contact plates, t is the time during the experiment, A is the geometric contact area, and c_p is the heat capacity of the specimen.

The heat-transfer coefficient, α , is calculated at a particular time, t , from the aforementioned

equation, and the corresponding contact pressure is measured from the experiment.

The contact pressure ranges from 0 to 40 MPa (0 to 6 ksi). The specimens were heated to the austenitization temperature of 950 °C (1740 °F) for 5 min. The experiments were repeated for five specimens ($n = 5$). The heat-transfer coefficient increases as a function of pressure due to the increase in contact surface area; the results are given in Fig. 7.16.

Lechler (Ref 7.14) studied the variation of heat-transfer coefficient as a function of contact distance between die and sheet surface. The results showed that the heat-transfer coefficient between die and sheet material is almost constant ($\sim 100 \text{ W/m}^2 \cdot \text{K}$) until the contact distance reaches 0.5 mm (0.02 in.), and the value increases steeply to $1200 \text{ W/m}^2 \cdot \text{K}$ when the die touches the sheet material. The results are given in Fig. 7.17.

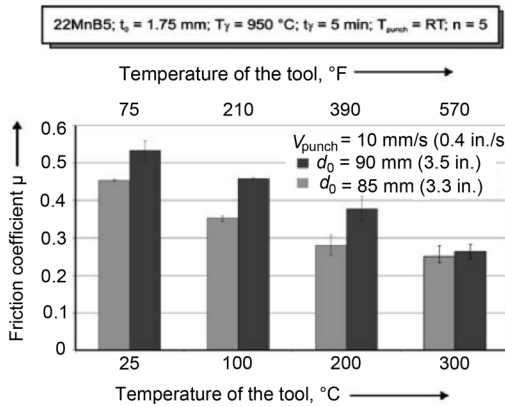


Fig. 7.13 Evolution of friction coefficient, μ , with different tool temperature, maintaining punch at room temperature for 22MnB5. Sheet thickness $t_0 = 1.75 \text{ mm}$ (0.069 in.); austenitization temperature $T_\gamma = 950 \text{ °C}$ (1740 °F); austenitization time $t_\gamma = 5 \text{ min}$; punch velocity $V_{\text{punch}} = 10 \text{ mm/s}$ (0.4 in./s); $d_0 =$ initial blank diameter. Source: Ref 7.11

7.2 Material Flow and Process Simulation

It is important to predict the final properties of the hot-stamped component early in the product development process. If precise predictions of the part geometry and microstructure can be obtained with numerical simulations, it is possible to create components with tailored properties and functionalities in different zones of the

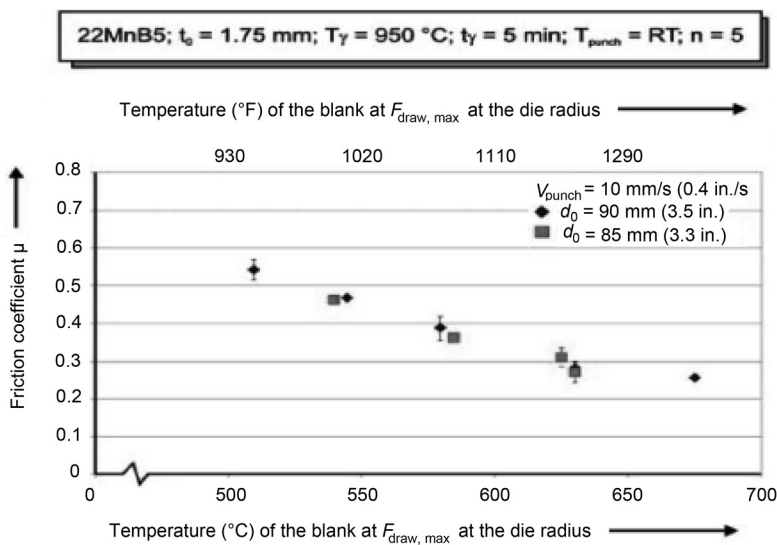


Fig. 7.14 Friction coefficient, μ , as function of blank temperature in contact area at die radius at moment of maximum drawing force for 22MnB5. Sheet thickness $t_0 = 1.75 \text{ mm}$ (0.069 in.); austenitization temperature $T_\gamma = 950 \text{ °C}$ (1740 °F); austenitization time $t_\gamma = 5 \text{ min}$; punch velocity $V_{\text{punch}} = 10 \text{ mm/s}$ (0.4 in./s). Source: Ref 7.11

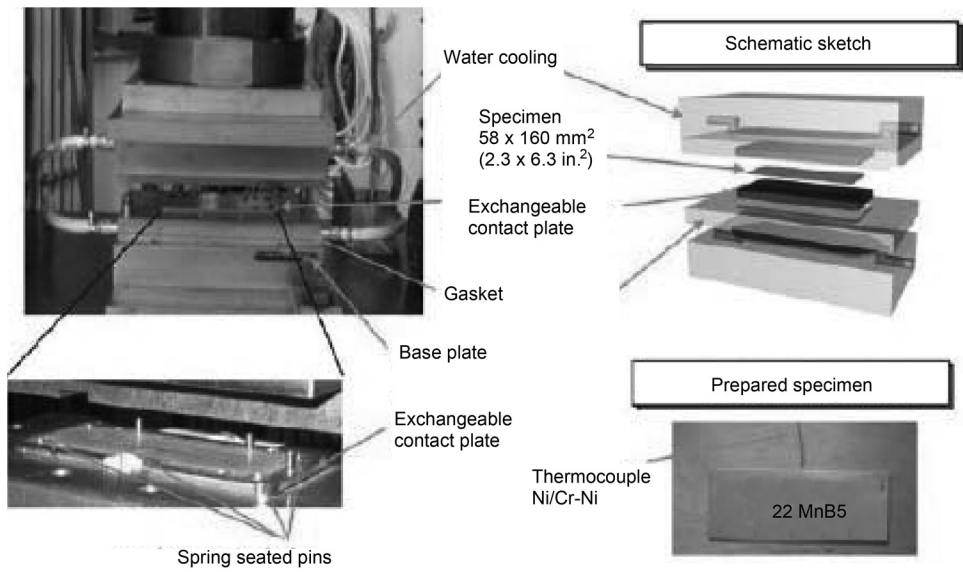


Fig. 7.15 Experimental setup for finding heat-transfer coefficient. Source: Ref 7.13

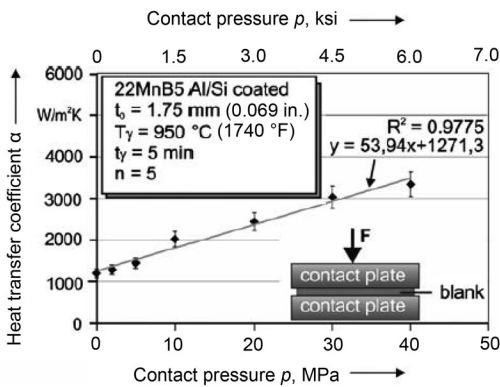


Fig. 7.16 Heat-transfer coefficient as a function of pressure for both-sided metallic contact. Source: Ref 7.11

component. For example, a B-pillar can be manufactured with a softer material zone at its lower end. By allowing controlled buckling in this lower area, severe buckling at a higher location with a possible penetration into the passenger compartment can be prevented (Ref 7.15).

Simulation of Coupled Thermomechanical and Microstructure Evolution. Hot stamping simulation involves combined thermomechanical and microstructure evolution simulation. Hein (Ref 7.16) identified the following challenges in the finite-element simulation of the hot stamping process:

- Temperature - and strain-rate-dependent material parameters (thermal and mechanical)
- Heat transfer between the blank and the die (depending on current contact conditions)
- Coupled thermomechanical calculation
- Evolution of microstructure of the material as a function of temperature, time, and deformation

The interaction between the mechanical field, thermal field, and the microstructure evolution during the hot stamping process is given in the schematic in Fig. 7.18. A description of the different interaction parameters shown in Fig. 7.18 is given in Table 7.2.

The effects of some of the interaction parameters are important, and some parameters can be neglected in the simulation. For example, the heat generation due to plastic deformation and friction can be neglected compared to the overall heat transfer between the blank and the tools (Ref 7.18).

In Table 7.2, parameter 1a, thermal boundary conditions based on deformation, represents the contact heat-transfer coefficient between the die and blank as a function of pressure. Parameter 1b can be neglected in the simulation because of its negligible amount compared to the overall heat transfer between the blank and die. Parameters 2 and 5b can be included in the simulation by considering the variation of thermal dilatation value as a function of temperature. Param-

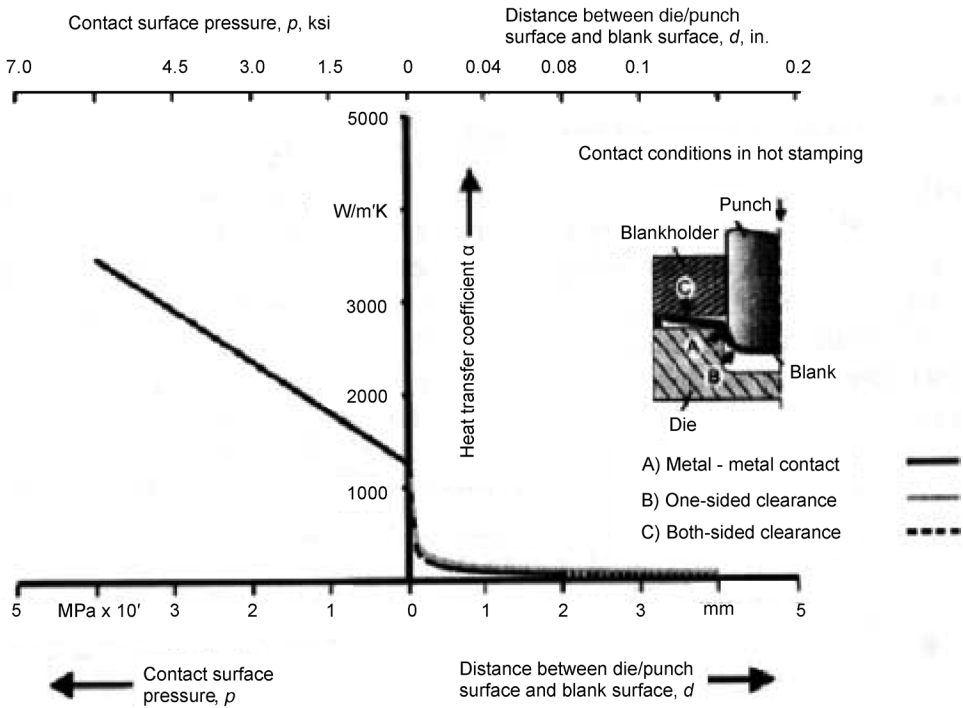


Fig. 7.17 Contact heat-transfer coefficient as a function of contact pressure and distance between tool and sheet material surface. Source: Ref 7.14

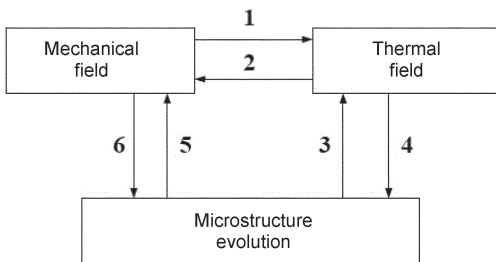


Fig. 7.18 Interactions between the mechanical field, thermal field, and microstructure evolution. Source: Ref 7.17

Table 7.2 Descriptions of interactions in Fig. 7.18

No.	Interaction description
1a	Thermal boundary conditions are deformation dependent.
1b	Heat generation due to plastic dissipation and friction (not accounted for in this work)
2	Thermal expansion
3a	Latent heat due to phase transformations
3b	Thermal material properties depend on microstructure evolution.
4	Microstructure evolution depends on the temperature.
5a	Mechanical properties depend on microstructure evolution.
5b	Volume change due to phase transformations
5c	Transformation plasticity
5d	Memory of plastic strains during phase transformations
6	Phase transformations depend on stress and strain

Source: Ref 7.17

eter 3a can be included in the simulation by considering the variation of heat capacity of the material with respect to temperature. Parameters 3b and 5a represent the dependency of material parameters on the microstructure evolution based on a certain temperature history. There are two methods of considering these effects in the simulation. First, based on the information of volume fraction of different phases (austenite, ferrite, pearlite, bainite, and martensite) and their properties, the overall material property can be calculated using mixture rules. Secondly, this effect can be considered directly by suitable material characterization experiments

following appropriate temperature history. The second method is used widely. Parameter 4 can be calculated from the temperature history and equations such as Koistinen-Marburger (for martensite evolution) (Ref 7.19).

Parameter 5c, transformation plasticity, is an irreversible deformation that occurs when a material undergoes phase transformation under applied stress well below the yield strength of the material. Parameter 5d is not considered in the finite-element simulation.

Thermal and Mechanical Properties Required for High-Temperature Forming Simulation (Ref 7.8)

Reliable flow-stress data as a function of strain, temperature, and strain rate for both blank and die material are important for accurate numerical simulation. These data are obtained by tensile test or compression test at high temperature.

Young's Modulus as a Function of Temperature. Young's modulus is a description of the mechanical stiffness of the material. It is temperature dependent and decreases at high temperatures.

Poisson's Ratio as a Function of Temperature. Poisson's ratio relates the axial and lateral strain in uniaxial compression or tension.

Thermal Dilatation due to Thermal Expansion and Phase Transformation. Thermal expansion and volume change due to transformation of austenite to martensite under controlled cooling conditions, evaluated by using dilatation tests, are required for the numerical simulation.

Thermal Conductivity as a Function of Temperature. Thermal conductivity defines the ability of a material to transfer heat. This property is phase and material dependent.

Heat Capacity as a Function of Temperature. The heat capacity of a material represents the amount of energy required to produce a unit temperature rise. This property is phase and temperature dependent. The heat capacity function includes the effects of the latent heat released during transformation from austenite to martensite.

Heat-transfer coefficient between die and sheet material during the hot stamping process changes as a function of distance until the die actually touches the sheet material and as a function of pressure during the deformation process.

Transformation-Induced Plasticity. During phase transformations, the material undergoes plastic deformation even if the applied stress is lower than the yield stress. It occurs by two mechanisms:

- The volume difference between the phases generates internal stresses large enough to cause plastic deformation in the weaker phase (Greenwood-Johnson mechanism).
- The formation of the new phase (martensite in this case) occurs in a preferred orientation

that influences the global shape of the material (Magee mechanism).

Constitutive Model for Hot Stamping by Akerstrom

A thermoelastic-plastic constitutive model based on the von Mises yield criterion with associated plastic flow was developed by Akerstrom from Lulea University of Technology, Sweden (Ref 7.20, 7.21). This model includes the effect of austenite decomposition and transformation-induced plasticity. This model is suitable for finite-element simulation using the explicit method.

In this model, the total strain increment during each time step of hot stamping simulation is given by (Ref 7.21):

$$\Delta \epsilon_{ij} = \Delta \epsilon_{ij}^e + \Delta \epsilon_{ij}^{th} + \Delta \epsilon_{ij}^{tr} + \Delta \epsilon_{ij}^p \quad (\text{Eq 7.3})$$

where $\Delta \epsilon_{ij}^e$ is the elastic strain increment, $\Delta \epsilon_{ij}^{th}$ is the thermal strain increment, $\Delta \epsilon_{ij}^{tr}$ is the isotropic transformation strain increment, and $\Delta \epsilon_{ij}^p$ is the plastic strain increment.

Constitutive Model for Hot Stamping by Behrens

The model developed by Behrens et al. (Ref. 7.22) can be used for implicit simulation methods, which are more efficient for heat-transfer simulations that involve longer duration and small deformations. This model uses the Johnson-Mehl-Avrami equation for diffusion-controlled austenite transformation and the Koistinen-Marburger equation for diffusionless transformation (austenite to martensite). This model was implemented in LS-Dyna version 971. The total strain increment in each step for this thermo-elastic-plastic-metallurgical material model is given by:

$$d\epsilon_{ij} = d\epsilon_{ij}^{el} + d\epsilon_{ij}^{pl} + d\epsilon_{ij}^{th} + d\epsilon_{ij}^{tr} + d\epsilon_{ij}^{tp} \quad (\text{Eq 7.4})$$

which is the sum of elastic, plastic, thermal, isotropic transformation, and the transformation-induced plasticity strain increments.

Based on the work from Akerstrom (Ref 7.15, 7.20), material model *MAT_244 was developed and implemented in LS-Dyna for hot stamping application. This model is quite computing-intensive. Using this model, final phase and hardness values at different parts of the geometry can be predicted.

7.3 Finite-Element Simulation of Hot Stamping

Simulation of B-Pillar Using LS-Dyna (Ref 7.23). AUDI proposed virtual modeling of the hot stamping process of a B-pillar reinforcement (Fig. 7.19). Simulation for the proposed problem done by Shapiro (Ref 7.23) using LS-Dyna was presented at the Seventh European LS-Dyna Conference, held in Salzburg, Austria, in 2009. The objective is to predict the sheet thickness distribution, necking failure, and local degree of hardness in the final part. The process steps involve:

1. Heating of the blank to 940 °C (1720 °F)
2. Transport from the oven into the tool (6.5 s)
3. Forming of part geometry in the tool (1.6 s)
 - a. Temperature of the blank at the beginning of the die movement: 810 °C (1490 °F)
 - b. Temperature of the tools: 75 °C (165 °F)
 - c. Travel curve for the die (die stroke versus time)

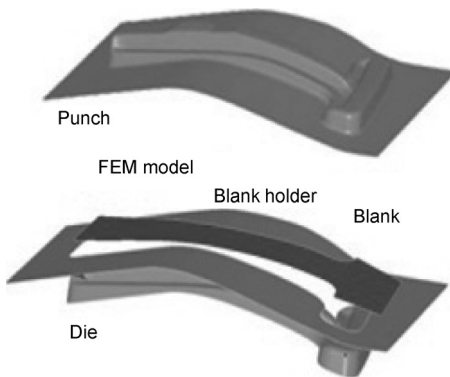
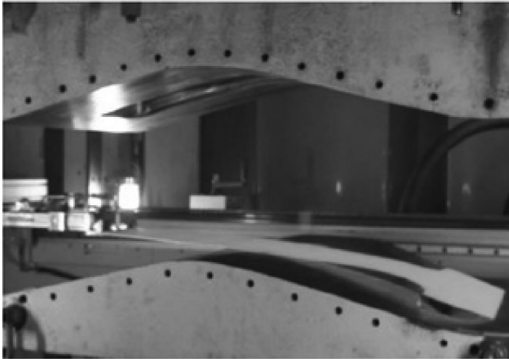


Fig. 7.19 Actual tools and finite-element model (FEM) of the proposed problem. Source: Ref 7.23

- d. Punch is fixed
4. Quenching time in the tool (20 s)
 - a. Double-sided tool contact

The blank material used is 22MnB5 plus aluminum-silicon of 1.95 mm (0.077 in.) thickness. The mechanical and thermal properties of 22MnB5 as given by AUDI are shown in Table 7.3.

The flow-stress data of 22MnB5 as a function of temperature, strain, and strain rate, from the University of Erlangen, Germany, are given as input. In addition to the flow-stress data given for different strain rates, the viscous effects can be accounted for by using the Cowper-Symonds coefficients c and p , and the flow-stress data can be scaled by $(1 + \dot{\epsilon}^p/c)^{1/p}$ for different strain rates. The thermomechanical properties for 22MnB5 as received from DYNAmore GmbH, Stuttgart, Germany, are given in Table 7.4.

In Table 7.4, E is the Young's modulus, ν is Poisson's ratio, c and p are the Cowper-Symonds coefficients for flow-stress calculation, k is the thermal conductivity for 22MnB5, and C_p is the heat capacity of 22MnB5. Material model 244 (MAT-244), which is specific for modeling phase-transformation kinetics of UHSS, is used for the quenching process. It requires latent heat of transformation of austenite into ferrite, pearlite, and bainite (590 MJ/m³) and the latent heat of transformation for austenite into martensite (640 MJ/m³).

Heating the Blank. An initial temperature condition of 25 °C (75 °F) is considered for the blank, which is heated to 940 °C (1725 °F). Finite-element modeling resulted in a thickness change from 1.95 to 1.97 mm (0.077 to 0.078 in.) due to thermal expansion.

Transport from Oven to Press. The heat-transfer coefficients can be entered as a function of temperature by a data curve in LS-Dyna. Us-

Table 7.3 Mechanical and thermal material properties of 22MnB5 (AUDI)

Young's modulus	E	100 GPa (14.5×10^6 psi)
Poisson's ratio	ν	0.3
Coefficient of thermal expansion	α	$0.13 \times 10^{-6}/K$ ($0.072 \times 10^{-6}/°F$)
Heat conductivity	K	32 W/m · K [18 Btu/(h · ft · °F)]
Heat-transfer coefficient	h_{air}	160 W/m ² · K
	h_{tool}	$p = 0$ MPa, 1300 W/m ² · K
		$p = 20$ MPa (3 ksi), 4000 W/m ² · K
		$p = 35$ MPa (5 ksi), 4500 W/m ² · K
Friction	μ	0.4

Source: Ref 7.24

Table 7.4 Mechanical and thermal material properties of 22MnB5 (DYNAMORE GmbH)

Temperature, °C (°F)	E, MPa (ksi)	ν	ρ	c	k , W/m · °C [Btu/(h · ft · °F)]	C_p , J/kg (Btu/lb)
20 (70)	212 (31)	0.284	4.28	6.2×10^9	30.7 (17.7)	444 (0.191)
100 (210)	207 (30)	0.286	4.21	8.4×10^5	31.1 (18.0)	487 (0.210)
200 (390)	199 (29)	0.289	4.10	1.5×10^4	30.0 (17.3)	520 (0.224)
300 (570)	193 (28)	0.293	3.97	1.4×10^3	27.5 (15.9)	544 (0.234)
400 (750)	166 (24)	0.298	3.83	25.8	21.7 (12.5)	561 (0.241)
500 (930)	158 (23)	0.303	3.69	78.4	...	573 (0.247)
600 (1110)	150 (22)	0.310	3.53	35.4	23.6 (13.6)	581 (0.250)
700 (1290)	142 (21)	0.317	3.37	23.3	...	586 (0.252)
800 (1470)	134 (19)	0.325	3.21	22.2	25.6 (14.8)	590 (0.254)
900 (1650)	126 (18)	0.334	3.04	30.3	...	596 (0.256)
1000 (1830)	118 (17)	0.343	2.87	55.2	27.6 (16.0)	603 (0.259)

Source: Ref 7.23

ing standard empirical relations, the convective heat-transfer coefficient, h_{conv} , and radiation heat-transfer coefficient, h_{rad} , were calculated. The effective heat-transfer coefficient, h_{eff} , is calculated by adding h_{conv} and h_{rad} ; the results are shown in Table 7.5.

Forming Process. The hot blank is at 810 °C (1490 °F) when it reaches the tool (75 °C, or 165 °F), and its lower surface begins to cool due to contact, as shown in Fig. 7.20. The metal-to-metal contact conductance ($\sim 2000 \text{ W/m}^2 \cdot \text{K}$) is much greater than the convection ($\sim 8.46 \text{ W/m}^2 \cdot \text{K}$) and radiation ($\sim 76.6 \text{ W/m}^2 \cdot \text{K}$) coefficients, and this mode of heat transfer (convection and radiation) becomes negligible. There is a through-thickness temperature gradient in the blank due to the difference in heat loss rates from the top and bottom. This thermal gradient is calculated by using a twelve-node shell element developed at Lulea University. This element has four nodes in the plane and three nodes along the thickness direction to accurately calculate the through-thickness temperature gradient.

The contact heat-transfer coefficient, $h(P)$, is the most critical parameter controlling cooling of the blank during forming and quenching, and it has high uncertainty. The values given by Merklein at 550 °C (1020 °F) are shown in Table 7.6 (Ref 7.23). Shvets presents the following equation for finding the heat-transfer coefficient as a function of pressure (Ref 7.25):

$$h(P) = \frac{k_{air}\pi}{4\lambda} \left[1 + 85 \left(\frac{P}{\sigma_r} \right)^{0.8} \right] \quad (\text{Eq 7.5})$$

where λ is the roughness parameter, σ_r is the rupture stress, and P is the contact pressure. The two end points of Merklein data are used to cal-

Table 7.5 Convection, radiation, and effective heat-transfer coefficients

Temperature		h_{conv} , W/m ² · °C	h_{rad} , W/m ² · °C	h_{eff} , W/m ² · °C
°C	°F			
50	120	5.68	5.31	11.0
100	210	6.80	6.8	13.6
200	390	7.80	10.8	18.6
300	570	8.23	16.3	24.5
400	750	8.43	23.6	32.0
500	930	8.51	33.0	41.5
600	1110	8.52	44.8	53.3
700	1290	8.50	59.3	67.8
800	1470	8.46	76.6	85.1
900	1650	8.39	97.2	106
1000	1830	8.32	121	129

Source: Ref 7.23

culate parameters λ and σ_r . Then, the equation can be used for calculating h at other pressures; the results are shown in Table 7.6.

Two analyses were conducted:

- All parts are modeled using shell elements. The tools are held at constant temperature at 75 °C (165 °F). The blank is modeled with a four-node thin-shell element that does not allow calculation of a through-thickness temperature gradient; however, it calculates the thickness variation.
- The tools are modeled with solid elements, allowing the calculation of tool temperature changes. The blank is modeled with a twelve-node thick-shell formulation, allowing through-thickness temperature gradient and thickness changes.

The results of both analyses are given in Table 7.7.

Quenching Process. The blank is held in the tools for 20 s during the quenching process. The

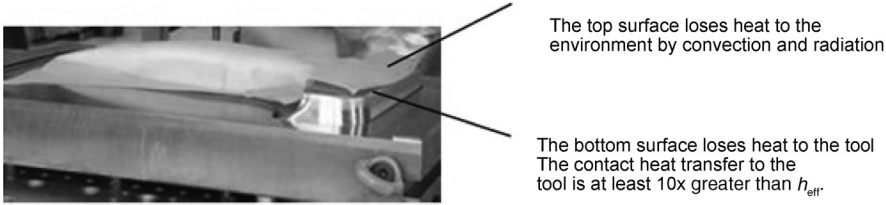


Fig. 7.20 Contact heat transfer from the blank to the tool. Source: Ref 7.23

Table 7.6 Contact heat-transfer coefficient as a function of interface pressure

Pressure		Merklein data: h at 550 °C (1020 °F), W/m ² · °C		Shvets formula: h , W/m ² · °C	Numisheet BM03: h , W/m ² · °C
MPa	ksi				
0	0	750	750	1300	...
5	0.7	1330	1330
10	1.5	1750	1770
20	3.0	2500	2520	4000	...
35	5.1	4500	...
40	5.8	3830	3830

Source: Ref 7.23

Table 7.7 Blank thickness and temperature results after forming

	Analysis 1	Analysis 2
Thickness, mm (in.)		
Minimum	1.36 (0.054)	1.43 (0.056)
Maximum	2.19 (0.086)	2.19 (0.086)
Temperature, °C (°F)		
Minimum	633 (1170)	650 (1200)
Maximum	828 (1520)	808 (1485)

Source: Ref 7.23

cooling rate affects the microstructure and hardness properties of the material. Curve 1 in Fig. 7.21 shows analysis 1, where the tool temperature is kept constant at 75 °C (165 °F), leading to a higher cooling rate. Curve 2 shows analysis 2, where the tool temperature is allowed to change, leading to a lower cooling rate. The LS-Dyna thermal material model allows specification of the latent heat (640 MJ/m³) and the phase-temperature change interval (230 to 410 °C, or 445 to 770 °F) for the austenite-to-martensite transition. Including the latent heat further slows down the cooling rate, as shown by curve 3.

Material model MAT-244 calculates material phase fractions and Vickers hardness throughout the part.

Simulation of Hat Shape Using DEFORM (conducted at the Center for Precision Forming/The Ohio State University). An example part and die geometry was chosen from Ref 7.20. The die geometry used for simulation is given in Fig. 7.22.

During the experiment conducted by Akerstrom et al. (Ref 7.26), the following parameters were measured:

- Forming force versus time
- Temperature at the edge of the steel strip, as shown in Fig. 7.23

The simulation was conducted using DEFORM-3D. The following materials data were used as input parameters:

- Sheet material: 22MnB5
- Die material: AISI-H13
- Flow-stress data for 22MnB5 (Ref 7.24)
- Emissivity of 22MnB5 = 0.6
- Thermal conductivity of 22MnB5 = 32 W/m · K [18 Btu/(h · ft · °F)] (constant)
- Specific heat capacity of 22MnB5 = 650 J/kg · K (0.16 cal/g · °C) (constant)
- Material properties for AISI-H13 are available in the DEFORM database.

The following process parameters were used:

- Velocity of punch = 10 mm/s (0.4 in./s)
- Duration of forming process = 5 s
- Initial temperature of tool = 26 °C (80 °F)
- Temperature of the environment = 30 °C (85 °F)
- Heat-transfer coefficient between sheet and die = 6500 W/m² · K (constant)
- Coefficient of friction = 0.3

The sheet material type is chosen as plastic and meshed with eight-node brick elements, and the die is meshed with a four-node tetrahedral element. Only one-quarter of the geometry

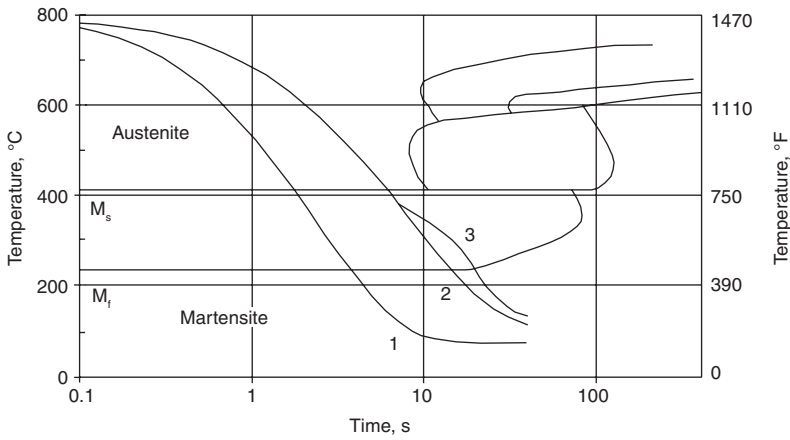


Fig. 7.21 Quenching temperature history for three modeling scenarios overlaid on a continuous cooling transformation diagram for 22MnB5 steel. Source: Ref 7.23

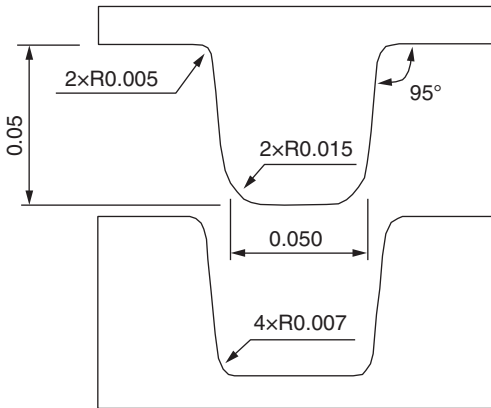


Fig. 7.22 Die geometry for hat shape. All dimensions are in meters. Source: Ref 7.20

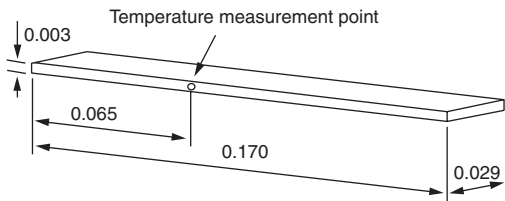


Fig. 7.23 Steel strip used for the experiment and the temperature measurement point. Dimensions are in meters. Source: Ref 7.20

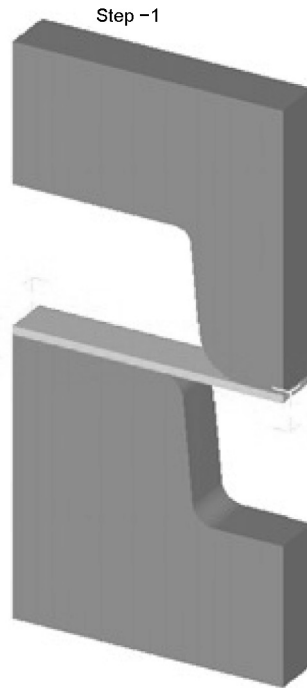


Fig. 7.24 Initial simulation setup in DEFORM. Source: Ref 7.27

is modeled due to planar symmetry. The initial simulation setup is given in Fig. 7.24. The results of the simulation are given in Fig. 7.25 and 7.26.

The temperature was measured at the edge of the steel strip at a given point, as shown in Fig. 7.23. In the simulation, an average temperature is calculated at three nodes at the specified location.

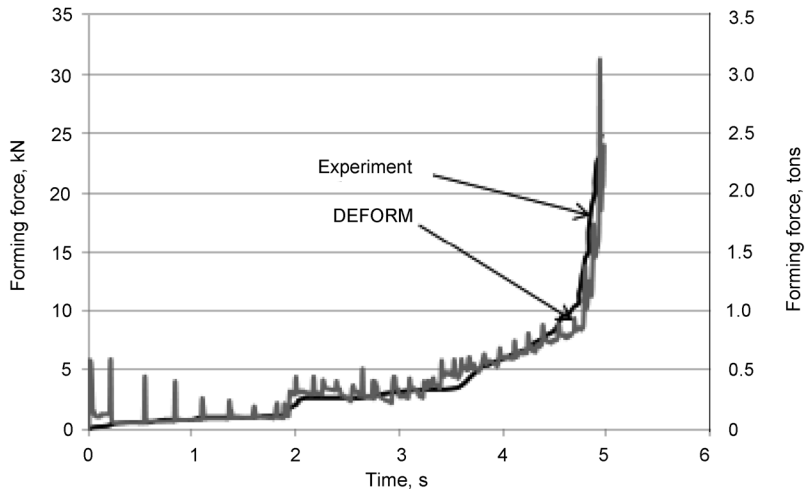


Fig. 7.25 Comparison of experimental and calculated forming force versus time. Source: Ref 7.27

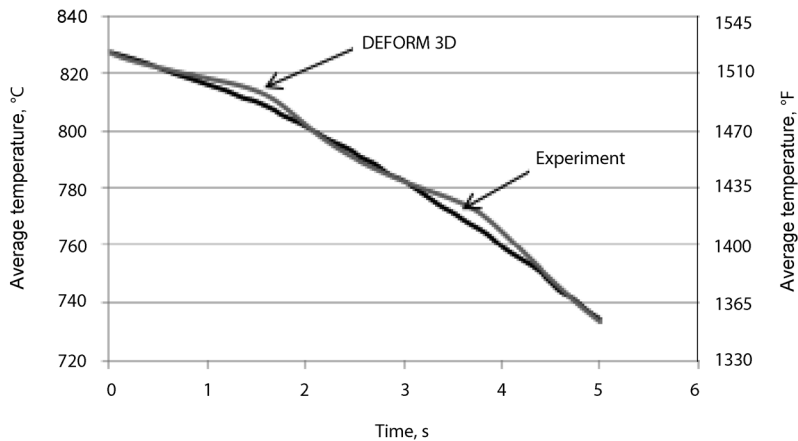


Fig. 7.26 Comparison of experimental and calculated temperature versus time. Source: Ref 7.27

7.4 Heating Methods

In the conventional hot stamping process, continuous furnaces are used whereby the blank is heated by radiation and convective flow of heat. The furnaces are heated with gas or electricity. The heating rate of the blanks is controlled by the speed of rollers or walking beams in the furnace. For 22MnB5 steel with an aluminum-silicon coating, a heating rate of 12 K/s (22 °F/s) is recommended to avoid melting of the aluminum-silicon layer and to improve the diffusion of iron into the aluminum-silicon layer. For complete austenitization, a dwell time of 145 s is

necessary at 950 °C (1740 °F), independent of the steel supplier and thickness of the aluminum-silicon coating, for a sheet thickness of 1 mm (0.04 in.). With increase in sheet thickness, the austenitization time also increases: 165 s for 1.5 mm (0.06 in.), 180 s for 1.75 mm (0.069 in.), and 240 s for 2.5 mm (0.1 in.) (Ref 7.28).

Conductive Heating. During the hot stamping process, the sheet is transferred from the furnace to the press. During this transfer, the sheet metal loses heat and also oxidizes. This may be avoided in the conductive heating method by directly heating the sheets, set into the dies by means of electrical resistance.

In the conduction heating method, the component is connected to a series of power sources. Due to the electric resistance of the component, the heat is generated proportional to the loss of power. This method can be used for partial heating of the sheet metal. In the field of sheet metal forming, conduction heating is currently used at the laboratory level in material characterization experiments (Ref 7.28).

The resistance heating method is rapid enough to synchronize with a press during the hot stamping process. Figure 7.27 shows a schematic of the resistance heating method developed by Mori et al. (Ref 7.29). The sheet material is kept in between the dies, and the electric

current is passed through the electrodes. The time interval between the end of heating to the beginning of the forming process is 0.2 s. A holding pressure of 7.4 MPa (1073 psi) was applied to maintain sufficient contact between the sheet and electrode. During the electrification process, the sheet is not in contact with the die, blank holder, and punch to avoid loss of heat.

Induction Heating. Similar to the conduction heating method, induction heating is used at the laboratory level for hot stamping applications. It contains two major components: a high-frequency generator and an induction coil (inductor). When an electricity-conducting component enters the inductor, an electric current is induced in the component, which generates heat. This eddy current depends on the operating frequency, electrical conductivity, and the permeability of the material. The frequency of the generator determines the depth of heating. Low frequencies lead to high penetration depth, and high frequencies lead to low penetration depth.

There are three types of induction coils available: longitudinal field, cross-field, and face-field inductors, as shown in the Fig. 7.28.

The type of inductor determines the position of the magnetic field in reference to the workpiece, resulting in different efficiency. Heating steel sheets up to their Curie temperature in a longitudinal field inductor is characterized by an efficiency of 93%. The Curie temperature for different steel grades ranges between 720 and 745 °C (1330 and 1375 °F). This method gives a homogeneous temperature distribution. For further rise in temperature, a face inductor is necessary, changing the orientation of the magnetic field. In a face inductor, the efficiency factor is 60%, and the temperature distribution is not as homogeneous as a longitudinal field inductor. Heating sheet metal from room temperature to 950 °C (1740 °F) with only a face inductor leads

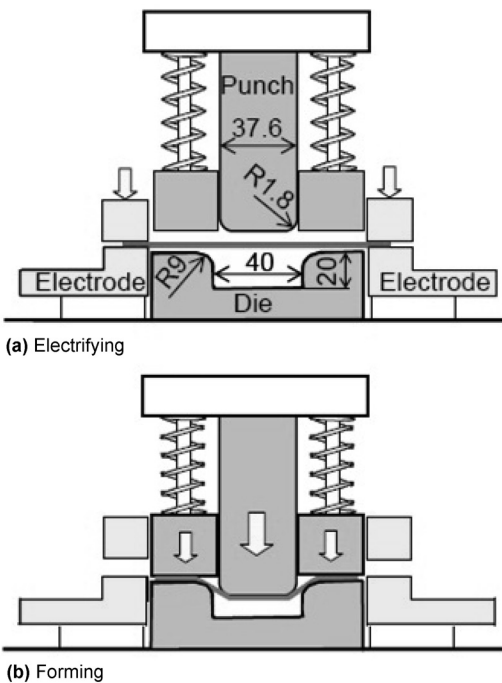


Fig. 7.27 Hot stamping process using resistance heating. Source: Ref 7.29

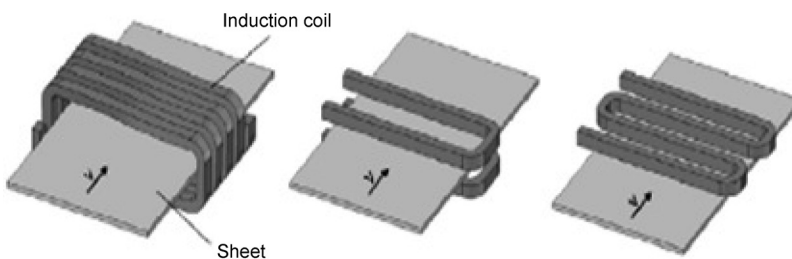


Fig. 7.28 Principle of design of longitudinal field, transverse field, and face inductors. Source: Ref 7.28

to a temperature deviation of 50 °C (90 °F) along the specimen. Thus, it is recommended to use face induction as a second heating step from Curie temperature to austenitization temperature, as shown in Fig. 7.29. This leads to maximum temperature deviations of ± 10 °C (± 18 °F).

Kolleck et al. (Ref 7.28) used a two-step induction heating device (Fig. 7.29) to heat a 22MnB5 steel specimen. The system contains a longitudinal field inductor with a maximum connected power of 120 kW and a face inductor with a maximum connected power of 150 kW. The transport of the blank is done with a chain drive fixed to the blank.

In the longitudinal field inductor, feed speed affects the heating rate. In the face inductor, the distance between sheet surface and induction coil is the governing parameter for achieving the required temperature.

7.5 Tools (Dies) for Hot Stamping

The complete tooling solution contains the tool steel, die design and construction, die coating, process parameters, and die maintenance (Ref 7.30).

Die Design. Two main functions of the hot stamping die are forming the part and extracting the heat from the blank. The tool must be able to achieve a minimum cooling rate of 27 K/s (50 °F/s) to guarantee a complete martensitic transformation. Furthermore, the heat-extraction capability of the die determines the productivity of the hot stamping line (Ref 7.30). The die must absorb and evacuate an amount of energy up to 100 kW by means of integrated cooling devices (Ref 7.31). This results in high-temperature gradients (up to 25 K/mm, or 1145

°F/in.) and induces high stresses in the surface layers. The total mechanical loading is a combination of the stresses caused by temperature gradients and the direct mechanical loadings (forming and closing pressure). Researchers (Ref 7.30, 7.31) note that hot stamping dies are usually designed to work without a blank holder in order to minimize heat loss in the flange area during the forming operation.

Because the heat-transfer coefficient depends on contact pressure, excellent contact over the whole part is essential to avoid hot spots during quenching. This requires precise tool design and good surface condition. Three principles to improve heat transfer in the tooling include using a die material with higher heat conductivity, avoiding thermal barriers, and optimizing the cooling strategy (Ref 7.30).

To maintain the dimensional tolerances and the efficiency in heat transfer desirable during hot stamping, the wear resistance of the tool material is an important issue (Ref 7.30). Paar et al. (Ref 7.30) specify the most typical failure mechanisms of hot stamping tools to be cracking, wear, and sticking of the sheet coating on the die surface. Paar et al. (Ref 7.30) further explain that the cracks usually occur at the cooling channel and then grow to the die surface.

Die Steels. Wilsius et al. (Ref 7.31) remark that in selecting die materials, it is necessary to make a compromise between good wear resistance over a wide temperature range and a good thermal conductivity. Increasing the alloying elements in die steel improves the hardness but negatively affects the heat conductivity. Paar et al. (Ref 7.30) state that most hot stamping dies are made of hot working steel (hardness > 44 HRC). Because the mechanical loads on the tool are not excessively high, a tool material

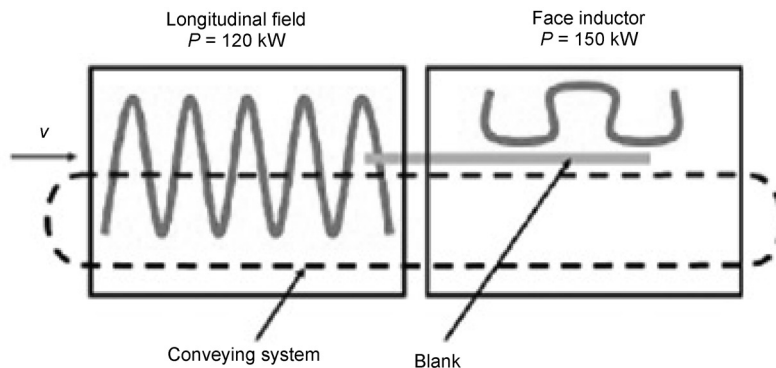


Fig. 7.29 Fundamental principle of a two-step induction heating device. Source: Ref 7.28

with strength above 1500 MPa (220 ksi) prevents plastic tool deformation.

Optimizing Locations of Cooling Channels in Hot Stamping Dies. In the hot stamping process, tool motion (time required to deform the part) requires a relatively short time compared to the quenching process. Optimization of the cooling system in hot stamping tools will greatly reduce the cycle time, because cooling the part after the dies are closed is critical to achieve the desired cooling rate (Ref 7.32).

The following factors are identified to affect heat transfer between the drawn part and die (Ref 7.33):

- Heat transfer from the drawn part to the tool depends on surface scaling effects and the gap between the part and the tool surface.
- Heat conductivity of the tool material depends on the choice of tool material.
- Design of the cooling ducts is defined by the size, location, and distribution of the cooling ducts.
- The type of coolant and the temperature difference between the coolant and tool affects the heat transfer.

A method for optimizing the design of cooling channels was developed by Steinbeiss et al. (Ref 7.33) at the Institute of Metal Forming and Casting, Technische Universität München, Garching, Germany. The tests conducted and the results obtained by Steinbeiss et al. are summarized in the following sections.

The die arrangement and test geometry of the blank and the drawn part for the optimization experiment are shown in Fig. 7.30. To provide an effective cooling system, the four tool components—punch, counterpunch, female die, and blank holder—are actively cooled with cooling ducts.

Method for Optimizing the Cooling System Design. Any tool surface can be divided into loaded and unloaded contours based on the subjected thermal and mechanical loading conditions.

The constraints for the tool design are (Ref 7.32) (Fig. 7.31):

- Minimum distance between loaded die surface (contour) and cooling duct (x)
- Minimum distance between unloaded die surface (contour) and cooling duct (a)
- Minimum distance between the cooling ducts (s)
- Size of available sealing plugs, which are used to divert the flow of coolants in the cooling duct
- Position of the cooling duct

As a first step in the tool design, the aforementioned parameters are calculated based on expertise or the results of preliminary finite-element calculations. The optimization is carried out using an evolutionary algorithm (EA) considering the criteria of cooling intensity of the tool (cooling rate to be achieved) and uniform cooling. The EA was used to place the

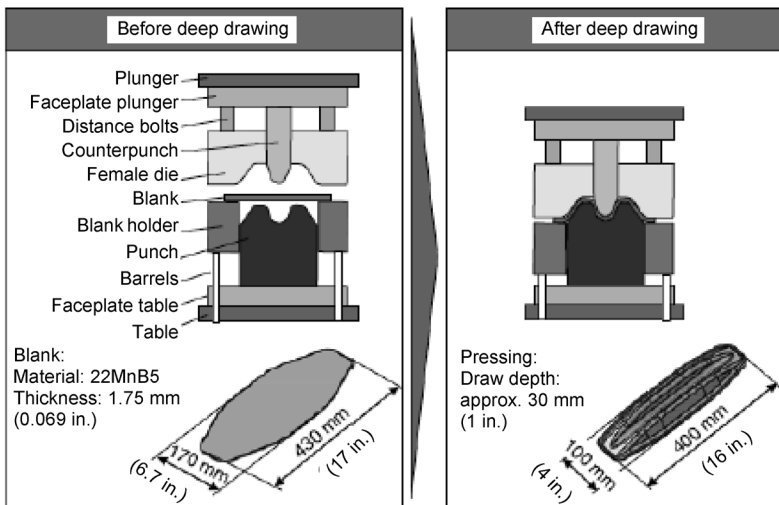


Fig. 7.30 Test geometry and drawn part. Source: Ref 7.33

cooling channels optimally according to the given input and constraints. Figure 7.32 gives the flow chart for the EA.

Figure 7.33 gives an example of the optimized design of a cooling system for a chosen drill hole diameter.

Hot Stamping Dies with Cast Cooling Channels. The method of casting cooling channels in hot stamping dies was carried out by Kolleck et al. (Ref 7.34) at the Institute of Tools and Forming, Graz University of Technology, Austria. This method improves the cooling performance of the tool and reduces the overall process cycle time.

Hot stamping tools with cooling ducts must meet the following requirements:

- Accuracy in achieving the desired cooling rate
- Uniform temperature distribution on the surface of the tool (maximum deviation ± 5 °C, or ± 9 °F)

The conventional method of constructing cooling channels by drilling and milling has the following disadvantages:

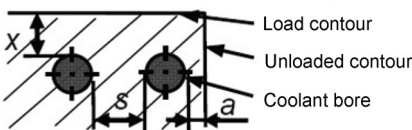


Fig. 7.31 Schematic of the tool surface. Source: Ref 7.32

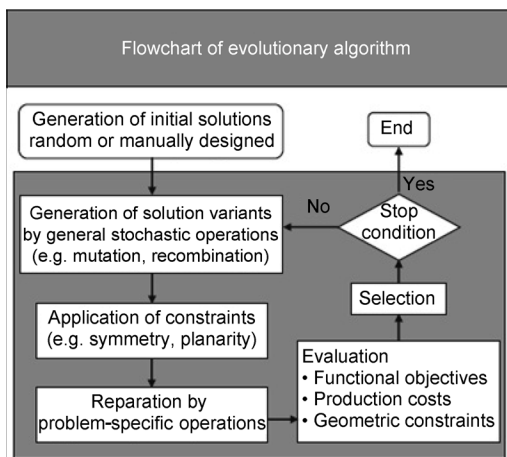


Fig. 7.32 Flow chart of the evolutionary algorithm. Source: Ref 7.33

- Complex cooling duct geometries cannot be made due to limited access.
- A higher amount of material removal leads to a high cost factor.

These disadvantages are overcome by casting cooling channels in the die block. The cooling channels can be accurately cast nearer to the tool surface to achieve the required cooling rate and temperature distribution.

Steps involved in building the tools (Fig. 7.34) include the following:

1. Optimal or near-perfect cooling ducts are fabricated.
2. The fabricated cooling ducts are cast into gray cast iron or ductile graphite iron. (High-strength copper alloys can also be used as base material.)
3. Using direct metal deposition technology, the tool surface is deposited with hard materials.

During the casting process, proper care must be taken in the following areas:

- During the process of bonding between the molten metal and the tubes of the cooling duct, air gaps may be formed, affecting heat transfer.
- The tubes of the cooling duct may distort during casting, affecting the flow of coolants.

The flow analysis of the coolants in the cooling ducts was done using AVL Swift (computational fluid dynamics software).

Tailor-Made Die Materials for Hot Stamping (Ref 7.35). A correct compromise between tooling variables such as initial tooling cost, durability, attainment of desired properties on the component, and allowed productivity is key to increasing the competitiveness of the hot stamping dies.

Introduction of extreme high-thermal-conductivity tool steels enabled the reduction of cycle time by reducing the holding time. Die materials such as HTCS-117 (nickel, chromium, and molybdenum die steel) reduced closed-die cycle times from 10 to 15 to 4 to 6 s. Now with the introduction of HTCS-130 (high-thermal-conductivity tool steel originally developed for aluminum die casting), HTCS-150, and HTCS-170, the cycle time is further reduced to 2 to 3 s. These tool materials, along with a reduction in sheet transfer time from oven to die and an in-

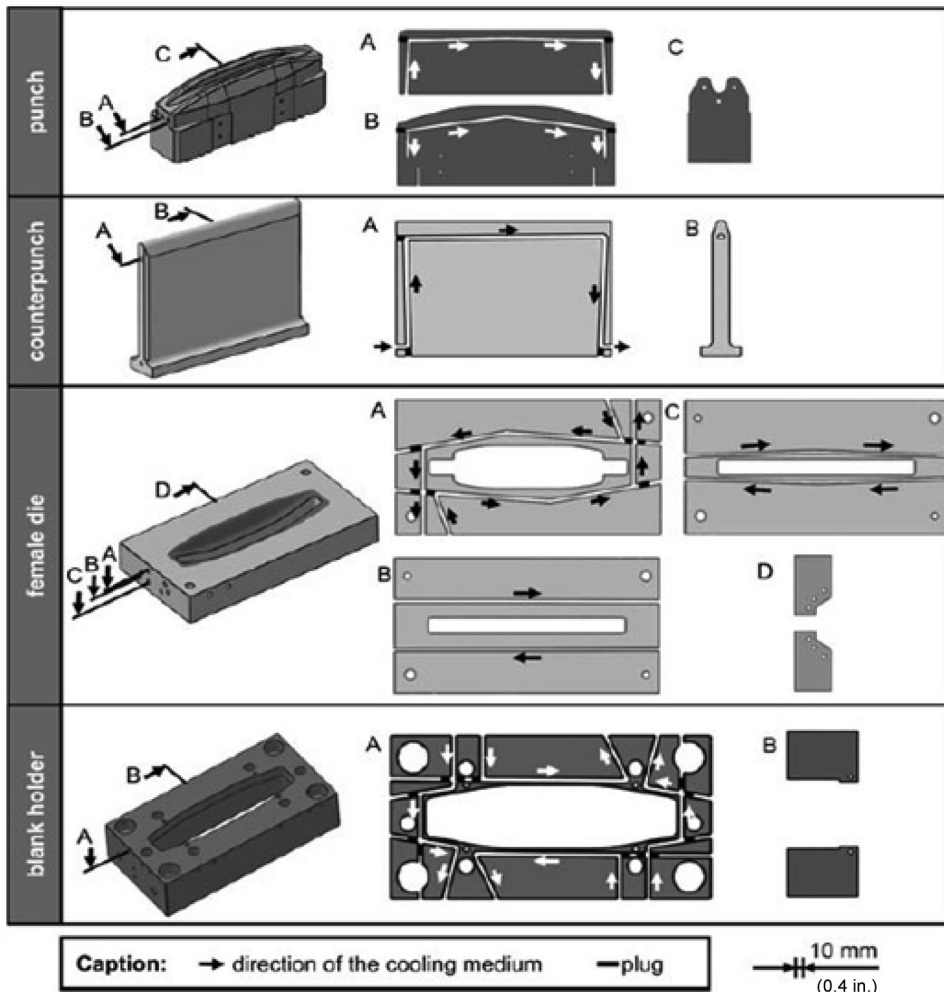


Fig. 7.33 Optimized design of the cooling ducts for the tool components punch, female die, counterpunch, and counterblank holder. Source: Ref 7.33

crease in press speed, are important parameters to optimize the hot stamping process.

Researchers are working on developing locally differentiated heat treatments in the hot-stamped components to improve crash performance or to facilitate posterior cutting operations. One of the preferred ways of achieving this is by having tools with varying thermal conductivities. The recently developed nanocasting technology can develop tools with complex cooling strategies at a reasonable price and any desired gradual or abrupt thermal conductivity variation in the range of 7 to 66 W/m · K [4 to 38 Btu/(h · ft · °F)].

A study was conducted by Casas et al. (Ref 7.35) on developing dies with gradually varying thermal conductivities, from 60 W/m · K to 5 to

10 W/m · K [35 Btu/(h · ft · °F) to 3 to 6 Btu/(h · ft · °F)], using nanocasting technology at Rovalma, Spain. Some welding materials used for repairing hot stamping dies and implementing dimensional changes were also studied by Casas et al. (Ref 7.35), with various base materials with different postheat treatments. Two high-thermal-conductivity welding alloys have been developed; one is available as tungsten inert gas wire (HTCS-Rod), and the other is available as a refurbished electrode (HTCS-RE). Postweld heat treatment severely increases heat conductivity and resilience and is always recommended.

Hard Trimming of Quenched Parts and Characterization Tests. The shearing and blanking of press-hardened components is extremely demanding. The HWS steels (cold work tool

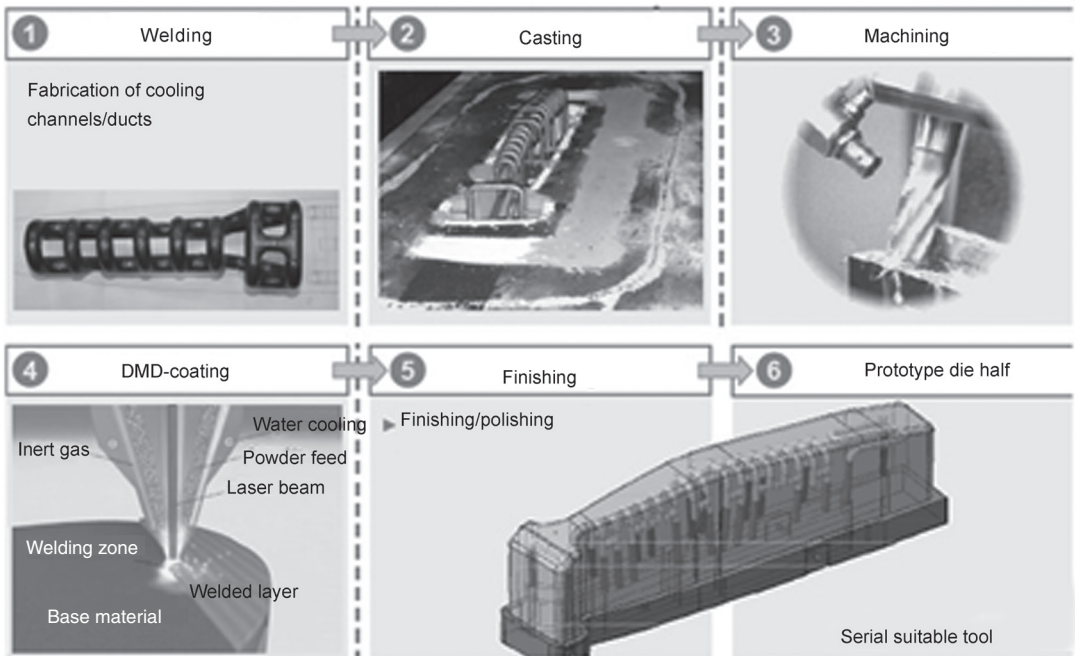


Fig. 7.34 Steps involved in casting cooling ducts. DMD, direct metal deposition. Source: Ref 7.34

steels) are used for these applications, provided they are robustly built and cutting angles and clearances are very well adjusted. Trimming tool performance is affected by the following factors:

- Slight blank movement in the moment of shearing/trimming
- Local clearance maladjustment
- Die cleanliness effect, leading to material buildup near the cutting edge
- Increase of blank thickness (poor scrap extraction or two blanks remaining under the press)

A small variation in the aforementioned factors increases the stress intensity at the cutting edge, leading to premature failure in the form of chipping. Using HWS, sheets with hardness in excess of 1800 MPa (260 ksi) and press-hardened components of more than 2 mm (0.08 in.) thickness have been successfully sheared under close tolerances (Ref 7.35).

7.6 Coatings for Oxidation Prevention

Coating the blanks before heating is important for reducing oxidation and maintaining a good surface finish. The 22MnB5 steel is gener-

ally supplied with an aluminum-silicon coating. ThyssenKrupp Steel supplied 22MnB5 steel for the production of the Volkswagen Passat with nanotechnology-based coating (MBW-K 1500 plus X-Tec), which gives short-term corrosion protection and acts as a lubricant during hot stamping (Ref 7.36). Mori et al. (Ref 7.37) tested different lubricant oils supplied by Nihon Kohsakuyu Co., Ltd., Japan, for their oxidation-prevention properties during the hot stamping process. These oils are generally used as lubricants for warm stamping of stainless steels and titanium sheets.

Effect of Coating. Researchers (Ref 7.31, 7.38) explained that the heating of uncoated blanks must be carried out under protective atmosphere to avoid oxidation (scaling) and surface decarburization. They indicate that there is direct contact with atmospheric oxygen during the transfer of the blank from furnace to press; oxidation occurs and forms an irregular and abrasive scale layer (iron oxides) on the blank surface. In this case, it is almost impossible to avoid some superficial decarburization (up to 60 μm), which is harmful for final properties of the parts. Because the scale is characterized by extreme hardness, the hot stamping process may result in high die wear. Moreover, these parts should be shotblasted or sandblasted to remove

the scale layer. Shotblasting is costly and can be harmful to the geometrical tolerances of thin parts. This scaling during the hot stamping process can be largely avoided by means of surface coating.

Aluminum-Silicon-Base Coating. USIBOR 1500P supplied by Arcelor possesses an aluminum-base precoat layer with a thickness between 23 and 32 μm . Researchers (Ref 7.31, 7.38) indicate that the aluminum-silicon coating is transformed into an Fe-Al-Si layer during heating in the furnace. Wilsius et al. (Ref 7.31) emphasized that the heating rate must not exceed 12 K/s (22 $^{\circ}\text{F/s}$), because too-rapid heating causes melting of the aluminum-silicon coating before transformation into the heat-resistant Fe-Al-Si layer can take place. Furthermore, Wilsius et al. (Ref 7.31) recommend a proper dwell time in the furnace to guarantee complete alloying of the coating.

Iron-Zinc-Base Coating. Boron steel is hot dip galvanized. Due to diffusion processes during the austenitization phase, the zinc layer transforms into a zinc-iron layer (Ref 7.39). Voestalpine developed a zinc-base coating that offers scaling protection as well as cathodic corrosion protection (Ref 7.40). Hence, the corrosion protection is maintained even if the zinc surface is damaged or interrupted for constructive reasons (Ref 7.39). Furthermore, the lower layer hardness compared to aluminum-iron coatings results in lower die wear. Until now, galvanized 22MnB5 was applicable for indirect hot stamping only (Ref 7.41).

X-Tec—Nanotechnology-Based Coating. ThyssenKrupp developed the X-Tec coating. References 7.41 and 7.42 describe the nanotechnology-based painting, which is applied on the steel coil. According to Ref 7.42, this coating protects the blank against corrosion and improves the lubrication between sheets and dies.

7.7 Other Areas of Importance (Ref 7.43)

To improve the crash performance and weight reduction in hot-stamped components, tailor-welded blanks are used. These have different steel grades with different thicknesses on the same blank. This allows adjusting the strength and elongation properties along the part, leading to different deformation modes under crash situations. Variation in properties is also obtained by partial heating of the blank in the fur-

nace and partial quenching of the part in hot stamping dies.

REFERENCES

- 7.1 B. Macek, “Developing a Deep Drawn Hot Stamped Fuel Tank Guard,” Great Designs in Steel Seminar, 2007
- 7.2 M. Merklein and M. Lechler, Investigation of the Thermo-Mechanical Properties of Hot Stamping Steels, *J. Mater. Process. Technol.*, Vol 177, 2006, p 452–455
- 7.3 H. Karbasian and A.E. Tekkaya, A Review on Hot Stamping, *J. Mater. Process. Technol.*, Vol 210 (No. 15), 2010, p 2103–2118
- 7.4 G. Berglund, The History of Hardening of Boron Steel in Northern Sweden, *First International Conference on Hot Sheet Metal Forming of High Performance Steel* (Kassel, Germany), 2008, p 175–177
- 7.5 J. Aspacher, Forming Hardening Concepts, *First International Conference on Hot Sheet Metal Forming of High Performance Steel* (Kassel, Germany), 2008, p 77–81
- 7.6 H. Engels, O. Schalmin, and C. Müller-Bollenhagen, Controlling and Monitoring of the Hot-Stamping Process of Boron-Alloyed Heat-Treated Steels, *The International Conference on New Development in Sheet Metal Forming Technology* (Stuttgart, Germany), 2006, p 135–150
- 7.7 D. Berglund, K. Amundsson, and L.O. Hellgren, Hot Stamped Components with “Soft Zones” for Improved Crashworthiness Simulation and Validation of Product Performance, *International Deep Drawing Research Group Proceedings* (Olofström, Sweden), June 2008
- 7.8 M. Eriksson, M. Oldenburg, M.C. Somani, and L.P. Karjalainen, Testing and Evaluation of Material Data for Analysis of Forming and Hardening of Boron Steel Components, *Model. Simul. Mater. Sci. Eng.*, 2002, p 277–294
- 7.9 M. Merklein, M. Lechler, and M. Geiger, Characterization of the Flow Properties of the Quenchable Ultra High Strength Steel 22MnB5, *CIRP Ann.*, Vol 55 (No.1), 2006

- 7.10 A. Yanagida and A. Azushima, "Evaluation of Coefficients of Friction for Hot Stamping by Newly Developed Tribosimulator," IDDRG 2009 International Conference (Golden, CO), International Deep Drawing Research Group, 2009
- 7.11 M. Geiger, M. Merklein, and J. Lechler, "Determination of Tribological Conditions within Hot Stamping," German Academic Society for Production Engineering, 2008
- 7.12 E. Siebel, Beisswanger H, Tiefziehen, Munchen-Hanser, 1955
- 7.13 M. Merklein, J. Lechler, and T. Stoehr, Characterization of Tribological and Thermal Properties of Metallic Coatings for Hot Stamping Boron Manganese Steels, *Proceedings of the Seventh International Conference on Coatings in Manufacturing Engineering*, Oct 1–3, 2008, p 219–228
- 7.14 J. Lechler, *Pressharten von Bor-Manganstahlen*, Fertigungstechnik-Erlangen, 2009, p 200
- 7.15 P. Akerstrom and M. Oldenburg, Austenite Decomposition during Press Hardening of Boron Steel, *J. Mater. Process. Technol.*, Vol 174, 2006, p 399–406
- 7.16 P. Hein, A Global Approach of the Finite Element Simulation of Hot Stamping, *Adv. Mater. Res.*, Vol 6–8, 2005, p 763–770
- 7.17 M. Oldenburg, P. akerstrom, G. Bergman, and P. Salomonsson, Modeling of Microstructure and Material Response in the Press Hardening Process, *International Deep Drawing Research Group Proceedings*, June 2008 (Olofstrom, Sweden)
- 7.18 G. Bergman, "Modeling and Simulation of Simultaneous Forming and Quenching," Division of Computer Aided Design, Department of Mechanical Engineering, Lulea University of Technology, Sweden, 1999
- 7.19 D.P. Koistinen and R.E. Marburger, A General Equation Prescribing the Extent of the Austenite-Martensite Transformations in Pure Iron-Carbon Alloys and Plain Carbon Steels, *Acta Metall.*, Vol 7, 1959, p 59–60
- 7.20 P. Akerstrom, "Modeling and Simulation of Hot Stamping," Doctoral thesis, Department of Applied Physics and Mechanical Engineering, Lulea University of Technology, Sweden, 2006
- 7.21 P. Akerstrom, G. Bergman, and M. Oldenburg, Numerical Implementation of a Constitutive Model for Simulation of Hot Stamping, *Model. Simul. Mater. Sci. Eng.*, Vol 15, 2007, p 105–119
- 7.22 B. Behrens, P. Olle, and C. Schaffner, "Process Simulation of Hot Stamping in Consideration of Transformation Induced Stresses," Numisheet 2008 (Interlaken, Switzerland), 2008
- 7.23 A.B. Shapiro, "Using LS-Dyna for Hot Stamping," Seventh European LS-Dyna Conference, 2009
- 7.24 "The Numisheet Benchmark Study, Benchmark Problem BM03," Numisheet 2008, Sept 2008 (Interlaken, Switzerland)
- 7.25 I.T. Shvets, Contact Heat Transfer between Plane Metal Surfaces, *Int. Chem. Eng.*, Vol 4 (No. 4), 1964, p 621
- 7.26 P. Akerstrom, B. Wikman, and M. Oldenburg, Material Parameter Estimation for Boron Steel from Simultaneous Cooling and Compression Experiments, *Model. Simul. Mater. Sci. Eng.*, Vol 13, 2005, p 1291–1308
- 7.27 N. Ambikapathy and T. Altan, "Hot Stamping Technology—Fundamentals and Applications," Report CPF-5.5/10/01, Center for Precision Forming, The Ohio State University
- 7.28 R. Kolleck, R. Veit, M. Merklein, J. Lechler, and M. Geiger, Investigation on Induction Heating for Hot Stamping of Boron Alloyed Steels, *CIRP Ann.*, 2009, p 275–278
- 7.29 K. Mori, S. Maki, and Y. Tanaka, Warm and Hot Stamping of Ultra High Tensile Strength Steel Sheets Using Resistance Heating, *CIRP Ann.*, Vol 54 (No. 1), 2005
- 7.30 U. Paar and I.Valls, "Werkzeugstahle und Strategie fur Warmumformung und Hartbeschneiden," Erlangener Workshop Warmblechumformung 2007, Bamberg, Meisenbach, 2007
- 7.31 J. Wilsius, P. Hein, and R. Kefferstein, "Status and Future Trends of Hot Stamping of USIBOR 1500 P," Erlangener Workshop Warmblechumformung 2006, Bamberg, Meisenbach, 2006
- 7.32 H. Hoffmann, H. So, and H. Steinbeiss, Design of Hot Stamping Tools with Cooling System, *CIRP Ann.*, Vol 56 (No. 1), 2007

- 7.33 H. Steinbeiss, H. So, T. Michelitsch, and H. Hoffmann, Method for Optimizing the Cooling Design of Hot Stamping Tools, *Prod. Eng. Res. Dev.*, Vol 1 (No. 2), 2007, p 149–155
- 7.34 R. Kolleck, S. Pfanner, E.-P. Warnke, and R. Ganter, “New Concept for Tempering Sheet Metal Forming Tools,” Report 28, Chemnitz Car Body Colloquium, IWV, 2005
- 7.35 B. Casas, D. Latre, N. Rodriguez, and I. Valls, Tailor Made Tool Materials for the Present and Upcoming Tooling Solutions in Hot Sheet Metal Forming, *Steel Grips*, Vol 6, Suppl. CHS2, 2008
- 7.36 F.J. Lenze, J. Banik, and S. Sikora, Applications of Hot Formed Parts for Body in White, *International Deep Drawing Research Group Proceedings*, June 2008 (Olofström, Sweden)
- 7.37 K. Mori and D. Ito, Prevention of Oxidation in Hot Stamping of Quenchable Steel Sheet by Oxidation Preventive Oil, *CIRP Ann.*, 2009, p 267–270
- 7.38 T. Altan and A. Yadav, Hot Stamping Boron-Alloyed Steels for Automotive Parts—Part II, *Stamp. J.*, Jan 2007
- 7.39 T. Laumann and M. Pfestorf, “Potential verzinkter Warmumformteile für den Einsatz in der Rohkarosserie,” Erlangerer Workshop Warmblechumformung 2007, Bamberg, Meisenbach, 2007
- 7.40 J. Faderl and K.M. Radlmayr, “Ultraform und Ultraform PHS—Innovation Made by Voestaplina,” Erlangerer Workshop Warmblechumformung 2007, Bamberg, Meisenbach, 2006
- 7.41 R. Stopp, L. Schaller, K. Lamprecht, E. Keupp, and G. Deinzer, “Warmblechumformen in der Automobil-Serienfertigung—Status, Trends, Potenziale,” Erlangerer Workshop Warmblechumformung 2007, Bamberg, Meisenbach, 2007
- 7.42 F.-J. Lenze, J. Bian, and S. Sikora, “Einsatz pressgehärteter Stähle im Karosseriebau: Stand und Trends der Entwicklung,” Erlangerer Workshop Warmblechumformung 2007, Bamberg, Meisenbach, 2007
- 7.43 E. Schaeper and J. Wilsius, Prediction of the Formability of Hot Stamped Parts, *International Conference on New Developments in Sheet Metal Forming*, May 2010 (Stuttgart, Germany), p 305–319

CHAPTER 8

Sheet Hydroforming

A. Yadav, Caterpillar Technical Center
M. Trompeter, Technical University of Dortmund

SHEET METAL FORMING using pressurized liquid media is called sheet hydroforming (Fig. 8.1) and is classified as sheet hydroforming with punch (SHF-P) and sheet hydroforming with die (SHF-D), depending on the male (punch) or the female (die) tool that has the shape/impression to be formed. SHF-P is synonymous with hydromechanical deep drawing. Similarly, SHF-D is synonymous with high-pressure sheet hydroforming. SHF-D is further classified into hydroforming of a single or double blank, depending on the number of blanks being used in the forming process.

8.1 The Room-Temperature Sheet Hydroforming System

Successful application of the SHF-P or SHF-D process requires careful consideration of all the components of the sheet hydroforming system (Fig. 8.2), namely:

- Properties and dimensions of the incoming sheet
- Die-workpiece interface issues (friction and lubrication)
- Tool material and geometry

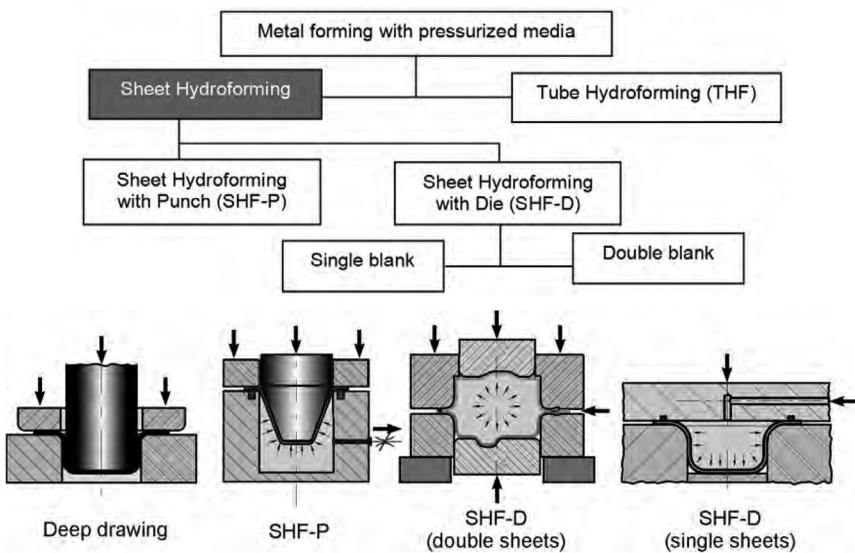


Fig. 8.1 Classification of forming processes using liquid media. Source: Ref 8.1

- Relationship between the internal fluid pressure (or pot pressure) and the blank holder force (BHF)
- Press design and characteristics, including pressure and load capacity and ram speed
- Dimensions and properties of the hydroformed part

8.2 Process Description, Advantages, and Disadvantages

Sheet Hydroforming with Punch. In SHF-P, the female die used in conventional stamping is replaced by a pressure pot. The sheet is deep drawn to form over the punch surface, against a counterpressure in the pressure pot generated by a pressurizing fluid (Fig. 8.3). The liquid in the pressure pot can be actively pressurized and controlled by an external pump or passively pressurized and controlled during the forward stroke of the punch by controlling the pressure with a relief valve, allowing some fluid to escape as the punch and the sheet are pushed into the pot.

Sheet Hydroforming with Die. In SHF-D, the sheet is formed against the female die by the hydraulic pressure of the fluid, as shown in Fig. 8.4(a). During the forming process, the blank holder controls the material movement from the flange into the cavity and also seals the fluid medium to avoid leakage.

The forming operation in SHF-D can be divided into two phases (Fig. 8.4b). Phase I involves free forming, where the sheet bulges freely in the die cavity until it contacts the die. Phase II involves forcing the sheet against the

die cavity to obtain the desired shape. The forming parameters (BHF and pot pressure) can be varied to obtain the desired strain path in the sheet for optimal use of formability of the material, which is part geometry dependent. Viscous pressure forming (Fig. 8.5) is similar to SHF-D in which pressure acting on the sheet is generated by compressing a viscous medium rather than hydraulic fluid/water.

8.3 Advantages and Disadvantages

Advantages include the following:

- Better formability
 In SHF-P, the fluid pressure acting on the sheet metal results in a high friction force at the sheet-punch interface that prevents stretching of the sheet material after it comes in contact with the punch. Therefore, compared to stamping, the sheet metal in the cup wall is not stretched as much in the SHF-P process, resulting in a more uniform wall thickness and higher limiting draw ratio.

Free bulging of the sheet in SHF-D introduces a uniform strain distribution throughout the sheet. In contrast, in conventional stamping the deforming sheet experiences high local deformation at the punch corner radius. Therefore, the formability of the material is used effectively in SHF-D. SHF-D is a viable alternative in fabrication of automotive parts from low-formability advanced high-strength steel grades and aluminum alloys in producing small quantities where die cost per part is large.

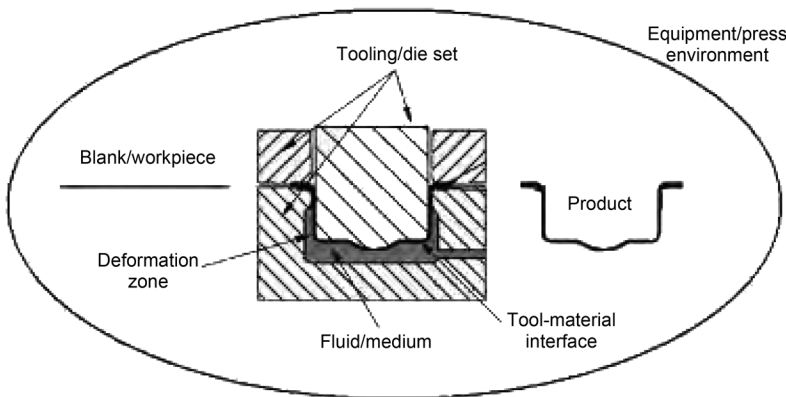


Fig. 8.2 Components of the sheet hydroforming system. Source: Ref 8.2

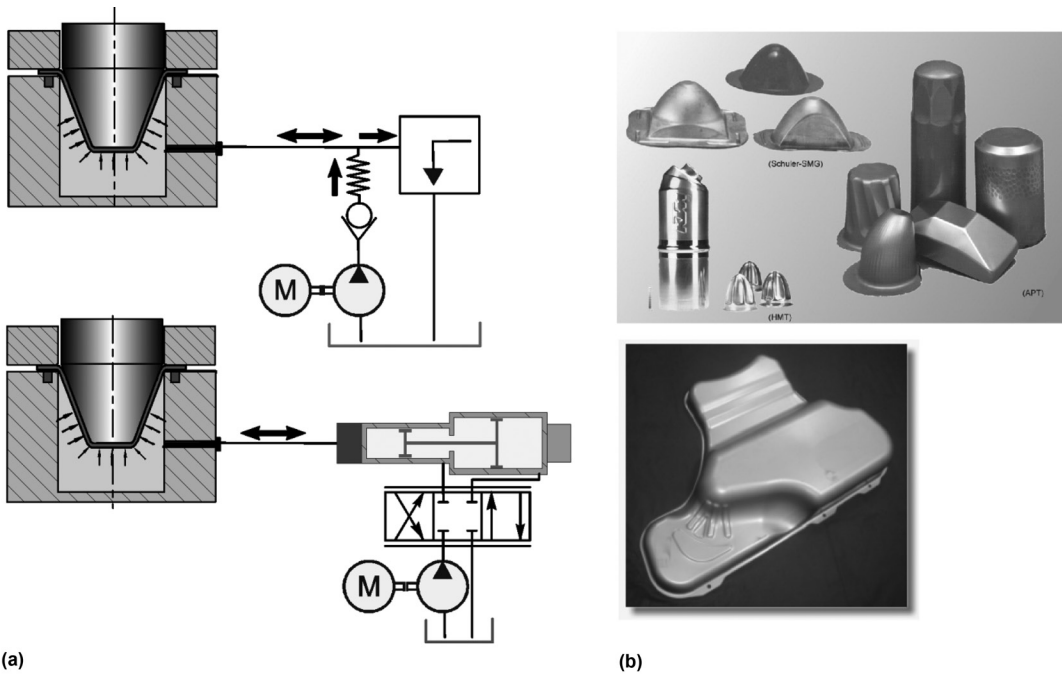


Fig. 8.3 Sheet hydroforming with punch process. (a) Schematic. (b) Example parts (to be modified). Source: Ref 8.3

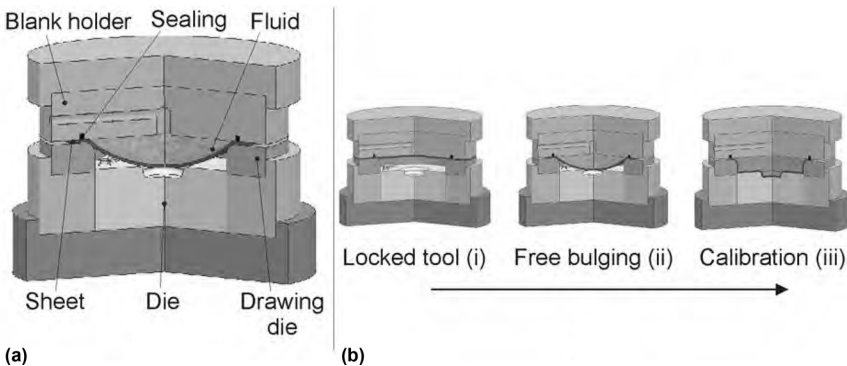
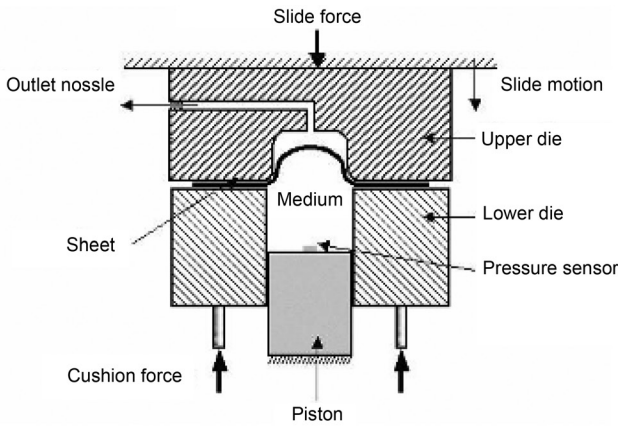


Fig. 8.4 Sheet hydroforming with die process. (a) Schematic. (b) Forming operation. Source: Ref 8.4

- Improved dent resistance
 - Strain hardening of the material during stretching in SHF-D improves the dent resistance of the hydroformed part as compared to the stamped part, because parts under the punch face are hardly stretched/strained during conventional stamping.
- Lower tooling cost
 - Elimination of one of the tools (punch or die) results in lower tool cost and reduced development time.
- Better surface quality
 - Elimination of sidewall wrinkles during sheet hydroforming, due to applied pot pressure, results in better surface quality and thus allows for more freedom in designing auto body panels.
- Fewer forming operations
 - The ability to form complicated shapes and features results in fewer forming operations compared to conventional stamping, which reduces die and manufacturing costs.



(a)



(b)

Fig. 8.5 Viscous pressure forming process. (a) Process schematic. (b) Formed part. Source: Ref 8.5

SHF-P processes can also be combined with regular stamping operations to reduce forming stages.

- Economical for small-lot production

The SHF-P process is economical for small-lot production, which is the current trend in manufacturing for products of short life cycle (Ref 8.6).

- Higher dimensional accuracy

Better surface quality can be achieved because the outer surface of the sheet is in contact with fluid, thereby reducing the chance of tool marks (Ref 8.7). A higher dimensional accuracy also can be achieved for simple symmetric parts.

Limitations include the following:

- High cycle time
- High ram forces needed/high press cost

SHF-P requires presses of higher capacity compared to stamping because of the pot pressure that acts against the punch. Thus, SHF-P presses are relatively expensive and require higher capital investment. Depending on the part geometry, production volume, and part mix, the higher press cost may not be offset by the lower tool cost (Ref 8.8).

In SHF-D, high pot pressure is required to form the sharp corners in the part. This pot pressure depends on the sheet material, thickness, and the smallest corner radius in the die geometry.

8.4 Sheet Hydroforming—Process Variations

Flexform Fluid Cell/Rubber Pad Forming.

This flexible-die sheet metal forming process is carried out in a fluid-form cell (Fig. 8.6). The press ram with oil and a flexible rubber diaphragm replaces the solid punch. The blank is kept on the rigid tool half, which defines the shape of the part. The hydroforming unit moves downward while the die cavity, blank, and blank holder are stationary. Under the oil pressure, the rubber diaphragm wraps the form and holds the blank over the die cavity.

The flexform fluid cell process was first developed by ASEA (ABB, Sweden). Due to the flexibility of the rubber diaphragm, parts with undercuts and sharp contours can be formed, even for sheets with different initial thickness. The hydroform process (developed by Cincinnati Machine Tools) and the wheelon process (developed by Verson, Chicago) are similar in principle to the flexforming process. Recently, Pryer Machine Co. also developed a diaphragm hydroforming press that offers similar capabilities (Ref 8.10).

Combination of SHF-P Process with Regular Stamping Operations. In this “active” SHF-P process, an external pump generates the pot pressure. The blank is initially forced to bulge upward (prestretching or prebulging) by the pot pressure before the SHF-P process (Fig. 8.7a). Prestretching or prebulging before the SHF-P process produces plastic strain and a fa-

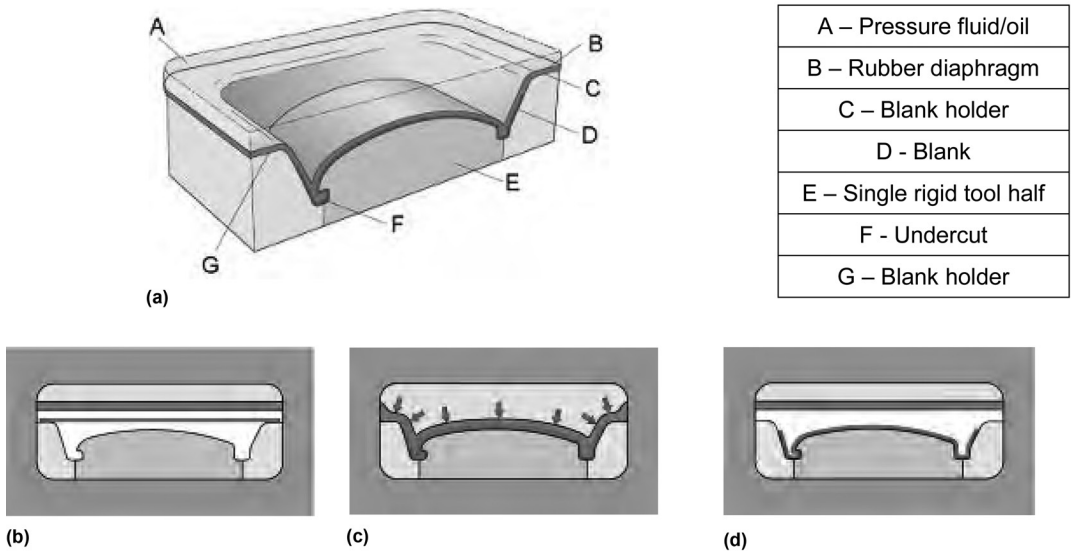


Fig. 8.6 Flexforming process. (a) Components of the process. (b)–(d) Steps in the flexforming process. Source: Ref 8.9

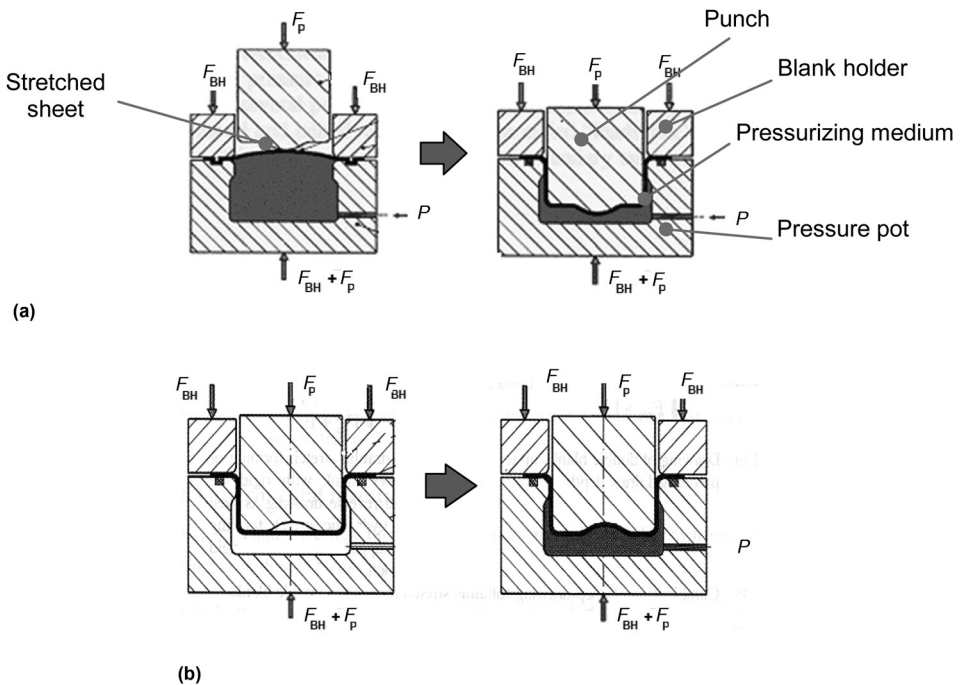


Fig. 8.7 Combination of sheet hydroforming with punch (SHF-P) with stretching and deep drawing to produce complex parts in forming operation. (a) Prestretching followed by SHF-P. (b) Deep drawing followed by SHF-P. Source: Ref 8.11

avorable state of stress, resulting in a higher dent resistance (Ref 8.6). Prebulging also suppresses wrinkles and improves the thickness distribution, thereby increasing the limiting drawing

ratio. Figure 8.7(b) shows the combination of SHF-P with regular stamping, resulting in a reduction in forming stages during forming of complex parts.

Double-Blank Hydroforming/Parallel-Plate Hydroforming. Two flat or preshaped sheets that can be of different thicknesses, different shape welded, or unwelded at the edges constitute the input blank for the parallel-plate hydroforming process. The input blank is placed in the tool that has both upper and lower die containing the shape to be formed. The blank is held at the edges, and the pressurizing medium is introduced between the sheets using a special docking mechanism. Sheets are formed against the top and bottom die to obtain the desired shape by fluid pressure. This variation of SHF-D offers some increases in productivity. However, it has not found acceptance in practice due to technical difficulties involved (Ref 8.12).

Rubber Forming. In a strict sense, rubber forming is not a sheet hydroforming process. Nevertheless, it is similar to hydroforming and used in low-volume industrial production, especially in the aerospace industry. In rubber forming, the die is replaced by a rubber pad supported by a pad holder. As the pad holder moves down, the rubber or elastomer comes in contact with the sheet/workpiece located on the punch. The deforming elastomer exerts a hydrostatic pressure on the sheet metal, causing it to conform to the shape of the punch. Rubber-forming technology is particularly suited to the production of prototypes and small series that are typical in the aerospace industry (Fig. 8.8).

8.5 Sheet Hydroforming Presses

Presses for Sheet Hydroforming with Punch. SHF-P is usually conducted in hydraulic presses that provide high ram forces and have a counter-pressure pot. Modern hydroforming (sheet or tube) presses use a long-stroke, high-speed cylinder to move the ram rapidly to reduce the cycle time. After the ram reaches the end of the stroke, two laterally-movable cylinders are activated to engage the locking system. Thus, after the position of the ram is fixed with the mechanical locking system, the short-stroke, high-pressure hydraulic clamping cylinders are activated to secure the sealing of the pot with the blank holder (Fig. 8.9).

The press seen in Fig. 8.9 allows independent control of the BHF and pot pressure as well as reduction in cycle time and cost by decreasing the amount of high-pressure hydraulic fluid to be handled by the system. This press is equipped with multipoint cushion (MPC) systems that al-

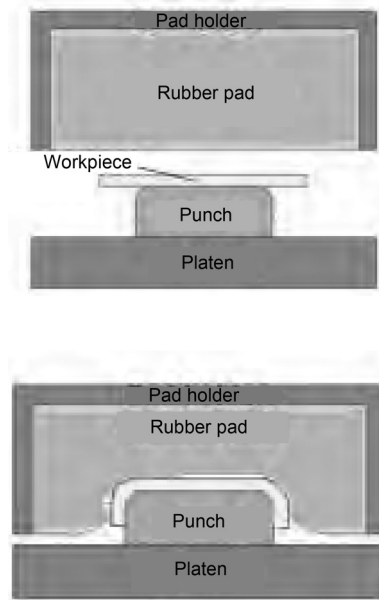


Fig. 8.8 Schematic of rubber die or rubber-forming process. Source: Ref 8.13

low changing the BHF in space over the flange area and during the SHF-P process. The MPC system is used to control local pressure on the flange so that the metal flow is optimized and leakage is reduced.

A similar active hydromechanical press is also offered by Schuler (Ref 8.15). The process allows prebulging of the blank prior to SHF-P and allows for increased strain hardening of the sheet during forming, which increases the dent resistance of automobile body panels (Fig. 8.10). An external hydraulic unit is used to generate the pressure required for prebulging the blank. Six hydraulic cylinders located in the press crown apply the required BHF, while eight cylinders located in the press bed apply the pressing force from below. The punch is fixed during forming by six adjustable mechanical stops.

Presses for Sheet Hydroforming with Die. The SHF-D presses and tools are designed and manufactured based on the technology developed and available in tube hydroforming. However, in SHF-D, a higher locking force due to the large area of the sheet and blank holding mechanism must be considered. University of Dortmund (IUL), Germany, in cooperation with Siempelkamp Pressen Systeme, Germany, has built a 100 MN press for SHF-D of large automotive parts (Fig. 8.11).

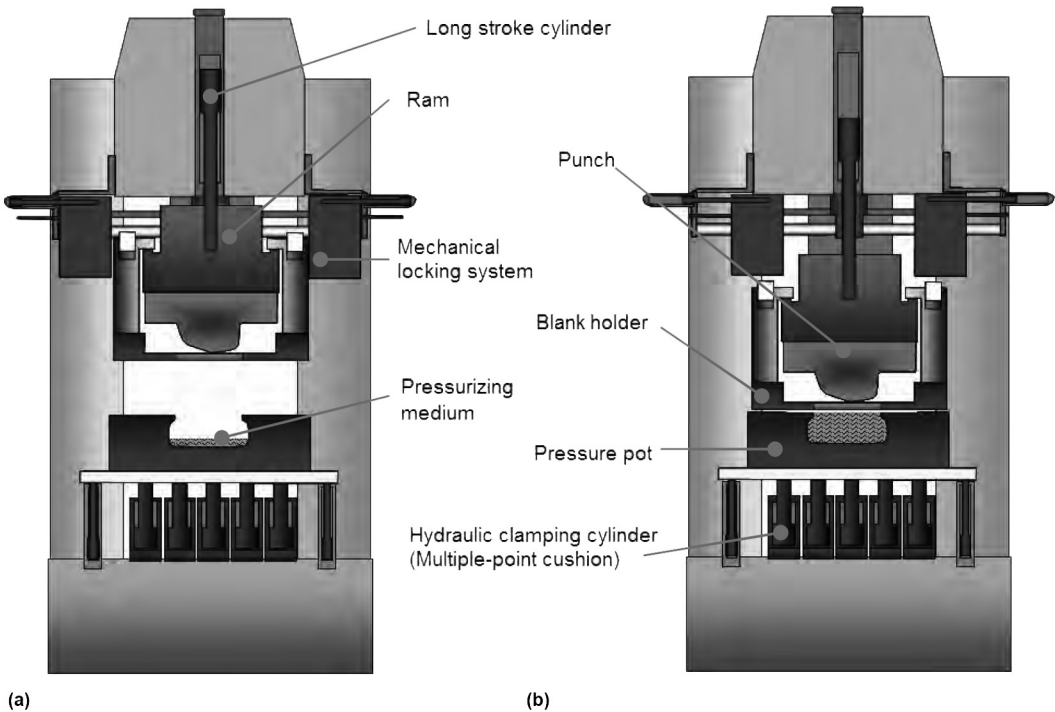


Fig. 8.9 Sheet hydroforming with punch short-stroke press. (a) Open position. (b) Closed position. Mechanical locks are engaged, and hydraulic clamping cylinders apply blank holder force. Source: Ref 8.14

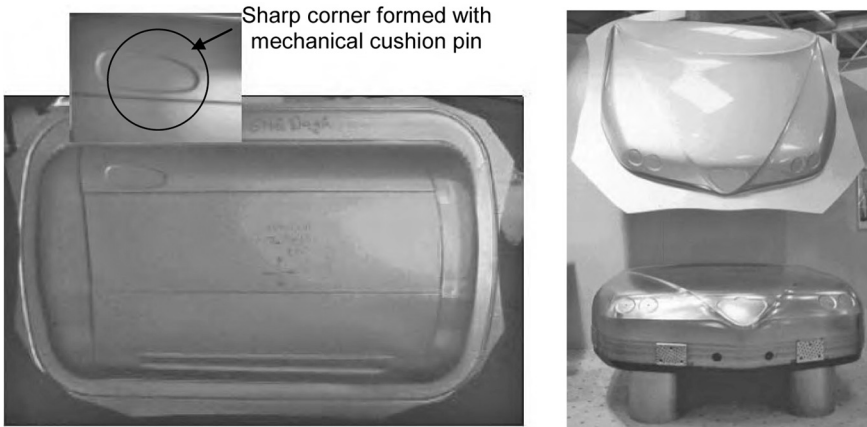


Fig. 8.10 Example parts formed by the Schuler active hydromechanical process. Source: Ref 8.15

The press is designed to have horizontal mounting for easy handling of the workpiece and fluid and for avoiding an expensive foundation. The inexpensive compact design could be achieved by using a cast frame that is prestressed by wire winding to withstand high tensile stresses resulting from the locking force and

by limiting the stroke of the locking cylinder that requires a part changeout of the press frame.

The working medium is supplied in a two-step sequence. The first step consists of a filling cylinder that provides high flow rates at a pressure of 31.5 MPa (4.6 ksi). This step is adequate for preforming the part, because large amounts

of fluid at relatively low pressures are required. However, a second step is used to calibrate the final part geometry. This step consists of a pressure intensifier that generates 200 MPa (29 ksi) at low flow rates. The main closing cylinder works at 70 MPa (10 ksi) and has an area of 1.4 m² (15.1 ft²). Thus, the closing cylinder can produce 100 MN (11,240 U.S. tons) of closing force, which allows the forming of sheet metal parts of 1 by 1 m (3 by 3 ft), up to a fluid pressure of 100 MPa (15 ksi).

Presses for Flexform Fluid Cell Processes. Quintus fluid cell presses are manufactured with rectangular trays with usable tool areas from 0.9 by 2 m (3 by 7 ft) up to 2 by 4 m (7 by 13 ft) (Fig. 8.12). The cycle time is normally between 1 and 3 min, depending on press size, formed parts,

and selected pressure. Maximum forming pressures are 100 MPa (14.5 ksi) and 140 MPa (20 ksi). For increased productivity, the fluid cell presses can be equipped with pallet systems. Using such a system, the tools and blanks are loaded onto a pallet that is lifted into and out of the tray with lifting pins, operating through the tray bottom. These presses are used in aerospace manufacturing, where small production lots are common, as well as in automotive prototyping.

8.6 Tool Design

Tool design for sheet hydroforming is similar to regular stamping; the achievable minimum radius on the part depends on the available max-



Fig. 8.11 Schematic of horizontal sheet hydroforming with die press located at the University of Dortmund's Light Forming Technology Center. Source: Ref 8.16

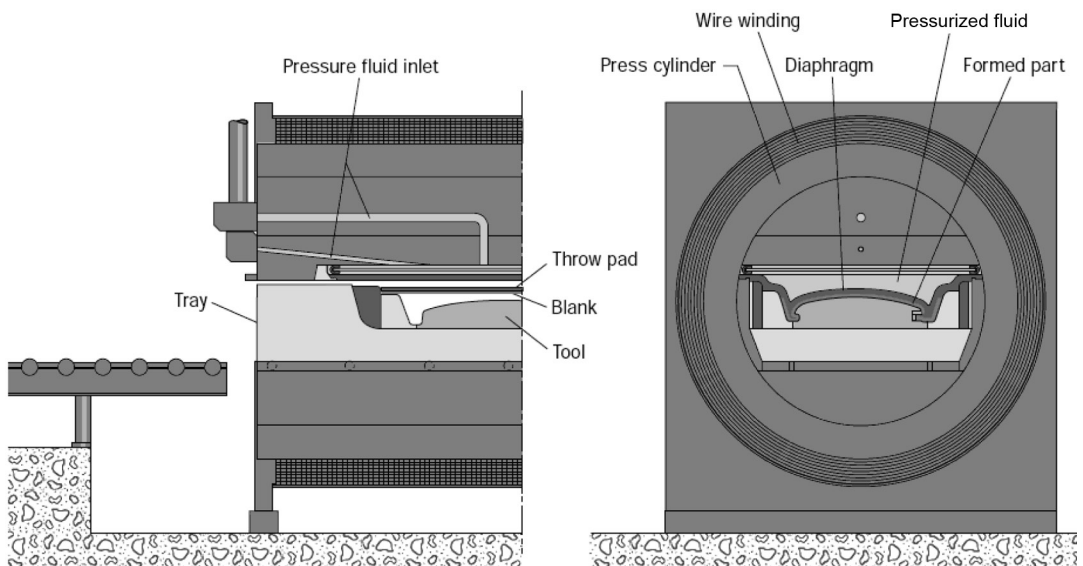


Fig. 8.12 Flexform fluid cell press. Source: Ref 8.9

imum liquid pressure. In SHF-P, punch and blank holder are specifically designed for the part shape, while the pressure pot remains common for all parts. The pressure pot and punch in SHF-P are designed to withstand high pot pressure. Also, careful consideration is required for sealing at the pressure pot/sheet interface to avoid leakage of the fluid during SHF-P.

Methods to Avoid Sheet Bulging. SHF-P of parts with tapered sidewalls results in bulging of the sheet in the gap between the blank holder and the punch due to pot pressure during forming (Fig. 8.13). This bulging could result in excessive thinning and fracture at higher pot pressures. Several design concepts have been developed as part of hydroforming research conducted at the University of Stuttgart (IFU) (Ref 8.17).

Elastic Cushion to Form Sharp Corners. The pot pressure required to completely form the part depends on the smallest corner radius in the part. Thus, parts with sharp corners require a press with very high capacity, resulting in an

increase in the investment cost. By using elastic cushions mounted in the pressure pot (Fig. 8.14), it is possible to form sharp corners mechanically by the cushions rather than the pot pressure, thus resulting in reduction of the required press capacity and investment (Ref 8.15).

Multipoint Blank Holder Control. In conventional SHF-D tooling (Fig. 8.4b), the intermediate plate applies the required force to avoid wrinkling and to seal the pressurizing medium. Hence, the surface pressure in the flange area depends on the internal pressure, p_i , which increases the friction during the calibrating stage. Furthermore, it is difficult to precisely apply the required BHF on the sheet. An advanced tool design is based on a functional separation between BHF and locking force, as shown in Fig. 8.15. The locking force is applied by the intermediate plate, while the blank holder, mounted in the flange portion of the die, applies the BHF independent from the internal pressure, p_i . Furthermore, such a tool design guarantees an effective compensation of tool deflections and opens new

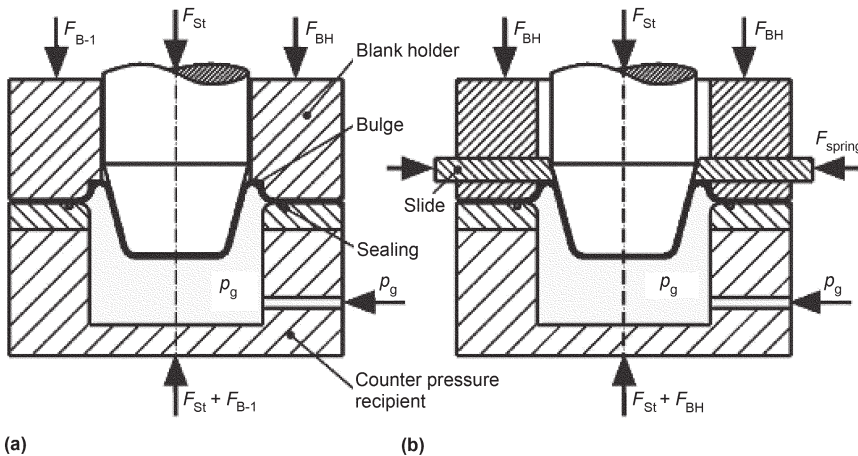


Fig. 8.13 Bulge height control techniques. (a) Using a modified blank holder. (b) Using a mechanical sliding mechanism. Source: Ref 8.17

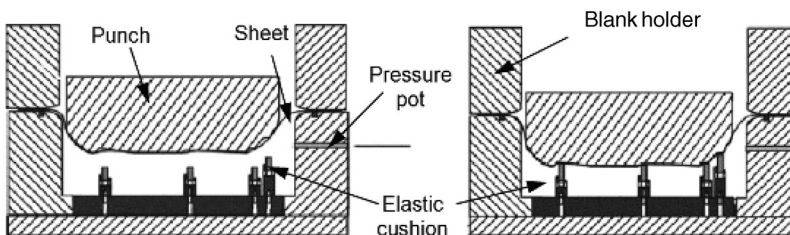
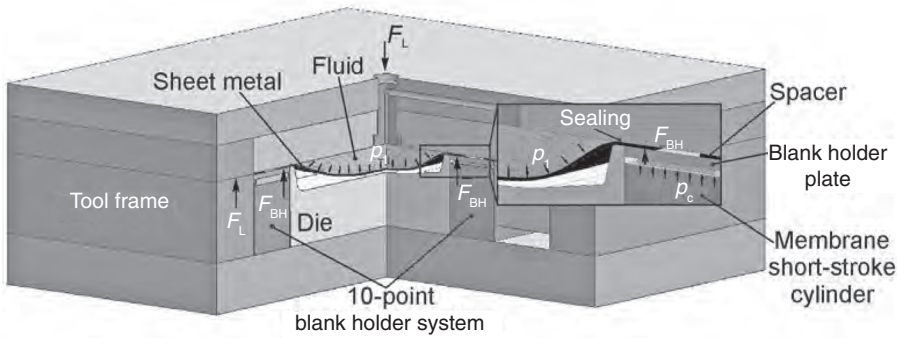
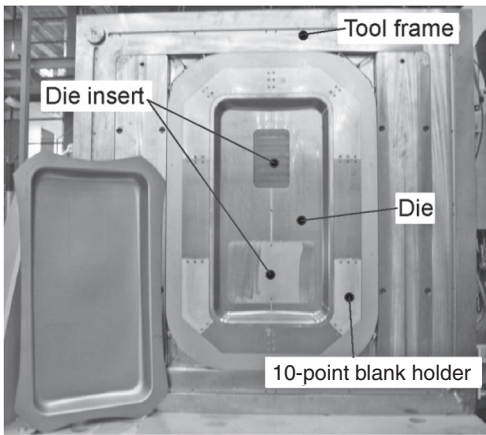


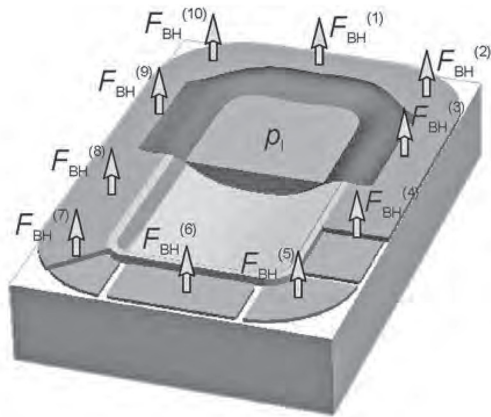
Fig. 8.14 Schematic of pressure pot with mechanical/elastic cushions to form sharp corners in sheet hydroforming with punch. Source: Ref 8.15



(a)



(b)



(c)

Fig. 8.15 Sheet hydroforming with dies used at the Technical University of Dortmund. (a) Schematic showing elements of the blank holder. (b) Photograph of the vertical blank holder segments, with an example hydroformed rectangular part with overall dimensions of 900 × 460 mm (35 × 18 in.). (c) The ten blank holder segments in the die for blank holder force application

possibilities for control of the process. By a combined variation of the process parameters—BHF, working media pressure, and volume flow—it also becomes possible to precisely control the forming history as desired and thus to achieve an optimal utilization of the formability of the material used. The University of Dortmund developed a modular tooling design with multipoint blank holder, as shown in Fig. 8.15, where the force at each cylinder can be varied independently. Thus, material flow from the flange can be controlled precisely by closed-loop process control strategies (Ref 8.16).

Elastic Blank Holder. In SHF-P, the sheet is pressed against the moving punch so that friction between the punch and the sheet is increased and relative sliding is reduced. Nevertheless, the material in the flange area is drawn in, in a manner similar to the conventional deep-drawing process. Thus, blank holder design also plays an important role in SHF-P because the

applied BHF controls the material flow during draw-in and also applies the necessary force to avoid leakage of the pressurizing medium during the forming process. In forming nonsymmetric parts using conventional blank holders, thickening in the flange is not uniform, resulting in a gap between the rigid blank holder and sheet. This causes leakage of the pressurizing medium.

At the University of Stuttgart (IFU), Germany, a segmented elastic blank holder (originally designed for stamping) was used for SHF-P (Fig. 8.16). The flexible blank holder deflects elastically under applied BHF and ensures uniform contact with the sheet metal despite nonuniform sheet thickening during the process. Thus, leakage of pressurizing medium can be avoided (Ref 8.18). Using the segmented elastic blank holder concept, additional experimental investigations were conducted at the University of Stuttgart to form automotive fender geometry

by SHF-P. A flat binder surface allowed for easier sealing and better leakage control. For the same part depth, less thinning was observed in parts formed with the curved binder.

Counterpunch. The use of counterpunches can increase the process window of SHF-D. The counterpunch applies a counterforce onto the blank opposite the main forming direction. As a consequence, smaller bottom radii can be reached, and the strain paths can be shifted to tension-compression strains (Fig. 8.17). Furthermore, the strain state, which occurs in the early process stages, can be conserved during the entire process, and local geometry details can already be calibrated at the process start using the complete formability of the sheet material.

8.7 Process Limits, Defects, and Process Window in SHF-P

Formed part quality in SHF-P is dependent on part geometry, incoming sheet material properties, interface conditions (friction), and pro-

cess parameters (namely, pot pressure and BHF) during forming. Common defects in SHF-P include:

- Excessive thinning leading to fracture
- Flange wrinkles leading to leaking of the pressurizing medium
- Sidewall wrinkles
- Excessive bulging leading to fracture (Fig. 8.18a)
- Surface marks (Fig. 8.18b).

In forming nonsymmetric parts (such as automotive fenders) by SHF-P, bulging of the sheet is observed more commonly in the straight sections of a die, where the deformation is in plane strain. This is because sheet material shows lower resistance to deformation in this state of stress. Sheet bulging is less common at the die corners, where the state of stress is approximately axisymmetric.

A process window is defined as a combination of process parameters for which the part can be formed with no defects. Figure 8.19 schematically shows a process window defined

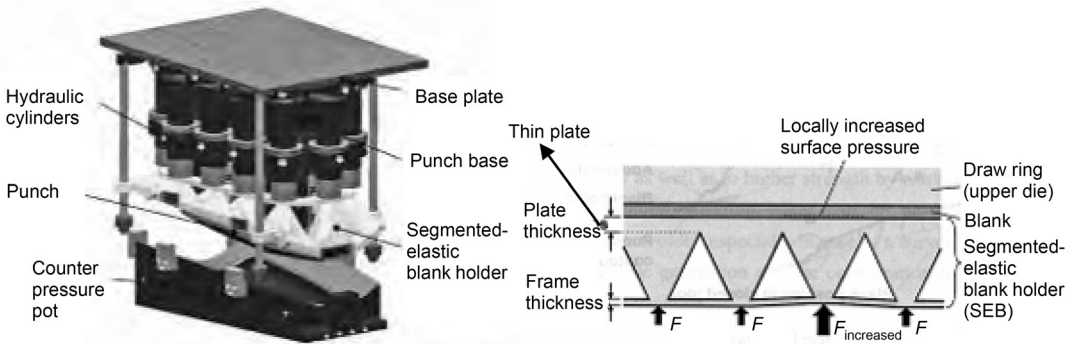


Fig. 8.16 Schematic of die assembly with segmented elastic blank holder for sheet hydroforming with punch. Source: Ref 8.18

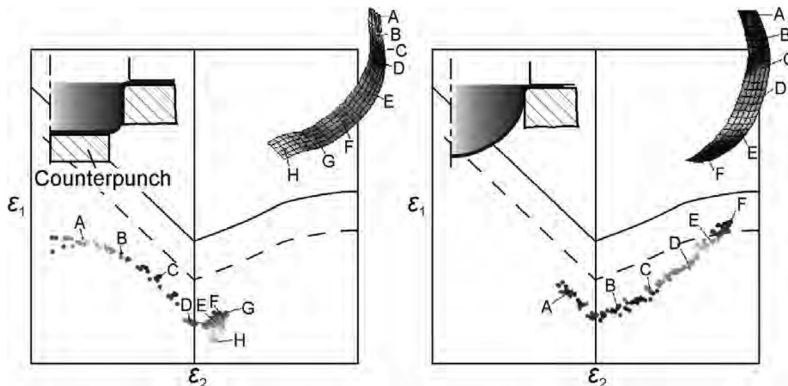


Fig. 8.17 Manipulation of strain state by the use of a counterpunch. Source: Ref 8.19

by using BHF and pot pressure as process parameters. Flange wrinkling occurs when the BHF is insufficient. Sidewall wrinkles can be attributed to insufficient pot pressure, part geometry (e.g., punch with tapered walls), and/or excessive flange wrinkling. Fracture occurs after excessive thinning due to high BHF and/or insufficient pot pressure (point A in Fig. 8.19). Fracture can be avoided/postponed by increasing the pot pressure (moving from A to A'' in

Fig. 8.19) or by decreasing the BHF (moving from A to A' in Fig. 8.19).

Leaking of the pressurizing medium and bulging against the drawing direction are unique possible modes of failure in SHF-P. Leaking occurs when the BHF is insufficient, resulting in flange wrinkling followed by leaking of the pressurizing medium (point B in Fig. 8.19). Leaking results in reduction of fluid pressure in the pot, which could result in fracture of the

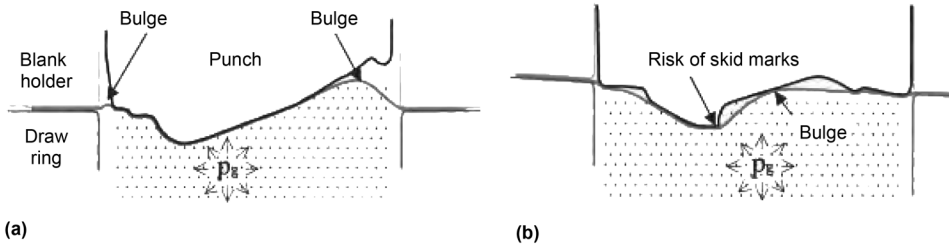


Fig. 8.18 Bulge formation in sheet hydroforming with punch. (a) Bulge at punch/blank holder interface and at inclined/tapered punch locations. (b) Due to uneven contact between sheet and tool, skid marks can occur because of sheet rubbing at sharp punch corners. Source: Ref 8.20

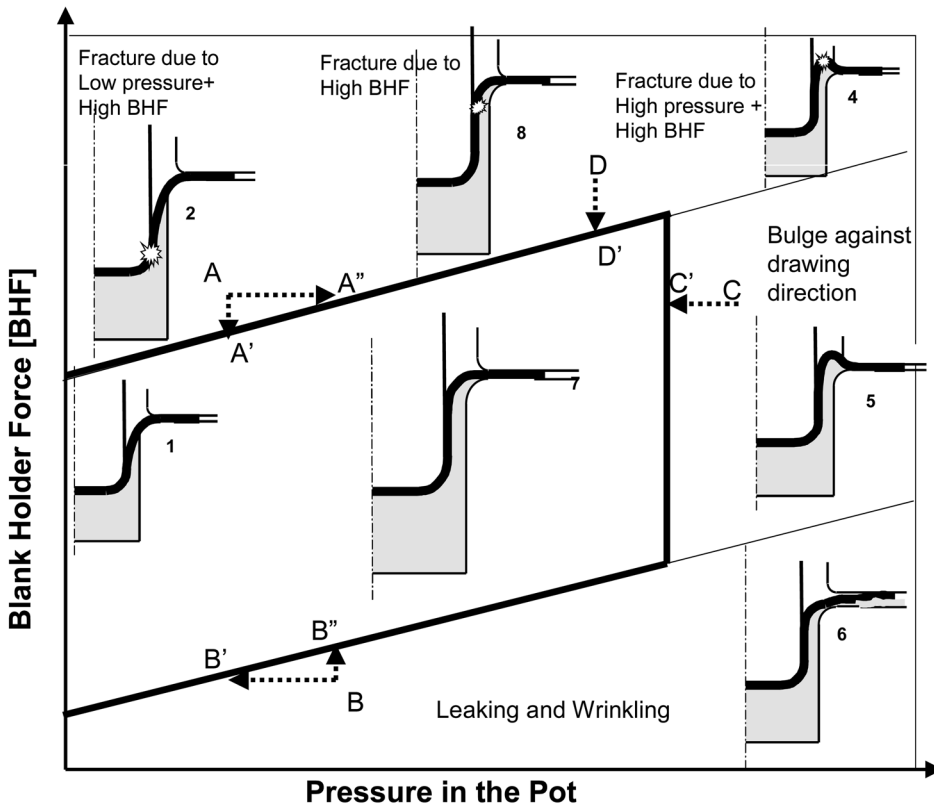


Fig. 8.19 Process window for the sheet hydroforming with punch process. Source: Ref 8.21

part. Leaking can be avoided by increasing the BHF (moving from B to B'' in Fig. 8.19) or by reducing the pressure in the pot (moving from B to B' in Fig. 8.19). Also, seals may be used to reduce the possibility of leaking during the SHF-P process. Bulging against the drawing direction occurs due to excessive fluid pressure. This is usually observed in parts with tapered walls. Bulging can be avoided by decreasing the pot pressure (moving from C to C' in Fig. 8.19).

8.8 Process Simulation—Room-Temperature Sheet Hydroforming

Numerous investigations on deformation mechanics in the SHF-P process have been conducted by researchers (Ref 8.18, 8.22, 8.23) who estimated the process parameters through trial-and-error experiments and finite-element simulation, which are costly and time-consuming. Furthermore, the estimated process parameters may not be robust to variations in the manufacturing process.

Application to Sheet Hydroforming with Die. The Engineering Research Center for Net Shape Manufacturing (ERC/NSM) worked in cooperation with the University of Dortmund, Germany, in optimizing the SHF-D process for a rectangular part (Fig. 8.15 and 8.20) formed us-

ing a multipoint cushion system with a segmented blank holder. This cushion system allows different BHF's to be applied at ten different locations around the rectangular blank. The BHF can also be varied with time in each of these locations.

For a multipoint cushion system, there are four possible ways of applying the BHF during the hydroforming process, namely:

- Blank holder force constant in space and time
- Blank holder force variable in space and constant in time
- Blank holder force variable in time and constant in space
- Blank holder force variable in space and time

Optimum values for all four possible modes of application of BHF to form the rectangular part were estimated (Ref 8.24).

Application to Sheet Hydroforming with Punch. Figure 8.21 shows a finite-element model of the SHF-P process of an automotive part (trunk lid-outer). The BHF is applied by a multipoint cushion system where the cylinders are connected in groups. All the cylinders in a group apply the same force, while each group can apply different forces. One-half geometry was modeled due to symmetry conditions. The process was modeled using the Aquadraw module in PAMSTAMP 2000. Sheet material properties

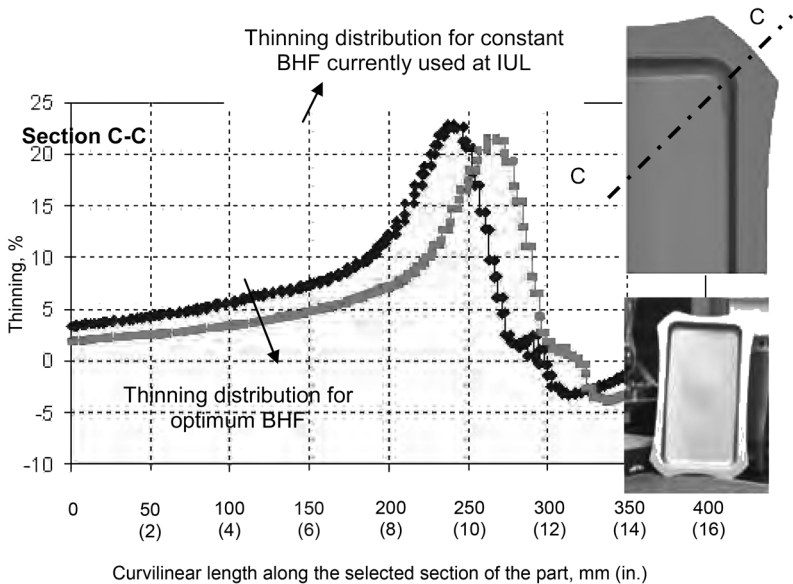


Fig. 8.20 Thinning distribution comparison along section C-C predicted by finite-element simulation for optimum blank holder force (BHF) compared with part currently formed using constant BHF at University of Dortmund (IUL), Germany. Source: Ref 8.24

(extradeep-drawing-quality steel, $t = 1$ mm, or 0.04 in.) were obtained from a tensile test. In finite-element simulation, $\mu = 0.15$ was used, because no lubricant was used in the process. The blank holder was modeled as an elastic object to account for elastic deflection that significantly complements the multipoint cushion system to form the part. In the experiments, the pot pressure could be adjusted to the desired trajectory. Therefore, pressure obtained from preliminary experiments was used as an input, and only BHF was estimated through finite-element analysis. Maximum pot pressure was limited to 100 MPa (15 ksi) due to limitations in die design.

Results and Experimental Validation. The BHF varying in space and constant in stroke was estimated using finite-element simulation (Fig. 8.22a). The predicted BHF resulted in maximum thinning of 25% and was sufficient enough to avoid wrinkling in the formed part in the finite-

element simulation. Figure 8.22(b) shows a photograph of the formed part that was formed without splits. However, minor wrinkles were observed in the geometry at location “A.” The wrinkle could not be eliminated by changing the BHF. The punch geometry was modified near location “A” to eliminate wrinkles in the die tryouts.

Optimization of SHF-P Process. Analysis and optimization of the SHF-P process for a $\varnothing 90$ mm (3.5 in.) cylindrical cup was conducted by the ERC/NSM in cooperation with Schnupp Hydraulik, Germany (Ref 8.8). The pot pressure was limited to a maximum value of 40 MPa (6 ksi) due to limitation of the machine capacity. Figure 8.23 shows the optimized BHF profile path for hydroforming a 90 mm diameter round cup from aluminum-killed drawing-quality steel to a depth of 105 mm (4.1 in.) in a single forming operation. Blank holder force was observed to increase toward the end of the forming process to restrain material flow and avoid excessive flange thickening, which would result in flange wrinkles and leakage. Using this optimized BHF profile, round parts were successfully hydroformed at Schnupp Hydraulik. Comparison of part thinning from experiment and from finite-element predictions is seen in Fig. 8.24.

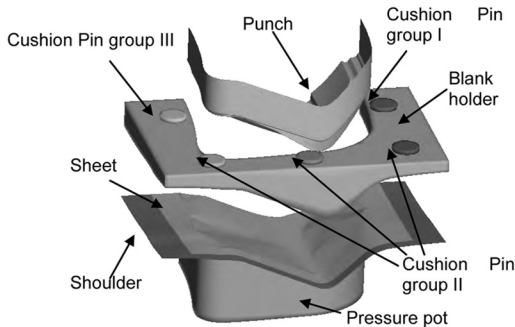


Fig. 8.21 Schematic of finite-element model for sheet hydroforming with punch process of a trunk lid-outer. Source: Ref 8.8

8.9 Elevated-Temperature Sheet Hydroforming

Warm sheet hydroforming is a relatively new technology that combines the advantages of

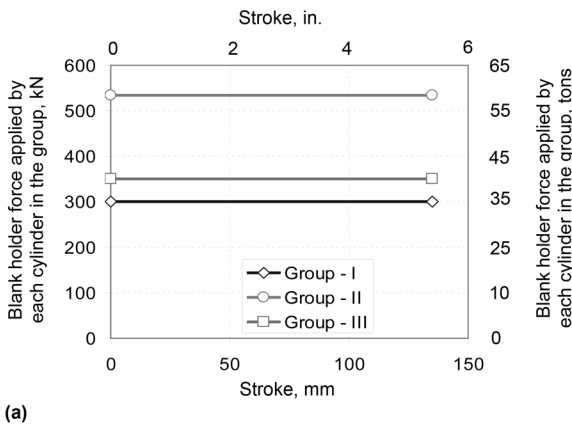


Fig. 8.22 Sheet hydroforming with die of an automotive part. (a) Blank holder force (BHF) varying in space estimated through finite-element simulation for trunk lid-outer part geometry. (b) Formed part (trunk lid-outer) using BHF (variable in space and constant in time) predicted by finite-element simulation. Source: Ref 8.8

elevated-temperature sheet metal forming with sheet hydroforming.

Warm Sheet Hydroforming with Punch.

In warm SHF-P, the sheet and flange portion of the die and blank holder are heated to the required temperature (Fig. 8.25a). The punch is cooled while the pressurizing fluid temperature is kept slightly higher than room temperature. During the process, the lower temperature of the punch and pressurizing medium cools the sheet adjacent to the punch, thereby increasing the strength of the sheet to carry the drawing load. This postpones failure caused by excessive thinning. As a result, a limiting draw ratio (LDR) of 3.0 was obtained for drawing an aluminum alloy cylindrical cup at a forming temperature of 250 °C (480 °F) (Ref 8.25). The

pressure medium is a high-temperature oil that can be heated to 300 °C (570 °F) without excessive smoking and burning.

The IFU Stuttgart (Ref 8.27) conducted warm SHF-P experiments with heated Ø 50 mm (2 in.) cylindrical cup tooling to investigate improvement in formability for magnesium alloys (AZ31). Conventional deep drawing at elevated temperature of 200 °C (390 °F) showed an LDR of 1.8. In warm SHF-P, an LDR of 3.0 was achieved experimentally. Aside from improved formability, the formed cup showed lower thinning in the cup wall and lower strains compared to conventionally drawn cups.

Warm Sheet Hydroforming with Die.

Figure 8.25(b) shows a schematic of the warm SHF-D process. In this process, the sheet, die,

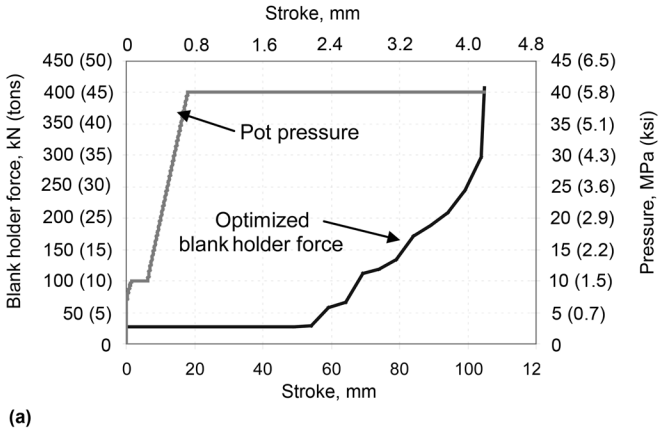


Fig. 8.23 Results of research study in sheet hydroforming with punch. (a) Pot pressure curve and optimum blank holder force (BHF) curve predicted using numerical optimization techniques coupled with finite-element modeling. (b) Wrinkles in the round cup were eliminated by using optimum BHF.

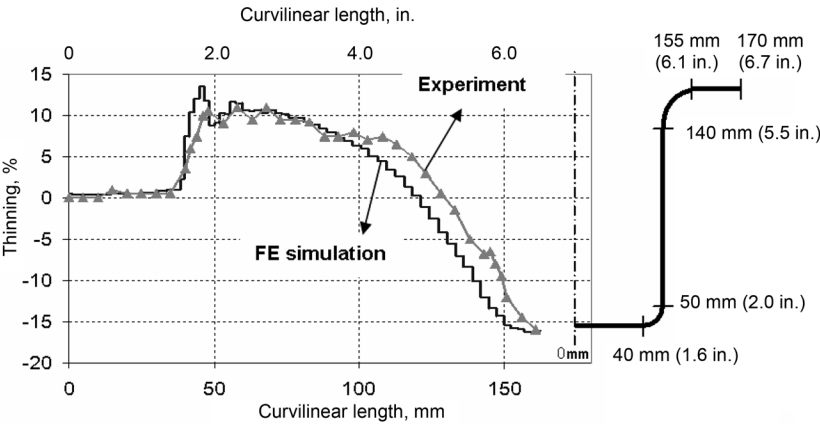


Fig. 8.24 Comparison of predicted and measured wall thickness. FE, finite-element

and pressurizing medium/fluid are heated to the desired temperature. The tooling consists of an upper and lower die. The upper die is heated with cartridges, while the lower die is heated by a band heater. Heat transfer/loss is minimized by thermal insulation. During the process, the pressurizing medium, nitrogen gas, is supplied through the upper die (with pressure p_i). The pressurizing medium deforms the sheet into the lower die cavity, which has the shape/impression to be formed. In this setup, the counterpressure in the lower die cavity can also be controlled. With this setup, door inner reinforcements were made from magnesium alloy AZ31 of 2.9 mm (0.1 in.) thickness at 400 °C (750 °F) with a forming pressure of 1.1 MPa (0.16 ksi) (Ref 8.26). At LFT, University of Erlangen-Nuernburg, sample automotive parts from aluminum alloy A6061, A5182 sheets, and aluminum-magnesium alloy tubes were hydroformed at a temperature of 220 °C (430 °F) (Ref 8.28).

Challenges in Warm Sheet Hydroforming/Issues in Process Simulation. The ERC/NSM has investigated warm sheet forming using finite-element (FE) simulations, and predictions were compared with experimental results available in the literature. Magnesium alloys were used in this investigation. Warm drawing of a cylindrical

cup and a rectangular pan from magnesium alloy was simulated using commercial code DEFORM-2D and 3D. In this investigation, it was observed that FE simulations predict all the major trends shown in the experimental data. However, the FE analysis overpredicts the punch force and thinning distribution compared to the experiment. This is despite the fact that material property inputs for the FE simulation were obtained through rigorous material testing (based on tensile test data) (Ref 8.29).

For accurate FE simulation of the sheet hydroforming process, the mechanical and thermal variations in the workpiece must be predicted (Table 8.1). Thus, it is necessary to have the following as input to FE process simulation: sheet material data (flow stress, yield surface, and material anisotropy) over the range of forming temperatures (25 to 350 °C, or 75 to 660 °F) and deformation rates (strain rates). Data on heat transfer and friction between the workpiece and tools are also needed.

Sheet Material Flow-Stress Data. As seen in Chapter 5 on warm sheet metal forming, prior research on elevated-temperature behavior of materials in warm stamping/hydroforming process simulation focused on determining the flow stress of sheet metal as a function of tempera-

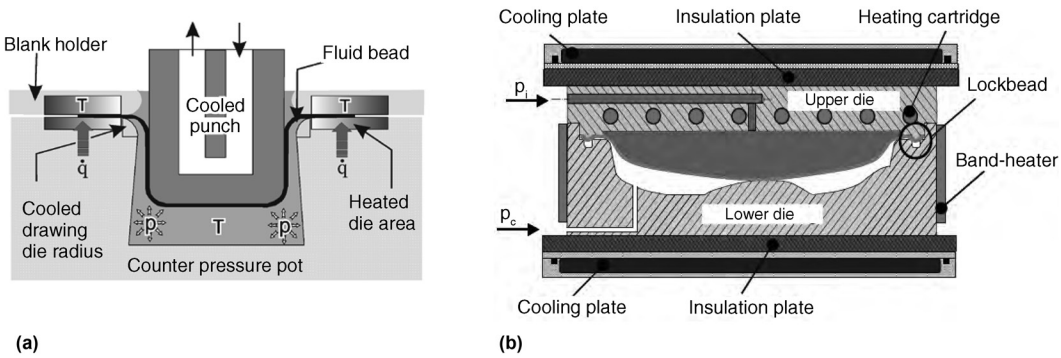


Fig. 8.25 Warm sheet hydroforming. (a) With punch using cylindrical punch. Source: Ref 8.25. (b) With die. Source: Ref 8.26

Table 8.1 Data required as input to finite-element modeling for accurate process simulation of the warm sheet hydroforming process

Mechanical data (for sheet)	Thermal data (for sheet, forming medium, and hard tools)	Process data
Young's modulus	Thermal expansion	Friction between sheet and tools (function of interface pressure and sheet temperature)
True stress-strain data (function of temperature and strain rate)	Thermal conductivity	Temperature (sheet and tools)
Yield surface (function of temperature)	Heat capacity	Interface pressure
Anisotropy coefficients (function of temperature)	Heat transfer	Process parameters (forming or pot pressure, applied blank holder force)
	Heat dissipation	

ture and strain rate. The effect of elevated temperature on yield surface and anisotropy coefficients, especially for aluminum alloys, is still a subject of research.

Commercially available FE codes do not offer specialized material models developed for specific materials and processes. Therefore, user subroutines must be programmed to model material behavior as a function of temperature and strain rate.

Heat-Transfer and Interface Heat-Transfer Coefficients. The pressurizing fluid and the dies have larger heat capacity due to their relatively larger masses compared to the sheet. Also, the selected sheet materials (aluminum and magnesium alloys) have low heat capacity. Therefore, for a simplified analysis, a valid assumption would be to assume a stepwise constant temperature of the dies and fluid (Ref 8.28).

To ensure accurate heat-transfer calculation, correct tool, sheet, and pressurizing medium interface heat-transfer coefficients must be known. At present, in most commercial finite-element modeling (FEM) codes the interface heat-transfer coefficient is assumed to be constant. However, the heat transfer between the sheet and the tools is dependent on the interface contact pressure. Because contact pressure varies with location, it is desirable to input to FEM the heat-transfer coefficient as a function of pressure. Therefore, user subroutines in FEM are needed to input the heat-transfer coefficient as a function of pressure.

Interface Friction Coefficient. At present, in FEM the interface friction coefficient is assumed to be constant. A detailed investigation on the influence of temperature and interface pressure on the friction coefficient is needed.

8.10 Industrial Applications of Sheet Hydroforming

Room-Temperature Applications—High-Strength Steels. The manufacturability of the SHF-P process for forming a roof outer panel of an Opel Vectra was demonstrated in a study conducted by Siebenwurst GmbH (Germany) in cooperation with ThyssenKrupp, Germany. The part was formed in a 3630 metric tons (4000 ton) Schnupp hydromechanical press from two high-strength steels: a 0.6 mm (0.02 in.) thick dual-phase DP-K 30/50 steel (H300X) and a 0.7 mm (0.03 in) thick BH180 (H180B) steel (Ref 8.30).

Room-Temperature Applications—Flexible Multiforming System. A new concept production cell was recently developed by Amino Corporation for medium-volume production (10,000 to 60,000 parts/year). The main press in the production cell is a sheet hydroforming press for draw operation (up to 2720 metric tons, or 3000 tons, with 725 metric ton, or 800 ton, blank holder tonnage capacity, part size up to 2.8 m, or 9.2 ft, with part depth 400 mm, or 16 in.). The second and third presses in the line are link-servo presses used for subsequent trimming and bending (up to 800 ton capacity each). This forming system, used in combination with a quick die-change mechanism, was used for production of numerous body panels, such as the 2006 Pontiac Solstice (Ref 8.31).

Elevated-Temperature Application—Quick Plastic Forming at General Motors. Quick plastic forming is a hot blow forming technology to manufacture complex panels at traditional automotive volumes (Fig. 8.26). General Motors has applied this technology in the forming of aluminum alloy closures and body panels (AA 5083). The main advantage of this technology is the enhanced formability of the aluminum, which enables complex designs, lower tool costs, simpler construction, and improved control of dimensional variations.

In this process, aluminum sheet blanks are sent into a preheater and heated to a temperature of 450 to 510 °C (840 to 950 °F). The hot blanks are then transferred into a hydraulic press and pressurized against an electrically heated top die using warm air, at 1.7 to 3.5 MPa (0.25 to 0.5 ksi). Once the parts are formed, they are transferred to a cooling fixture to bring them down to handling temperature (Ref 8.32).

8.11 Sheet Hydroforming Process Economics

In most cases, the practical application of SHF-P requires a cost advantage in comparison with conventional stamping. Currently, manufacturing cost calculators for stamping and SHF-P processes are not commercially available, and calculations are proprietary to a company. Therefore, in this study, a Microsoft Excel-based calculator (SHEETCOST) was developed based on technical cost modeling (Ref 8.33) to assist process planners in deciding how to manufacture the part, either by stamping or by sheet hydroforming. Using SHEETCOST, the cost of the

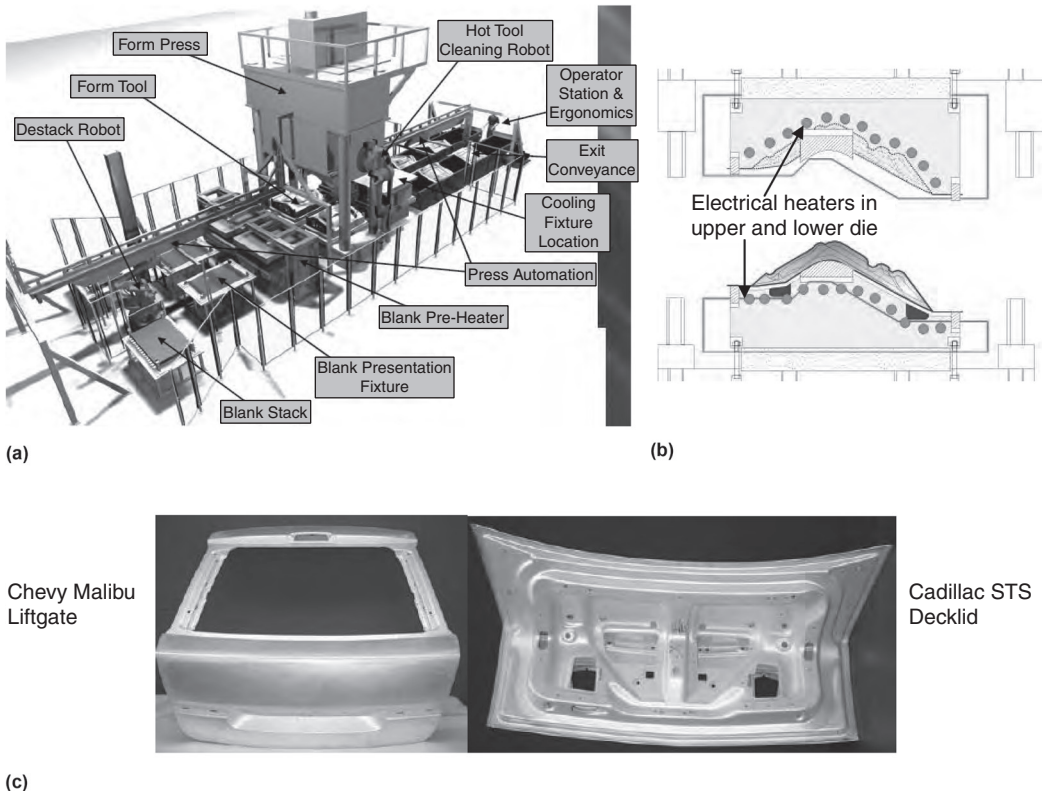


Fig. 8.26 Quick plastic forming process. (a) Schematic of production forming cell at General Motors. (b) Schematic of the heated tool. (c) Example formed production parts

each stage in production is calculated to obtain the final cost. Calculation results depend on the accuracy of the input data (Ref 8.8).

Inputs to the SHEETCOST calculator include the following.

General inputs are subdivided into inputs for stamping and for sheet hydroforming. The input data are the same for both stamping and sheet hydroforming and include:

- Expected production volume per year
- Part life
- Working days per year
- Working hours
- Line cycle time
- Wages
- Energy unit cost
- Interest
- Equipment life
- Building cost

Process-related inputs are subdivided into inputs for stamping and sheet hydroforming. These are further divided into general informa-

tion, common to all stages in the stamping/sheet hydroforming process, and stage-specific information, which is specific to each stage of the forming process. The general information includes:

- Material cost
- Material density
- Scrap cost
- Rejection scrap rate
- Unplanned downtime
- Number of workers in stamping/hydroforming line
- Number of indirect workers in stamping/hydroforming line
- Tool-changing time
- Part-handling investment
- Line space
- Line equipment maintenance cost

The required stage-specific information for the deep drawing stage example includes press investment, press power requirement, tooling investment, and tooling maintenance.

Outputs from the Calculator. The costs calculated for stamping and sheet hydroforming lines are presented in two different formats. In format I, the total manufacturing cost of the part by stamping and sheet hydroforming is broken down to fixed cost and variable cost. In format II, the total manufacturing cost of the part is broken down to process steps, as calculated (Fig. 8.27). Also, bar charts are provided to compare

the various components of the fixed and variable costs between the sheet hydroforming and stamping processes.

Case Study 1—Rear Door Panel. A rear door panel-outer (Fig. 8.28) was used in a study conducted by Auto Steel Partnership in cooperation with Porsche Engineering and Schuler SMG. In this example, it was observed that the material cost as well as the tooling and

COST SUMMARY				
<i>Costbreakdown by Variable and Fixed Costs:</i>				
	Stamping (DD)		Hydroforming	
Material cost	\$6.69	77.1%	\$6.69	64.9%
Direct labor cost	\$0.33	3.8%	\$1.19	11.5%
Indirect labor cost	\$0.33	3.8%	\$1.19	11.5%
Direct energy cost	\$0.11	1.2%	\$0.11	1.1%
Indirect energy cost	\$0.00	0.0%	\$0.00	0.0%
Material handling cost	\$0.02	0.2%	\$0.00	0.0%
Total Variable Costs	\$7.47	86.0%	\$9.18	89.1%
Equipment cost	\$0.20	2.3%	\$0.61	5.9%
Tooling cost	\$0.96	11.1%	\$0.49	4.8%
Building cost	\$0.00	0.0%	\$0.00	0.0%
Maintenance cost	\$0.05	0.6%	\$0.02	0.2%
Total Fixed Costs	\$1.21	14.0%	\$1.13	10.9%
Part Manufacturing Costs	\$8.68	100.0%	\$10.31	100.0%

Costbreakdown by individual Process Steps:

Stamping (DD)			Hydroforming				
Line costs			Line costs				
Material Cost	\$6.69	77.1%	Material Cost	\$6.69	64.9%		
Direct labor cost	\$0.33	3.8%	Direct Labor cost	\$1.19	11.5%		
Line maintenance cost per part	\$0.00	0.0%	Maintenance cost for line	\$0.00	0.0%		
Material handling cost	\$0.02	0.2%	Material handling cost	\$0.00	0.0%		
Indirect labor cost	\$0.33	3.8%	Indirect labor cost	\$1.19	11.5%		
Indirect energy cost	\$0.00	0.0%	Indirect energy cost	\$0.00	0.0%		
Building cost	\$0.00	0.0%	Building cost	\$0.00	0.0%		
Step costs			Step costs				
BLANKING	\$0.02	0.3%	BLANKING	\$0.02	0.2%		
DRAWING	\$0.28	3.2%	HYDROFORMING	\$0.35	3.4%		
TRIM AND PIERCE	\$0.25	2.9%	LASER TRIM	\$0.19	1.8%		
FLANGING	\$0.25	2.9%	CAM FLANGE	\$0.34	3.3%		
CAM FLANGE	\$0.25	2.9%	CAM FLANGE AND PIERCE	\$0.34	3.3%		
CAM PIERCE AND TRIM	\$0.25	2.9%		0	\$0.00	0.0%	
	0	\$0.00	0.0%		0	\$0.00	0.0%
	0	\$0.00	0.0%		0	\$0.00	0.0%
Part Manufacturing Cost	\$8.68	100.0%	Part Manufacturing Cost	\$10.31	100.0%		

Fig. 8.27 Example output from SHEETCOST

press investment cost contribute significantly to the total cost for both stamping and sheet hydroforming processes.

Figure 8.28 shows the change in the part cost with changes in annual production volume, assuming the part life is fixed. It was calculated that sheet hydroforming was economical only if the annual production volume was less than 60,000 parts/year. This developed tool can be used to conduct a sensitivity analysis mainly to answer some of the “what-if” questions. For example, a sensitivity analysis conducted by changing the line cycle time indicated that manufacturing cost per part changes by \$0.10/s for both stamping and sheet hydroforming lines. Also, a change in direct labor indicated that manufacturing cost per part changes by \$0.10/personnel in the stamping line and \$0.40/personnel in the sheet hydroforming line.

Case Study 2—Fifteen Body Panel Parts.

In this case study, SHEETCOST was used to calculate the manufacturing cost of 15 body panel parts of a new car model to be produced at Adam Opel AG by either stamping or sheet hydroforming. In the analysis, it was assumed that the original equipment manufacturer would invest in a new line, and therefore, any additional capacity would be wasted. Thus, investment costs needed to be assimilated in the parts produced. Also, indirect costs, energy costs, and material handling cost were not considered due to a lack of reliable information. Costs were calculated for making 50,000 of each part per year for a period of 6 years.

Figure 8.29 shows the cost per part for stamping and sheet hydroforming. It is seen that the costs per part by stamping are nearly twice that of sheet hydroforming. Costs from stamping are

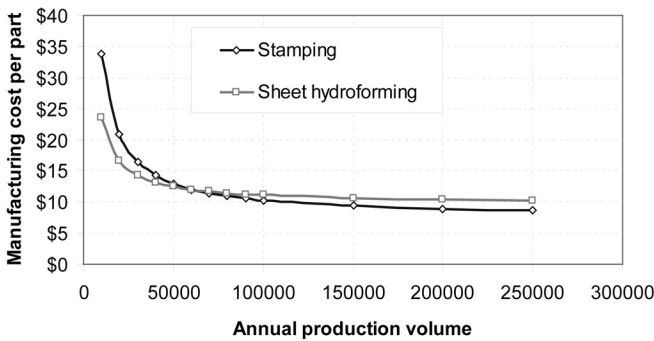


Fig 8.28 Comparison of cost per part from stamping and sheet hydroforming for different annual production volumes.

	Stamping (DD)		Hydroforming	
Material cost	\$0.00	0.0%	\$0.00	0.0%
Direct labor cost	\$1.10	32.3%	\$0.66	34.8%
Indirect labor cost	\$0.00	0.0%	\$0.00	0.0%
Direct energy cost	\$0.00	0.0%	\$0.00	0.0%
Indirect energy cost	\$0.00	0.0%	\$0.00	0.0%
Material handling cost	\$0.00	0.0%	\$0.00	0.0%
Total Variable Costs	\$1.10	32.3%	\$0.66	34.8%
Equipment cost	\$2.02	59.3%	\$1.11	58.4%
Tooling cost	\$0.18	5.3%	\$0.07	3.7%
Building cost	\$0.00	0.0%	\$0.00	0.0%
Maintenance cost	\$0.11	3.1%	\$0.06	3.1%
Total Fixed Costs	\$2.30	67.7%	\$1.24	65.2%
Part Manufacturing Costs	\$3.40	100.0%	\$1.90	100.0%

Fig. 8.29 Comparison of the cost per part in stamping and sheet hydroforming for manufacturing 15 different parts

higher because a large capacity of the new stamping line that will be installed to produce the parts will be underutilized due to a shorter cycle time in stamping. In sheet hydroforming, the new line will be used 100% of its capacity to produce parts due to a long cycle time. Furthermore, the investment for the stamping line was higher compared to the sheet hydroforming line.

REFERENCES

- 8.1 H. Rosen, S. Schwarz, A. Birkert, and S. Schneider, Hydroforming for the Automobile Industry, *Hydroforming of Tubes, Extrusions and Sheet Metals*, Vol 2, K. Siegert, Ed., IFU-Stuttgart, 2001, p 135–157
- 8.2 T. Altan, S. Oh, and H.L. Gegel, *Metal Forming: Fundamentals and Applications*, American Society for Metals, 1983
- 8.3 M. Aust, Modified Hydromechanical Deep-Drawing, *New Developments in Sheet Metal Forming*, Vol 2, *Hydroforming of Tubes, Extrusions and Sheet Metals*, K. Siegert, Ed., IFU-Stuttgart, 2001, p 215–234
- 8.4 M. Kleiner, V. Hellinger, W. Homberg, and Ch. Klimmek, Trends in Sheet Metal Hydroforming, *Hydroforming of Tubes, Extrusions and Sheet Metals*, Vol 1, K. Siegert, Ed., IFU-Stuttgart, 1999, p 249–260
- 8.5 J. Liu, B. Westhoff, M. Ahmetoglu, and T. Altan, Application of Viscous Pressure Forming (VPF) to Low Volume Stamping of Difficult to Form Alloys—Results of Preliminary FE Simulations, *J. Mater. Process. Technol.*, Vol 59, 1996, p 49–58
- 8.6 H. Hoffmann, S. Semmler, M. Golle, and M. Kerschner, Technological Characteristics of Hydro-Formed Parts, *Hydroforming of Tubes, Extrusions and Sheet Metals*, Vol 2, K. Siegert, Ed., IFU-Stuttgart, 2001, p 235–247
- 8.7 T. Maki, Current Status of Fluid Forming in the Automotive Industry, *Hydroforming of Tubes, Extrusions and Sheet Metals*, Vol 3, K. Siegert, Ed., IFU-Stuttgart, 2003, p 25–44
- 8.8 H. Palaniswamy, A. Yadav, M. Braedel, M. Ujevic, and T. Altan, IDDRG 2008 International Conference, June 16–18, 2008 (Olofström, Sweden), International Deep Drawing Research Group
- 8.9 Quintus Flexform Presses, Avure Technologies, Inc., www.avure.com
- 8.10 T. Altan, Increasing Diaphragm Hydroforming Productivity with Rapid Prototyping, *Stamp. J.*, May 2009, p 12
- 8.11 K. Siegert and B. Losch, Sheet Metal Hydroforming, *Hydroforming of Tubes, Extrusions and Sheet Metals*, Vol 1, K. Siegert, Ed., IFU-Stuttgart, 1999, p 221–248
- 8.12 M. Schroder, Recent Developments in the Hydroforming of Tubular and Sheet Blanks—Semi Productive and Productive, *Hydroforming of Tubes, Extrusions and Sheet Metals*, Vol 3, K. Siegert, Ed., IFU-Stuttgart, 2003, p 165–183
- 8.13 M. Rashid, C. Kim, E.F. Ryntz, F.I. Saunders, R. Verma, and S. Kim, Quick Plastic Forming of Aluminum Alloy Sheet Metal, U.S. Patent 6,253,588 B1, July 3, 2001
- 8.14 K. Schnupp and M. Kerschner, Presses for Hydromechanical Drawing of Panels for Automobiles, *Hydroforming of Tubes, Extrusions and Sheet Metals*, Vol 3, K. Siegert, Ed., IFU-Stuttgart, 2003, p 409–448
- 8.15 D. Stremme, H. Cherek, and R. Kolleck, Manufacturing of Large Size Outer Panels Using Active Hydromechanical Sheet Metal Forming, *Hydroforming of Tubes, Extrusions and Sheet Metals*, Vol 2, K. Siegert, Ed., IFU-Stuttgart, 2001, p 249–258
- 8.16 M. Kleiner and W. Homberg, New 100,000 kN Press for Sheet Metal Hydroforming, *Hydroforming of Tubes, Extrusions and Sheet Metals*, Vol 2, K. Siegert, Ed., 2001, p 351–362
- 8.17 T. Khandeparakar, “Hydromechanical Deep Drawing under the Influence of High Fluid Pressures,” Ph.D. dissertation, Institut für Umformtechnik, University of Stuttgart, Germany, 2007
- 8.18 K. Siegert, B. Oberpriller, and H. Markstadter, Hydromechanical Deep Drawing of Car Outer Panels, *Hydroforming of Tubes, Extrusions and Sheet Metals*, Vol 3, K. Siegert, Ed., IFU-Stuttgart, 2003, p 551–567
- 8.19 W. Homberg, “Investigation of Process Control and Manufacturing System of High-Pressure Sheet Metal Forming,”

- Dr.-Ing. thesis, University of Dortmund, Germany, 2000
- 8.20 B. Oberpriller, M. Liewald, K. Siegert, J. Liehkauf, and C. Wehe, Hydromechanical Deep Drawing of Outer Body Panels, *International Conference on New Developments in Sheet Metal Forming*, M. Liewald, Ed., IFU-Stuttgart, 2006, p 429–452
- 8.21 M. Braedel, H. Palaniswamy, and T. Altan, “Estimation of the Optimal Blank Holder Force and Forming Pressure Trajectory for Sheet Hydroforming Process with Punch,” Report ERC/NSM-05-R-21, ERC/NSM, The Ohio State University, Columbus, OH, 2005
- 8.22 N. Abedrabbo, M.A. Zampaloni, and D. Pourboghrat, Wrinkling Control in Aluminum Sheet Hydroforming, *Int. J. Mech. Sci.*, Vol 47 (No. 3), March 2005, p 333–358
- 8.23 L. Lang, J. Danckert, K. Nielsen, D. Kang, and S. Zhang, Key Technologies of the Simulation of the Hydrodynamic Deep Drawing of Irregular Parts, *J. Mater. Process. Technol.*, Vol 150, 2004, p 40–47
- 8.24 V. Vavilikolane, “Estimation of Optimum Process Parameters to Form a Rectangular Part Geometry by Sheet Hydroforming with Die (SHF-D) Process Using Finite Element Method,” Master’s thesis, The Ohio State University, Columbus, OH, 2005
- 8.25 P. Groche, R. Huber, J. Dorr, and D. Schmoeckel, Hydromechanical Deep Drawing of Aluminum Alloys at Elevated Temperatures, *CIRP Ann.*, Vol 51 (No. 1), 2002, p 215–218
- 8.26 S. Jäger, “Forming of Magnesium Sheet Metal,” Ph.D. dissertation, IFU, University of Stuttgart, 2005 (in German)
- 8.27 B.A. Behrens, G. Kurz, and S. Hubner, Heated Hydro-Mechanical Deep Drawing of Magnesium Sheet Metal, *New Developments in Sheet Metal Forming*, IFU-Stuttgart, 2004, p 379–398
- 8.28 M. Geiger, M. Celeghini, G. Haldenwanger, and M. Prier, Sheet and Tube Hydroforming at Elevated Temperatures, *Hydroforming of Tubes, Extrusions and Sheet Metals*, Vol 3, K. Siegert, IFU-Stuttgart, 2003, p 259–278
- 8.29 K. Dröder, “Analysis on Forming of Thin Magnesium Sheets,” Ph.D. dissertation, IFUM, University of Hanover, 1999 (in German)
- 8.30 C. Siebenwurst, S. Schwarz, M. Rupp, H. Rothe, and K. Schnupp, Production of a High Strength Steel Roof Outer Panel by AHU Hydromechanical Sheet Forming, *Hydroforming of Tubes, Extrusions and Sheet Metals*, Papers of the International Conference on Hydroforming in Fellbach (near Stuttgart), Germany, Vol 4, M. Liewald, Ed., 2005, p 37–58
- 8.31 T. Maki, Sheet Hydroforming of Automotive Body Panels, *Hydroforming of Tubes, Extrusions and Sheet Metals*, Vol 4, M. Liewald, Ed., 2005, p 187–202
- 8.32 J. Carsley, P. Krajewski, J. Schroth, and T. Lee, Aluminum Forming Technologies—Status and Research Opportunities, *New Developments in Sheet Metal Forming*, IFU-Stuttgart, 2006
- 8.33 F.R. Field, Lecture notes for “Introduction to Technical Cost Modeling Concepts and Illustrations,” Department of Material Science Engineering, MIT Open Courseware, Massachusetts Institute of Technology, Cambridge, MA, 2005, www.mit.edu

CHAPTER 9

Tube Hydroforming

Gracious Ngaile, North Carolina State University

TUBE HYDROFORMING (THF) is a material-forming process that uses a pressurized fluid in place of a hard tool to plastically deform a given tubular material into a desired shape (Fig. 9.1). At stage A, the tube is placed on the die cavity, the dies are closed, and the axial cylinders push the punches toward the tube end and seal the tube. Forming starts at stage B. Axial feed and increase in internal pressure are controlled simultaneously to improve the material-shaping capabilities. After the tube is completely formed (stage C), the punches are retracted and the part is ejected (stage D).

9.1 Applications

Tube hydroforming is widely used for making parts in the automotive and motorcycle/

bicycle industries, as well as for making components for sanitary use, such as faucets, and other household appliances, such as refrigerator handles and so on. Typical automotive parts that are produced using THF include exhaust manifolds, chassis parts, engine cradles, catalytic converters, radiator frames, and shock absorber housings. Figure 9.2 shows examples of parts made by THF for different applications.

Tube hydroforming offers several advantages compared to conventional manufacturing via stamping and welding (Ref 9.2):

- Part consolidation. For example, stamped and welded sections to form a box section can be formed as one single piece.
- Weight reduction through more efficient section design and tailoring of the wall thickness in structural components

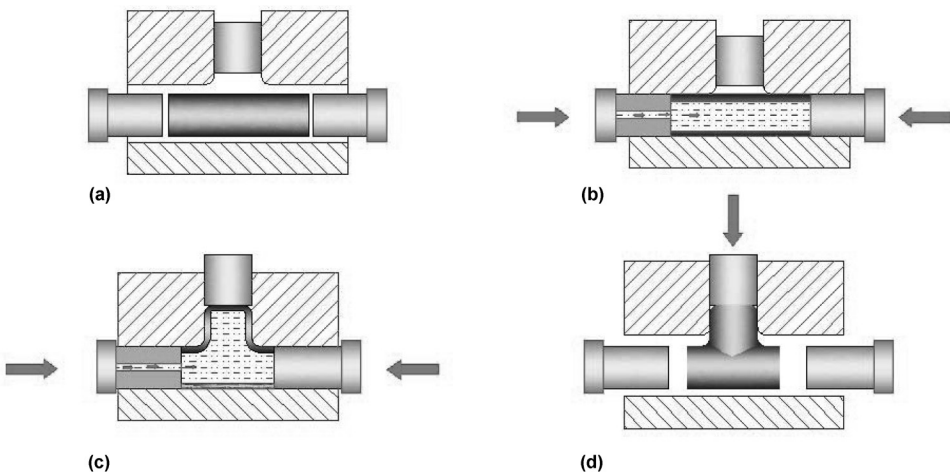


Fig. 9.1 Tube hydroforming process sequence

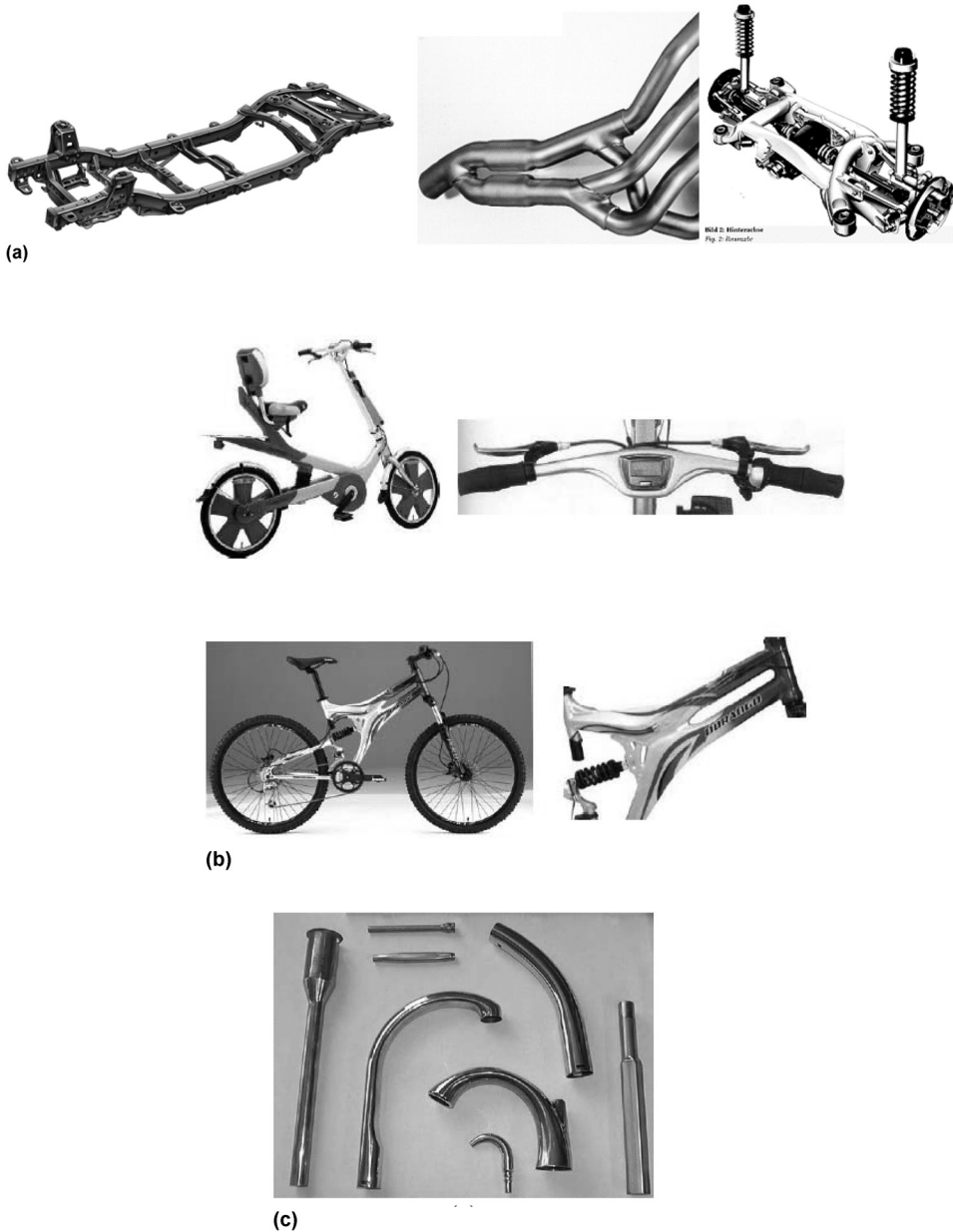


Fig. 9.2 Examples of parts made by tube hydroforming. (a) Automotive applications. (b) Motorcycle and bicycle applications. (c) Applications for household appliances. Source: Ref 9.1

- Improved structural strength and stiffness via optimized section geometry
- Lower tooling costs due to fewer parts
- Fewer secondary operations (less welding and punching of holes during hydroforming)
- Tighter tolerances and reduced springback, both of which facilitate assembly
- Reduced scrap, because trimming of excess

material is far less in THF than in stamping

The drawbacks of THF are the large cycle time and initial investment cost compared to stamping processes.

Tube hydroforming processes can be classified into various categories, as shown in Fig. 9.3.

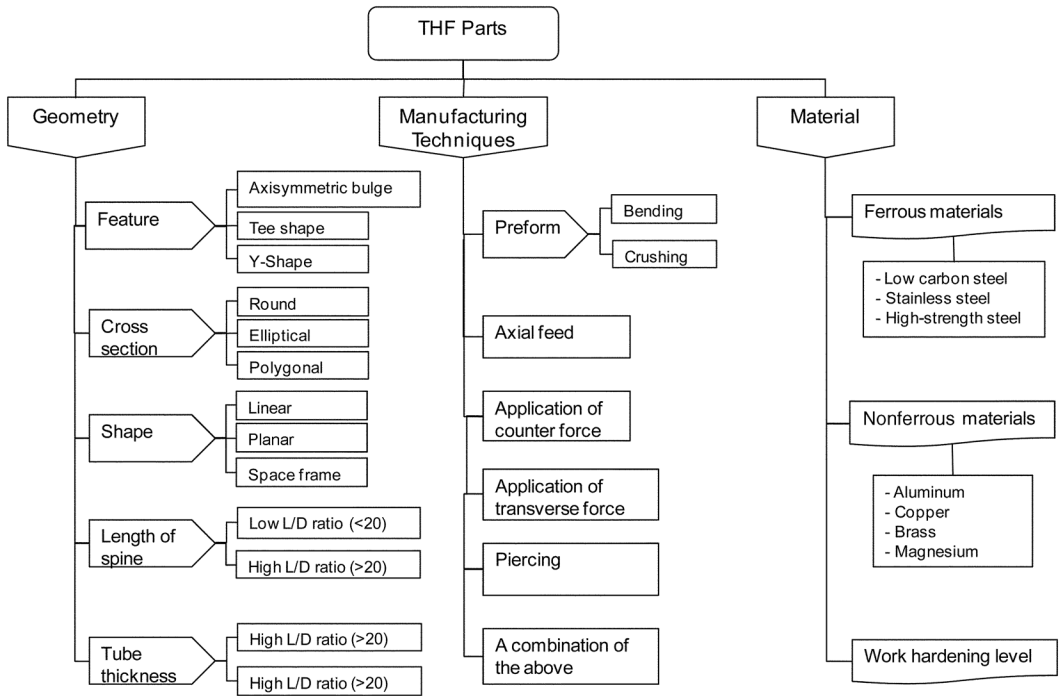


Fig. 9.3 Classification of parts and processes in tube hydroforming (THF)

9.2 Tube Hydroforming as a System

A fundamental understanding of all the system variables is essential for establishing a robust, productive, and cost-effective process technology. As shown in Fig. 9.4, the THF system comprises incoming material, preforming, tool-workpiece interface, tools and dies, deformation mechanics, equipment, and the hydroformed tubular part.

9.3 Materials for Tube Hydroforming

The quality of the incoming tube material is critical to the success of any THF process. Factors such as final properties of the part, forming process, and potential failure during deformation play an important role in the selection of materials.

Variation of tube material properties or variation in wall thickness may result in premature fracture. Of equal importance is the surface texture/morphology of the tube, which can have a drastic influence on lubrication mechanisms. Any tube material with good formability can be

used in THF. Formability can also be enhanced by conducting THF at elevated temperature. Steel and aluminum alloys are widely used in manufacturing products for the automotive, aerospace, and motorcycle/bicycle industries. Brass and copper alloys are typical material for THF products for piping and household appliances. Steel and aluminum alloys commonly used in THF are listed in Table 9.1 (Ref 9.4–9.6).

Other materials that are becoming common in THF include advanced high-strength steels (dual phase) and magnesium alloys. The latter can be hydroformed only at elevated temperatures.

The manufacturing processes for tubular materials used in THF can be divided into two groups: seamless (mainly aluminum and copper alloys) and welded tubing (steels). Seamless tubes (aluminum or copper alloys) are produced mainly by extrusion, whereas steel tubes are produced by roll forming and welding. The design of the roll forming sequence affects the strain distribution in the tube, in the circumferential direction. The resulting circumferential nonuniformity of strain may affect formability in THF (Ref 9.7, 9.8).

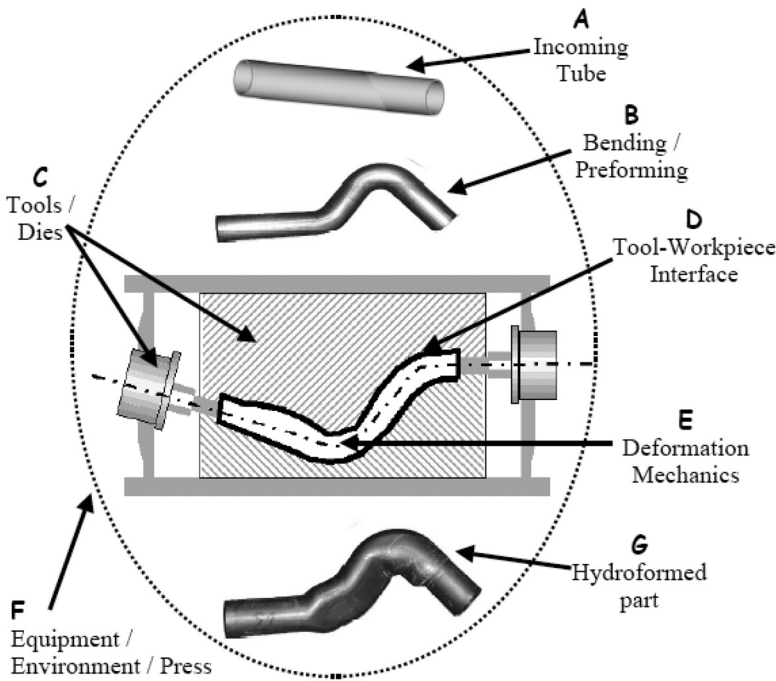


Fig. 9.4 Hydroforming system components. Source: Ref 9.3

Table 9.1 Steel and aluminum alloys used in tube hydroforming

Steel alloys	Aluminum alloys
AISI 1008, 1010, 1015, 1020, 1055; SS 304, 409	Al 5005, 5056, 6020-T4, 6022-T4, 6061-T4, 6064-T4, 7075, 6082

The welding seam introduces inhomogeneity in the tube. However, in general, good quality welding does not affect THF. Aluminum tubing for THF can be produced by either roll forming or extrusion, depending on the type of the alloy. Usually, 5000-series alloy tubes are produced by roll forming and 6000-series by extrusion (Ref 9.9).

Flow Stress and Formability. A complex part can be hydroformed if the incoming tubular material has sufficient formability. When a tubular material is plastically deformed, it strain or work hardens, which enhances formability. Before THF is carried out, the tubular preform often undergoes bending and, in some cases, crushing operations. All these deformation steps further consume tube formability. Quantification of formability is therefore important for determining the feasibility of hydroforming a part without failure.

There are various methods that are used to determine tube formability, namely, the tensile test, ring hoop test, tube bulge test, and cone test. The schematics of these tests are given in Fig. 9.5 and 9.6.

The elongation obtained in a tensile test can be used to quantify the formability of tube material. When using the tensile test, it is important to use specimens cut from a tube to account for the formability that has been consumed in the tubemaking process. Taking specimens at different locations along the cross section helps to determine the variation in the material characteristics along the tube circumference. Experimental studies have shown that tubes produced by roll forming exhibit a significant degree of anisotropy (Ref 9.10). One of the drawbacks of the tensile test is that the curved specimens cut from the tube must be flattened prior to the test, which affects formability. The hoop test was developed to eliminate this drawback (Fig. 9.5b). Although the hoop test gives a good indication of formability, the test setup can be used only for a specific tube size. The quantification of tube formability using the hydraulic bulge test (Fig. 9.6) is based on the maximum bulge height the tube can attain at a specific hydraulic pres-

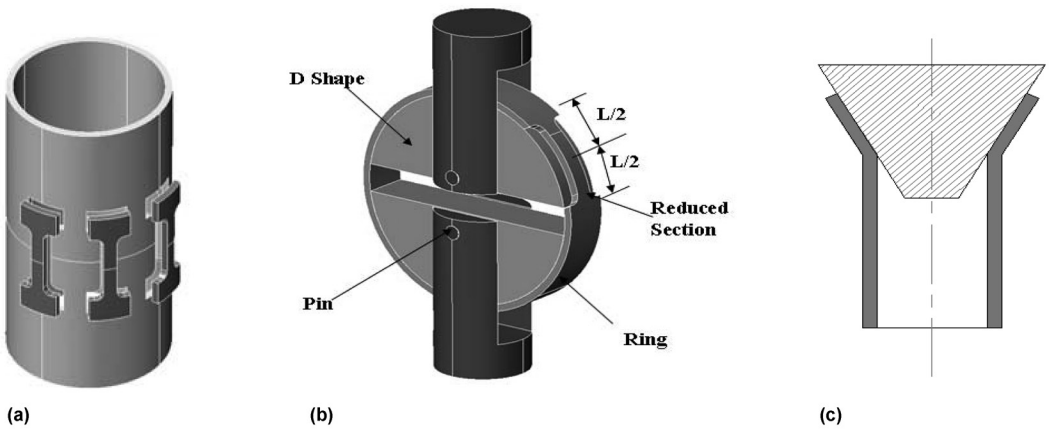


Fig. 9.5 Formability tests. (a) Tensile test. (b) Hoop test. (c) Cone expansion test

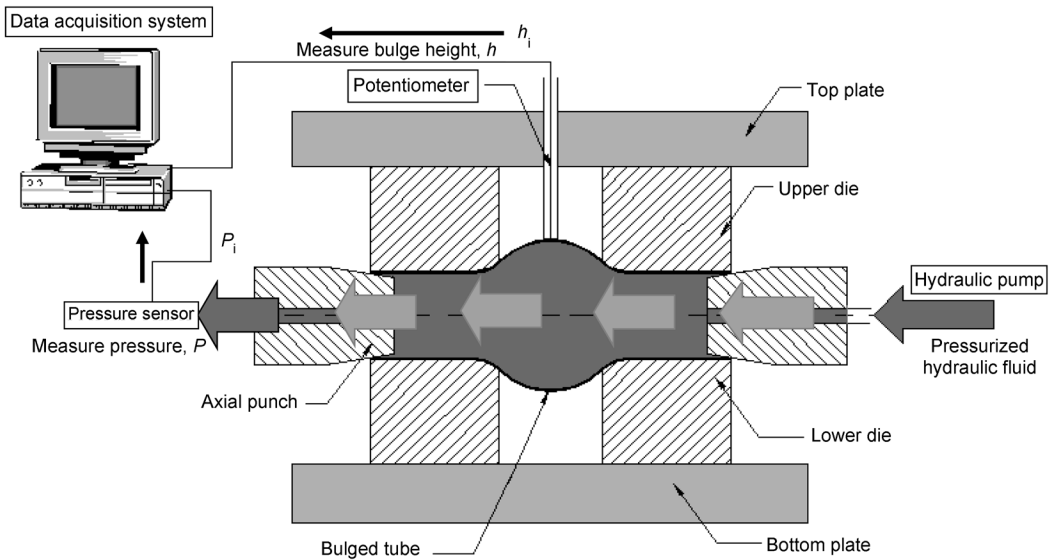


Fig. 9.6 Schematic of the hydraulic bulge test tooling for determining formability of tubular materials. Source: Ref 9.5

sure. The burst pressure can also be used to quantify the formability of the tube. In the cone expansion test (Fig. 9.5c), a tube is bulged at the end of the tube using a conical punch until fracture. The cone geometry obtained is a measure of tube formability. However, because friction is present at the cone-tube interface, the results must be interpreted carefully.

The accurate measurement of the flow stress of tubular materials is necessary for preparing material input data for the finite-element simulation of THF. For this purpose, in addition to tensile tests, the biaxial tube bulge tests are used

(Fig. 9.7 and 9.8). In conducting the tube bulge test, it is necessary to measure only the pressure and the corresponding maximum bulge diameter (Ref 9.5).

The flow stress of materials used in computer modeling is often expressed as a power law given by:

$$\bar{\sigma} = K(\bar{\epsilon}_0 + \bar{\epsilon})^n \tag{Eq 9.1}$$

To determine the quantities given in Eq 9.1, start by taking the equilibrium of forces at the apex of the bulge (Fig. 9.7), which will result in

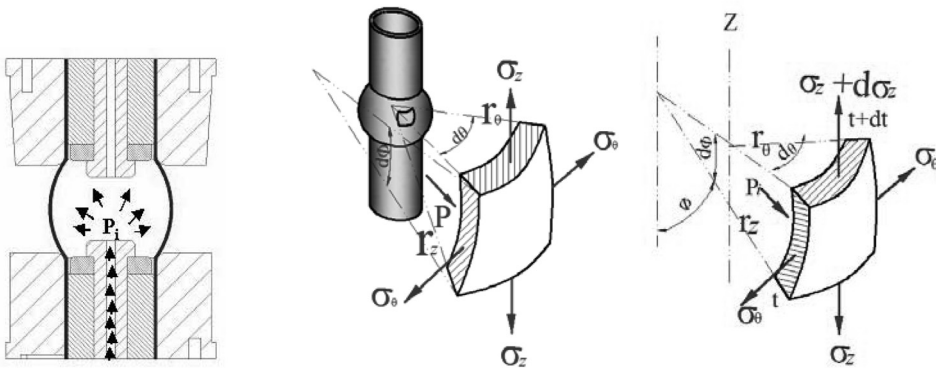
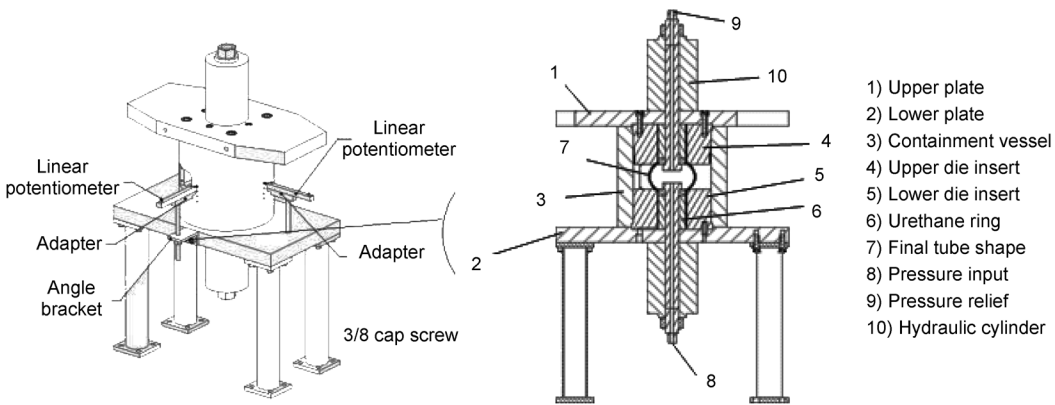


Fig. 9.7 Schematic of bulge test and state of stress



- 1) Upper plate
- 2) Lower plate
- 3) Containment vessel
- 4) Upper die insert
- 5) Lower die insert
- 6) Urethane ring
- 7) Final tube shape
- 8) Pressure input
- 9) Pressure relief
- 10) Hydraulic cylinder

Fig. 9.8 Schematic of bulge test setup. Source: Ref 9.11

Eq 9.2. Taking σ_z as a subject, the longitudinal stress can be obtained (Eq 9.3):

$$\frac{P_i}{t} = \frac{\sigma_\theta}{r_\theta} + \frac{\sigma_z}{r_z} \tag{Eq 9.2}$$

$$\sigma_z = \left(\frac{P_i}{t} - \frac{\sigma_\theta}{r_\theta} \right) r_z \tag{Eq 9.3}$$

where t is the thickness of the bulged tube, and r_θ and r_z are the radii of curvature in the hoop and longitudinal directions, respectively. Because the tubes used in THF usually have thin walls (the diameter-to-thickness ratio does not exceed 10), membrane theory can be used. By using the flow rule, the hoop and longitudinal stresses can be related to the hoop and longitudinal strains as in Eq 9.4. By combining Eq 9.3 and 9.4, the hoop stress can be expressed in

terms of known quantities obtained from the hydraulic bulge test (Ref 9.12). The hoop stress is given by Eq 9.5:

$$\frac{\epsilon_\theta}{\sigma_\theta - \frac{1}{2}\sigma_z} = \frac{\epsilon_z}{\sigma_z - \frac{1}{2}\sigma_\theta} \tag{Eq 9.4}$$

$$\sigma_\theta = \frac{pr_\theta r_z}{t} \left(\frac{1 + 2\frac{\epsilon_\theta}{\epsilon_z}}{2r_\theta + r_z + \frac{\epsilon_\theta}{\epsilon_z}(2r_z + r_\theta)} \right) \tag{Eq 9.5}$$

The thickness strain can be obtained by relating the original tube thickness and the instantaneous thickness of the tube (Eq 9.6). The hoop strain can be determined from the change in the diameter (Eq 9.7). Using volume constancy, the longitudinal strain can be established (Eq 9.8). Using von Mises yield criteria, the effective

stress and strain can now be determined at any given pressure using Eq 9.9 and 9.10, respectively:

$$\epsilon_t = \ln\left(\frac{t_1}{t_0}\right) \tag{Eq 9.6}$$

$$\epsilon_\theta = \ln\left(\frac{r_\theta}{r_0}\right) \tag{Eq 9.7}$$

$$\epsilon_z = -(\epsilon_\theta + \epsilon_t) \tag{Eq 9.8}$$

$$\bar{\sigma} = \sqrt{\sigma_\theta^2 - \sigma_\theta\sigma_z + \sigma_z^2} \tag{Eq 9.9}$$

$$\bar{\epsilon} = \sqrt{\frac{2}{3}(\epsilon_\theta^2 + \epsilon_z^2 + \epsilon_t^2)} \tag{Eq 9.10}$$

By carrying out the hydraulic bulge test at different pressure levels using several tube samples and by determining effective stress and effective strain at each pressure level, a flow-stress curve can be plotted. Using the least square fit, the material strength coefficient, K , and strain-hardening coefficient, n , can be obtained. The effective prestrain, $\bar{\epsilon}_0$, given in Eq 9.1, accounts for the consumed formability during tubemaking. A schematic of hydraulic bulge tooling and the major components is shown in Fig. 9.8. The tooling system consists of two hydraulic cylinders at the upper and lower die. Each hydraulic cylinder provides a force to compress a urethane plug, to seal and lock both ends of the tube. As an example, Fig. 9.9 shows a flow-stress curve for SS 304 obtained from the bulge test. Table 9.2 shows material flow stress

determined by the hydraulic bulge test for three metals.

9.4 Tube Bending

Figure 9.10 shows typical THF parts that require bending or preforming prior to hydroforming. When the geometry of the bent tube is designed correctly, not only can the tube be easily oriented into the hydroformed die cavity, but also the quality of the formed part can be improved (Ref 9.14). More importantly, correct design of the geometry of the bend will reduce local consumption of material formability, which is critical for the success of THF.

Characteristics of the Tube-Bending Process. During bending, the tube wall at both edges will tend to move toward the centerline of the tube, and consequently, the cross section of the circular tube will become oval. This phenomenon is generally referred to as flattening or collapse of the tube (Fig. 9.11). As the tube is bent, the outer wall (extrados) and inside wall (intrados) undergo tensile and compressive stresses,

Table 9.2 Material flow stress ($\bar{\sigma} = K(\epsilon_0 + \bar{\epsilon})^n$) determined by the hydraulic bulge test

Material	Strength coefficient, K		Prestrain, ϵ_0	Strain-hardening exponent, n
	MPa	ksi		
Low-carbon steel, LCS 1008	589	85	0.028	0.28
Aluminum alloy, AA 6260-T4	301	44	0.011	0.19
Stainless steel, SS 304	1323	190	0.055	0.62

Source: Ref 9.13

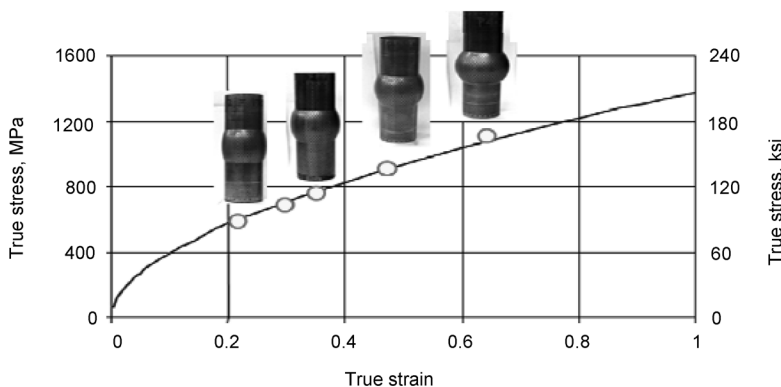


Fig. 9.9 Flow-stress curve for SS 304, obtained using the hydraulic tube bulge test. Source: Ref 9.5

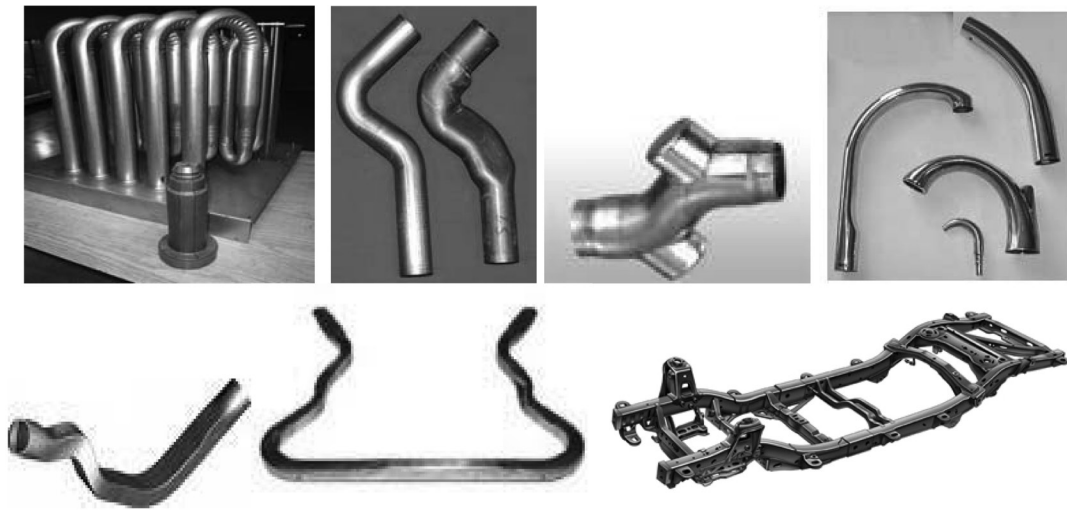


Fig. 9.10 Tube hydroformed parts that require preforming

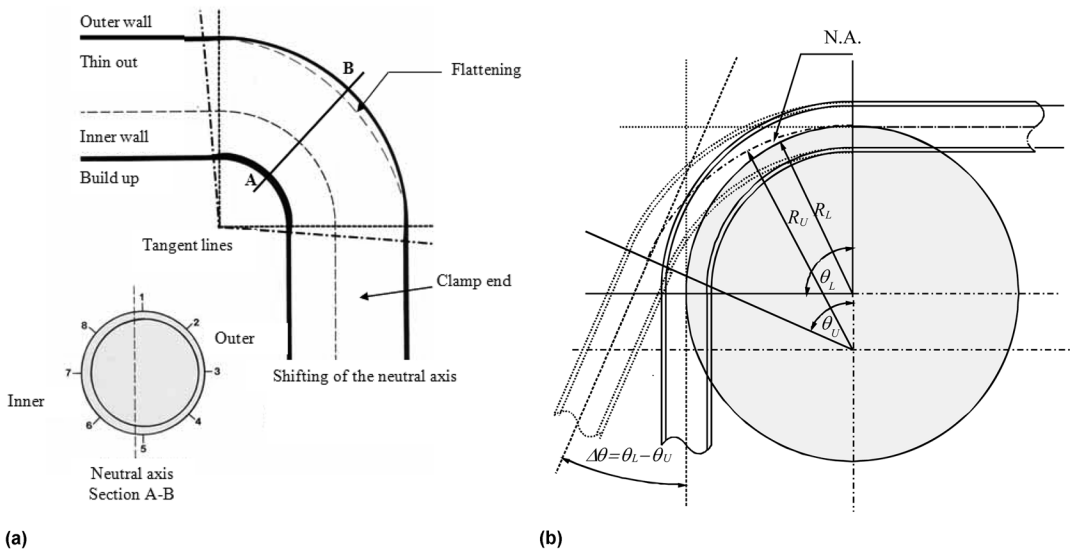


Fig. 9.11 (a) Thickness distribution around and along the cross section of the bent tube. (b) Springback. Source: Ref 9.15

respectively. These stresses result in wall thinning at the outer wall and thickening at the inner wall.

Also, during the bending process, the neutral axis will shift toward the intrados. The higher the ratio of tube radius to bending radius, the higher the thickening and thinning ratio becomes. Because the neutral axis shifts toward the intrados, the length of the centerline is larger than the original neutral axis, and the total length of the tube after bending is therefore larger than that of the original tube.

Because of the nonuniform stress distribution across the bent section, springback is bound to occur when the bending load is removed. Springback will cause the bending radius and bending angle to increase. The springback effect can be compensated by overbending the tube. For THF preforms that require several bends in series, geometrical errors pertaining to springback will accumulate, and the total error will thus be magnified. Under these circumstances, accuracy in springback prediction becomes crucial.

Tube-Bending Defects. There are four main categories of defects that may occur in tube bending: wall thinning, ovality, buckling, and surface defects. The first three are largely associated with the evolution of tensile stresses at the extrados and compressive stresses at the intrados during the bending operation. Before the tensile stress at the extrados reaches the ultimate tensile strength, compressive stresses at the intrados reach the buckling point and cause the tube to collapse. When the collapse of the tube is not severe, only the shape of the cross section is changed, and there is no serious effect on the appearance and strength of the part. However, if the tube is subjected to excessive compressive stresses, buckling and wrinkling may occur at the intrados, and high thinning and flattening may occur at the extrados. The tendency for buckling to occur is more severe for thin-walled tubing and smaller bend radii. Most of the surface defects are caused by markings left by the clamping dies or insufficient lubrication between the tube and the mandrel. Some of the defects can be prevented by selecting an appropriate bending method.

Bending Methods. The various tube-bending methods can be categorized into four groups: rotary draw bending, compression bending, ram bending, and press bending (Fig. 9.12).

In rotary draw bending, the tube is clamped before the front tangent point, and the tube is drawn into the die by the clamp (Fig. 9.12a). The tools move/rotate with the tube, and there is no relative movement between the tooling/workpiece surfaces. Draw bending is the most common method in industry. This type of bending has the largest variety of tooling options and offers the best quality and accuracy, particularly for tight radii and thin-walled tubes. With the improvement of digital technology, most rotary bending machines use computer numerical control to improve accuracy and repeatability (Ref 9.16).

In compression bending (Fig. 9.12b), a rotary arm is used to compress the tube onto the die surface. The tube is clamped behind the rear tangent point. All the tooling parts and the tube remain stationary except the rotary arm. This bending method is simpler and cheaper than rotary draw bending. However, the quality of the bend, as measured by such factors as ovality and wall thinning, is inferior to that obtained in draw bending. Compression bending is particularly suitable for tubes with large wall thicknesses and small tube radii.

Ram bending (Fig. 9.12c) is one of the oldest and simplest methods of mechanical bending. This bending process has many limitations, such as the minimum achievable radii compared with other bending methods. However, the advantage of this method is that a large-diameter pipe can be bent at a relatively low cost.

Press bending (Fig. 9.12d) is another variation that is essentially a combination of ram and compression bending techniques.

Rotary Draw Bending. The rotary draw bending method (Fig. 9.12a) is the tube-bending method most commonly used in industry (Ref 9.16, 9.17). Figure 9.13 shows a rotary draw bending machine and a list of major components. The rotary draw bending process uses multiple dies that have been designed primarily to control the tensile and compressive stresses occurring at the extrados and intrados. As a result, severe flattening, wall thinning, buckling, and wrinkling can be avoided.

The bend die determines the radius of bend. The circumferential groove on the bend die gives external support to the workpiece along the inside of the bend and provides a means to confine the compressive stresses incurred in the material during bending. The straight section of the bend die can hold the tube with pressure applied by the opposing clamp die. In the rotary draw bending process, tubes are held by the clamp just beyond the front tangent point. The tube is drawn onto the die surface with the aid of a swing arm.

The clamp die should give enough clamp force to hold the tube in position, and it should be wide enough to provide good gripping of the tube. In severe situations, such as when a tube with very thin wall thickness is bent into a small radius, it is necessary to use a mandrel and a wiper die. Interfaces between the tube and these components will increase the friction/drag forces significantly. Thus, higher clamp force is needed to draw the tube onto the bend die surface and hold the tube in position. When the clamp cannot offer enough force to draw the tube into the deformation area, slip will occur and cause the tube to undergo excessive buckling. Higher clamping force can provide higher drawing force to hold the tube in position. However, excessive clamping force may crush the tube. To avoid tube crushing, a clamp plug may be inserted to give internal support.

The pressure die is used to hold the unbent tube in position. With the pressure acting on the tube surface, the tube can be closely attached to

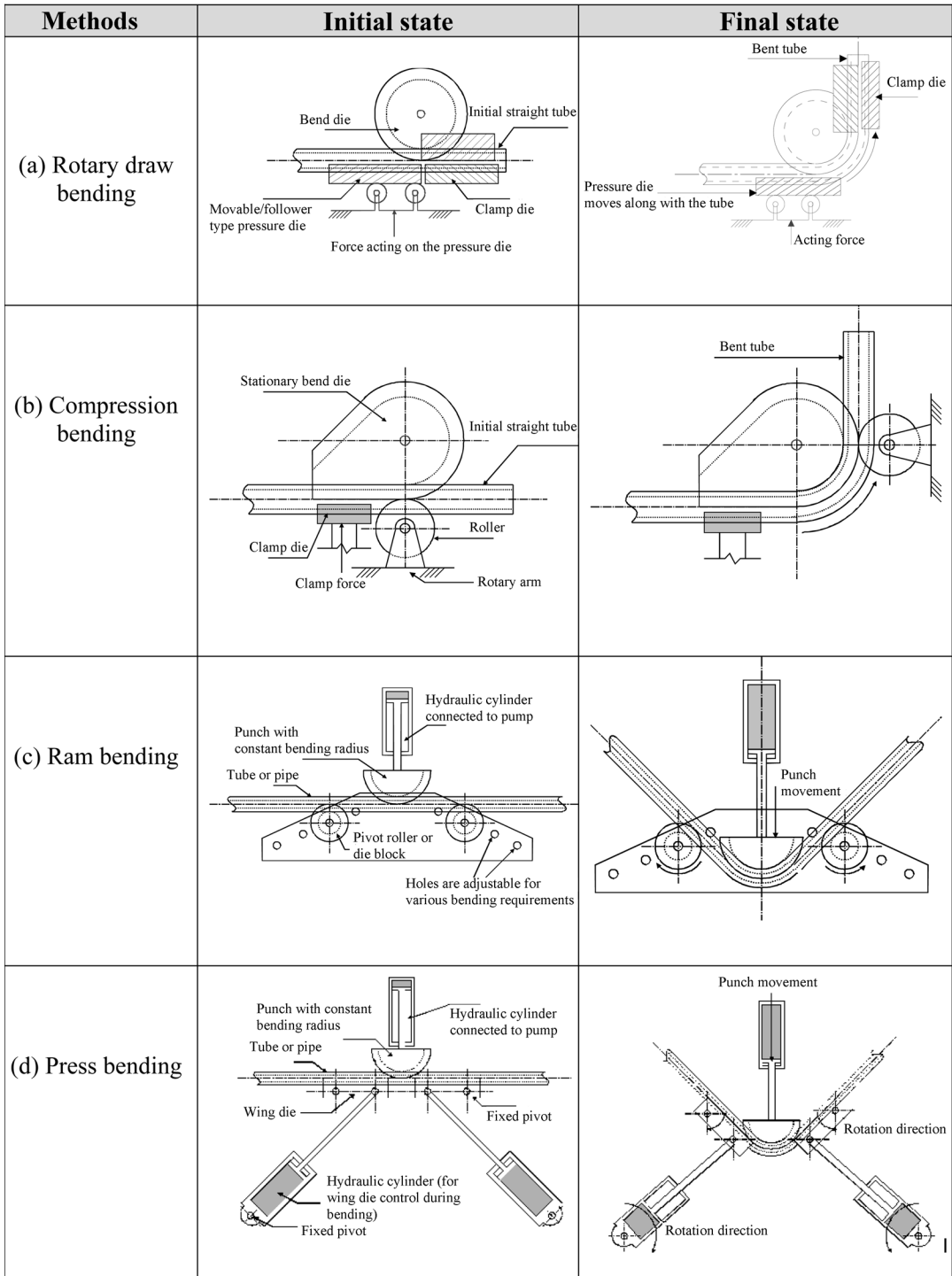


Fig. 9.12 Schematics of bending methods. Source: Ref 9.15

the bend die surface. When the tube is drawn into the deformation area with a static pressure die, the bender must overcome the friction force coming from the static pressure die. The roller-type pressure die eliminates the friction force at the interface. By placing a mandrel inside the tube, the ovality of the tube can be reduced significantly. In addition, the mandrel can transfer the force of the pressure die to the inner wall of the bend to prevent wrinkling occurring at the intrados. For bending very thin tubular material, the mandrel can sometimes function as a sizing tool. Thus, the wrinkles can actually be ironed out during the bending operation by stroking the mandrel. When bending thin-walled tubing to a tight radius, the tube may buckle into a bump or series of wrinkles at the intrados.

Adding a wiper die fitted into the peripheral surface between the bend die and the tube near the tangent line can control the tendency toward wrinkling. The wiper die can absorb the force from the pressure die and confine the metal flow to a smooth surface. However, the wiper die cannot wipe out existing wrinkles, only prevent their initial formation. Because the wiper die is wiping against both the tube and the bend die, the tip can be worn out after a certain number of bends, so good lubrication is necessary.

Because tube bending is a preforming operation, knowing how much material formability remains on the bent tube is essential to assess whether the hydroforming operation will be successful. For simple bending of a circular tube, thickness distribution can be determined by the analytical relationship given in Eq 9.11 and 9.12 (Ref 9.20):

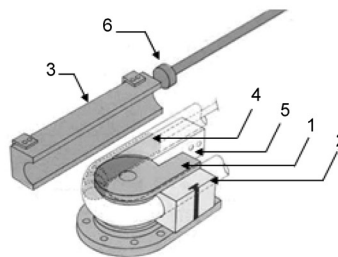
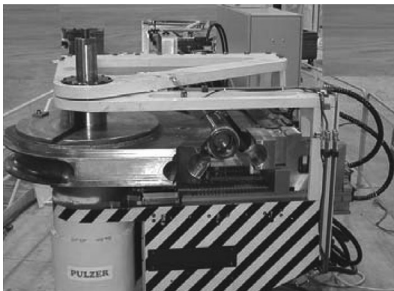
$$t = \frac{1}{\sqrt{1+k \sin \theta}} \cdot t_0 \quad (\text{Eq 9.11})$$

$$\text{Thinning}(\%) = \frac{t-t_0}{t_0} = \left(\frac{1}{\sqrt{1+k \sin \theta}} - 1 \right) \cdot 100\% \quad (\text{Eq 9.12})$$

where $k = r/R$ is the ratio of the tube radius to the bending radius, t is the tube wall thickness, t_0 is the initial tube wall thickness, and θ is the degree of bend. For a complex bending operation, the finite-element method will provide a more accurate thickness distribution. Figure 9.14 shows the thickness distribution on the middle cross section of a 90° bend. The comparison between finite-element simulation results and analytical calculations shows good agreement. Material properties and dimensions used for the bending analysis are given in Table 9.3. The wall thinning at the extrados is 7%, and wall thickening at the intrados is 8.8%.

9.5 Mechanics of Tube Hydroforming

The mechanics of hydroforming can be examined by considering a bulge-shaped part, shown in Fig. 9.15. To form this part successfully, accurate loading paths, that is, internal pressure and axial feeding-versus-time profiles, must be used. An accurate loading path should fall within the hydroforming process control limits shown in Fig. 9.16. Any deviation from the forming zone process window will lead to part failure (e.g., wrinkling, folding, buckling, and bursting). Both wrinkling and bursting failures are related to limits pertaining to the local state of stress and strain. The local state of stress also varies with process time. There are theories and methods that can be used to determine the correlation between forming load, stress state, and strain (Ref 9.21–9.27).



1. Bend die
2. Clamp die
3. Pressure die
4. Mandrel
5. Wiper die
6. Pressure die assistance

Fig. 9.13 Draw bending machine. Source: Ref 9.18, 9.19

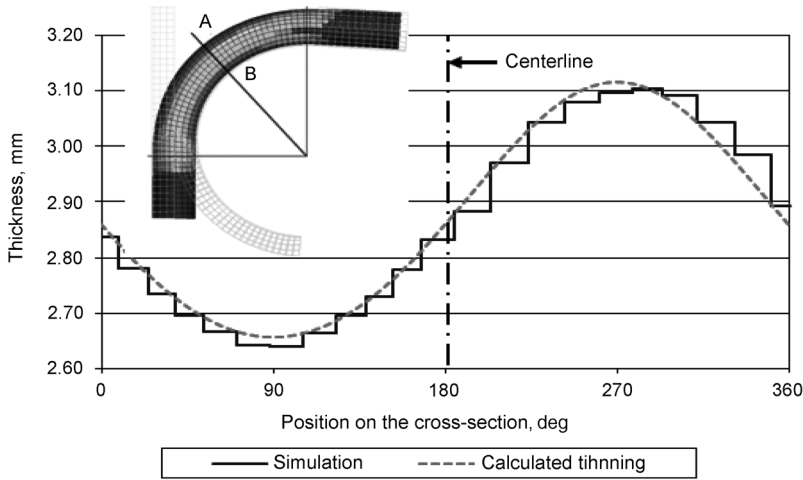


Fig. 9.14 Tube wall thickness distribution on the middle cross section (A-B) of a 90° bend. Source: Ref 9.15

Table 9.3 Tube dimensions and material properties, used in the simulation given in Fig. 9.14

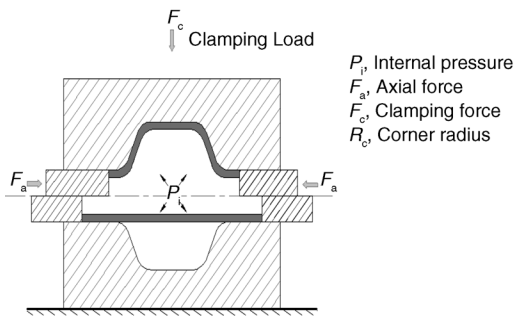
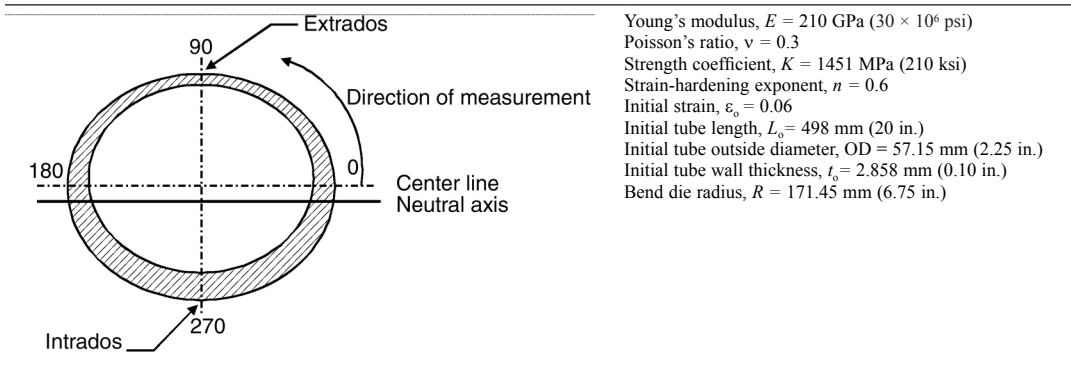


Fig. 9.15 Example of a simple hydroformed part

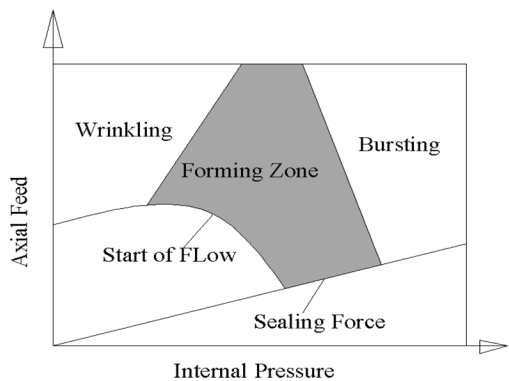


Fig. 9.16 Tube hydroforming process control limits

The majority of existing solutions for modeling hydroforming processes are based on (Ref 9.9):

- Membrane theory, which assumes thin-walled structures with constant stresses over the thickness and negligible bending stress
- Shell theory, which, in addition to the normal force and shear forces, considers transverse forces, bending moment, and twisting moment within the surface structure

- Continuum theory of plasticity, which enables the correlation between the state of stress and resulting strain rate of ductile continuum to be described
- Finite-element modeling, which discretizes the structure into a number of finite elements. Finite-element simulation examples on the determination of loading paths are given in section 9.8, “Tube Hydroforming Process Design and Design Guidelines,” in this chapter.

The strain state at the apex of the bulged part as calculated using membrane theory is shown in Fig. 9.17.

Under the assumption that the volume is constant, the sum of the three strain components is zero:

$$\epsilon_\theta + \epsilon_\phi + \epsilon_t = 0 \tag{Eq 9.13}$$

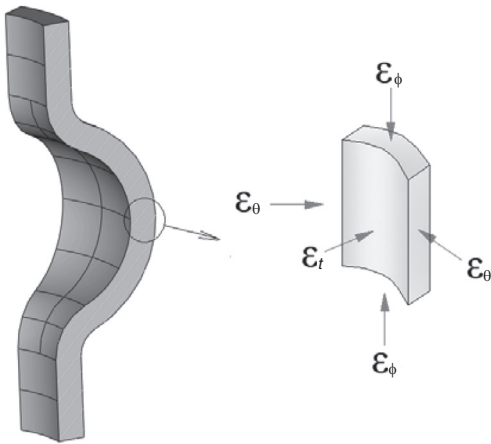


Fig 9.17 State of strain on the bulge shape

where ϵ_θ is the strain in the hoop direction, ϵ_ϕ is the strain in the longitudinal direction, and ϵ_t is the strain in the thickness direction.

The hoop strain can be given by:

$$\epsilon_\theta = \ln \frac{r_\theta}{r_{\theta_0}} \tag{Eq 9.14}$$

where r_θ is the instantaneous bulge radius, and r_{θ_0} is tube radius prior to deformation.

The thickness strain is given by:

$$\epsilon_t = \ln \frac{t}{t_0} \tag{Eq 9.15}$$

where t is the instantaneous bulge thickness, and t_0 is the original tube thickness. The state of the stress at the apex of the bulge shape is similar to the state of stress given in Fig. 9.7. Thus, the relationship among the instantaneous fluid pressure, P_i , the hoop stress, σ_θ , and the longitudinal stress, σ_z , can be obtained from Eq 9.2 as follows:

$$\frac{P_i}{t} = \frac{\sigma_\theta}{r_\theta} + \frac{\sigma_z}{r_z} \tag{Eq 9.16}$$

where t is the thickness of the bulged tube, and r_θ and r_z are radii of curvature in the hoop and longitudinal directions, respectively. When r_z is very large compared to r_θ , the second term in Eq 9.16 vanishes. Hence, P_i becomes a function of t , σ_θ , and r :

$$P_i = \frac{t\sigma_\theta}{r_\theta} \tag{Eq 9.17}$$

From the bulge shape shown in Fig. 9.18, the forces F_a acting on the punch can be determined.

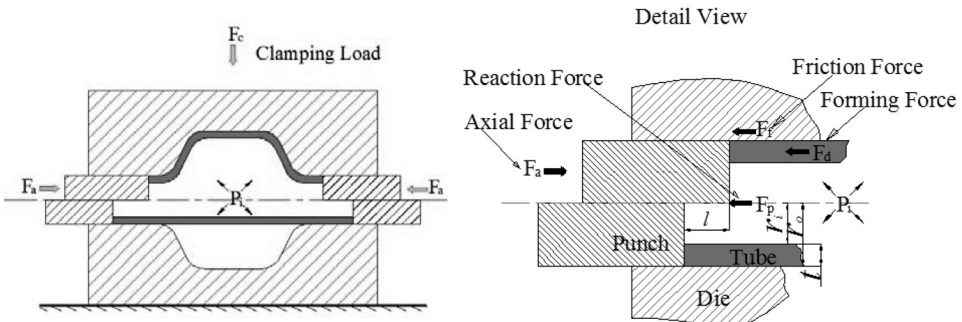


Fig. 9.18 Components of punch force in tube hydroforming

A close-up view of the interface between the punch and the deforming tube shows that the forces acting on the punch are a result of three force components, F_p , F_f , and F_d :

$$F_a = F_p + F_f + F_d \tag{Eq 9.18}$$

where F_p is the force acting on the punch due to the fluid pressure inside the tube, F_f is the friction force, and F_d is the tube forming force.

The force F_p can be determined by:

$$F_p = \pi(r_o - t)^2 p_i \tag{Eq 9.19}$$

where r_o is the tube outer radius, and t is the thickness of the tube.

The friction force F_{pf} can be determined by:

$$F_f = A\tau_s = \frac{2}{\sqrt{3}} \pi r_l l m \sigma_f \tag{Eq 9.20}$$

$$\tau_s = mk = \frac{m}{\sqrt{3}} \sigma_f$$

where τ_s is the shear stress exhibited at the tube-die contact surface; m is the friction factor, which varies from 0 to 1; σ_f is the yield stress of the tube materials; k is the shear strength of the tube material; and l is the effective length the punch has traveled.

The tube deformation force F_d is determined by:

$$F_d = \pi(r_o^2 - r_i^2) \sigma_z \tag{Eq 9.21}$$

where σ_z is the longitudinal stress acting on the tube ends. It should be noted that the clamping load, F_c , is obtained by multiplying the maximum pressure with the projected area. This value determines the press capacity to be used.

The previous discussion has shown the relationship between the variables in THF of a simple bulge shape. For complicated THF parts, closed-form solutions are difficult to obtain. Thus, numerical solutions via the finite-element method are often used to determine parameters of interest in the design of THF processes.

9.6 Friction and Lubrication in Tube Hydroforming

As the tube material flows into the die cavity (Fig. 9.19), due to axial feeding and fluid pressure, P_f , a pressure is built up at the interface,

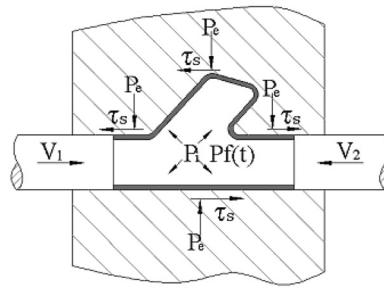


Fig. 9.19 Die-workpiece interface variables at macro scale for tube hydroforming

P_e , and a shear stress, τ_s , is generated by friction. Depending on part geometry and variation in the fluid pressure, the interface pressure (P_e) and shear stress will vary locally along the interface. To obtain a sound THF part, an optimal combination of fluid pressure, P_i , tube feeding velocity, V , material characteristics (flow stress), and tribological conditions must be achieved.

Coulomb's law is given by $\tau = \mu P$. The shear friction law is given by:

$$\tau = mk = \frac{m}{\sqrt{3}} \bar{\sigma}$$

where τ is the friction shear stress, μ is the coefficient of friction, P is the interface pressure, σ is the flow stress of the tube material, k is the shear strength of the tube material, and $0 < m < 1$.

Parameters That Influence Friction, Lubrication, and Wear in THF. The variables that affect lubrication, friction, and wear in THF can be subdivided into three groups, as seen in Fig. 9.20:

- *Interface pressure:* A change in the interface pressure affects the friction stress as well as the viscosity of the lubricant, the surface contact morphology, and the lubricant film thickness (Fig. 9.21).
- *Surface expansion/contraction:* Surface expansion during deformation leads to generation of virgin surfaces and change in surface morphology. This causes thinning and breakdown of the lubricant film and may accelerate the chemical reactivity of the lubricant on the newly generated surfaces. On the other hand, surface contraction may cause lubricant film delamination or change the surface pocket volume size and morphology (Ref 9.29, 9.30).

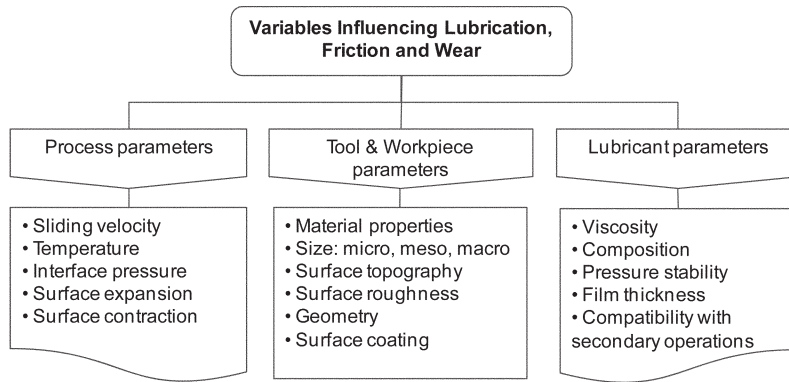


Fig. 9.20 Parameters that influence friction, lubrication, and wear in tube hydroforming

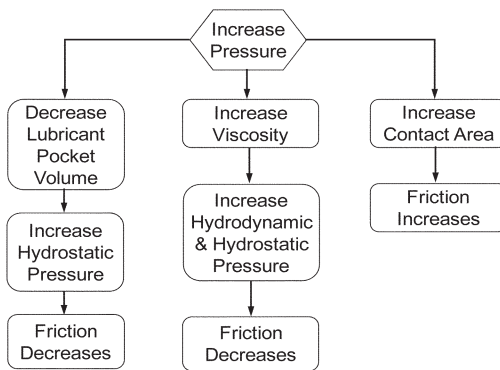


Fig. 9.21 Effect of increased interface pressure on friction. Source: Ref 9.28

- *Sliding velocity*: Sliding between the die and the deforming material will generate frictional heat. As a result, lubricant rheology will be changed, flow stress of the surface asperities and subsurface material will be decreased, and chemical reactivity between the deforming material and the lubricant will increase (Fig. 9.22).

Friction Zones and Characteristics. In a typical THF process, three different friction zones are observed: the guiding zone, transition zone, and expansion zone (Fig. 9.23) (Ref 9.31, 9.32). In the guiding zone, the workpiece and the die are in full contact, and material deformation is limited to wall thickening. However, the material is pushed into the deformation zone by means of axial cylinders. Most THF processes require the material to be fed toward the expansion zone. Therefore, depending on the geometry of the part, a high relative sliding velocity

(50 to 100 mm/s) between the workpiece and die may be present.

Because of the difference in the local state of stress and material deformation modes in various friction zones, the tribological conditions will differ and thereby lead to different lubrication mechanisms. This fact poses a challenge in developing lubricants or lubrication systems that will be effective in all friction zones. Concerning lubrication and friction, the most important friction zone in THF is the guiding zone. Thus, lubrication in this zone is critical for a successful THF operation.

Experiments using guiding zone tests to evaluate lubricants have shown that very low values of the coefficient of friction (on the order of $\mu = 0.02$ or lower) may occur (Ref 9.33). To understand possible lubrication mechanisms at the guiding zone, microscopic surfaces can be treated as composed of surface asperities, which form peaks and valleys. The surface valleys can act as lubricant retainers.

In contrast, at the boundaries of the expansion zone, lubricant trapped at the interface can escape as a consequence of multiple die-workpiece clearances as the tube gradually establishes contact with the die when the pressure increases.

One practical method of reducing friction and increasing formability is to hydroform, for example, T-shapes, by using pulsating pressure (Ref 9.34).

9.7 Presses and Tooling

The main functions of hydroforming equipment are to close the die set, provide clamping load during forming, pump high fluid pressure

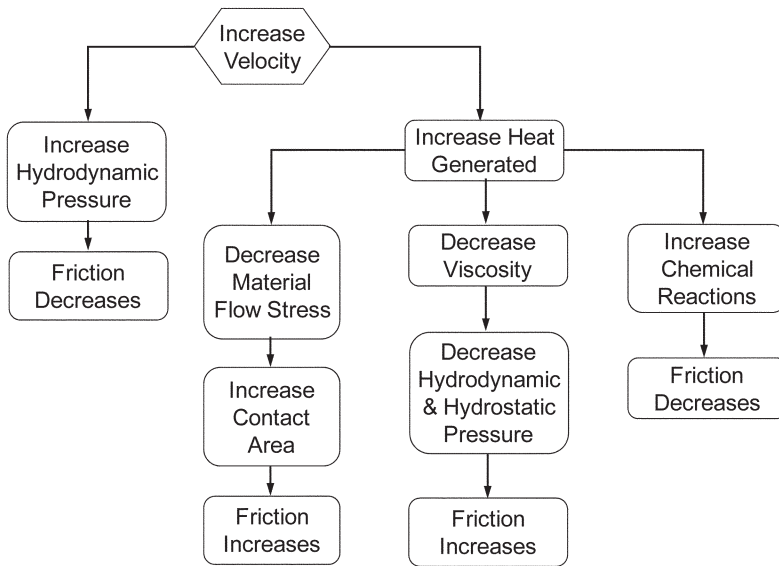


Fig. 9.22 Effects of increased sliding velocity on friction. Source: Ref 9.28

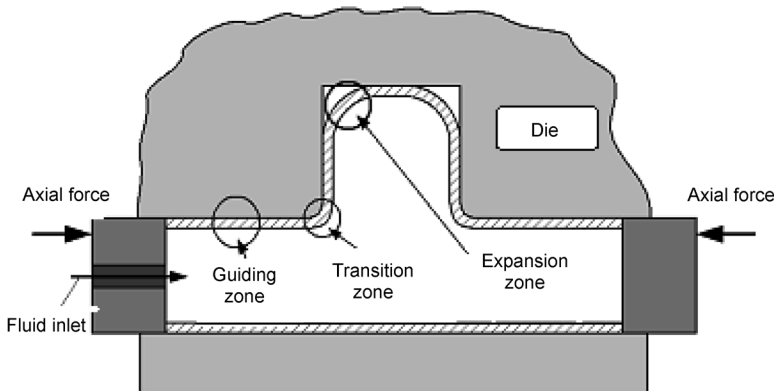


Fig. 9.23 Friction zones in tube hydroforming

into the tube, and transmit the axial force to the tube ends to feed the material. Tube hydroforming equipment comprises a press, tooling, a hydraulic pressure intensifier, and a control system. Hydraulic presses are typically used in THF, and their main function is to provide the die clamping force. The tooling for THF consists of upper and lower dies, piercing punches, ejectors, and axial cylinders that provide the force to feed the material to the die cavity. The control system is used for press closure sequencing, part sealing, part feeding, pressure intensification, piercing operation, part ejection, and so on.

Depending on the quantity of parts to be hydroformed, a THF production line where most of

the operations are automated may be economical. In this case, a centralized control unit may be used to sequence various operations, such as tube bending, lubrication, preforming, hydroforming, hydropiercing, cleaning, and trimming. Figure 9.24 shows a schematic of a THF line; Fig. 9.25 shows typical hydraulic presses used in THF.

One major issue in THF is the length of the process cycle time. All press manufacturers are trying to reduce this time by improving the frame design, reducing the fluid transfer time, increasing the press ram speed, and optimizing the sequence of various operations in the press.

Press Frame Designs. For THF of large parts, the press must have plenty of daylight for

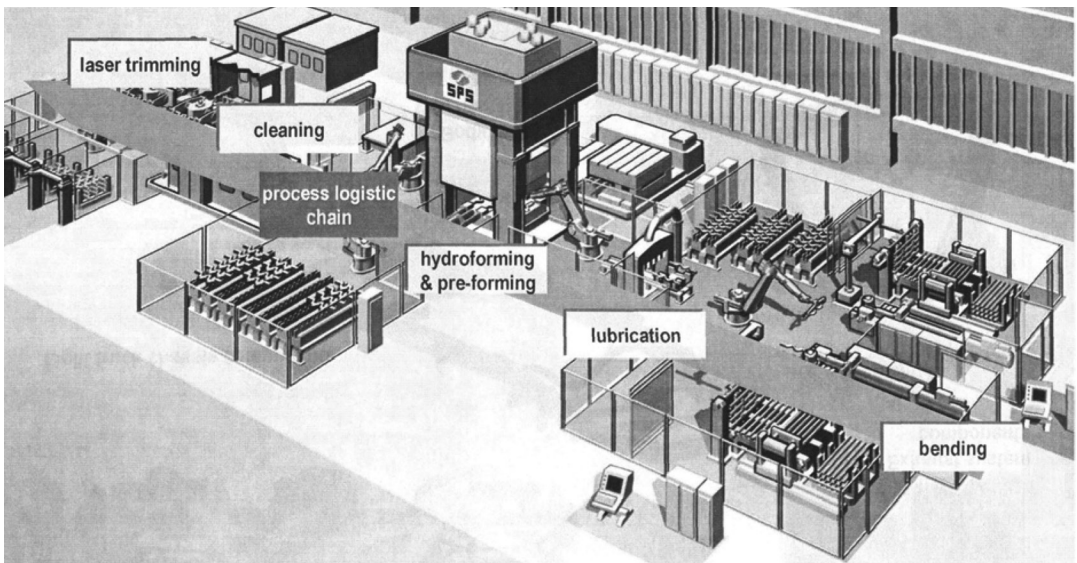


Fig. 9.24 Tube hydroforming production line. Source: Ref 9.35

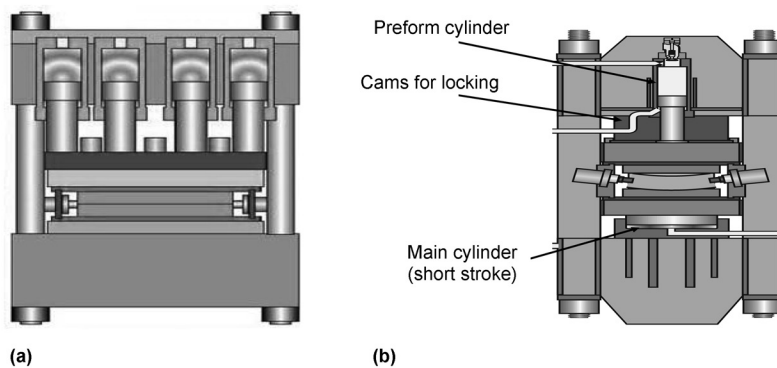


Fig. 9.25 Typical tube hydroforming (THF) presses used in THF. (a) Standard large-stroke press. (b) Short-stroke press with rapid ram motion, side cams for locking after the ram moves down, and the main cylinder that exerts the total press load to close the dies and keep them closed during hydroforming

the installation of dies, as well as a massive press ram and piston, which in turn require large and fast-motion cylinders. Moving the fluid and the ram to close the dies may take a considerable amount of time. Furthermore, the increase in part size increases the cost of equipment drastically. Because the competitiveness of THF is governed by the cycle time, various press concepts have been introduced (Fig. 9.26).

The underlying principle behind press concept A is that in THF, the maximum ram force is needed only for clamping the die along with a relatively short stroke during the hydroforming stage. However, maximum stroke length is needed to open and close the die for loading and unloading the die and the tube. To reduce the

cycle time, die closing is done in two stages. In the first stage, a long-stroke, small-diameter cylinder is activated, and the top ram is rapidly brought down until it touches the bottom dies. In the second stage, the short stroke is activated to move the bottom ram slowly and closes the dies. High pressure is thus built up by a short-stroke cylinder mounted below the bottom die. In this type of press, the upper ram is locked by using horizontal side cylinders before the high-pressure cylinder is activated (Fig. 9.26a) (Ref 9.36). With the short-stroke press, the cycle time can be reduced by 25% (Ref 9.37).

The THF concept shown in Fig. 9.26b uses a design that can provide a larger die closure force and a C-frame for clamping the dies. Be-

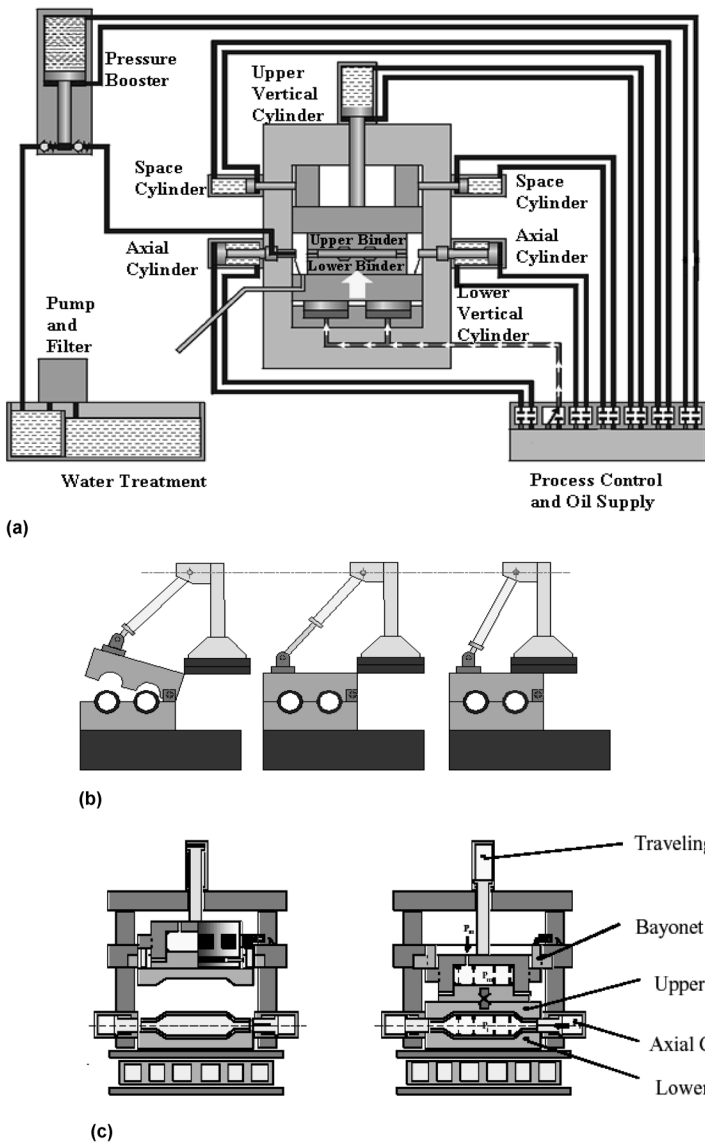


Fig. 9.26 Schematic of several tube hydroforming press concepts. (a) Concept A. (b) Concept B. (c) Concept C

cause of the wedging action, this design is capable of handling forces comparable to those in a conventional press, but at a fraction of the cost (Ref 9.38). The die assembly is supported on a bed, which includes a slideway that allows the die assembly to be shifted. The upper crown has a pressure-activated bladder for pressing the platens together with a large force. Fluid cylinders not only open and close the die but can also mechanically preform the tube.

In concept C, the ram and the upper die are moved up and down by a long-stroke, low-

pressure cylinder. For die closing, two hydraulic cylinders, which are located horizontally on the head plate, rotate the bayonet body (Fig. 9.26c). The upper and lower dies are locked together by the mechanical bayonet die-locking system (Ref 9.39). To compensate for the elastic deformation of the base frame, that is, to prevent the die from opening during the forming process, a hydraulically operated membrane in the form of a pressure cushion is integrated into the upper ram. The force of this membrane is controlled automatically in proportion to the projected sur-

face area of the part and the internal pressure in the tube during the forming process.

Measures for Productivity Enhancement.

Productivity in THF can be increased by the reduction of part-filling times, the integration of faster forming processes, an increase in forming speed, or integrated sequence control of the process (Ref 9.40).

When hydroforming large parts, the time necessary to fill the tube becomes important. The conventional method of filling the tube via the forming tool may cause air bubbles and limit the volumetric flow. To prevent this from happening, quick-filling systems have been developed that fill the component with forming fluid at the same time as such other process steps as tool closing, forming, force buildup, and tube sealing. The advantage of this approach is that the filling time is largely independent of the part size. Thus, filling volume flow rates of more than 20 L/s (1200 L/min) are achieved. Tube hydroforming components that require fluid volume up to 30 L and more can be filled within 2 to 3 s (Ref 9.40).

Many components that are flat in various areas or have bends in the tool-closing direction can be formed directly in the hydroforming tool. By supporting the preform (tube) with internal pressure, a more homogeneous material distribution is achieved and wrinkling is avoided (Ref 9.40). However, a disadvantage of using the hydroforming clamping device for this forming process is that it requires large installed press capacities that increase the cycle times. By using fast preforming techniques (Fig. 9.27), cycle times can be kept to a minimum with small installed pumping capacities.

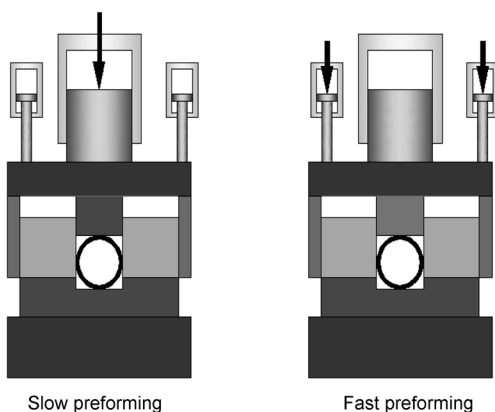


Fig. 9.27 Optimization of the integrated forming process. Source: Ref 9.40

Tandem presses make use of two rams, which increase production capacity (Fig. 9.28). They are characterized by alternating tool-closing movements. While forming takes place in one tool, the other tool is loaded with the preform. This mode of operation also allows coupling of both rams to provide higher clamping forces and accommodate larger dies.

Tube Hydroforming Tooling. Major components of THF tooling are shown in Fig. 9.29. The functions of these components are summarized in Table 9.4. As shown in Fig. 9.29(b), the upper and lower dies are divided into several die inserts that can be individually replaced. For example, feeding inserts are expected to wear faster than other inserts and require repairs because the guiding zone regions are subjected to high sliding velocities.

Classification of Tooling. Based on the applications, THF dies can be designed in different ways, as discussed subsequently.

Open and Closed Dies. As shown in Fig. 9.30, the movements of the vertically operated die blocks are different for open and closed dies. They can be used for production of rotationally symmetrical parts, in which the axis of symmetry is the same for the part and the initial tube (Ref 9.22). In closed-die forming, the forming die is divided laterally and is closed prior to the start of the THF process. There are guides for holding the tubular blank at each end. The blank is pushed by punches throughout the forming process. By using the closed die, the free length of the tube can be kept to a minimum, ensuring good tube guidance and reducing the danger of buckling.

In the open-die setup, the die is open at the beginning of the process. The distance of the opening corresponds to the difference in the length of the tubular blank and the final workpiece. As the process progresses, the die walls are closed and the expanded tube comes into contact with the die surface. One of the advantages of the open-die setup is that friction is minimized by the reduced relative movement between the tube and the dies. The drawback of this process, however, is the greater risk of tube buckling compared to the closed-die setup (Ref 9.22).

Crosswise and Lengthwise Split Dies. Crosswise split dies (Fig. 9.31) are cheaper to produce than lengthwise split dies. They also have the advantage that predefined diameter dimensions can be better controlled. Moreover, closing forces are smaller. However, lengthwise

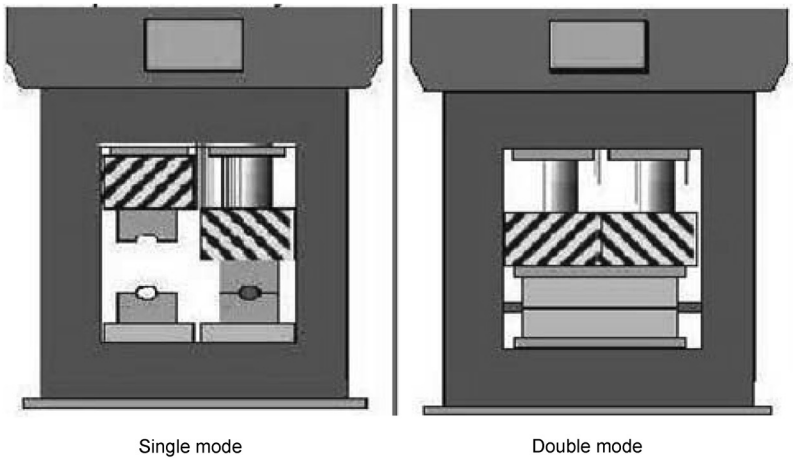
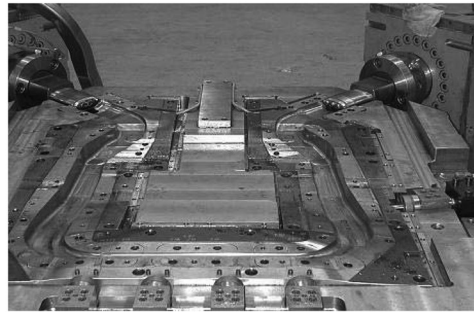
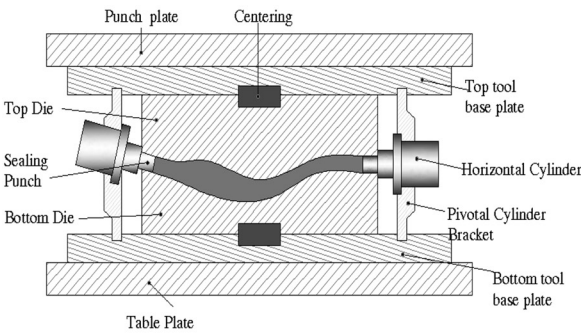
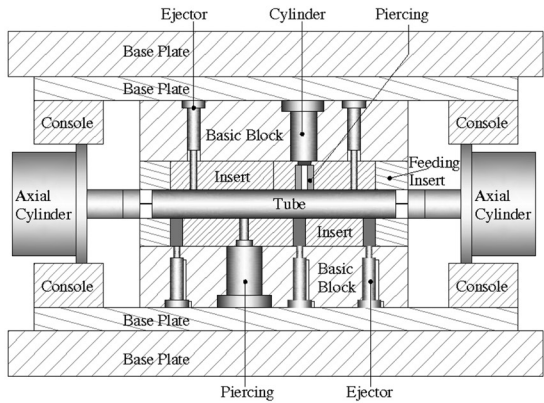


Fig. 9.28 Tandem press. Source: Ref 9.41



(a)

(b)



(c)

Fig. 9.29 Tube hydroforming (THF) tooling composition. (a) Major THF tooling components. (b) Typical tooling for engine cradle. (c) Detailed tooling cross section. Source: Ref 9.18, 9.19

split dies must be used if the workpiece has bends or subsidiary shapes perpendicular to the main axis of the tubular preform (Ref 9.22).

Dies for Prototyping and Production. Prototyping dies are built to shorten development

time at minimum die cost. Hence, the die is constructed as a monoblock. However, in designing for mass production, it is vital to take into account the service life of the dies. For this reason, die inserts are added to enable quicker and

economical replacement of the damaged or worn-out inserts (Fig. 9.32) (Ref 9.18, 9.19). The inserts can be surface-coated to improve their wear resistance. The die inserts have other functions as well. They can increase flexibility with regard to geometry changes, die materials, heat treatment condition, and coatings; they can act as ejectors, preventing the part from sticking in the top half of the die; they can accommodate piercing tooling; and they can serve as channels for quick filling of the tube (Ref 9.42).

Tool Design Considerations. The forces that can act on a hydroforming die are shown in Fig. 9.33. The forces caused by internal pressure and the motion of the axial punches can be significantly high and can even cause plastic deformation of the die.

Table 9.4 Tube hydroforming tooling parts

Upper and lower dies	Permit the tube material to deform and take the desired shape of the final product
Die holder plates	Permit adjustment of the assembly height prescribed by the press stroke or height of the cylinder holder brackets
Sealing punches	Seal and push the tube ends during the hydroforming process
Horizontal cylinders	Activate the punches. They are displacement dependent or pressure dependent and controlled.
Cylinder holder brackets	Absorb the axial forces and align the horizontal cylinders concentrically with the end guides. These can be moved and positioned on the bed or slide plate of the press.
Transverse counterpunches	May also be incorporated in the forming die to form protrusions. Transverse counterpunches may also be used to punch holes in the workpiece at the end of the forming process.
Ejector cylinders	For ejecting the part upon completion of the process

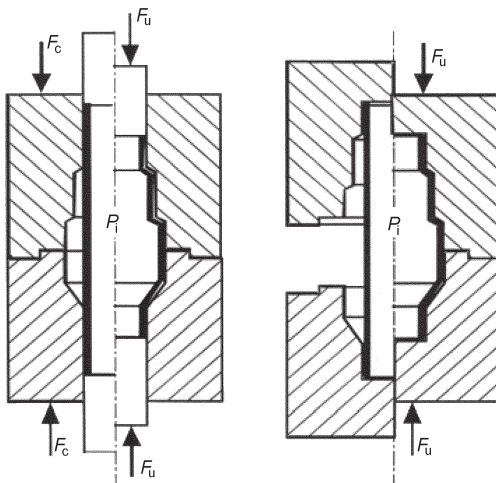


Fig. 9.30 Closed- and open-die systems. Source: Ref 9.22

Figure 9.33(b) shows a close-up view of the guiding zone in THF of a T-shape. Due to the friction stress, τ , the pressure (P_d) at the interface between the die and the tube can increase significantly. Analytical models have been developed to determine die contact pressure distribution when a tube is fed to the die cavity (Ref 9.27). Figure 9.34 shows a comparison between the analytical model and finite-element results on the induced pressure at the tube-die interface when a constant hydraulic fluid pressure of 60 MPa (8700 psi) is used. The contact stress at the tube-die interface increases rapidly as friction increases, and the increase in the contact pressure is also influenced by the increase in the tube length. Some of the factors to be considered when designing dies for THF are summarized in Table 9.5.

Tube Hydro piercing. Most THF parts are designed to be integrated into an assembly with other structural components. Various methods are used to assemble these units, including welding, riveting, bolting, self-threading screws, threaded fasteners, and so on. Most of these joining methods require a hole or an opening on the structure through which a fastening device may be inserted. Hydro piercing is one method of producing a hole in a THF part. Figure 9.35 shows an engine cradle and a front wheel mount for an Opel Astra ready for installation. The multiple holes on the engine cradle can be produced during the hydroforming cycle via hydro piercing. Alternatively, the holes can be produced in a secondary, post-THF operation by methods such as drilling, milling, conventional punching, laser cutting, waterjet cutting, and so on.

In addition to reducing the cycle time of producing a part, combining hydroforming and hydro piercing into a single operation ensures that the hole will always be punched in the correct orientation to the surface. The high degree of

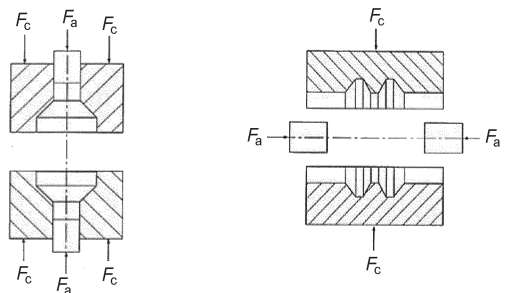


Fig. 9.31 Crosswise and lengthwise split dies. Source: Ref 9.22

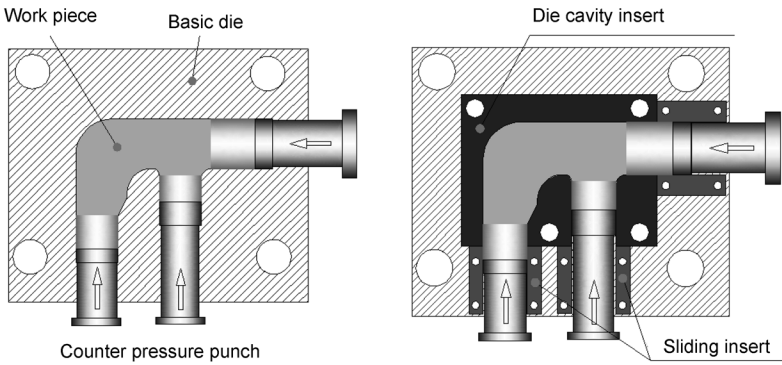


Fig. 9.32 Prototype die (left) and production dies (right). Source: Ref 9.18, 9.19

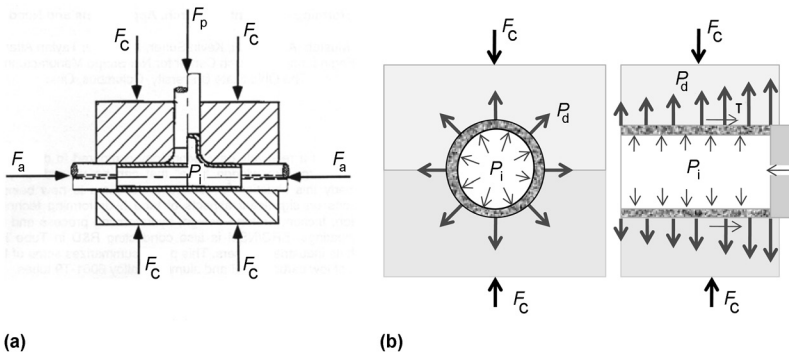


Fig. 9.33 Forces acting on a T-shape tube hydroforming die

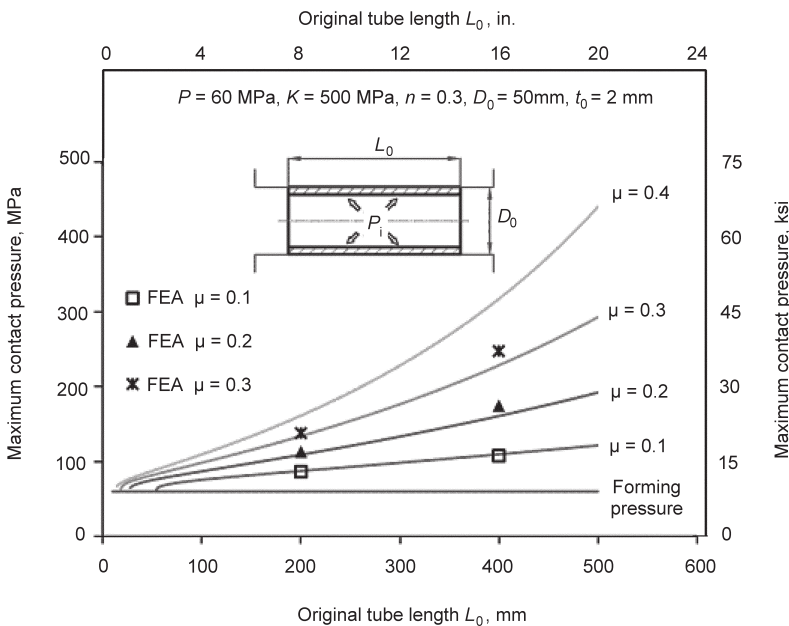


Fig. 9.34 Example of pressures generated in the guiding zone for a tubular material with $K = 500 \text{ MPa}$ (75 ksi), $n = 0.3$ (for $\sigma = K\epsilon^n$), and internal pressure = 60 MPa (9 ksi). FEA, finite-element analysis. Source: Ref 9.27

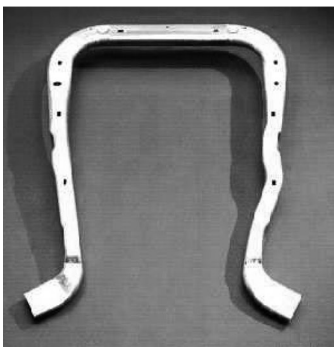
repeatability thus achieved helps to eliminate potential assembly problems (Ref 9.43).

Figure 9.36 shows variations of inward hydropiercing processes. The mechanics of shearing is such that in the course of hydropiercing, deflection will occur in the vicinity of the hole (Fig. 9.36b). This deflection is commonly re-

ferred to as countersink. The countersink depth and width will decrease with increasing hydraulic pressure. There are cases in which countersink is considerable; in such cases, outward hydropiercing can be used as an alternative. As shown in Fig. 9.36(c), when a self-threading fastener is required, hydropiercing can be done

Table 9.5 Factors to be considered in die design

Die geometry	Critical corners should have relatively large radii.
Die inserts	Active die inserts should be parted at critical notching points to avoid the possibility of die fracture due to plastic deformation. The fitting of inserts is important, especially for irregular die geometries where it is not possible to match all the parting lines by surface grinding. Even the smallest gaps between die inserts and other active parts, such as slides used to prevent undercutting and so on, will cause active parts to be displaced or tilted under high pressures. This will have a direct bearing on the dimensional accuracy of the hydroformed components.
Parting line	Spotting of the parting line is required to achieve evenly distributed loading between top and bottom die halves. The parting plane must be designed and finished so that the die is not damaged even when the maximum clamping load is applied without the presence of internal pressure. The position of the parting line and the orientation of the die geometry must be such that it does not create pinching of the workpiece during closing of the die.
Material	The use of cast materials is very attractive when deep pockets or cavities must be milled out of the basic body, and when a large number of inserts, slides, and hydraulic piercing cylinders must be accommodated. High metal-cutting volumes are also generally required for production of components with multilevel three-dimensional curvature. Base plate SAE 1020/1045; mold insert H13; feeding insert D2
Tool wear	Risk of wear exists at sharp edges, the sealing zone at the tube end, and in exposed active areas such as concave contour zones. In selecting the die material, criteria to be considered in addition to the basic functionality, that is, strength and toughness, include aspects such as machining, polishing, hardening capacity, and suitability for wear-resistant coatings. Weldability is also important because good weldability can reduce repair/modification costs for the die blocks.

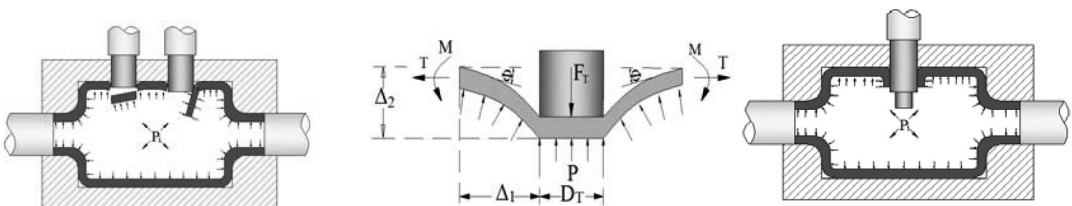


(a)



(b)

Fig. 9.35 Hydroformed engine cradle with multiple holes. (a) Hydropierced holes on engine cradle. (b) Ready for installation. Courtesy of Adam Opel AG



(a)

(b)

(c)

Fig. 9.36 Schematic of inward hydropierced holes. Source: Ref 9.44

with a stepped punch to produce a flange. The formed flange provides better engagement of self-threading fasteners (Ref 9.43–9.45).

In the outward hydropiercing process (Fig. 9.37), countersink will not occur. Some design considerations for incorporating hydropiercing into THF tooling are summarized in Table 9.6.

9.8 Tube Hydroforming Process Design and Design Guidelines

The focus in the process design phase is the determination of optimal process conditions that will prevent such failures as buckling, wrinkling, bursting, folding, and unacceptable surface quality. Figure 9.38 shows typical failures encountered in THF.

Buckling usually occurs at the start of the operation as a result of a high axial force acting on the tube. Buckling is more likely to occur if the tube wall thickness is not uniform. Wrinkling usually occurs in the early stages of hydroforming when the axial force is too high in relation to the internal pressure. Wrinkles can be eliminated by increasing the internal pressure, provided that the wrinkle has not surpassed a critical shape that cannot be removed. Bursting or fracture occurs as a result of excessively high internal tube pressure. The complex nature of the THF process makes complete optimization of the process difficult to attain. However, with the aid of finite-element simulations, good process parameters can be obtained in a cost-effective manner.

As is done in the design of all other sheet metal forming processes, finite-element analysis (FEA)-based process simulation is also used with great success in the design of THF processes. Thus, process and tool development time and costs are reduced.

Determination of Loading Paths. The main controllable process parameters in THF are pressure versus time, axial feed(s) versus time, and (when present) counterpunch force versus time. These variables are often referred to as loading paths. Loading paths may be determined by experience, by trial and error, or more effectively by using FEA-based process simulation. In this last case, one of the well-known commercial codes (e.g., PAMSTAMP, LS-DYNA, or AUTOFORM) is used.

Self-Feeding Approach (Ref 9.46). The self-feeding (SF) approach is a finite-element simulation technique that limits the search for the loading paths to a proper family of curves for selecting the optimum loading paths within

Table 9.6 Design considerations for hydropiercing

Maintaining hydroforming pressure	If multiple holes are needed, fluid pressure can be maintained by leaving the punch in each hole to act as a plug until all punching is completed.
Countersink depth and width	The countersink depth and width are functions of several variables (hydraulic pressure, material, process, punch design). Numerical modeling via finite-element analysis can provide data that will help to decide if inward hydropiercing should be used.
Accessibility	The tooling used to create the hole must have easy access to the location of the hole.

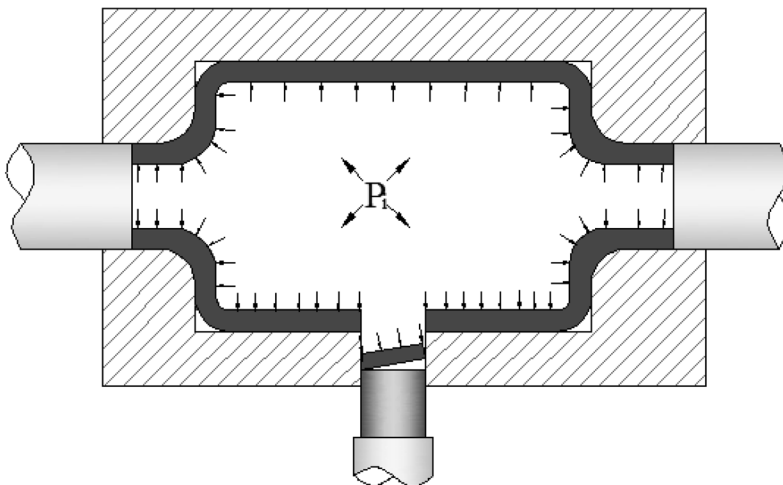


Fig. 9.37 Schematic of outward hydroforming

this family. The main advantage of this approach is that it reduces the computation time and assures some degree of optimization of the process parameters. The starting point of the approach is to run an initial tube-bulging simulation without any boundary conditions on the tube ends, with zero friction on the tube-die interface, and with only internal pressure forcing the tube toward the bulging area (Fig. 9.39). This initial simulation provides values for the minimum axial feed (called self-feeding axial feed or natural axial feed) required from both tube ends; these axial feed values are the smallest that will suffice to form the part in the absence of interface friction. Then, the amounts of axial feed are proportionally increased and applied in iterative simulation runs with the presence of tube-die interface friction until a sound part is achieved. The approach is not appropriate for THF parts for which the natural axial feed is prohibited or restricted by the geometry

of the dies, for example, when the bulge area is strongly nonaxisymmetric, as in T- and Y-shapes. However, the approach provides good results for a variety of structural and frame parts.

This approach is illustrated by an example involving an automotive structural part with a length of 820 mm that was hydroformed from a low-carbon steel tube of 63.5 mm (2.5 in.) diameter and 2.3 mm (0.1 in.) wall thickness. Successful loading paths (Fig. 9.40) were determined through an SF approach. A few simulations were conducted systematically, starting from SF simulations and normal simulations where tube-die interface friction was applied (Table 9.7). The first SF simulation (free bulging, FEM-SF No. 1) with no friction was conducted with a linear pressure curve (up to calibration pressure). The linear pressure curve was then modified and applied in FEM-SF No. 2 to reduce the axial feed speed to a reasonable level. The resulting axial feed curves from SF

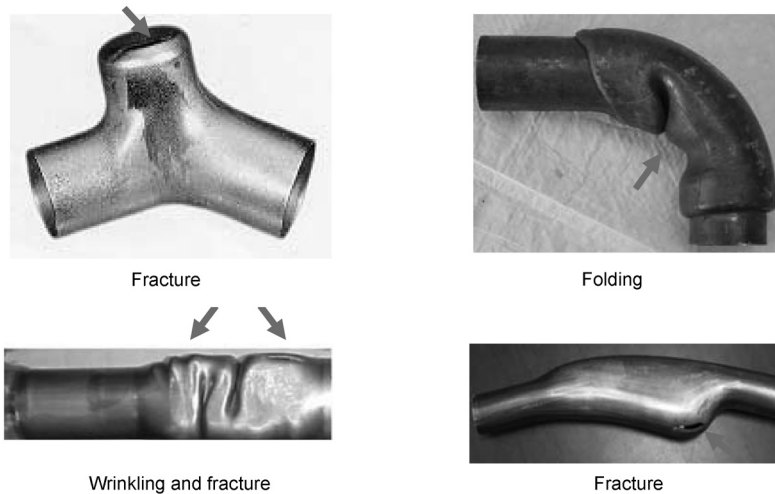


Fig. 9.38 Typical failures in tube hydroforming

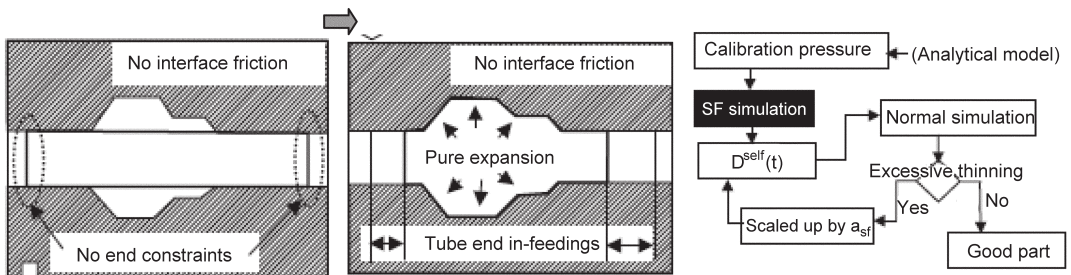


Fig. 9.39 Self-feeding (SF) approach

No. 2 were scaled up and applied to the rest of the normal simulations (with friction) to achieve a sound part with acceptable maximum thinning (<25%). The best axial feed curves were obtained from FEM No. 4 and the modified pressure curve (Fig. 9.40). These loading paths formed the part with 23% maximum thinning.

Adaptive Simulation Approach (Ref 9.3). The adaptive simulation (AS) approach is based on the ability to detect the onset and growth of defects during the process, identify the defects, and promptly counter them. With such ability, loading paths can be adjusted within the same simulation run to correct the defects. The ultimate goal is to select a set of feasible loading paths with a minimum number of simulations, or even within a single run. Compared to the optimization class of methods (Ref 9.47), the required computational time is greatly reduced, but the optimized process is harder to find and it can be determined only locally. The AS algorithm readjusts loading paths at predetermined time intervals within a single simulation run to avoid the growth of wrinkles and to delay bursting (Fig. 9.41). The algorithm for the AS ap-

proach is summarized in the flow chart given in Fig. 9.42.

The main goal of AS is to quickly obtain a set of feasible loading paths. The general strategy of the proposed method is to maximize axial feed and minimize pressure while preventing the generation of irreversible wrinkles. The strategy of this adaptive approach generates very low or negative values of the stress ratio $\alpha = \sigma_z / \sigma_\theta$ (where σ_z is the axial stress, and σ_θ is the hoop stress), which has been proved to be beneficial. The stress ratio α should therefore be kept as small as possible. Unfortunately, the lower limit of this ratio also marks the onset of wrinkling. It therefore seems that optimal loading paths should push the process a little above the edge of wrinkling, let a limited number of recoverable wrinkles grow, and finally flatten them out during the calibration phase.

One crucial issue in the AS strategy is therefore the availability of reliable wrinkle indicators (Ref 9.47, 9.48). Two simple wrinkle indicators were devised at The Ohio State University Engineering Research Center (Ref 9.47). The first wrinkle indicator, called the slope cri-

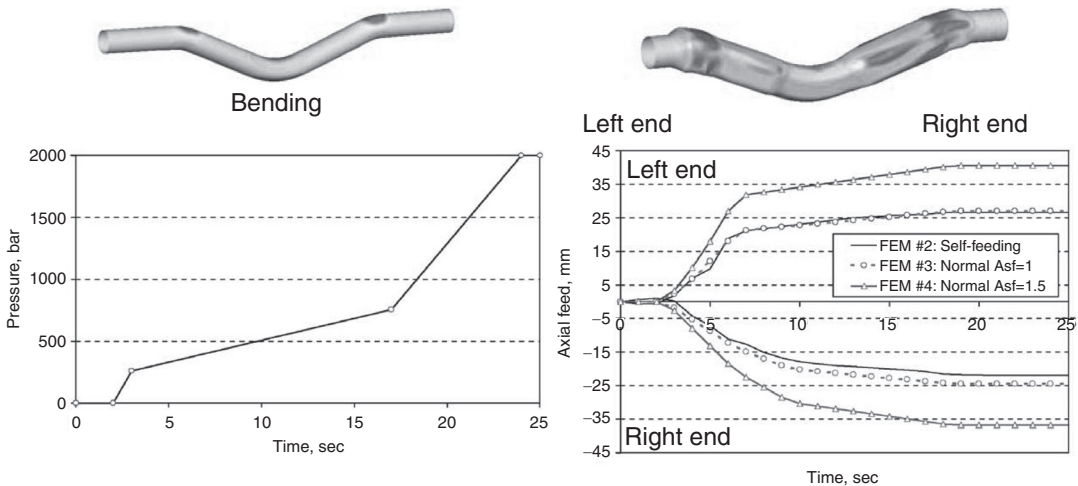


Fig. 9.40 Pressure curve and axial feed curves determined through self-feeding approach in an example tube hydroforming operation. Asf = axial self-feeding = ratio of tube material fed by axial punch versus material that is self-fed by internal pressure only

Table 9.7 Simulations conducted through self-feeding (SF) approach

Approach	Description	Thinning/wrinkle
1. SF	Free bulging ($\mu = 0$)	32%, no wrinkle
2. SF	Same as No. 1, modified pressure	36%, no wrinkle
3. Normal: Asf = 1 (Asf, feeding factor)	Pressure curve from No. 2, axial feed curves from No. 2 (smoothened), friction ($\mu = 0.06$)	43%, wrinkle removed later, burst part
4. Normal: Asf = 1.5	Loading curves same as No. 3, with scaled-up axial	23%, wrinkle removed later, sound part

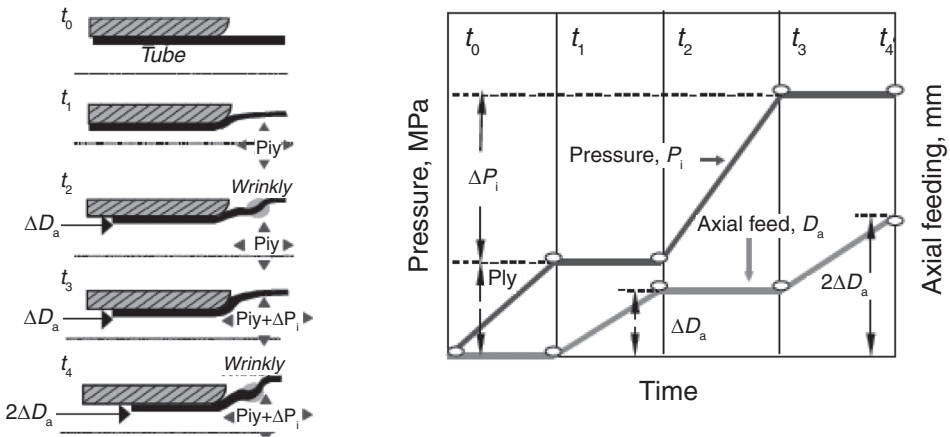


Fig. 9.41 Schematic of adaptive simulation procedure. P_{iy} , yielding pressure; ΔP_i , pressure increment; ΔD_a , axial feed increment

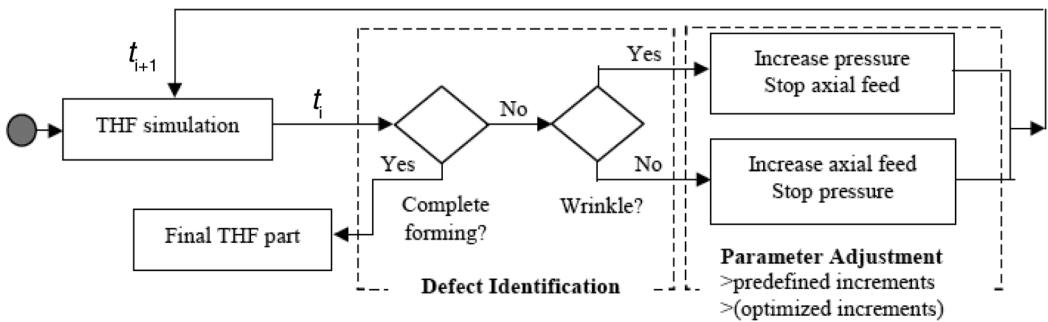


Fig. 9.42 Adaptive simulation approach flow chart (running at each simulation time step $t_i - t_{i+1}$). THF, tube hydroforming

terion, simply considers the slopes of a deforming tube profile. The second wrinkle indicator, called the surface-to-volume criterion, is based on the ratio of the deforming part surface to its volume. The use of tube profile slope as a wrinkle indicator becomes limited when dealing with complex part geometries. The main shortcoming is that the slope criterion cannot distinguish the curvature of the die geometry from possible wrinkle geometry. Knowledge of the die geometry must be considered to enhance the slope wrinkle-detection criterion.

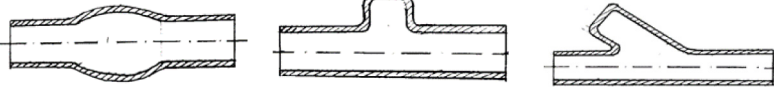

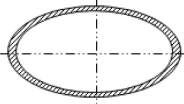
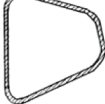
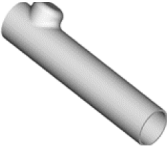


A new wrinkle indicator was devised to solve the potential problem of the slope criterion. The new criterion, called the surface-to-volume criterion, is based on the observation that for the same internal volume, a wrinkled part will have a larger surface area than that of the corresponding wrinkle-free part. An application example of the AS approach based on this criterion is given in Ref 9.47.

Design Guidelines. In designing THF for the production of structural components, a number of factors must be taken into account to ensure technically and economically viable production. This section provides general design guidelines and approximate equations for rapid feasibility assessment to find out whether the product in question is a good candidate for THF or not.

Table 9.8 shows the general guidelines that can be used in the early stages of designing a THF part. These guidelines are based on geometric variables, such as the length of spline, the number of bends on a part, and the number of bulges and protrusion sections on the parts. The level of difficulty in forming a part increases drastically as the number of protrusions, bulges, or bends increases.

The capacity and size of the THF equipment should also be considered early in the design stage, because these can significantly influence

Table 9.8 General guidelines for hydroforming of various shapes

Based on feature geometry	
Based on cross section of final part	<div style="display: flex; justify-content: space-around;"> <div style="text-align: center;">  Round </div> <div style="text-align: center;">  Elliptical </div> <div style="text-align: center;">  Polygonal </div> </div>
Based on profile of longitudinal axis	<div style="display: flex; justify-content: space-around;"> <div style="text-align: center;">  Linear </div> <div style="text-align: center;">  Planar </div> <div style="text-align: center;">  Space frame </div> </div>
Length of spline	For a given tube initial outer diameter, the longer the spline is, the higher the effect of friction forces, and the more difficult feeding becomes.
Number and geometry of bends	Feeding becomes difficult when the part has many bends, especially if bends are sharp (bend angle $\geq 90^\circ$, $\leq 120^\circ$). If a part has more than two sharp bends, axial feeding becomes virtually impossible, except at the very ends of the part.
Number of bulges	The need for axial feeding increases as the number of bulges along the spline increases. More than three bulges are difficult to form. Even with three bulges, the central one could not be easily fed.
Number of protrusions	Feeding becomes necessary when a part has a protrusion (T- or Y-shape), unless the protrusion has a very small height. The higher the number of protrusions, the higher the amount of feeding required. If a part has more than two protrusions on different positions along the spline, feeding the central protrusions becomes very difficult, and the part may not be producible with a conventional one-step hydroforming process. Most parts with protrusions require the use of a counterpunch.

the cost of producing the part. It is therefore important to have a good estimate of the maximum pressure required to form tight corner radii, the die clamping load, and so on. Table 9.9 shows equations that can be used to approximate the yield and burst pressure as a function of the yield strength of the tubular material and tube size. The table also gives an equation to approximate the internal pressure for forming a given corner radius.

Overall success in hydroforming a product depends heavily on the material properties of the incoming tubular material. Tables 9.10 and 9.11 list expansion limits of commonly used materials in THF and the formability classes based on the material strain-hardening exponent, n , and plastic anisotropy, r .

REFERENCES

- 9.1 M. Koc, *Hydroforming for Advanced Manufacturing*, Woodhead Publishing Limited, 2008
- 9.2 M. Ahmetoglu and T. Altan, *Tube Hy-*

Table 9.9 Approximate formulae for tube hydroforming

Variable	Approximate formulae
Yield pressure estimate	$(P_i)_{yp} = \sigma_{yp} \frac{2t_o}{(2R_o - t_o)} = \sigma_{yp} \frac{2t_o}{(D_o - t_o)}$ <p>where: $(P_i)_{yp}$ = yield pressure σ_{yp} = yield strength of material t_o = initial thickness of tube R_o = initial mean radius of tube</p>
Bursting pressure estimate	$(P_i)_B = \sigma_{uts} \frac{4t_o}{(2R_o - t_o)} = \sigma_{uts} \frac{4t_o}{(D_o - t_o)}$ <p>where: $(P_i)_B$ = bursting pressure σ_{uts} = ultimate tensile strength t_o = initial thickness of tube R_o = initial mean radius of tube</p>
Internal pressure for forming a given corner radius	$(P_i)_{max} = \frac{2}{\sqrt{3}} \sigma_{yp} \ln \left(\frac{r_c}{r_c - t} \right) \left[2 - \frac{\sigma_{yp}}{\sigma_{uts}} \right]$ <p>where: $(P_i)_{max}$ = maximum pressure required to form the corner radius σ_{yp} = yield strength of material r_c = outside corner radius t = thickness of tube σ_{uts} = ultimate tensile strength of material</p>

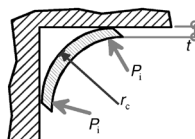


Table 9.10 Expansion percentage limits for various materials

Material	Expansion limit, %
Aluminum, AA 6260	12–14
Low-carbon steel, LCS 1008	15–18
Stainless steel, SS 304	Up to 30

Source: Ref 9.49

Table 9.11 Classification of formability of tubes according to n - and r -values

Formability classes	Poor	Average	Good
n -value	<0.14	0.14–0.2	>0.2
r -value	«1	~1	»1

Source: Ref 9.50

- droforming: State-of-the-Art and Future Trends, *J. Mater. Process. Technol.*, Vol 98 (No. 1), Jan 15, 2000, p 25–33
- 9.3 S. Jirathearanat, “Advanced Methods for Finite Element Simulations for Part and Process Design in Tube Hydroforming,” Ph.D. dissertation, The Ohio State University, 2004
- 9.4 M. Ahmetoglu, K. Sutter, X.J. Li, and T. Altan, Tube Hydroforming: Current Research, Applications and Need for Training, *J. Mater. Process. Technol.*, Vol 98 (No. 2), Jan 29, 2000, p 224–231
- 9.5 M. Koc, Y. Aue-u-lan, and T. Altan, On the Characteristics of Tubular Materials for Hydroforming—Experimentation and Analysis, *Int. J. Mach. Tools Manuf.*, Vol 41 (No. 5), April 2001, p 761–772
- 9.6 C. Hartl, Materials and Their Characterization for Hydroforming, *Hydroforming for Advanced Manufacturing*, M. Koc, Ed. Woodhead Publishing Limited, 2008, p 77–91
- 9.7 P. Groche and G. von Breitenbach, Conference of Tube Manufacturing Processes on Hydroforming, *Prod. Eng.*, 2006, p 109
- 9.8 S. Patil et al., Variations in the Material Properties of Tubes Used for Hydroforming, *TPJ-Hydroform. J.*, Sept 2002, p 76
- 9.9 C. Hartl, Deformation Mechanisms and Fundamental of Hydroforming, *Hydroforming for Advanced Manufacturing*, M. Koc, Ed., Woodhead Publishing Limited, 2008, p 52–75
- 9.10 D.E. Green, Formability Analysis for Tubular Hydroforming, *Hydroforming for Advanced Manufacturing*, M. Koc, Ed., Woodhead Publishing Limited, 2008, p 93–120
- 9.11 T. Sokolowski, K. Gerke, M. Ahmetoglu, and T. Altan, Evaluation of Tube Formability and Material Characteristics: Hydraulic Bulge Testing of Tubes, *J. Mater. Process. Technol.*, Vol 98 (No. 1), Jan 15, 2000, p 34–40
- 9.12 P. Bortot, E. Ceretti, and C. Giardini, The Determination of Flow Stress of Tubular Material for Hydroforming Applications, *J. Mater. Process. Technol.*, Vol 203 (No. 1–3), July 18, 2008, p 381–388
- 9.13 S. Kulukuru, Y. Aue-u-lan, and T. Altan, Determination of Flow Stress of Tubes for Hydroforming, *TPJ-Hydroform. J.*, March 2002, p 10
- 9.14 F. Dohmann and C. Hartl, Hydroforming—Applications of Coherent FE Simulations to the Development of Products and Processes, *J. Mater. Process. Technol.*, Vol 150, 2004, p 18–24
- 9.15 A. Shr and T. Altan, “Bending of Tubes for Hydroforming: A State of the Art Review and Analysis,” Report THF/ERC/NSM-99-R-1, Engineering Research Center for Net Shape Manufacturing, Columbus, OH, 1999
- 9.16 G. Khodayari, Pre-Forming: Tube Rotary Draw Bending and Pre-Flattening/Crushing in Hydroforming, *Hydroforming for Advanced Manufacturing*, M. Koc, Ed., Woodhead Publishing Limited, 2008, p 181–201
- 9.17 H. Li, H. Yang, M. Zhan, and Y.L. Kou, Deformation Behaviors of Thin-Walled Tube in Rotary Draw Bending under Push Assistant Loading Conditions, *J. Mater. Process. Technol.*, Vol 210 (No. 1), Jan 1, 2010, p 143–158
- 9.18 Schäfer Hydroforming, 11,000-Ton Press for Tube and Sheet Metal, Hydroforming, *Proc. of Third Annual Symposium on Metal Forming and the Manufacturing Environment*, June 1998 (Dearborn, MI), p 14–15
- 9.19 G. Schuler, Hydroforming: Die Engineering, *Metal Forming Handbook*, Springer, 1998
- 9.20 R.J. Kervick and R.K. Springborn, “Cold Bending and Forming Tube and Other

- Sections,” American Society of Tool and Manufacturing Engineers, 1966
- 9.21 S. Fuchizawa, Influence of Strain Hardening Exponent on the Deformation of Thin-Walled Tube of Finite Length Subjected to Hydrostatic Internal Pressure, *Adv. Tech. Plastic. Conf.*, 1984, p 297–302
- 9.22 F. Dohmann and C. Hartl, Hydroforming—A Method to Manufacture Lightweight Parts, *J. Mater. Process. Technol.*, Vol 60, 1996, p 669–676
- 9.23 M. Ahmed and M.S.J. Hashmi, Estimation of Machine Parameters for Hydraulic Bulge Forming of Tubular Components, *J. Mater. Process. Technol.*, Vol 64 (No. 1–3), Feb 1997, p 9–23
- 9.24 N. Asnafi and A. Skogsgårdh, Theoretical and Experimental Analysis of Stroke-Controlled Tube Hydroforming, *Mater. Sci. Eng. A*, Vol 279 (No. 1–2), Feb 29, 2000, p 95–110
- 9.25 C. Yang and G. Ngaile, Analytical Model for Planar Hydroforming: Prediction of Formed Shape, Corner Fill, Wall Thinning, and Forming Pressure, *Int. J. Mech. Sci.*, Vol 50 (No. 8), Aug 2008, p 1263–1279
- 9.26 G. Ngaile and C. Yang, Part 1: Analytical Model for Characterizing the Pear Shape Tribotest for Tube Hydroforming, *Proc. IMechE, J. Eng. Manuf. B*, Vol 222, 2008, p 849–863
- 9.27 G. Ngaile and C. Yang, Analytical Model for the Characterization of Guiding Zone Tribo-Test for Tube Hydroforming, *ASME J. Manuf. Sci.*, Vol 131, April 2009, p 021008-1
- 9.28 M. Gariety, “Enhancement of Tribological Condition in Tube Hydroforming and the Viability of Twist Compression Test for Screening Tube Hydroforming Lubricants,” Master’s thesis, The Ohio State University, 2003, p 39–40
- 9.29 G. Ngaile and C. Yang, Part 2: Application of Analytical Model for Characterizing the Pear Shape Tribotest for Tube Hydroforming, *Proc. IMechE, J. Eng. Manuf.*, Vol 222 (Part B), 2008, p 865–873
- 9.30 G. Ngaile, Tribological Aspects in Hydroforming, *Hydroforming for Advanced Manufacturing*, M. Koc, Ed., Woodhead Publishing Limited, 2008, p 144–178
- 9.31 M. Prier and D. Schmoekkel, Tribology of Internal High Pressure Forming, *MAT-INFO Werkstoff-Informationsgesellschaft mbH*, Humburger Allee 26, D-60486, Frankfurt, 1999, p 379–390
- 9.32 G. Ngaile and T. Altan, Practical Methods for Evaluation Lubricants for Tube Hydroforming, *Hydroform. J.*, March 2001, p 8–12
- 9.33 M. Plancak, F. Vollertsen, and J. Woitschig, Analysis, Finite Element Simulation and Experimental Investigation of Friction in Tube Hydroforming, *J. Mater. Process. Technol.*, Vol 170, 2005, p 220–228
- 9.34 M. Loh-Mousavi et al., Improvement of Formability in T-Shape Hydroforming of Tubes by Pulsating Pressure, *Mech. E. Proc. B*, Vol 222 (No. 1), 2008, p 1139
- 9.35 H. Lucke, Hydroforming Manufacturing Concepts, *International Conference on Hydroforming* (Stuttgart), 2003, p 423–434
- 9.36 K. Siegert, M. Häussermann, B. Lösch, and R. Rieger, Recent Developments in Hydroforming Technology, *J. Mater. Process. Technol.*, Vol 98 (No. 2), Jan 29, 2000, p 251–258
- 9.37 W. Osen, Specific Design Concept for Hydroforming Presses, *International Conference on Hydroforming* (Stuttgart), 1999, p 139–148
- 9.38 Benteler Industries, Inc., U.S. Patent 5,600,983, 1997
- 9.39 P. Bieling, Industrial Applications of Tube Hydroforming, *Proc. of Second International Conference on Innovations in Hydroforming Technology* (Columbus, OH), 1997, p 2–5
- 9.40 A. Nottrot, Hydroforming Machines and Plants, *International Conference on Tube Hydroforming* (Stuttgart, Germany), 1999, p 149–160
- 9.41 K. Siegert and M. Aust, A Survey of Presses for Hydroforming Tubes, Extrusions, *Fabricator*, Oct 9, 2003
- 9.42 A. Birkert and J. Neubert, Dies and Die-Tryout for the Hydroforming of Tubes and Profiles, *International Conference on Hydroforming* (Stuttgart), 2001, p 271–287
- 9.43 G. Morphy, “Tube Hydroforming Design Flexibility,” *TheFabricator.com—Metal*

- Fabricating News, Products, and Articles, 2005, www.thefabricator.com
- 9.44 L.M. Smith, Hydroforming: Hydro-piercing, End-Cutting, and Welding, *Hydroforming for Advanced Manufacturing*, M. Koc, Ed., Woodhead Publishing Limited, 2008, p 202–215
- 9.45 S.K. Choi, W.T. Kim, and Y.H. Moon, Analysis of Deformation Surrounding a Hole Produced by Tube Hydro-Piercing, *Proc. Inst. Eng. B, Eng. Manuf.*, Vol 218, 2004, p 1091–1097
- 9.46 M. Strano, S. Jirathearanat, S.-G. Shr, and T. Altan, Virtual Process Development in Tube Hydroforming, *J. Mater. Process. Technol.*, Vol 146 (No. 1), Feb 15, 2004, p 130–136
- 9.47 M. Strano, S. Jirathearanat, and T. Altan, Adaptive FEM Simulation for Tube Hydroforming: A Geometry-Based Approach for Wrinkle Detection, *CIRP Ann., Manuf. Technol.*, Vol 50 (No. 1), 2001, p 185–190
- 9.48 P. Nordlund, Adaptivity and Wrinkle Indication in Sheet Metal Forming, *Comput. Meth. Appl. Mech. Eng.*, Vol 161, 1998, p 127–143
- 9.49 S. Kaya, “Investigation of the Formability Limits in THF by Engineering Extruded Aluminum Profile,” ERC/NSM report in cooperation with Mold Tooling Systems Inc., 2001
- 9.50 M. Strano, Design and Modeling of Parts, Process and Tooling in Tube Hydroforming, *Hydroforming for Advanced Manufacturing*, M. Koc, Ed., Woodhead Publishing Limited, 2008, p 121–143

CHAPTER 10

Roll Forming

Okan Gortan, Technical University Darmstadt
Haydar Livatyali, Tubitak, Turkey
Peter Groche, Technical University Darmstadt

IN ITS GENERAL FORM, roll forming is defined as a process in which flat strip or sheet material with a constant thickness is continuously and progressively formed by bending it in the lateral direction without any desired change in thickness. Thus, a product with a desired cross-sectional profile is formed by passing the flat strip through a series of contoured rotating roll pairs arranged in tandem (Fig. 10.1).

A wide range of standard products can be produced economically by roll forming (Fig. 10.2). These products can be classified into four different groups: open sections, closed sections, narrow strip sections, and wide strip sections. Different types of profiles can be produced on the same roll forming machine by changing the roll pairs. However, due to the high number of

forming steps, the setup of an entire roll forming line with a new roll set is time-consuming. Therefore, low-volume items do not normally justify the expenditures involved. This aspect is seen as the main disadvantage of the roll forming process.

On the other hand, the output of the roll forming process is extremely high. Line speed can go up to 260 m/min (850 ft/min). After the appropriate setup of the line, the labor requirements are usually minimal. Different materials such as steel, stainless steel, aluminum, brass, and copper with thicknesses varying from 0.025 to 25 mm (0.001 to 1.0 in.) can be processed successfully. With careful roll and process design, the cross-sectional tolerances may decrease to 0.01 mm (0.0004 in.) (Ref 10.1–10.4). Be-

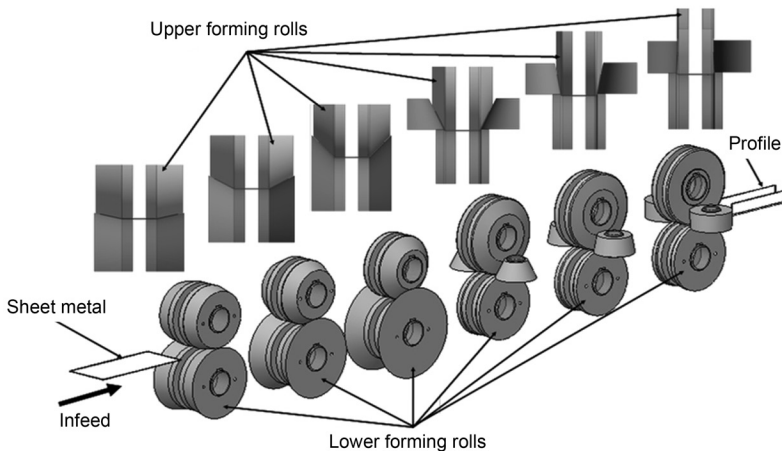


Fig. 10.1 Schematic illustration of the roll forming process

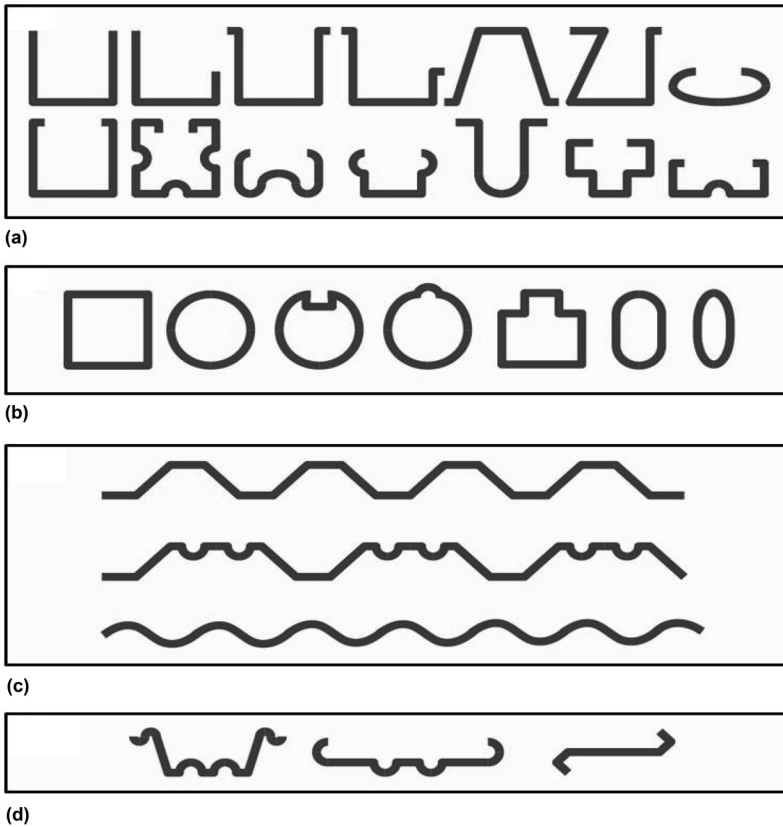


Fig. 10.2 Some product examples made using the roll forming process. (a) Open sections. (b) Closed sections. (c) Wide strip. (d) Narrow strip

cause of the stepwise nature of roll forming, alloys with low ductility that do not lend themselves to standard bending operations can be formed via this process. In addition, most pre-finished materials, such as enameled, painted, lithographed, plated, galvanized, vinyl-coated, and prepunched, can be successfully roll formed to end products or semifinished materials. In some cases, dissimilar metals such as stainless steel and plain carbon steel are roll formed together to form composite products. Roll forming can even produce metal-nonmetal composites such as aluminum with felt, rubber or plastic sealing, and thermoplastic-matrix composites (Ref 10.1, 10.5). Materials such as titanium, nickel, chromium, magnesium, and their alloys are roll formed mainly at elevated temperatures. In these applications, either the full strip or selected bending zones can be preheated locally.

Due to the wide variety of the product geometries that can be roll formed and the high output and flexibility of roll forming, it is used in many different applications, such as:

- Road vehicles (passenger cars, heavy trucks and buses)
- Aircraft parts
- Shipbuilding
- Wagon building
- Agricultural equipment parts
- Metal building panels and structure, window regulators and guides, ceiling grids and tiles, tailgates and garage doors, roof and siding panels
- Warehouse equipment parts
- Furniture parts
- Tubes and pipes
- Constructional steelwork

10.1 Roll Forming Lines

A roll forming line is defined as a machine that continuously transforms flat strip or sheet material into profiles. The major parts of a typical roll forming line are the roll stands (stations or passes), which are mounted on a steel base.

Each of the stands is designed for holding one pair of rolls (top and bottom, or left and right). The actual forming takes place in between these roll pairs. A roll forming machine may involve as few as three or four sets of rolls and, except in very rare cases, will not exceed 30 stands. Aside from the forming rolls, a roll forming line contains many additional features that support the process (Fig. 10.3).

Roll forming lines start with a decoiler device where the strip material is kept in coil form, unless precut blanks are fed. In a standard line with a decoiler, the process is stopped during coil change. For high-speed roll forming applications, it is advantageous to use double-decoiler systems to reduce downtimes. In cases where large and heavy coils are used, a coil cradle is usually preferred. In addition to the decoiler, a multiarm entry coil holder (turnstile), a holdup/down roll, and a coil car usually running on rails are used for practical coil handling.

A coil loop or a horizontal or vertical accumulator is usually included in roll forming lines for high production speeds and quantities after the decoiler. They enable the storage of the sheet during coil change and the necessary welding of the strip ends.

After decoiling, the unevenness in the sheet is straightened with a roll straightening machine. This type of machine reduces the residual stresses by bending and rebending the sheet and eliminates the undesired cracking of the strip or blank. During bending, the yield strength of the material must be exceeded to eliminate the elastic recovery in the uneven sections of the sheet. Depending on the product tolerances, it is advisable to use a band edge milling machine after straightening to adjust the width of the strip to the desired range.

An entrance table is an essential part of every roll forming machine. It is designed basically to keep the stock in proper alignment with the first pair of forming rolls as the strip is fed into the machine.

Some additional operations such as embossing are usually performed in the last station of

the roll former; however, it may also be done in the first station when necessary or practical. Perforating and piercing operations are done on a set of rolls in the process of forming or by stamping before or after roll forming (Ref 10.2, 10.5, 10.6).

Roll forming is predominantly a cold forming process. However, some hard metals or pre-painted materials must be preheated prior to the process to enable forming or to avoid cracking and peeling of the paint layer (Ref 10.7). The heating is achieved either with induction heaters or with furnaces. In special cases, only the selected bending zones are preheated locally.

Roll stands (stations) are mounted on a fabricated steel base that has close-tolerance machined and finished surfaces, so that all machine equipment and auxiliary units can be mounted in accurate alignment with each other. Both main housings and outboard stands are usually made from cast or rolled steel. Stands on one side are usually removable for quick and easy changeover of roller dies.

Important components of a roll stand are the shafts. The main functions of shafts are the carriage of the forming rolls and the transmission of the rotation movement to the rolls. The conventional or standard mills can be classified roughly into four groups, including outboard, inboard, double-head, and raft types, which are advantageous for different roll forming applications.

The outboard (overhung or cantilevered) machine is the most economical type usually preferred for some light narrow shapes. In this machine, working shafts protrude from the gear housing and are supported at one end only. Thus, better visibility and access to the machine in changing and adjusting the tooling is provided (Fig. 10.4a). Inboard-type machines, in which spindles are supported at both ends, are necessary for the thicker-gage shapes where higher pressures are required in forming (Fig. 10.4b). Double-head (panel or duplex) machines can be used only if side forms must be produced on wide panels (e.g., wall and ceiling elements, side panels of home appliances, shelf panels). In this

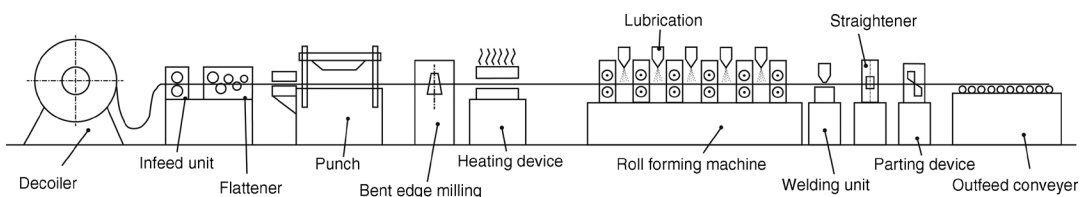


Fig. 10.3 Schematic illustration of a typical roll forming machine. Source: Ref 10.3

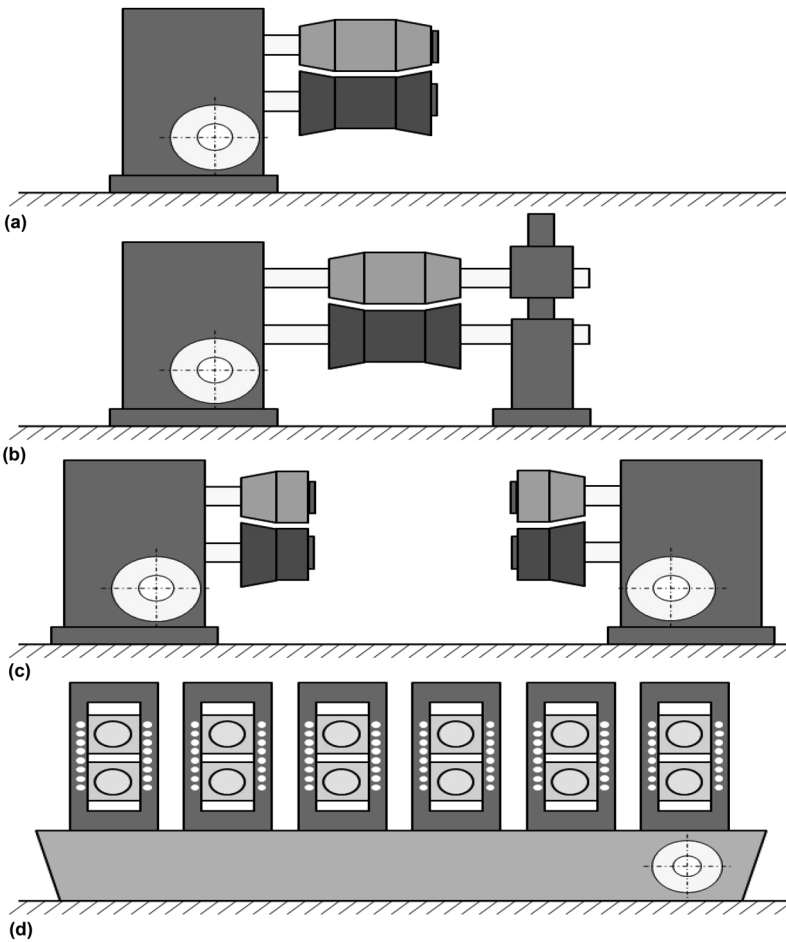


Fig. 10.4 Common roll forming mill configurations. (a) Outboard, (b) Inboard, (c) Double-head, and (d) Raft types

case, roll forming machines with working shafts in cantilever design are arranged opposite to one another (Fig. 10.4c). In raft-type (rafted) machines, roll stands are mounted on rafts or sub-plates that are removable from the mill base. In this type of mill, the whole setup work is done outside the operating roll forming machine. This aspect enables quick changeover of the rolls for maintenance or product change (Fig. 10.4d).

The machine may be furnished with either a fixed- or a variable-speed drive unit that is powered by an alternating current (ac) or a direct current (dc) motor. A simple system has a high-torque ac drive and a starter sized to permit jogging operation. The dc motors and variable-frequency ac motors have a variable-speed feature, whereas classic ac motors will make a variable (stepless) transmission box necessary and are not suitable for numerical control. Variable-

speed feature, however, is useful in threading and tryout, emergency reverse, smooth starting, and controlled stopping. Multimotor systems are also used in some applications, but they are costly. Servomotors can be used not only to drive rolls but also to adjust the height or orientation of roller dies (Ref 10.5).

Side roll (guide) stands can be used to guide or help the strip being formed into the next set of dies. Moreover, they are, especially in tube roll forming, used to form the material rather than guide it. Side rolls are usually idler rolls mounted on a vertical shaft and adjustable in a horizontal plane. Aside from side roll stands, bronze shoes or plastic guides may be used in addition to contoured rolls to better guide the sheet during the process. Straighteners following the last roll stand are used to eliminate any twist or bow existing in the rolled product.

In forming closed profiles, mostly welding units are used to close the cross sections after the last forming stand. An important aspect of selecting the welding type is the speed of the line. Arc welding is a low-cost solution. However, it is appropriate for slow lines, whereas high-frequency welding is a costly but fast alternative for bonding operations. In addition to these two types, laser, plasma, and induction welding, and soldering and brazing techniques can be incorporated within roll forming lines.

Cut-off machines are needed in postcut-type roll forming. The cut-off machine is combined with a length measurement system. There are three common types of cut-off machines: flying shear press, rotary disc cutter, and circular saw. Components such as cut-off machines or stamping presses do not operate continuously. They can be integrated into roll forming lines either on moving linear tables or by providing storage stations before or after cut-off. In some applications, a start-stop operation is used. In this kind of operation, the roll-formed strip is stopped during the discontinuous operations.

The roll forming machines are also often furnished with a lubrication system. Lubrication is essential to avoid wear, galling, or metal pickup and to remove the heat generated during the process. It is usually applied as a flooding system. However, other lubrication techniques can be used, such as dripping, wiping, roller coating, and spraying.

A main control unit is needed so that the different components of the roll forming line function in harmony. A closed-loop system can be integrated to the control system to measure the geometric parameters of the end profile. That way, a quality-assurance system can be achieved. Such a system is necessary in roll forming of high- and ultrahigh-strength materials, where a significant deviation in mechanical properties may be possible within a coil.

In addition to the equipment discussed previously, other types of peripheral units can be integrated into the roll forming lines, such as a run-out table for handling finished parts, a packaging unit, and a painting unit.

10.2 Roll Design

Tool design for roll forming is an experience-based process. No definite scientific rules or format have been established that would apply to the wide variety of sections required in industry.

The contours of a set of rolls for a given section may vary considerably, depending on the designer. However, the main objective of every designer is the same: design an appropriate roll system for a particular product with the least number of forming stations. The designed system must be able to produce products in the desired quality and productivity. This highly sophisticated task requires a deep understanding of the roll forming principles and the reasons for defects potentially occurring in roll-formed products.

Principles of Roll Forming. The major mode of deformation during roll forming is transversal or lateral bending. During deformation of the metal strip, a stress distribution with tensile and compressive stresses occurs in the bending zone in the thickness direction of the sheet material. Tensile stress is induced at the outer side of the profile, while the inner side is loaded with a compressive stress.

In addition to lateral bending, metal strips are subjected to other stresses in roll forming processes that are mostly undesirable and may cause defects in roll-formed products. The workpiece, whether it is a strip at the beginning of a roll forming process or a profile in between the rolls, always performs a linear movement tangential to the rotating forming rolls. However, the strip follows a spatial path in the free space between the roll pairs. Within that path, the edge of the strip usually travels another distance than the bending line (Fig. 10.5). Due to this difference, stresses are generated in the longitudinal direction in the strip material. Unless these stresses are below the plastic deformation limit of the material, an unintended deformation emerges in the edge of the strip as a defect.

The spatial path of the strip in between two consecutive forming roll pairs is mostly nonlinear but has convex and concave sections that result in additional bending and rebending of the strip near to the edge. In the first bending zone, additional tension is superimposed on the outer side of the strip in the longitudinal direction. Meanwhile, the inner section of the strip edge is pressed in the same direction. While the strip is bent back, the stresses change their direction. In this case, the outer section is pressed and the inner section is stretched. These additional stresses contribute to the undesired elongation in the strip sections near to the edge in the longitudinal direction and may cause the formation of defects in the product.

During roll forming of wide panels, the strip edge is pulled toward the center when the mid-

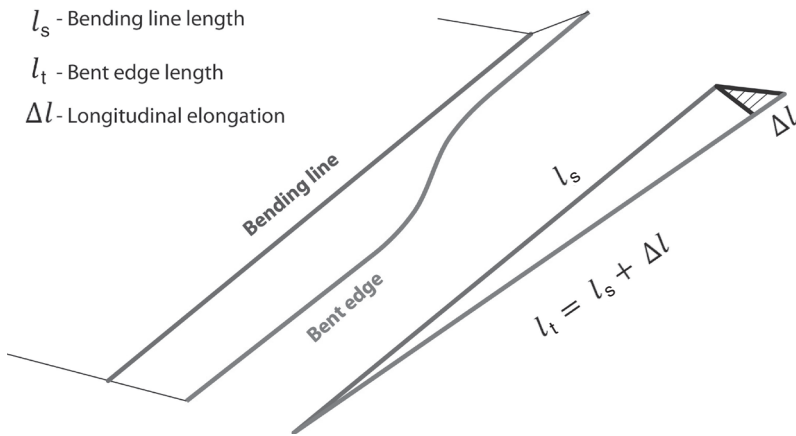


Fig. 10.5 Schematic illustration of longitudinal bending occurring by roll forming

dle section of the metal strip is formed. This pulling results in tensile stresses in the transversal direction in the profile.

Strip Width Calculation. As in most other forming operations, the forming process design phase for roll-formed products also starts with the end geometry. In the first stage of the design phase, the calculation of the strip width for the desired cross-sectional geometry is made. Therefore, the final shape of the profile is divided into straight and curved sections. The total length is the sum of these sections. The length of the straight sections remains constant during forming.

In the bending zone, the thinning of the material is very high compared to the rest of the strip. This thinning also causes an elongation of the strip in the width direction. Therefore, the calculation of the strip width in the curved sections with the assumption that the centerline (neutral axis) lies in the center of the curvature results in incorrect values.

To compensate for this deviation, it is necessary to shift the neutral axis to the inner side of the curved section (Fig. 10.6). The shifting of the axis is defined with a bend allowance, k . However, this factor foresees a regular shifting of the neutral line and does not take the corner of the bending zone into consideration. Therefore, methods involving the bend allowance to compensate for the thinning of the metal strip in the bend section are based on an empirical approach and are capable of defining the strip width at least approximately (Ref 10.5).

The major factors affecting the bend allowance are the material thickness, mechanical

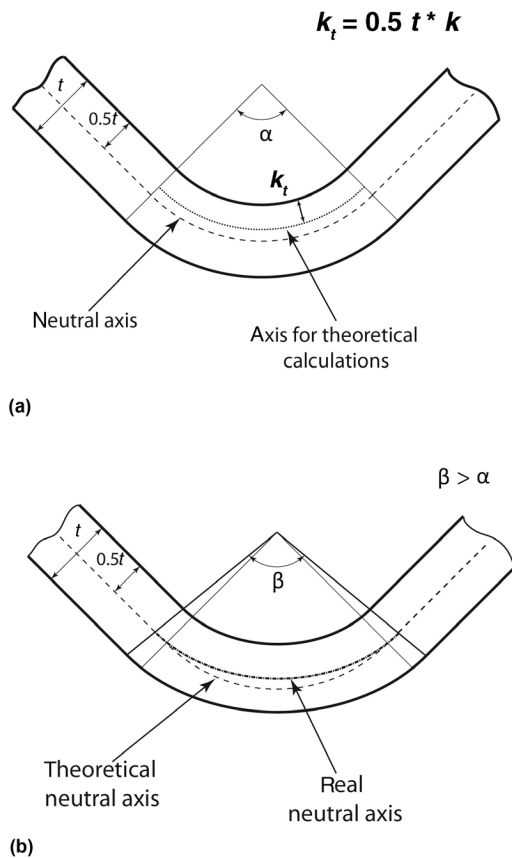


Fig. 10.6 (a) Theoretical approach used by the strip width calculation. (b) Real behavior of the bending zone

properties of the material, and the inside radius of the bend. Generally, harder materials show more resistance to thinning and thus have a higher k -value. Likewise, the higher the bending radius, the lower the thinning in the sheet. Moreover, thinner materials have a higher k -value.

Roll Forming Strategies. In roll forming, a flat sheet material is formed to the desired product geometry in many forming steps. This gradual forming requires the design of a bending sequence. The roll form designer's work is to ensure the production of the desired profile within the predefined geometrical tolerances using the minimum number of forming stages. After the establishment of the forming stages or passes, the visualization of the cross section in every pass defines a so-called flower diagram or the flower pattern of the roll forming process (Fig. 10.7).

The determination of the bending sequence is a highly knowledge-based process. Different roll form designers may generate different flower diagrams for one specific product geometry. However, there are certain roll forming strategies that every designer should consider by the definition of the bending sequence.

Roll forming can be categorized as shape (or profile) roll forming and tube forming. Tube forming refers to roll forming of seam-welded round and rectangular tubes, whereas the term *shape* or *profile* roll forming is used to refer to roll forming of all other kinds of sections. The roll forming strategies of these categories also differ from each other.

The two major forming strategies in profile roll forming—constant arc length forming and constant radius forming—are mainly related to the bending zone of the profile (Fig. 10.8). The constant arc length method assumes the material usage in the radius to remain constant. In this method, the radius is large in the first form-

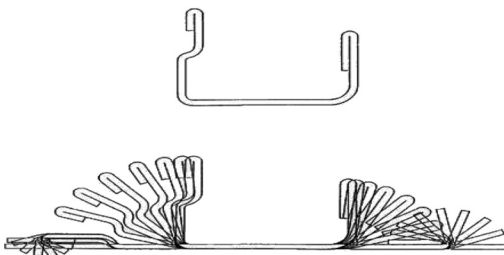


Fig. 10.7 Flower diagram of a roll-formed product. Source: Ref 10.3

ing stages, because the bend angle is small. Increasing bend angles reduce the bending radius.

In the constant radius method, the bend radius is kept constant from pass to pass. Because a smaller angle requires less material than a larger bend with the same radius, there is extra material in any incomplete bend. This extra material is gradually added to the bending area in every pass. The constant radius forming method usually gives a more broken or unsteady radius than the constant arc length method. However, because the bending radius is always smaller than the one in the constant arc length method, except for the last pass, this method is more appropriate for reducing springback.

Three different bending sequences regarding flower patterns are widely accepted for tube production in relevant industrial applications (Fig. 10.9a). Both the single- and the multiple-radius forming strategies show a steady orientation of the bending sequence toward the closed,

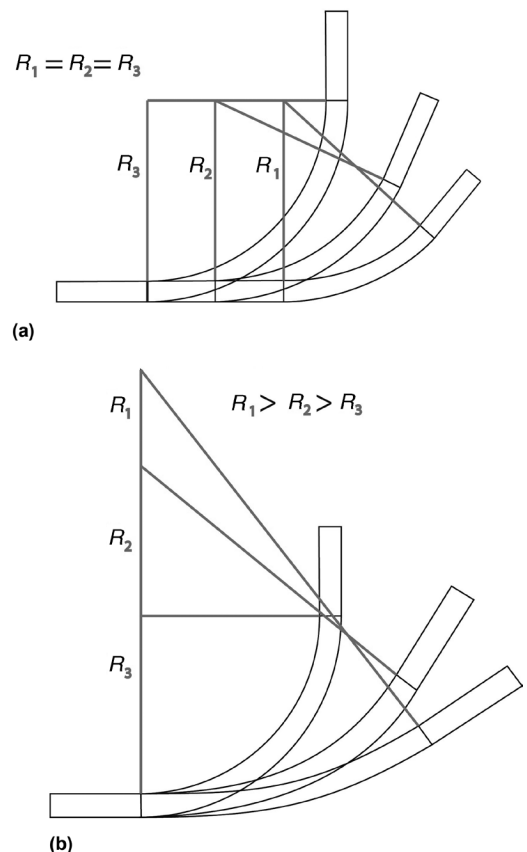


Fig. 10.8 Schematic illustration of (a) constant radius bending and (b) constant arc length bending methods

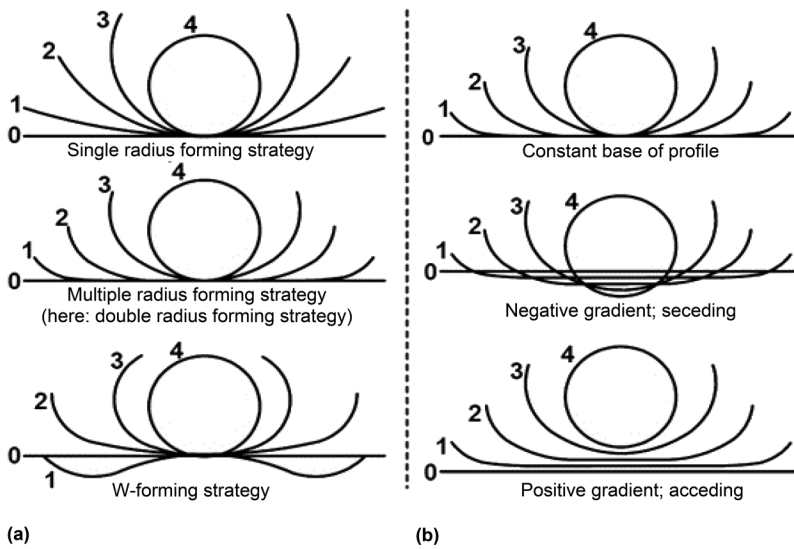


Fig. 10.9 Schematic illustration of (a) bending sequences and (b) vertical leveling strategies. Source: Ref 10.8

round tube cross section. Typically, these two strategies are applied to thin-walled tubes with a high diameter-to-wall-thickness ratio. When the diameter-to-wall-thickness ratio decreases, the so-called W-forming strategy is often applied. This strategy introduces the final tube radius in a wide region next to both band edges already in the first stands. Here, an upper and a lower roll can directly form the geometry easily with a correlating rolling gap. In order not to provoke an undercut or a high slippage rate in the first stand, it is necessary to introduce a geometrically opposed bending region (Fig. 10.9a, W-forming strategy, stand 1).

The challenge with the single- and multiple-radius forming strategies is to form the tube radius near the band edges when the profile is already closed and an upper roll can no longer support the profile from inside. The fin pass rolls, which surround the complete tube on the outside and support the band edges with a circumferential fin or knife, compress the tube into the roll cavity.

Vertical leveling is another important aspect that influences the tube forming strategy. Different strategies are known and established (Fig. 10.9b). They can be altered by the machine adjustment without tool changes. That is why this strategy is often used in production to tune and adapt a given bending sequence to the needs of a certain application. By raising or lowering single stands, the band edge position and the

gap in between can be influenced. Here, the tube manufacturer must take into consideration that not only the inlet but also the outlet of the split strip will change at the shifted stand. Therefore, the loading as well as the forming conditions will be significantly altered due to leveling.

Defects in Roll-Formed Parts. Part defects in roll forming can be defined as the deviation between the target and the actual geometry of the product. Basically, these defects can be divided into two major groups according to their reason of appearance. The first one is the cracks on the outside surface of the bending section. These cracks are related to the minimum bending radius, which is dependent mainly on the material used and its thickness. Using a bending radius that is smaller than the minimum allowable value results in cracks on the outside of the profile.

The second group involves the defects that are caused by the incorrect design of the flower pattern and the forming tools or inappropriate adjustment of the gap in between forming rolls. These defects may appear mainly in the form of longitudinal bow, sweep, twist, flare, edge waviness, oil canning, or springback (Fig. 10.10).

The occurrence of longitudinal bow, sweep, twist, and edge waviness is related to the longitudinal strain. Due to the characteristics of roll forming, the bend edge travels a longer distance than the bend line in between two consecutive

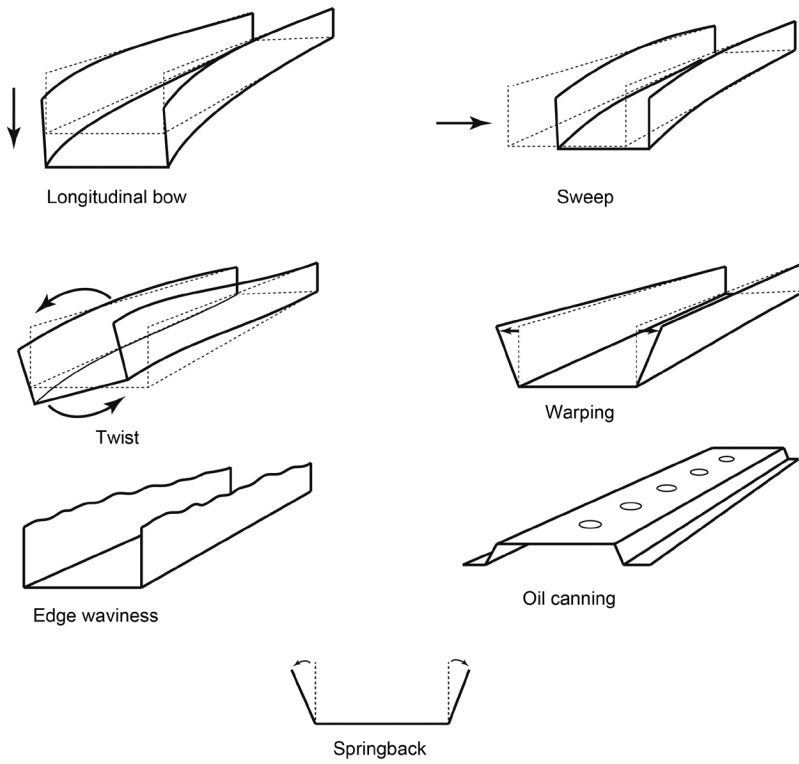


Fig. 10.10 Defects that occur during roll forming

forming stations. Thus, the edge stretches and shrinks consecutively during forming. If the strain at the bend edge in the longitudinal direction exceeds the elastic-plastic limit of the material, permanent edge waviness occurs in the profile. It is basically the buckling of the edge section of a roll-formed profile. This defect is usually observed in products with a small thickness or large depth. Thick sheets are less sensitive to edge waviness.

Longitudinal bow appears mainly in narrow products due to the excessive longitudinal strain. However, this type of defect is usually observed in products made of thick materials. Camber and twist defects occur due to the nonuniform distribution of the longitudinal strains in the transversal direction along the profile.

The longitudinal strain in roll forming is inevitable. However, it can be controlled or minimized to avoid form defects. For this reason, the number of forming passes can be increased or the forming sequence can be adjusted. Another option is to optimize the distance between the forming stands. This distance should be longer than the forming length of the profile. There-

fore, small distances between roll stands should be avoided.

Another important form defect that usually emerges in wide sections of wide profiles, used in manufacturing roof panels or garage doors, is center buckling or oil canning. This defect occurs due to the compressive stresses in the longitudinal direction in the nonformed central sections. When a wide panel is roll formed, the outer sections are pulled toward the centerline, which causes a tensile stress in the transversal direction in the center section of the sheet. Additionally, bending in the transversal direction supports this tension. However, due to the bending, shrinkage in the longitudinal direction is observed along the bend line in the profile. This shrinkage induces excessive compressive stresses in the nonbent sections. As a result, buckling takes place in the wide center section with poor stiffness compared to the rest of the sheet. Center buckling can be minimized by optimizing the roll gap. A tight gap may support transversal elongation and increase buckling.

Another defect that may appear in the product after cutting to the desired length is the flare

in the entry and exit cross section of the profile. This defect is caused by the residual stresses in the thickness direction of the sheet. During bending, the outer section of the strip material reaches the forming rolls first. Afterward, the inner section follows the outer one. However, this delayed forming between outer and inner section results in shear stresses along the thickness in the profile. The shear stresses cause residual stresses, which cause a flare-form deviation after cutting the product to the desired length. The effect of the residual shear stresses can be minimized by overbending or backbending the profile after the last forming step. Thus, the residual stresses can be equalized. Another alternative is to use discontinuous calibration operations at the profile end after roll forming.

Springback is an inevitable aspect of every bending process, due to the elastic recovery of the material in the bending line. It refers in general to the change in bending angle and bending radius when unloading the part. Important geometric parameters that influence the amount of springback are the inner bending radius, the sheet thickness, and the forming strategy (i.e., design of the flower pattern). Whereas an increasing inner bending radius leads to a higher springback angle, increasing sheet metal thickness decreases this value. Young's modulus, yield stress, strain-hardening coefficient, and anisotropy affect springback. Springback increases with increasing yield stress and decreasing Young's modulus and is present after every forming station. It can be reduced only after the last forming pass with an additional overbending unit.

Selection of Roll Materials. The roll design phase also requires the selection of roll materials. The most commonly used roll materials include low-carbon steel; gray cast iron (such as class 30); case-hardened carbon steel (ASTM 8613); low-alloy tool steel (such as O1 or L6); high-carbon, high-chromium tool steel (such as D2); cobalt-molybdenum high-speed steel (such as M42); and aluminum bronze (Ref 10.9).

Rolls made of low-carbon steel or gray iron are commonly used in short-run production or in medium- to long-run production with rather soft materials and generous corner radii. They are preferred because of their low cost and good machinability.

Tool steels such as O1 or L6, which can be hardened up to 60 to 63 HRC, are preferred in medium-run production. For increased tool life and reduced galling or scratching of the work

metal, these rolls can be plated with up to 25 μm of chromium (Ref 10.5, 10.9). In general applications where a smooth-finish steel strip is to be formed, often AISI 8670 is used (Ref 10.6). This alloy is a 70% C, Cr-Ni-Mo oil-hardening tool steel that is heat treated to 58 HRC. Such tooling is expected to roll form 10 to 16 million meters (3 to 5 million feet) of thin-gage cold-rolled mild steel strip before regrinding, and up to four to five regrinds can be made. For longer tool life, a high-carbon, high-chromium cold working steel, such as AISI D2, which can be heat treated to 63 HRC, is recommended. Such tooling is reported to yield 100 to 150% longer life at only 30 to 50% additional cost. To reduce galling and thus increase the tool life, the use of cobalt-molybdenum high-speed steels is preferred for forming of ultra-high-strength materials.

In applications such as roll forming of light-gage stainless steels, aluminum alloys, or pre-coated and prepainted material, where the cosmetic quality of the product is important, softer rolls are used to avoid surface damage. Aluminum bronze is a good choice in such cases.

Considering the cost of tooling materials, roll wear is a significant problem in roll forming. Factors affecting the tooling cost are the initial cost of the rolls (materials, coatings, machining, and heat treatment), total length of product that can be made before refinish, cost of refinishing and/or recoating, number of refinishes that can be done, and type and cost of lubricant.

In cases where split rolls are used, different tool materials can be combined in one tool set, depending on the shape of the rolls. The cylindrical parts that are subject to galling due to high gripping pressure can be made of D2 steel hardened to 63 HRC and hard chromium coated. On the other hand, conical side surfaces, which are subject to high sliding speeds rather than high pressures, can be nitrided or coated with a certain kind of ceramic.

Computer-Aided Roll Form Design. A standard roll forming line may have as much as 30 forming passes with at least two rolls in each pass, many spacers, and peripheral components. Each forming stand may have hundreds of dimensions. These numbers indicate the complexity of the design of a roll forming line. General computer-aided design (CAD) tools can simplify the designer's work and therefore have been widely used in roll forming firms for more than 30 years. However, there are also several specific CAD programs for roll forming to

support the roll form designers in roll-formed product design, bending sequence determination, and roll design. Additionally, in-house developments of the design programs are common.

Modern commercial roll forming software allows the import of roll geometries into finite-element (FE) programs and enables the fully automatic FE model generation of a complete process chain, as well as the automated evaluation of the FE simulation results (Ref 10.10–10.13). These features allow fast investigations of the stress and strain distributions during roll forming of a particular profile and the determination of the final geometry of the same profile. However, it is still the designer's job to interpret the results of the computer program and make a judgment about the end design.

10.3 Recent Developments and the Future of Roll Forming Technology

The development of roll forming technology can be divided into three major phases. In the first phase until the 1970s, roll forming was primarily used for the production of structural elements and welded tubes and pipes. The roll forming design process was mainly based on the designer's knowledge.

Roll forming technology developed rapidly during the second phase, beginning from the 1970s until the mid-1990s. In this time period, the product range of roll-formed parts increased considerably. Research led to new design tools such as CAD-based software and FE packages. In addition to computerized process design, some new computer numerical controlled roll forming mills with section plates, hydraulic quick clamping, and fast release clutches were built. These lines, which are programmable to produce different types of products and reduce scrap and changeover times, were necessary to implement computerized management and just-in-time manufacturing systems. They can deliver information such as production level, number of parts manufactured, batch quantities, part numbers, material usage, and downtime. This information can make preventive maintenance more efficient and reduce the amount of defective products.

The third and present phase of roll forming is mainly driven by the lightweight production philosophy. Up until now, conventional steel was the major roll forming material. Strips with constant thickness and cross-sectional geometry

were the main production materials. However, the idea of generating load-optimized tailored products mainly for the automotive industry motivated researchers to investigate new roll forming concepts such as flexible roll forming (FRF) (Ref 10.14). Flexible roll forming enables roll forming of profiles with variable cross sections in the longitudinal direction. In this method, the forming rolls are not fixed in their position, as by the conventional roll forming, but are moved along a predetermined path on the profile.

Flexible Roll Forming. The FRF process enables the production of profiles with a variable cross section in the rolling direction. This new forming process offers high flexibility because it can be numerically controlled (Ref 10.15, 10.16). The first geometry considered was a symmetrical U-section, and by adding further conventional roll forming steps, more complex profiles such as hat sections or closed profiles can be achieved, as shown in Fig. 10.11.

Flexible Roll Forming Tooling. A recently developed roll forming system can produce profiles that have nonconstant cross sections along the longitudinal axis (Ref 10.18). The forming rolls in such a flexible stand are not driven, so that conventional stands are used for feeding the sheet metal. The line connecting the axes of the forming rolls (inner and an outer roll) in the forming unit is always perpendicular to the bending edge (Fig. 10.12). They are movable by rotation or translation by two spindles driven by servomotors. The desired forming edge can be generated in a CAD system and read by a control program developed specifically for this tool setup. The control of the servomotors depends on the feed rate of the sheet metal. The feed rate is measured with the help of a friction wheel rolling on the sheet metal.

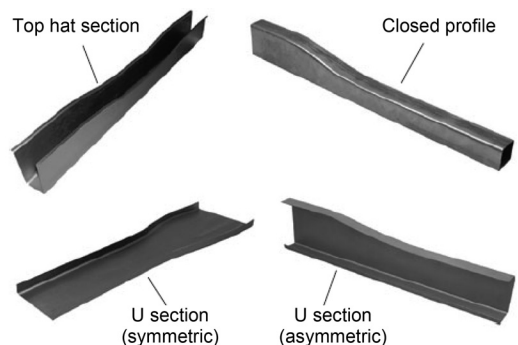


Fig. 10.11 Prototype profiles produced by flexible roll forming. Source: Ref 10.17

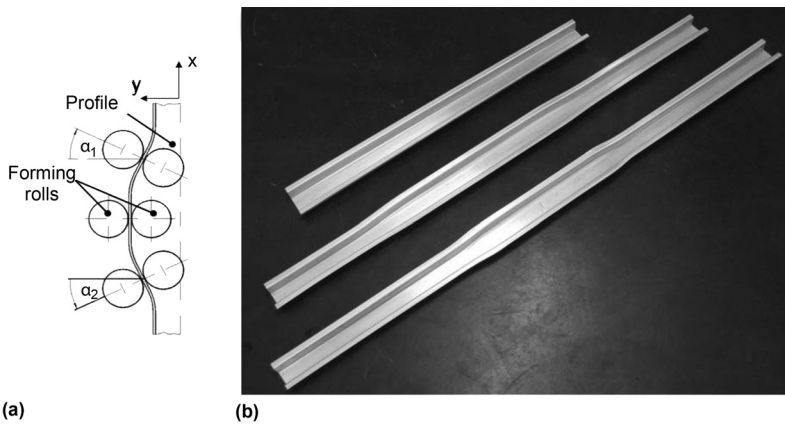


Fig. 10.12 (a) Kinematics of flexible roll forming. (b) Flexible roll-formed products. Source: Ref 10.18

Figure 10.13 shows another FRF mill prototype that was developed by Ona et al. (Ref 10.19, 10.20), who controlled the flexible cold roll forming machine by a progressive logic controller unit to form products with flexible cross sections.

Finite-Element Analysis of Flexible Roll Forming. During early investigations of the FRF process, the process limits were detected in terms of wrinkles or other geometric instabilities. So far, the producibility of a new geometry has been proven either by FE analyses or laboratory tests. References 10.15, 10.21, and 10.22 are examples of published papers on the FRF topic.

Groche et al. (Ref 10.15) found that it was possible to create a model to mimic the stresses in the formed part by assuming that the entire process was being done in a single step. The main objective of this study was to develop a one-step model to check the feasibility of a specific geometry in a very short time. This feasibility check focuses only on the occurrence of wrinkles along flanges in the transition zone. Figure 10.14 shows the model used by Groche et al. (Ref 10.15). Finite-element simulations were carried out to determine the results of various geometrical parameters, namely, contour radius (R), sheet thickness (t), and flange height (s_h). The failure mode in the final part was that of buckling (wrinkles) in the compression zone of the flange. The wrinkles occurred as a result of raising the flange height (s_h), reducing the sheet thickness (t), or reducing the contour radius (R).

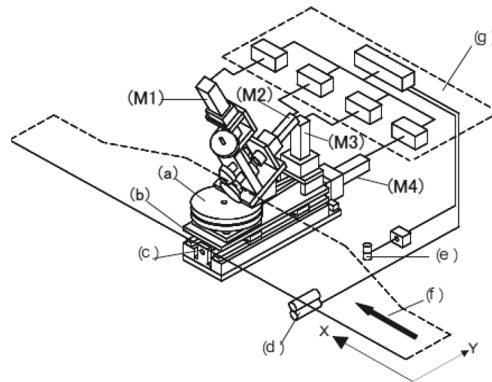


Fig. 10.13 Flexible roll forming mill prototype. Servomotors: (M1) for light rolling; (M2) for driving rolls; (M3) for rotating turn table; and (M4) for translating base table. (a) Turn table. (b) Base table. (c) Guide actuator. (d) Rotary encoder. (e) Linear encoder. (f) Blank sheet. (g) Controller. Source: Ref 10.19, 10.20

As a result of these FE analyses, a characteristic strain distribution in the area of the profile flange was identified. Using a precut sheet metal leads to the creation of compression and stretching zones along the profile flange. The FE results also show that the predominant plastic strain in the longitudinal (x) direction can be described by a combination of the major strain along the stretching zone and the minor strain in the compression zone. The actual lay-out procedure no longer considers a one-dimensional strain state but a three-dimensional strain state along the flange, summed up by the equivalent plastic strain. This helps to obtain more accurate values for the resulting stress in the flange.

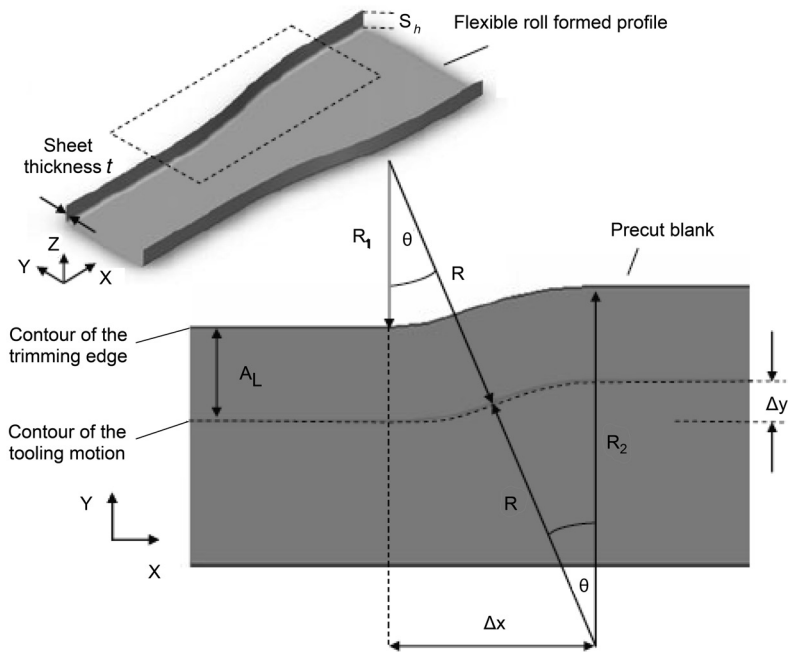


Fig. 10.14 Geometric parameters for profile definition. Source: Ref 10.15

Larranaga et al. (Ref 10.21) also conducted two different FE simulations of the laser-assisted FRF process: heating the corner of the part and heating the flange of the part. They concluded that in these studies, the most important parameter affecting geometrical defects was the flange length. When the flange length increases, geometrical distortions increase as well. Also, local laser-assisted FRF was studied, and it was shown that considerable improvements can be achieved when the flanges are heated.

Variable Strip Geometries. Another research issue in the roll forming industry is the use of strip geometries other than strips with constant thickness and width as incoming material. The major examples for these geometries are tailored rolled blanks (TRB) and branched profiles (Fig. 10.15). The main idea of the tailored products lies in the use of the material where it is most needed to reduce the total weight of the product. The production of the roll formed TRBs requires a change in the forming path and the numerical control of the forming rolls.

An innovative method to produce branched profiles is linear flow splitting (Ref 10.8). During that process, a plain sheet metal is formed using obtuse-angled splitting rolls as well as

supporting rolls to form the strip to have additional flanges at the ends. Roll forming of the branched profiles generates totally new product classes that are suitable for lightweight applications (Fig. 10.16) (Ref 10.23).

New Materials. The philosophy of light weight also changes the materials used in roll-formed products. In the automobile industry, conventional steel types are being replaced by high-strength steel (HSS) and advanced high-strength steel (AHSS). The use of lighter materials such as aluminum, magnesium, and titanium is also increasing in the roll forming industry. Some of these materials require elevated temperatures for forming. Therefore, a current topic for the roll forming industry is the local heating of the profiles on the bending zone (Ref 10.24). In that way, the accuracy of the products can be increased without heating the whole product.

Roll forming of HSS and AHSS is only possible with specific precautions. Due to their high yield strength and high elastic recovery rate, the springback values are high compared to mild steels. Furthermore, the springback of these types of materials are more sensitive to the fluctuations in the material mechanical properties. An innovative approach foresees an

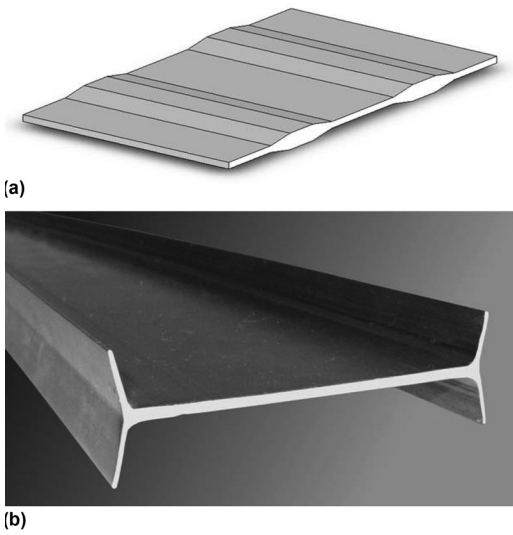


Fig. 10.15 Examples of (a) tailored rolled blank and (b) branched profile that can be used in roll forming

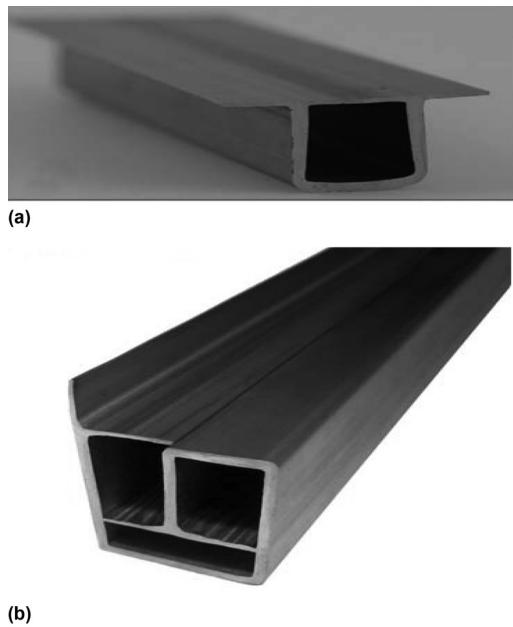


Fig. 10.16 Example profiles roll formed from branched profiles. (a) One chamber and (b) multichamber profiles. Source: Ref 10.23

inline quality-control system for the geometrical accuracy of HSS and AHSS. In this system, the profile geometry is measured after forming, and, depending on the springback rate, a corrective overbending angle is defined in a closed-loop system. Thus, real-time springback com-

pensation can be realized, and the effects of the material property fluctuations can be omitted. With this system, it is possible to minimize reject rates and to achieve close tolerances by roll forming of HSS and AHSS (Ref 10.8).

10.4 Future of Roll Forming

It is fair to say that there have been some great changes in the basic roll forming process in the last decades. However, there is significant improvement potential in roll forming technology. The numerical modeling of roll forming is still time-consuming. Therefore, a larger body of research on basics and numerical modeling of roll forming is expected in the future. The limits and the effects of warm and hot roll forming have not been investigated sufficiently. In the future, more warm roll-formed products are expected in order to increase the accuracy of the profiles to produce ready-to-assemble parts. The long set-up times are still a major problem of every roll forming plant. To increase the profitability of the roll forming process even for small-batch production, the disturbance factors in this process should be studied deeply. Thus, the application areas of roll forming can be extended, and the efficiency of the process can be improved significantly.

Research on three-dimensional (flexible) roll forming is still in its beginnings. When designing a traditional roll forming machine, it is necessary to know the number of forming steps, the tool design, and the springback. Furthermore, it is equally important to know the limitations of radius changes in both depth and width when designing a three-dimensional roll forming machine or a profile.

Today, a computer-aided engineering program can be used to estimate how many forming steps a profile needs. Such a program also proposes the design of the steps. Nevertheless, the experience of a toolmaker is necessary to decide if the proposed tool design is adequate. This is where FE simulations can support the toolmaker in the design and manufacturing of rolls.

Research will also be focused toward development of an integrated production line. The goal of such a production line is the continuous and need-based production of any user-defined profile shape by variation of the control parameters, as well as establishing minimum radius in width/depth for a flexible rolled process.

REFERENCES

- 10.1 F.L. Church, Roll Forming: What It Is, What It Can Do, *Mod. Met.*, Vol 46, 1990, p 64–70
- 10.2 *Up to Date Cold Roll Forming Technology*, Dreistern-Werk, Maschinenbau GmbH & Co., Germany, 1991
- 10.3 G.T. Halmos, *Roll Forming Handbook*, CRC Press, 2005
- 10.4 O. Pösse, “Nagel Profiliertechnik—Starker Partner bei der Entwicklung kundenspezifischer Technologien,” Fachtagung Walzprofilieren, 2010
- 10.5 “Roll Form Theory & Applications,” No. 525, Maplewood—The Metal-Formers, Rockford, IL, 1975
- 10.6 “Profile Roll Forming Systems, A Company Brochure,” Yoder Mfg. Co., Cleveland, OH, 1989
- 10.7 J. Ivaska, Jr., Choosing the Correct Lubricant for Modern Roll Forming Operations, *The Fabricator*, Vol 23, 1993, p 24–27
- 10.8 P. Groche and M. Henkelmann, Dimensional Deviation of Roll Formed Components Made of High Strength Steel, *Key Eng. Mater.*, Vol 344, 2007, p 285–292
- 10.9 S.L. Semiatin, Ed., *Forming and Forging*, Vol 14, *Metals Handbook*, 9th ed., ASM International, 1988, p 624–635
- 10.10 A. Sedlmaier and J. Tann, Process Simulation and Quality Management for the Roll Forming Industry, *Advanced Technology of Plasticity/Proceedings of the Sixth International Conference of Technology of Plasticity*, Sept 19–24, 1999 (Nuremberg), p 2381
- 10.11 A. Sedlmaier and J. Tann, Process Simulation and Quality Control in the Roll Forming Industry, *Proceedings of Roll Forming Technology*, April 5–6, 2000 (Arlington Heights, IL), Society of Manufacturing Engineers
- 10.12 F. Pfeiffer, *Virtuelle Rollformanlage*, Blech in Form 01, 2000, p 52
- 10.13 R. Brandegger, Predicting Stress and Strain in Roll Formed Profiles, *The Fabricator*, May 2004
- 10.14 A. Istrate, “Verfahrensentwicklung zum Walzprofilieren von Strukturbauteilen mit der Längsachse veränderlichen Querschnitten,” Dissertation, Institute for Production Engineering and Forming Machines (PtU), TU Darmstadt, 2002 (in German)
- 10.15 P. Groche, A. Zettler, and S. Berner, Development and Verification of a One-Step Model for the Design of Flexible Roll Formed Parts, *Int. J. Mater. Form.*, 2010
- 10.16 ORTIC AB, www.ortic.se
- 10.17 A. Abee, S. Berner, and A. Sedlmaier, Accuracy Improvement of Roll Formed Profiles with Variable Cross Sections, *JCTP* (Korea), 2008, p 520
- 10.18 S. Berner, M. Storbeck, and P. Groche, A Study on Flexible Roll Formed Products Accuracy by Means of FEA and Experimental Test, *Proceedings of the 14th Int. ESAFORM Conference, ESAFORM 2011*, p 345
- 10.19 H. Ona, T. Jimma, and N. Fukaya, Experiments on the Forming of Straight Asymmetrical Channels—Research on the High Accuracy Cold Roll Forming Process of Channel Type Cross Sections III, *J. Jpn. Soc. Technol. Plast.*, Vol 22, 1981, p 1244–1251
- 10.20 H. Ona, T. Jimma, and H. Kozono, A Computer Aided Design System for Cold Roll Forming, *Adv. Technol. Plastic., Proc. First Int. Conf. on Technology of Plasticity*, The Japanese Society for Technology of Plasticity, 1984, p 422–427
- 10.21 J. Larranaga, L. Galdos, C. Garcia, R. Ortubay, and G. Arrizabalaga, “Flexible Roll Forming Process and Reliability Optimization Methods,” ICTP 2008, The Ninth International Conference on Technology of Plasticity, 2008
- 10.22 “What You Should Know about COPRA, Computer Oriented Profiling Assistant,” Data M GmBh, Germany, www.datam.de
- 10.23 M.O. Görtan, D. Vucic, P. Groche, and H. Livatyali, Roll-Forming of Branched Profiles, *J. Mater. Process. Technol.*, Vol 209, 2009, p 5837–5844
- 10.24 J. Larranaga and L. Galdos, “Geometrical Accuracy Improvement of Flexibly Roll Formed Profiles by Means of Local Heating,” First International Congress on Roll Forming (Bilbao, Spain), 2009

CHAPTER 11

High-Velocity Forming

Verena Psyk and Désiree Risch, Technische Universität Dortmund, Germany

HIGH-VELOCITY FORMING (also called impulse forming, high-energy-rate forming, high-strain-rate forming, or high-rate forming) includes all processes converting stored energy in a very short time to plastic deformation of parts (Ref 11.1). As illustrated in Fig. 11.1, the high-velocity forming technologies can be subdivided into high-velocity hydroforming, high-velocity mechanical forming, and energy-based high-velocity forming.

In high-velocity forming, process strain rates in the range of 10^2 to 10^4 s⁻¹ are achieved. Thus, the duration of the process is typically in the range of microseconds or milliseconds. Therefore, cycle times are determined mainly by the duration of the handling operations and the pro-

cess preparation, which can be complex and time-consuming in some techniques. To illustrate the differences between high-velocity forming and conventional processes, the approximate forming speeds are given in Table 11.1.

Due to the high strain rates, in high-velocity forming of several materials, including aluminum alloys, titanium alloys, steels, copper, and some magnesium wrought alloys, increased formability can be achieved. This phenomenon is often called hyperplasticity and was investigated by a large number of researchers (Ref 11.4–11.7). Other advantages of high-velocity forming processes are reduced wrinkling and springback effects and the possibility to use inertia locking mechanisms in the tool design,

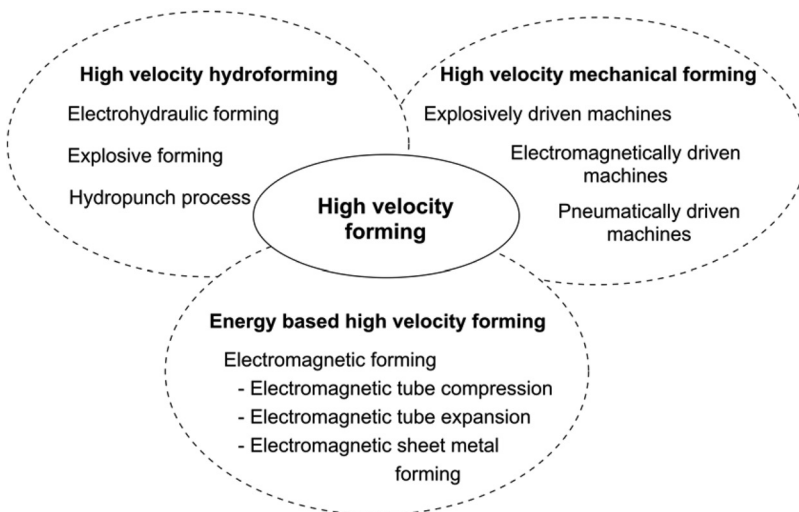


Fig. 11.1 Classification of high-velocity forming technologies. Source: Ref 11.2

Table 11.1 Approximate forming velocities in various conventional and high-velocity forming processes with subsequent strain rates

Process	Forming velocity		Strain rate (order of magnitude), s ⁻¹
	m/s	ft/s	
Hydraulic press	0.03	0.1	10 ⁰
Brake press	0.03	0.1	10 ⁰
Mechanical press	0.03–0.73	0.1–2.4	10 ⁰ –10 ¹
Drop hammer	0.24–4.2	0.79–14	10 ¹ –10 ²
Gas-actuated ram	2.4–82	7.9–269	10 ²
Explosive forming	9–228	30–748	10 ² –10 ⁴
Magnetic forming	27–228	89–748	10 ³ –10 ⁴
Electrohydraulic forming	27–228	89–748	10 ³ –10 ⁴

Source: Ref 11.3

allowing the use of smaller-capacity presses. Furthermore, due to the short forming time, the process can be considered to be adiabatic and the forming heat can be used more efficiently for deformation than in conventional quasistatic forming operations.

On the other hand, due to the high forming velocities, advanced sensing and measurement methods are needed for process monitoring and control. In special technologies, for example, electromagnetic forming, measuring is complicated due to the process-related high-magnetic fields, from which the sensors must be shielded. High acoustic emissions during the process and the necessity of evacuating the air from the die before the forming operation are other disadvantages of high-velocity forming technologies.

11.1 High-Velocity Hydroforming

High-velocity hydroforming can be used for deep drawing and stretch forming as well as for the expansion of tubular semifinished parts. In these processes, only one forming tool (die) is required, while the force application is advanced by a solid, fluid, or gaseous working medium. For a target-oriented and regulated use of energy for a specific forming operation, knowledge about basic relations between energy transfer and propagation, the material behavior, and the tool loading is required (Ref 11.8).

Process Principle

In high-velocity hydroforming, the pressure applied to an enclosed fluid is not conveyed continuously and uniformly to every part of the fluid and to the surfaces of its container. Instead,

a pressure impulse propagates throughout the fluid. If the propagation velocity is higher than the specific sonic speed in the medium, the pressure impulse is called a shock wave. As soon as this wave strikes the workpiece, a part of the mechanical energy carried by the wave is transferred to the workpiece, which is accelerated in the propagation direction of the shock wave. Thus, the forming process is significantly influenced by the specific impulse of the shock wave, which in turn depends on the maximum pressure and duration of the pressure pulse. The impulse transferred to the workpiece determines the velocity during the deformation process. Due to the fast movement of the workpiece and a tension wave that runs in the direction opposed to the propagation direction of the shock wave, cavitation can occur directly behind the workpiece.

Process Variations

According to the initiation mechanisms of the shock wave, three different process variations exist. The processes are electrohydraulic forming, explosive forming, and the hydropunch process.

Electrohydraulic Forming. In electrohydraulic forming, the electric energy, stored in a capacitor, is suddenly discharged through a spark gap, which is positioned in a working medium, for example, water. During the discharge, the water is ionized and vaporized, resulting in the shock wave, leading to workpiece deformation. Thus, electric energy is transformed directly to mechanical energy.

In electrohydraulic forming, two different process setups can be distinguished according to the type of spark gap used. These are electrohydraulic forming with discharge through a wire (i.e., the electrodes are connected to each other by a wire bridge) and electrohydraulic forming with discharge through a gap (i.e., there is no connection between the electrodes). The corresponding setups are shown in Fig. 11.2 (Ref 11.8). The advantages of a wire bridge are that the discharge can be better controlled and shaped, the process is more efficient and can be operated at lower voltages and using longer distances between the electrodes. On the other hand, this setup requires a more time-consuming preparation of the process.

Explosive Forming. In explosive forming, the shock wave is initiated by a detonation

whereby not only the detonation of high explosives but also propellant forming techniques, for example, gas forming, can often be used.

In one variation of explosive forming, the contact operation shown in Fig. 11.3(a), one surface of the workpiece is covered with the explosive. The emerging detonation wave accelerates the workpiece directly within microseconds to velocities in the range of several meters per second. The workpiece is formed into a male or female die. This process variation is typically applied if a high pressure is required, but it is a relatively imprecise operation and is limited to forming of thick plates. Furthermore, a shock wave hardening occurs due to the direct contact of workpiece and explosive before the actual forming process starts.

In the standoff operation, the workpiece and the die are submerged into a working medium, preferably a fluid or amorphous substance, and the explosive is ignited some distance from the workpiece (Fig. 11.3b) (Ref 11.8). In this process variation, the shock wave propagates through the working medium before causing deformation of the workpiece. In addition, a high-pressure gaseous bubble is produced, which expands with a lower velocity than the actual shock wave pushing the working media and thus accelerating the workpiece a second time. Compared to the contact operation, the achievable pressures are significantly lower. It is shown that the working pressure increases with decreasing distance between explosive and workpiece (Ref 11.10). Especially in cases where this

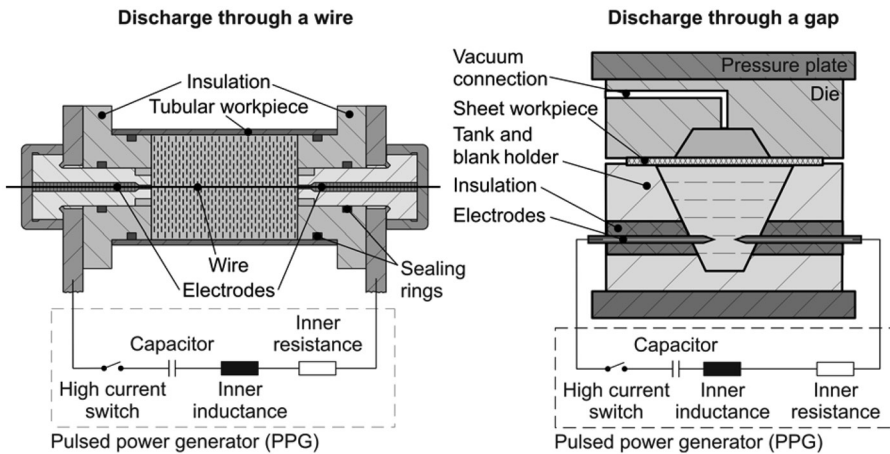


Fig. 11.2 Different setups used in electrohydraulic forming according to German patent DE 1806283

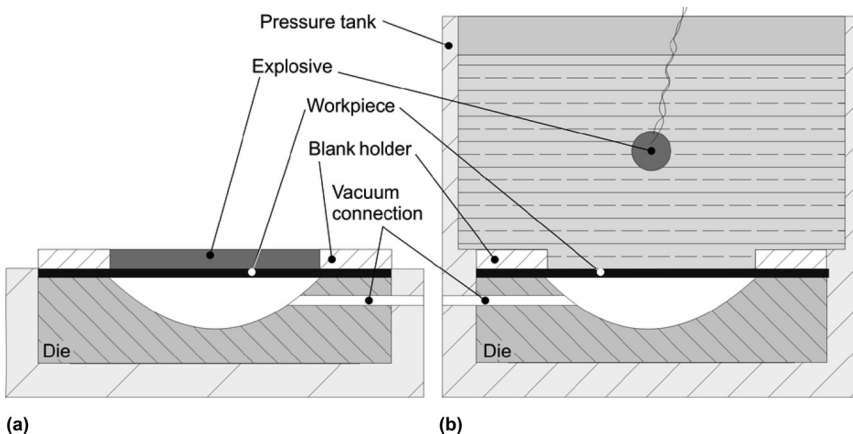


Fig. 11.3 Process variations of explosive forming techniques. (a) Contact operation. Source: Ref 11.8. (b) Standoff operation. Source: Ref 11.9

distance cannot be adjusted (e.g., inside a tubular workpiece), the choice of a suitable working medium affects the process design. Lower densities of the working media as well as a lower humidity of less than 15% lead to a significant decrease of the working pressure and the transfer speed. In some cases, this condition is desirable because some materials fracture when a critical transfer speed is exceeded.

For the gas forming technique, gas mixtures are used as the energy source, and the pressure wave is generated by the burning propellant. Thus, the detonating gas is the actuator of the process as well as the working medium (Ref 11.11). Suitable explosive gases are hydrogen (H_2) and hydrocarbons (C_nH_m). In addition, oxygen (O_2), with nitrogen (N_2), carbon dioxide (CO_2), and argon (Ar), is required for the chemical reaction. A thorough mixing of the different gases is required for the process and can be achieved by suitable mixing equipment (Ref 11.12).

Different variations for forming of tubes and sheet metal workpieces are shown in Fig. 11.4. In all cases, the reaction takes place in a small detonation zone, which propagates through the detonation tube toward the workpiece to be formed. The detonation velocities are in the range of 1500 to 4500 m/s (4900 to 15,000 ft/s), while temperatures of up to 4500 °C (8100 °F) and pressures of several hundred megapascals are achieved (Ref 11.12).

High-Velocity Hydropunching. As shown in Fig. 11.5, the principle setup of hydropunching consists of a compressed air system, accel-

erating a plunger up to velocities in the range of 30 m/s (100 ft/s) before it dips into the working medium. Due to the impact, the fluid is compressed and pressed into the tool unit. The resulting pressure forms the workpiece into the die cavity (Ref 11.13).

Equipment

Electrohydraulic Forming. The equipment required for an electrohydraulic forming operation includes the pulsed power generator (PPG), the spark gap, and the die, including a reflector if applicable. A PPG consists mainly of capacitor banks, a high-voltage charging device, a trigger unit, and high-current switches (Ref 11.14).

Connected to the PPG is the spark gap, which is the actual tool in an electrohydraulic forming operation. It consists of two electrodes, which can be arranged opposed or coaxial to each other, as shown in Fig. 11.6. For electrodes arranged opposed to each other, the insulation can be realized more easily, while coaxially arranged electrodes are usually less inductive and therefore more efficient (Ref 11.1). The energy transferred into the exploding wire and the arc between the electrodes, respectively, can amount to 90 to 95% of the capacitor charging energy if the wire and the distance between the electrodes are well chosen. However, the energy transferred to the shock wave is only in the range of 20% (Ref 11.15).

To focus the shock wave during an electrohydraulic forming process and increase the process efficiency, the closing of the die can be

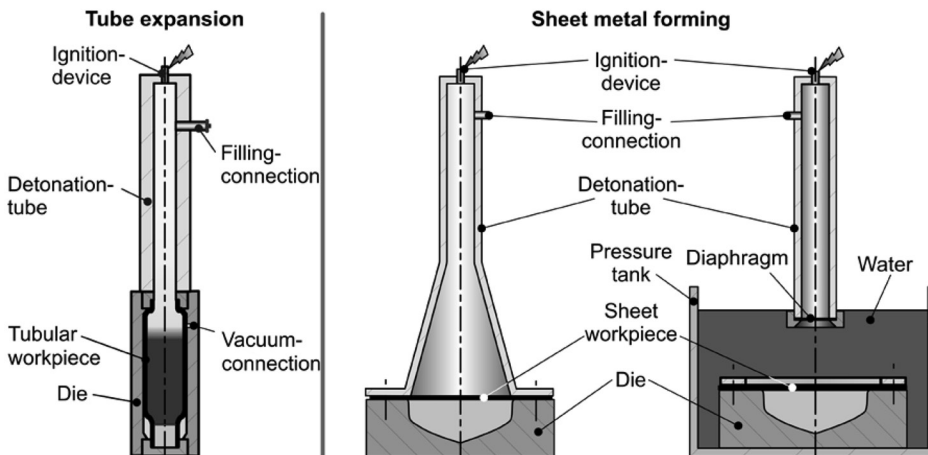


Fig. 11.4 Propellant forming. Source: Ref 11.12

achieved by a suitable reflector. The geometry of this additional tool must be adapted to the special forming task; for example, an elliptic reflector can be used to calibrate geometric details in a sheet metal forming process (Ref 11.16). To do so, the spark gap initiating the shock wave is positioned within the first focal point, while the detail to be formed is located close to the second focal point. Consequently, the shock waves spread from the initiating focus spherically in all directions, are reflected, and converge in the

position of the target area, as shown in Fig. 11.7(a). Figure 11.7(b) and (c) show reflection geometries suitable for electrohydraulic bulging of tubes with various tube diameter-to-length (d/l) ratios.

Explosive Forming. Usually, explosive forming is applied for extremely large parts and small batch sizes. Consequently, the equipment cost should be kept as low as possible. Due to safety issues, the process is often carried out in a (natural or artificial) lake or river (Ref 11.17) or in an underground mine (Ref 11.18) and not in a factory site. Thus, the development costs for explosive forming are usually low compared to conventional forming technologies, but, on the other hand, the setup time and effort is larger so that the economic efficiency must be evaluated for every individual application.

Hydropunching. According to Ref 11.19, the piston is a significant component in hydro-punching (Fig. 11.5). The energy available for the forming operations depends directly on the kinetic energy when the piston contacts the water surface. This energy is determined by the mass and the velocity of the piston. The velocity is influenced mainly by the driving mechanism, for example, pneumatic pressure; the acceleration distance, that is, the length of the acceleration tube; and the piston geometry (due to aerodynamic reasons).

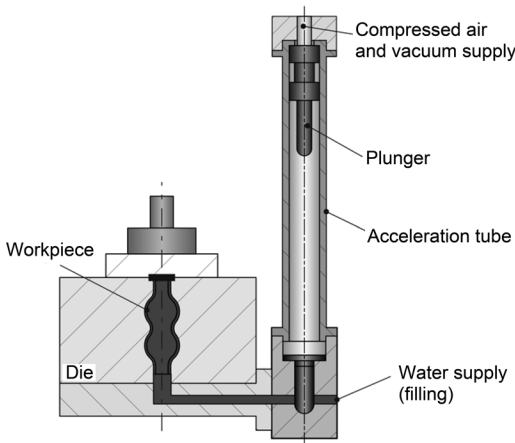


Fig.11.5 Principle sketch of the hydropunch process. Source: Ref 11.13

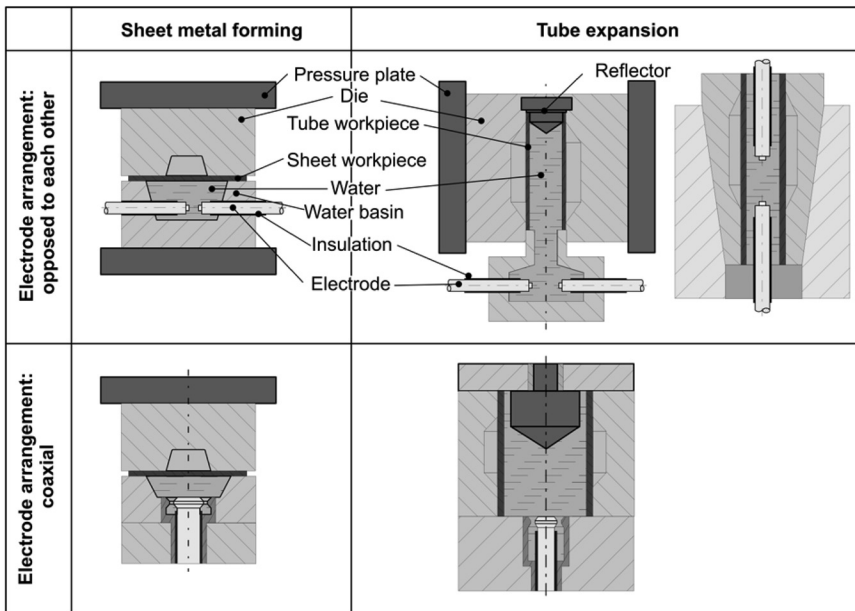


Fig. 11.6 Possible arrangements of spark gaps for electrohydraulic forming. Source: Ref 11.1

Applications

Electrohydraulic Forming. Applications of electrohydraulic forming include air conditioning technology and the automotive sector as well as aerospace applications. The technology allows fabricating complex parts with small corner radii and reduced springback effects (Ref 11.20). Due to loading by the shock wave, wrinkling

is prevented during the drawing of conical workpieces. Examples of parts produced by electrohydraulic forming are presented in Fig. 11.8.

Explosive Forming. Explosive forming and propellant forming technologies are multipurpose processes, suitable to form workpieces of complex geometries from materials that are difficult to form by conventional methods (Ref

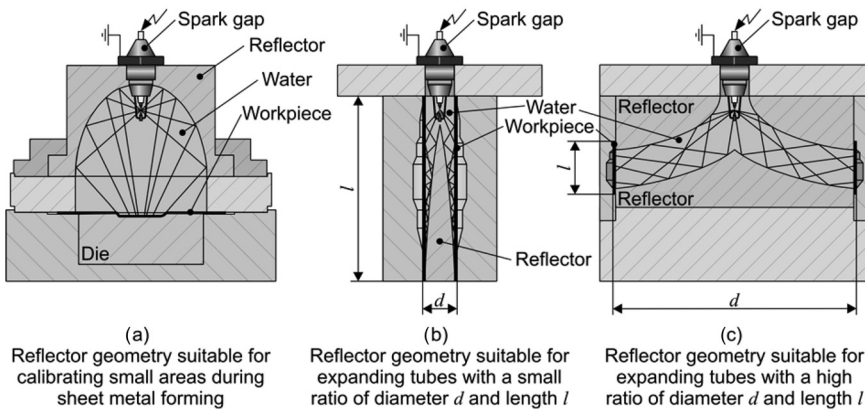
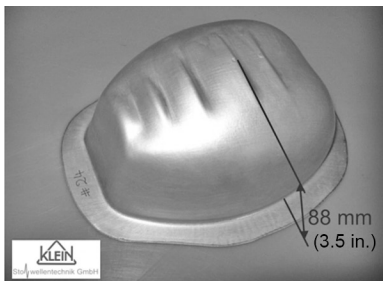
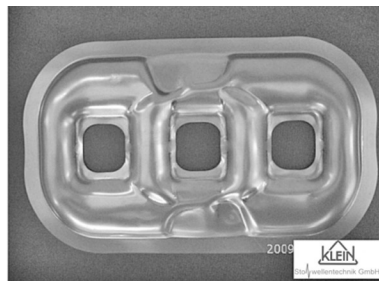


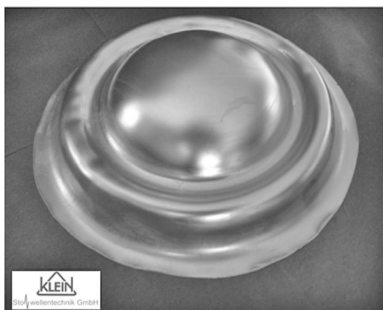
Fig. 11.7 Principle of shock wave focusing. (a) To calibrate small details in sheet metal forming. Source: Ref 11.16. (b) and (c) For bulging tubes with different measurement ratios. Source: Ref 11.1



Reflector for street lamp
Material: EN AW 1085



Exhaust Gas Collector Part
(after forming and after cutting)
Material: 1.4301



Spherical cap
Material: 1.4301

Fig. 11.8 Parts produced by electrohydraulic forming

11.1). The applicable sheet thicknesses range from very thin-walled sheets and profiles (especially in propellant forming) to rather thick-walled semifinished parts (especially in forming with high explosives using the contact operation). Different technologies can be applied for steel and aluminum alloys as well as for forming high-strength titanium alloys. Thereby, forming using high explosives is especially suitable for the manufacturing of large parts, for which the forces of conventional presses are not sufficient.

Hydropunch. The hydropunch process can be used for forming parts with high tolerances and surface quality. As discussed in Ref 11.13 with the example of a pulley, combined processes, including forming with a hydropunch as well as conventional forming, may also be used. Further applications are fittings, flute tubes, and small but complex sheet metal parts for heat exchangers.

11.2 High-Velocity Mechanical Forming

Process Principle. High-velocity mechanical forming uses presses with special drive systems that can provide relatively high punch velocities of up to 20 m/s (65 ft/s). Such high-velocity forming operations can be considered to be essentially adiabatic, because the temperature loss is overcompensated by the heat generated by forming. Thus, the forming of the workpiece is performed at higher temperatures than in a conventional process.

The high-velocity forming processes were extensively investigated for forging applications in the 1970s and 1980s. In these processes, due to high impact forces, tool life is relatively short and the cycle times are low. Consequently, the application of this technology has been quite limited.

Process Variations and Equipment. According to the drive mechanism, high-velocity mechanical forming machines can be subdivided into:

- Pneumatically-driven machines
- Explosively-driven machines
- Electromagnetically-driven machines

Among these, currently only electromagnetically-driven machines, such as the blanking press shown in Fig. 11.9, are relevant, while the other machine types have vanished. As shown

in Fig. 11.10, the principle of the electromagnetically driven press consists of:

- A pulsed power generator, represented here by its equivalent circuit diagram, mainly consisting of a capacitor and a high-current switch
- An acceleration coil, which is a flat coil consisting of several spirally wound turns, similar to a tool coil for electromagnetic sheet metal forming
- A piston with an electrically high conductive surface that accelerates the punch
- The punch

To start the process, the capacitor is charged up to the desired energy by the corresponding voltage. Then, the high-current switch is closed, and thus, the capacitor is discharged through the

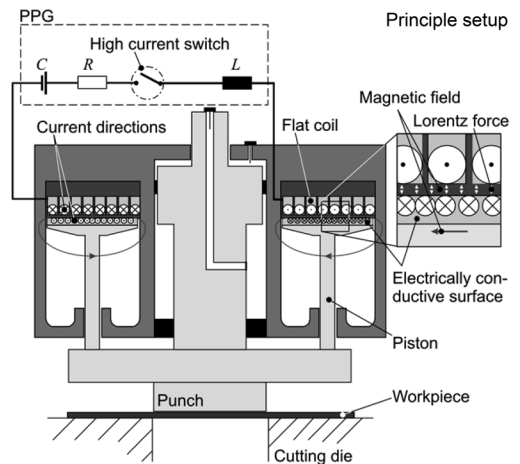


Fig. 11.9 Principle of an electromagnetically-driven blanking press (die cutter) according to German patent DE 1955400. PPG, pulsed power generator

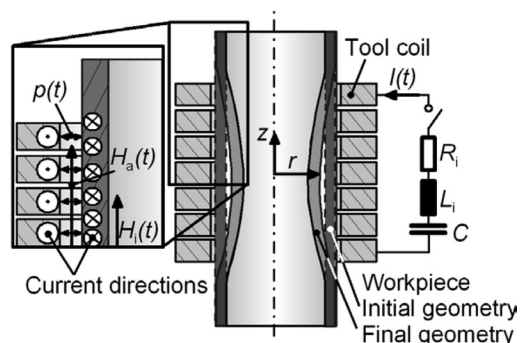


Fig. 11.10 Principle of the electromagnetic compression process according to U.S. patent 2976907

acceleration coil. Due to the coil current and the induced currents in the piston surface, Lorentz forces result and accelerate the piston, which in turn accelerates the punch. Thus, a sheet metal forming or cutting operation can be initiated. The backward movement of the punch and the piston can be achieved pneumatically. A small electromagnetic press (working surface 400 by 500 mm, or 16 by 20 in.), with a maximum stroke of 40 mm (2 in.) and maximum stroking rate of 300/min, is commercially used for blanking of thin sheet from various materials (Ref 11.21). High-velocity mechanical forming processes are limited to use for special forging operations, for compaction of metal and ceramic powders, as well as in special cases for sheet metal forming operations (Ref 11.1).

11.3 Electromagnetic Forming

According to Ref 11.8, electromagnetic forming (EMF) includes all production processes using pulsed magnetic fields to apply forces and thus deform a sheet metal workpiece of an electrically conductive material. The main advantages of EMF can be summarized as follows:

- Because the magnetic field itself represents the active tool, no working medium is required, and the forces are applied to the workpiece without mechanical contact. Therefore, the process can be performed under special conditions, for example, in a clean room or a vacuum, and the surface quality of the workpiece is not deteriorated. Even forming of coated or painted semifinished parts is possible as long as the adhesion of the coating and the coating itself endures the deformation without peeling off.
- The process is environmentally friendly, because no lubricant is used. Thus, no impurities are involved, and there is no need for cleaning the workpiece after the EMF process.
- A high repeatability can be achieved once the forming machine is adjusted. The adjustment of the applied forces via the charging energy and the voltage, respectively, is very accurate so that joints between metals, on one hand, and glass, polymers, composites, or metals, on the other hand, are possible without damaging even brittle materials.
- In contrast to conventional sheet metal forming, the electromagnetic sheet metal forming process uses only one form-defining tool,

the (female) die. Hence, the tool costs can be decreased significantly.

- Due to the high strain rates for several materials, including aluminum alloys, for example, the formability is higher compared to conventional quasistatic forming processes.

Some disadvantages of EMF are:

- Due to the physics of the process, this technology is limited to electrically high-conductive materials, and the process efficiency increases with increasing conductivity and decreasing flow stress. If the conductivity of the workpiece material itself is not sufficient, so-called drivers can be applied, but this technique increases the process costs and the handling and positioning effort.
- Safety aspects of the process and equipment must be considered, because of the high currents, high voltages, and high magnetic fields (Ref 11.22, 11.23).

Process Principle

The typical EMF setup consists of a PPG, similar to those used for electrohydraulic forming; a tool coil, including a fieldshaper (i.e., a usually axisymmetric component made of an electrically high-conductive material featuring one or more axial slots that is positioned between the tool coil and workpiece), if applicable; and the workpiece itself. If the workpiece to be formed is not made of an electrically high-conductive material, such as copper or an aluminum or magnesium alloy, a so-called driver is required to build up the forming forces. Therefore, the tool coil and the workpiece, including the fieldshaper and the driver, where required, represent the consumer unit, while the PPG is the energy supplier. After charging the capacitor of the PPG, the closing of the high-current switch affects a sudden discharge in the form of a damped sinusoidal current through the tool coil. Typical amplitudes are approximately 10 to 200 kA, while typical frequencies range from 70 to 75 kHz (Ref 11.24). Consequently, magnetic fields with a field strength of 20 to 100 T are induced for a very short period of time, in the range of microseconds.

The electrically conductive workpiece and the driver can be considered as a short-circuited secondary winding of a current transformer. Therefore, a secondary current, directed opposed to the coil current according to Lenz's law, is induced. Due to the skin effect, the cur-

rents flow only in those areas of the workpiece and the coil surface that face each other directly. Lorentz forces are acting on both the workpiece as well as the tool coil. These volume forces can be transformed mathematically to virtual surface forces, the so-called magnetic pressure, p , which corresponds to the energy density of the magnetic field and acts orthogonally to the current directions and the magnetic field lines. If the resulting stresses in the workpiece reach the flow stress of the workpiece material, the workpiece is accelerated in the direction away from the tool coil. Thereby, velocities up to 300 m/s (1000 ft/s) and strain rates in the range of 10^3 to $10^4/s$ are reached (Ref 11.25). The arrangement of tool coil and workpiece, and the directions of the currents and fields as well as of the magnetic pressure, is shown in Fig. 11.11 for the electromagnetic compression, which is the most common process variation.

During the process, the magnetic field penetrates into the workpiece. This effect is influenced significantly by the frequency of the discharging current; the workpiece geometry, which is characterized by radius and wall thickness; and the electrical conductivity of the material. The magnetic pressure can be calculated from the magnetic field outside the workpiece, the penetrated magnetic field, and the permeability (Ref 11.15).

For successful EMF, the following essential characteristics of the tube material are required:

- A closed cross-sectional geometry of the workpiece is essential for the working mechanism of the EMF process. Only if this prerequisite is granted, a closed path for the eddy currents is provided in the workpiece, and Lorentz forces can be established in those areas of the workpiece that are located close to the coil winding.

- Sufficient formability of the material under the highly dynamic conditions of the EMF process is necessary.
- High electrical conductivity of the workpiece is necessary to allow high efficiency of the process. An overview about electrical conductivities of different metallic materials is given in Table 11.2.

Process Variations

In addition to electromagnetic compression, other well-known process variations of EMF are tube expansion and forming of sheet metal. Typical arrangements and coil geometries for all three process types are shown in Fig. 11.11. For accomplishing an electromagnetic compression process, the tubular workpiece is positioned inside a cylindrical coil, while in electromagnetic expansion, the coil is positioned inside the workpiece. During sheet forming, so-called flat coils are used for forming flat or three-dimensionally preformed semifinished parts. All three process variations have in common that the deformation of the workpiece is always directed away from the tool coil.

Table 11.2 Electrical conductivities of various metallic materials

Material	Electrical conductivity, MS/m
Silver	62
Copper	58
Gold	44
Aluminum (pure)	36
EN AW-6060	28
Magnesium (pure)	21
EN AW-5754	19
Brass (CuZn37)	15
AZ31	10
DC06	8
Titan	2.6
Stainless steel (1.4301)	1.4

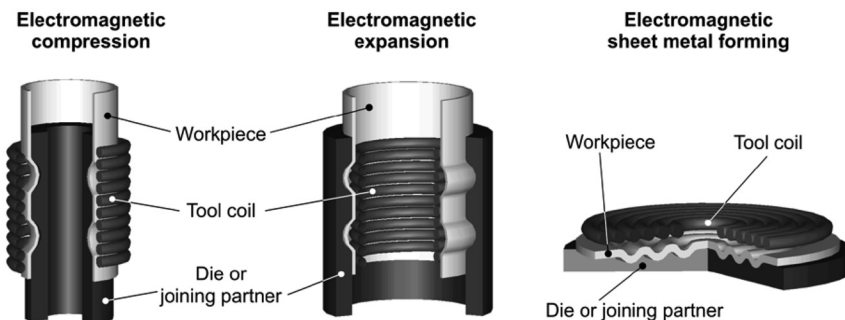


Fig. 11.11 Common process variants of electromagnetic forming. Source: Ref 11.14

In electromagnetic sheet metal forming processes, numerous and significantly different geometries of coil winding are possible. So-called pancake tool coils, that is, spirally wound ones, are frequently applied in literature; this geometry is considered here, Fig. 11.12.

In all EMF variations, the magnetic pressure acts only in those areas where the winding of

the tool coil is located. Thus, in a spirally wound coil, the maximum pressure occurs in the area of the mean coil radius, while in the center of the coil there is no magnetic pressure (Fig. 11.13). Therefore, the deformation starts in the form of a toroidal bulge directly above the coil winding, while the center of the workpiece remains in its initial position for several microsec-

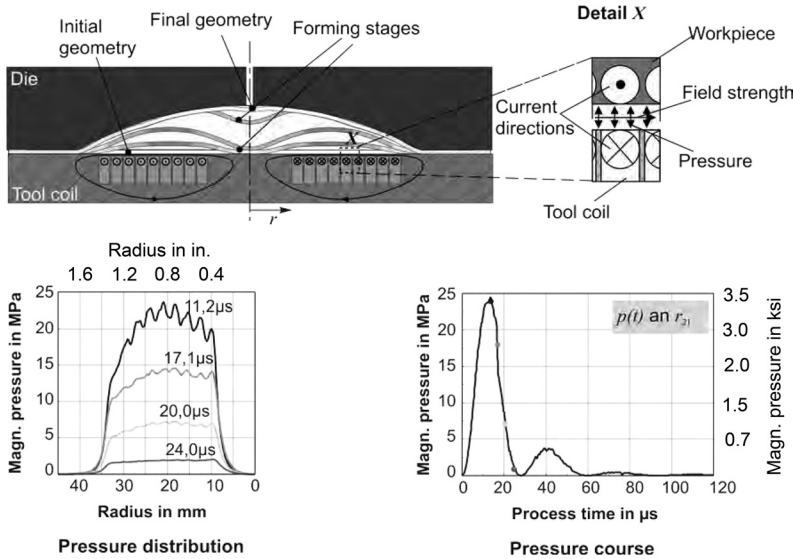


Fig. 11.12 Process principle of electromagnetic forming of sheet metal. Source: Ref 11.26

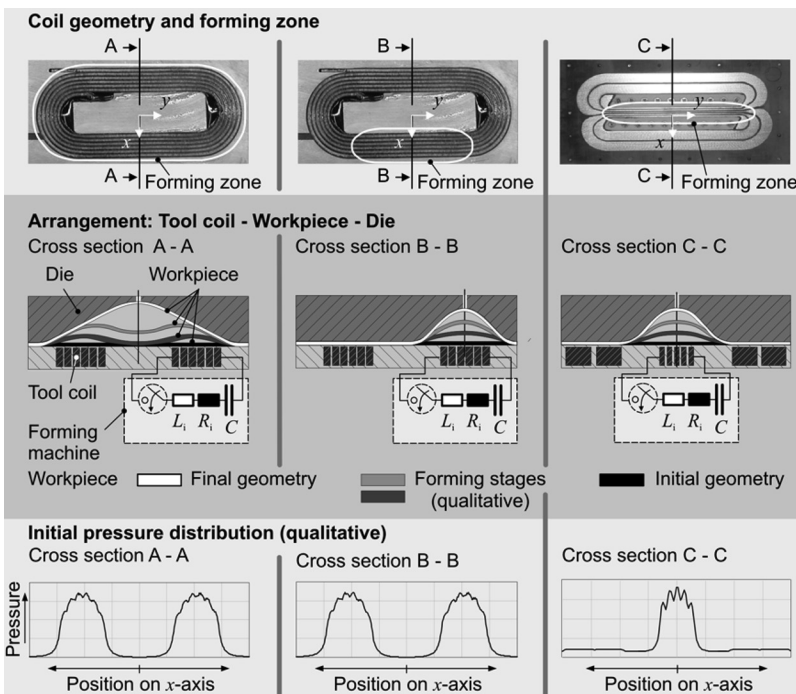


Fig. 11.13 Adaptation of pressure distribution and die cavity in electromagnetic sheet metal forming. Source: Ref 11.27

onds. Due to the increasing gap volume between tool coil and workpiece, the energy density of the magnetic field, which equals the magnetic pressure, decreases rapidly. However, even after the decrease of applied magnetic pressure to a negligible level, the deformation process continues due to inertia forces. These inertia forces can also cause an acceleration of the workpiece center. Depending on the dimensions of workpiece, tool coil, and die and on the process design, the workpiece center can even achieve the highest forming velocities and strains, although no magnetic pressure is applied here throughout the complete duration of the forming process.

Some special processes, such as forming with a discharging current in the workpiece, can also be found. In this case, the current flowing in the workpiece is not an induced short-circuit current but is imposed via contacting the semifinished part. To expand a tube, a ring-shaped supply can be attached to one end of the tube, so that the current is fed into the workpiece here. The second contact should be realized at the other end of the tube, and the current should be conducted through the inner tube by a mandrel. Radial Lorentz forces result from the interaction of the current in the tube and in the mandrel. Because the directions of the current in the tool coil and workpiece are opposed to each other, the forces are rejective and lead to an expansion of the tube. The smaller the gap between the workpiece and the conducting tool, the higher the efficiency of this process variant (Ref 11.28).

Another special process is forming with attractive forces, by which convex forms can be achieved in such locations that cannot be reached from the other side of the material. To realize such forces, a high magnetic field, which was established slowly, is suddenly abolished. For this purpose, the coil must be short-circuited in the moment when the current supply is stopped. Due to the decrease of the magnetic field, a voltage is induced in the coil and in the workpiece. Consequently, currents flow in the

coil and workpiece that are equally directed, resulting in attractive Lorentz forces (Ref 11.28).

Equipment

Similar to the electrohydraulic forming operation, as well as in EMF, high electrical energies are required in a short time, necessitating appropriate energy storage. Here again, a PPG similar to those applied in electrohydraulic forming can be used, because a capacitor is the most economic storage solution. For forming smaller parts, PPGs with a maximum storable energy of 6 to 20 kJ are typically sufficient (Ref 11.24). The biggest machine known was used for forming large parts for the Saturn V moon rocket. It offered a maximum chargeable energy of 240 kJ (Ref 11.29). Parameters of representative machines currently available or in use can be found in Table 11.3 (Ref 11.30).

A low self-inductance is favorable for the EMF process. The self-inductance of the PPG is the inductance measured if the machine is short-circuited without any forming load in the form of a tool coil and a workpiece. This value represents a lower limit for inductance of the oscillating circuit, which will be lowered when connecting a tool coil. Thus, a low-inductive PPG offers maximum flexibility for adapting the circuit parameters and therefore the temporary behavior of the discharging current, which in turn can influence the process efficiency (Ref 11.26, 11.32) and the forming results (Ref 11.33). Such an adaptation can be done by applying a tool coil with suitable parameters, considering the number of turns (Ref 11.14). The forming coil is the actual tool in EMF and must be designed considering the properties of the PPG, on one hand, and the special forming task to be fulfilled, on the other hand. The major tasks of the coil are to conduct the current and to apply a suitable temporary trajectory and spatial distribution of the so-called magnetic pressure. Therefore, it is necessary to consider that the

Table 11.3 Characteristics of current pulsed power generators

Machine type/manufacturer	Maximum charging energy, kJ	Maximum charging voltage, kV	Capacitance, μF	Maximum allowable current, kA	Short-circuit frequency, kHz
Magneform 7000-er series (USA)	32	8	1000	800	23
Poynting SMU2000 (Germany)	2	6.1	107	100	65
Poynting SMU modular (Germany)	<54	<8	...	<1440	30–50
PS16-10 Blue Wave (PST Products, Germany)	16	25	51	240	100
PS112-16 Blue Wave (PST Products, Germany)	112	25	384	1680	100
Pulsar Model 20/9 (Israel)	20	9	494	800	36
Pulsar Model 100/25 (Israel)	100	25	320	1600	65

Source: Ref 11.30, 11.31

forces applied to form the workpiece also act on the coil and must be endured permanently (Ref 11.34). For a durable coil, a lifetime of 10^6 forming operations is desired. (Especially in small-batch productions, the application of disposable coils used for only one or very few forming operations can also be an alternative, Ref 11.35. These are constructed more easily, but the economic efficiency of this approach must be evaluated for every single application.) To reach this goal, special design considerations are required. Moreover, an efficient transfer of capacitor charging energy to magnetic pressure is desired. Thus, the energy initially stored in the capacitor, and consequently the load acting on the tool coil, can be reduced. In this case, a reduction of the coil resistance by applying electrically high-conductive material is essential. To achieve high conductivity as well as sufficient mechanical strength, various approaches have been suggested and applied.

One possibility is to use a composite winding consisting of a high-strength steel body and an electrically high-conductive copper layer (Ref 11.36). Due to the skin effect also in the coil, the current only flows close to the surface facing the workpiece and not in the complete cross section. The use of copper-beryllium alloys is another alternative, because these materials offer a good compromise of strength and conductivity and can be hardened up to their flow stress (Ref 11.37).

The choice of the number of windings is crucial, because it significantly influences the resistance and inductivity of the coil and the coil-workpiece unit, respectively. Here, it should be considered that the gap width between the single turns should not be smaller than 2 mm (0.08 in.), and the width of the turns should be at least 5 mm (0.2 in.) to guarantee the required stiffness (Ref 11.38).

Possible production strategies for manufacturing the coil winding are spooling an isolated wire as well as machining processes such as milling, laser and jet cutting, and eroding (Ref 11.39). The machining alternatives offer the additional potential to modify the pressure distribution by selecting the width of the turns locally (Ref 11.40).

The arrangement of tool coil, workpiece, and die is important concerning the deformation behavior of the workpiece. As shown in Fig. 11.14, depending on the forming task, it can be reasonable to use only parts of the winding for deformation to avoid the typical distinctive bending and unbending effect in sheet metal forming that results from the inhomogeneous pressure distribution described in previous sections (Ref 11.27).

A similar approach is used in Ref 11.42. The researcher uses a helically wound tool coil (actuator), which is surrounded by an electrically conductive frame at three sides. The fourth open side of the actuator is positioned close to the

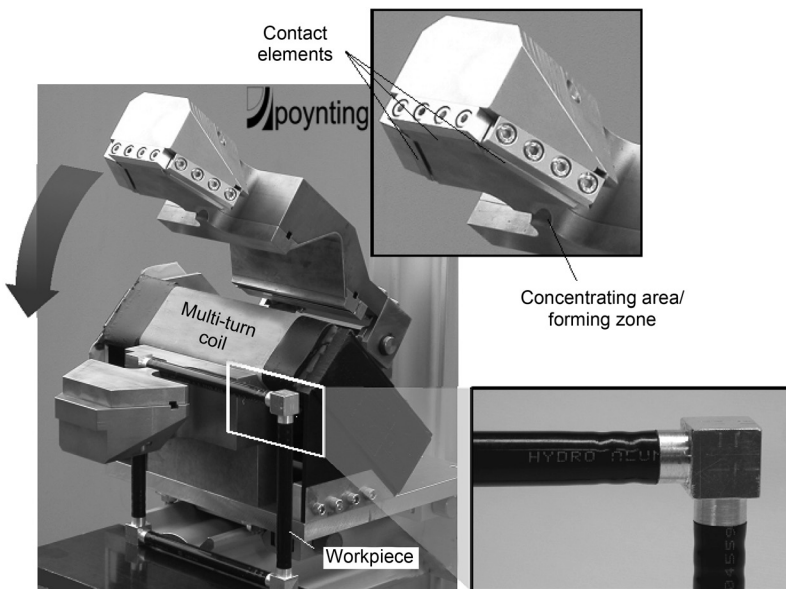


Fig. 11.14 Example of a separable tool coil. Source: Ref 11.41

sheet workpiece, which is electrically connected to the frame. As soon as a current flows through the coil, a secondary current is induced in the workpiece as well as in the frame. Thus, the pressure distribution acting on the workpiece is relatively homogeneous, so that this coil is called a uniform pressure actuator. As shown in Ref 11.43, this tool coil is suitable for forming, coining, and cutting sheet metal workpieces. The application is especially promising in the production of fuel cell components (Ref 11.42).

In compression coils, recent developments focus on the design of separable coils to allow the joining of closed structures (Ref 11.14, 11.41). The problem here is that welding effects caused by the high current density must be avoided. An example of a separable tool coil is shown in Fig. 11.15.

In many practical applications, the described setup for electromagnetic compression, consisting of the PPG, a tool coil, and the workpiece, is supplemented by a so-called fieldshaper. This increases the flexibility of the process (Ref 11.45) and can lead to reduction of the coil load and thus to an increase of the coil lifetime. At the same time, however, the process efficiency may be reduced.

A fieldshaper is usually an axisymmetric part with one or several axial slots made of a material of high electrical conductivity that is positioned between the tool coil and workpiece, as shown in Fig. 11.15. In this process variation, the sudden discharge of the capacitor causes a current, I_{Coil} , in the tool coil, inducing a secondary current in the fieldshaper, $I_{\text{Fieldshaper}}$. Due to the skin effect and Lenz's law, this current flows in the opposite direction to the coil current at the outer side of the fieldshaper and in the same direction as the coil current at the inner side. Here, the current in the fieldshaper in turn induces a current in the workpiece. In the begin-

ning of the process, the magnetic field is limited to the volume of the gap between the tool coil and fieldshaper, in the axial slot of the fieldshaper, and between the fieldshaper and workpiece. Usually, this inner surface of the fieldshaper is significantly smaller than the outer one, so that the current density as well as the magnetic field strength are higher here in the so-called concentrating area. If the resulting pressure acting on the workpiece is high enough, deformation is achieved.

In principle, a fieldshaper can be used in electromagnetic expansion or in a sheet metal forming process as well, but these variations are extremely rare. Exceptions dealing with the application of fieldshapers in electromagnetic expansion are described in Ref 11.46.

Applications

The most common and most efficient application of EMF is the joining of hollow profiles, particularly in sheet metal forming operations. Furthermore, the technology can be applied to primary shaping by powder compaction (Ref 11.47) and cutting operations (Ref 11.48, 11.49).

Joining can be achieved by compressing the tubular workpiece onto a mandrel or by expanding it into a collar (Ref 11.50). Moreover, the joining of sheet metal is possible (Ref 11.51). Example applications are shown in Fig. 11.16.

Tube joining operations can be divided into three different mechanisms, as follows:

- Force -fit or interference-fit
- Form-fit
- Metallic connections

A force-fit or interference-fit is based on an elastic-plastic bracing of tube and mandrel and tube and hub, respectively (Fig. 11.17). To realize this, the joining partners are positioned, if

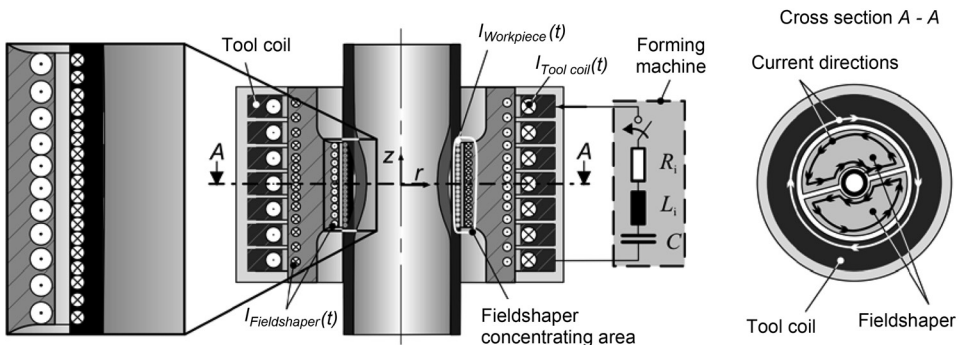


Fig. 11.15 Principle of electromagnetic compression using a fieldshaper. Source: Ref 11.44

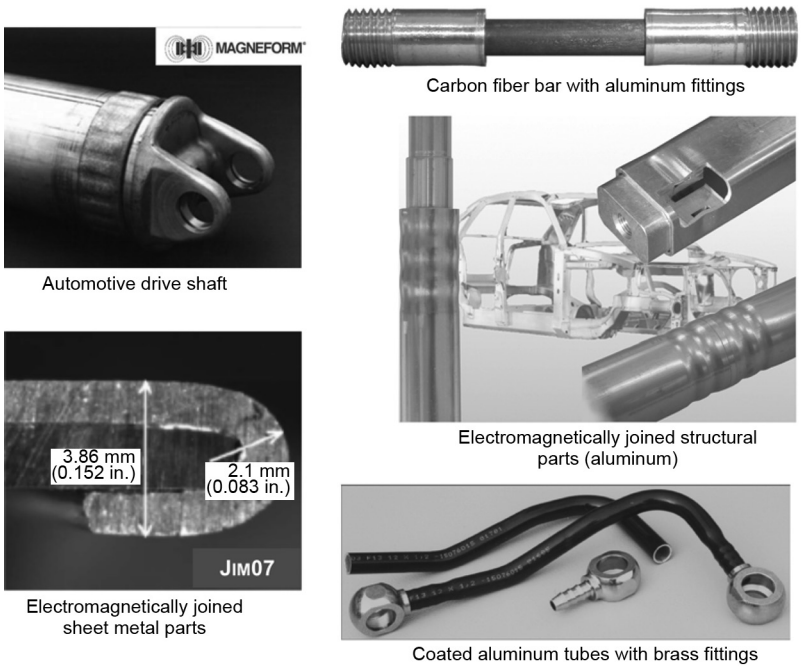


Fig. 11.16 Application examples for joining. Source: Ref 11.51–11.53

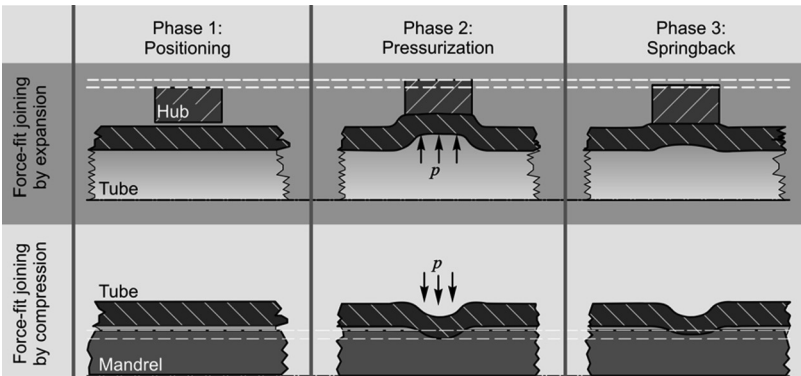


Fig. 11.17 Principle of force-fit joining by expansion and compression

applicable, with a radial gap between the two. Due to radial pressure that is applied to the tube, it aligns to the mandrel and the hub, respectively, and then both joining partners are deformed together up to a maximum radial displacement. The tube is thereby deformed plastically, while the deformation of the mandrel or the hub should be just elastic. After the decay of the magnetic pressure, springback of both joining partners takes place. A force-fit results if the complete springback of the mandrel is inhibited by the deformed tube.

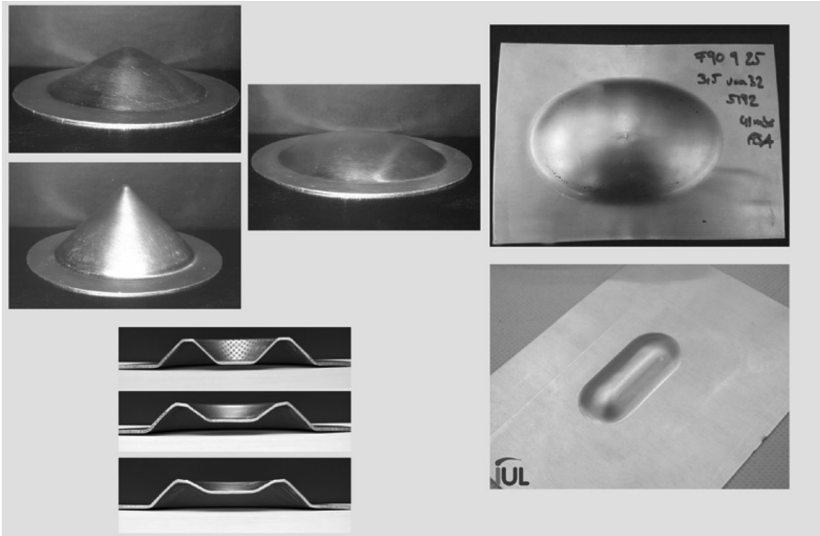
For a form-fit connection, one joining partner (typically the mandrel) features geometry elements such as grooves or beads so that during the deformation of the other joining partner, material flows into these grooves and forms an undercut. Depending on the geometry and the arrangement of these elements, the joint can be optimized with regard to the transfer of radial or axial loads, for example.

A metallic connection is based on joggling on a microstructural level. To realize this, the joining partners are positioned with a special dis-

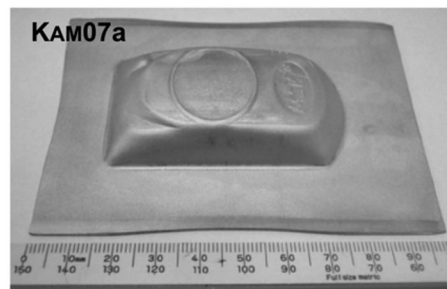
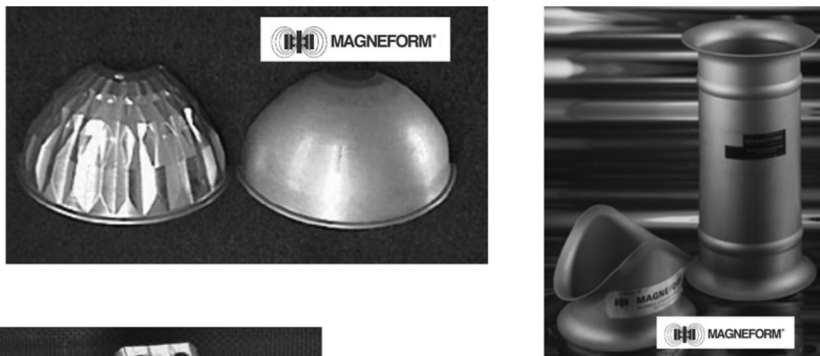
tance and angle between them. Then, one joining partner is accelerated and, analogue to explosive cladding, the partners approach each other to atomic distance and thus bond on an atomic level. At the collision point, the joining partners take a highly viscous stage, so that a

wavy interface is formed, as shown in Fig. 11.18.

Metallic connections can be achieved for tubular workpieces as well as for sheet metal (Ref 11.57). The most important process parameters influencing weld geometry and shearing strength



(a)



(b)

Fig. 11.18 Principle of joining on the basis of a metallic connection. (a) Example parts manufactured by forming. (b) Example industrial parts manufactured by electromagnetic forming. Source: Ref 11.52, 11.54–11.56

are the impact velocity, which is significantly influenced by the charging energy and standoff distance; the impact angle; and the velocity of the collision point. These parameters must be adjusted to the materials to be welded to each other (Ref 11.58). Here, it is also possible to combine different materials, which can hardly be welded using conventional methods due to such factors as significantly different melting points (Ref 11.59, 11.60).

Applications of electromagnetic joining can be found in:

- The aircraft and automotive industry, for example, when connecting tubes and fittings (Ref 11.61) or during the assembly of cooling systems and air conditionings
- In the electrical industry, for example, when joining eyelets or sockets to flexible cables, copper or brass casings to resistors, and dynamos of small electric motors that are joined by aluminum shells (Ref 11.62)
- In the defense industry (Ref 11.63)
- In the assembly of shell and tube heat exchangers (Ref 11.61)
- In the assembly of spaceframe constructions (Ref 11.64)

Joining two metallic workpieces or joining of an aluminum or copper tube to a nonmetal core from polyurethane, ceramics, or carbon-fiber-reinforced plastic can also be achieved (Ref 11.65). In sheet metal, form-fit joints (Ref 11.51) and continuous metallic connections are possible (Ref 11.60). In electromagnetic sheet metal, forming was used for beading of axially symmetrical parts (Ref 11.66). Parts of different aluminum alloys and different shapes were beaded along the outer edge. Additionally, rings were beaded along their inner edge using mandrels as dies. Reference 11.67 describes newer developments and analysis results of this application area. Within these applications, the beading was complemented by one process step called clinching.

Forming. In tubular workpieces, forming applications are less common than joining examples. However, the process offers a high potential for the calibration of extruded profiles (e.g., to produce tubes with close-tolerance diameter for a subsequent bonding operation).

Electromagnetic sheet metal forming is often used for shaping processes. The technology is especially suitable for the processing of small parts or local areas in larger components. It is not limited to flat sheets but can also be used for

the further processing of three-dimensionally preformed parts (Ref 11.49). Figure 11.18(a) shows exemplary part geometries realized in feasibility studies and demonstrates the strength of the process, considering the forming of sharp edges and small radii.

In Fig. 11.18(b), more practical parts are depicted. Here, the result of a two-step strategy is included for manufacturing of mobile phone cases with the material Al 2219-0 (Ref 11.56, 11.68). At first, the part is electromagnetically preformed in the requested shape. The missing details of the geometry are electromagnetically calibrated in a second forming step by using a driver made of copper. These parts show good mold filling and no material failure. The geometries were reached with the developed uniform pressure actuator, which generates a homogeneous pressure allocation in the forming zone (Ref 11.43). A multiple-step forming technique is also used for manufacturing of a door handle (Ref 11.23).

In Fig. 11.18(b), lamp reflectors before and after EMF are also presented (Ref 11.52). The complex pattern of the diamondlike surface was produced by electromagnetic calibration. Thus, a better shape was accomplished, but in particular, considerably better reflecting attributes were achieved compared to conventional manufacturing processes. Another advantage consists of the abandonment of an additional grinding operation, because the tool touched just one side of the part (Ref 11.69).

Blanking and Piercing. By applying suitable blanking dies, piercing operations can be achieved for sheet metal workpieces as well as for hollow profiles. The blanking process can be performed as a separate production step or integrated into a forming operation (Ref 11.70). Examples are shown in Fig. 11.19.

Combined Conventional and Electromagnetic Processing. Innovative approaches combine electromagnetic and conventional forming operations to exploit the process-specific advantages complementarily. The feasibility of the following process combinations and integrations could already be proven successfully:

- Combined deep drawing and electromagnetic calibration (Ref 11.72)
- Integrated deep drawing and electromagnetic calibration (Ref 11.73, 11.74)
- Combined profile bending, electromagnetic compression, and tube hydroforming (Ref 11.33, 11.75)

- Combined extrusion and electromagnetic compression (Ref 11.76)
- Combined bending and electromagnetic calibration

By combining conventional deep drawing and subsequent electromagnetic calibration, higher strains can be realized compared to the mere deep drawing process (Ref 11.72). In such a combination, the deep drawing process can be applied profitably to realize the overall shape of a large component, while EMF can be used beneficially to calibrate smaller details. As shown in Fig. 11.20, it is possible to sharpen a radius to a measurement that, due to cracking, is not achievable by means of deep drawing (Ref 11.32, 11.72). To do so, the tool coil must be integrated into the deep drawing punch. Furthermore, it is

possible to form a door handle or similar shapes. Therefore, the tool coil should be integrated into the deep drawing die. In the latter case, good form filling can be achieved if a relatively homogeneous pressure distribution is applied. This can be realized by a so-called double-pancake flat tool coil (Ref 11.77) or a uniform pressure actuator (Ref 11.42). Alternatively, accordingly shaped pancake coils can be used, but then the dimensioning must be carried out very thoroughly, because the forming result reacts extremely sensitively to small changes in the coil geometry, for example, considering the width of the turns (Ref 11.74).

An integration of electromagnetic sheet metal forming into a conventional deep drawing process is presented in Ref 11.74 and 11.78. In these investigations, a three-dimensionally curved

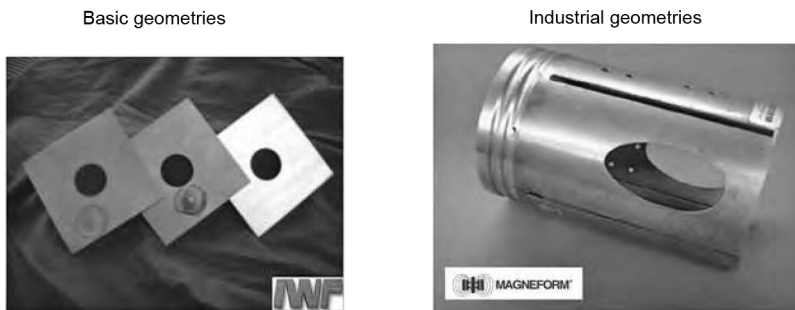


Fig. 11.19 Example parts manufactured by blanking and piercing. Source: Ref 11.52, 11.71

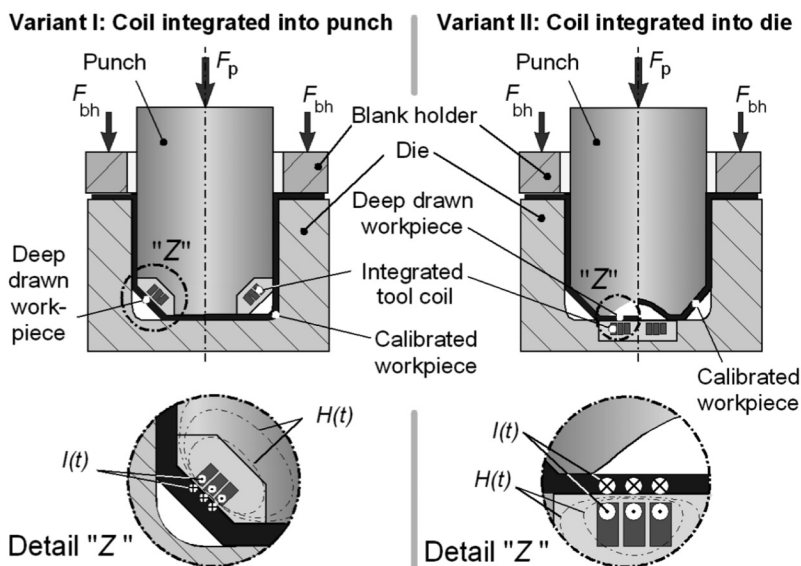


Fig. 11.20 Combined deep drawing and electromagnetic sheet metal forming. Source: Ref 11.73

tool coil was integrated into the deep drawing tool, and the EMF process was carried out in the bottom dead center of the deep drawing punch under full deep drawing load. In Ref 11.78, the tool coil was integrated into the deep drawing punch, while in Ref 11.74, the tool coil was implemented in the deep drawing die, as shown in Fig. 11.20. The forming task could be achieved in both examples in good order.

Another process combination offers the possibility to enhance the forming limits of the conventional hydroforming process. Starting with a semifinished part of a medium-sized diameter, the cross section is locally reduced by electromagnetic compression. This precontoured semifinished part is then applied to a hydroforming process to enlarge the cross-section locally and calibrate the preformed regions (Ref 11.33, 11.79). Thus, the spectrum of cross-sectional geometries achievable within one and the same part can be increased. This principle is illustrated in Fig. 11.21.

A further enhancement of the forming limits can be achieved by a suitable heat treatment between the single forming steps, but such addi-

tional production steps will lead to an increased production time and energy consumption and thus to rising production costs. As an alternative, electromagnetic compression can be directly coupled to an extrusion process. This means that the extruded strand is guided through and compressed by the tool coil, and subsequently a controlled cooling of the workpiece material is realized to adjust the microstructure (Ref 11.76). A setup used for first feasibility tests considering this combination is shown in Fig. 11.22.

In this process combination, electromagnetic compression is carried out as a hot working operation, so that the resulting influences on the relevant material properties must be considered. For example, the flow stress is significantly decreased so that only a lower magnetic pressure is required to achieve a special strain. At the same time, the maximum formability can be increased significantly. On the other hand, the electrical conductivity decreases with increasing temperature, and the thermal load of the equipment—and especially the tool coil—must be compensated by suitable cooling mecha-

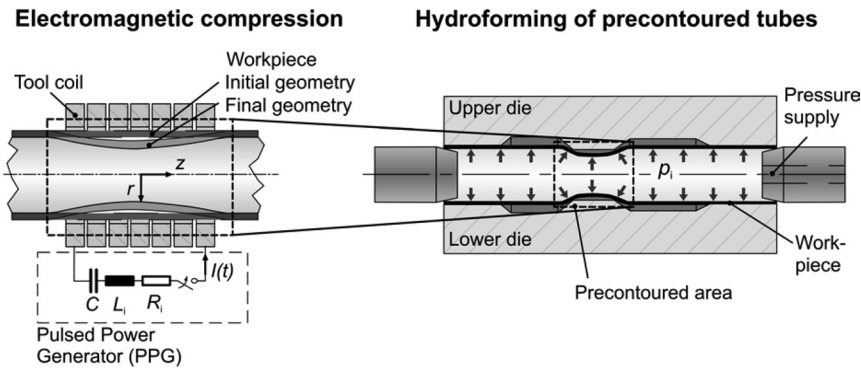


Fig. 11.21 Principle of combined electromagnetic compression and hydroforming. Source: Ref 11.33

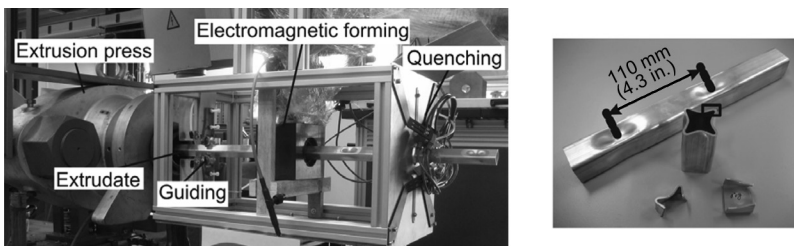


Fig. 11.22 Feasibility tests considering combined extrusion and electromagnetic compression. Source: Ref 11.76

nisms, for example, water or air cooling or by implementing heat-conveying metal parts in the armouring (Ref 11.80).

A process combination consisting of bending and electromagnetic calibration steps was investigated (Ref 11.81). Here, profiles with an L- or U-shaped cross section are produced by conventional sheet metal bending operations. Subsequently, a springback calibration by means of EMF is performed. The industrial applicability of this concept was shown on the example of a jet nozzle from the aerospace industry (Ref 11.82).

REFERENCES

- 11.1 K. Lange, Umformtechnik, Handbuch für Industrie und Wissenschaft, Band 4, *Sonderverfahren, Prozesssimulation, Werkzeugtechnik, Produktion*, Monographie, 1993
- 11.2 M. Kleiner, W. Homberg, A. Brosius, and D. Risch, Ein Überblick über die Verfahren der wirkmedienbasierten Hochgeschwindigkeitsumformung, *Abschlussbericht zum DFG-Schwerpunktprogramm, SPP1098 2000-2006, Wirkmedienbasierte Fertigungstechniken zur Blechumformung*, 2006, p 55–66
- 11.3 M.C. Noland, H.M. Gadberry, J.B. Loser, and E.C. Sneegas, “High-Velocity Metalworking—A Survey,” Office of Technology Utilization, National Aeronautics and Space Administration, 1967
- 11.4 M. Altynova, X. Hu, and G. Daehn, Increased Ductility in High Velocity Electromagnetic Ring Expansion, *Mater. Mater. Trans. A, Phys. Metall. Mater. Sci.*, Vol 27 (No. 7), 1996, p 1837–1844
- 11.5 E. El-Magd and M. Abouridane, High Speed Forming of the Light-Weight Wrought Alloys, *Proceedings of the First International Conference on High Speed Forming, ICHSF 2004* (Dortmund, Germany), 2004, p 3–12
- 11.6 V. Psyk, C. Beerwald, A. Klaus, and M. Kleiner, Characterisation of Extruded Magnesium Profiles for Electro-Magnetical Joining, *J. Mater. Process. Technol.*, Vol 177, 2006, p 266–269
- 11.7 H. Weisshaupt, “Verformungsverhalten metallischer Werkstoffe,” Dr.-Ing. dissertation, Aachen, 1995
- 11.8 A. Neubauer, H. Stroppe, H. Wolf, et al., *Hochgeschwindigkeitstechnologie der Metallbearbeitung*, 1988
- 11.9 J. Schinnerling, Die Explosivumformung—Eine neue Verfahrenstechnik der Umformung, *Werkstatt Betr.*, Vol 104 (No. 3), 1971, p 183–186
- 11.10 A. Neubauer, H. Steinicke, K. Vinzens, and H. Schmicker, New Processes for Explosive Metal Forming of Sheet Parts in Batch Production, *Adv. Technol. Plastic.*, Vol I, 1984, p 379–384
- 11.11 M. Weber, M. Hermes, A. Brosius, C. Beerwald, G. Gersteyn, H. Olivier, M. Kleiner, and Fr.-W. Bach, Process Investigation of Tube Expansion by Gas Detonation, *Proceedings of the Second ICHSF 2006* (Dortmund, Germany), p 161–174
- 11.12 V.T. Vovk, Gasexplosion als, *Werkzeug in der Fertigungstechnik*, Magdeburg, Habilitationsschrift, 1999
- 11.13 R. Ratjen and M. Takamatsu, Hoehenenergie-Umformverfahren Hydropunch, *Werkstatt Betr.*, Vol 104 (No. 1), 1971, p 41–45
- 11.14 C. Beerwald, “Grundlagen der Prozessauslegung und—Gestaltung bei der elektomagnetischen Umformung,” Dr.-Ing. dissertation, Technische Universität Dortmund, Institut für Umformtechnik und Leichtbau, 2005
- 11.15 R. Winkler, *Hochgeschwindigkeitsbearbeitung*, VEB-Verlag Technik, Berlin, 1973
- 11.16 M. Kleiner, C. Beerwald, and W. Homberg, Machine Tools and Process Strategies for Sheet Metal Hydroforming, *Proceedings of the Ninth International Conference on Sheet Metal*, April 2–4, 2001 (Leuven, Belgium)
- 11.17 F.W. Wilson, “High-Velocity Forming of Metals,” ASTM Manufacturing Data Series, 1964
- 11.18 M. Koschlig, M. Veehmayer, and D. Raabe, Production of Steel-Light Metal Compounds with Explosive Metal Cladding, *Proceedings of the Third International Conference on High Speed Forming—ICHSF*, March 11–12, 2008 (Dortmund, Germany), p 23–32
- 11.19 O.E. Kosing and B.W. Skews, “The Use

- of Liquid Shock Waves for Metal Forming,” 21st International Symposium on Shock Waves, July 20–25, 1997 (Great Keppel Island, Australia)
- 11.20 R. Prümmer, Explosivumformung von Mittel- und Grobblechen, *DFBO Mitteilung.*, Vol 25 (No. 1), 1974, p 3–9
- 11.21 Netronics Research and Development, Ltd., New Milford, CT, www.netronics-research.com
- 11.22 M. Plum, Electromagnetic Forming, *Forming and Forging*, Vol 14, *ASM Handbook*, ASM International, 1988, p 644–653
- 11.23 F. Löschmann, “Anlagentechnische Grundlagen für die Elektromagnetumformung im Automobilbau,” Dissertation, Technische Universität Chemnitz, 2007
- 11.24 S.T.S. Al-Hassani, J.L. Duncan, and W. Johnson, Analysis of the Electromagnetic Forming Process, *Proceedings of the International Conference on Manufacturing Technology 1967* (Ann Arbor, MI), 1967, p 854–882
- 11.25 S.T.S. Al-Hassani, J.L. Duncan, and W. Johnson, On the Parameters of the Magnetic Forming Process, *J. Mech. Eng. Sci.*, Vol 16 (No. 1), 1974, p 1–9
- 11.26 D. Risch, “Energietransfer und Analyse der Einflussparameter bei der formgebundenen elektromagnetischen Blechumformung,” Dr.-Ing. dissertation, Technische Universität Dortmund, 2009
- 11.27 V. Psyk, C. Beerwald, M. Kleiner, M. Beerwald, and A. Henselek, Use of Electromagnetic Forming in Process Combinations for the Production of Automotive Parts, *Proceedings of the Second European Pulsed Power Symposium—EPPS 2004*, 2004, p 82–86
- 11.28 H. Furth and R. Waniek, New Ideas on Magnetic Forming, *Am. Machin./Metalwork. Manuf.*, Vol 106, 1962, p 92–95
- 11.29 R.J. Schwinghamer, Shaping Metal Magnetically, *New Sci.*, 1966, p 478
- 11.30 C. Beerwald, Current Trends in EMF Tools and Process Technology, *Proceedings: First Technical Conference on Industrialized Magnetic Pulse Welding and Forming 2008* (Munich, Germany), 2008
- 11.31 S. Kallee, R. Schäfer, and P. Pasquale, “The Industrial Use of EMPT, State of the Art and Future Applications,” International Conference and User Meeting, April 22, 2010 (Alzenau, Germany)
- 11.32 V. Psyk, A. Brosius, and A.E. Tekkaya, Target-Oriented Adaptation of the Pressure Course in Electromagnetic Tube Compression Processes, *Proceedings of the First International Conference on High Speed Industrial Manufacturing Processes* (Frankreich), Cetim, 2007
- 11.33 V. Psyk, “Prozesskette Krümmen—Elektromagnetisch Komprimieren-Innenhochdruckumformen für Rohre und profilförmige Bauteile,” Dr.-Ing. dissertation, Technische Universität Dortmund, 2010
- 11.34 V. Fischer, “Gestaltung und Einsatz von Flachspulen für die elektromagnetische Umformung,” Dissertation, TH Magdeburg, 1983
- 11.35 S. Woodward, C. Weddeling, G. Daehn, V. Psyk, B. Carson, and A.E. Tekkaya, Agile Production of Sheet Metal Aviation Components Using Disposable Electromagnetic Actuators, *Proceedings of the Fourth International Conference on High Speed Forming (ICHSF 2010)*, March 9–10, 2010 (Columbus, OH), 2010, p 35–46
- 11.36 V. Schmidt, “Untersuchung der magnetischen Induktion, Stromdichte und Kraftwirkung bei der Magnetumformung,” Dr.-Ing. dissertation, Universität Stuttgart, 1976
- 11.37 J. Daube and A. Borowski, Auswechselbare Arbeitsspule mit Einspannvorrichtung für eine elektromagnetische Umformanlage, *Drittes Kolloquium über Grundlagen der elektrischen Hochgeschwindigkeitsbearbeitung*, Jan 27–30, 1969 (Berlin), p 67–77
- 11.38 S. Golovashchenko, Methodology of Design of Pulsed Electromagnetic Joining of Tubes, *Proceedings of the Second Global Symposium on Innovation in Material Processing and Manufacturing: Sheet Materials*, TMS Annual Meeting (New Orleans, LA), 2001
- 11.39 S. Golovashchenko, N. Bessonov, and R. Davies, Design and Testing of Coils for Pulsed Electromagnetic Forming, *Proceedings of the Second International Conference on High Speed Forming* (Dortmund, Germany), 2006, p 141–151

- 11.40 M. Beerwald and A. Henselek, *Spiralförmige Spule zur magnetischen Umformung von Blechen*, Offenlegungsschrift De 102 07 655 A 1, 2003
- 11.41 A. Henselek, M. Beerwald, and C. Beerwald, Design and Adaptation of EMF Equipment—From Direct Acting Multi-Turn Coils to Separable Tool Coils for Electromagnetic Tube Compression, *Proceedings of the First International Conference on High Speed Forming, ICHSF 2004* (Dortmund, Germany), 2004, p 275–284
- 11.42 G. Daehn, Electromagnetic Metal Forming, U.S. Patent, 2005/0217333 A1, 2005
- 11.43 M. Kamal, “A Uniform Pressure Electromagnetic Actuator for Forming Flat Sheets,” Ph.D. thesis, The Ohio State University, 2005
- 11.44 H. Dietz, H.J. Lippmann, and H. Schenk, Theorie des Magneform-Verfahrens: Erreichbarer Druck, *Elektron. Z. A*, Vol 88 (No. 9), 1967, p 217–222
- 11.45 R. Hahn, “Werkzeuge zum impuls-magnetischen Warmfügen von Profilen aus Aluminium- und Magnesiumlegierungen,” Dr.-Ing. dissertation, Technische Universität Berlin, 2004
- 11.46 C. Li, J. Zhang, Z. Zhao, Y. Wang, and J. Li, Experimental Research of Field Shaper for Bulging, *J. Harbin Inst. Technol.*, Vol 32 (No. 4), 2000, p 107–109
- 11.47 A.G. Mamalis, D.E. Manolakos, A.G. Kladas, and A.K. Koumoutsos, Electromagnetic Forming and Powder Processing: Trends and Developments, *Appl. Mech. Rev.*, Vol 57 (No. 4), 2004, p 299–324
- 11.48 T. Kautz, “Impuls-magnetisches Beschneiden von dünnwandigen Hohlprofilen,” Dr.-Ing. dissertation, Otto von Guericke Universität, Magdeburg, 2008
- 11.49 R. Neugebauer, H. Bräunlich, and V. Kräusel, Hochgeschwindigkeitsbearbeitung für die ressourceneffiziente Karosseriefertigung, *MM Maschinenmarkt—Das Industriemagazin*, Vol 3, 2009, p 28–29
- 11.50 D. Jurgasch and K. Damavandi, Berührungsloses Umformen im Zeitraffer, *Berliner Runde, Prozess, Struktur und Simulation rund um die Werkzeugmaschine*, 2006, p 33–51
- 11.51 P. Jimbert, I. Perez, I. Eguia, and G. Daehn, Straight Hemming of Aluminum Sheet Panels Using the Electromagnetic Forming Technology: First Approach, *Key Eng. Mater.*, 2007, p 365–372
- 11.52 Maxwell Magneform Products, www.magneform.com/apps.html, July 22, 2008
- 11.53 V. Psyk, C. Beerwald, M. Kleiner, and C. Dreesen, Berührungslos in Form, *Maschinenmarkt*, Vol 6, 2005, p 20–22
- 11.54 PST Products, www.pstproducts.com, Sept 16, 2009
- 11.55 D. Risch, C. Beerwald, A. Brosius, and M. Kleiner, On the Significance of the Die Design for the Electromagnetic Sheet Metal Forming, *Proceedings of the First International Conference on High Speed Forming, ICHSF 2004*, March 31–Apr 1, 2004 (Dortmund, Germany), p 191–200
- 11.56 M. Kamal, J. Shang, V. Cheng, S. Hatkevich, and G.S. Daehn, Agile Manufacturing of a Micro-Embossed Case by a Two-Step Electromagnetic Forming Process, *J. Mater. Process. Technol.*, Vol 190, 2007, p 41–50
- 11.57 T. Aizawa, Magnetic Pressure Seam Welding Method for Aluminium Sheets, *J. Light Met. Weld. Constr.*, Vol 41 (No. 3), 2003, p 20–25
- 11.58 V. Shribman and Y. Tomer, Magnetic Pulse Technology for Improved Tube Joining and Forming, *Tube Pipe Technol.*, 2006, p 91–95
- 11.59 V. Shribman, Magnetic Pulse Welding for Dissimilar and Similar Materials, *Proceedings of the Third International Conference on High Speed Forming* (Dortmund, Germany), 2008, p 13–22
- 11.60 S.D. Kore, P.P. Date, and S.V. Kulkarni, Electromagnetic Impact Welding of Aluminium to Stainless Steel Sheets, *J. Mater. Process. Technol.*, 2008
- 11.61 H. Wolf and M. Meinel, Fügen durch Magnetumformung—Erreichbare Effekte, *Fertigungstech. Betr.*, Vol 39 (No. 11), 1989, p 672–673
- 11.62 H. Bühler and E. von Finckenstein, Beitrag zur Herstellung von Ummantelungen und Sickenverbindungen rohrförmiger Teile durch Magnetumformung, *Bänder Bleche Rohre*, Vol 10 (No. 7), 1969, p 413–418

- 11.63 G. Zittel, Getting the Most Out of Electromagnetic Forming, *Assem. Eng.*, 1976, p 26–29
- 11.64 E. Uhlmann, U. Forstmann, and M. Scholz, Flachumformen mit Impulsmagnetfeldern, *Werkstattstechnik*, Vol 89 (No. 5), 1999, p 265–268
- 11.65 W.S. Hwang, N.H. Kim, H.S. Sohn, and J.S. Lee, Joining of Copper Tube to Polyurethane Tube by Electromagnetic Pulse Forming, *J. Mater. Process. Technol.*, Vol 37, 1993, p 83–93
- 11.66 G. Lebedev, A. Komarov, G. Isarovic, and D. Lysenko, Umbördeln der Öffnungen und des Außenrandes von Blechteilen durch Magnetumformung, *Umformtechnik*, Vol 4 (No. 6), 1970, p 13–20
- 11.67 P. Jimbert, I. Eguia, I. Perez, B. Gonzalez, and G.S. Daehn, Hemming of Aluminum Sheet Panels Using the Electromagnetic Forming Technology, *Proceedings of the IDDRG 2007 International Conference*, May 21–23, 2007 (Győr, Hungary), p 283–290
- 11.68 M. Kamal and G.S. Daehn, A Uniform Pressure Electromagnetic Actuator for Forming Flat Sheets, *J. Manuf. Sci. Eng.*, Vol 129, April 2007, p 369–379
- 11.69 G. Zittel, Magneform: An Accepted Production Tool, *Proceedings of the Fifth International Conference on High Energy Rate Fabrication*, June 11–26, 1975 (Denver, CO), p 3.1.1–3.1.35
- 11.70 E. Uhlmann and U. Forstmann, Impulsmagnetische Umformung, *Z. Wirtsch. Fabrikbetr.*, Vol 93, 1998, p 286–289
- 11.71 Institut für Werkzeugmaschinen und Fabrikbetrieb IWF, <http://www.iwf.tu-berlin.de>, Feb 11, 2010
- 11.72 V. Vohnout, “A Hybrid Quasi-Static/Dynamic Process for Forming Large Sheet Metal Parts from Aluminium Alloys,” Ph.D. dissertation, The Ohio State University, 1998
- 11.73 V. Psyk, D. Risch, C. Beerwald, and A.E. Tekkaya, Investigation of Combined Electromagnetic and Conventional Forming, *IDDRG International Deep Drawing Research Group Best in Class Stamping* (Olofström, Sweden), 2008, p 487–498
- 11.74 D. Risch, G. Gersteyn, W. Dudzinski, C. Beerwald, A. Brosius, M. Schaper, A.E. Tekkaya, and F.-W. Bach, Design and Analysis of a Deep Drawing and In Process Electromagnetic Sheet Metal Forming Process, *Proceedings of the Third International Conference on High Speed Forming, ICHSF 2008* (Dortmund, Germany), 2008, p 201–212
- 11.75 V. Psyk, C. Beerwald, W. Homberg, M. Kleiner, M. Beerwald, and A. Henselek, Investigation of the Process Chain Bending-Electromagnetic Compression-Hydroforming on the Basis of an Industrial Demonstrator Part, *Proceedings of the Second International Conference on High Speed Forming—ICHSF 2006* (Dortmund, Germany), 2006, p 117–127
- 11.76 A. Jäger, D. Risch, and A.E. Tekkaya, Verfahren und Vorrichtung zum Strangpressen und nachfolgender elektromagnetischer Umformung, German patent DE 10 2009 039 759.0, 2009
- 11.77 R. Burden, L. Snowden, K. Hasegawa, D. Newman, and D. Bauer, Elektromagnetisches Umformen (EMF), *Neuere Entwicklungen in der Blechumformung*, K. Siegert, Ed., 2000, p 331–343
- 11.78 V. Psyk, C. Beerwald, A. Henselek, W. Homberg, A. Brosius, and M. Kleiner, Integration of Electromagnetic Calibration into a Deep Drawing Process of an Industrial Demonstrator Part, *Key Eng. Mater.*, Vol 344, 2007, p 435–442, <http://www.scientific.net>
- 11.79 V. Psyk, C. Beerwald, W. Homberg, and M. Kleiner, Electromagnetic Compression as a Preforming Operation for Tubular Hydroforming Parts, *Proceedings of the First International Conference on High Speed Forming, ICHSF 2004* (Dortmund, Germany), 2004, p 171–180
- 11.80 H. Beerwald, Mehrwindungsspule zur Erzeugung starker Magnetfeldimpulse, German patent DE 100 20 708 C 2, 2003
- 11.81 E. Iriondo, “Electromagnetically Impulsed Springback Calibration,” Ph.D. dissertation, The University of the Basque Country, 2007
- 11.82 E. Iriondo, B. Gonzalez, M. Gutierrez, V. Vohnout, G. Daehn, and B. Hayes, Electromagnetic Springback Reshaping, *Proceedings of the Second International Conference on High Speed Forming—ICHSF 2006* (Dortmund, Germany), 2006, p 153–160

CHAPTER 12

Spinning, Shear Forming, and Flow Forming

L. Kwiatkowski, Technische Universität Dortmund, Germany

SHEET METAL SPINNING is a forming technique to manufacture axially symmetrical hollow bodies with nearly arbitrary contour. The parts are formed incrementally from circular blanks or preformed hollow bodies. The main characteristic of this process is the locally confined forming zone. Spinning is a generic expression that covers several process variations and can be divided into three main processes: spinning, shear forming, and flow forming. Figure 12.1 presents a comprehensive overview of the main characteristics of these three processes. The spinning process is often combined with flow forming and shear spinning operations to manufacture complex parts.

12.1 Spinning

Figure 12.2 shows the components of a spinning machine as well as a typical process sequence. A blank (1) is clamped between the tail stock (2) and a mandrel (3). The mandrel must be manufactured to have the shape of the desired part and rotates with the main spindle. The forming tool is a roller (4). Conventionally, the roller tool can be moved on two linear axes, which are mounted as a support on the machine bed. The roller tool moves along a predefined tool path (5) and forms the blank stepwise into the desired shape (6). During the forming operation, the blank holder (7) supports the workpiece to prevent wrinkling. After spinning, further forming or cutting operations are possible, which require additional tooling (8).

The ability of the material to be formed from a blank into a hollow body is limited by the occurrence of a failure such as wrinkling or tearing. The spinning ratio, β , has been introduced as a characteristic value (Fig. 12.3). The value is determined by dividing the diameter of the initial blank, D_0 , by the diameter of the mandrel, d ($\beta = D_0/d$). The maximum spinning ratio depends on many process parameters, especially the tool path. This ratio can only be derived for a single-cycle spinning process, where the tool moves axially and the tool mandrel clearance is equal to the original sheet thickness.

Process Variations. The spinning process is classified in DIN 8584 (DIN = German Industry Standard), and it is subdivided into three variations: spinning of hollow bodies, expanding, and necking. Workpieces can be expanded or necked by the use of a part-specific mandrel, as shown in Fig. 12.4(b) or (i). Using split or eccentric mandrels (Fig. 12.4f), undercuts can be obtained by necking-in a part. Furthermore, spinning can be used to deform the edge of flat sheets or of tubular workpieces, as shown in Fig. 12.4(d), (e), and (g).

Stress States and Failure Modes. The stress state initiated by the spinning process depends strongly on the forming direction (Fig. 12.5). Moving the tool beginning at the mandrel toward the free edge of the sheet initiates tensile stresses in the radial direction because the material is elongated radially. Due to volume constancy, a tangential compression occurs while the workpiece diameter is reduced. Moving in the opposite direction, beginning at the free

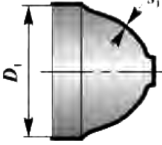
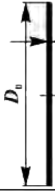
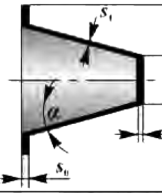
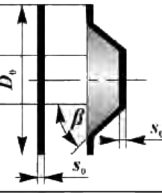
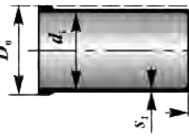
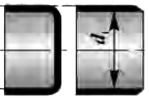
Standard		Procedure	Initial component	Wall thickness
Tensile - compressive forming according to DIN 8582	Metal spinning according to DIN 8584, T4	Metal spinning 	 Circular blank $D_0 > D_1$	Approximately constant $s_1 = s_0$
		Shear spinning 	Circular blank or preform 	In the bottom $s_1 = s_0$ In the formed area $s_1 = s_0 \frac{\sin \alpha}{\sin \beta}$
Compressive forming according to DIN 8582	Flow forming according to DIN 8584, T2	Flow forming 	Cup or tin 	In the formed wall (of a drawn cup) $s_1 = \frac{1}{2} (D_1 - d_1)$

Fig. 12.1 Characterization of spinning. Source: Ref 12.1

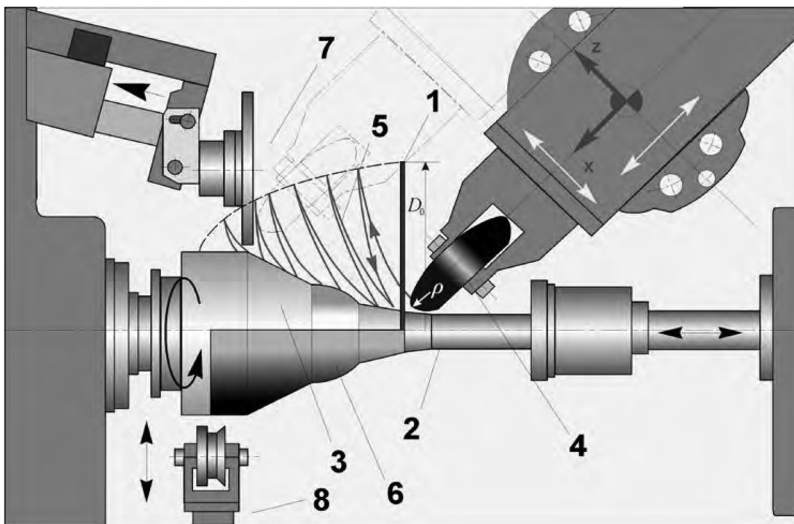


Fig. 12.2 Top view of the machine setup for spinning. Source: Ref 12.2

edge and forming toward the mandrel, compressive stresses act in the radial direction because the material is upset radially. Tangential stresses occur as well, caused again by the tangential compression. The radial compression of the part

can be observed as a buckle, which appears in front of the tool.

Based on the states of stress, a spinning operation is limited by the following failure modes (Fig. 12.6):

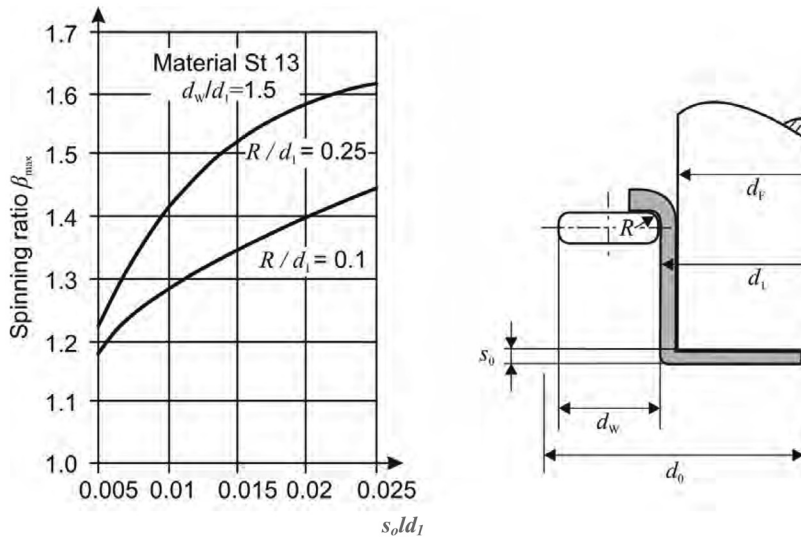


Fig. 12.3 Spinning ratio in single-cycle spinning. Source: Ref 12.3

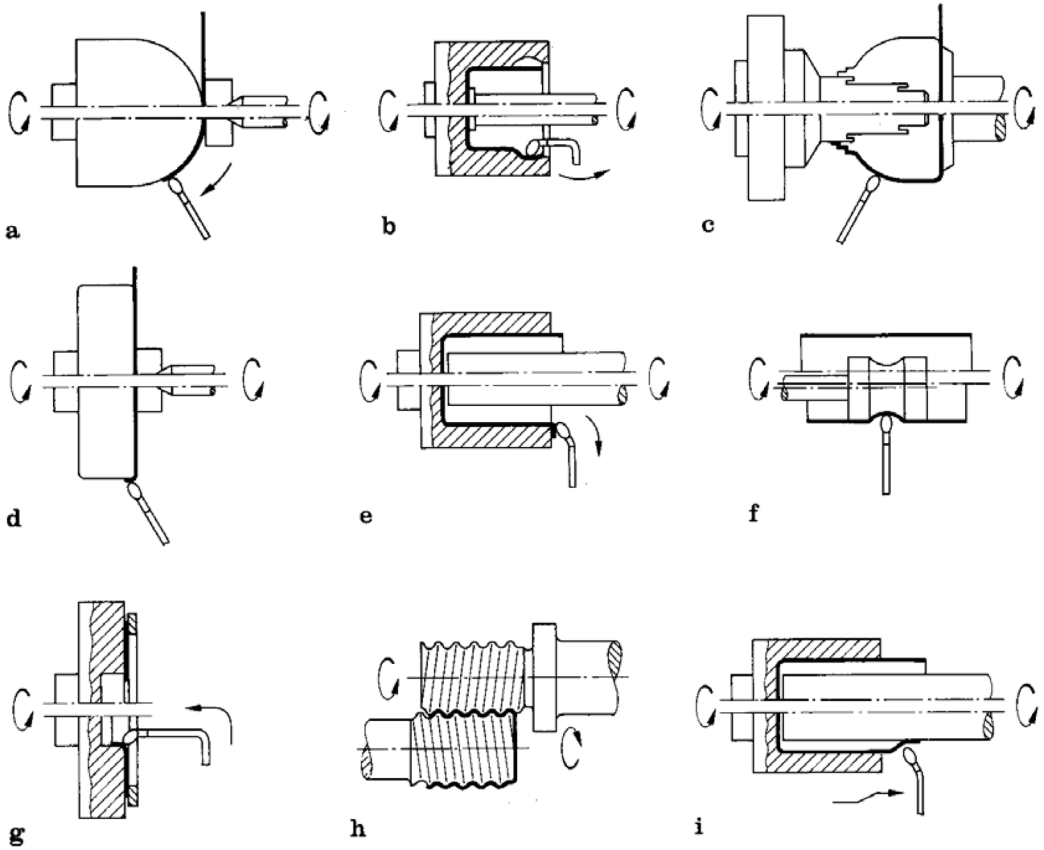


Fig. 12.4 Spinning variations. (a) Conventional spinning. (b) Expanding. (c), (f), and (i) Necking. (d), (e), and (g) Flange forming. (h) Thread forming. Source: Ref 12.4

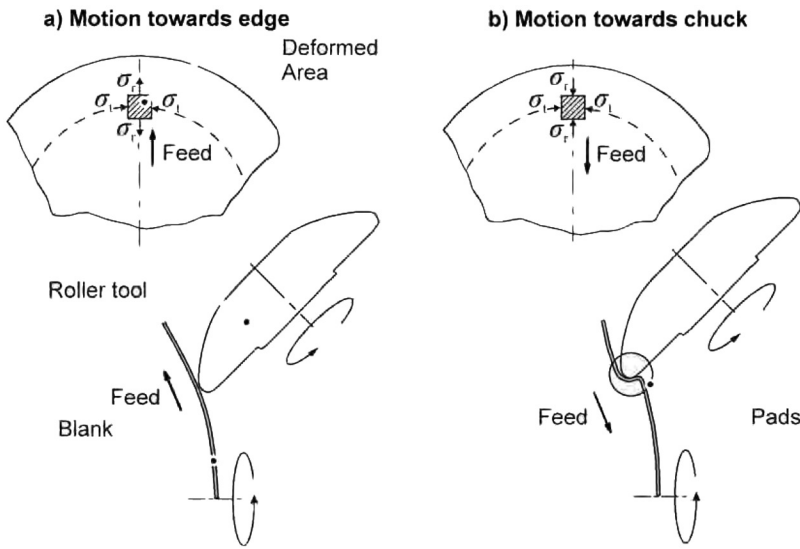


Fig. 12.5 Stress state in spinning. Source: Ref 12.2

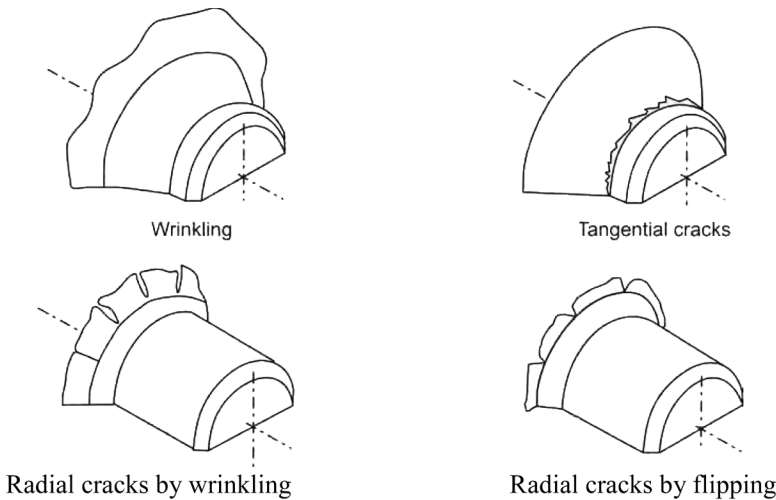


Fig. 12.6 Failure modes in spinning. Source: Ref 12.5

- Wrinkling:** Wrinkling may occur in the free flange of the blank. This instability of the blank is caused by the limited ability of the material to withstand tangential stresses. Wrinkling limits the maximum diameter reduction that can be attained with the blank, as well as the minimum sheet thickness that can be used in spinning. The potential for wrinkling increases with increasing blank diameter and decreasing sheet thickness. The limit is reached when wrinkles cannot be flattened in subsequent spinning passes.
- Tangential Cracks:** Tangential cracks appear in the vicinity of the mandrel in the transition zone between the free flange and the portion of the part that has already been formed. They are caused by tensile stresses during the tool motion ahead of the edge of the blank. Consequently, the trend to tangential cracks increases with decreasing sheet thickness. The appearance of tangential cracks depends on several machine and process parameters. A choice of a small working radius of the tool ($r < 3 s_0$), a high feed

rate, f_r , or a highly curved tool path may lead to this failure mode.

- **Radial Cracks:** These cracks are initiated by previous wrinkles in the flange that are initiated by tangential compressive stress. The subsequent forming passes can lead to further bending of those wrinkles instead of flattening the sheet. The material will overlap within the bent area when the process is continued. This results in radial cracking of the overlapped material.

During a forming cycle, the remaining flange may flip backward similar to a disc spring. This flipping depends mostly on the chosen tool path. A highly curved tool path enhances this effect. During this flipping action, tension stresses act

in the tangential direction and may lead to radial cracks.

Tool Path Planning. The tool path is selected by trial-and-error and by the experience and skills of the craftsmen. This leads to a huge amount of possible tool paths that are in common use. Figure 12.7 presents a systematic overview of linear and curved tool paths. These different types of passes are not standardized, and the spinning process must be learned over years of individual experience.

To allow a systematic description of the tool path, several parameters can be introduced. Figure 12.8 presents a linear tool path used to manufacture a cup. The tool motion can be characterized by using the number of passes, n , a distribution of the tool path contact points on

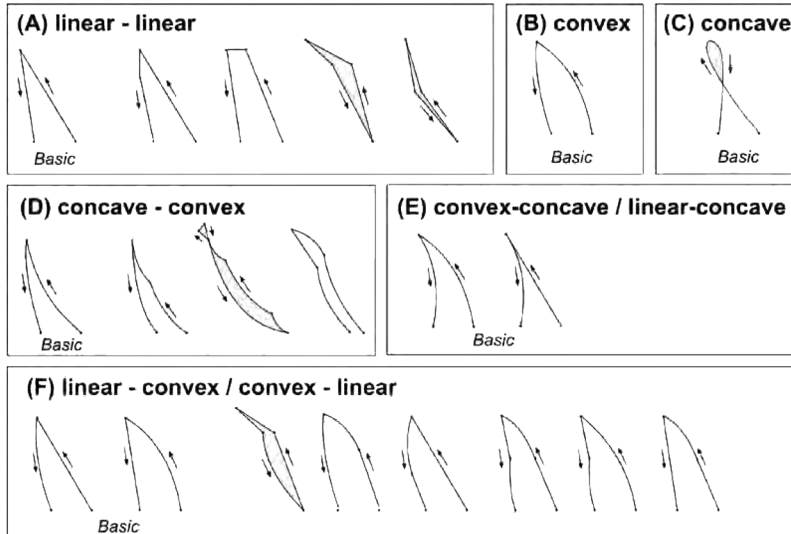


Fig. 12.7 Composition of different tool paths in spinning. Source: Ref 12.6

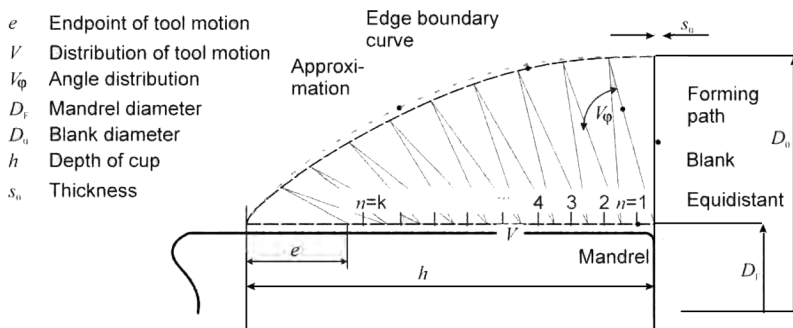


Fig. 12.8 Parametrized tool path. Source: Ref 12.6

the mandrel, v , as well as the distribution of the tool motion inclination, V_ϕ . Information about the curvature of the tool path is necessary to describe a nonlinear motion.

To design the tool path, the local thickness, s , the local diameter, D , as well as the final cup depth, h , of the part must be considered to estimate the part volume. This is required to calculate the required diameter of the blank, D_0 . To identify the points of the tool motion return during the process, the determination of two curves is important. The equidistant curve limits the tool motion with respect to the mandrel to avoid undesired thinning of the material or a tool crash. The edge boundary curve limits the tool motion at the free flange of the part. A return of the tool before reaching the part edge will cause a flange of material that is not formed, causing a tear in the part. If the tool returns beyond the part edge, a crash with the material is unavoidable in most cases. For a proper calculation of the edge boundary curve, the volume of the already-formed part must be compared with the initial volume. Analyzing each forming step, N , the volume of the flange exhibits the point of return. The edge boundary curve can be approximated by a combination of a straight line and a parabola. Preferring an involute tool path, a graphical solution is possible. Figure 12.9 presents a construction method that uses well-defined parameters for the tool path description. The edge boundary curve must be calculated by the volume. Both presented methods for tool path determination must be adjusted individually based on the part material. Different materials will thin differently, which requires the adjustment of the tool path.

For a qualitative understanding of how the process is affected, Table 12.1 shows the effects

of different process parameters on produced cups. The final cup depth (h), the maximum diameter (D_{max}), the minimal wall thickness (s_{min}), the tendency of wrinkling (TW), and the effects on the surface quality (SQ) are considered.

In addition to tool path parameters, the spinning process must be adjusted for the properties of the sheet material. Due to the great number of parameters that must be considered at the same time, the process is still set up by trial-and-error. A first feasible parameter setting can be used to adjust the spindle speed as well as the feed of the tool motion. Figure 12.10 presents recommended values for initial setup of a feasible number of spinning cycles for various sheet materials. Tables 12.2 and 12.3 give recommended spindle speeds and feed rates, respectively.

To introduce the design step of a spinning process into a computer-aided manufacturing (CAM) system, different approaches have been developed for systematic storage of already produced parts. In general, those methods separate the shape of the part along its longitudinal axis into different zones, which can be compared with standard geometries such as straight lines, cones, or circular arcs. Each standard geometry introduces a specialized tool path that must be adjusted to the current production task. The combination of these separated tool paths results in the final tool motion. A transfer of the machine parameters from already-produced parts to a new production task is an additional challenge requiring the transfer of craftsmen's knowledge to a systematic and transferable database. All these knowledge-based approaches are still in the development stage.

Machines. Spinning has been developed from an art to the present production process. Today, computer numerical-controlled (CNC) machines

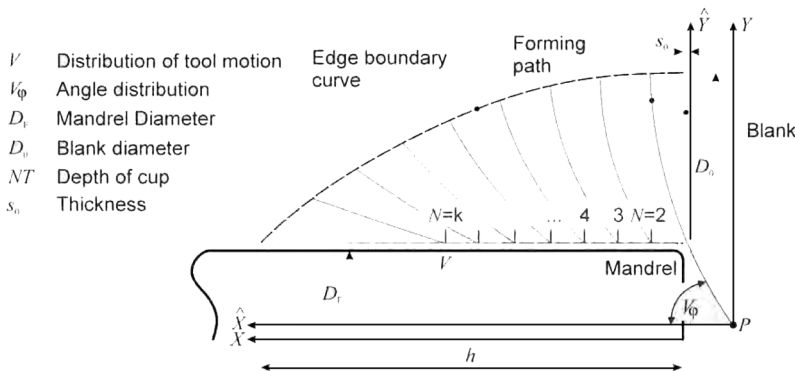


Fig. 12.9 Involute tool path. Source: Ref 12.7

Table 12.1 Effect of process variables in forming of a round cup by spinning

Parameter/target value	<i>h</i>	<i>D</i> _{max}	<i>s</i> _{min}	TW	SQ
Round-off radius (\bar{r})	↑	↓	↑	↑	↑
Feed (<i>f</i>)	↑	↔	↔	↑	↓
Spindle speed (<i>s</i>)	↓	↔	↓	↑	↑
Number of passes (<i>n</i>)	↔	↔	↓	↓	↑
Endpoint on mandrel (<i>e</i>)	↓	↔	↓	↑	↔
Distribution on <i>v</i>	=	↔	=	=	↔
Blank holder	↓	↔	↓	↑	↑
Lubrication	↔	↔	↔	↔	↑

Note: ↑, increase of value requires an increase of parameter; ↓, increase of value requires a decrease of parameter; ↔, no effect; =, best setting in the middle range. Source: Ref 12.6

Table 12.2 Recommended spindle speed as a function of blank diameter and material

Material	Spindle speed (<i>s</i>), 1/min					
	Ø50 mm (2 in.)	Ø100 mm (4 in.)	Ø200 mm (8 in.)	Ø300 mm (12 in.)	Ø400 mm (16 in.)	Ø500 mm (20 in.)
Al-99.5	3000	2150	1150	900	550	400
Al-Mg-Si	2600	1750	900	700	400	350
Soft steel	2000	1250	800	600	400	300
Stainless steel	1000	800	600	350	250	150
Cu	1800	1350	700	600	300	300
Mg	1500	1200	600	450	300	250

Source: Ref 12.8, 12.9

are available with a maximum power of up to 150 kW. They can form blanks with an initial diameter of up to 5000 mm (195 in.). The design of a spinning machine can be compared to a conventional turning lathe, as presented in Fig. 12.2. The blank is clamped between the mandrel and the tailstock, and the mandrel is rotated.

Even today, some parts are spun by hand (Fig. 12.11). Manual spinning is done using a forming bar or a stick. This stick is pivoted on a T-rest and a pin and is moved forward and backward on the part surface by the spinner. To allow the forming of a complete part, the pin can be repositioned. A backstick is used to support the blank to avoid wrinkles. To have support, the craftsman can be linked with the spinning machine by a harness. A roller tool can also be used in this manual process. Today, manual spinning is used for the manufacturing of parts in very small batches with a high surface quality.

To apply a larger force, which is necessary to spin larger and thicker parts, the forming tool can be mounted on two linear mechanical axes, which are driven by hydraulics or electric power (Fig. 12.12). Two manually controlled linear

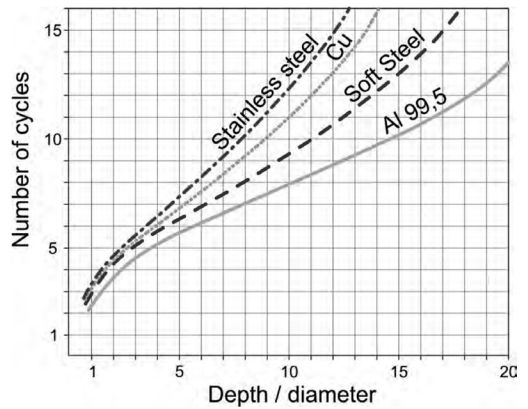


Fig. 12.10 Recommended number of spinning cycles as a function of cup geometry. Source: Ref 12.8, 12.9

Table 12.3 Recommended feed rate as a function of blank diameter and material

Material	Feed (<i>f</i>), mm/min					
	Ø50 mm (2 in.)	Ø100 mm (4 in.)	Ø200 mm (8 in.)	Ø300 mm (12 in.)	Ø400 mm (16 in.)	Ø500 mm (20 in.)
Al-99.5	525	525	350	350	350	300
Al-Mg-Si	400	400	300	300	300	300
Soft steel	350	350	350	250	250	250
Stainless steel	250	250	250	250	175	150
Cu	300	300	300	300	250	250
Mg	250	250	250	250	250	200

Source: Ref 12.8, 12.9

axes are applied to create a nonlinear tool motion. The craftsman must coordinate the forming tool by hand-operated switch keys. Hence, this technique is quite complicated, with an increased risk of tool crash.

Modern production processes require short production times. This led to the development of CNC spinning machines in the 1970s. The tool motion is controlled using numerical axes, which can be programmed offline using CAM software. The degree of automation is expanded further compared to a copying machine, because the complete production task, including all necessary handling operations, can be considered within the program. A manipulation of the tool path is completed by a change in the CNC program.

Due to the lack of basic knowledge for setting up a spinning tool path, the programming of the pure CNC code can be quite complicated. To apply the operator's individual knowledge to the spinning process, many spinning machines

are equipped with a teach-in panel (Fig. 12.13). By using a joystick to move the forming tool, an individual tool path can be recorded and transferred to a CNC code. In a playback mode, this tool path can be repeated to allow a computer-controlled production of the part. Additionally,

the playback mode can be executed at an increased forming speed to reach a higher level of productivity.

Spinning requires sophisticated development of a tool path for each individual part. The task depends on many geometrical- as well as material-dependent parameters. The use of a CNC machine can only consider the geometrical requirements. To consider material effects as well as other random process variations, an adaptive control is necessary. The adjustment of the tool path to the current state of forming is achieved by continuous monitoring and analysis of the forming force, the tool displacement, and the actual shape of the part. Such adaptive controlled machines are currently in the development stage.

Tooling. The mandrel gives its shape to the final product (Fig. 12.4). Different types of mandrels exist to allow external or internal forming of the part. Undercuts in the part shape can be achieved using split tools. For prototyping, mandrels can be made of wood. To manufacture parts with large dimensions, locally supported mandrels are used. Figure 12.14 shows a specialized machine used to manufacture gas tank housings. Additional machine axes are necessary to move the localized mandrel.

Spinning can also be used to manufacture products with an oval shape after implementing a specialized mandrel. The part is mounted on a separate rotation axis, which is positioned eccentrically to the main spindle axis (Fig. 12.15). Oval spinning can be used to manufacture exhaust systems.

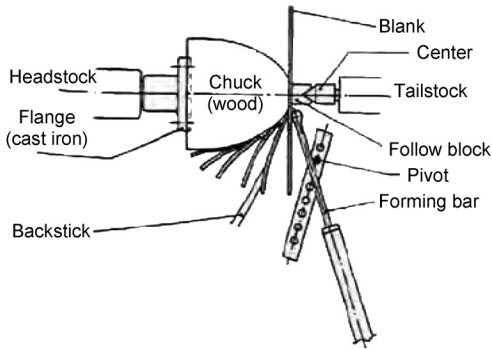


Fig. 12.11 Spinning by hand. Source: Ref 12.10

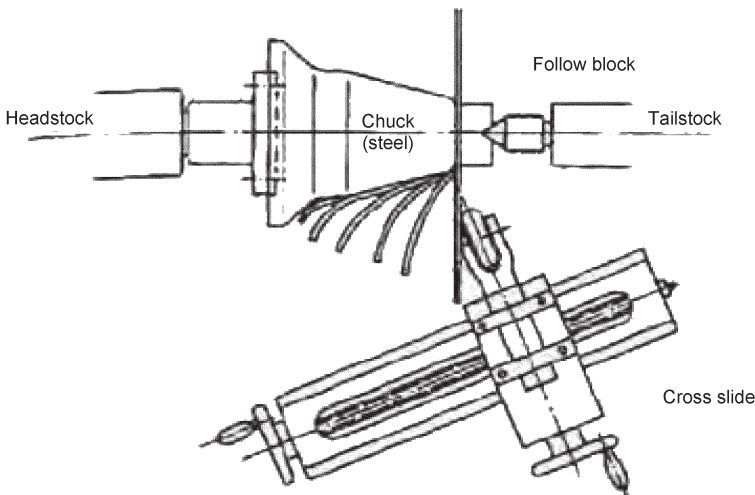


Fig. 12.12 Spinning with hydraulic or electric drives in two linear axes. Source: Ref 12.10



Fig. 12.13 Spinning by teach-in. Source: Ref 12.11

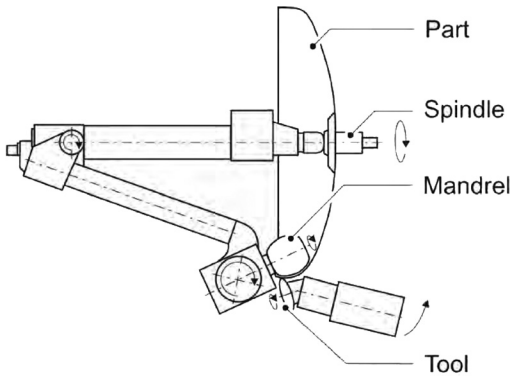


Fig. 12.14 Spinning of big parts. Source: Ref 12.12

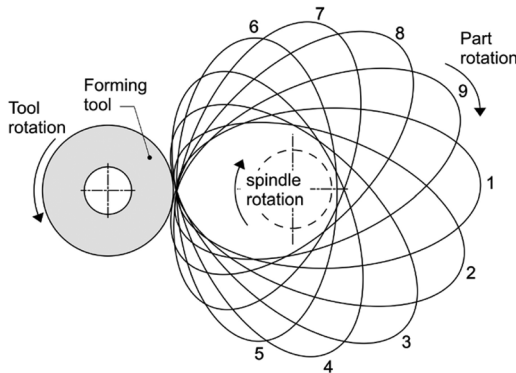


Fig. 12.15 Oval spinning. Source: Ref 12.13

Conventionally, forming tools used in spinning are rollers made of tool steel with a chromium content of approximately 12% and a surface hardness between 60 and 64 HRC. To increase the life cycle of these tools, physical vapor deposition coatings can be used. The roller tools must resist temperatures over 500 °C (930 °F), which is generated through dissipated heat, friction, or even through external heating to increase the formability of the sheet material. The roller is clamped by a bracket with a fork design or as an overhang arrangement. The tools either turn freely or are driven externally by an additional drive to avoid slip marks. Tool storage devices are used for rapid tool changing.

To produce very smooth surfaces, or to form thin materials, rollers made from plastics can be used. These rollers are made of phenolic resin and deform elastically within the forming zone. Hence, the typical spiral structure on the part surface can be avoided. To further improve the part surface finish, elastic tool clampings are used. Here, the tool is no longer controlled by the displacement but by the forming force. Elastic clamping can be achieved by introducing springs combined with pneumatic devices.

Different roller-type tool designs can be used in metal spinning (Fig. 12.16). Tools A and C are used for manufacturing parts by spinning from a flat blank. Design B is used for necking,

that is, diameter reduction of the parts. To flatten the surface of a part, a flat roller such as type D is necessary. Roller designs such as type E are applied in the shear spinning process. Type F can be used to process combinations of shear spinning and flow forming. It is known that a larger round-off radius, r , of the tool increases the spinning ratio, β .

In addition to the tool used for the main forming operation, other tools can be mounted on the spinning machine to simplify handling or to allow secondary processing, as shown in Fig. 12.17. A centering device allows quick adjustment of the blank in the machine rotating spindle. A cutter can be used to constrain the remaining flange to a dedicated diameter. The part edge can be formed by a roller tool with a concave shape, which is mounted on a linear axis. Likewise, a cutting roller can trim the part to a desired height after forming. A roller tool with a customized design must be used to form complicated shapes or to form local zones that are not accessible by the main forming tool. These profiled tools are also mounted on additional machine axes.

Part Properties. In general, any cold forming material can be shaped by the spinning process.

Materials with a low formability, such as titanium and tungsten, with an initial thickness of more than 20 mm (0.8 in.) can be formed by using an external heating device. The formability can be increased further when annealing steps are introduced into the process chain.

Spinning is suitable to reach high geometrical accuracy of the produced parts, especially when a final rolling pass along the desired contour is included after the main forming operation. For the resulting thickness, the deviations are less than ± 0.1 mm (0.004 in.) for parts smaller than 500 mm (20 in.) and approximately ± 0.4 mm (0.02 in.) for parts with a diameter of 3000 mm (120 in.) and an initial thickness of 10 mm (0.4 in.). Table 12.4 presents an overview of feasible tolerances for the given outer part diameters. The surface quality of the parts can be increased by using a larger round-off radius of the tool or by decreasing the feed rate of the tool motion. However, the accuracy depends on the quality of the tools and can differ depending on the tool material and surface finish.

Applications. Spinning is suitable to manufacture a variety of parts with different diameters. One common characteristic of the process is the high precision of the produced parts. Typical parts produced by spinning include (Fig. 12.18):

- Braking and hydraulic cylinders
- Pulleys
- Barrels
- Exhaust silencers
- Wheel rims
- Cooking pots
- Gas containers
- Parts for jet engines, rockets, and missiles
- Lamp housings and reflectors

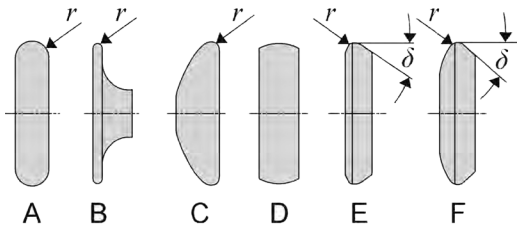


Fig. 12.16 Tool designs for spinning. Source: Ref 12.2

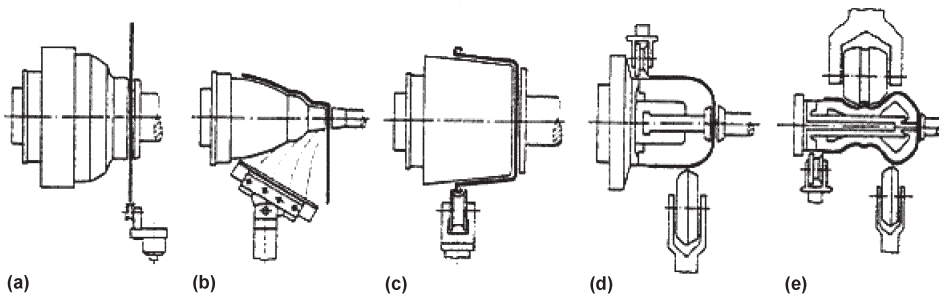


Fig. 12.17 Additional assisting tool devices. (a) Centering. (b) Cutter. (c) Edging roller. (d) Cutting roller. (e) Profiled roller. Source: Ref 12.12

12.2 Flow Forming

Flow forming is a bulk metal forming process to manufacture axially symmetrical parts with high precision and surface quality as well as high strains up to 90%. Flow forming allows the manufacturing of internal and external net-shape gear teeth only by forming. The parts are manufactured almost always from tubular semifinished parts or preforms such as cups. Such preforms can be produced either by spinning or by other metal forming processes. Flow forming can be divided into flow forming of hollow parts with cylindrical shape, which is also known as tube spinning, and flow forming of hollow parts with conical or different shape, which is better known as shear spinning (see the section “Shear Spinning” in this chapter).

Process Description. As illustrated in Fig. 12.19, in forward flow forming, a cup (1) is clamped between a tail stock (2) and a mandrel

(3). The mandrel is driven by the main spindle and gives its shape to the workpiece. The forming tool (4) is moved in a plane along a predefined tool path (5). During the forming operation, the wall thickness of the part is reduced. Thus, the part elongates in the axial direction (z). As seen in Fig. 12.19, the tool path defines a gap between the mandrel and the forming tool. Due to local variations in this gap, the wall thickness of the final part (6) can be adjusted to a desired value. The internal diameter of the part is given by the shape of the mandrel.

Flow forming has two types. Figure 12.19 shows the machine setup for forward flow forming. Here, the material flow is in the same direction as the axial feed of the forming tool. To perform a forward forming process, the use of cups as semifinished parts is required in order to clamp the workpiece between the tail stock and the mandrel.

Figure 12.20 illustrates a backward forming process. Here, the material flow is in the opposite direction as the feed of the forming tool. The backward flow forming process is performed by using tubular semifinished parts (1). The mandrel is equipped with planar teething (3). During the forming operation, the forming tool (4) pushes the workpiece against the teething to transmit the rotation of the spindle (2) to the part. The desired diameter of the part is achieved by adjusting a gap between the forming tool and the workpiece within the tool path

Table 12.4 Accuracy in spinning

Without rolling pass				With rolling pass			
Part diameter		Tolerance		Part diameter		Tolerance	
mm	in.	mm	in.	mm	in.	mm	in.
<600	<24	0.8–1.6	0.03–0.06	≤500	≤20	±0.2	±0.008
600–1200	24–47	1.6–3.2	0.06–0.13
1200–3000	47–118	3.2–6.4	0.13–0.25	>500	>20	±0.4	±0.02

Source: Ref 12.14

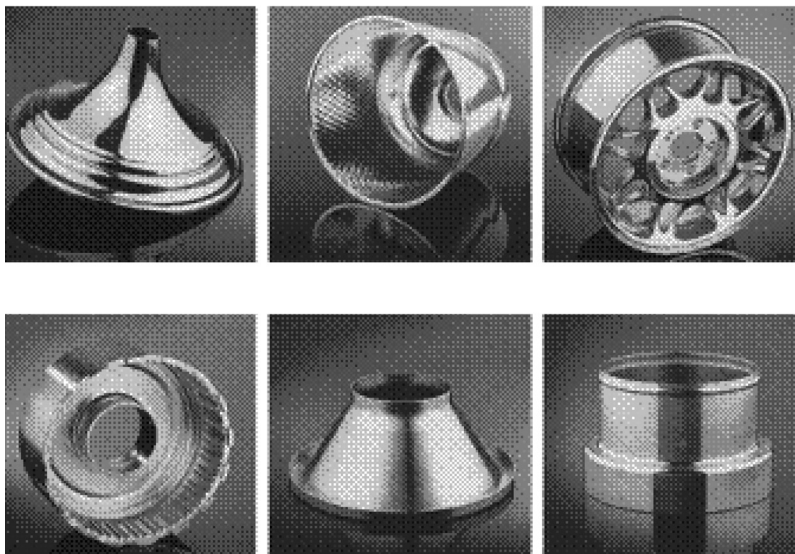


Fig. 12.18 Spinning parts. Source: Ref 12.15

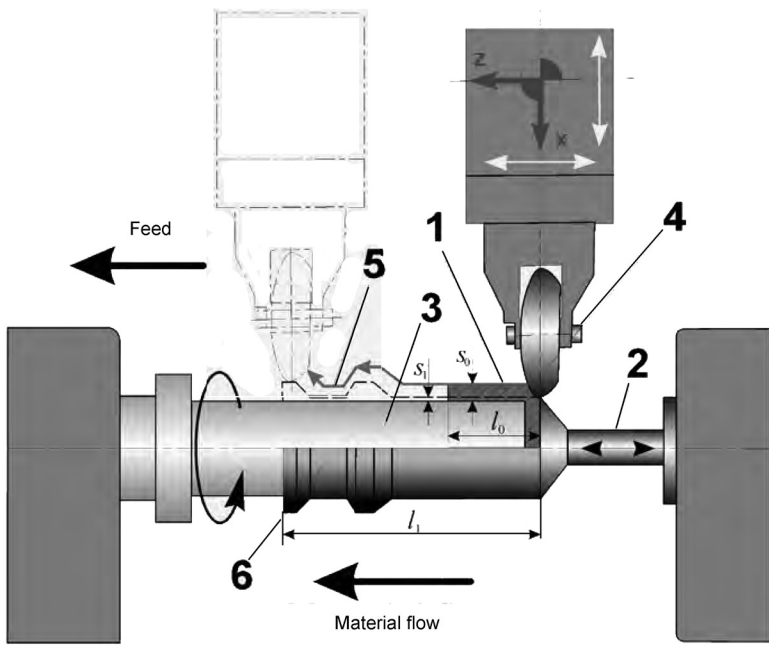


Fig. 12.19 Machine setup for forward flow forming. Source: Ref 12.12

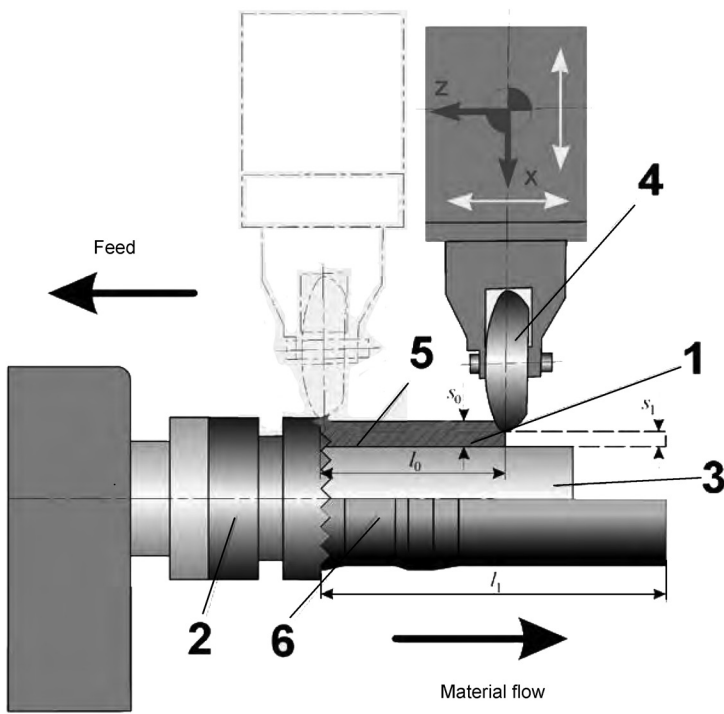


Fig. 12.20 Machine setup for backward flow forming. Source: Ref 12.12

(5). The material flows beneath the forming tool and the workpiece. In backward flow forming, the length of the formed part (6) is not restricted by the length of the mandrel.

Due to volume constancy, the final length of the part, which must be manufactured, can be calculated beforehand using Eq 12.1:

$$l_1 = l_0 \cdot \frac{s_0(d_i + s_0)}{s_1(d_i + s_1)} \quad (\text{Eq 12.1})$$

When using a flat blank to manufacture a preform that is used thereafter in forward flow forming, the initial diameter, D_0 , of the blank can be approximated as:

$$D_0 \approx \sqrt{4d_i h_1 \frac{s_1}{s_0} + d_i^2} \quad (\text{Eq 12.2})$$

In Eq 12.1 and 12.2, l_1 is the length of the product after deformation, l_0 is the length of the preform before deformation, s_0 is the initial wall thickness, s_1 is the final wall thickness, d_i is the inner diameter, and h_1 is the height (depth) of the cup after forming.

In practice, the calculated value for D_0 is increased by adding an offset of approximately 5 to 10 mm (0.2 to 0.4 in.). This is done to compensate for the cutting operation performed before the flow forming operation in order to obtain a perfectly centered blank, and the cutting operation after flow forming in order to finish the edge of the formed part.

Forming Forces, Stress State, and Failure Modes. In flow forming, the plastic forming

zone is limited to a local area. This causes an inhomogeneous stress state along the workpiece. For a better understanding of the failure modes in flow forming, Fig. 12.21 illustrates schematically the major forming zones and the acting forces, as well as the principal stress states.

Flow forming allows a great reduction of the wall thickness, up to 90% or more. Due to the locally limited forming zone, the displaced material often leads to a bulge in front of the roller tool (Fig. 12.22). This bulge is affected by several process parameters, listed in Table 12.5.

The appearance of the bulge cannot be avoided completely. In practice, the forming process is aborted before moving the forming tool over the remaining bulge at the part edge. This procedure increases the durability of the forming tools. However, the remaining material that includes the bulge must be cut off after the main forming cycle. In any case, the appearance of a bulge must be minimized as much as possible, because it leads to an undesired change in the part diameter. Additionally, a larger increase of the bulge leads to radial cracks at the upper surface or to bending of the bulge itself (Fig. 12.23). Such bulges cannot be flattened any more in a subsequent forming cycle.

Flow forming is restricted by the minimum value of the wall reduction in each pass, which is approximately 20%. Lower values cause high shear strains between the outside and the inside surface of the part and lead to shearing of the outside surface.

In a forward forming process, the maximum reduction is limited by the capability of the re-

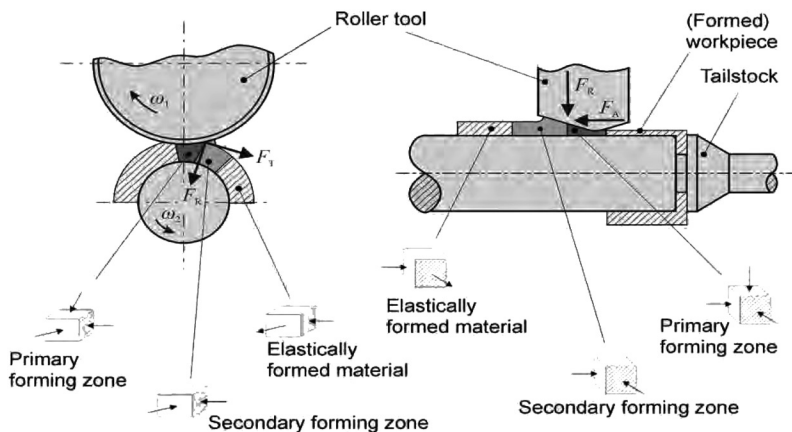


Fig. 12.21 Forces and stress states in forward flow forming. Source: Ref 12.2, 12.16

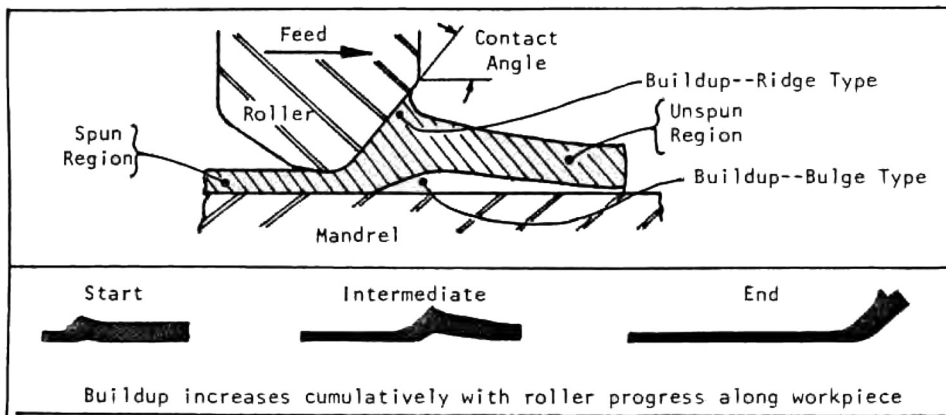


Fig. 12.22 Effects of process parameters on bulging during flow forming. Source: Ref 12.17

Table 12.5 Factors that influence the occurrence of a bulge during flow forming

Factor	Effect
Process variant	Forward flow forming leads to minor bulges compared to backward flow forming.
Cone angle of tool	Bulge increases with greater cone angle
Tool diameter/mandrel diameter	Slight increase when increasing factor
Pitch (feed/spindle speed)	Decrease when decreasing pitch
Friction between work-piece and tool	Low friction reduces bulge
Friction between work-piece and mandrel	High friction reduces bulge
Reduction of wall thickness	Significant increase in bulges when increasing the reduction of the wall thickness in one cycle
Wall thickness	Great wall thickness reduces bulge

duced wall thickness to withstand tensile stresses. These stresses are initiated by the forming tool, which pushes forward the thick and underformed material at the front face of the tool. The maximum strain limit can be increased by including an annealing operation into the flow forming cycle.

Machines, Process Variations, and Specialized Tools. As illustrated in Fig. 12.24, three roller tools are generally used in a typical flow forming machine. This minimizes the tangential flow of the material, which leads to an undesired increase of the diameter of the workpiece. Additionally, it is possible to reduce the cycle time when applying several tools at the same time. To manufacture precise parts, bending of the mandrel must be avoided by applying more than one forming tool to compensate bending moments caused by the local forming

forces. Usually, three tools are arranged with an angle of 120° between each tool.

Conventional flow forming machines are designed to manufacture tubes with dimensions between 30 and 300 mm (1 and 10 in.) in diameter. Parts up to a total length of 13 m (43 ft) can be manufactured as well. To manufacture tubular parts with a diameter up to 3.2 m (10.5 ft), the mandrel is replaced by roller tools that act as counter tools (Fig. 12.25). To manufacture cylindrical parts with smaller diameters, a miniaturized tool module, with a similar function as conventional three-roller supports, can be mounted on the support of a lathe. Thus, flow forming operations can be used to manufacture parts as small as 4 mm (0.16 in.) in diameter (Ref 12.19).

Although flow forming is conventionally a cold forming process, the dissipated heat during the forming operation leads to an increase of the temperature. Often, the part must be cooled during forming. Flow forming is also applied to manufacture gas cylinders where the preform is locally heated (Fig. 12.26).

Additional novel applications of flow forming include the split forming of flat disks, as illustrated in Fig. 12.27. Research in flow forming often focuses on the improvement of tolerances and on warm forming of difficult-to-form alloys, such as magnesium and aluminum alloys, as well as stainless steels (Ref 12.21).

Roller Tools for Flow Forming. The roller tool design is one of the most important parameters in flow forming and affects the achievable part quality. Figure 12.28 shows five tool designs with characteristic differences. A round

roller tool (Fig. 12.28a) is used as a basic tool to flow form preformed aluminum blanks. As a rule of thumb, the round-off radius, R , can be increased for a softer material. In Fig. 12.28(b), the tool is featured with an additional collar, determined by the depressor angle, β . This collar can be used to prevent the rising of the material in front of the tool. The clearance angle, γ , at the rear face of the tool is responsible for the surface quality of the part. Beyond the function of burnishing of the surface of the part, the clearance angle also affects the expansion of the formed component for easy removal from the machine after forming. The sophisticated design of the roller in Fig. 12.28(c) is used to flow form aluminum from flat disks. The conical roller in Fig. 12.28(d) is used for forming stainless steel or high-alloyed, high-strength steels. Figure

12.28(e) illustrates a roller tool that introduces multiple forming zones in the workpiece. Although this tool design significantly reduces the flexibility of the process, it also reduces the process cycle time.

In flow forming, the material flow in tangential direction must be avoided to achieve good part quality. The ratio between the longitudinal and the axial material flow is highly affected by the contact zone of the tool on the workpiece.

In addition to roller tools, ball-shaped tools are also known to form long and precise thin-walled tubes and cylinders (Fig. 12.29). Due to their smaller dimensions, they can be applied in greater numbers. Thus, the feed of the forming tool can be increased, which reduces the required cycle time.

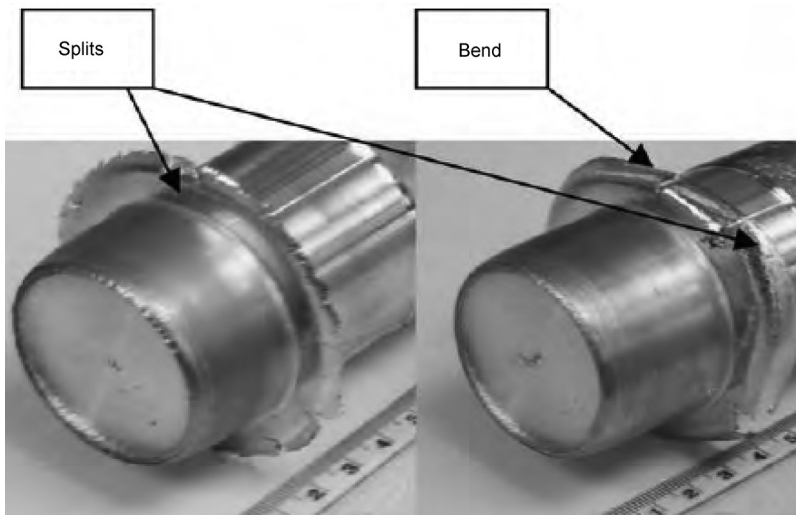


Fig. 12.23 Cracks caused by a large amount of bulging. Source: Ref 12.10

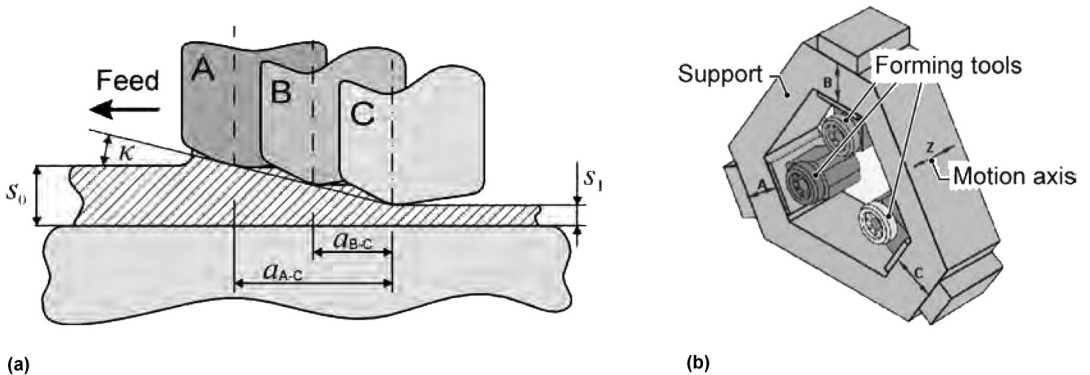


Fig. 12.24 (a) Flow forming by three forming tools (illustrated in one cross section). Source: Ref 12.2. (b) Closed support design

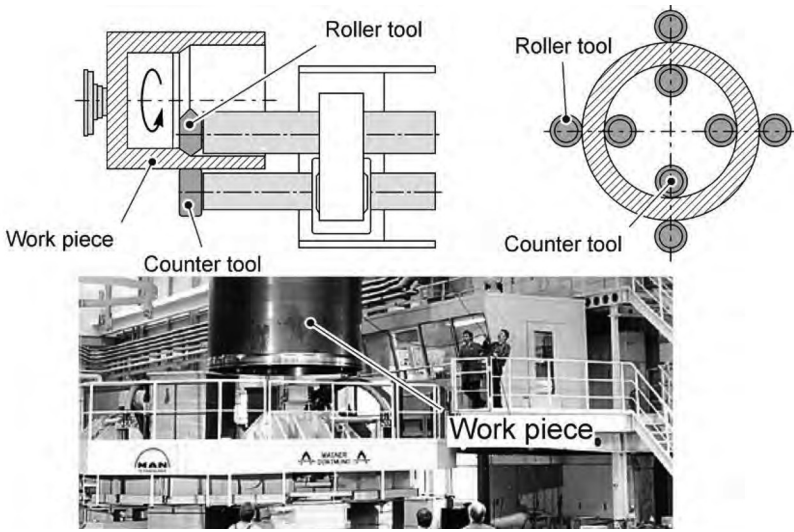


Fig. 12.25 Flow forming of great diameters with counter rolls. Source: Ref 12.17, 12.18

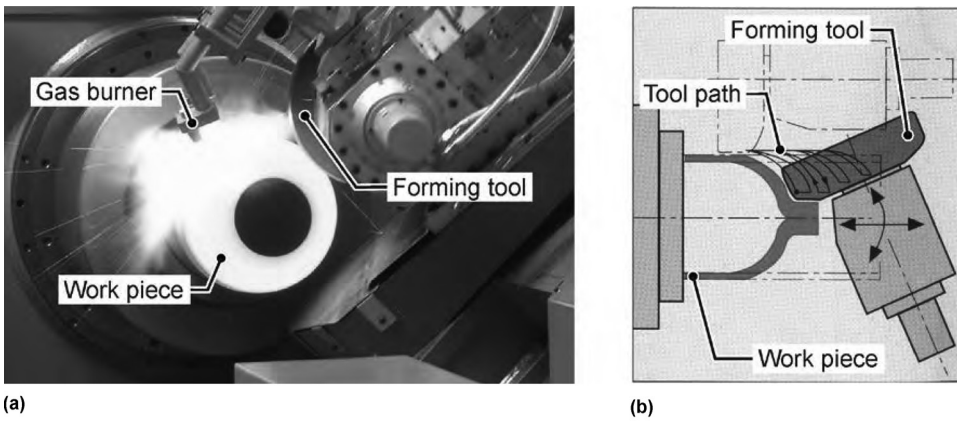


Fig. 12.26 (a) Necking-in machine to manufacture gas cylinders. Source: Ref 12.15. (b) Process kinematic. Source: Ref 12.2

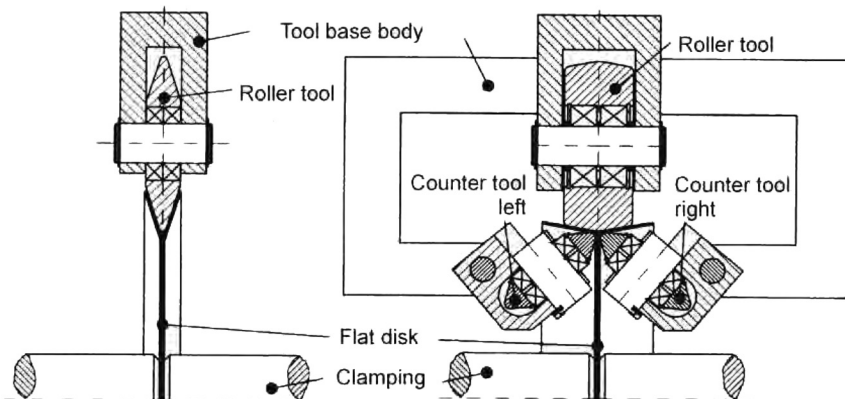


Fig. 12.27 Splitting of disks by flow forming. Source: Ref 12.20

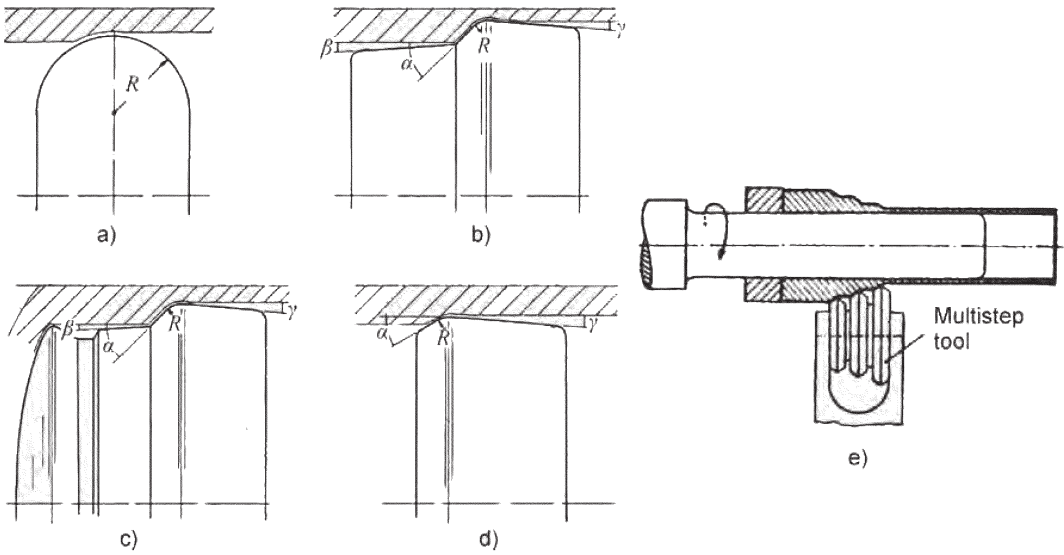


Fig. 12.28 Different shapes of roller tools used for flow forming. Source: Ref 12.22–12.24

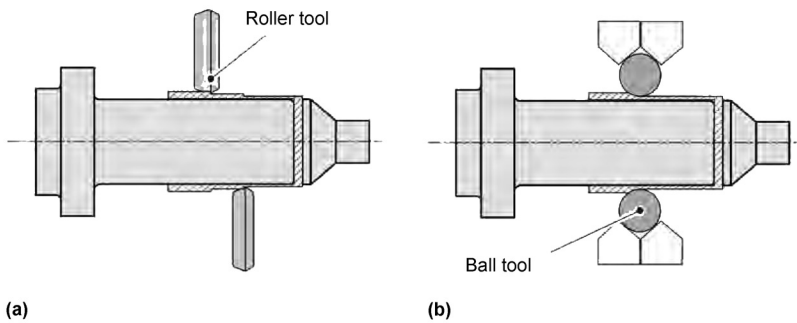


Fig. 12.29 Flow forming with (a) roller tools and (b) ball tools. Source: Ref 12.25

The manufacturing of parts with gear teeth requires specialized tooling for each different geometry to be formed. To form a part with internal teeth, for example, a mandrel with the negative profile of the desired shape is necessary (Fig. 12.30).

Part Properties. The geometrical precision of the flow forming of tubes is presented in Table 12.6. The data are divided into three different dimensions of the workpiece.

Applications. Flow forming is applicable to form nearly all metals. For example, flow forming allows the manufacturing of a hollow cylinder with a length-to-diameter ratio of >20 and a diameter-to-wall thickness ratio of >500 . In low-volume production, flow forming offers the advantage of low investment in tooling (Fig. 12.31, 12.32).

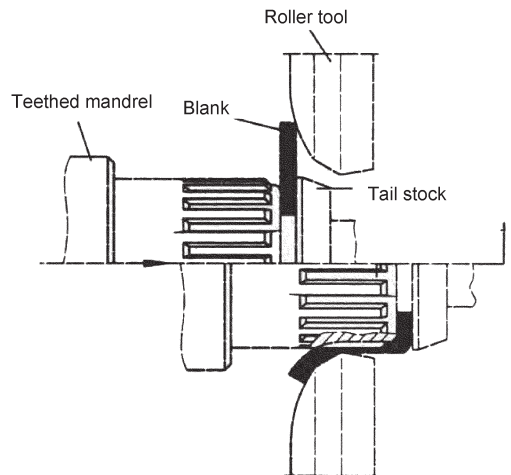


Fig. 12.30 Mandrel to flow form an internal gear tooth form. Source: Ref 12.2

Table 12.6 Tolerances in flow-formed cylinders

Part dimensions for flow forming of cylinders			
Internal diameter, mm (in.)	≤100 (<4)	≤250 (≤10)	≤400 (≤16)
Final thickness, mm (in.)	≥2 (≥0.08)	≥3 (≥0.1)	≥4 (≥0.2)
	Quality properties		Tolerance value
Circularity, mm (in.)	≤0.1 (≤0.004)	≤0.2 (≤0.008)	≤0.3 (≤0.01)
Straightness, mm (in.)	≤0.1 (≤0.004)	≤0.15 (≤0.006)	≤0.2 (≤0.008)
Wall thickness in circumferential direction, mm (in.)	±0.02 (±0.0008)	±0.025 (±0.001)	±0.04 (±0.002)
Wall thickness in longitudinal direction, mm (in.)	±0.02 (±0.0008)	±0.03 (±0.001)	±0.04 (±0.002)
Roughness outer surface, im	±0.4	±0.05	±0.06
Roughness inner surface, im	±0.1	±0.1	±0.15

Source: Ref 12.2

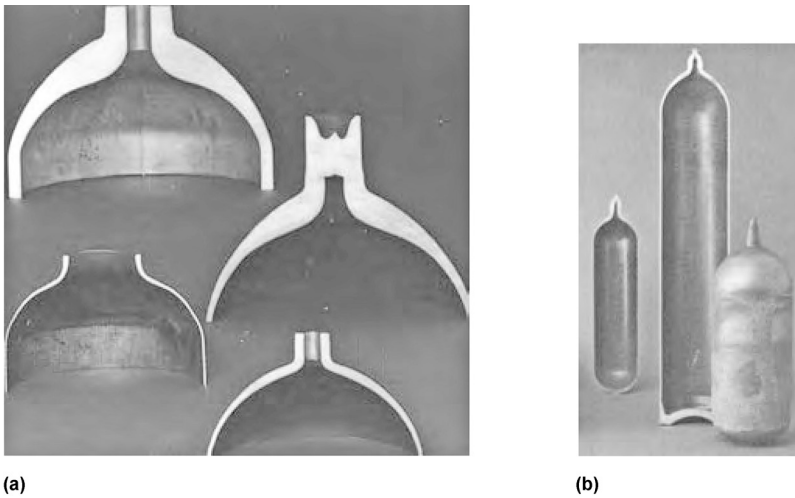


Fig. 12.31 (a) Gas bottle neck, formed by hot flow forming. (b) Gas liner. Source: Ref 12.15

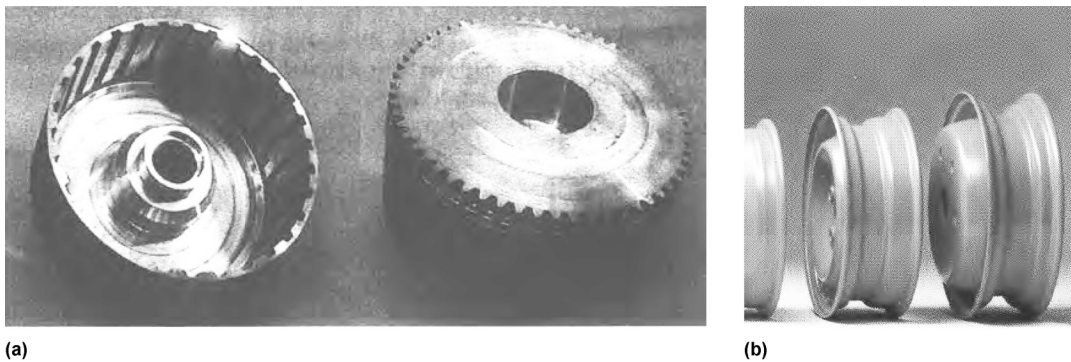


Fig. 12.32 (a) Clutch housing. (b) Aluminum automotive wheel. Source: Ref 12.15

12.3 Shear Spinning

Shear spinning is used to manufacture conical, convex, or concave parts from sheet metal or preformed workpieces. In shear spinning, the material thickness is reduced significantly, while the outer diameter of the part remains constant.

Process Description. In shear spinning, which is sometimes called power spinning or spin forging (Fig. 12.33), the blank (1) is clamped between a tailstock (2) and a mandrel (3), which is driven by the main spindle and gives its shape to the part. In contrast to conventional spinning, the part is formed in only one cycle (5). There-

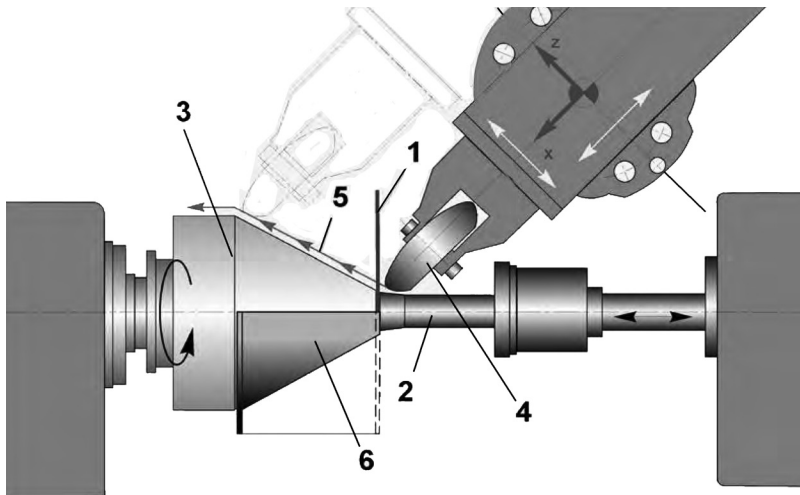


Fig. 12.33 Process kinematic in shear spinning

fore, the roller tool (4) moves with a predefined gap along the contour of the mandrel until the part (6) is formed.

Figure 12.34 demonstrates schematically the deformation of the part during the shear spinning process. The material is projected horizontally on the shape of the mandrel, while the outer diameter, D_0 , does not change. The material thickness, s_1 , normal to the part surface remains constant, and it is reduced from its initial value, s_0 . The angle, α , determines the final cone angle and defines the complete cone angle.

Considering the constancy in volume and using the symbols given in Fig. 12.34, the final thickness of the part can be calculated by the sine law:

$$s_1 = s_0 \sin\left(\frac{\alpha}{2}\right) \quad (\text{Eq 12.3})$$

In practice, this formula must be used to adjust the gap between the mandrel and roller tool. In manufacturing of curved shapes (Fig. 12.35), there is a gradual change of the wall thickness. Thus, the gap between the tool and the mandrel must be adjusted locally to give the required value.

Failure Modes. Figure 12.36 presents typical failure modes when the sine law is neglected during shear spinning. A greater clearance, s_p , than what is required (underreduction, Fig. 12.36a) will lead to wrinkles in the remaining part. On the other hand, an adjustment of a

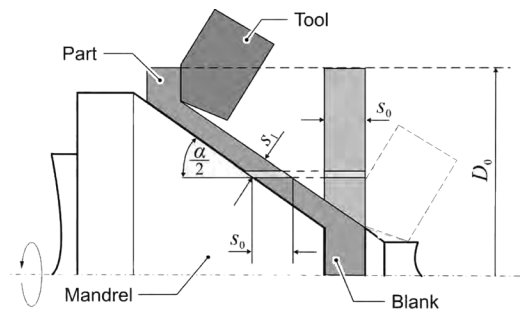


Fig. 12.34 Shear spinning of a cone. Source: Ref 12.14

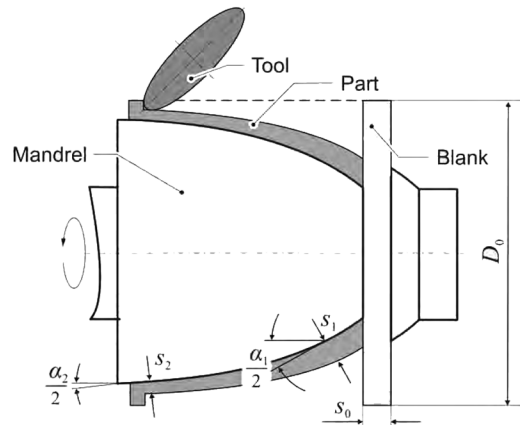


Fig. 12.35 Shear spinning of convex shapes. Source: Ref 12.14

gap, s_f , smaller than the required one (overreduction, Fig. 12.36b) will lead to circular flaring in front of the roller tool, which may lead to circumferential cracks (Fig. 12.36c). A straight and flat flange indicates that the gap, s_f , has the correct magnitude.

Process Design. In shear spinning, the part dimensions can only be affected by changing the initial sheet thickness, s_0 , or by the cone angle, α . Figure 12.37 gives some examples that show how a variation of the blank initial thickness and shape affects the final shape of the part.

In Fig. 12.38, a circular blank with an initial diameter, D_0 , and thickness, s_0 , is formed by conventional spinning to a cone with a diameter, D , and an angle, α_1 . Due to the process kinematics of conventional spinning, the wall

thickness did not change significantly while the outer diameter is reduced. In the next step, the part is formed by shear spinning. The required reduction of the wall thickness is smaller when compared to a forming operation using shear spinning directly without the intermediate preforming step. The final wall thickness of the part, when using an intermediate preform step, can be obtained by:

$$s_2 = s_0 \frac{\sin \alpha_1}{\sin \alpha_2} \tag{Eq 12.4}$$

Machines and Tools. In principle, the same machines can be used for shear spinning as well as the conventional spinning process. However, shear spinning causes larger forces during forming. This results in high bending moments on

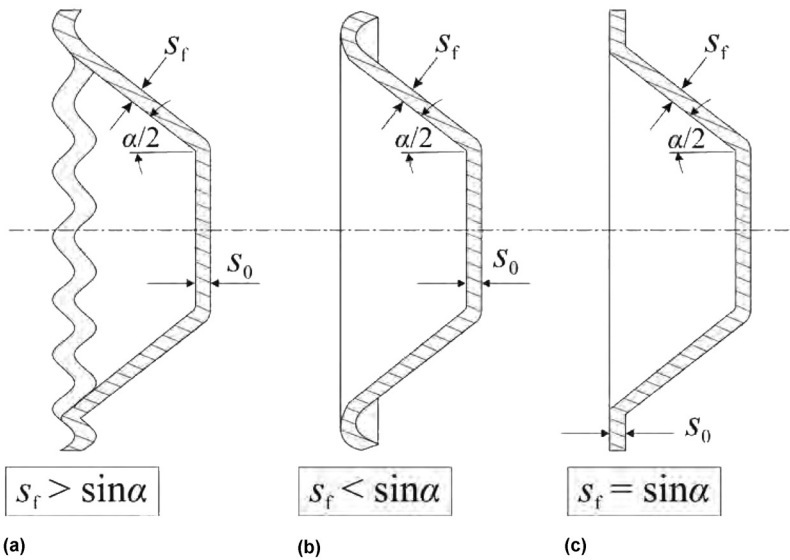


Fig. 12.36 Failure modes in shear spinning. (a) Wrinkling. (b) Flaring. (c) Sufficient part. Source: Ref 12.26

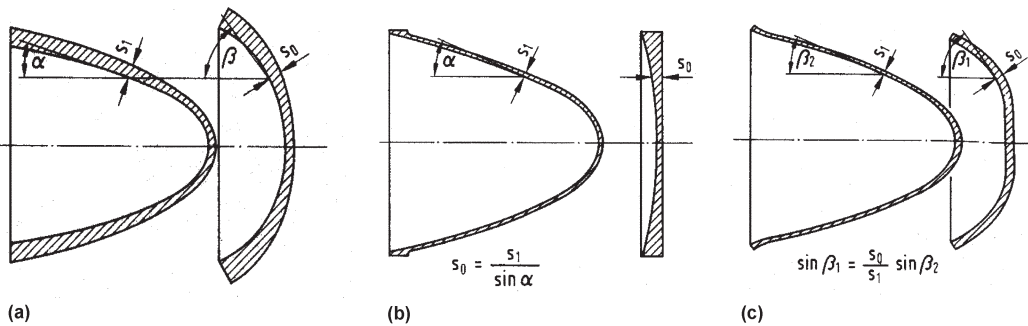


Fig. 12.37 Examples of preforms of the blank to vary the final thickness. Source: Ref 12.15

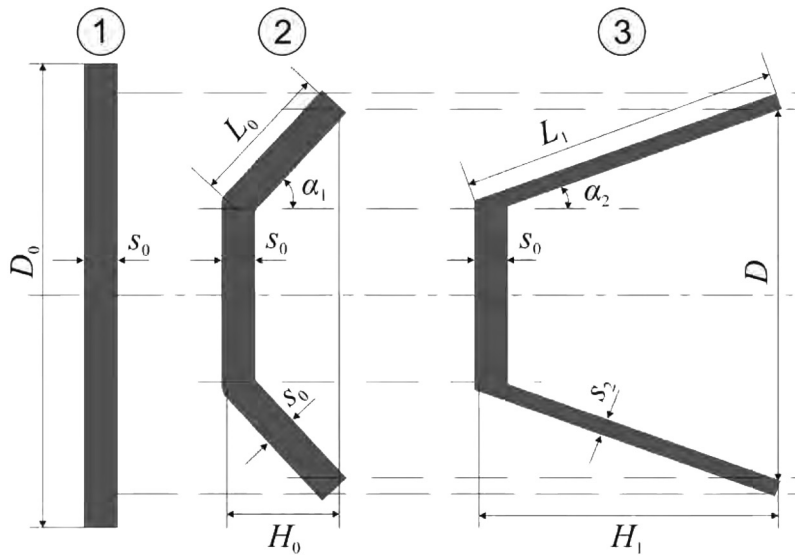


Fig. 12.38 Process combination of conventional and shear spinning. Source: Ref 12.27

the mandrel as well as asymmetric loads on the machine. To compensate for these asymmetric acting forces, machines with two symmetric roller tool-heads that act simultaneously on the workpiece have been developed.

When geometrical tolerances of the workpiece are not critical, the shear spinning process can even be performed with a simple mandrel, used for holding the blank (Fig. 12.39). Thus, parts with different shapes can be obtained with the same mechanical setup.

Part Properties. The production accuracy of parts manufactured by shear spinning is comparable to that of machined parts. Table 12.7 gives an overview of achievable tolerances in some selected applications.

For a given initial thickness, s_0 , the maximum angle, α_{limit} , that can be achieved by shear spinning depends on the material. Table 12.8 presents an overview of cone angles reached by experimental investigations. Flat, circular blanks with an initial thickness of $s_0 = 5 \text{ mm}$ (0.2 in.) have been formed into conical parts with a constant angle. In further experiments, parts were formed to achieve a hemispherical shape. The manufactured parts have a constant thickness. This was reached by preforming flat blanks by machining to a convex shape at one surface, such as in Fig. 12.37(b).

Applications. Typical applications for parts made by shear spinning are conical shapes, as presented in Fig. 12.40.

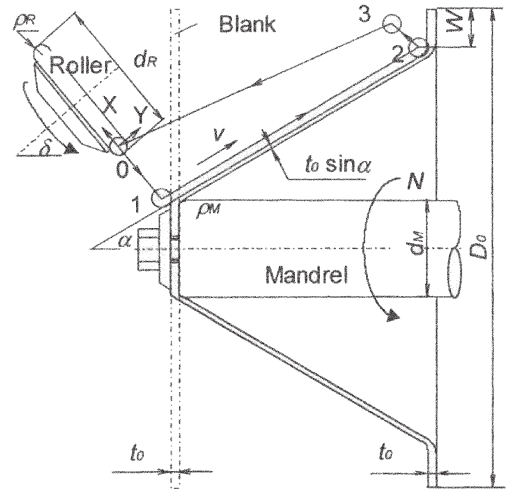


Fig. 12.39 Dieless shear spinning. Source: Ref 12.28

Table 12.7 Tolerances in shear spinning

Part-dependent value		Tolerance value	
Height of cone, mm (in.)	50–300 (2–12)	Thickness in axial direction, mm (in.)	± 0.03 (± 0.001)
Diameter, mm (in.)	40–300 (1.5–12)	Thickness in circumferential direction, mm (in.)	± 0.02 (± 0.0008)
Angle, degrees	25–50	Circularity (blank = round), mm (in.)	< 0.04 (< 0.002)
Final thickness, mm (in.)	2–10 (0.08–0.4)	Circularity (blank = square), mm (in.)	< 0.08 (< 0.003)
Initial thickness, mm (in.)	5–13 (0.2–0.5)	Angle of inclination of surface line, mm (in.)	± 0.05 (± 0.002)
Material	Cu 99.9	Average roughness (R_a), μm	< 0.4

Source: Ref 12.15

Table 12.8 Maximum angles obtainable in shear spinning

Material	Cone	Curvilinear	Material	Cone	Curvilinear
Ferrous alloys			Nonferrous alloys		
321 SS	75	50	3000 Al	60	50
347 SS	75	50	6061 Al	50	75
17-7 PH SS	66	45	2024 Al	50	...
17-4 PH SS	66	45	2014 Al	40	50
410 SS	60	50	5086 Al	65	50
A-286	70	55	7075	65	50
Waspalloy	40	30	Copper	75	...
Rene 41	40	35			
Maraging 250	75	60			
Maraging 300	65	50	Com Pure	45	...
Maraging 350	45	30	6-4	55	...
D6AC	70	50	B120VCA	30	...
4340	70	50	6-6-4	50	...
6434	70	50			
4130	75	55			
H11 tool steel	50	35			
			Tungsten	45	...
			Beryllium	35	...
			Ti-molybdenum	60	45

(a) These alloys are spun at elevated temperature; all others at room temperature. Source: Ref 12.29

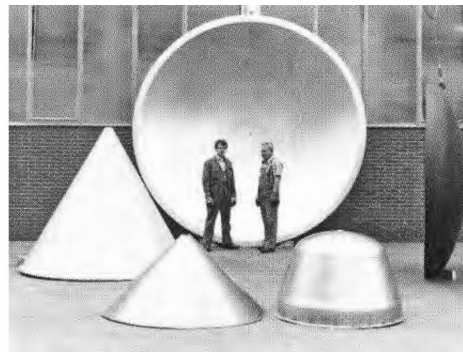


Fig. 12.40 Example parts manufactured by shear spinning. Source: Ref 12.15

REFERENCES

12.1 H.-J. Dreikandt, “Untersuchungen über das Drückwalzen zylindrischer Hohlkörper und Beitrag zur Berechnung der gedrückten Fläche und der Kräfte,” Dissertation, Universität Stuttgart, 1973

12.2 M. Runge, Drücken und Drückwalzen, *Die Bibliothek der Technik*, 1993, p 72

12.3 K.-H. Dröge, “Kräfte und Materialfluss beim Drücken,” Dissertation, Universität Stuttgart, 1954

12.4 “Fertigungsverfahren Zugdruckumformen—Drücken,” DIN 8584, 1971, p 1–2

12.5 R. Köhne, “Rechnergestützte Ermittlung und Verarbeitung von Umformparametern für das Fertigungsverfahren Drücken,” Dissertation, TU Dortmund, 1984

12.6 R. Ewers, “Prozessauslegung und Optimierung des CNC—gesteuerten Formdrückens,” Dissertation, TU Dortmund, 2005

12.7 M. Hayama, H. Kudo, and T. Mutara, Development of Roller Pass Programming for Spinning Shells of Various Shapes, *JSTP*, Vol 33, 1992, p 510–518 (in Japanese)

12.8 H. Maschke, Das Drücken dünner Bleche—1, *Teil, Blech*, Vol 5, 1963, p 265–267

12.9 H. Maschke, Das Drücken dünner Bleche—2, *Teil, Blech*, Vol 7, 1963, p 448–454

12.10 C.C. Wong, T.A. Dean, and J. Lin, A

- Review of Spinning, Shear Forming and Flow Forming Processes, *Int. J. Mach. Tools Manuf.*, Vol 43 (No. 14), 2003, p 1419–1435
- 12.11 M. Runge, Automatisches Drückprogramm-Generieren als Alternative zum Playback-Steuern, *BÄnder Bleche Rohre*, Vol 8, 1989, p 65–71
- 12.12 K. Lange, *Umformtechnik—Handbuch für Industrie und Wissenschaft*, Band 2, Springer Verlag, 1988
- 12.13 O. Music, J. Allwood, and K. Kawai, A Review of the Mechanics of Metal Spinning, *J. Mater. Process. Technol.*, Vol 210, 2010, p 3–23
- 12.14 W. König, *Fertigungsverfahren Band 5, Blechumformung*, VDI 5, 1990, p 88–104
- 12.15 Liefeld Metal Spinning GmbH, 1993, <http://www.leifeldms.de/en/home.html>
- 12.16 G. Herold, S. Gorbauch, and H. Hartwig, Kraft- und Drehmomentbedarf beim Drückwalzen, *Blech Rohre Profile*, Vol 42 (No. 11), 1995, p 708–712
- 12.17 S. Kalpakjian and S. Rajagopal, Spinning of Tubes: A Review, *J. Appl. Metalwork.*, Vol 2 (No. 3), 1982, p 211–223
- 12.18 M. Eckert and E. Nold, Gegenrollen-Drückwalzen: Ein neues Verfahren zum Herstellen großer, hochfester, rohrförmiger Werkstücke, *Werkstatt Betr.*, Vol 125 (No. 1), 1992, p 64–68
- 12.19 F. Garreis and K. Adler, Fließdrücken auf Drehmaschinen, *Fertigungstech. Betr.*, Vol 18 (No. 5), 1968, p 304–308
- 12.20 S. Hauk, “Grundlagen des Fließspaltens von Blechrollen,” Dissertation, TU Darmstadt, 1999
- 12.21 A. Danno, “Effects of Forming Conditions on Diameter Accuracies of Short Cylindrical Hollow Cup after Flow Forming,” ICTP 2011 (Aachen, Germany)
- 12.22 C.L. Packham, Metal Spinning and Shear and Flow Forming, *Sheet Met. Ind.*, 1977, p 382–389
- 12.23 C.L. Packham, Metal Spinning and Shear and Flow Forming, Part 2, *Sheet Met. Ind.*, 1977, p 485–492
- 12.24 C.L. Packham, Metal Spinning and Shear and Flow Forming, Part 3, *Sheet Met. Ind.*, 1977, p 586–590
- 12.25 S. Gorbauch, K.-H. Heidel, and S. Kühmel, Entwicklungsstand und Anwendungsmöglichkeiten des Abstreckdrücken, *Fertigungstech. Betr.*, Vol 28, 1978, p 174–177
- 12.26 B. Avitzur and C.T. Yang, Analysis of Power Spinning of Cones, *J. Eng. Ind.*, 1960, p 231–245
- 12.27 J. Faulhaber, Drücken und Fließdrücken, Verfahren und Maschinen, Teil 1+2, *Blech Rohre Profile*, Vol 34 (No. 2), 1987, p 199–285
- 12.28 K. Kawai, H. Koyama, T. Kamei, and W. Kim, Boss Forming, An Environment-Friendly Rotary Forming, *Key Eng. Mater.*, Vol 344, 2007, p 947–953
- 12.29 J.D. Steward, Shear Spinning Rewards Designer with Automatically Precise Parts, *SAE J.*, Vol 78 (No. 2), 1970, p 43–45

SELECTED REFERENCES

- J.M. Allwood and H. Utsunomiya, A Survey of Flexible Forming Processes in Japan, *Int. J. Mach. Tools Manuf.*, Vol 46 (No. 15), 2006, p 1939–1960
- W. Blaschke, “Analytische Untersuchung des Drei-Rollen-Drückwalzens zum Erhalt notwendiger Umformbedingungen,” Dissertation, TU München, 1991
- W. Bosch, Spanlose Formgebung durch Drücken und Fließdrücken, *Maschinenmarkt*, Vol 20, 1969, p 49–79
- H. Dierig, “CNC-Drücken mit adaptiver Regelung,” Dissertation, TU Dortmund, 1992
- H.-J. Dreikandt, Ordnungsschema für drückwalzbare Werkstückformen, *Ind.-Anz.*, Vol 93 (No. 28, 37), 1971, p 587–591, 832–835
- K. Grüning, Drücken, Vieweg Verlag, *Umformtechnik*, Vol 3, Auflage, 1982, p 151–156
- M. Hayama, Roller Pass Programming and Selection of Working Conditions in Conventional Spinning, *J. JSTP*, Vol 345, 1989, p 1403–1410
- M. Hayama, H. Kudo, and T. Shinokura, Study of the Pass Schedule in Conventional Simple Spinning, *Bull. JSME*, Vol 13, 1969, p 1358–1365
- M. Hayama and T. Murota, On the Study of Metal Spinning, *Bull. Faculty Eng.*, Yohohama National University, Vol 12, 1963, p 54–88

- M. Hayama, T. Murota, and H. Kudo, Deformation Modes and Wrinkling of Flange on Shear Spinning, *Bull. JSME*, Vol 9 (No. 34), 1966, p 423–433
- W. Hofen and R. Wenke, Stand und Entwicklungstendenz des Fließdrückens, *Fertigungstech. Betr.*, Vol 30 (No. 10), 1980, p 584–587
- H. Jacob and F. Garreis, Rollenordnung und Rollenform beim Fließdrücken kreiszylindrischer Hohlkörper, *Fertigungstech. Betr.*, 1965, p 279–283
- H. Jacob and F. Garreis, Fließdrücken mit Schrägstellung der Rollen und deren Auswirkung auf den Werkstofffluß und die Umformkräfte (Dreh-Umformmaschine), *Fertigungstech. Betr.*, 1966, p 42–45
- K. Kawai and M. Hayama, Roller Pass Programming in Conventional Spinning by NC Spinning Machine, *Adv. Technol. Plastic.*, Vol 11, 1987, p 711–718
- K. Kawai, L.-N. Yang, and H. Kudo, Dieless Shear Spinning of Truncated Conical Shells, *Adv. Technol. Plastic., Proc. of the Sixth ICTP* (Erlangen), 1999, p 1089–1094
- S. Kobayashi, Instability in Conventional Spinning of Cones, *Trans. ASME*, 1963, p 44–48
- H. Labetzke, “Untersuchung zum Einziehen von Metallhohlkörpern durch Drücken,” Dissertation, TH Zwickau, 1992
- W. Lehmann, Das Metalldrücken, *Tech. Rundsch.*, Vol 4040, 1965, p 71–75
- H.J. Ludwig, Grundlagen und Anwendungsgebiete der Drückverfahren (I), *Bänder Bleche Rohre*, Vol 10 (No. 9), 1969, p 540–548
- H.J. Ludwig, Grundlagen und Anwendungsgebiete der Drückverfahren (II), *Bänder Bleche Rohre*, Vol 10 (No. 10), 1969, p 623–629
- H.J. Ludwig, Grundlagen und Anwendungsgebiete der Drückverfahren (III), *Bänder Bleche Rohre*, Vol 10 (No. 11), 1969, p 667–676
- P. Merkel, Zahnräder aus Ronden, *Ind.-Anz.*, 1994, p 16–17
- G. Micha and T. Jehuda, Plastic Flow Instability Under Compressive Loading during Shear Spinning Process, *J. Eng. Ind.*, Vol 104, 1982, p 17–22
- F.J. Pistol, Modern Spinning Methods, *Sheet Met. Ind.*, 1970, p 131–136
- S. Rajagopal and S. Kalpakjian, Some Aspects of Internal Shear Forging to Produce Large, Internally Ribbed Aluminium Alloy Tubes, *Second International Conference on Rotary Metalworking Processes*, Oct 6–8, 1982 (Stratford upon Avon, England), p 287–298
- W. Sellin, *Metalldrücken*, Springer Verlag, 1955, p 1–71
- G. Spur, *Handbuch der Fertigungstechnik—Umformen*, Band 2/1, G. Spur, Ed., Hanser Verlag, 1983
- E. von Finckenstein and H. Dierig, CNC-Drücken, *CIRP Ann.*, Vol 39 (No. 1), 1990, p 267–270
- H.K. Winkel, Drückwalzen, *Handbuch der Fertigungstechnik—Umformen*, Band 2/1, G. Spur, Ed., Hanser Verlag, p 535–547

CHAPTER 13

Incremental Sheet Forming

G. Hirt and M. Bambach, RWTH Aachen University

DEEP DRAWING is a very cost-effective and well-established process for the mass production of sheet metal components. However, because of the high costs and long lead time for die manufacturing, it is not economical for small-batch production, rapid prototyping, and large sheet components with a complex geometry. To achieve cost-effective small-batch production and prototyping of sheet metal parts, incremental sheet metal forming processes based on computer numerical-controlled (CNC) machines have been developed. The basic idea behind incremental sheet metal forming is to form sheet metal parts using a CNC forming tool. The forming tool follows the contour of the desired part and imposes a localized plastic deformation. These localized plastic deformations add up to create the final shape of the part.

By means of a moving forming tool, the need for dedicated tooling can be reduced or even avoided.

Incremental sheet forming (ISF) was first described in 1967 in a patent (Ref 13.1) at a time when CNC was not yet technically feasible. Starting from the early 1990s, the process has been investigated and developed by an ever-growing number of research teams and companies. A selection of parts that were produced using ISF is shown in Fig. 13.1. This chapter provides an overview of ISF, covering the existing variations of the process, the machines and equipment used, the process limits, advanced forming strategies, process simulation, and recent developments in the field of hybrid ISF, that is, process combinations of ISF with stretch forming and laser heating.

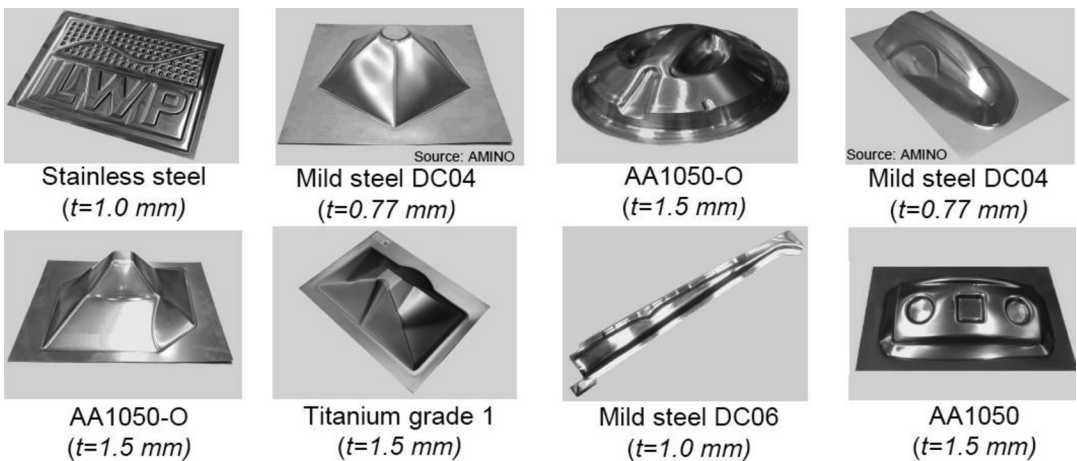


Fig. 13.1 Various parts manufactured by incremental sheet forming. t , initial sheet thickness of the blank. Source: Ref 13.2

13.1 Process Variations of ISF

A definition for ISF has been given in Ref 13.3. It states that ISF is a process which:

- Has a solid, small-sized forming tool
- Does not have large, dedicated dies
- Has a forming tool that is in continuous contact with sheet metal
- Has a tool that moves under control, in three-dimensional space
- Can produce symmetric as well as asymmetric sheet metal shapes

Incremental sheet forming includes the following process variations.

Single-Point Incremental Forming (SPIF). The characteristic feature of SPIF is that a part is shaped by the action of a CNC forming tool that has a single-point contact with the sheet metal. The blank is clamped in a blank holder that remains at a constant height (Fig.13.2). This process variation can be truly dieless when no support tool is used. In most cases, however, a dedicated rig or backplate is employed to create a defined transition between the flange and the part. Both variations of the SPIF process are shown in Fig.13.2. There is no single-point contact when a backplate is used. Nevertheless, the acronym SPIF is well-established and often used for the process variations shown in Fig.13.2.

Two-Point Incremental Forming (TPIF). In some cases, a full or partial positive die is required to expand the range of possible geometries or enhance the accuracy of the process (Fig. 13.3). A full support is particularly important for geometries with defined curvature changes. Those parts of the component that were formed in the beginning of the process must not be deformed in later stages. This can be ensured by a support tool. The process variations using a positive die are called TPIF. In the TPIF process, the sheet is again clamped in a blank holder and formed by a CNC forming tool. In contrast to SPIF, the sheet approaches the final shape from the outside, using a blank holder that descends over the die. Two-point incremental forming is not dieless. However, tooling for ISF can be made of less expensive materials than for stamping, which is still an advantage. In some cases, it is possible to use a partial die (Fig. 13.3, right) to manufacture variations of a part design with the same setup by adjusting the tool path only.

Kinematic Incremental Sheet Forming (KISF). A new development is the use of two forming tools (one on either side of the blank), which are actuated simultaneously (Fig. 13.4). This process variation is a truly dieless sheet metal forming process, thus offering additional flexibility over the SPIF process. It was first de-

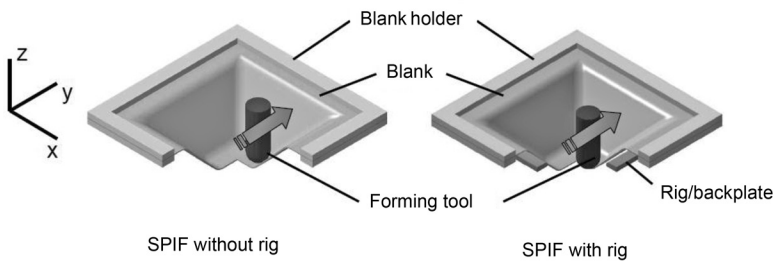


Fig. 13.2 Single-point incremental sheet forming (SPIF). Source: Ref 13.2

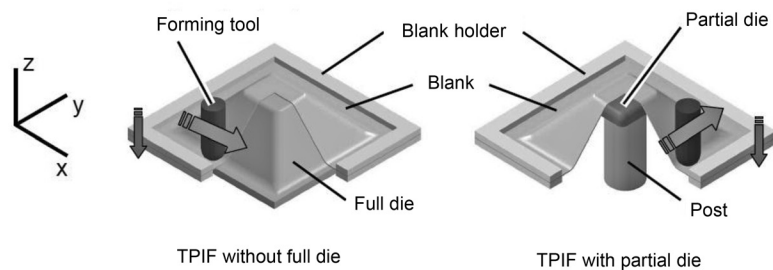


Fig. 13.3 Two-point incremental sheet forming (TPIF). Source: Ref 13.2

scribed in a Japanese patent (Ref 13.4). It is sometimes referred to as fully kinematic ISF or roboforming. Currently, the biggest challenges in the development of KISF are the definition and synchronization of the tool paths of the master and slave tool so that the slave tool can act as a support tool during forming, and the control of dimensional accuracy of the parts, especially when using two synchronized robots.

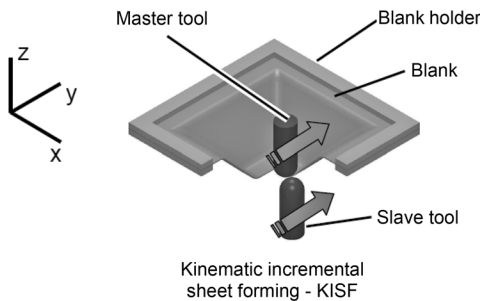


Fig. 13.4 Kinematic incremental sheet forming using two forming tools. Source: Ref 13.2

13.2 Equipment and Basic Process Parameters

Machines Used for ISF. In principle, any computer-controlled machine that allows a forming tool to move along a defined tool trajectory in space can be used to perform ISF. The selection of machines used in practice includes the following:

- CNC milling machines
- Industrial robots
- Hexapods
- Dedicated machine designs

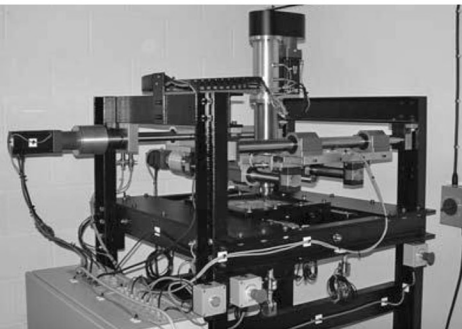
Availability, speed, working volume, stiffness, and costs are the key factors in the decision for a machine type. Figure 13.5 shows typical machine setups for ISF: an upgraded conventional milling machine with moveable blank holder (Fig. 13.5a), a specially designed ISF machine distributed by the Japanese company AMINO (Fig. 13.5b), a special incremental sheet-forming machine built at the University of



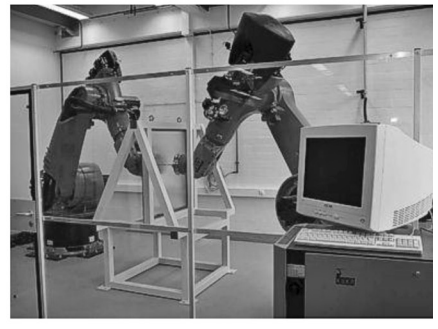
(a)



(b)



(c)



(d)

Fig. 13.5 Machines used for incremental sheet forming (ISF). (a) Upgraded milling machine. (b) Dedicated machine for ISF by AMINO. (c) A special ISF machine built at the University of Cambridge. (d) Roboforming process using two robots. (a) to (c) Source: Ref 13.3. (d) Source: Ref 13.5

Cambridge (Fig. 13.5c), and the roboforming process that uses two cooperating industrial robots (Fig. 13.5d).

Milling machines are often used because they are available in many shop floors and can be adapted easily to the requirements of ISF. Industrial robots are a good alternative because of their moderate prices. However, because of their low stiffness, additional efforts must be made to prevent the forming tool from deviating from the prescribed trajectory.

An alternative forming process using industrial robots is the incremental hammering process. Instead of a rigid forming tool, incremental hammering uses a forming tool that has a fast oscillating movement, thus beating the sheet into the desired shape.

Forming Tools. A solid forming tool with a hemispherical head is generally used for ISF (Fig. 13.6). The tool radius has considerable effects on the process. It influences the surface quality, forming limits, and springback. If the part contains features with small radii, a forming tool with a matching radius must be used. The tools are made of tool steel, stellite, or plastic. Typically, rotating tools are used with milling machines, whereas other machines, such as single-purpose AMINO machines, use rigid tools that do not rotate. This use of nonrotating tools has considerable effects on the frictional conditions compared to actively or passively rotating tools. Cold forming oil is usually spread on the surface of the sheet to reduce friction.

Work Flow and Forming Parameters. A significant advantage of ISF is that it enables parts to be devised and produced within a short period of time. In the case of SPIF, the tool path can be planned from a computer-aided design (CAD) model, and the part can be formed directly without the need for dedicated dies. For TPIF, either a full or partial positive die must be manufactured, but because forming forces are relatively low, cheap and easy-to-mill materials such as plastics, resin, or wood can be used. Hence, the time needed to form a part from a CAD model can be kept short. If the geometry is simple, manufacturing a part using ISF is straightforward and comprises the steps shown in Fig. 13.7.

Most software applications on the market that can generate CNC programs for milling can be used for the generation of tool paths for ISF. The most common type of tool path used in ISF consists of a series of contour lines at different levels along the forming direction (usually the *z*-axis). The vertical distance between the contours, the tool pitch, is an important process parameter (Fig. 13.8).

The manufacturing of parts using *z*-level tool paths shall be referred to as the standard forming strategy. Besides the tool pitch, the most important process parameters are as follows (Fig. 13.9, middle):

- Size and shape of the moving forming tool (Fig. 13.9, left), tool material, and tool velocity



Fig. 13.6 Forming tools (left to right): satellite tools with radii of 3, 5, and 15 mm, respectively, and a 15 mm plastic tool. Source: Ref 13.3

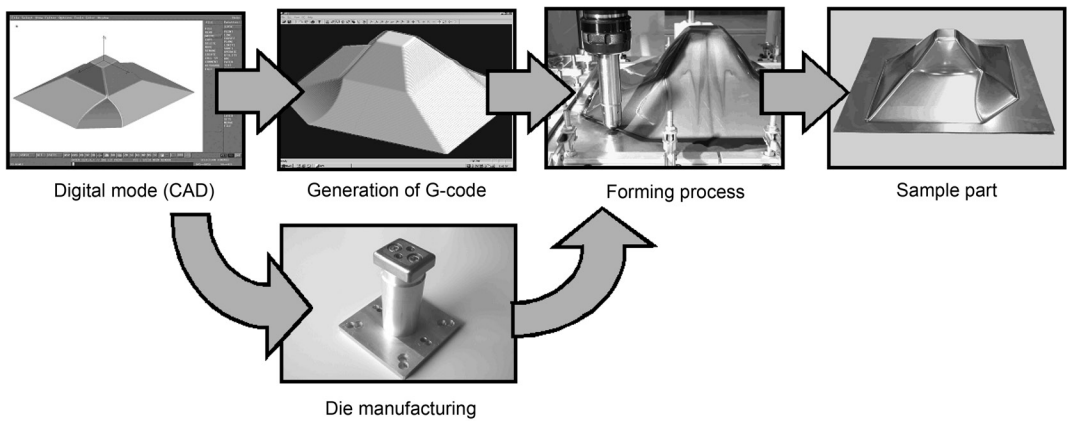


Fig. 13.7 Computer-aided design (CAD)/computer-aided manufacturing process chain for incremental sheet forming. Source: Ref 13.6

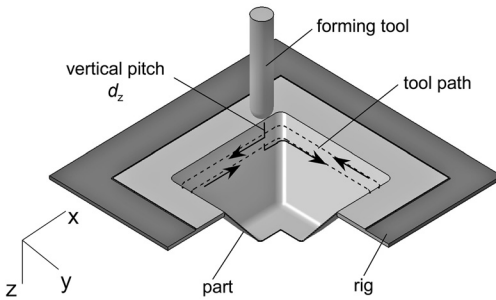


Fig. 13.8 Tool path and tool pitch for a sample geometry. Source: Ref 13.2

- Sheet thickness
- Direction of tool motion (Fig. 13.9, right)
- Blank holder force, temperature, lubrication, and forming speed

Truly dieless SPIF can be applied only to relatively simple geometries. For more complex shapes, it is required either to use a backplate in SPIF or to use the TPIF process, which yields a better accuracy and allows the production of more complicated shapes. In that case, a solid die must be manufactured.

The work flow shown in Fig. 13.7 is valid only for simple parts. Very often, the fabrication of parts using ISF is not straightforward; parts are often designed for stamping rather than for ISF, which makes it hard to generate these shapes by ISF. Another limiting factor may be that the application requires a very good geometrical accuracy or does not allow for much sheet thinning.

13.3 Process Mechanics and Process Limits

The process mechanics of ISF are strongly influenced by the fact that the plastic deformation zone is localized. On-line deformation measurements using a stereovision system indicate that the deformation zone is indeed very small and limited to the contact area between tool and workpiece (Ref 13.8). As a consequence of the localized deformation, the process mechanics of ISF are complex and still the subject of current research. Questions of scientific interest include:

- Why does ISF show extended forming limits compared to traditional forming limit diagrams?
- What is the predominant deformation mechanism: stretching, shear, or bending?
- What can be done to reduce sheet thinning in ISF?
- How can the geometrical accuracy of parts made by ISF be improved?

Sheet Thinning. Measurements of the surface strains on testpieces with stereovision systems show macroscopic deformation modes on flat surfaces that are very close to plane-strain conditions. These surface strains do not give any insight into the through-thickness deformation but are often used to calculate the thickness strains. Assuming that ISF induces a projection of the undeformed material onto the surface of the final part, the so-called sine law can be derived if a one-dimensional section through the part is considered. The sine law allows an esti-

mate of the actual sheet thickness (t_1) from the initial sheet thickness (t_0) as a function of the wall angle, α (Fig. 13.10):

$$t_1 = t_0 \cdot \sin(\pi/2 - \alpha) \tag{Eq 13.1}$$

For nonflat surfaces, it is easier to calculate the thickness change as a function of the area ratio of the undeformed and deformed state. This leads to the simple equation:

$$t_1 = t_0 \cdot A_0/A \tag{Eq 13.2}$$

for a surface element (Fig. 13.10).

It can be shown that under the assumption of a pure projection of surface elements, the sine law does not take into account minor strains and therefore gives quite inaccurate predictions of the thickness after forming for areas in which the sheet metal is not flat. To remedy this restriction of the sine law, a simplified modeling approach (SMA) using kinematically admissible velocity fields has been developed (Ref 13.9). This approach draws upon the fact that the deformation in ISF is determined to a great

extent by the geometrical constraints imposed by the moving forming tool. Figure 13.11 gives a comparison of the sheet thickness calculated by the sine law and the SMA with experimental data, showing that the sine law, unlike the SMA, gives wrong estimates of the sheet thickness in the corners of the test shape. Hence, the SMA algorithm allows the calculation of surface strain estimates within minutes, which is useful for evaluating the feasibility of a given part design.

Forming Limits. The sine law indicates that sheet thinning increases rapidly when the inclination of the part surface with respect to the plane sheet increases. At a wall angle of 60° , the sheet thickness after forming will be half of the initial value. If the wall angle increases, necking can be observed, as shown in Fig. 13.12 for a cross section through a pyramidal test shape. If the wall angle is increased beyond 60 to 65° , the sheet will break.

Sheet thinning limits the range of possible wall angles to approximately 60 to 65° for most applications. As a consequence, the forming kinematics inherent in ISF entail the following drawbacks:

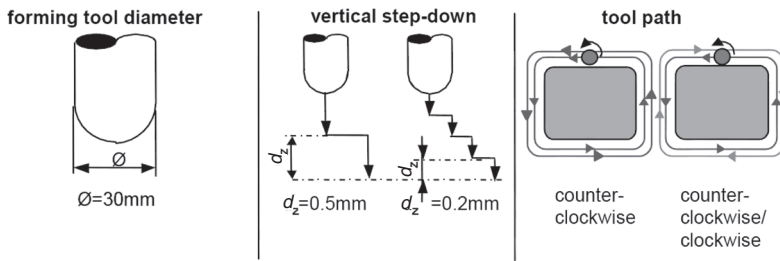


Fig. 13.9 Some important process parameters of incremental sheet forming. Source: Ref 13.7

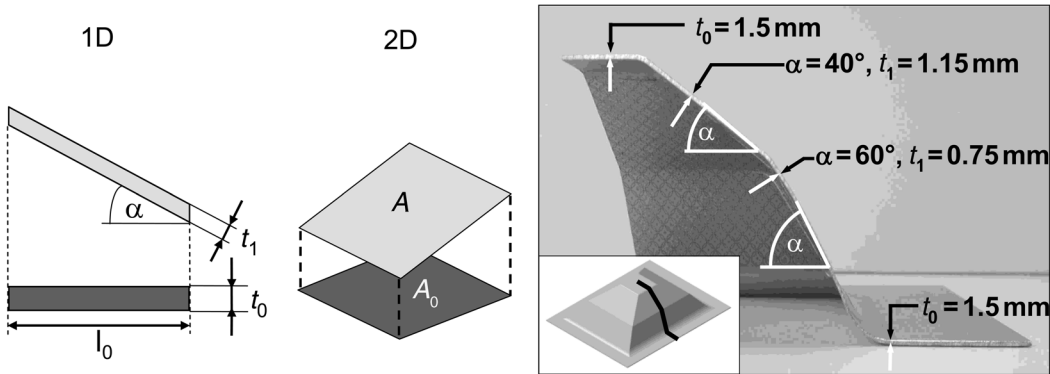


Fig. 13.10 Sheet thinning in incremental sheet metal forming. Source: Ref 13.3

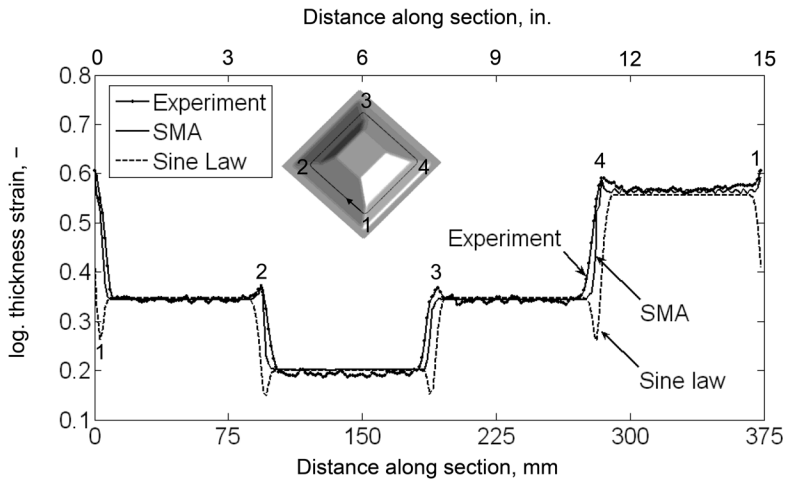


Fig. 13.11 Comparison of sheet thickness predicted by the sine law and a simplified modeling approach (SMA) with experimental data. Source: Ref 13.2

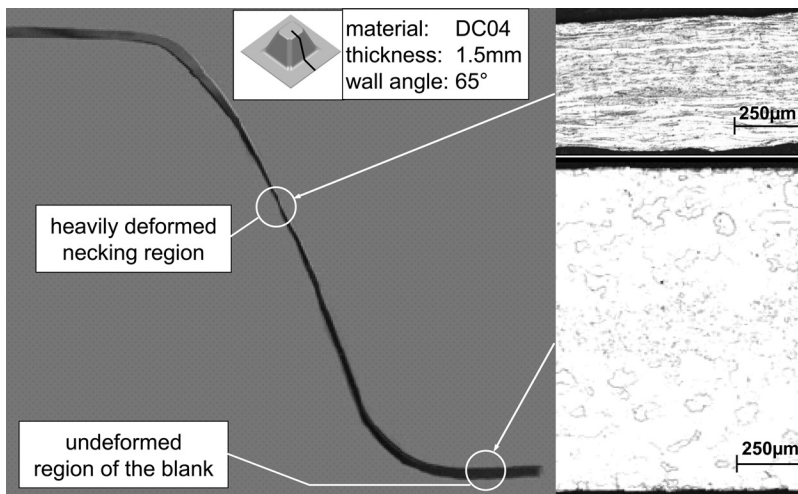


Fig. 13.12 Cross section through the side wall of a pyramidal test shape. Source: Ref 13.7

- The limitation on the maximum wall angle restricts the potential scope of shapes and applications.
- The strong dependence of sheet thinning on the feature angle can lead to an inhomogeneous thickness distribution in the final part.

These drawbacks have motivated research into multistage forming strategies and new hybrid process variations.

Early investigations showed that the forming limits observed in ISF are significantly larger than expected from a typical forming limit curve. Forming limit diagrams for ISF were obtained by plotting the fracture strains obtained

with various test shapes into a classic forming limit diagram, as shown in Fig. 13.13.

The limit strains measured in ISF roughly match with the fracture limit strains obtained from a Nakajima test but are much larger than the necking strains obtained in a Nakajima test. Recent research has shown the following:

- A clear distinction between necking and fracture should be made when evaluating limit strains in ISF.
- The surface strains at necking in ISF are still much larger than typical necking strains obtained from Nakajima tests.
- The deformation in ISF is nonproportional.

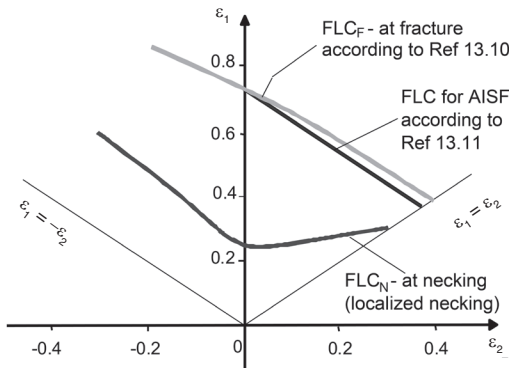


Fig. 13.13 Comparison of forming limit curves (FLCs) at necking and fracture and an FLC for the incremental sheet forming process. Source: Ref 13.2

In fact, serrated strain paths are obtained. Forming limit curves are valid only for linear strain paths. Hence, they cannot be applied to ISF.

The nature of the forming limits in ISF is not yet comprehensively understood. Reference 13.12 attributes the large attainable strains in ISF to shear, Ref 13.13 to cyclic bending, and Ref 13.14 to the nonlinear strain paths; Ref 13.15 treats the limit strains using a low-cycle fatigue model.

There are several factors that determine the onset of necking and fracture in sheet metal forming. It is unlikely that the large strains can be attributed to just one phenomenon alone. To understand the forming limits in ISF, it seems necessary to understand the interplay of process mechanics and material behavior. Reference 13.2 lists a number of effects that can act in a stabilizing way in ISF:

- *Punch Curvature, Tool Pressure, and Triaxiality:* The typical punch diameter according to the ISO 12004 guidelines is 100 mm. Punches in ISF are usually smaller, for example, 6 to 30 mm (0.24 to 1.18 in.), such as the ones shown in Fig. 13.6. This means that the forming tools in ISF will generally produce larger thickness gradients, which stabilize the deformation. Also, the surface pressure in ISF leads to triaxiality ratios below zero under the immediate action of the tool, which can have a stabilizing effect on the deformation.
- *Stress State:* In ISF, the immediate action of the forming tool imposes a biaxial in-plane

state of stress on the sheet. A change in stress state is necessary for a localized neck to develop. The stress state under the tool could give an explanation why, for some test shapes used in ISF, fracture is not preceded by localized necking, but for others, it is.

- *Localized Deformation:* The plastic deformation in ISF is localized; that is, the plastic zone is always embedded in the surrounding material, which behaves elastically and supports the forming zone. This can have important effects on the development of a localized neck.
- *Cyclic Deformation:* As shown by Ref 13.13, superimposed cyclic bending can stabilize the stretch deformation of a strip. This effect seems to be important for ISF, too, because cyclic bending is present in ISF.
- *Through-Thickness Shear:* Reference 13.12 puts forward the idea that through-thickness shear is mainly responsible for the extended forming limits in ISF. It is shown in Ref 13.12 that superimposed shear indeed lifts the level of the forming limit curve, but it has not yet been shown that enough shear is created in ISF to allow for the increase in limit strains that are observed experimentally.
- *Feed Rate, Strain Rate, Temperature, and Friction:* The feed rate in a Nakajima test is sufficiently low that strain-rate effects and an excessive increase in temperature can be neglected. In contrast, ISF experiments performed at two different feed rates show that an increase in feed rate (thus entailing a change in strain rate, frictional conditions, and temperature) can stabilize the deformation, so that larger failure depths can be reached.
- *Tool Movements:* Assume that the stretching created by the forming tool should principally lead to necking (or rupture), just as in the Nakajima test. The difference between the Nakajima test and ISF lies in the moving tool. In ISF, the forming tool imposes a small, moving bulge on the sheet and creates a groove as it is dragged over the sheet metal. The moving bulge generates in-plane strain gradients in front of it, coupled with in-plane shear stresses that act in a stabilizing manner on the groove that is created by the moving tool. In addition, a rigid moving tool causes friction forces that act in a stabilizing way.

Geometrical Accuracy. The tool path is generated exclusively from the geometric information specified in the CAD model of the desired part. Following this tool path, the tool tries to impose the desired shape on the sheet metal. This strategy would be successful if the deformation were purely plastic. However, ISF gives rise to a number of springback effects that stem from elastic deformations:

- *Localized Springback:* This type of springback takes place continuously throughout the process. As the tool moves along its trajectory, portions of the part are continuously freed from constraints so that they can relax,

giving rise to a continuous localized springback behind the tool (Fig. 13.14a).

- *Orbital Motions:* During forming, the part is always inclined toward the forming tool, resulting in global orbiting motions (Fig. 13.14b). This effect is due to the asymmetry of loading with a single forming tool. The effect becomes more dominant with increasing part size and decreasing stiffness of the part.
- *Springback on Removal of the Forming Tool:* This type of springback occurs at the end of forming when the tool is removed and during forming whenever the tool is lifted and moved to a different position. On removal of

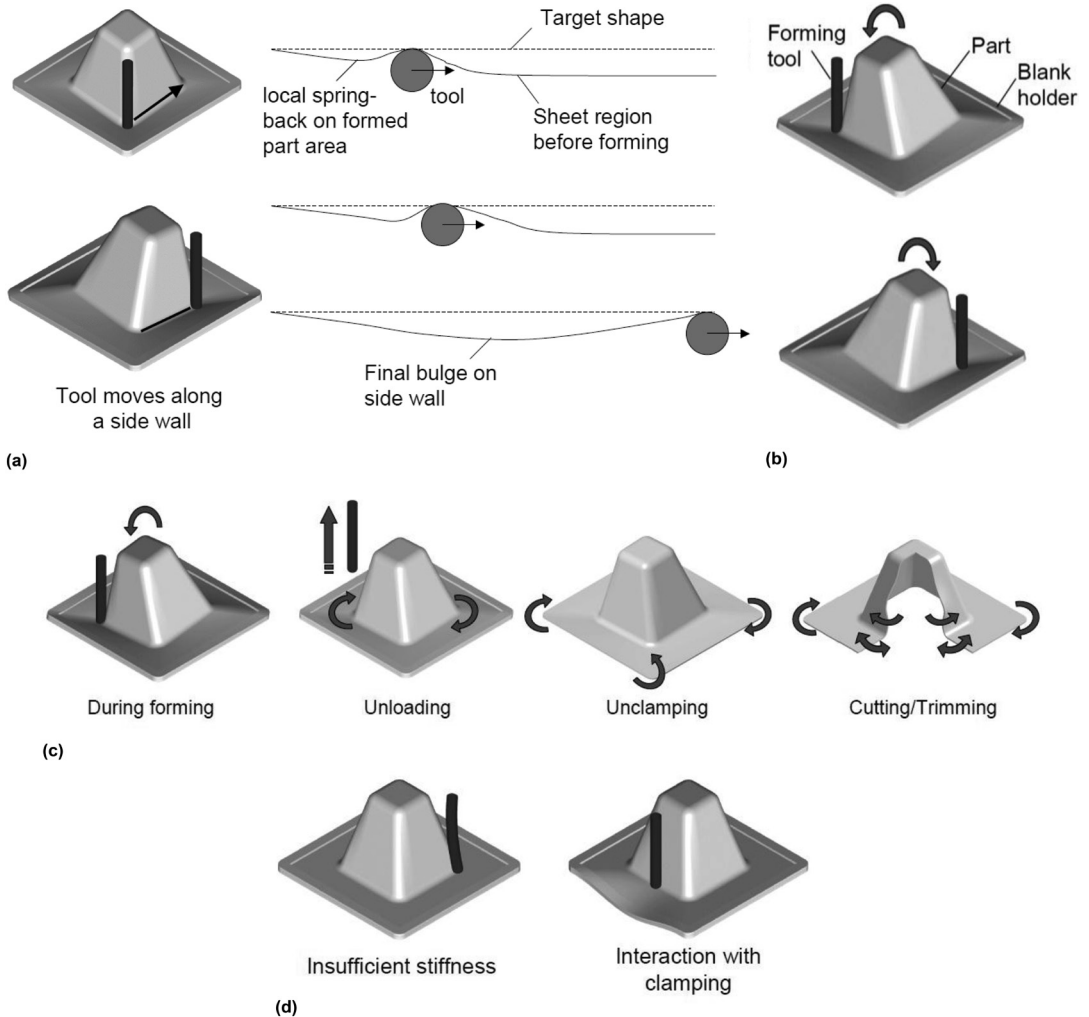


Fig. 13.14 Elastic effects and springback in incremental sheet forming. (a) Local springback under the tool. (b) Orbital motions of a part around the die. (c) Elastic deformations upon unloading, unclamping, and cutting/trimming. (d) Interaction with the machine structure. Source: Ref 13.2

the tool, the elastic deformations induced locally under the tool (type 1) and those induced globally (type 2) are recovered.

- *Springback on Unclamping:* This is a typical type of springback. When the part is removed from the blank holder, shape changes can occur when the part assumes a new state of equilibrium.
- *Springback on Trimming:* Most parts made by ISF require a trimming operation because they usually have addendum surfaces that are necessary for forming. Residual stresses in the part can lead to shape changes during cutting. Types 2 to 5 are illustrated in Fig. 13.14(c).
- *Process-Machine Interactions:* Interactions of the forming process with the machine structure may affect the accuracy of the formed part. This point is particularly important when the stiffness of the machines used for forming is low, for example, for robot-based ISF. Also, the parts of the machine or the blank holder can be elastically deformed when forces are too large (Fig. 13.14d). Another possible effect in this category is the slipping of the sheet in the clamps when the clamping force is insufficient.

In addition, residual stresses are built up in the part as a result of cyclic loading into the plastic range and unloading. These residual stresses can lead to considerable deviations from the target geometry. The amount of deviation depends on the material to be formed, the sheet thickness, and a number of process parameters. As a rough first approximation, Ref 13.16 states that, typically, deviations of less than 1 mm are hard to achieve (on typical sheet metal parts). However, recent developments show that the geometrical accuracy can be improved by using adapted multistage forming strategies (Ref 13.17) or process combinations with stretch forming (Ref 13.18), as discussed in section 13.6, “Hybrid Process Variations,” in this chapter.

13.4 Multistage Forming Strategies

The process limits of ISF have motivated research into multistage forming strategies. Inspired by the forming strategies used in sheet metal spinning, multistage forming strategies for nonaxisymmetric parts were developed. The following stages constitute a typical multistage forming strategy:

1. In the preforming stage (Fig. 13.15a), the blank is clamped in the blank holder, and a preform with a shallow wall angle (45° in this example) is produced by using the regular ISF process and a partial die.
2. Then, a number of stages follow in which the forming direction of the forming tool alternates from upward (Fig. 13.15b) to downward (Fig. 13.15c) and vice versa.
3. From one stage to the next, the tool path is generally designed with an increase in angle of 3° or 5° . This means that 9 to 15 stages are needed to produce components with a wall angle of 90° .

With this forming strategy, it was possible to produce a four-sided pyramid with rectangular side walls (Fig. 13.16).

Despite the successful application of multistage forming strategies to many problems, perhaps the biggest hindrance for using multistage forming strategies is the drastic increase in processing time. For the square box shown in Fig. 13.16, seven hours are needed. The large number of forming stages cannot be decreased, because the part otherwise may wrinkle in the corners and material may fail at the bottom of the sidewalls.

This drawback has led to the development of bending/stretching strategies, which create a preform that roughly approximates the final shape of the part by stretching the sheet metal harshly over the die using a tool path with a large vertical pitch. After the preform is created, a forming stage generates the final shape of the

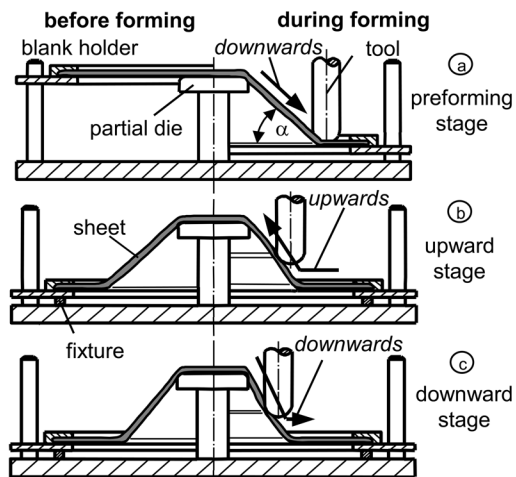


Fig. 13.15 Multistage incremental sheet forming strategy. Source: Ref 13.7

part using a very small pitch to ensure a good surface finish (Fig. 13.17).

If a preform is created by stretching the sheet metal over the die using incremental forming, large tool forces are observed. It is therefore easier to stretch the sheet over the die using stretch-forming equipment. Besides reducing the risk of overloading the CNC machine, stretch forming leads to a reduction in process time and improves the accuracy of the part. The combination of stretch forming and ISF is discussed in section 13.6, “Hybrid Process Variations,” in this chapter.

Multistage forming strategies can also be used to reduce the geometrical deviations produced by the standard forming strategy. Multistage forming can be applied in single-point forming and two-point forming. In single-point forming, the basic idea is to create a preform that is smaller than the final part and to stretch it out during the consecutive forming steps in order to flatten the bulges of the preform. A similar effect can be observed in TPIF. Figure 13.18 shows a comparison of a part made by single and multistage forming, showing that multistage forming improves the accuracy of the part after forming. Trimming a part after forming

can induce shape changes. Sometimes, it is necessary to perform stress-relief annealing before trimming to preserve the accuracy obtained in the forming process.

13.5 Process Modeling

Because of the large number of degrees of freedom that ISF offers, it is sometimes tedious to find and optimize forming strategies for a given part by experience or trial-and-error. A suitable process model is needed to estimate whether a part is feasible with ISF and to identify suitable forming strategies. In principle, the finite-element method is well established in sheet metal forming to analyze and optimize, for example, stamping processes. However, the following difficulties exist with regard to the finite-element process simulation of incremental sheet metal forming processes (Ref 13.2):

- Incremental sheet forming processes are characterized by a small plastic zone in relation to the component volume. This plastic zone moves continuously, or step by step, through the component that behaves elastically in all other respects. To be able to adequately measure the prevailing local gradients of the field variables in the plastic zone, this zone must be finely discretized. Together with the migratory motion, this gives rise to the need for a fine mesh of the entire structure. Because at times the number of load cycles is extremely high, relatively long processing times are the norm. This fact, together with considerable geometric and material nonlinearity, results in unacceptably long computation times.
- Furthermore, the movement of the plastic zone is also linked to continuous changes in the contact between the workpiece and tool for small load changes. This can lead to con-

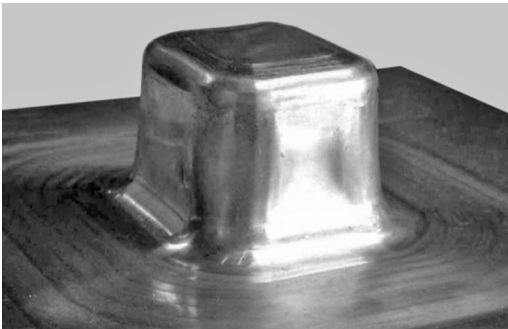
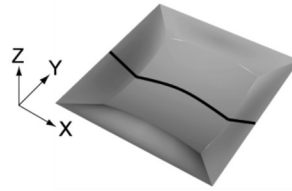


Fig. 13.16 Pyramidal frustum with vertical walls. Source: Ref 13.7

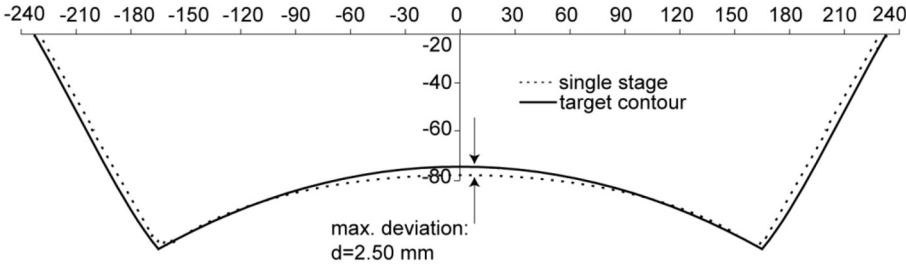


Fig. 13.17 Stiffening brace manufactured by incremental sheet metal forming. Source: Ref 13.9

Evaluation of the cross section in X



single stage forming strategy



multistage forming strategy

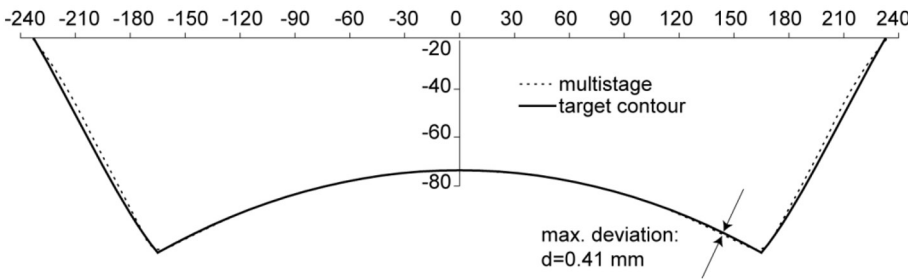


Fig. 13.18 Comparison of single and multistage forming with respect to the accuracy of formed parts. Source: Ref 13.17

vergence problems in finite-element method simulations with implicit time integration.

- Individual workpiece areas cycle during the forming process; in certain circumstances, they undergo a range of cycles of plastification and unloading, whereby changes in the direction of loading can occur. Therefore, materials modeling for incremental forming faces increased challenges.

An efficient simulation technique must be able to handle the aforementioned challenges. Depending on the process chosen, different approaches are possible.

Modern specialized programs for the simulation of sheet metal forming processes often use explicit time integration algorithms (LS-DYNA, PAMSTAMP, etc.). In contrast to implicit methods, these methods include mass, inertial forces, and damping, so that velocity and acceleration play an important role in the simulation. The

maximum time step that can be specified depends on the speed of sound, c_d , in the blank material and the element dimensions, L_{min} , of the smallest element in the meshed component:

$$\Delta t = \frac{L_{min}}{c_d} \propto \sqrt{\rho} \tag{Eq 13.3}$$

The critical time step is therefore proportional to the density and mass of the blank material. To increase the efficiency, a procedure known as mass scaling is often applied; that is, the finite-element system assumes that the blank material has a larger mass than it really does. This means that the critical time step can be increased and the calculation can be performed with significantly fewer time steps. The advantage of a shorter computation time, however, comes hand-in-hand with potential errors in the calculation results.

During the forming process, the tools transfer kinetic energy to the workpiece through their movement. As a result of mass scaling, the workpiece now has a larger kinetic energy for a given tool velocity than it would have in the real process. This surplus kinetic energy is transformed into additional plastic deformation, which can lead to unexpected results.

In addition, sound waves are generated in the component. The calculation result is therefore also influenced by the definition of the tool trajectory. Long tool path lengths in ISF give rise to the following difficulties for explicit time integration. Without mass scaling, the computation times would be at least of the same order of magnitude as for the implicit process, yet with mass scaling, errors can add up over the duration of the calculation, negatively influencing the quality of the computation results.

To alleviate this problem, care must be taken to use a tool trajectory with continuous velocity and acceleration. The maximum acceleration values determine the maximum allowable time step. If discontinuities in the tool velocity and acceleration are avoided and if a suitable time step is chosen, finite-element simulations with a good quality can be obtained using codes with explicit time integration (Ref 13.2).

13.6 Hybrid Process Variations

The conventional incremental sheet metal forming method is suitable for the production of small and medium quantities of sheet metal parts from cold workable materials. It has the following disadvantages:

- The process time is relatively large and scales proportionally to the surface area of the part.

- The sheet thickness distribution on formed parts is inhomogeneous.
- The cyclic loading can produce considerable residual stresses and hence inaccuracies.

Another drawback is that there are parts made from titanium or magnesium alloys that are needed in small quantities and cannot be manufactured using ISF because of their limited workability at room temperature. These drawbacks have motivated research into hybrid process combinations of ISF with stretch forming and laser heating. Figure 13.19 gives the process principles for both processes.

Stretch Forming and ISF. Compared to ISF, stretch forming is relatively fast, produces parts with a good dimensional accuracy, and shows a material flow that creates sheet thinning in areas that would not be deformed in ISF. This makes a combination of ISF and stretch forming promising in view of reducing the drawbacks of ISF. Figure 13.20 shows a sheet metal forming center that is equipped with four independently movable stretch forming modules and the capability to perform five-axis ISF. This setup allows the creation of preforms in a relatively short amount of time via stretch forming, while using ISF to create those features of the part that cannot be formed in the stretch forming process.

Laser-Assisted ISF. Figure 13.21 (left) shows the setup of the hybrid process in which the sheet metal is heated locally in front of the moving forming tool by means of laser radiation. Figure 13.21 (right) shows the forming depth reached with sheets of the titanium alloy Ti-6Al-4V and the magnesium alloy AZ31. The sheets were formed at room temperature until fracture occurred. In contrast to cold forming, laser-assisted forming produces a higher forming depth with a simultaneous reduction of the forming forces.

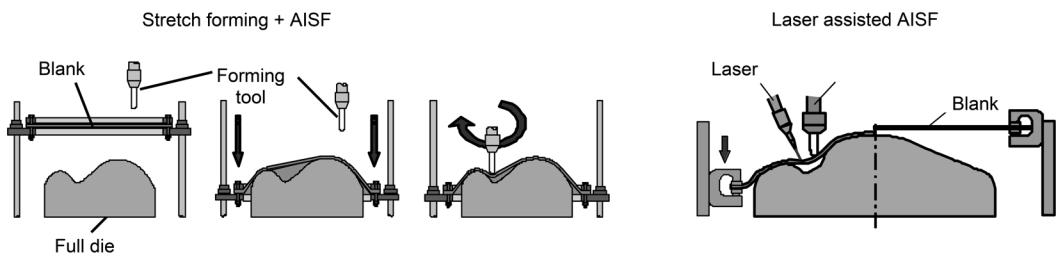


Fig. 13.19 Process principles of the hybrid processes stretch forming plus incremental sheet forming (ISF) and laser-assisted ISF. Source: Ref 13.19

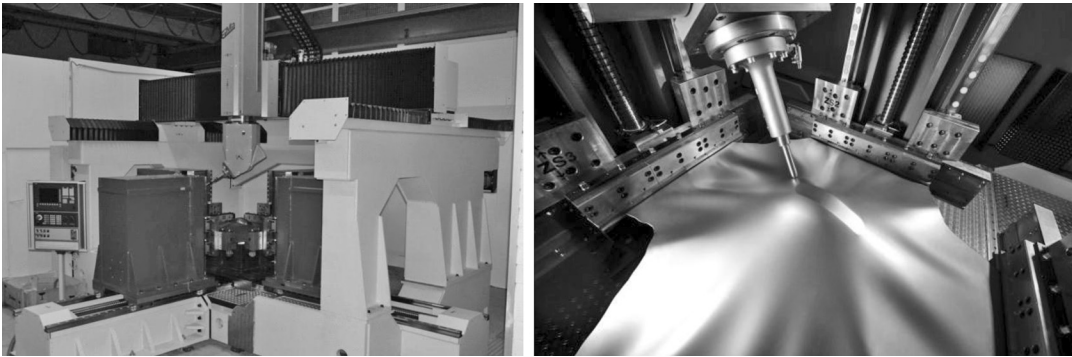


Fig. 13.20 Sheet metal forming center combining stretch forming and five-axis incremental sheet forming. Source: Ref 13.19

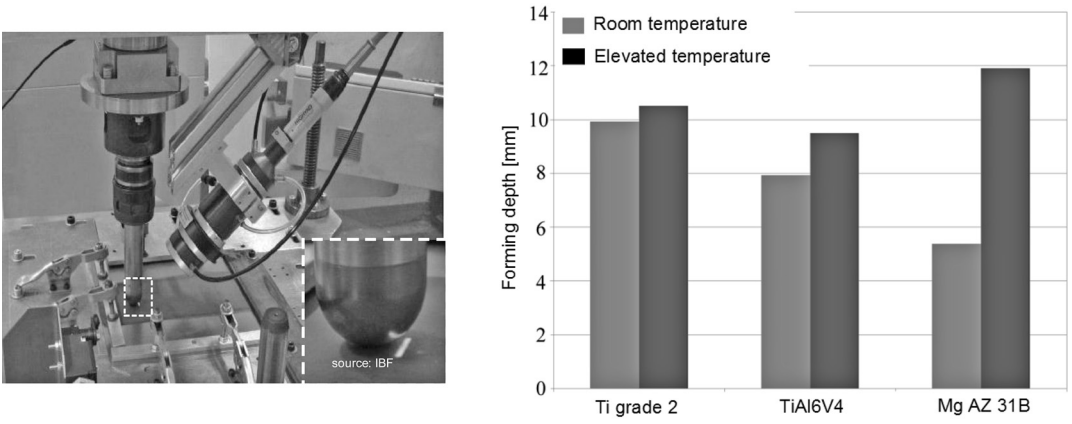


Fig. 13.21 Laser-assisted incremental sheet forming. Setup (left) and first results (right). Source: Ref 13.20

REFERENCES

13.1 E. Leszak, Apparatus and Process for Incremental Dieless Forming, U.S. Patent 3342051A1, 1967

13.2 M. Bambach, Process Strategies and Modelling Approaches for Asymmetric Incremental Sheet Forming, *Umformtechnische Schriften*, Vol 139, Shaker, Aachen, 2008

13.3 J. Jeswiet, F. Micari, G. Hirt, A. Bramley, J. Dufloy, and J. Allwood, Asymmetric Single Point Incremental Forming of Sheet Metal, *CIRP Ann.*, Vol 54, 2005, p 623–649

13.4 A. Shima, T. Yoshikawa, K. Nakamura, Y. Sudo, and S. Suzuki, Formation of Successively Expanding Metallic Plate and Apparatus Therefore, Japanese Patent JP9085355, 1997

13.5 H. Meier, B. Buff, L. Laurischkat, and V. Smukala, Increasing the Part Accuracy in Dieless Robot-Based Incremental Sheet Metal Forming, *CIRP Ann., Manuf. Technol.*, Vol 58 (No. 1), 2009, p 233–238

13.6 G. Hirt, J. Ames, M. Bambach, and R. Kopp, Forming Strategies and Process Modelling for CNC Incremental Sheet Forming, *CIRP Ann.*, Vol 53 (No.1), 2004, p 203–206

13.7 S. Junk, “Inkrementelle Blechumformung mit CNC Werkzeugmaschinen: Verfahrensgrenzen und Umformstrategien,” Ph.D. thesis, Universität des Saarlandes, Germany, 2003 (in German)

13.8 J. Ames, Systematische Beeinflussung des Werstoffflusses bei der Inkrementellen Blechumformung mit CNC-

- Werkzeugmaschinen, *Umformtechnische Schriften*, Vol 140, Shaker, Aachen, 2008 (in German)
- 13.9 G. Hirt, J. Ames, and M. Bambach, A New Forming Strategy to Realise Parts Designed for Deep Drawing by Incremental CNC Sheet Forming, *Steel Res.*, Vol 71 (No. 2–3), 2005, p 160–166
- 13.10 H. Takuda, K. Mori, N. Takakura, and K. Yamaguchi, Finite Element Analysis of Limit Strains in Biaxial Stretching of Sheet Metals Allowing for Ductile Fracture, *Int. J. Mech. Sci.*, Vol 42, 2000, p 785–798
- 13.11 L. Filice, L. Fratini, and F. Micari, Analysis of Material Formability in Incremental Forming, *CIRP Ann.*, Vol 51 (No. 1), 2002, p 199–202
- 13.12 J.M. Allwood, D.R. Shouler, and A.E. Tekkaya, The Increased Forming Limits of Incremental Sheet Forming Processes, *Proceedings of the 12th International Conference on Sheet Metal*, 2007, p 621–628
- 13.13 A. Hadoush, A.H. van den Boogaard, and J. Huétink, Stable Incremental Deformation of a Strip to High Strain, *Proceedings of the 12th International Conference on Sheet Metal*, 2007, p 615–620
- 13.14 P. Eyckens, S. He, A.V. Bael, P.V. Houtte, and J. Dufloy, Forming Limit Prediction for the Serrated Strain Paths in Single Point Incremental Sheet Forming, *AIP Conference Proceedings*, Vol 908, American Institute of Physics, 2007, p 141–146
- 13.15 K. Kitazawa, T. Oka, and Y. Sato, Forming Limit in Incremental Stretching of Sheet Metals, *Proceedings of the 54th Japanese Joint Conference for the Technology of Plasticity*, 2003, p 421–422
- 13.16 J.M. Allwood, G.P. King, and J. Dufloy, A Structured Search for Applications of the Incremental Sheet-Forming Process by Product Segmentation, *Proc. IMECHE Part B, J. Eng. Manuf.*, Vol 6, 2005, p 239–244
- 13.17 M. Bambach, B. Taleb Araghi, and G. Hirt, Strategies to Improve the Geometric Accuracy in Asymmetric Single Point Incremental Forming, *Prod. Eng., Res. Develop.*, Vol 3 (No. 2), 2009, p 145–154
- 13.18 B. Taleb Araghi, G.L. Manco, M. Bambach, and G. Hirt, Investigation into a New Hybrid Forming Process: Incremental Sheet Forming Combined with Stretch Forming, *CIRP Ann., Manuf. Technol.*, Vol 58 (No. 1), 2009, p 225–228
- 13.19 Institute of Metal Forming, RWTH Aachen University, Germany, 2009, www.ibf.rwth-aachen.de
- 13.20 T. Biermann, A. Goettmann, J. Zettler, M. Bambach, A. Weisheit, G. Hirt, and R. Poprawe, Hybrid Laser-Assisted Incremental Sheet Forming—Improving Formability of Ti- and Mg-Based Alloys, *Proceedings of the Fifth International WLT—Conference on Lasers in Manufacturing 2009*, June 2009 (Munich, Germany)

CHAPTER 14

Mechanical Joining by Forming

Deepak Rammohan and Jose L. Gonzalez-Mendez, The Ohio State University

MECHANICAL JOINING is a process where two or more components are held together through the use of either an integral feature of components or through fasteners. In these types of joining, loads are transferred from one component to another through the development of mechanical forces arising from the interlocking and resulting interference of two or more elements and/or fasteners. Joining by forming includes all processes where parts being joined are formed locally and sometimes fully. The deformation forces are generated mechanically or electromagnetically. A positive interlock is formed between the materials, and the joint is formed. Commonly used processes in the industry are riveting, clinching, and crimping (Ref 14.1).

Major applications of mechanical joining by forming are found in automobile and aircraft industry, household appliances, ventilation and air conditioning, as well as in electronics and medical appliances.

The advantages of mechanical joining include:

- Versatile and easy to use
- Allows easy dismantling of the product
- Allows different materials to be joined with ease
- No thermal or structural transformation of components takes place. Therefore, neither distortion nor embrittlement is present.
- Pre- and posttreatment of workpieces is rarely necessary.

The disadvantages of mechanical joining include:

- Fasteners do not seal the joint against liquids or gases.

- Prone to failure at the hole where the fastener goes through
- Formability required is a constraint
- Stress concentration is present in most methods at points of fastening.

The main focus of this chapter is on riveting, crimping, clinching, self-pierce riveting, and their combinations with other processes.

14.1 Riveting

A rivet is a metallic pin with a head, used for joining together plates or pieces of materials by passing it through them and then beating or pressing down the point so that it shall spread out and form a second head, a pin, or bolt headed or clinched at both ends. The process in which this technique is implemented is called riveting (Ref 14.1).

Two main types of riveting processes are punch riveting and self-pierce riveting.

Punch Riveting. Figure 14.1 shows the riveting process in four steps. First, the parts to be joined are fixed by the blank holder (view 1). As the punch moves down, the punch rivet penetrates both the sheet layers, and the scrap is ejected (view 2). As the punch moves on, the conical head of the rivet begins to mold into the upper sheet layer (view 3). Once the head is fully molded in, the ring on the face of the die presses the lower layer of sheet material into the groove of the rivet shank, creating a positive lock (from closure) overlaid by nonpositive radial compressive stresses (view 4).

The advantages of the punch riveting process are illustrated in Fig. 14.1, which shows the smoothness of the joint at the head area and its

flush fit on both sides. These advantages are often a criterion for the use of this process. The main range of application for this joint is between $s = 1.5$ and 5 mm (0.06 and 0.2 in.) thickness, the lower layer requiring a minimum thickness of approximately 1 mm (0.04 in.) to fill the groove in the shank.

Some of the features of punch riveting include:

- Even materials of high tensile strength, $R_m > 1000$ MPa (145 ksi), can also be joined.
- Formability is not a constraint in this case.
- Thin materials (<1 mm, or <0.04 in.) and nonmetals can also be processed.
- Materials that are brittle can also be processed.

Future developments of this process appear to include:

- Lower-cost rivets, tools, and equipment
- Finite-element method simulations and calculations
- Lower joining forces; accessibility from one side
- New rivet shapes and concepts
- Corrosion-resistant joints

- Combination with other methods (clinching and adhesion)

Self-Piercing Riveting. Figure 14.2 shows the self-piercing riveting process with a self-piercing semitubular rivet in four steps. First, the parts to be joined are fixed by the blank holder (view 1). As the punch moves down (view 2), the rivet pierces only the upper sheet layer nearest the punch, and the punched scrap is taken into the cavity of the semitubular rivet. As the punch moves on, the lower part of the self-piercing semitubular rivet splits open and the undercut is formed (view 3). Again, with this positive lock, radial compressive stresses remain, which create the nonpositive lock important for cyclic resilience (view 4) (Ref 14.1, 14.2). The self-piercing riveting can also be used to join dissimilar materials (Ref 14.3).

The advantages of self-piercing riveting include:

- Joint strength is high in the self-piercing semitubular rivet joint.
- Materials with high tensile strength, R_m up to 1000 MPa (145 ksi), can be joined.
- Brittle materials can be joined, but they are placed on the punch side.

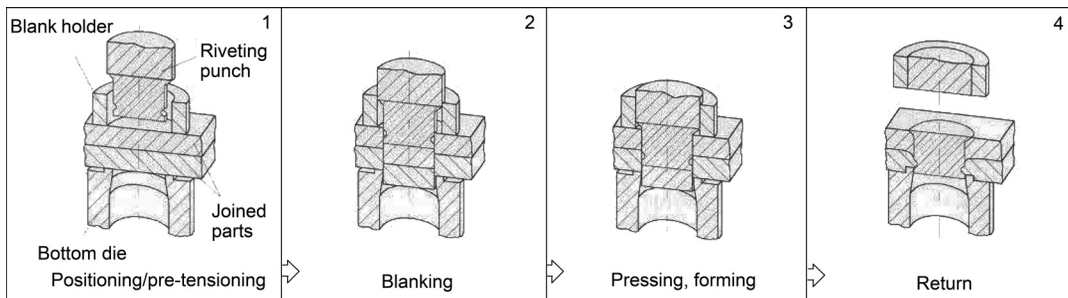


Fig. 14.1 Illustration of the principle of punch riveting. Source: Ref 14.1

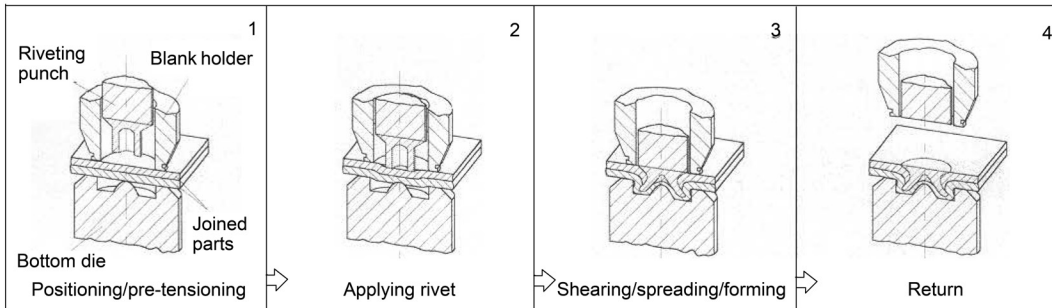


Fig. 14.2 Schematic diagram of self-piercing riveting with semitubular rivet. Source: Ref 14.1

- Used for thin sheet metals ($s = 1.5$ to 4 mm, or 0.06 to 0.2 in.)
- No need for a predrilled hole
- No waste material produced

The disadvantages of this process include:

- Access is required to both sides of the joint.
- Bulges and indents associated with the forming process may not be aesthetically acceptable.
- Relatively high force is required for the forming process.

Figure 14.3 shows the basic layout used for all self-piercing processes. It consists mainly of the blank holder, punch, and die.

To evaluate the strength of self-piercing riveting (SPR), some studies have conducted static and fatigue tests. Results show that static strength for SPR is lower than spot-welded joints. However, the fatigue strength of the SPR joints is superior to that of the spot-welded joints in aluminum alloys used in the automotive industry. Other studies such as those conducted for shear tests demonstrate that SPR shows a high peak load, ductility, and initial stiffness when compared to clinching, self-tapping screws, and pop riveting.

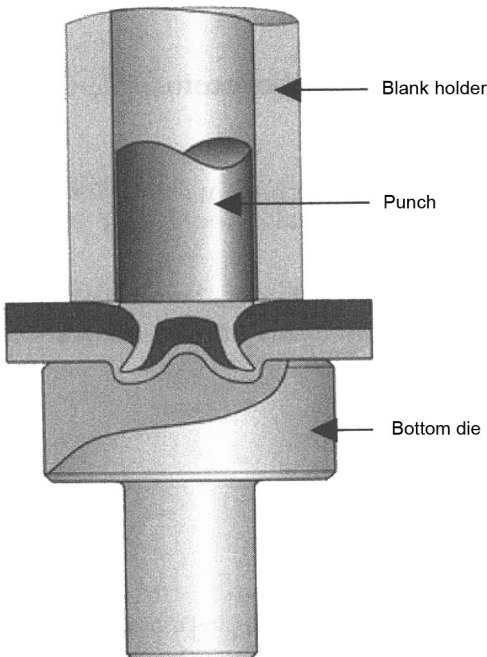


Fig. 14.3 Cross section of components used during semitubular self-piercing riveting. Source: Ref 14.4

Usually, the fretting wear phenomenon accompanies crack formation in SPR at the rivet-to-sheet interface and the sheet-to-sheet interface. The severity of fretting wear increases with sheet thickness.

Surface irregularities or crevices caused by SPR increase the risk of corrosion problems. Crevice corrosion is a severe form of highly localized corrosion attack and results from the presence of an electrolyte in a crevice. Galvanic corrosion occurs when dissimilar, conductive materials are joined and the ingress of water forms an electrolytic cell. This type of corrosion can be avoided if the rivet is manufactured from the same material as the sheets being joined.

At early stages of finite-element modeling of SPR, finite-element analysis in two dimensions was used to calculate setting forces, displacements, and component deformations to be compared with that of actual fastenings. The option of three-dimensional analysis has helped to define accurately the stresses in the SPR process. Other more elaborate models have been applied by several authors to study a number of phenomena: numerical modeling of SPR process parameters such as friction coefficients of the different interfaces and the value of kinetic energy used in a quasi-static analysis, and modeling the characteristics of SPR in aluminum parts and structures subjected to impact, lap shear joints, crash testing, load-induced local distributions of relative slip, contact pressure, and bulk stress in joints (Ref 14.5, 14.6).

Continuous research on this process is aimed at:

- Cost reduction
- Improved joinability for high-strength sheets
- Use of high-strength rivets and workpiece heating
- Process stability and monitoring
- Realistic calculation of the processes
- Reduction of joining force
- Resistance to corrosion

Hydro-Self-Pierce Riveting (HSPR). The manufacturing of complicated workpieces often requires medium-based forming processes, or hydroforming. Thus, some parts may be difficult to reach, that is, a few parts are inaccessible, and joining such parts is difficult. To overcome this difficulty, the combination of SPR and hydroforming has been developed, resulting in a dieless process with accurately formed parts (Ref 14.7).

A schematic diagram of the process is shown in Fig. 14.4. It is mainly carried out in three stages. In step A, the hydroformed sheet (5) and the part to be attached (4) are brought in contact with the hydroforming tool (2) by the fluid (6). The rivet (3) is positioned on the surface of the parts (4). In steps B and C, the punch (1) presses the spreading rivet (3) into the sheets. The high-pressure fluid (6) prevents excessive bending of the hydroformed sheet (5). To the axial movement of the punch, a wobble movement can be overlaid to decrease the necessary joining force and thus limit the necessary pressure of the fluid. Finite-element modeling has been used to design and optimize the HSPR process (Ref 14.7).

The effective stress distribution at the end of the joining operation is calculated for the

HSPR process by using the software package DEFORM. The material behavior is considered to be elastic/plastic. The tool elements are considered to be rigid with the computing time. The mesh generated is a very fine mesh within the rivet foot area. The sheet metal properties are determined by quasi-static tensile testing. Figure 14.5 shows the stress distribution obtained from such a finite-element simulation.

To simulate crack generation in the riveting process, a damage criterion is necessary. The damage value is based on a macromechanical integral value and is calculated from maximum principal stress and effective strain. This is implemented in the simulation by the simple elimination of the elements damaged beyond a given threshold value, followed by remeshing (Ref 14.7).

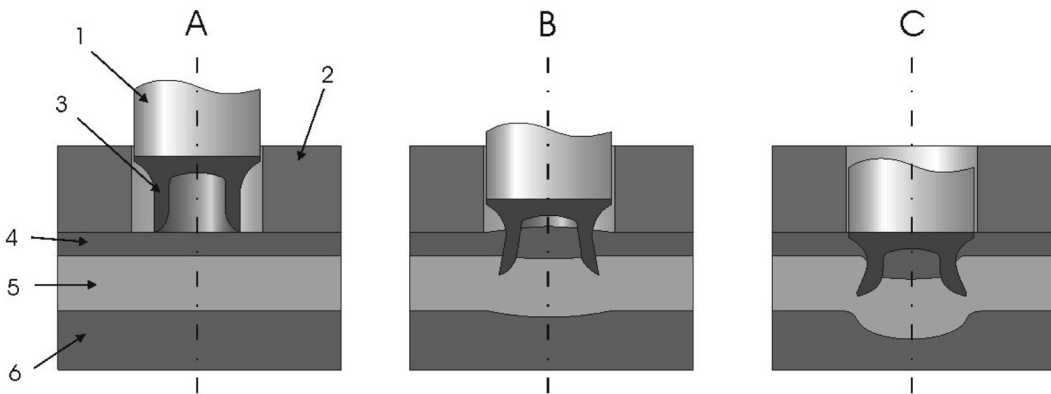


Fig. 14.4 Operational sequence of the hydro-self-piercing riveting process. Source: Ref 14.7

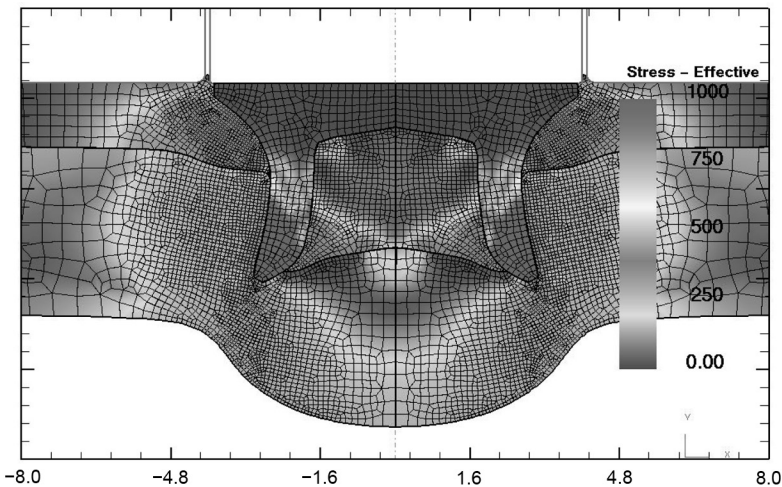


Fig. 14.5 Effective stress distributions at the end of the joining procedure. Source: Ref 14.7

The main difference between HSPR and SPR is that, due to the absence of a die, there exists a different stress condition in the upper sheet metal on the verge of the material separation. As a function of the fluid pressure, the yield stress, and the geometry of the rivet foot, compression stresses at the foot of the rivet are superposed in all directions. The damage value is much higher in the vicinity of the rivet shaft, as shown in Fig. 14.6.

Self-Piercing Riveting at Elevated Temperatures. The formability of some materials, such as magnesium alloys, increases considerably at elevated temperatures. The SPR process can be modified to meet the temperature requirements. For the forming of magnesium alloys, parts are locally heated to approximately 300 °C (570 °F) in the direct joining area by using induction or resistance heating (Ref 14.8).

Different materials can also be joined, including magnesium-carbon-reinforced plastic pairings, with the magnesium part positioned on the die side. For this process, the load-bearing capacity is found acceptable, particularly under shear stress. Only low characteristic load-bearing capacity values were achieved when the joint was subjected to peeling stress, because

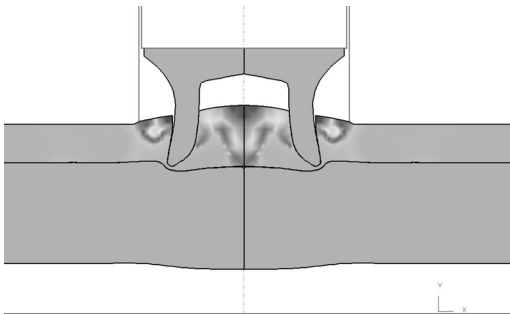


Fig. 14.6 Damage value distribution at the material separation. Source: Ref 14.7

premature joint failure occurred due to popping out as a result of the low diameter of the self-piercing rivet head (Ref 14.9).

14.2 Clinching

Clinching is also known as press joining. It is a process by which two or more sheets of material are stretched and deformed into a die that creates a button on one side of the sheets. This button forms a leakproof mechanical interlock between the sheets (Ref 14.10). The clinching process does not require preassembly steps such as drilling/punching of holes for fasteners or surface preparation for welding. Therefore, clinching is a very cost-effective process (Ref 14.1, 14.11). The tool design for clinching can be optimized by using finite-element analysis (Ref 14.6, 14.12).

Four steps in clinching with a fixed die are illustrated schematically in Fig. 14.7. Once the sheets have been positioned using the blank holder (view 1), the material below the punch is pushed through and compressed (view 2). The material, pressed outward radially, forms a button (undercut) between the sheets (view 3). In addition to this positive lock, at the same time, residual radial compressive stresses develop, creating a nonpositive lock (view 4).

Clinching is used extensively in the manufacturing of cars, household appliances, air conditioners, and other electronic and electrical products.

The advantages of clinching include (Ref 14.14):

- Low cost
- Can be used to connect sheet, profile, and die-cast parts
- Used up to sheet metal thickness of 4 mm (0.2 in.)

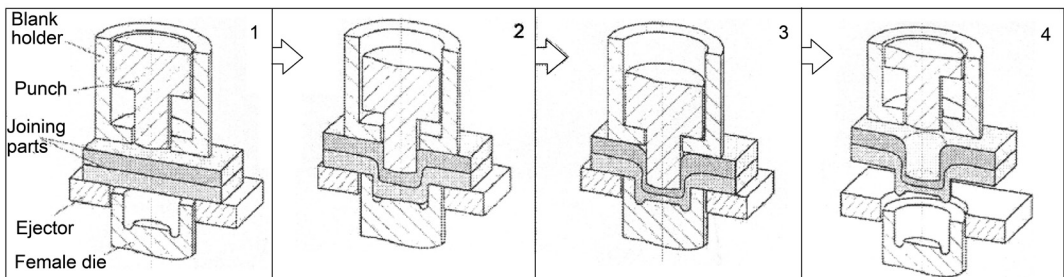


Fig. 14.7 Principle of the clinching process with a fixed die. Source: Ref 14.13

- Materials with high tensile strength, R_m up to 1000 MPa (145 ksi), can be joined
- Process can be monitored in real-time for quality control
- Can also join unweldable and dissimilar material combinations
- Increased fatigue life compared to spot-welded joints
- Automated process with low cycle time

The disadvantages of this process can be considered to be:

- Access is required to both sides of the joint.
- Joint appearance may be a concern for some applications.
- Lower static strength when compared to spot-welded steel
- Button formed by clinching may be undesirable
- Metals to be joined must be sufficiently ductile.

Currently there are several clinching techniques available from companies such as TOX Pressotechnik GmbH, BTM Corporation, and Eckold GmbH. These clinching processes are discussed briefly in the following sections. There are many clinching geometries available in practice. However, only axisymmetric joints are discussed, because they are most commonly used due to their ability to bear nominally equal loading in all directions with high maximum shearing loads (Ref 14.6).

TOX Pressotechnik GmbH (Ref 14.15). This clinching technique uses a simple punch geometry to press two sheet materials into a round die, which contains an anvil and outer ring groove. The process is shown in Fig. 14.8.

Once the sheets enter the die, they come in contact with the anvil. Upsetting occurs, forcing material to flow into the outer ring groove. Upon filling of the ring groove, further upsetting causes the punch-side material to spread outward within the die-side material. The final joint is a round button with no sharp edges or burrs. The load-carrying capability of the joint depends on the button diameter, sheet thickness, and the materials being joined.

BTM Corporation (Ref 14.16). The BTM Corporation has developed a clinching technology called Tog-L-Loc. This process uses a round punch, split die with anvil and moving blades, and an elastomeric ring. A schematic diagram describing the Tog-L-Loc clinching process is shown in Fig. 14.9.

The Tog-L-Loc process is completed in the following stages:

1. Pressure pad around the punch clamps the material (prevents upward extrusion of metal around punch)
2. Punch draws metal into the die and upsets the material against an anvil
3. Moving blades allow metal to flow outward during upsetting
4. Expanding diameter forms a circular lock, which is strong
5. Pressure pad allows for punch removal upon completion of the process

The die used for Tog-L-Loc clinching is shown in Fig. 14.10. The figure shows that the three moving blades, which are split and thus free to move independently, encompass the die anvil. An elastomeric ring is located around the moving blades. The elastomeric ring allows the blades to move outward while applying a re-

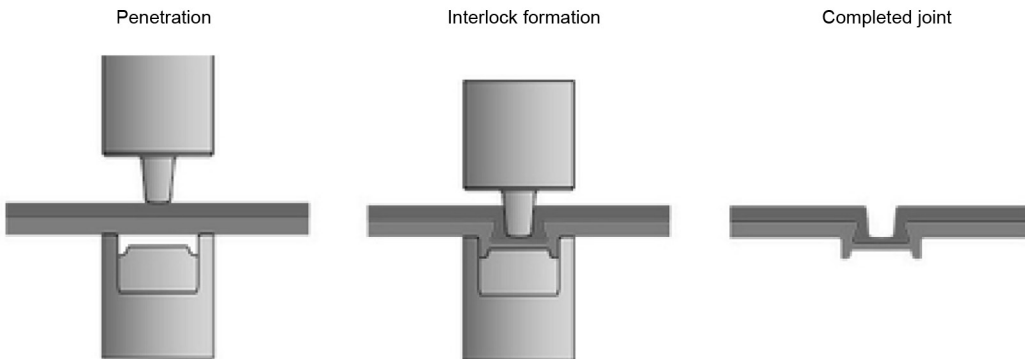


Fig. 14.8 Schematic illustration of TOX clinching method. Source: Ref 14.15

straining force, which causes the blades to pinch the sheet material.

The moving blades reduce the force required to form the joint because the material must overcome the restraining force applied by the elastomeric ring to flow outward.

Eckold GmbH Corporation (Ref 14.17). Eckold GmbH, based in St. Andreasburg, Ger-

many, also produces clinching equipment. Their process is similar to that of TOX Pressotechnik GmbH and BTM Corporation. Eckold GmbH uses a round punch and die with an anvil and flexible split ring. The split ring components are controlled by flexible blades, which act as springs to produce restraining force. The process is shown in Fig. 14.11. A punch forces the mate-

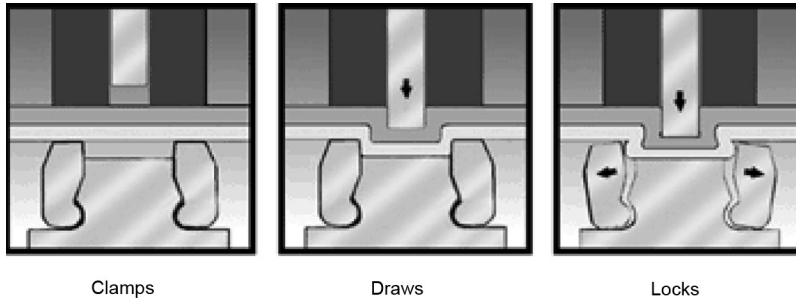


Fig. 14.9 Tog-L-Loc mechanical clinching. Source: Ref 14.16

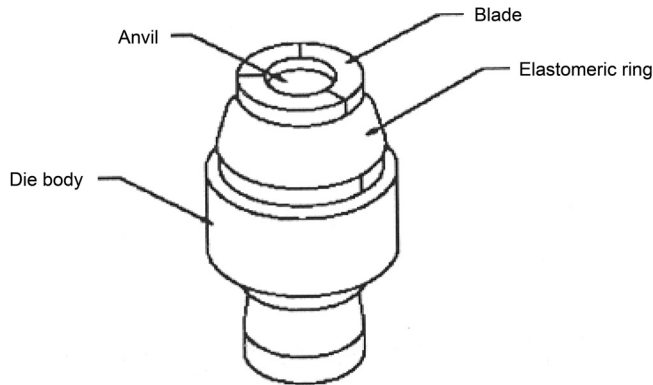


Fig. 14.10 Die used for Tog-L-Loc clinching. Source: Ref 14.16

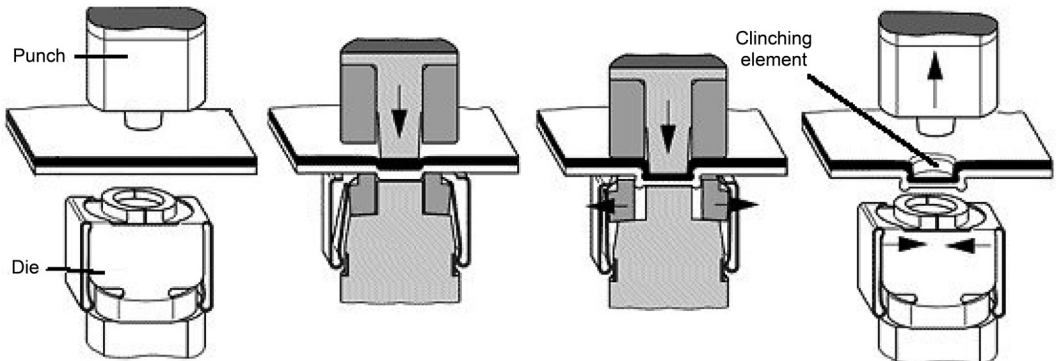


Fig. 14.11 Illustration of the mechanical clinching process. Source: Ref 14.17

rial into the die, where it is upset against an anvil. The split ring assembly allows the material to flow outward from the die.

14.3 Future Trends

In conventional joining by forming methods such as clinching or SPR, the contoured die must be positioned to the punch with high accuracy. A misalignment between punch and die would result in both decreasing strength of the formed connection and shortened tool life. The process reliability is affected in some cases by deposits in the die, by wear of the die, by joints getting stuck in the die at the end of the joining process, or even by partial damage at the rim of the die, which may go unnoticed by the process-monitoring system if it does not exceed a certain size. To improve this situation, two joining methods are introduced where a flat anvil re-

places the contoured die. These methods are referred to as dieless clinching and dieless rivet clinching (Ref 14.1, 14.5, 14.18).

Figure 14.12 shows the conventional clinching dies and a flat anvil for dieless clinching.

Dieless Joining. The principle of dieless joining by forming can be explained using the example of dieless clinching. As seen in Fig. 14.13, an upper part (1) will be joined with a bottom part (2). At the beginning of the joining process, these two parts to be joined (1, 2) are lying partially overlapped on the flat counter tool or anvil (3). For forming the connection, the clamp (5) and the punch (4) are moved toward the parts to be joined (1, 2). First, the clamp (5) contacts the upper part (1), and a limited pressure is applied on the parts without deforming them. Then, the punch is pressed into the parts with a high force. The material of the parts is displaced partially and flows in the opposite direction to the movement of the punch, thereby pushing the clamp

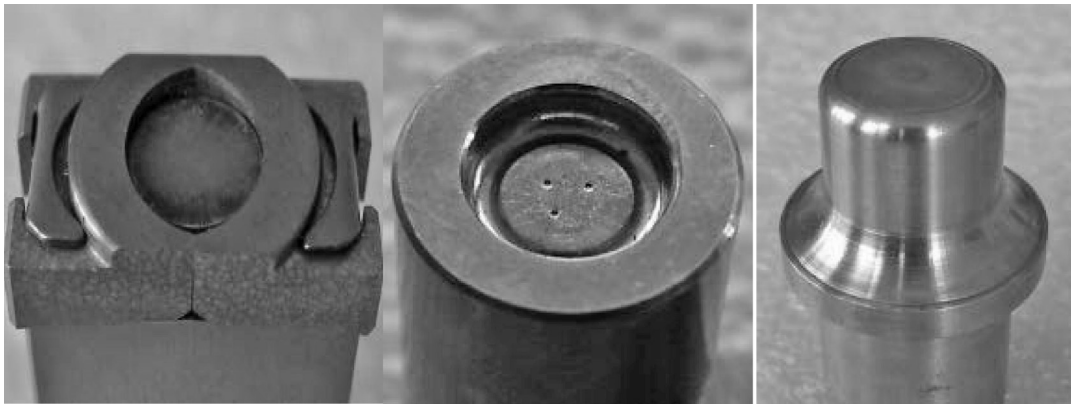


Fig. 14.12 Conventional clinching dies (left, middle) and flat anvil for dieless clinching (right). Source: Ref 14.5

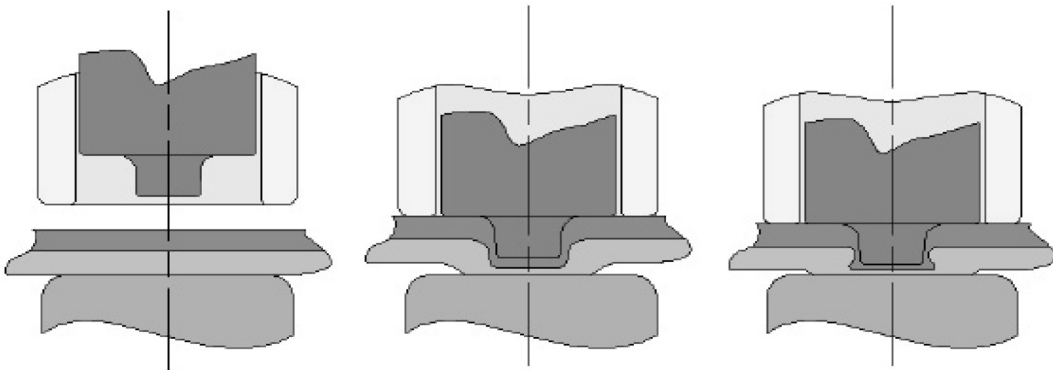


Fig. 14.13 Schematic diagram of dieless clinching. Source: Ref 14.5

upward. Thus, an elevation is formed on the downside of the bottom sheet, because it is important that the clamp pressure is sufficient to avoid warping of the parts but still allows for formation of the elevation. The size of this elevation increases further as the punch is pressed into the parts. As soon as the material of the upper part has come into contact with the shoulder of the punch, the material flow against the movement of the punch is stopped. When the punch is pressed even further into the parts, the elevation at the downside of the bottom part is flattened, and the material displaced by the punch is forced to flow in a radial direction, thus forming an interlock between the parts. The connection has been formed in a single step. The material volume that the punch displaces is directed entirely toward the formation of the elevation (Ref 14.5).

Dieless rivet clinching is based on the same principle as dieless clinching. However, instead of the punch in dieless clinching, which is pulled out of the connection after forming it, the rivet-clinched connection is formed with an auxiliary part. This part stays in the connection and thereby stabilizes it, thus substantially increasing the shear strength. The shape of the rivet and its deformation in the joining process can additionally support the formation of the interlock.

The advantages of dieless joining include:

- The flat countertool can be used for all joining tasks.
- Tool costs and set-up time are reduced, and defective joints caused by inaccurate joint geometries are eliminated.
- Low-cost equipment is used.
- Process reliability is increased, because this leads to no tool wear in the anvil.
- No slag deposits are formed in the cavities.
- Joining of brittle materials is easier.

Dieless Clinching at Elevated Temperatures (Ref 14.8). The process described previously can be used to mechanically join materials such as aluminum and steel under room-temperature conditions. On the other hand, mechanical joining of other materials, such as magnesium alloys, is restricted by the limited forming capability presented by these materials at room temperature, because in forming these alloys, cracks may form even at low levels of strain. The cause of this limitation comes from the material microstructure (e.g., the hexagonal lattice structure in the case of magnesium). However, the forming capability of magnesium alloys improves signifi-

cantly at higher temperatures. Therefore, it is possible to form joints without cracks by using joining methods such as clinching if the tooling is heated to temperatures up to 220 °C (430 °F) or more. This is achieved by transferring heat from the heated anvil to the components to be joined at the exact moment of clamping between the insulated part of the clamp and the heated anvil (Ref 14.19).

In this process, it is only the flat countertool that is heated through a heating cartridge with temperature control. Thanks to this system, it is not necessary to heat the clinching punch, even if both parts to be joined are made of magnesium. The required heating time depends on the magnesium alloy used, the thickness of the parts to join, and the temperature of the anvil. Some studies have shown that the heating time range varies from 3 to 6 s (Ref 14.8). In addition, any warping in the tool caused by heat does not have an impact on the quality of the joints, because there are only very slight demands made on the concentric alignment between the punch and the anvil in dieless clinching. In other words, the addition of a cooling system to prevent position discrepancies between the joining tools is not necessary.

A finite-element analysis tool has been used to conduct parametric studies on the geometry of the dieless clinching of magnesium. According to Ref 14.8, the process is sensitive to any change in the punch edge radius, which should not be larger than 0.1 mm (0.004 in.). If the radius is too large, the interlocking strength of the joint decreases. Another important parameter is the punch diameter; the larger this is, the larger the neck thickness. In contrast, punch diameters below 6 mm (0.2 in.) result in lower joint interlocking if the overall component thickness is below 3 mm (0.1 in.).

Hydroforming and Clinching. Figure 14.14 shows the operational sequence of hydroclinching. In this case, the fluid acts as a punch. The principle of this process is the same as that of HSPR (Ref 14.7) and is as follows:

1. The hydroformed sheet (4) and the part to be attached (3) are brought in contact with the hydroforming tool (2) and the fluid (5).
2. During calibration, the hydroformed sheet (4) is pressed through a hole in the part to be attached (3). The punch (1) is withdrawn to avoid bursting and to ensure a higher forming level at the produced bulge in the sheet.

- Subsequently, the punch is set toward the high-pressure fluid. Because the high-pressure fluid prevents back forming, the material that has been pressed through the hole spreads out and develops an interlock.

There is also the option of joining without active punch movement. Supported by the hole chamfering of the part to be attached (3), the interlock forms automatically when the bulge is pushed through the hole.

14.4 Fatigue Behavior of Clinched Joints

Experimental studies on the quality of clinched joints have been conducted (Ref 14.18). In these studies, two FePO₂ thin sheets (150 by 50 by 1 mm, or 6 by 2 by 0.04 in.) are joined by clinching. As seen in Fig. 14.15, the joints are located in a transversal and longitudinal manner to in-

vestigate the influence of load direction on the strength of such joints. The clinching process was conducted at the same conditions (i.e., same tools and pressing force equal to 40 kN, or 4.5 tons) for all joints.

Fatigue tests were conducted at different stress ratios (*R*), the ratio between the minimum stress and maximum stress, equal to 0.1, 0.3, and 0.7 at a frequency equal to 50 Hz, and run-out experiments defined at 2×10^7 cycles. As seen in Fig. 14.16, the stress-number of cycles curves were obtained for each indentation configuration (longitudinal and transverse). Carboni (Ref 14.18) observed that the joint configuration (longitudinal and transverse) does not have a significant influence on the fatigue behavior of clinched joints within the stress ratio *R* range of 0.1 and 0.3. This important finding proves an advantage of clinching over spot welding: the fatigue limit for clinched joints with *R* = 0.1 and *R* = 0.3 is very similar and equal to approximately 50% of the obtained ul-

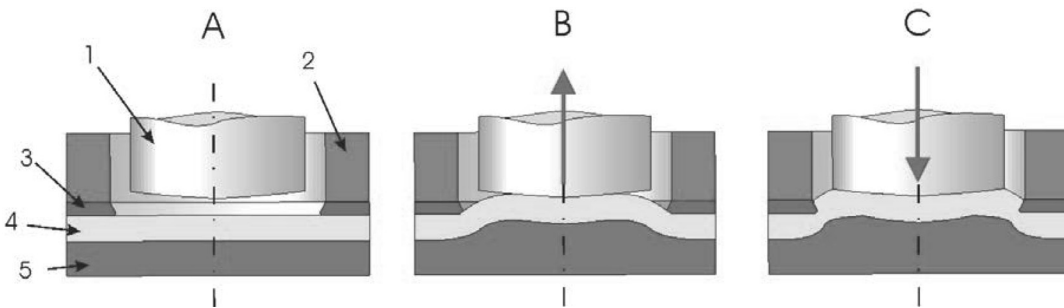


Fig. 14.14 Operational sequence of hydroclinching. Source: Ref 14.7

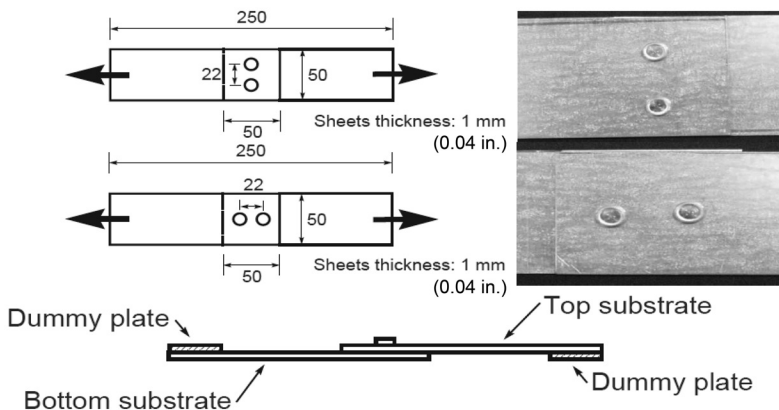


Fig. 14.15 Experimental tests on longitudinal and transverse clinching indentations. Source: Ref 14.18

timate stress; meanwhile, the spot welding typical fatigue limit is approximately 30 to 40%. The author also mentions that in the case of $R = 0.7$, the fatigue limit is quite different from the other considered R values (0.1 and 0.3), suggesting that for high mean stresses ($R = 0.7$), a complete change in failure mode occurs.

14.5 Crimping

Crimping is used to assemble tubular components. In an example application, a bullet or usually a cylindrical solid rod is assembled into a tubular part with a specific geometry called a casing. Thus, during crimping, the bullet is lowered into the casing to a predetermined depth, and then segmented crimpers/dies are pushed

into the casing by hydraulic or mechanical rams, forming the crimp (Fig. 14.17). The tube is deformed to fill a groove, which was machined on the solid cylinder. A very common application of the crimping process in manufacturing is in the field of electrical engineering for assembling composite insulators. These insulators consist of a glass-reinforced polymer rod with two metal end fittings, which are radially crimped onto it (Ref 14.20, 14.21).

Traditionally, the design of crimping operations has relied on experience and costly trial-and-error experiments. However, some studies (Ref 14.20, 14.21) discuss the application of the finite-element method to optimize the mechanical crimping process, to enhance the performance of the assembly by determining the optimum process and geometrical parameters.

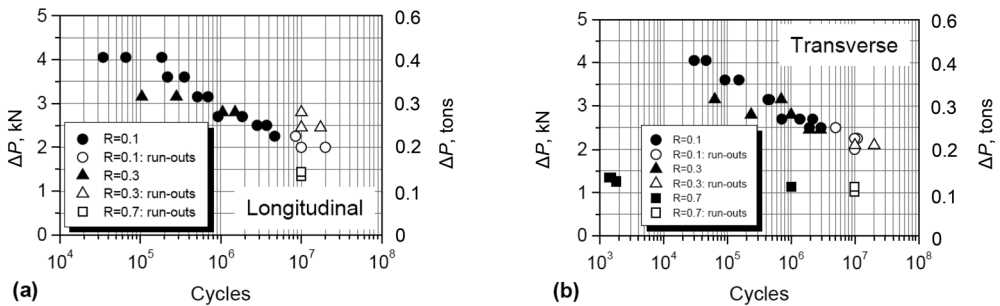


Fig. 14.16 Stress-number of cycles curves obtained by means of fatigue tests. Source: Ref 14.18

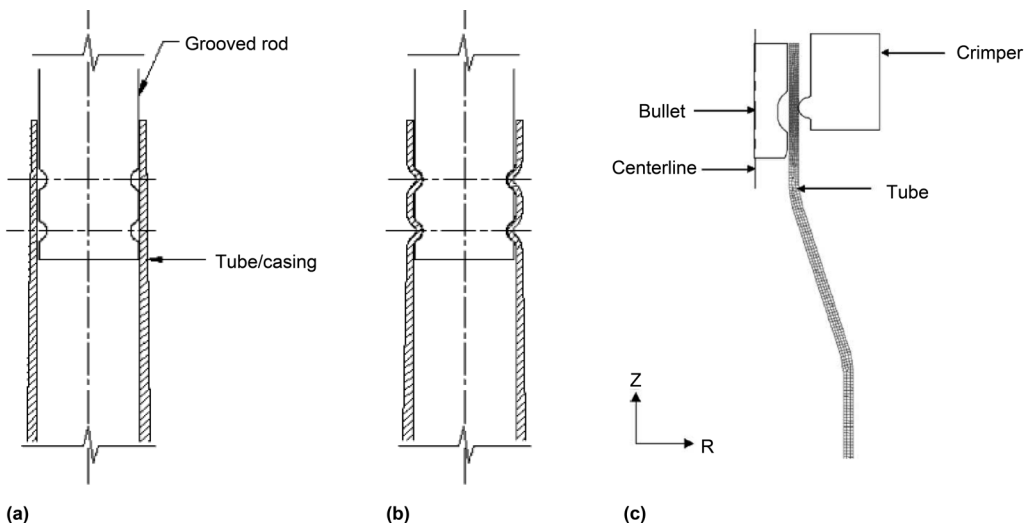


Fig. 14.17 Schematic diagram of crimping process. (a) Before crimping. (b) After crimping. (c) Finite-element model of crimping. Source: Ref 14.20, 14.21

The crimp quality, which is critical to the final performance of the assembly, is evaluated by a test that measures the force required to pull the rod from the tube, the so-called pullout test. A variation in the geometrical properties of the crimp will cause variations in the strength and quality of the assembly that must satisfy certain specifications. During the pullout test, the tube rarely ruptures. However, when it does, the damage is normally near the crimp. The quality of the crimping procedure can also be improved by the selection of an optimum alignment of tooling and the evaluation of different die designs (e.g., round-nosed crimpers, flat-nosed crimpers) through finite-element analysis.

REFERENCES

- 14.1 H. Tschaetsch, *Metal Forming Practice: Processes, Machines and Tools*, Springer-Verlag, 2006, p 250–260
- 14.2 X. He, I. Pearson, and K. Young, Self-Pierce Riveting for Sheet Materials: State of the Art, *J. Mater. Process. Technol.*, Vol 199, 2008, p 27–36
- 14.3 K. Mori, T. Kato, Y. Abe, and Y. Ravshanbek, Plastic Joining of Ultra High Strength Steel and Aluminum Alloy Sheets by Self Piercing Rivet, *CIRP Ann. Manuf. Technol.*, Vol 55 (No. 1), 2006, p 283–286
- 14.4 Böllhoff Rivnut Inc., www.bollhoff.com
- 14.5 R. Neugebauer, R. Mauermann, and S. Dietrich, Chances and Challenges in Joining by Forming with a Flat Counter Tool, *Adv. Mater. Res.*, Vol (6–8), 2005, p 203–208
- 14.6 P. Wenning, “Design and Analysis of a Mechanical Joining Process Using FEM,” M.S. thesis, The Ohio State University, Columbus, OH, 2003
- 14.7 R. Neugebauer, R. Mauermann, and R. Grutzner, Combination of Hydro Forming and Joining, *Steel Res. Int.*, Vol 76 (No. 12), 2005, p 939–944
- 14.8 R. Neugebauer, C. Kraus, and S. Dietrich, Advances in Mechanical Joining of Magnesium, *CIRP Ann. Manuf. Technol.*, Vol 57, 2008, p 283–286
- 14.9 H. Friedrich and B. Mordike, *Magnesium Technology—Metallurgy, Design Data, Applications*, Springer, Germany, 2006
- 14.10 J. Varis, Ensuring the Integrity in Clinching Process, *J. Mater. Process. Technol.*, Vol 174, 2006, p 277–285
- 14.11 C. Lee, J. Kim, S. Lee, D. Ko, and B. Kim, Design of Mechanical Clinching Tools for Joining of Aluminium Alloy Sheets, *Mater. Des.*, Vol 31, 2010, p 1854–1861
- 14.12 ERC/NSM, Clinching for Assembly: Process Simulation Case Study—R&D Update, *Stamp. J.*, March/April 2003
- 14.13 W. Voelkner, F. Jesche, and L. Lachmann, Joining by Forming—Newer Developments, *J. Technol. Plastic.*, Vol 14, 2002
- 14.14 W. Voelkner, Present and Future Developments of Metal Forming—Selected Examples, *J. Mater. Process. Technol.*, Vol 106, 2000, p 239
- 14.15 TOX Pressotechnik GmbH, <http://www.tox-us.com>
- 14.16 BTM Corporation, <http://www.btmcorp.com>
- 14.17 Eckold GmbH, <http://www.eckold.de>
- 14.18 M. Carboni, S. Beretta, and M. Monno, “Fatigue Behavior of Clinched Joints,” 15th European Conference of Fracture (Stockholm, Sweden), 2004
- 14.19 B.A. Behrens and S. Huebner, Heated Clinching of Magnesium Sheet Metal, *Prod. Eng.*, Vol X11 (No. 1), 2005, p 59
- 14.20 M. Shirgaokar, G. Ngaile, T. Altan, J. Yu, J. Balconi, R. Rentfrow, and W. Worrell, Hydraulic Crimping: Application to the Assembly of Tubular Components, *J. Mater. Process. Technol.*, Vol 146, 2004, p 44–51
- 14.21 M. Shirgaokar, C. Hyunjoong, G. Ngaile, T. Altan, J. Yu, J. Balconi, R. Rentfrow, and W. Worrell, Optimization of Mechanical Crimping to Assemble Tubular Components, *J. Mater. Process. Technol.*, Vol 146, 2004, p 35–43

CHAPTER 15

Sensors for Sheet Metal Forming

Deepak Ravindran and Yu-Chih Su, The Ohio State University

IN SHEET METAL FORMING, the quality of formed parts is affected by variables such as sheet material, die material and surface, lubrication, and press characteristics. Therefore, monitoring these variables and controlling their effects to produce high-quality products is critical and essential. The purpose of using sensor technologies is to improve the sheet metal forming process by increasing tool and machine uptimes, reducing setup and downtimes, and reducing scrap. For example, a failure in the tool is usually detected in the form of defects on the workpiece after many defective parts are produced. This could lead to an increase in scrap, especially in a large production-rate process. Identifying and rectifying the problem consumes time and hence disrupts production; furthermore, the corrected tool may not be guaranteed to produce the same part quality as before (Ref 15.1). Identifying possible failure modes and their frequency of occurrence proactively can eliminate the aforementioned problems. Thus, with increasing emphasis on quality, cost, and lead time, the use of sensors gained critical importance.

Some of the advantages of using sensors are (Ref 15.2):

- Improved part quality due to better monitoring and correction of faults and errors
- Protection of expensive and complex multi-stage tools against breakage and subsequent damage
- Protection of machine overload
- Detection and prevention of errors due to errors in part feeding
- Longer production without the need for manual supervision
- Reduced downtime due to proactive identification and correction of process disturbances

- When sensors are coupled with control systems, automatic control of the processes and tools reduces the need for manual labor.

15.1 Measurement of Forces

Just as a speedometer provides important information for operating a vehicle, a force sensor provides important information for operating a press by measuring the press loads (Ref 15.3). Force sensors are also referred to as tonnage monitors. Typically, they output the load values as a function of slide displacement, time, or crank angles (in the case of mechanical presses). This information is also called force or tonnage signatures. Several different types of monitoring systems are available. The sensor may be used to display the peak force during each cycle and may be connected to an alarm that gives a signal when this peak force exceeds the preset limit. In other cases, the complete force signature is monitored and displayed, providing additional information to the operator. Force sensors can help to achieve the following objectives (Ref 15.2):

- Protection of machine from overload
- Monitoring of tool wear
- Detection of changes in stock thickness and hardness
- Detection of changes in part lubrication
- Detection of parts that may be stuck in the die
- Detection of misfeeds

Load cells and piezoelectric force sensors are the most commonly used force-monitoring devices.

Load Cells. A load cell is a force transducer that converts force into an electric signal. Although there are different types of load cells, strain-gage-based load cells (Fig. 15.1) are the most commonly used type. Strain gages are made up of a long, thin strip of conductive material arranged in a zigzag manner (Fig. 15.2). Load cells typically contain multiple strain gages aligned and wired in a Wheatstone bridge circuit (Fig. 15.3). When stress is applied to a strain gage, the resistance of the strain gage changes and unbalances the Wheatstone bridge,



Fig. 15.1 Strain gage load cell. Source: Ref 15.4

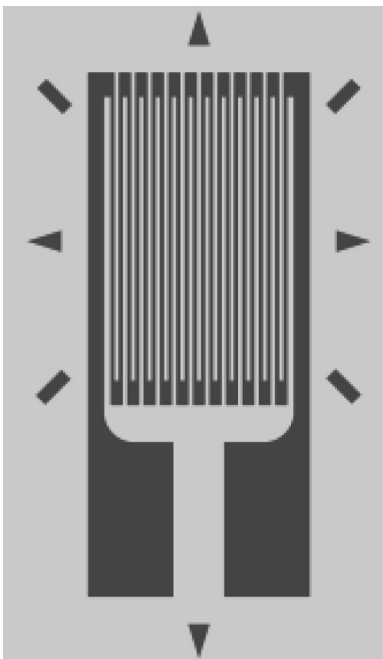


Fig. 15.2 Schematic of a strain gage. Source: Ref 15.5

resulting in a signal output (voltage) that is proportional to the stress.

Load cells usually come in a variety of different shapes and designs, such as columns, beams, and rings, with strain gages bonded onto them. The size, type of force measured (tensile, compressive, bending, shear), and cost are some of the factors that determine the type of the load cell to be used. Load cells typically work under compressive load conditions but are also used to measure tensile, bending, and shear forces. Apart from strain gage (electrical)-based load cells, there are also hydraulic and pneumatic load cells. Here, the force is measured by the variation of pressure of the fluid inside a diaphragm chamber. Thus, load cells can be classified based on their output signal (electrical, pneumatic, or hydraulic), on the type of force they detect (tensile, compressive, bending, or shear), or on their design (beam, column, ring, etc.). Calibration of load cells is done using standard calibration load cells that are known to provide accurate readings. These standard calibration load cells are placed on the press and load is applied. The readouts from the standard calibration cell are then compared with that of the load cell used in production conditions.

Piezoelectric force sensors operate on the principle of the piezoelectric effect. Materials such as quartz, lithium sulfate, and zirconate titanate exhibit this effect, which results in an output voltage when these materials are elastically deformed. The deflection in the material is proportional to the load applied, and thus, the electrical output generated is proportional to the load as well. The primary advantage of piezoelectric sensors is their high sensitivity and their ability to measure dynamic forces, because they have a very rapid response time (Ref 15.7).

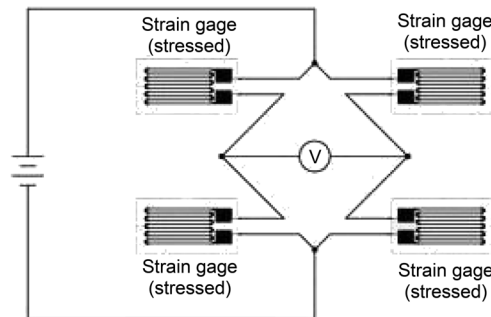


Fig. 15.3 Strain gages aligned in a Wheatstone bridge circuit. Source: Ref 15.6

Installation of Force Sensors. The force sensors, placed at different locations on the press, give different readings of loads. The greater the distance of the sensor from the process, the greater the noise in the signal. Therefore, the location of the sensor is crucial for its effective application. Typically, force sensors are placed in the press frame, the connecting rods, the slide, or directly in the tool, as shown in Fig. 15.4.

Frame Mounting. Placing force sensors in press frames is the most commonly used method. Furthermore, because they are easy to install and have a relatively longer life, frame-mounted sensors do not need to be replaced every time a new tool is used. These sensors measure the strain induced on the press frames caused by the forming loads. The presses are designed such that the frame deflection is relatively small. Therefore, a frame-mounted sensor cannot detect minor changes in load within the process. They are used primarily for protection from press overloads. Figure 15.5 shows the location of sensors in straight-side and C-frame presses. Typically,

one force sensor is installed in the middle of each press column for straight-side presses. For C-frame presses (gap presses and open back inclinable), two force sensors are usually used. One is mounted on the front side of the C-frame for measuring the tensile forces. The other is installed on the back side of the C-frame for measuring the compression forces (Ref 15.3, 15.9).

In-Die Mounting. Mounting force sensors directly in the dies provides accurate force signals. In this case, the sensors are usually mounted in the upper or lower tool. They provide more detailed information about the process than frame-mounted sensors. For example, in-die force sensors can detect improper positioning of tools within the press. Figure 15.6 shows a comparison of the force-versus-time readings between a proper tool setup and a tighter tool setup (both readings were taken with the sensor mounted on the tool). In the tighter tool setup, the position of the upper tool is 0.6 mm (0.02 in.) lower than the actual setup. This causes unnecessary high forces toward the lower dead center, which is

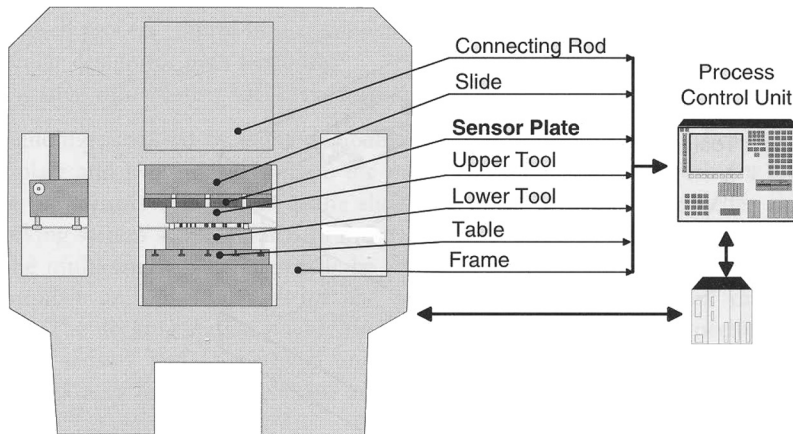


Fig. 15.4 Possible force sensor locations in a sheet metal forming press. Source: Ref 15.2

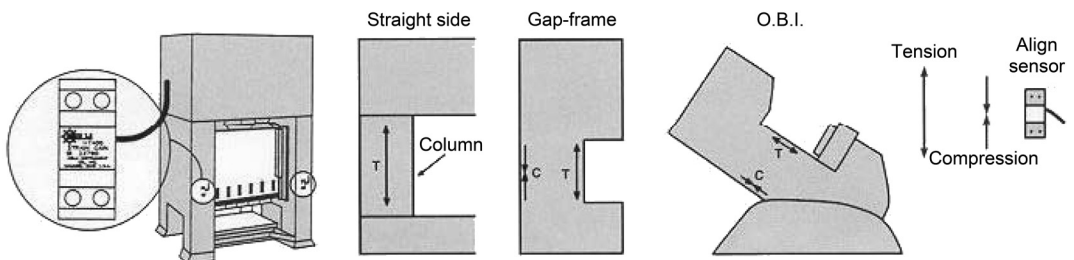


Fig. 15.5 Frame mounting locations for force sensors. O.B.I., open back inclinable. Source: Ref 15.8

detected through the significant second peak from the output of the tighter tool setup (Ref 15.2).

Die Plug Installation. Another method for measuring forming forces is to install force sensors into dies in the form of a die plug sensor (Ref 15.10). This sensor uses either piezoelectric or strain gage sensing elements at the end of a tube with cables running through the middle (Fig. 15.7). This method provides an easy and convenient way to mount the sensor. First, a hole is machined into the die or the tool holder, and the sensor is glued in place with high-strength epoxy applied inside the tube. The epoxy holds the sensor in place and fills in the hole, creating a solid mounting for the sensor (Ref 15.8).

15.2 Displacement Sensors

The primary purpose of displacement sensors is die protection, that is, to avoid die crash.

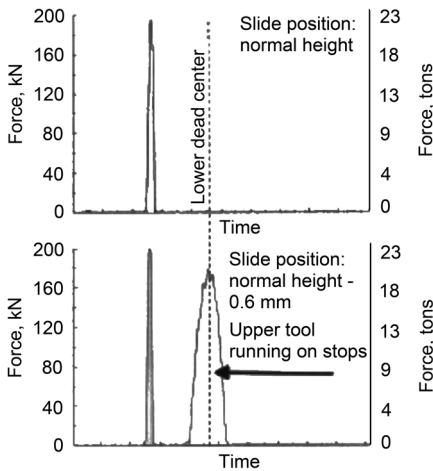


Fig. 15.6 Force signals obtained from a normal and an incorrect tool setup. Source: Ref 15.2

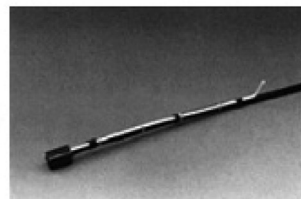
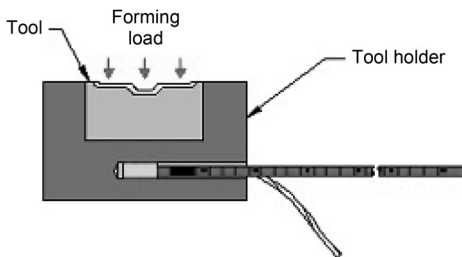


Fig. 15.7 Die plug sensor. Source: Ref 15.8

crashes may occur due to material misfeed and improper part or slug ejection. Proximity sensors, photoelectric sensors, and ultrasonic sensors are the most commonly used sensors for detection of objects, and a linear variable differential transformer is the most commonly used sensor for measuring displacement.

Linear variable differential transformers (LVDTs) are electromechanical transducers that convert the straight-line motion of an object into an electrical signal. The LVDTs are usually tubular in shape. The inside of the tube has a primary winding in the center, surrounded by a pair of secondary windings spaced symmetrically on either side (Fig. 15.8). The primary and secondary windings form the stationary component of the transformer. The moving member of the transformer is called the core and is made of magnetically permeable material. This core is free to move axially inside the transformer. The primary winding is energized by an alternating current. The magnetic flux resulting from this alternating current is coupled by the core to the secondary windings. Initially, when the core is positioned symmetrically with respect to the secondary windings, the voltage generated at the two secondary windings is the same. Thus, the differential voltage between the two secondary windings is zero. If the core is moved closer to one of the two secondary windings, the voltage generated in that coil is larger than that developed in the other coil, resulting in a differential voltage. The closer the core gets to one coil, the greater the voltage in that coil, and the greater the differential voltage. This difference in voltage gives a measure of the distance traversed by the core and, in turn, by the object to which it is coupled (Ref 15.11).

The LVDTs are commonly installed on the press slide to measure the displacement of the slide during each stroke. They are also used for monitoring and controlling slide parallelism, avoiding ram misalignment, and for adjusting

and verifying the shut height. In automated feed mechanisms, LVDTs can be used to provide the position feedback of the servo-motor-driven feed for automatic control (Ref 15.11, 15.12).

Proximity sensors are used for die protection due to their low cost and compact size. There are three basic types: inductive, capacitive, and magnetic. Inductive proximity sensors are most commonly used and consist of a coil through which a current is applied (Ref 15.13) (Fig. 15.9). As a result of this current, an electromagnetic field is generated around the coil. When a magnetic object (metal) enters the vicinity of the sensor, eddy currents build up in the object. This reduces the strength of the sensor's own current. When, the reduction in the sensor's own oscillation field reaches a certain

level, an output circuitry triggers an output indicating the presence of the object (Ref 15.15). Because the sensors do not come into physical contact with the target, there is no problem of wear (Ref 15.13).

Proximity sensors do not have any moving parts. Additionally, they are not easily affected by oils, coolants, or other liquids. They can be integrated into the dies in many different styles and shapes, such as rectangular, low profile, and ring (Ref 15.1). For example, as shown in Fig. 15.10, a flatpack sensor can be used for monitoring slug ejection (Ref 15.16). Proximity sensors can also be used to check material feed progression and part ejection in progressive dies.

Photoelectric sensors are used when a larger sensing range is needed. This sensor works by sending a beam of light from a transmitter to a receiver. The part being sensed interrupts this beam, which triggers a signal. Photoelectric sensors consist of four main components: light source, light detector, lenses, and output switching device. The light source or transmitter is a light-emitting diode (LED) that emits light when a current is applied. These LEDs are made to emit a specific wavelength or color of light. Infrared, visible red, green, and blue LEDs are used as the light source (emitter). The light detectors or receivers are usually photodiodes or phototransistors that are solid-state devices that undergo a change in conducting current based on the amount of light detected. Because LEDs emit light over a wide area, and photodetectors can detect light over a wide area, lenses are used to narrow down the emitting and sensing areas (Ref 15.17).

Opposed-mode photoelectric sensors are also referred to as through-beam or transmitted beam

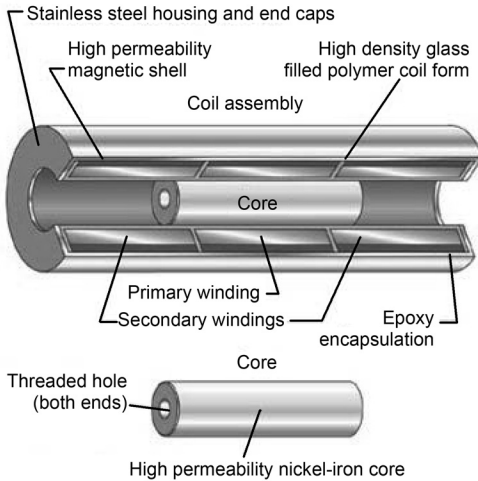


Fig. 15.8 Schematic design of linear variable differential transformer. Source: Ref 15.11

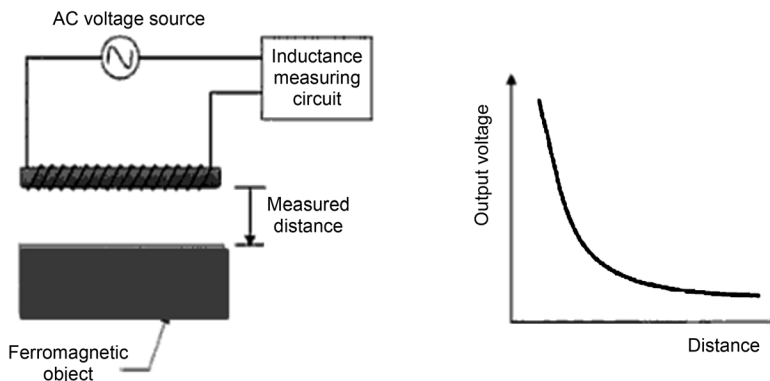


Fig. 15.9 Working principle of an inductive proximity sensor. AC, alternating current. Source: Ref 15.14

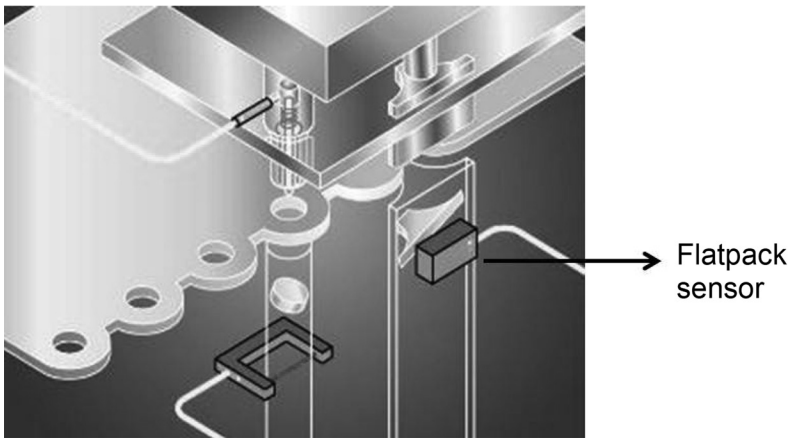


Fig. 15.10 Flatpack proximity sensor used for slug ejection. Source: Ref 15.16

sensors. In this mode, the light source and receiver are contained in separate housings. These two units are positioned opposite each other so that the light from the light source shines directly on the receiver (Fig. 15.11). If an object is present between the two, it blocks the beam (Ref 15.17). The biggest advantage of these sensors is that they have very long sensing distances. However, the presence of two separate housings requires the transmitter and receiver to be wired separately, which may lead to installation difficulties (Ref 15.13).

Direct Reflective Photoelectric Sensors. In direct reflective, or retroreflective or reflex, sensors, both the transmitter and receiver are contained in a single housing. The light beam emitted by the transmitter reflects off the part to be sensed and then is detected by the receiver (Fig. 15.12). These sensors will not work when they are too close to a background, because the sensor may mistakenly detect the background and provide a false reading. For this sensor to function properly, the part being detected must be reflective by nature, because the intensity of the reflected beam is what is used to detect the presence of the object (Ref 15.13).

Optical Convergent Photoelectric Sensors. Optical convergent or diffuse sensors help detect an object near a background without detecting the background. Unlike the aforementioned two methods where the intensity of the beam is used to detect the object, optical convergent sensors use the triangulation method to sense an object. Here, the angle, and not the intensity, of the incoming light determines the presence of an object (Fig. 15.13). The receiver consists of a photosensitive strip instead of a simple photo-

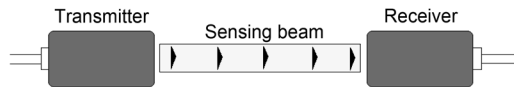


Fig. 15.11 Principle of operation of opposed-mode photoelectric sensor

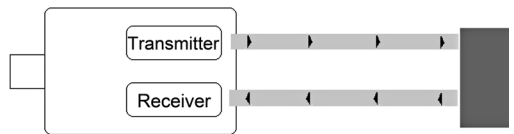


Fig. 15.12 Principle of operation of direct reflective photoelectric sensors

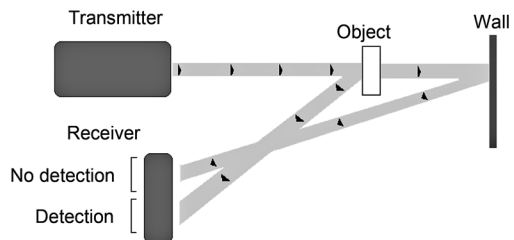


Fig. 15.13 Principle of operation of optical convergent photoelectric sensors

detector. The sensor is actuated only when the light strikes on a particular place on the strip. For the light to strike this particular place, it must be at a certain angle to the strip. The sensor is positioned in such a way that when the object is present, it reflects the light onto the detecting region of the receiver. Because detection of the object is based on geometry rather

than reflectivity, even a nonreflective object placed near a reflective background can be detected accurately (Ref 15.13).

Like proximity sensors, photoelectric sensors do not have any moving parts. Their primary advantage is the fact that they offer much longer sensing ranges than the proximity sensors. However, they are very likely to fail in dirty environments, that is, when they come in contact with oil, dust, or other materials that may block the light. The most common use for photoelectric sensors is to monitor part ejection (Fig. 15.14), slug ejection, and for monitoring strip feed (Ref 15.1).

Ultrasonic sensors operate by emitting and receiving high-frequency sound waves. The frequency is usually on the order of 200 kHz, which is beyond the audible range of the human ear. When an object to be detected comes into the path of the ultrasonic signal, the pulses are either reflected or echoed back from the target to the sensor (Ref 15.17). The sensor determines the distance of the object from the sensor by measuring the length of time for this echo to return.

The sensing distance for operation depends on the target material, shape, size, position, and temperature. The ideal target is a smooth, flat surface. Rounded or uneven objects can also be detected, but the sensing distance may be reduced. To obtain the best performance, the sensor should be aligned such that the sensor face is parallel to the target surface (Ref 15.17).

15.3 Detection of Tool Breakage and Flaws in Parts

Acoustic emission sensors are used to detect disturbances or failures, that is, tool break-

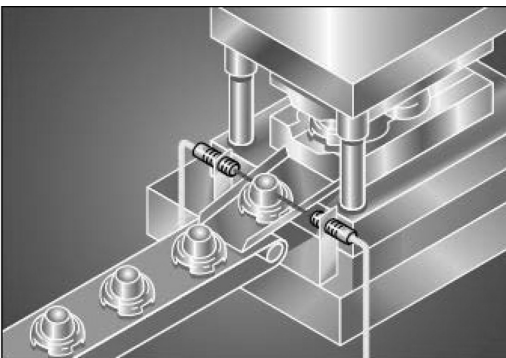


Fig. 15.14 Example application of a photosensor for monitoring part ejection. Source: Ref 15.16

age and cracks in parts, during the forming process. When a crack is generated in the workpiece or tool during forming, stress waves are produced from this crack that travel throughout the workpiece or tool, similar to an earthquake that propagates from an epicenter (Ref 15.18). These stress waves are accompanied by an acoustic emission. The acoustic emission excites a piezoelectric transducer that produces an output voltage, thereby indicating a crack in the workpiece or breakage in the tool (Fig. 15.15).

When locating an acoustic emission sensor, it is very important that mechanical disturbances such as vibrations are avoided. A greater distance between the source and the sensor will increase noise signals. The gap between the forming process and the sensor will also filter (reduce) the strength of the acoustic emission. Therefore, an acoustic emission sensor must be placed as close as possible to the process (Ref 15.2). Typical locations are upper or lower tool or as close as possible to the tool, such as the slide and bolster plate. Owing to their more significant responses to tool breakage or overload events than force signals, acoustic emission sensors are recommended for detecting tool breakages. Figure 15.16 shows the signals of force and acoustic emission, respectively, under normal and punch breakage conditions. It is shown that when the punch breaks, there is only a slight change in the force signal. However, in the case of acoustic emission sensors, a significant second peak in the acoustic emission signals is observed, which indicates tool breakage. Acoustic emission sensors can also be used to detect changes in friction properties, lubrication conditions, stick-slip phenomenon, and galling (Ref 15.20).

Ultrasonic Sensors. Ultrasonic inspection is a method in which high-frequency sound waves are introduced into workpiece materials to detect surface or subsurface flaws. The sensor typically consists of an ultrasonic transducer that serves as both a pulsar (emitter) and a re-

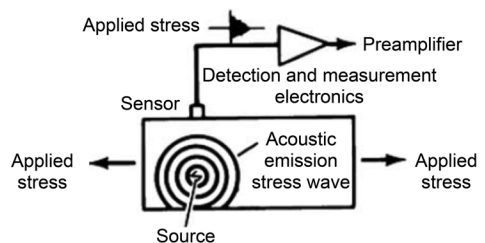


Fig. 15.15 Principle of acoustic emission sensor. Source: Ref 15.19

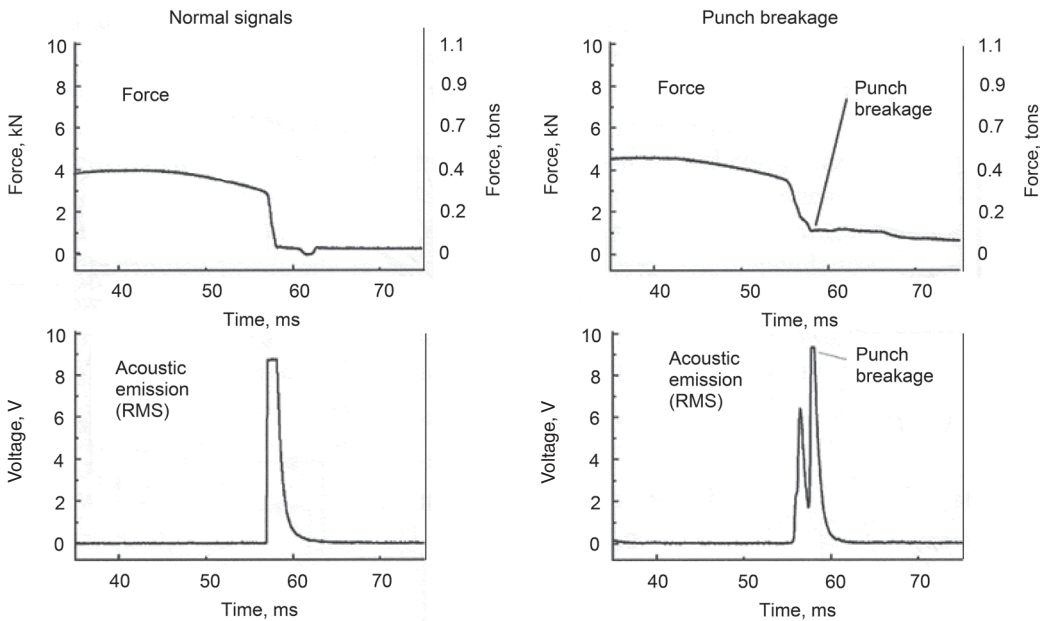


Fig. 15.16 Force and acoustic emission signals for a breaking punch. Source: Ref 15.2

ceiver. This ultrasonic transducer can convert electrical energy into high-frequency sound energy or vice versa. The ultrasonic transducer generates sound waves that travel through the workpiece. Sound waves travel through a medium (solid, liquid, or gas) at a specific speed in a predictable direction. When these sound waves enter a boundary with a different medium, some of the sound waves are reflected back (Ref 15.21). Using standard tests, the standard reference attenuation and echo response for a “good” part can be found. When a flaw such as a crack is present in the workpiece, the sound waves are reflected and scattered, and the attenuation in sound energy is different from the standard reference attenuation of a flawless part. Thus, the attenuation in the echo detected by the ultrasonic transducer can be used to determine the presence of discontinuities in the workpiece. The time-of-flight between the initial pulse to the reception of the echo produced by the flaw can be used to detect the depth at which the flaw is located (Ref 15.19). The same principle can also be used to detect the thickness of the part.

Eddy current sensors consist of an electric coil carrying an alternating current. When a part to be inspected is brought near this coil, the alternating current in the coil causes eddy currents to flow in the metallic part as a result of electromagnetic induction. These eddy currents

flow in closed loops within the part with a certain amplitude and phase. The flow of eddy currents in the part depends on the electrical characteristics of the part, the presence or absence of flaws or discontinuities in the part, and the total electromagnetic field within the part (Ref 15.19). Flaws such as cracks can be detected by the change in flow of eddy currents in the part (Ref 15.19).

15.4 Measurement of Material Flow during Forming

By measuring certain material flow parameters, such as the displacement of the workpiece material, velocity of its movement, draw-in, and the detection of wrinkles, the progress of the forming process can be verified and controlled. By comparing these measurements for the current process with standard reference measurements obtained for an ideal process, any deviations in the progress of the forming process can be identified and controlled (Ref 15.22).

Two different types of sensors were developed for laboratory research purposes (yet to be used on the shop floor) for the detection and measurement of direction, displacement, and velocity of material flow, namely, roller ball sensors and contactless optical sensors.

Roller Ball Sensor. The roller ball sensor is a contact-type sensor that measures the material flow through a ball contacting over the material surface. When the material moves, the movement drives the ball. Then, the relative motions of the ball with respect to the metal surface are detected and recorded, similar to the principle of a computer mouse. Thus, the direction, distance, and velocity of material movement can be detected (Ref 15.22). The principles and operations of these sensors are shown in Fig. 15.17.

Contactless Optical Sensor. A contactless optical sensor for material flow measurement was developed by the Institute for Metal Forming and Metal Forming Machine Tools (IFUM) at the University of Hannover. The sensor consists of two LEDs and a lens and works on the principle of image processing. The sheet is illuminated by the LEDs, and the image is detected by a metal oxide semiconductor chip. The changes in the topography of the sheet are sensed and observed over a series of recorded images to measure the movement of the sheet. The sensor can record up to 1500 images/second. The movement of the sheet is detected over two orthogonal directions (Ref 15.22).

Draw-In Sensor. Measurement of the draw-in in deep drawing provides useful information about the progress of the deep drawing process and on part quality. The displacement of the workpiece edge from its initial position when placed in the tools to its current location at any time during the forming process is called draw-in or flange insertion. An LVDT-based draw-in sensor is the most common type of draw-in sen-

sor currently used in research and in various laboratories for detecting wrinkles and failure (Fig. 15.18) (Ref 15.2).

Wrinkle Sensor. The sensor consists of two separate position sensors, one placed in the die and the other placed in the blank holder (Fig. 15.19). The system measures the distance between the two sensors. Thus, when wrinkles occur, the distance between the two sensors increases, and this is detected by the sensors.

15.5 Machine Vision Systems

Machine vision systems are used for automated quality-control purposes. They provide geometrical information about the entire part. They work by acquiring an image of the part to be tested; processing this image to check for quality, irregularities, or sometimes even to evaluate material properties; and then output these results (Fig. 15.20). They also provide the strain distribution on the parts, thinning, and information for forming limit diagrams (Ref 15.24). All machine vision systems can be considered to be operating in three stages:

- Image acquisition
- Image processing and analysis
- Interpretation

In the image acquisition stage, the part to be processed is illuminated by a lighting system that projects a fringe pattern on the part to be inspected, and then an image of this illuminated part is captured using cameras. Alternatively, in systems such as ARGUS, a three-dimensional

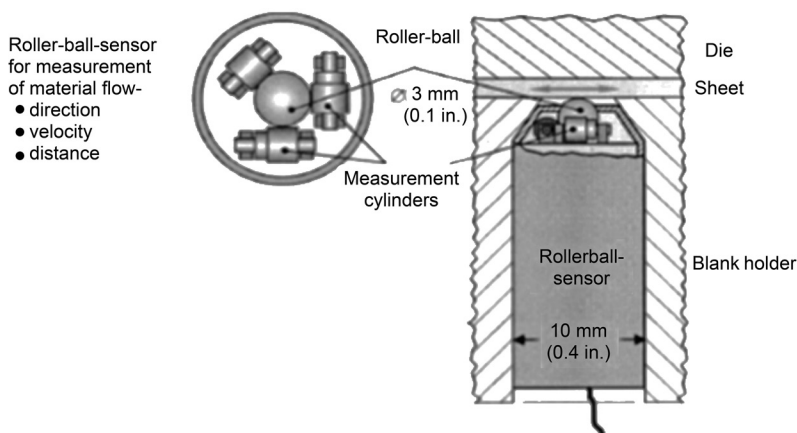


Fig. 15.17 Principles and operation of a prototype roller ball sensor. Source: Ref 15.22

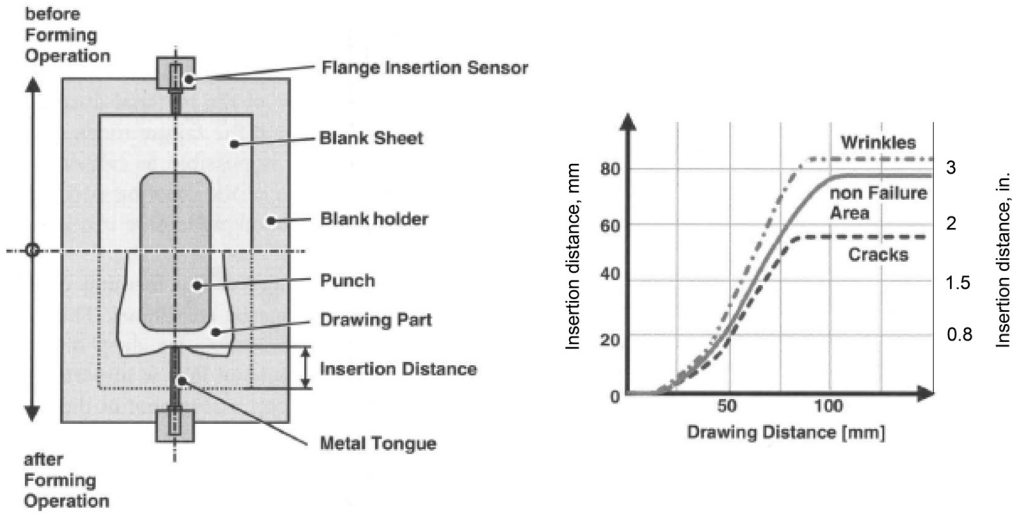


Fig. 15.18 Flange insertion or draw-in sensor to measure draw-in in deep drawing tool. Source: Ref 15.2

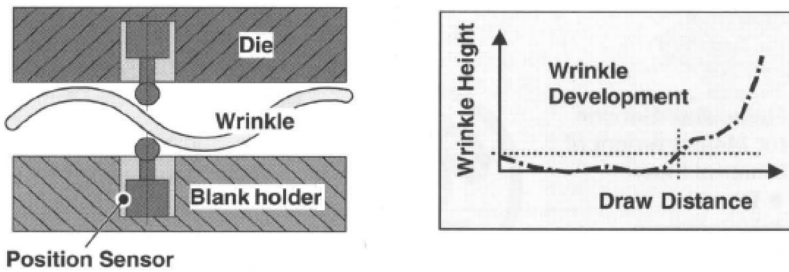


Fig. 15.19 Wrinkle-detection sensor. Source: Ref 15.2

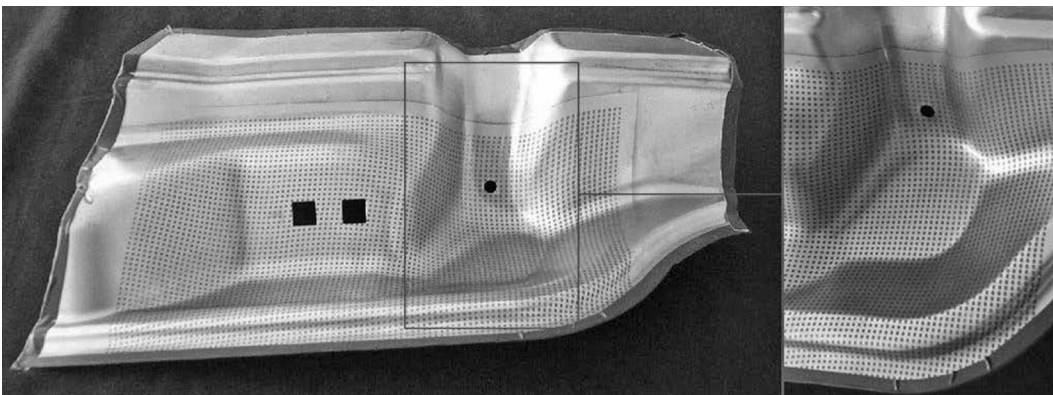


Fig. 15.20 Sheet metal part with a grid of dots after forming. Source: Ref 15.23

(3-D) optical measuring system developed by GOM GmbH, instead of using a fringe pattern, the sheet metal is marked with a grid of dots, either through chemical etching or laser marking, and then formed (Fig. 15.20). Images of the

formed part are then taken using cameras for processing (Ref 15.23). Charge-coupled device and charge-injection device cameras are the most commonly used type of cameras. For a complete 3-D image of the part, several images

must be taken from different angles and then combined.

In the image processing stage, the coordinates of the various points of the image with a fringe pattern, or the coordinates of the dots in the case of the ARGUS system, are automatically calculated by software, and a 3-D geometry of the part is obtained. For transforming the coordinates of the points into a global coordinate system, reference points are used on the sheet metal. The calculated 3-D points form the geometry of the part, which is then used for quality-control purposes.

Finally, the results of the image analysis are presented to the user on a screen, or, in cases where automatic control is enabled, the system makes a decision and triggers an actuation mechanism such as removing defective parts from the good ones. The primary advantages of a machine vision system are its high accuracy, fast measuring process, and capability to compare the 3-D parts with computer-aided design or numerical simulation data (Ref 15.24). Its biggest disadvantage is that it is expensive to set up.

15.6 Online Material Property Evaluation

In sheet metal forming, mechanical properties have significant influence on part quality, because material formability is determined by its mechanical properties, such as yield stress, tensile strength, uniform elongation, elongation at fracture, hardness, and so on (Ref 15.25). However, these properties usually vary from coil to coil; therefore, to maintain part quality, it may be necessary to monitor the mechanical properties of the incoming sheet metal. Conventionally, material formability is determined through destructive methods, such as tensile test and bulge test. Nondestructive methods, such as eddy current testing, avoid this problem. Furthermore, these methods can be used online without disturbing the production rate as well as make it possible to automatically monitor each and every sheet (Ref 15.2, 15.25).

Theory of Eddy-Current-Based Material Properties Evaluation. The properties of a material are determined primarily by its microstructural composition, such as grain size, grain orientation, alloying elements, and dislocation density (Ref 15.2). A direct result of this is that the electromagnetic properties of a material have a strong correlation with its mechanical

properties. Thus, by monitoring the electromagnetic properties of a material, namely, permeability and conductivity, it is possible to estimate the mechanical properties of the material, such as yield stress, tensile strength, and hardness.

For nondestructive measurement of material properties, low-frequency eddy current sensors are used. The sensor is inserted into the process cycle after the uncoiling of the blank from the coil. A magnetic coil inside the sensor is excited through an alternating current and generates eddy currents in the blank and a second magnetic field with a direction opposite to the primary field (Fig. 15.21). The phase of the secondary field depends on the material composition and the electromagnetic properties, such as permeability and conductivity of the sheet material. Therefore, this sensing technique can be used only with conductive sheet materials.

The method explained previously uses a single-current frequency, while advanced techniques use multifrequency sensors. The use of several different frequencies makes it possible to evaluate different material properties at the same time and also helps to improve the accuracy of the measurements (Ref 15.27).

To ensure consistent and exact correlation between the eddy current readings and the material properties of the tested coil, the system must undergo a teaching or calibration phase. This teaching phase involves testing a few blanks from different batches/coils/heats by destructive evaluation tests (tensile or bulge test). Results from both evaluation methods are correlated to establish a relation between the two tests. The teaching phase is followed by a validation phase to verify the correlation model.

Figure 15.22(a) shows a comparison between the values of yield strength obtained from tensile tests and that obtained through eddy current tests for ETG-100 steel. This shows a 1% error band within the correlation model in the training phase. Figure 15.22(b) shows the results of the validation phase. A 2% error band is observed within the correlation model for the tested material yield strength values.

Figure 15.23(a) shows an error band of 2% within the correlation model built by using the eddy current test data and tensile test data for uniform elongation during the teaching phase for silver material. Figure 15.23(b) shows a 2% error band within the developed correlation model during the validation phase (Ref 15.25).

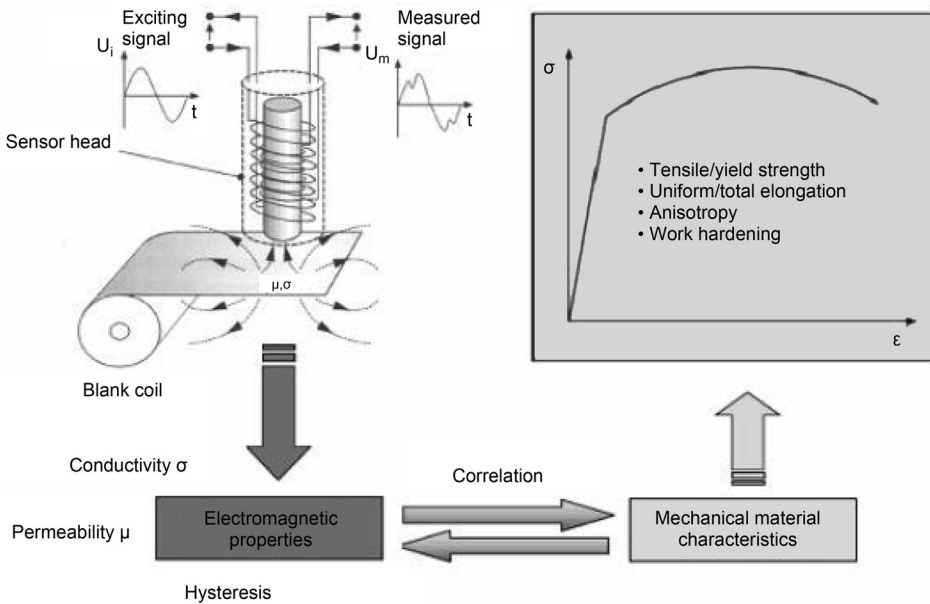


Fig. 15.21 Principle of eddy current material testing. Source: Ref 15.2, 15.26

15.7 Sensors for Lubrication

The formability during sheet metal forming processes is usually affected by the properties of lubrication. Uniform oil films on the metal separate the sheet from the die and permit constant material flow between blank holder and die. Excess lubrication can cause wrinkling, and reduced lubrication can cause tearing. Sensors based on high-resolution infrared spectrometry have been developed to measure the oil film thickness on metal surfaces. The sensor, as shown in Fig. 15.24, consists of a measurement head and a data collection unit. The working principle is based on the absorption of infrared radiation by the hydrocarbons present in the oil. The measurement is obtained by locating the sensor head on the metal surface. When the sensor is triggered, the data collection unit will collect the data and calculate the oil amount by comparing the measured data with precalibration data. The output result is the average of the measurements of different points on the surface. Calibration is required when measuring different types of materials, due to the optical differences in the surface textures of different materials such as copper, steel, and aluminum (Ref 15.2).

15.8 Summary

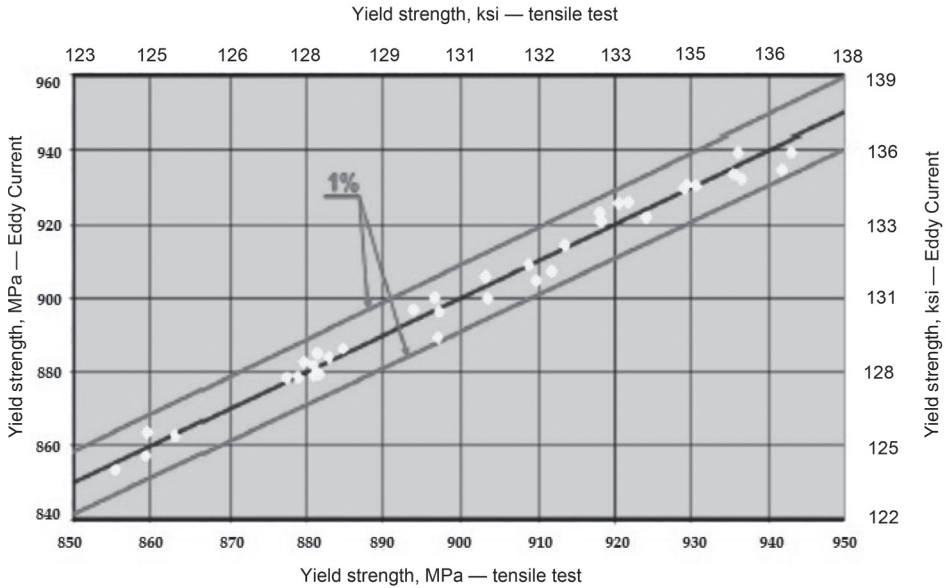
In modern sheet metal forming plants, sensors are widely used for monitoring of press load, part feed, tool failure, material flow in the dies, and for determining the variations in the mechanical properties of incoming material. Due to advances in sensor and control technology, electronics, and display devices, the cost of sensors and process monitoring systems decreased considerably. Thus, the integration of sensors and monitoring techniques in modern production represents a cost-effective investment to maintain part quality and production rate and to reduce scrap and downtime.

REFERENCES

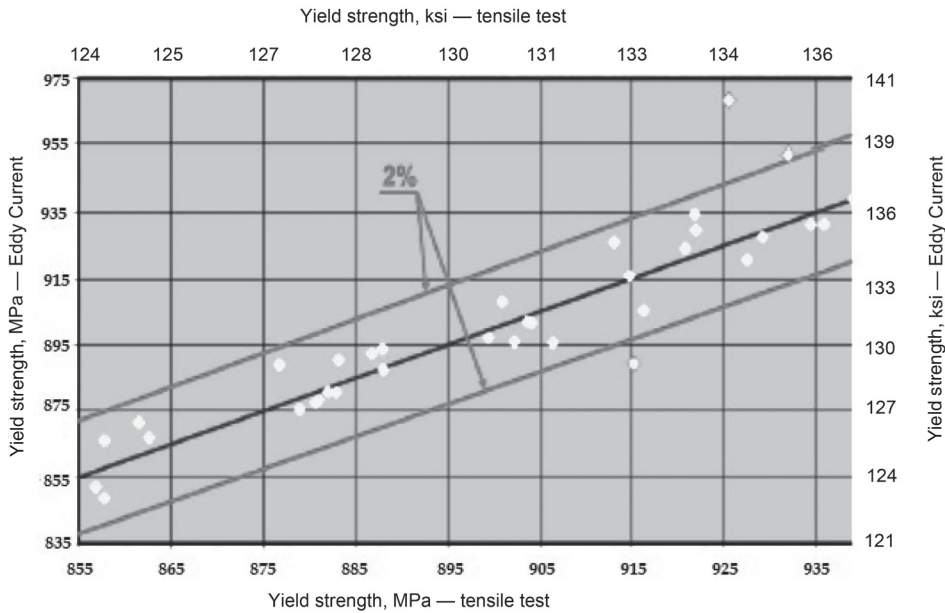
15.1 K. Keller, Protecting Metal Stamping Dies: How to Prevent Die Crashes with Sensors, *Stamp. J.*, Feb 2007
 15.2 E. Doege, F. Meiners, T. Mende, W. Strache, and J.W. Yun, Sensors for Process Monitoring: Metal Forming, Chap. 4.2, *Sensors in Manufacturing*, H.K. Tonshoff and I. Inasaki, Ed., Wiley-VCH, 2001, p 172–190

- 15.3 D. Falcone, Equipping Your Press with the Right Tonnage Monitor, *Stamp. J.*, Nov 2002
- 15.4 PULSElectronic, <http://www.pulselectronic.com>

- 15.5 Wikipedia, The Free Encyclopedia, <http://www.wikipedia.org>
- 15.6 Sensorland.com, The Information Centre for Sensors & Data Systems, <http://www.sensorland.com/>



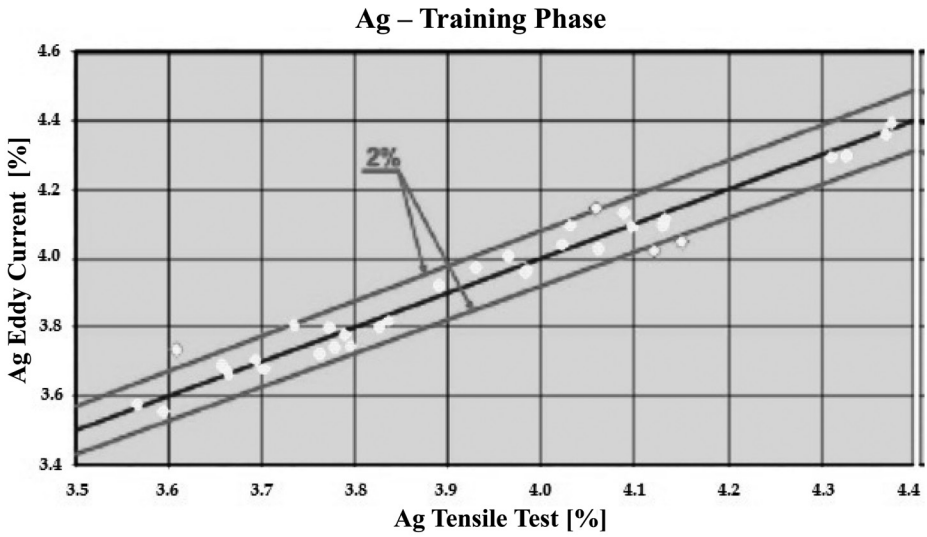
(a) Training/Calibration for yield strength



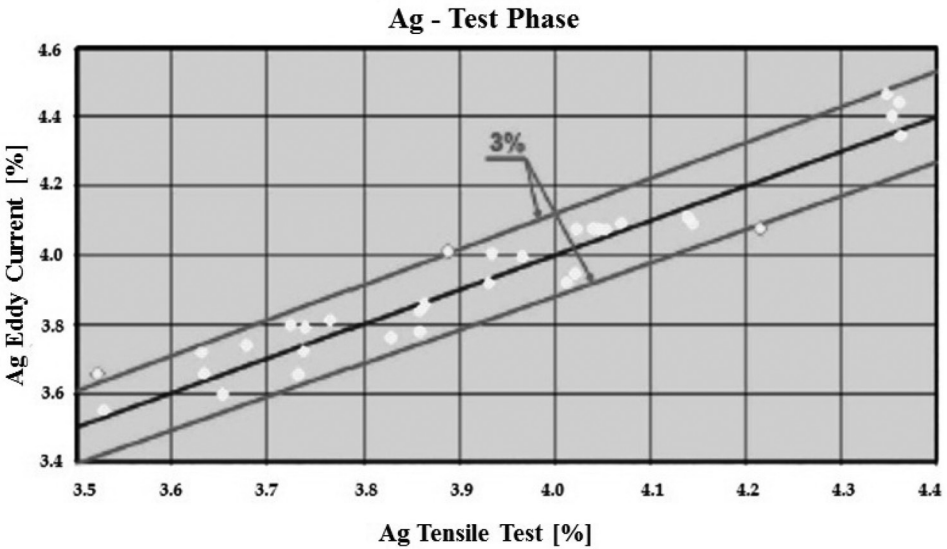
(b) Validation for yield strength

Fig. 15.22 Training and validation for material ETG-100 steel. Source: Ref 15.25

15.7	Kistler, http://www.kistler.com/	Chap. 18, <i>Handbook of Metalforming Processes</i> , H.E. Theis, Ed., Marcel Dekker, 1999, p 365–374	
15.8	Helm Instrument Co., Inc., http://www.helminstrument.com		
15.9	J. Breitling, B. Pfeiffer, T. Altan, and K. Siegert, <i>Process Control in Blanking</i> , <i>J. Mater. Process. Technol.</i> , Vol 71, 1997, p 190–192	15.11	AST/Macro Sensors, http://www.macrosensors.com/lvdt_tutorial.html
15.10	R. Wilhelm, <i>In-Die Force Monitoring</i> ,	15.12	Schuler, <i>Metal Forming Handbook</i> , Springer, 1998, p 80–82
		15.13	J.B. Finnerty, <i>Electronic Sensors for</i>



(a) Training for uniform elongation



(b) Validation for uniform elongation

Fig. 15.23 Training and validation for silver. Source: Ref 15.25

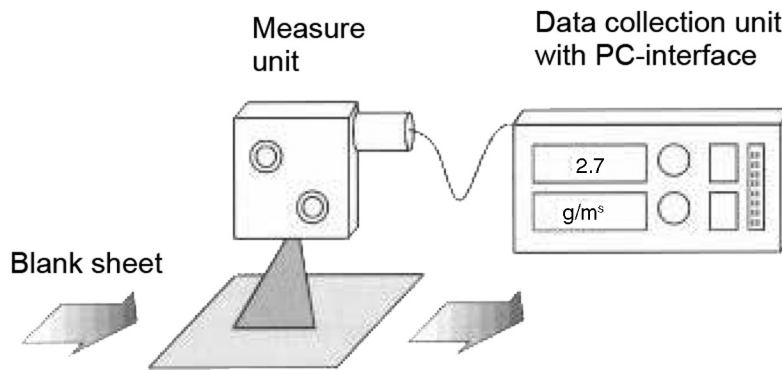


Fig. 15.24 Schematic diagram of a portable infrared analyzer. Source: Ref 15.2

- Die Protection, Chap. 17, *Handbook of Metal Forming Process*, H. Theis, Ed., Marcel Dekker, 1999, p 341–350
- 15.14 B. Benhabib, Instrumentation for Manufacturing Control, Chap. 13, *Manufacturing—Design, Production, Automation and Integration*, Marcel Dekker, 2003, p 377–455
- 15.15 PC Control Ltd., <http://www.pc-control.co.uk>
- 15.16 Balluff Sensors Worldwide, <http://www.balluff.com/Balluff>
- 15.17 Rockwell Automation, <http://www.rockwellautomation.com/>
- 15.18 Vallen Systeme GmbH, <http://www.vallen.de/>
- 15.19 Guide to Nondestructive Testing, *Adv. Mater. Process.*, Vol 165 (No. 11), Dec 2007, p 35–42
- 15.20 T. Jayakumar, C.K. Mukhopadhyay, S. Venugopal, S.L. Mannan, and B. Raj, A Review of the Application of Acoustic Emission Techniques for Monitoring Forming and Grinding Process, *J. Mater. Process. Technol.*, Vol 159, 2005, p 49–55
- 15.21 Olympus Corporation, <http://www.olympus-ims.com/en/>
- 15.22 E. Doege, H.J. Seidel, B. Griesbach, and J.W. Yun, Contactless Online Measurement of Material Flow for Closed Loop Control of Deep Drawing, *J. Mater. Process. Technol.*, Vol 130–131, 2002, p 95–96
- 15.23 GOM GmbH, <http://www.gom.com/>
- 15.24 K. Galanulis, Optical Measuring Technologies in Sheet Metal Processing, *Fourth International Conference and Exhibition on Design and Production of Machines and Dies/Molds*, 2007, p 403–411
- 15.25 3R Technics, <http://www.3r-technics.com>
- 15.26 T. Altan, Dissecting Defects—Part 2: Testing for Incoming Sheet Coil Variation, *Stamp. J.*, Nov 2007, p 22–23
- 15.27 Foerster USA, <http://www.foerstergroup.com/>

CHAPTER 16

Tool Materials, Treatments, and Coatings

Eren Billur, The Ohio State University

A STAMPING TOOL must be replaced or repaired periodically, when it fails to produce parts within the specified tolerance and/or required surface quality. This is mainly caused by wear, galling, cracking, chipping, or plastic deformation of the tools. Therefore, proper selection of tool materials, surface and heat treatments, and surface coatings is essential to optimize the tool life (i.e., number of acceptable stamped parts).

16.1 Background

Tool Failure Mechanisms in Sheet Metal Forming. Stamping tools fail in five different mechanisms, as shown in Table 16.1 (Ref 16.1, 16.2).

Wear is damage to a solid surface, involving loss or displacement of material. Wear is caused by sliding contact between the workpiece and tool and can be divided into two types:

- Abrasive wear is caused by hard particles forced against and moving along a solid surface.
- Adhesive wear is defined as wear due to localized bonding between contacting solid surfaces, leading to material transfer between the two surfaces or loss from either surface.

Plastic deformation is caused by high contact pressure, exceeding the compression yield stress (σ_{oc}) of the tool material.

Chipping is a result of high stresses, exceeding the fatigue strength of the tool material, usually at sharp edges.




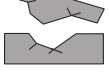

Cracking is caused by high stresses, exceeding the fracture toughness of the tool steel.

Galling is a form of damage caused by sliding of two solids. It often includes plastic flow, material transfer, or both.

Factors that affect galling and tool wear include the following.

Contact Pressure. All failure types (Table 16.1) can be avoided by reducing contact pressure. For a given sheet material, contact pressure can be reduced by die design, that is, using larger radii or reducing the sheet thickness. As the strength of the material is increased (for ex-

Table 16.1 Common tool failures and recommended changes in tools to prolong tool life

Tool failure	Recommended changes in tool	
	Increase	Decrease
 Wear	Hardness, ductility	Friction
 Plastic deformation	Hardness, yield stress	...
 Chipping	Toughness, ductility	...
 Cracking	Fracture toughness	Hardness, sharp corners
 Galling	Surface hardness	Friction

Source: Ref 16.2

ample, advanced high-strength steel compared to mild steel), contact pressure increases.

Surface Quality. Although the surface of the tool is much smoother than the surface of the sheet, galling is affected by the tool surface quality. Polishing the tool surfaces before and after coating helps to reduce galling. Roughness of the sheet has little influence on galling (Ref 16.3).

Tool Coating. Selection of proper coating is also crucial to avoid galling and tool wear. Coatings that may have lower coefficient of friction and high surface hardness help reduce tool failures (Ref 16.4). Tool coatings may require prior preparation of the tools (i.e., to harden or have surface roughness values below some threshold) (Ref 16.5, 16.6).

Lubrication helps to reduce wear and galling. Forming of higher-strength sheets will require better-performing lubricants, due to higher contact pressure and temperature during the process. Extreme-pressure additives may be required for forming advanced high-strength steels. Recently, due to environmental concerns and lean manufacturing purposes, some stampers are moving away from using additional lubricants, other than mill oil or dry lubricants. In such cases, low-friction coatings are recommended (Ref 16.3, 16.7, 16.8).

Estimation of Tool Wear. A study by Meng (Ref 16.9) showed that there are more than 300 equations to predict tool wear, each of which is a correlation of several parameters and is derived from various wear tests. Among these, the Archard wear equation (Eq) is commonly used for modeling tool wear in metal forming processes (Ref 16.10):

$$W = K \frac{PL}{H} \tag{Eq 16.1}$$

where W is the worn volume (volume loss, m^3 or $in.^3$), K is the coefficient of wear (dimensionless), P is the normal load (N or lb), L is the sliding distance (m or in.), and H is the surface hardness of the tool material (N/m^2 or psi). As seen in Eq 16.1, contact pressure must be reduced in order to reduce wear. Similarly, increasing the surface hardness would help. Archard’s equation does not consider surface roughness, lubricity, or friction coefficient. These effects can be included in the calculations by changing the value of K in the equation (Ref 16.11). Figure 16.1 shows a specific wear rate, K/H , determined by a lab test, for several com-

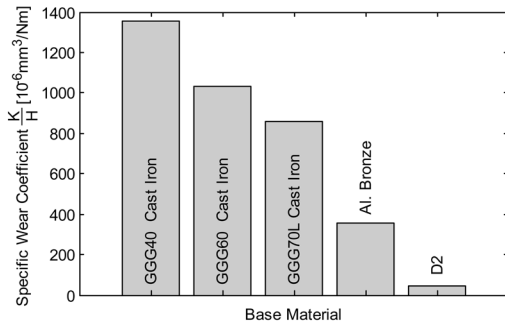


Fig. 16.1 Specific wear coefficient of several tool materials determined by dry sand/rubber wheel abrasion test. Source: Ref 16.12, 16.13

mon tool materials. Tests and methods to calculate the coefficient of wear (K) are discussed in a later section.

16.2 Tool Materials

The selection of tool material depends on batch size, severity of forming, and material to be formed. Tool materials can be classified into three main classes:

- **Nonmetallic Materials:** Two types of non-metallic materials are used for sheet metal forming tools: polymeric materials and ceramic materials. Polymeric materials are used to manufacture tools by rapid prototyping (Fig. 16.2) and are used for small series of metal stampings (on the order of 50 to 500 pieces) (Ref 16.14, 16.15). Ceramics, on the other hand, are used for a high number of stampings (>100,000). They have very high hardness; however, they are brittle. Therefore, they are mostly used as punches or inserts. Ceramics or hard metals, used in stamping, include but are not limited to tungsten carbide (WC), alumina (Al_2O_3), and zirconia (ZrO_2) (Ref 16.16, 16.17).
- **Nonferrous Metals:** Zinc and bismuth alloys are used for prototyping purposes and small-batch productions. Use of aluminum is not common, because tool surfaces may scratch easily (Ref 16.18). Aluminum bronze, an alloy of copper and aluminum, is used for forming carbon and stainless steels. These alloys have high resistance to galling; however, due to their low hardness, they fail by wear (Ref 16.13).

- **Ferrous Materials:** Ferrous tool materials may be cast iron, cast steel, or tool steels. These are the most common tool materials in the sheet metal forming industry and are explained in detail in the next sections.

Cast iron, by definition, is an alloy of iron, containing 2 to 4% C, 0.5 to 3.0% Si, and 0.4 to 1.0% Mn. Other elements may be added to further optimize mechanical properties, that is, control the microstructure and hardness. Cast iron is used extensively in large stamping dies, because the material is much less costly than steel. It may not be cost-efficient to use cast iron dies for small parts due to the cost of pattern-making (Ref 16.19).

Wear and galling may limit the life of cast iron dies. To overcome this, selective (flame/laser) hardening, hard chrome plating, and/or adding inserts to high-wear areas are common. These inserts may be manufactured from tool steels. Cast iron grades used in stamping are

gray cast iron (G2500, G3500, etc.) and ductile iron (D4512, D5506, D6510, and GGG70, among others) (Ref 16.8, 16.20).

Cast Steels. Similar to cast iron, cast steel is more cost-efficient for large dies, due to pattern costs. Cast steel is preferred when more toughness and resistance to abrasive wear are required. Steel dies may be costlier than cast iron dies because of higher material and machining costs. Cast steels may be flame hardened and can be rewelded with tool steel or aluminum bronze to improve resistance to galling. Cast steel tools may be preferred in restriking, flanging, and trimming operations (Ref 6.21, 6.22).

Cast steels used in stamping include 0030, 0050A, Carmo (1.2333), Caldie, GP4M, and SKD12. Similar to cast iron tools, high-wear areas may be hardened, coated, or fitted with inserts, as shown in Fig. 16.3(a). A novel method of casting iron and steel into one die is offered by a Swedish company. As shown in Fig. 16.3(b), the die shoe is cast from gray iron, and

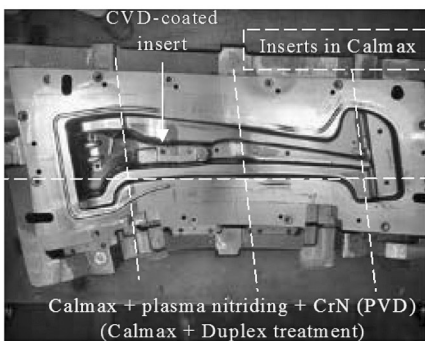


(a)

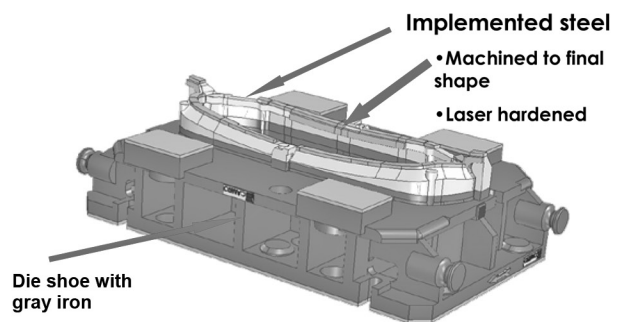


(b)

Fig. 16.2 Polymer tools manufactured by rapid prototyping. Source: Ref 16.15



(a)



(b)

Fig. 16.3 (a) Use of inserts in a cast steel stamping die. CVD, chemical vapor deposition; PVD, physical vapor deposition. Source: Ref 16.8. (b) Novel method of casting iron and steel. Source: Ref 16.23

functional surfaces are cast from steel and laser hardened (Ref 16.8, 16.20, 16.23, 16.24).

Tool steels are clean (free from inclusions), medium- to high-carbon, high-alloy steels designed to have high hardness, resistance to wear and deformation, dimensional stability, toughness, and through hardenability (Ref 16.25). Tool steels are classified by the American Iron and Steel Institute (AISI) based on alloying (i.e., tungsten, molybdenum), application (cold work, hot work steels), and heat treatment (i.e., water hardening, air hardening steels) (Table 16.2). Although AISI classification is widely used, many countries have their independent classifications, and some steel companies may prefer to use commercial names different than the AISI nomenclature (Ref 16.26).

16.3 Treatments to Harden the Tools

As seen in Archard’s equation (Eq 16.1), as surface hardness is increased, die wear is reduced. Therefore, increasing the hardness of the tools is desirable when wear is the main concern. However, there is a trade-off between hardness and toughness: a very hard die may be superior against wear but may fail by chipping or cracking (Table 16.1).

Rockwell and Vickers Hardness. Hardness of bulk materials (in stamping tools, core hardness of the tool) is measured by Rockwell B (HRB) or C (HRC) scale. The HRB test uses a 1.59 mm (0.0625 in.) diameter ball and requires a 100 kg (220 lb) load; the HRC test uses a diamond indenter and requires 150 kg (330 lb). Hardness number is calculated from the measurement of indentation depth (on the order of 60 to 160 μm in HRC). To have reliable results, the thickness of the material must be at least 10

times that of the indent depth (0.6 to 1.6 mm, or 0.02 to 0.06 in., minimum) (Ref 16.27).

Because of thickness limitations, Rockwell measurements are not reliable to check surface hardness when the surface is hardened or coated. In most cases, the thickness of the coating or depth of the hardened volume is on the order of 5 to 30 μm. In this scale, the Vickers microhardness test is used. This test uses a pyramid-shaped diamond indenter. After the load is applied, surface area is calculated by measuring the diagonal lengths. Vickers hardness number (HV) is found by dividing the load by the area and is often given in kgf/mm² (Ref 16.28).

There is no direct conversion between hardness scales by definition (Ref 16.27). However, curve fitting can be done to convert different scales for everyday purposes. One such curve fit was done by Qvarnström (Ref 16.29), as shown in Fig. 16.4. Similarly, compressive yield strength (σ_{CY}) can be approximated using Vickers hardness, by using Eq (Ref 16.30). By using both conversions, compressive yield strength can be approximated using Rockwell C hardness. Note that in Fig. 16.5, estimated compressive yield strength values are within ±10% of values given in various references:

$$\sigma_{CY} \approx \frac{HV}{3} \tag{Eq 16.2}$$

Through Hardening. Ferrous tool materials may be delivered as tempered to low hardness values so that they can be machined easily. Tools must be hardened in order to reduce plastic deformation (i.e., increasing compressive strength) and wear (Table 16.1). The basis of hardening is to transform the metal to a martensitic microstructure. To obtain this, a three-step heat treatment is applied:

1. Heating for austenite formation (austenitizing)
2. Cooling to transform austenite to martensite (quenching)
3. Tempering to eliminate retained austenite and form carbides, as shown in Fig. 16.6 (Ref 16.25, 16.26)

The material expands during heating and contracts during austenite formation. If the temperature is not uniform within the tool, it is possible that while one part is expanding, another may contract, which in turn will create internal stresses. To avoid these thermal stresses that

Table 16.2 Tool steels as classified by AISI

Identifying symbol	Group	Examples
W	Water hardening	W1, W2
S	Shock resisting	S5, S7
O	Oil hardening, cold work	O1, O2
A	Air hardening, medium alloy, cold work	A2, A6, A7
D	High carbon, high chromium, cold work	D2, D3, D5
H	Chromium, hot work	H10, H11, H13
	Tungsten, hot work	H21, H23
T	Tungsten, high speed	T2, T4, T5
M	Molybdenum, high speed	M2, M4, M6

Source: Ref 16.26

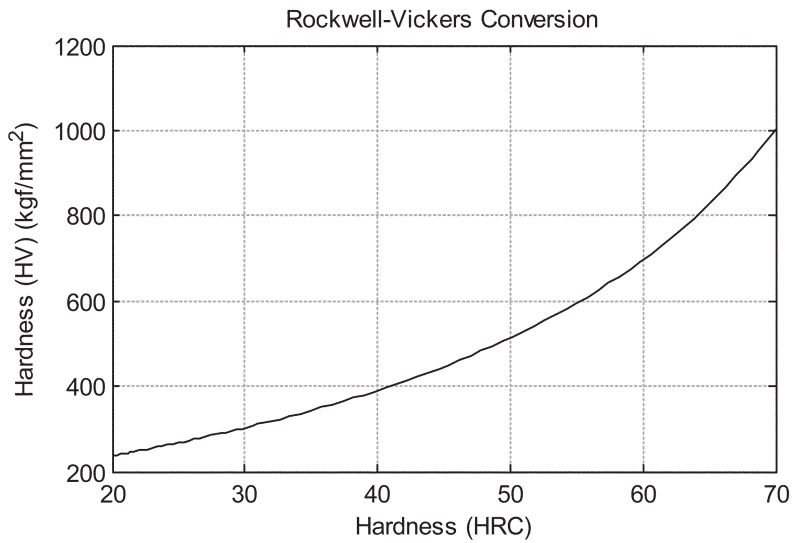


Fig. 16.4 Conversion of Rockwell and Vickers hardness values, based on curve fitting. Source: Ref 16.29

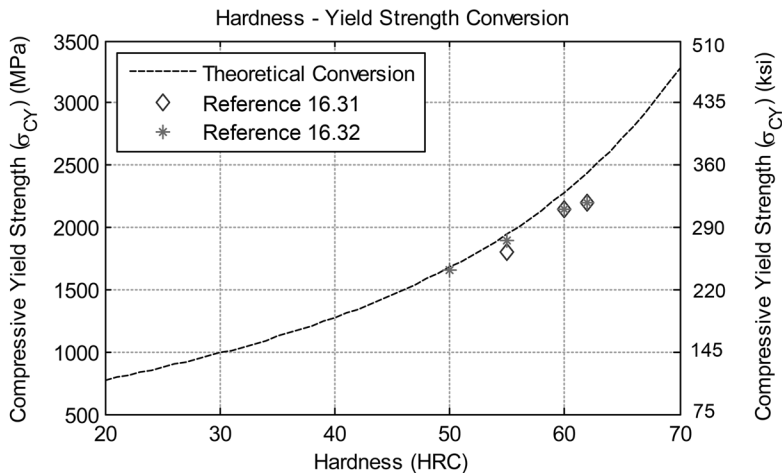


Fig. 16.5 Approximation of compressive yield strength using Rockwell hardness. Source: Ref 16.29–16.32

may cause distortion or cracks, preheating may be applied to establish more uniform temperature distribution (Fig. 16.6). Preheating is advised for high-alloyed materials. During this stage (step 1 in Fig. 16.6), the microstructure of the metal is composed mainly of ferrite and carbides (Ref 16.26, 16.33).

Once the austenite-forming temperature is reached, ferrite is transformed to austenite (step 2 in Fig. 16.6), and carbides are dissolved. If the material is cooled slowly, the microstructure

again transforms to ferrite and carbides (step 1). However, if it is cooled rapidly by soaking in water, a salt bath, or room-temperature air (i.e., quenched), then martensite is formed. When steel is hardened, it is never completely converted to martensite; some retained austenite and carbides are always left (step 3 in Fig. 16.6).

After quenching, the presence of the martensite microstructure greatly increases the hardness of the material (and yield strength) but causes it to be brittle. By increasing the temperature of

the material and keeping it at high temperature for some time, it is possible to temper the martensite (i.e., make it more stable) and transform some retained austenite to martensite. So, at step 4 in Fig. 16.6, the microstructure consists of tempered martensite, newly formed martensite, retained austenite, and carbides. This would increase the toughness of the material without sacrificing too much of its hardness or yield strength, as seen in Fig. 16.7. For tool steels, double tempering is advised in order to temper the newly formed martensite (step 5 in Fig. 16.6). For high-speed steels with high carbon content, three tempers are advised (Ref 16.26, 16.35, 16.36).

Case (Surface) Hardening. For wear resistance, surface hardness is important. In many applications, tool surfaces are hardened more than the core of the tool itself. This has two main advantages:

- The hard surface resists wear, while the relatively softer and tougher core resists impact loads.
- It is less costly to harden only the surface.

Some techniques are also favored for easy repair of the surface. There are three main classes of surface-hardening methods (Table 16.3) (Ref 16.37). Diffusion techniques and coatings/surface modifications are discussed in later sections. In this section, applied energy techniques are investigated.

Surface hardening using applied energy is similar to through hardening in terms of microstructure transformations. Applied energy is used to heat the surface layer 50 to 100 °C (90 to 180 °F) higher than the austenitizing temperature. Quenching can be done by so-called self-quenching, where bulk material can act as a heat sink and no additional quenchant is re-

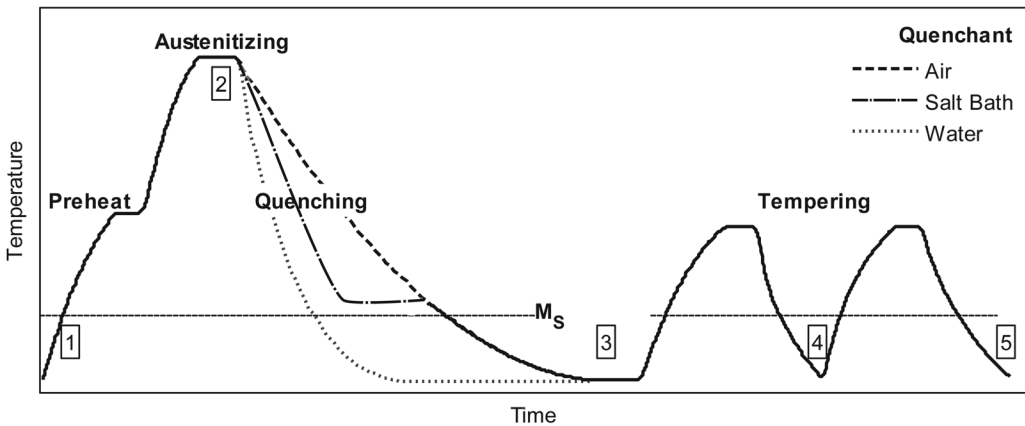


Fig. 16.6 Steps of heat treatment processes. Source: Ref 16.26

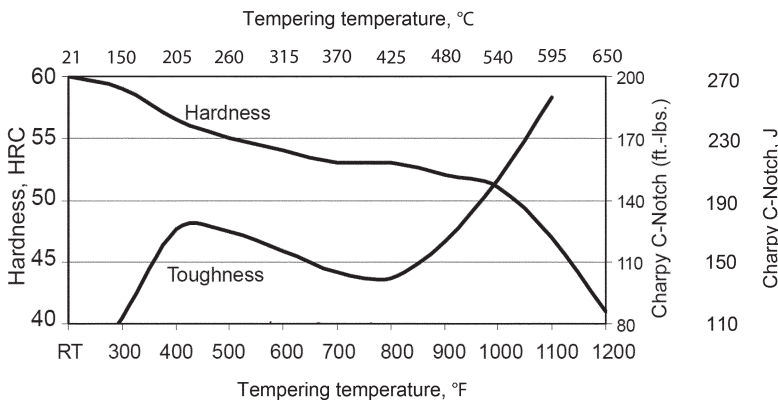


Fig. 16.7 Effect of tempering temperature on Rockwell hardness and toughness as determined by Charpy test. Source: Ref 16.34

quired; gaseous quenchant, such as air, forced air, or nitrogen; and liquid quenchant, such as water or oil. Additional tempers can be performed. Because only a small case depth (thickness) is heated, surface hardening takes much less time than through hardening (Ref 16.38, 16.39).

In flame hardening, heating is applied by an oxyfuel torch, followed by immediate quenching with water. This method requires low initial investment but high operator skills. Temperature and case depth can be controlled by time and fuel type (i.e., acetylene, propane). High energy is required for flame hardening. Therefore, quenching is necessary, and distortion may be a problem.

Induction hardening is suitable for axisymmetric parts (i.e., punches). An induction coil specific to the part would be required. Frequency of the alternating current and time are two variables used to control the temperature and case depth in induction hardening. Quench-

ing with water is common; however, oil and forced air may also be used.

Achievable surface hardness in flame and induction hardening is a function of carbon content. Figure 16.8 shows achievable surface hardness with water quenching after flame or induction heating. This applies to alloy steels, except those that contain chromium and vanadium (Ref 16.37).

In laser beam hardening, the workpiece is heated by absorbed energy of the laser (Fig. 16.9). The heating rate may be on the order of 1000 °C/s (1800 °F/s), so the surface is heated up very quickly. Due to the high thermal conductivity of metals, high-temperature surface layers are self-quenched rapidly. Therefore, additional quenchants are not required. The energy input in laser beam hardening is approxi-

Table 16.3 Common surface-hardening methods used in stamping tools

Diffusion techniques	Applied energy techniques	Coating/surface modifications
Nitriding	Flame hardening	Hard chrome plating
Thermal diffusion	Induction hardening	Chemical vapor deposition
	Laser beam hardening	Physical vapor deposition

Source: Ref 16.37

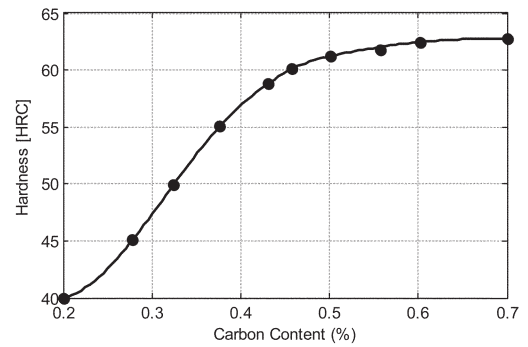
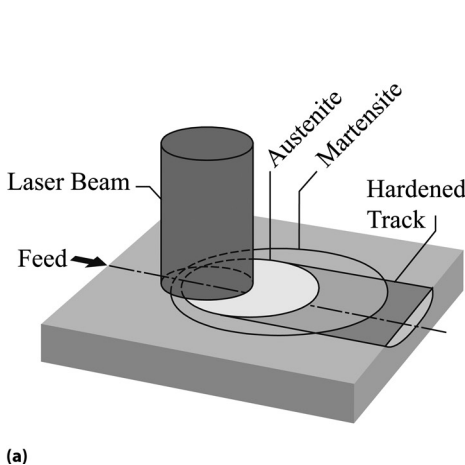
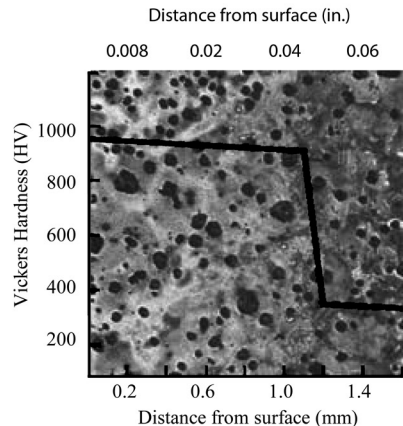


Fig. 16.8 Achievable surface hardness with flame or induction hardening. Source: Ref 16.37



(a)



(b)

Fig. 16.9 Laser hardening. (a) Schematic. Source: Ref 16.40. (b) Hardness profile and micrograph of laser-hardened cast iron (EN-GJ5-700). Source: Ref 16.41

mately 10% of flame hardening, which makes it more energy efficient and reduces distortion/cracking problems (Ref 16.37, 16.39).

Nitriding is a case-hardening process, where nitrogen is introduced (diffused) into the surface of a metal alloy. Nitriding processes are classified and named after the medium that provides nitrogen (Ref 16.42):

- *Gas Nitriding*: Nitrogen is introduced to the surface of hot metal (at 500 to 570 °C, or 930 to 1060 °F) via nitrogenous gas, usually ammonia. Quenching is not required.
- *Liquid (Salt Bath) Nitriding*: Takes place at similar temperature ranges as gas nitriding (510 to 580 °C, or 950 to 1075 °F) but employs a salt bath containing cyanides or cyanates. Liquid nitriding has lost favor due to environmental considerations.
- *Ion (Plasma) Nitriding*: Uses glow discharge technology to introduce nitrogen to the surface of the metal. The technique requires high-voltage electrical energy to form plasma in a low-pressure medium. This accelerates the gas (nitrogen) particles in the medium and creates an ion bombardment of the workpiece.

Nitriding is a diffusion (case)-hardening method. Therefore, there is no additional thickness layer (i.e., no deposition or coating). Figure 16.10 shows how the hardness changes with distance from the surface for D2 tool steel. Table 16.4 gives information about the effect of ion nitriding on surface hardness of some common tool materials.

Ion nitriding can be applied to large stamping dies up to 9.6 by 2.9 m (31.5 by 9.5 ft) and 40

metric tons (44 tons) (Ref 16.6, 16.46). Figure 16.11 shows an ion-nitrided stamping tool, used in the automotive industry (Ref 16.48).

16.4 Plating and Coating

Another method to increase wear resistance is to plate or coat the forming dies. Common methods are plating, physical vapor deposition (PVD) coatings, chemical vapor deposition (CVD) coatings, and thermal diffusion (TD) coatings, as explained in the following sections (Ref 16.49).

Hard Chrome Plating. In the metal industry, nickel, zinc, and chrome plating are commonly used for visual or functional purposes. For stamping dies, hard chrome plating is often applied. This is done by electrodeposition from a solution containing chromic acid (CrO₃) and a catalytic anion. If deep drawing tools are to be chrome plated, the base metal should be surface hardened to more than 50 HRC (Ref 16.49).

Hard chrome coating typically adds 2.5 to 500 μm of a hard layer, generally around 850 to 1100 HV (63 to 70 HRC equivalents). Several studies have shown that hard chrome coatings are favorable for mild steels but fail in forming of advanced high-strength steels (Ref 16.7, 16.50, 16.51) (Fig. 16.12).

Chrome coating has a high surface hardness but causes a sharp reduction in hardness from the chrome coating to the substrate material (Fig. 16.13). In addition, chrome coating is not reworkable, and if any repair is needed, the coating is required to be stripped first (Ref 16.6).

Physical vapor deposition coatings refer to a family of relatively low-temperature (compared to CVD and TD) atomistic deposition processes: vacuum evaporation, sputter deposi-

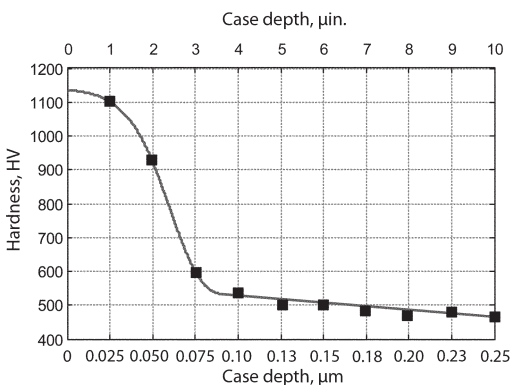


Fig. 16.10 Hardness profile of D2 tool steel after ion nitriding process. Source: Ref 16.43

Table 16.4 Surface hardness of several cast iron/steel grades and tool steels after ion nitriding

Base material	Depth, μm	Core hardness, HRC	Surface hardness, HV
A2: cold work tool steel	~8	54–60	750–1200
D2: cold work tool steel	5–8	61–64	750–1200
M2: high-speed tool steel	8–10	64–66	1050–1200
H13: hot work tool steel	~5	48–55	700–1350
0050A: cast steel	5–7	20–27	560–900
G3500: gray cast iron	7–10	20–27	330–610
D6510: ductile cast iron	~7	23–28	440–575

Source: Ref 16.43–16.47



Fig. 16.11 Ion-nitrided forming tool for hood outer panel. Source: Ref 16.48

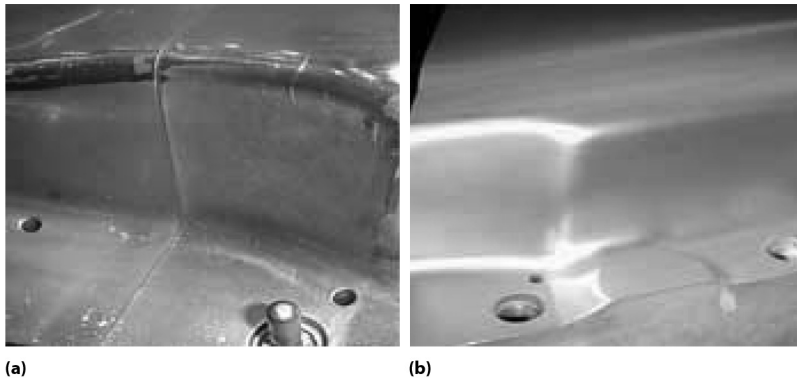


Fig. 16.12 (a) Hard-chrome-coated Carmo die after 50,000 stampings. (b) Physical vapor deposition CrN-coated Carmo die after 1,200,000 stampings. Source: Ref 16.7

tion (or sputtering), ion plating, and ion beam-assisted deposition (Ref 16.52).

As seen in Fig. 16.14, PVD has lower process temperatures (200 to 550 °C, or 390 to 1020 °F) compared to CVD (600 to 1000 °C, or 1110 to 1830 °F) and TD (870 to 1040 °C, or 1600 to 1905 °F) (Ref 16.7, 16.53). Lower process temperatures are often associated with several benefits (Ref 16.6):

- Less softening of tool material
- Less effect on corrosion resistance
- Less distortion or dimensional change

Physical vapor deposition allows coating only the area of interest, by using proper masking. On the other hand, this may limit the ability

to coat long, internal diameters. Table 16.5 lists the common PVD coatings, including solid-film lubricant (MoS_2) and diamondlike carbon. Figure 16.15 shows two applications of PVD coatings in the metal forming industry. In Fig. 16.15(a), PVD TiN is used for a soda can tab punch, and in Fig. 16.15(b), PVD TiCN is used to extrude AA battery casings. Note that both applications require a high production rate and volume (Ref 16.7, 16.52, 16.55).

An important issue in PVD coating is the base material hardness. It is noted that a minimum of 43 HRC (equivalent to ~430 HV) is required to hold the PVD coating. To achieve high substrate surface hardness, duplex coatings are employed, where the substrate material is

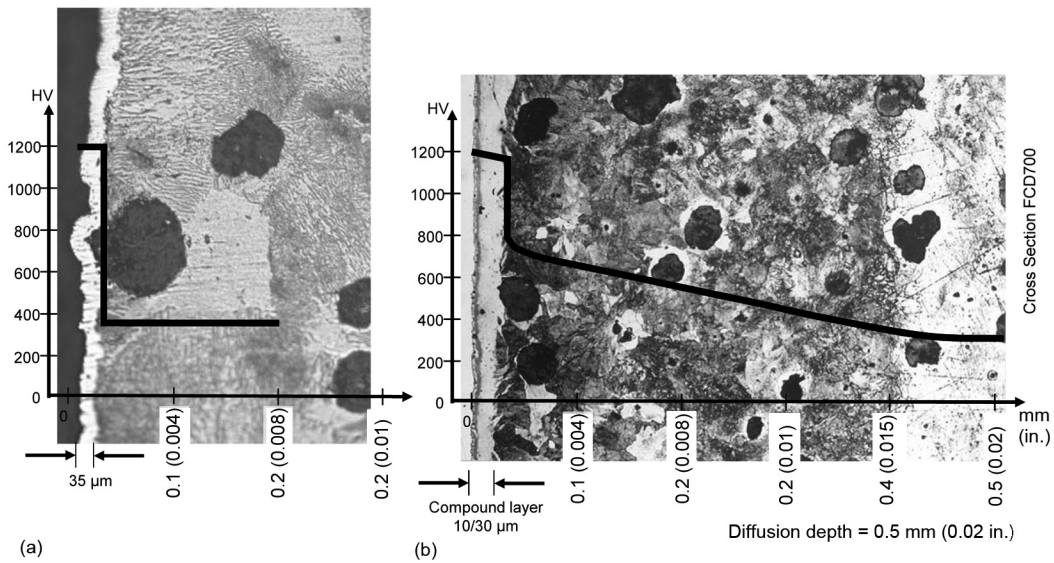


Fig. 16.13 Comparison of hardness profile and diffusion/deposition depth of (a) chrome coating and (b) ion nitriding on cast iron FCD700. Source: Ref 16.6

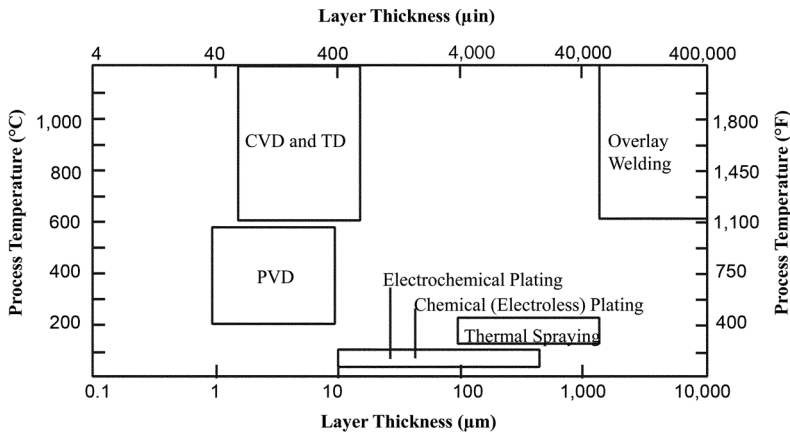


Fig. 16.14 Typical coating thicknesses and process temperature for common coating methods. CVD, chemical vapor deposition; TD, thermal diffusion; PVD, physical vapor deposition. Source: Ref 16.54

Table 16.5 Common physical vapor deposition coating materials and their properties

Coating(a)	Typical thickness, μm	Hardness, HV
B ₂ C	Up to 20	3000–4000
CrN	3–8	1800–2500
DLC (a-C:H)	Up to 5	1500–3000
DLC (ta-C)	1–4	5000–9000
MoS ₂	2–12	2000 min
TiAlN	2–5	2600–3400
TiCN	1–3	3200–4000
TiCrN	4–10	4200
TiN	3–5	2400–2900

(a) DLC, diamondlike carbon. Source: Ref 16.7, 16.55

first nitrided and then PVD is applied. Figure 16.16(a) shows how a soft substrate may cause cracks in the PVD coating. Figure 16.16(b) depicts the hardness profile as well as a micrograph of a duplex coating, where nitriding is applied to increase the surface hardness of the substrate to hold the PVD coating (Ref 16.5, 16.7).

Surface roughness of substrate materials also plays an important role in the life of the coating. Surface features such as ridges and grooves may create internal residual stresses in the coating, as shown in Fig. 16.17 (Ref 16.56). These

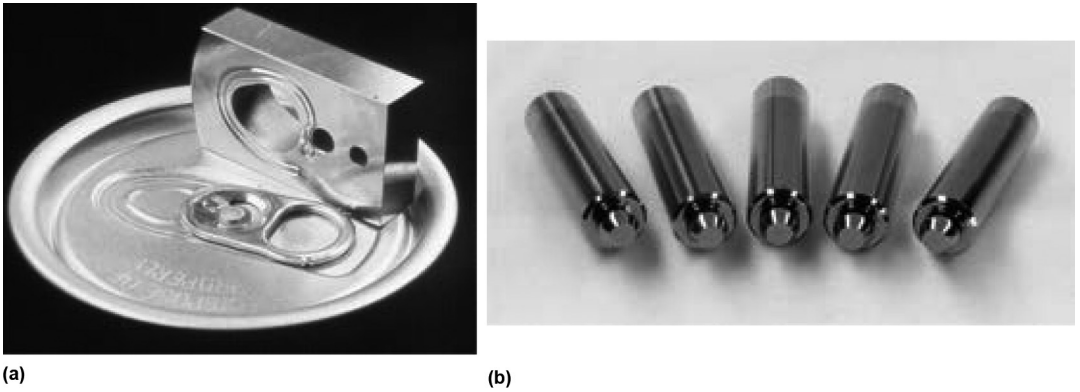


Fig. 16.15 Applications of physical vapor deposition (PVD) coatings. (a) PVD TiN used for soda can tab punch. (b) PVD TiCN used for AA battery casing extrusion punch. Source: Ref 16.55

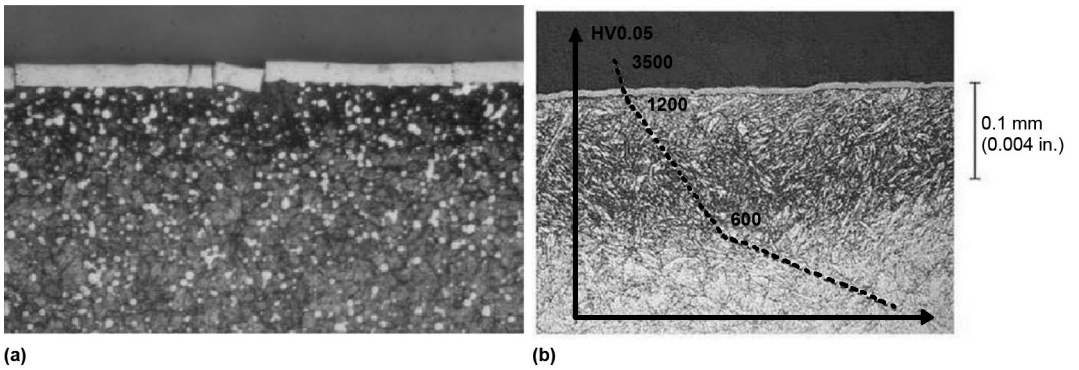


Fig. 16.16 (a) Crack in physical vapor deposition (PVD) layer due to low hardness of substrate. (b) A solution to this problem is duplex coating (nitriding + PVD). Source: Ref 16.5

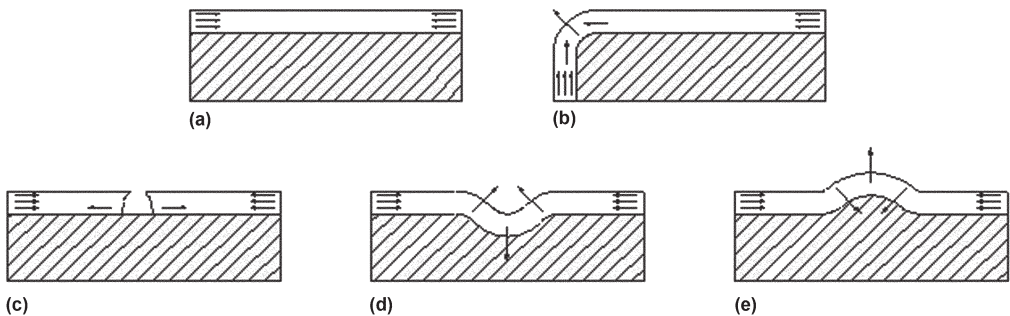


Fig. 16.17 Residual stresses caused by surface features in chemical vapor deposition or physical vapor deposition coating. (a) Ideal case. (b) Edge. (c) Coating edge. (d) Groove. (e) Ridge. Source: Ref 16.56

internal residual stresses may cause a crack in the hard coating. To avoid this type of failure, it is recommended to have a surface finish of more than $1\ \mu\text{m}$ (Fig. 16.18, 16.19) (Ref 16.6, 16.57).

Physical vapor deposition chambers have size and weight limitations. The largest cham-

bers available are approximately $\varnothing 2$ by 3 m (7 by 10 ft), and parts weighing up to 3.2 metric tons (3.5 tons) can be coated (Ref 16.58, 16.59). Current practice is to PVD-coat inserts in stamping tools in high-wear areas (Ref 16.8).

Chemical Vapor Deposition Coating. Chemical vapor deposition is defined as deposition of

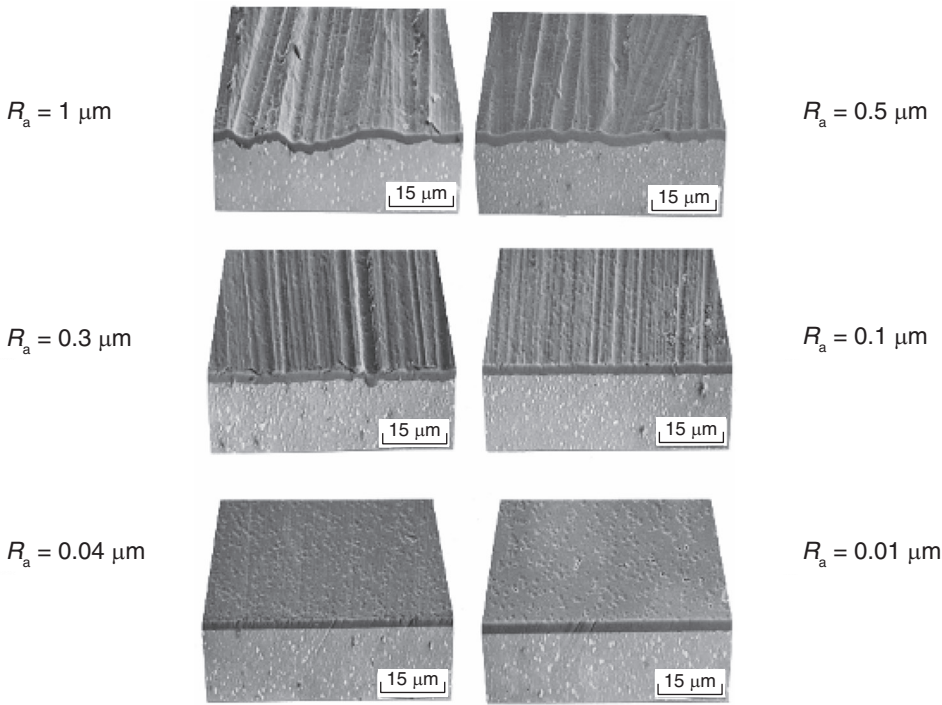


Fig. 16.18 Effect of surface roughness (R_a) on physical vapor deposition coating. Material is PM HSS, powder metallurgy high-speed steel. Source: Ref 16.6

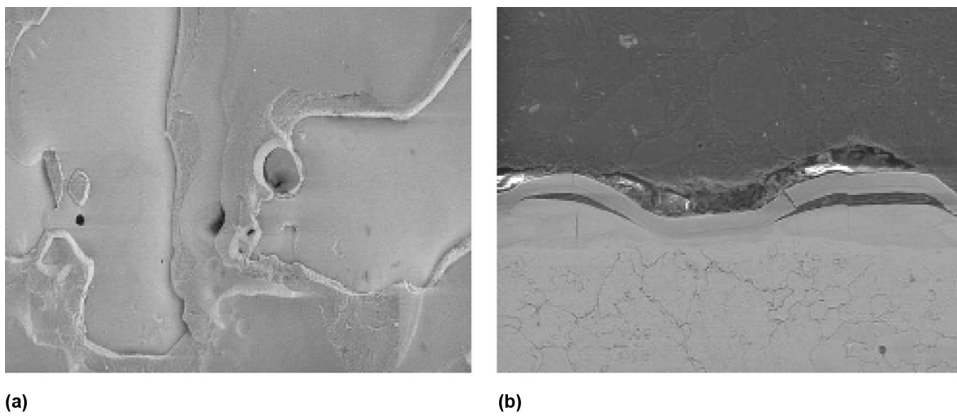


Fig. 16.19 Flaking of physical vapor deposition coating on a D2 tool steel, due to residual stresses caused by surface features. Source: Ref 16.6

a solid on heated surfaces by a chemical reaction in the vapor phase (Fig. 16.20). As shown in Fig. 16.14, typical coating thicknesses are 4 to 12 μm , and process temperatures are typically around 800 to 1050 $^\circ\text{C}$ (1475 to 1925 $^\circ\text{F}$). However, recent technology enabled plasma-assisted CVD (also known as plasma-enhanced CVD), which can reduce the process temperatures considerably. For the coatings used in the stamping industry (Table 16.6), plasma-assisted CVD can

be applied at approximately 500 $^\circ\text{C}$ (930 $^\circ\text{F}$) (Ref 16.7, 16.60).

Due to the high temperature of the process, softening and distortion are the problems to be addressed in stamping dies. Additional heat treating may be required after coating. Due to distortion, tight tolerances may not be achievable with CVD coatings. In addition, postcoating polishing may be required for good surface finish. Chemical vapor deposition is not recom-

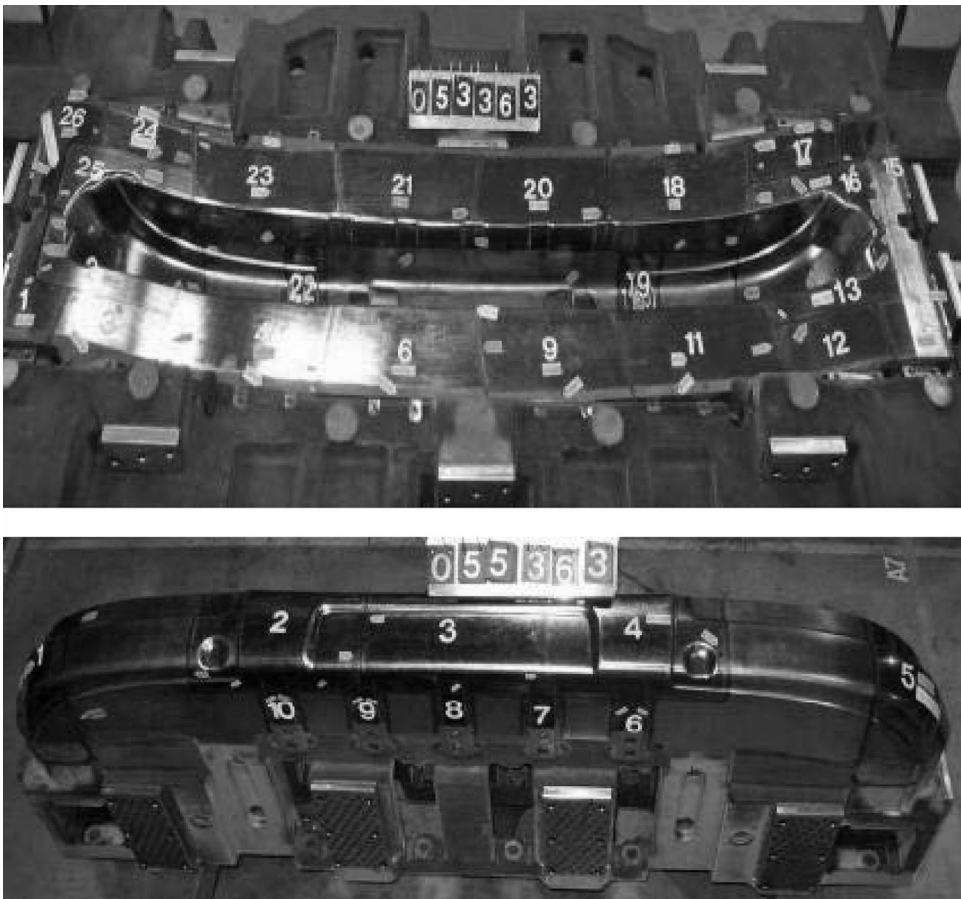


Fig. 16.20 Chemical vapor deposition coating applied to a stamping die for truck bumpers. Source: Ref 16.6

Table 16.6 Common chemical vapor deposition coating materials and their properties

Coating	Typical thickness, μm	Hardness, HV
Al_2O_3	8–12	3400
TiC	4–12	3000–3400
TiN	6–10	2200–3200

Source: Ref 16.7, 16.55

mended with A2 tool steel, because the process temperature is higher than the austenitizing temperature. Chemical vapor deposition chambers may be as large as $\text{\O}1.5$ by 2 m (5 by 7 ft) (Ref 16.7, 16.55, 16.57).

Thermal Diffusion Coating. Thermal diffusion, also known as thermal reactive coating, is a diffusion coating technology using various carbides, with vanadium carbide (VC) being the most common. The TD process is carried out in

a high-temperature (usually around 900 to 1050 $^{\circ}\text{C}$, or 1650 to 1920 $^{\circ}\text{F}$) salt bath filled with reactive chemicals in precise concentrations. Parts to be coated are first preheated and then soaked into the salt bath for a specific time and temperature (Ref 16.55).

Due to the high temperatures involved, distortion is an issue, and some materials may not be TD coated due to their thermal properties. It is stated that TD coating of A2 may cause problems, and some steels may not be compatible with TD, mainly because of the high temperature. General properties of TD coating are given in Table 16.7. Thermal diffusion coating can be applied to $\text{\O}0.7$ by 1.5 m (2 by 5 ft) dimensions.

16.5 Galling/Wear Tests

There are various conditions in which wear causes a problem, and therefore, there are nu-

Table 16.7 Thermal diffusion coating properties

Coating	Typical thickness, μm	Hardness, HV
VC	3–12	3200–4000

Source: Ref 16.55

merous wear test methods. Most of these methods are standardized by ASTM International and are classified into three groups:

- Evaluating a material response to a specific type of wear
- Screening materials, lubricants, and/or coatings
- Investigating fundamental aspects of wear (Ref 16.61)

However, none of the standard tests is tailored specifically to evaluate wear phenomena in sheet metal forming operations. Over the years, researchers have modified the standard tests and applied them to evaluate tool materials and coatings in sheet metal forming.

To be useful, the selected test must satisfy the following conditions (Ref 16.62):

- Plastic deformation must be similar to the real process; surface topography and mechanical properties of the sheet may change.
- Composition, treatment, and surface conditions of the tool specimen must be similar to that of a stamping die.
- The magnitude of friction and the regime of lubrication must emulate real conditions.

Scratching Tests. The standard pin-on-disk test (Fig. 16.21a) is used to determine wear in sliding material pairs, evaluate lubricants, or determine the friction coefficient. Because the material pair is in contact with the same surface (which is not the case in sheet metal forming), some modified tests (Fig. 16.21b) were introduced where the tool material is in contact with fresh sheet material throughout the test (Ref 16.63).

Although the sliding speeds and normal forces (therefore, the contact pressure) can be adjusted to a level that is similar to sheet metal forming processes, the effect of plastic deformation is ignored in these tests. Therefore, the results may not emulate the progression of tool wear in sheet metal forming.

Analysis of the pin-on-disk test (Fig. 16.21a) is standardized in ASTM G 99 (“Standard Test

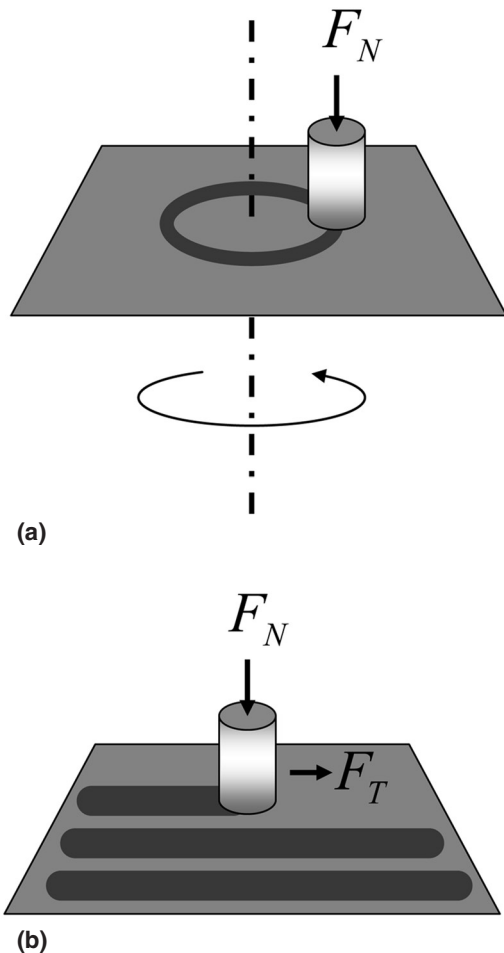


Fig. 16.21 Scratching tests. (a) Pin-on-disk test. (b) Slider-on-sheet test

Method for Wear Testing with a Pin-on-Disk Apparatus”) with respect to volume loss. The volume loss can be measured directly from the specimen dimensions before and after the test, or it can be calculated from mass loss. From this, the wear coefficient (K in Archard’s equation (Eq 16.1) can be calculated. If galling is present, volume loss may not reflect the tool wear, and therefore, this test method should not be used (Ref 16.64).

Twist Compression Test. In the twist compression test, a rotating button (tool material) is pressed against a fixed sheet metal, as depicted in Fig. 16.22(a). Rotation speed and pressure may be adjusted to simulate the metal forming process. However, similar to the pin-on-disk test, the tool material is rotating on the same

surface, not on a fresh sheet surface as in metal forming. Thus, surface conditions of sheet metal forming or stamping operations cannot be emulated.

This test is used to evaluate lubricant performance very quickly and to determine threshold galling stress for given sheet and die materials. To evaluate lubricant performance, transmitted torque is recorded in time, enabling calculation of the change in coefficient of friction in time. As a rule, when the coefficient of friction (μ) reaches 0.3 (Fig. 16.22b), the test is stopped (Ref 16.65).

Strip Reduction Tests. In strip reduction tests, the thickness of a sheet metal strip is reduced while it slides against the tested “tool material” (Fig. 16.23). This test is used to determine the galling tendency of a pair of materials (tool/sample) as well as to evaluate lubricants. For the first application, the length of strip that could be drawn using a given tool material without galling is recorded. The results are

compared within tool materials evaluated to determine which tool material and coating is best for drawing/reducing a specific sheet material. For evaluating the performance of various tool materials, coatings, and lubricants, the change in the surface finish of the tool after a reduction test may be used as a criterion (Ref 16.66, 16.68). Wear can be measured by volume/mass loss, provided that galling is not present (Ref 16.64, 16.67).

The tests discussed here include the effect of plastic deformation. Nevertheless, the state of deformation is limited to the thickness direction only. However, in deep drawing operations, the deformation is biaxial, and the sheet material undergoes thinning, thickening, and bending. All of these operations may change the surface texture, which cannot be emulated by strip reduction tests (Ref 16.62).

Forming tests are designed to emulate the actual state of deformation in sheet metal forming processes. Common tests found in the litera-

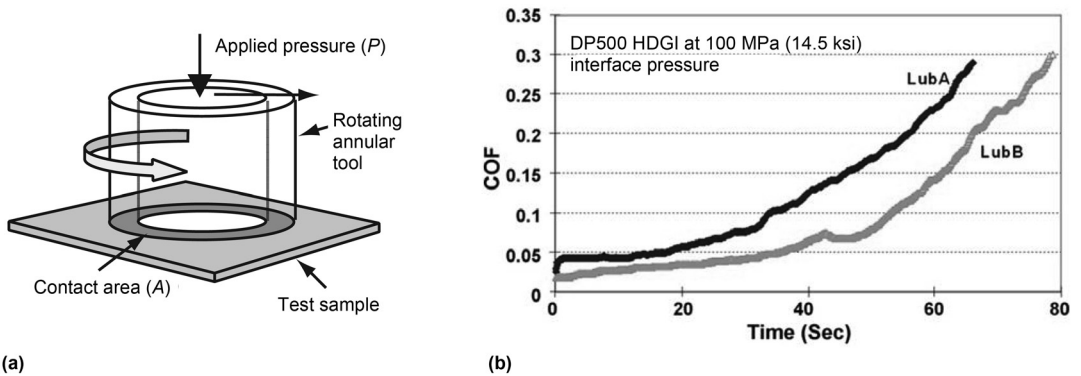


Fig. 16.22 Twist compression test (TCT). (a) Schematic of the test. (b) Sample output of lubricant evaluation using TCT. COF, coefficient of friction. Source: Ref 16.65

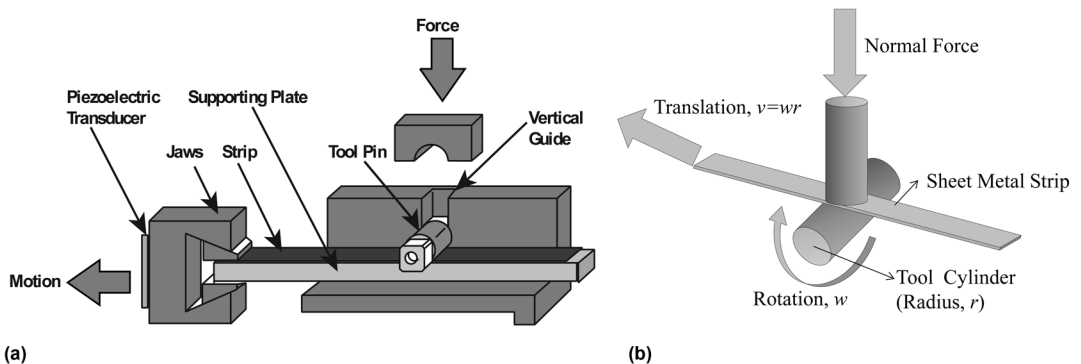


Fig. 16.23 Strip reduction tests. (a) As described by Ref 16.66. (b) Cylinder-on-strip test. Source: Ref 16.67

ture include, but are not limited to, the part forming test (Fig. 16.24a), the strip drawing/ironing test (Fig. 16.24b), the cup drawing test, and the drawbead simulator (Ref 16.2, 16.8, 16.69).

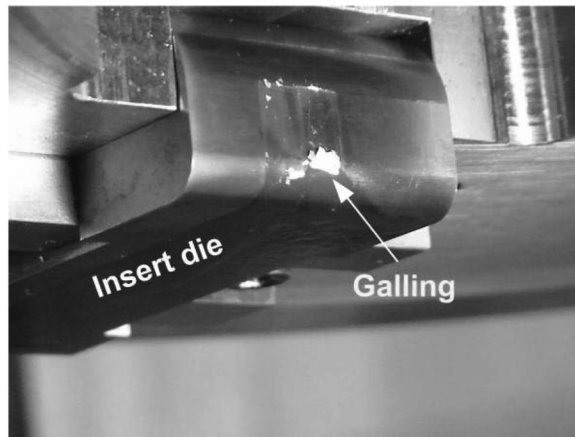
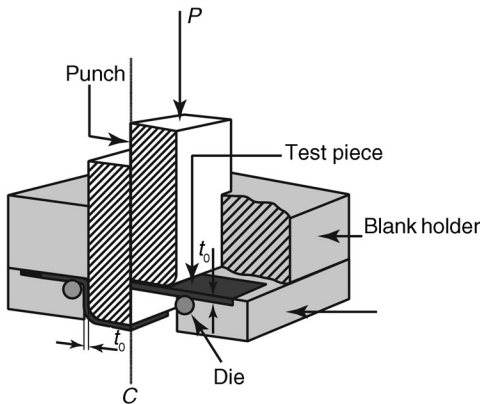
The forming tests are conducted either up to a certain number of pieces or until wear/galling or scratches on the workpiece are observed. In the former method, the number of parts produced without defects is an indication of tool performance. These tests can emulate the real production conditions as closely as possible, provided that parameters such as press speed, contact pressure, and lubrication are close to values used in actual production lines (Ref 16.8, 16.51). In the latter method, the surface area, where galling occurs, is measured. Change in surface roughness, as well as increase in forming load or friction coefficient, may also indicate galling.

16.6 Guidelines for Selecting Tool Materials, Treatments, and Coatings

Using the test methods explained earlier, many researchers and tool material companies have published guidelines for selecting tool materials, treatments, and coatings. These are best divided into three main classes.

Comparative Studies. These studies rank the tool materials by using a widely accepted wear test method but do not give quantitative information regarding tool life under practical stamping conditions. Table 16.8 gives a summary of recent studies on several steel grades. Note that the tests to rank these materials are not the same.

Benchmark studies give numeric comparison of tool life (number of good parts stamped) for a given tool material and coating. Forming tests are conducted until the stamped part has



(a)

(b)

Fig. 16.24 Forming tests. (a) Channel forming test. Source: Ref 16.8. (b) Visible galling on a strip drawing/ironing test. Source: Ref 16.2

Table 16.8 Ranking of tool materials, treatments, and coatings on several sheet materials

Reference	16.70	16.71	16.72	16.73
Sheet material	DC04 HDGI, draw-quality steel	AISI 304, stainless steel	DP980 HDGI, advanced high-strength steel	DP590 (at 400 °C, or 750 °F)
Test method	Strip reduction	Slider on sheet	Strip forming	Pin-on-disk
Best-ranked tool	D2 (1.2379) CVD TiC, TiN	Vanadis 6 + PVD DLC	DC53 + PVD TiCN	D2 + Belcoat SS
2nd	D2 PVD CrN	Vanadis 6 + nitriding	DC53 + PVD CrN	D2 + CVD TiC
3rd	D2 PVD TiN	Weartec full hardened	DC53 full hardened	D2 + TD (VC)
4th	D2 full hardened	Vanadis 6 full hardened	DC53 + PVD XNP	D2 + PVD CrN
5th	Gray cast iron + ion nitriding	Vanadis 6 + PVD TiN
6th	Gray cast iron + flame hardening
7th	Gray cast iron + Cr coating

CVD, chemical vapor deposition; PVD, physical vapor deposition; DLC, diamondlike carbon; TD, thermal diffusion

visible defects (i.e., scratches) or up to a certain predefined number of stampings.

A study done in Sweden (Ref 16.8) tested Sverker 21, Calmax, Sleipner, Weartec, Vanadis 6, and Vancron 40. The channel forming test (Fig. 16.24a) was done by a fully automated forming test setup that used a mechanical press with 55 strokes/min speed. The stamped parts were visually inspected for galling, and if scratches covered the entire part, the test was stopped. This test was done up to 50,000 strokes

(if a tool material did not show galling before). After the initial laboratory test, tool steels that did not show any sign of galling were selected for further production tests. Results from the first study give quantitative information about tool life in stamping DP600 (Fig. 16.25).

Another study was conducted (Ref 16.51) in which uncoated DP980 material was formed into a final part, as depicted in Fig. 16.26. A progressive die was used to emulate many stamping operations, such as forming, piercing,

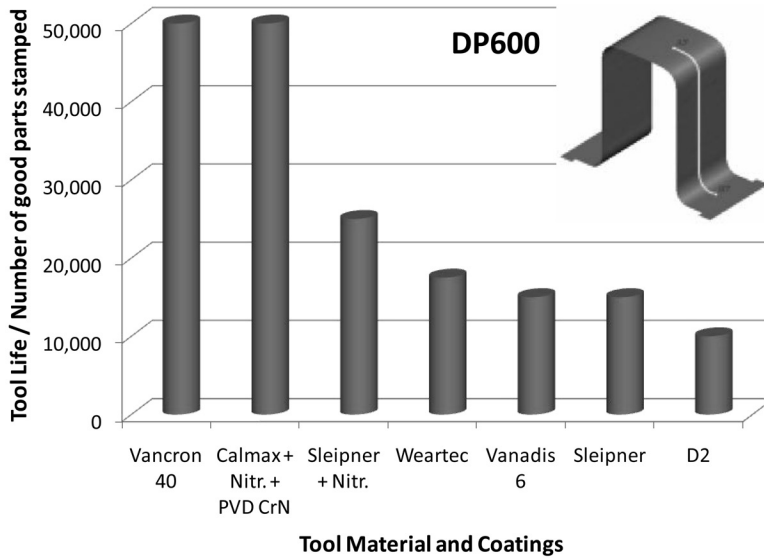


Fig. 16.25 Results of benchmark study by channel forming test with DP600. PVD, physical vapor deposition. Source: Ref 16.8

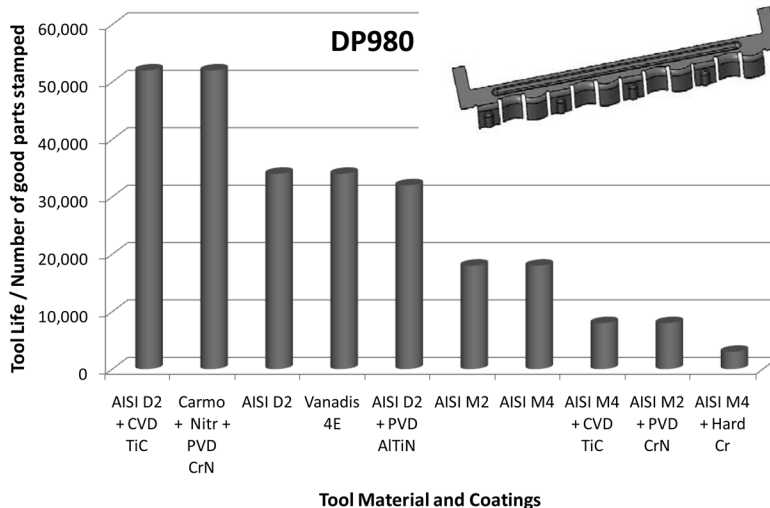


Fig. 16.26 Ranking of ten tool materials, treatments, and coatings, using a progressive die. CVD, chemical vapor deposition; PVD, physical vapor deposition. Source: Ref 16.51

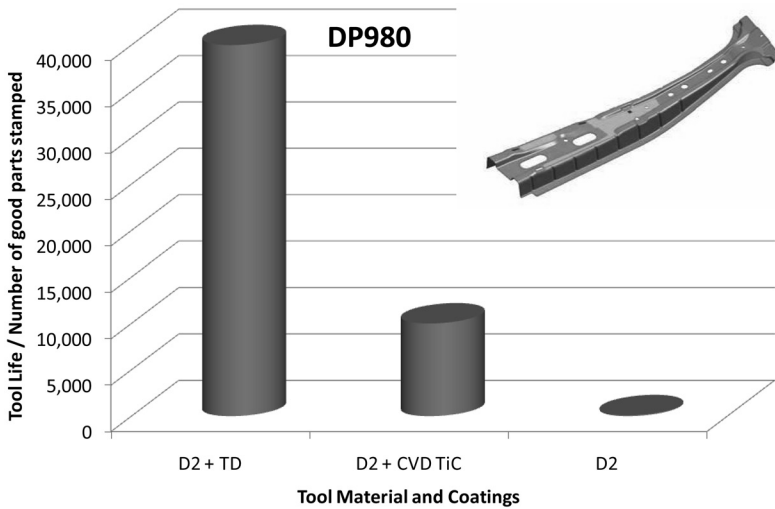


Fig. 16.27 B-pillar inner forming results for uncoated DP980. TD, thermal diffusion; CVD, chemical vapor deposition. Source: Ref 16.74

flanging, and trimming. Ten tool steels/coatings were tested, and the number of successful hits was used as an indication of performance.

As a benchmark, forming of a B-pillar inner also showed that conventional tool materials fail (due to heavy galling) with advanced high-strength steels as soon as a few hundred stampings are made. Figure 16.27 shows how the tool life of D2 changes with three different coatings (Ref 16.74).

Guidelines and Recommendations. Tool steel companies, industrial experts, and research facilities have come up with some recommended tool materials, treatments, and coatings for several workpiece grades (e.g., mild steel, advanced high-strength steel). Table 16.9 lists recommended coatings for forming and cutting advanced high-strength steel. Tables 16.10 and 16.11 show tool steel recommendations for forming sheet metal.

REFERENCES

16.1 “Standard Terminology Relating to Wear and Erosion,” G 40, ASTM International, 2005

16.2 H. Kim, “Tool Materials, Coatings and Lubricants to Reduce Tool Wear in Forming AHSS,” Workshop on Forming of AHSS, 2009

16.3 M.B.D. Rooij and D.J. Schipper, Analysis of Material Transfer from a Soft

Table 16.9 Recommendations of tool coatings for advanced high-strength steel

Application	Good	Better	Best
Piercing	PVD TiCN	PVD AlTiN PVD TiCrN	CVD TiC PVD solid-film lubricant
Blanking/ trimming	PVD TiCN	PVD TiCrN	PVD AlTiN
Forming/ drawing	PVD CrN	PVD TiCrN PVD AlTiN	CVD TiC TD PVD solid-film lubricant

PVD, physical vapor deposition; CVD, chemical vapor deposition; TD, thermal diffusion. Source: Ref 16.7

Workpiece to a Hard Tool, Part II: Experimental Verification of the Proposed Lump Growth Model, *J. Tribology*, Vol 123, 2001, p 474–478

16.4 B. Podgornik, S. Hogmark, and O. Sandberg, Proper Coating Selection for Improved Galling Performance of Forming Tool Steel, *Wear*, Vol 261, 2006, p 15–21

16.5 C. Constable, “Cost Reduction: By Improving Tool Life and Tool Performance,” Confederation of British Metalforming Event, 2008

16.6 A. Reiter, “Wear Protection for Punching/Forming Applications,” ISTMA Europe Conference, 2008

16.7 B. Janoss, Selecting, Using Tool Coatings to Stamp AHSS, *The Fabricator*, July 2008

Table 16.10 Tool steel selection for forming sheet materials

Type of sheet	Yield strength of sheet material		Tool steel grade	Base die		Inserts		Surface treatment(a)			
	MPa	ksi		Bar	Cast	Bar	Cast				
Soft/mild	<350	<50	Carmo	X	X	X	...	Not needed			
			Calmax	X	X	X	...				
			Sleipner	X	X	X	X				
High strength	350–570	50–85	Carmo	X	X	X	...	Optional/needed			
			Calmax	X	X	X	...				
			Caldie	X	X	X	X	Optional			
			Sleipner	X	X	X	X				
			Vanadis 4 extra	X	...	X	...				
			Extrahigh strength	570–800	85–115	Vanadis 6	X	...	X	...	Nitriding and PVD needed
						Carmo	X	X	X	...	
Calmax	X	X				X	...	PVD/CVD needed			
Caldie	X	X				X	X				
Sleipner	X	X				X	X				
Vanadis 4 extra	X	...				X	...				
Vanadis 6	X	...				X	...				
Vanadis 40	X	...				X	...				
Ultrahigh strength	>800	>115				Roltec	X	...	X	...	PVD/CVD needed
						Sleipner	X	X	X	X	
			Roltec	X	X	X	X				
			Weartec	X	...	X	...				
			Vanadis 4 extra	X	...	X	...				
			Vanadis 6	X	...	X	...				
			Vanadis 10	X	...	X	...				
			Vanadis 40	X	...	X	...				

(a) PVD, physical vapor deposition; CVD, chemical vapor deposition. Source: Ref 16.75

Table 16.11 Selection of tool materials for forming DP600, DP800, and DP1000

Tool	Sheet thickness (t), <1.2 mm (0.047 in.)		Sheet thickness (t), >1.2 mm (0.047 in.)		Comments
	Coated	Uncoated	Coated	Uncoated	
Sheet material: DP600					
Punch	GGG70L	GGG70L	GGG70L	GGG70L	Steel inserts at expected wear areas
Lower die Inserts	GG25	GG25	GG25	GG25	...
	Calmax + nitriding	Calmax + nitriding + PVD	Calmax + nitriding	Calmax + nitriding + PVD	All inserts are through hardened
Blank holder Inserts	Sleipner	Sleipner + PVD	Sleipner + nitriding	Sleipner + PVD	All inserts are through hardened
	GGG70L	GGG70L	GGG70L	GGG70L	Without drawbeads
	...	Calmax + nitriding + PVD	Calmax + nitriding + PVD	With drawbeads	
	...	Sleipner + PVD	Sleipner	Sleipner + PVD	With drawbeads
Sheet material: DP800					
Punch	Sleipner	Sleipner	Sleipner	Sleipner	Wrought and through hardened
	Calmax	Calmax	Calmax	Calmax	Through hardened
Lower die Inserts	GG25	GG25	GG25	GG25	...
	Sleipner + PVD	Sleipner + PVD	Sleipner + PVD	Sleipner + PVD	Wrought and through hardened
Blank holder	Sleipner 21 + PVD	Sleipner 21 + PVD	Sleipner 21 + PVD	Sleipner 21 + PVD	Through hardened
	Sleipner + PVD	Sleipner + PVD	Sleipner + PVD	Sleipner + PVD	Wrought and through hardened
	Sleipner 21 + PVD	Sleipner 21 + PVD	Sleipner 21 + PVD	Sleipner 21 + PVD	Through hardened
Sheet material: DP1000					
Punch	Sleipner	Sleipner	Sleipner	Sleipner	Wrought and through hardened
	Calmax	Calmax	Calmax	Calmax	Through hardened
Lower die Inserts	GG25	GG25	GG25	GG25	...
	Sleipner + PVD	Sleipner + PVD	Sleipner + PVD	Sleipner + PVD	Wrought and through hardened
Blank holder	Sleipner 21 + PVD	Sleipner 21 + PVD	Sleipner 21 + PVD	Sleipner 21 + PVD	Through hardened
	Sleipner + PVD	Sleipner + PVD	Sleipner + PVD	Sleipner + PVD	Wrought and through hardened
	Sleipner 21 + PVD	Sleipner 21 + PVD	Sleipner 21 + PVD	Sleipner 21 + PVD	Through hardened

PVD, physical vapor deposition. Source: Ref 16.8

- 16.8 M. Liljengren, K. Kjellsson, T. Johansson, and N. Asnafi, Die Materials, Hardening Methods and Surface Coatings for Forming of High, Extra High and Ultra High Strength Steel Sheets (HSS/EHSS/UHSS), *Proc. of the ID-DRG 2008*, 2008, p 597–604
- 16.9 H.C. Meng and K.C. Ludema, Wear Models and Predictive Equations: Their Form and Content, *Wear*, Vol 181–183, 1995, p 443–457
- 16.10 H. Hoffmann, C. Hwang, and K. Ersoy, Advanced Wear Simulation in Sheet Metal Forming, *CIRP Ann., Manuf. Technol.*, Vol 54, 2005, p 217–220
- 16.11 J. Thompson and M. Thompson, A Proposal for the Calculation of Wear, *Proc. of the 2006 International ANSYS Users Conference and Exhibition*, 2006
- 16.12 “Standard Test Method for Measuring Abrasion Using the Dry Sand/Rubber Wheel Apparatus,” G 65, ASTM International, 2004
- 16.13 E. van der Heide, E.D. Stam, H. Giraud, G. Lovato, N. Akdut, F. Clarysse, et al., Wear of Aluminium Bronze in Sliding Contact with Lubricated Stainless Steel Sheet Material, *Wear*, Vol 261, 2006, p 68
- 16.14 M. Liewald and J. de Souza, New Developments on the Use of Polymeric Materials in Sheet Metal Forming, *Prod. Eng.*, Vol 2, 2008, p 63–72
- 16.15 M. Mabie, “Metal Forming with FDM Tooling,” Fortus 3D Production Systems, Catalogue, 2010
- 16.16 C. DiRuggiero, Advanced Ceramics Excel in High-Speed Metalforming Tools, *Met. Form. Mag.*, Feb 2000, p 48–55
- 16.17 B. Lauwers, J.-P. Kruth, and W. Eeraerts, Wear Behaviour and Tool Life of Wire-EDM-ed and Ground Carbide Punches, *CIRP Ann., Manuf. Technol.*, Vol 54, 2005, p 163–166
- 16.18 T. Nakagawa, Advances in Prototype and Low Volume Sheet Forming and Tooling, *J. Mater. Process. Technol.*, Vol 98, 2000, p 244
- 16.19 *Forming and Forging*, Vol 14, *ASM Handbook*, 4th printing, ASM International, 1996
- 16.20 D. Piotrowski, “Index for Stamping Dies—Cast Materials,” NAAMS Standard, revised 2010
- 16.21 J.R. Newby, *Source Book on Forming of Steel Sheet: A Discriminative Selection of Outstanding Articles from the Periodical and Reference Literature*, American Society for Metals, 1976
- 16.22 B.F. Kuvin, Ford’s New DP 600 Die Standards, *Met. Form. Mag.*, Feb 2006
- 16.23 C. Svensson, “Cast Mix Tooling by CAMITO,” Novacast CD brochure, 2006
- 16.24 D. Young, “Cast Materials for Automotive Stamping Dies,” Uddeholm Automotive Tooling, Feb 1–4, 2006 (Sweden)
- 16.25 K.H. Grote and E.K. Antonsson, Ed., *Springer Handbook of Mechanical Engineering*, Springer, Würzburg, 2009
- 16.26 G.A. Roberts, G. Krauss, R. Kennedy, and R.L. Kennedy, *Tool Steels*, ASM International, 1998
- 16.27 “Standard Test Methods for Rockwell Hardness of Metallic Materials,” E 18, ASTM International, 2008
- 16.28 “Standard Test Method for Knoop and Vickers Hardness of Materials,” E 384, ASTM International, 2010
- 16.29 H. Qvarnström, Technical Note: A Mathematical Formula for Transformation between the Steel Hardness Scales of Rockwell C and Vickers, *J. Heat Treat.*, Vol 7, 1989, p 65–67
- 16.30 A.E. Tekkaya and K. Lange, An Improved Relationship between Vickers Hardness and Yield Stress for Cold Formed Materials and Its Experimental Verification, *CIRP Ann., Manuf. Technol.*, Vol 49, 2000, p 205
- 16.31 “A2 Cold Work Steel Data Sheet,” Uddeholm North America, 2000
- 16.32 “D2 Cold Work Steel Data Sheet,” Uddeholm North America, 2000
- 16.33 *Heat Treatment of Tool Steel*, 8th ed., Uddeholm, 2008
- 16.34 “AISI S7 Data Sheet,” Crucible Materials Corp., 2003
- 16.35 G.E. Totten, *Steel Heat Treatment: Metallurgy and Technologies*, Taylor and Francis, 2006
- 16.36 R.E. Smallman and A.H.W. Ngan, *Physical Metallurgy and Advanced Materials*, Butterworth Heinemann, 2007
- 16.37 J.R. Davis, *Surface Hardening of Steels: Understanding the Basics*, ASM International, 2002

- 16.38 “Heat Treatment of Ferrous Materials, Part 5: Surface Hardening,” DIN 17022-5, Deutsches Institut für Normung (German Institute for Standardization), 2000
- 16.39 J.C. Ion, Laser Transformation Hardening, *Surf. Eng.*, Vol 18, 2002, p 14–31
- 16.40 K. Wissenbach, Surface Treatment, *Tailored Light 2*, R. Poprawe, Ed., Springer, Berlin Heidelberg, 2011
- 16.41 “Laser Hardening of Large Tools and Complex Components,” Catalogue DE 507EN-1010, Oerlikon Balzers Coating GmbH, 2010
- 16.42 *Heat Treating*, Vol 4, *ASM Handbook*, 3rd printing, ASM International, 1995
- 16.43 E. Rolinski, G. Sharp, and A. Konieczny, Plasma Nitriding of Automotive Stamping Dies, *Heat Treat. Prog.*, Sept/Oct 2006
- 16.44 O. Salas, J. Oseguera, N. García, and U. Figueroa, Nitriding of an H13 Die Steel in a Dual Plasma Reactor, *J. Mater. Eng. Perform.*, Vol 10, 2001, p 649–655
- 16.45 X. Nie, L. Wang, Z.C. Yao, L. Zhang, and F. Cheng, Sliding Wear Behaviour of Electrolytic Plasma Nitrided Cast Iron and Steel, *Surf. Coat. Technol.*, Vol 200, 2005, p 1745–1750
- 16.46 E. Rolinski and G. Sharp, When and Why Ion Nitriding/Nitrocarburizing Makes Good Sense, *Ind. Heat.*, Aug 2005
- 16.47 J. Livezey, personal communication, 2009
- 16.48 J. Livezey, “High Performance Coatings for Stamping and Forming,” July 21, 2010 (Columbus, OH)
- 16.49 *Surface Engineering*, Vol 5, *ASM Handbook*, 2nd printing, ASM International, 1996
- 16.50 M. Masen, “Abrasive Tool Wear in Metal Forming Processes,” Ph.D. dissertation, University of Twente, 2004
- 16.51 D. Young, T. Mulholland, and M. Klein, “Investigation of Tooling Durability for Advanced High-Strength Steel,” Great Designs in Steel 2009, 2009
- 16.52 D. Mattox, *Handbook of Physical Vapor Deposition (PVD) Processing*, Noyes Publications, Park Ridge, NJ, 1998
- 16.53 H.M. Glaser, “The Application of Vanadium Carbide—The TD Process,” Fabtech International, Oct 14–17, 1991 (Rosemont, IL)
- 16.54 S. Hogmark, S. Jacobson, and M. Larsson, Design and Evaluation of Tribological Coatings, *Wear*, Vol 246, 2000, p 20–33
- 16.55 Y. Madorsky and M. Thompson, “New Developments in Wear-Resistance Tool Coatings for Stamping Applications,” Second Annual Stamping Journal Forum: Competing to Win with Less, May 11–12, 2004 (Detroit, MI)
- 16.56 U. Wiklund, J. Gunnars, and S. Hogmark, Influence of Residual Stresses on Fracture and Delamination of Thin Hard Coatings, *Wear*, Vol 232, 1999, p 262
- 16.57 L. Carreras, S. Bueno, and F. Montala, “Advanced Coatings for Automotive Industry Forming Dies,” Seventh International Conference of Trends in the Development of Machinery and Assisted Technology, 2003
- 16.58 T. Kacsich, When Size Matters: PVD Coatings on Large Tools for the Plastic Industry, *Coat. News*, No. 1, 2005, p 2–5
- 16.59 J. Destefani, Ramping Up PVD, *Products Finishing Magazine Online*, <http://www.pfonline.com/articles/0508tn1.html>, accessed April 15, 2010
- 16.60 H.O. Pierson, *Handbook of Chemical Vapor Deposition (CVD)*, Noyes Publications, Park Ridge, NJ, 1999
- 16.61 P.J. Blau and K.G. Budinski, Development and Use of ASTM Standards for Wear Testing, *Wear*, Vol 225–229, 1999, p 1159–1170
- 16.62 J. Schey, “A Critical Review of the Applicability of Tribometers to Sheet Metalworking,” SAE Technical Paper 970714, 1997
- 16.63 E. van der Heide, A.J. Huis in ‘t Veld, and D.J. Schipper, The Effect of Lubricant Selection on Galling in a Model Wear Test, *Wear*, Vol 251, 2001, p 973–979
- 16.64 “Standard Test Method for Wear Testing with a Pin-on-Disk Apparatus,” G 99, ASTM International, 2005
- 16.65 H. Kim, J.H. Sung, R. Sivakumar, and T. Altan, Evaluation of Stamping Lubricants Using the Deep Drawing Test, *Int.*

- J. Mach. Tools Manuf.*, Vol 47, 2007, p 2120
- 16.66 D.D. Olsson, N. Bay, and J.L. Andreasen, Prediction of Limits of Lubrication in Strip Reduction Testing, *CIRP Ann., Manuf. Technol.*, Vol 53, 2004, p 231–234
- 16.67 J. Cao, R. Zhou, Q. Wang, and Z.C. Xia, Strip-on-Cylinder Test Apparatus for Die Wear Characterization, *CIRP Ann., Manuf. Technol.*, Vol 58, 2009, p 251–254
- 16.68 J.L. Andreasen, N. Bay, and L. De Chiffre, Quantification of Galling in Sheet Metal Forming by Surface Topography Characterisation, *Int. J. Mach. Tools Manuf.*, Vol 38, 1998, p 503–510
- 16.69 M. Vermeulen and J. Scheers, Micro-Hydrodynamic Effects in EBT Textured Steel Sheet, *Int. J. Mach. Tools Manuf.*, Vol 41, 2001, p 1941–1951
- 16.70 C. Magny, “Tool Materials and Coatings: Optimization in Relation to the Stamping Behavior,” SAE 2002 World Congress, March 4–7, 2002 (Detroit, MI)
- 16.71 B. Podgornik, S. Hogmark, and J. Pezdirnik, Comparison between Different Test Methods for Evaluation of Galling Properties of Surface Engineered Tool Surfaces, *Wear*, Vol 257, 2004, p 843
- 16.72 H. Kim, “Prediction and Elimination of Galling in Forming Galvanized Advanced High Strength Steels (AHSS),” Ph.D. dissertation, The Ohio State University, 2008
- 16.73 K. Yamamoto, S. Kujime, T. Yasunaga, K. Akari, Y. Hosokawa, K. Takahara, et al., Application of Innovative PVD Coating to Stamping Dies for Processing Ultra-High Tensile Strength Steel Sheets, *SAE Int. J. Mater. Manuf.*, Vol 2, 2009, p 461–464
- 16.74 A. Mihail, M. Rozdik, and G. Nadkarni, “Design and Manufacturing a DP980 B-Pillar Inner for the GM Chevy Equinox/Pontiac Torrent,” Great Designs in Steel 2007, 2007
- 16.75 O. Sandberg and B. Johansson, “Tool Steels for Blanking and Forming—New Developments, Recent Advances in Manufacture and Use of Tools and Dies and Stamping of Steel Sheets,” Oct 5–6, 2004 (Olofström, Sweden)

Index

- 90° V-bend test, 116(F)
- 22MnB5
 - B-pillar simulation, 143(T)
 - chemical composition, 135(T)
 - coatings for oxidation prevention, 153–154
 - continuous cooling transformation diagram, 135(T)
 - flow-stress data, 135–136(F), 137(F)
 - friction coefficient, 138, 139(F)
 - galvanized, 154
 - hat shape simulation, 145–147(F)
 - induction heating, 149
- 2006 Pontiac Solstice, 173

- A**
- ABAQUS-Standard, 52(T)
- abrasive wear, 11, 317, 319
- acceleration coil, 233(F)
- Adam Opel AG, 176–177(F)
- adapted Rice and Tracey criterion, 55, 56
- adaptive simulation (AS) approach, 204–205(F)
- adhesive wear, 119, 319
- adiabatic blanking, 12
- adiabatic phenomenon, 12, 228
- adiabatic shear bands, 12
- adiabatic softening, 12
- advanced high-strength steels (AHSSs)
 - anisotropy, 112, 114
 - anisotropy (r) of various steels, 113(F)
 - bake hardening, 110–111, 114
 - banana curve, automotive steels, 108(F)
 - Bauschinger effect, 111–112
 - Bauschinger effect factor with plastic strain, 112(F)
- BEND, 31
- blanking presses, 125
 - punch-die clearances, 125(T)
 - snap-through forces, 125
- conventional steels, comparison, 113–114
- cracks, 116
- DEFORM-2D, 116
- ductility, 107
- edge cracking, 116
- elastic modulus, 109–110, 114
- engineering stress-strain curves, 109(F)
- FEA, 27, 116, 118(F)
- FEM simulations, 54
- flow curves, 109(F)
- flow stress, 108–109
- forming
 - achievable height/punch stroke, 117(F)
 - angular stretch bend test, 117(F)
 - bending, 115(F), 116(F)
 - combined bending and stretching, 117(F)
 - deep drawing, 115–116(F)
 - flanging/edge stretching, 116–117, 118(F)
 - FLCs, 117–119
 - stretching, 114–115(F)
- forming force and energy, 122–124
 - energy in forming DP 600, 124(T)
 - flow-stress curves of DP 699, 123(F)
 - flow-stress curves of HSLA 450, 123(F)
 - forming force predicted by FE and actual measurement, 124(T)
 - press force and pad force required to form a part, 123(F)
- hole flanging, 38
- hydraulic cushions, 124
- initial prestrain, baking temperature, and baking time, compared, 111(F)
- instantaneous n -value between DP 600 and TRIP 600, 114(F)
- instantaneous n -value with engineering strain for DP 350/600, 109(F)
- instantaneous n -value with engineering strain for HSLA 350/450, 109(F)
- instantaneous n -value with engineering strain for TRIP 350/600 steels, 109(F)
- under loading, 113–114
- material models, 114
- materials for body-in-white parts, 107(F)
- mechanical behavior, 108–114(F)
- metallurgy and general characteristics, 108(T)
- overview, 107–108
- postnecking deformation, 108
- reverse loading, 114
- roll forming, 223
- springback, 25(F) (*see also* springback in AHSS)
- stamping process, 114
- strain rate, 112
- stretch bending, 33

- advanced high-strength steels (AHSSs) (continued)
 - tandem press lines, 124–125
 - temperature, 112–113
 - temperature, effect of, 114
 - tensile strength, 114
 - tool coating recommendations, 334(T)
 - tooling construction
 - with cast steel, 125–126
 - cast steel materials for stamping tools, 126(F)
 - monoblock design, 125(T)
 - with tool steel, 126
 - total elongation, 108(F)
 - total elongation versus UTS, 108(F)
 - transfer presses, 124(F)
 - die setup in a transfer press, 124(F)
 - slide actions, 124
 - tribology in forming (*see* Tribology in forming AHSS)
 - types, 107
 - unloading *E*-modulus with true strain, 111(F)
 - UTS, 108
 - yield strength, 114
 - Young's modulus with plastic strain, 110(F)
- aerospace industry
 - electrohydraulic forming, 232
 - joining, 242
 - rubber-pad forming, 162(F)
- Aida Engineering Ltd., 103(F)
- AIDA servo press (110 ton), 97(F)
- air bending, 20(F), 28(F)
 - advantage of, 27
 - BEND, 30–31(F,T)
 - bend allowance, 28–29(F)
 - bend deduction, 28–29(F)
 - mathematical model, 29–30(F)
 - minimum bend radius, 32(F,T)
 - online process control strategies
 - direct process control, 47
 - indirect process control, 47
 - overview, 46–47
 - process control strategies, comparison, 47
 - overview, 27–29
 - springback, 23(F), 24(F), 28, 31(F)
 - test fixture, 32(F)
 - tractrix die bending, 31(F)
- air conditioning technology, 232
- AIRAM Press Co. Ltd., 12
- AISI 8670, 220
- AISI D2, 220
- Akerstrom constitutive model for hot stamping, 142, 145
- Altair Hypermesh software, 52
- aluminum
 - density, 83
 - roll forming, 211, 223
 - UHS, 12
- aluminum alloys
 - applications, 101–102(F)
 - Chevrolet Malibu Maxx lift gate, 102(F)
 - deep drawing (*see* deep drawing)
 - explosive forming, 233
 - formability, 83
 - General Motors lift gate, 102–103(F)
 - high-velocity forming, 227
 - Mercedes inner door panel, 104
 - roll forming, 220
 - THF, 181, 182(T)
- aluminum alloys, specific types
 - 24S-T (2024-T4), 98
 - 24S-T86 (2024-T86), 98
 - 75S-T (7075-T6), 98
 - 3003-H, 84(F), 85(T), 86(F), 87(T), 88(F)
 - 5754-O, 99–101(F,T)
 - A5182, 172
 - A6061, 172
 - Al 2024, 30(T)
 - Al 3003-H111, 87(T)
 - Al 5086, 83
 - Al 5182, 86(F), 87(F)
 - Al 5182-O, 86(T), 87(F)
 - Al 5741, 86(F), 87(F)
 - Al 5754-O, 99–101(F,T)
 - Al 57-54-O, 99–101(F,T)
 - Al 6111, 86(F), 87(F)
 - Al 6260-T4, 185(T)
 - AlMg0.4Si1.2, 85, 88(F)
- aluminum alloys, warm forming
 - bulge (biaxial) test, 85
 - Al 3003-H111 bulge test data, 87(T)
 - overview, 84–85
 - true stress versus true strain curves, 88(F)
 - E*-modulus and yield stress comparison, 83(F)
 - mechanical behavior, 83–84
 - overview, 83
 - specific strength and specific stiffness comparison, 84(F)
 - tensile (uniaxial) test, 85
 - Al 3003-H111 test data, 85(T)
 - AL 5182-O test data, 86(T)
 - engineering stress versus engineering strain curves, 86(F)
 - engineering stress-strain curves of 5182-O, 87(F)
 - overview, 84
 - strain-hardening rate with temperature, 87(F)
 - strain-rate sensitivity exponent with plastic strain, 87(F)
 - true stress versus true strain curves, 86(F)
- aluminum bronze, 220, 318, 319
- aluminum sheets
 - 1050-series, 98(F)
 - 5754-series, 98(F)
 - 6016-series, 98(F)
- aluminum-magnesium alloy tubes, 172
- Al-Zn-coated steel sheet, 120
- American Iron and Steel Institute (AISI), 320(T)
- AMINO, 275–276(F)
- Amino Corporation, 173
- angular stretch bend test, 116(F), 117(F)
- anisotropy
 - AHSS, 112, 113(F), 114, 126
 - deep drawing, round and rectangular cups, 58(T)
 - FE simulation, stamping with progressive dies, 58(T)
 - FE simulation, warm sheet hydroforming, 172(T), 173
 - springback, 22, 23(T), 66, 126, 220

state of stress, 21(T)
 THF, 182, 206
 antigalling properties, 121
 appliance industry
 clinching, 293
 warm forming, 96–97
 Aquadraw module, 169–170
 arc welding, 215
 Archard's equation, 320, 330
 ARGUS, 309–310, 311
 ASEA (ABB, Sweden), 160
 ASTM A36, 30
 ASTM A572 high-carbon steel, 83
 ASTM A1011 DS type B, 56
 ASTM B 557M-94, 84
 ASTM E 21 09, 84
 ASTM G 99, 332(F)
 ASTM 8613, 220
 atomistic deposition processes, 324–325
 austenite
 B-pillar simulation, 143
 continuous cooling transformation diagram, 135(T)
 hat shape simulation, 145
 high-temperature forming simulation, 142
 quenching temperature history, 146(F)
 through hardening, 320–322(F)
 22MnB5, 135
 Auto Crown, 45
 Auto Steel Partnership, 175–176
 AUTOFORM
 loading paths, 202
 progressive die design, 81–82
 AUTOFORM-Explicit, 52(T)
 AUTOFORM-one step, 52(T)
 automotive industry
 aluminum alloys, 101–102(F)
 clinching, 293
 electrohydraulic forming, 232
 high-strength steels, 53
 hole flanging, 38
 hot stamping, 133
 joining, 242
 magnesium alloys, 101–102(F)
 roll forming, 223
 THF, 179, 180(F)
 warm forming, 96–97
 automotive parts
 hemming, 39
 SHF-D, 162, 164(F)
 SHF-P, 167
 stretch bending, 32
 THF, 179
 warm SHF-D, 172
 AZ31-O, 90(F)

B

backing pads, 34, 35(F)
 bainite, 107, 113, 135(F), 136, 143
 bake hardening, 110–111(F)
 banana curve, 108(F)

Bauschinger effect, 111–112(F)
 Bauschinger effect factor (BEF), 112(F)
 Behrens model for hot stamping, 142
 BEND
 AHSS, 31
 aluminum 2024, 30(T)
 bend allowance, prediction of, 30
 bent sheet final dimensions, 30(F)
 low-carbon steels, 31
 overview, 30
 predicted and measured punch stroke values, 31(T)
 punch stroke versus springback angle, 31(F)
 springback, 30–31(F)
 bend die, 187, 189, 190(T)
 bending, 20(F), 35(F)
 AHSS, 115(F), 116(F)
 air bending (*see* air bending)
 bending under tension, 25–26
 contour flanging, 37, 38(F)
 draw bending, 187
 elastic recovery, 24(F)
 FEA analysis, 26–27
 hole flanging, 37–39(F)
 material-hardening models, 22(F)
 mechanics, 19–20
 overview, 19
 roll bending, 37(F)
 rotary bending, 35, 36(F)
 rotary draw bending, 187–189(F)
 sample part, 19(F)
 sheet bending, 20(F)
 simplified bending theory, 20
 springback, 22–23(F,T), 24(F), 25(F), 27
 springback, factors affecting, 23–25
 states of stress, 21–22(T)
 straight flanging, 35–37(F)
 strain, prediction of, 20–21(F)
 stress, prediction of, 21(F), 22
 stretch bending, 32–34(F)
 under tension, 25–26(F)
 terminology, 20(F)
 U-die bending, 34, 35(F)
 V-die bending, 26–27(F,T), 28(F), 34(F), 35(F)
 wipe die bending, 35–37
 bending angle, measuring
 angle measurement using four probes, 45(F)
 bending angle measurement, 44(F)
 bending with three sensors, 45(F)
 CCD cameras, 44(F)
 four-point measurement with sensor disks, 45(F)
 overview, 44
 sensor tool, 45(F)
 using contact method, 44–45(F)
 using non-contact method, 44(F)
 bending machines, 41(F)
 bending angle, measuring, 44–45(F)
 leaf bending machine, 47, 48(F)
 press brakes, 42 (*see also* press brake bending; press
 brake drive types)
 three-roll bending machine, 47
 bending moment, 22–23(F,T)

- biaxial tube bulge test, 183–184(F), 185(F)
- binder forces, 124
- bismuth alloys, 318
- blank holder
 - blanking, 2
 - riveting, 289
 - room-temperature sheet hydroforming, 170
 - SHF-D, 158
 - SHF-P, 165
- blank holder force (BHF)
 - AHSS, 129(T)
 - deep drawing round/rectangular cups, 57, 58
 - elastic blank holder, 166
 - hydroforming, 158
 - multipoint blank holder control, 165–166(F)
 - optimization, 59–60(F)
 - process simulation, 170, 171(F)
 - room-temperature sheet hydroforming, 158, 169(F), 170(F)
 - SHF-D, 158, 169–170(F)
 - SHF-P, 60, 162, 163(F), 166–171(F)
 - trunk lid-outer, 170(F)
- blanking, 1(F)
 - AHSS, 125
 - Aida Engineering Ltd. production line, 103(F)
 - breakthrough, 1(F), 2
 - burr, 4–5, 6(F)
 - burr length, 4–5(F), 6(F)
 - burr volume, 5(F)
 - damping systems, 10–11(F)
 - die geometry, 7(F)
 - blanking punch shapes, 7(T)
 - sheared dies, 7(F)
 - DP 590, 5(F)
 - electromagnetic forming, 242, 243(F)
 - FE simulations, 15–16
 - fine blanking, 12–14
 - force distribution, 2(F)
 - forces, 2–3
 - fracture, 2, 3
 - frictional forces, 2(F)
 - high-speed stamping, 8(F)
 - instantaneous shock, 8(F)
 - joining, 242
 - overview, 1
 - part edge characteristics
 - blanking clearance, effect of, 4
 - part edge quality, effect of material on, 5
 - punch-die clearance, 5(F)
 - tool wear, effect of, 4–5
 - zones, 4(F)
 - part-edge quality, 5(F)
 - phases, 1(F)
 - piercing, difference between, 1
 - presses, 10
 - process
 - breakthrough, 1(F), 2
 - contact of the punch, 1(F)
 - elastic deformation, 1(F)
 - load-stroke-curve, 3(F)
 - phases, 1(F)
 - plastic deformation, 1(F)
 - stripping, 1(F), 2
 - punch die clearance, 4, 5(F)
 - punch die clearance in high-speed stamping, 8
 - punch geometries, 3(F), 4(F)
 - punch life, factors affecting
 - clearance, 8
 - punch coatings, 7
 - punch materials, 7
 - punch misalignment, 8
 - punch point geometry, 8
 - punch rigidity during impact, 8
 - punch wear, effect of lubrication, 8–9(F)
 - punch-die clearance, 4, 5(F)
 - shearing (*see* shearing)
 - snap-through forces, 10–11(F)
 - springback, 2
 - stresses, 2–3
 - theoretical load-stroke curve, 3(F)
 - tool materials, 11
 - tooling
 - die geometry, 6–7
 - gibs, 10
 - pilots, 9–10(F)
 - punch geometry, 6
 - punch stagger, 7, 8(F)
 - spring stripper plate, 9(F)
 - stripper plate, 9 (F)
 - UHS, 12
- blanking dies, 10, 13, 242
- blanking presses
 - AHSS, 125
 - high-velocity mechanical forming, 233(F)
 - overview, 10
- blanking/piercing
 - AHSS, 125
 - case study, 54–56(F,T), 57(F)
- blanks
 - Aida Engineering Ltd. production line, 103(F)
 - aluminum, 263
 - B-pillar simulation, 143, 144
 - fine blanking, 12
 - flexform fluid cell process, 160
 - fluid cell presses, 164(F)
 - heating (*see* heating methods)
 - hot stamping, direct method, 133–134(F)
 - hydroforming, 157
 - KISF, 274
 - nanotechnology-based painting, 154
 - shear spinning, 266, 269(F)
 - shearing, 14
 - SHF-P, 160
 - spinning, 249, 255, 263
- body-in-white, 104, 107(F)
- boron alloyed steel 22MnB5, 133, 135(T). *See also* 22MnB5
- boron steel
 - hot dip galvanized, 154
 - hot stamping, 112
 - metallurgy and general characteristics, 108(T)
 - 22MnB5, 133, 135, 135(T)

- bottom dead center (BDC), 42, 44, 98(T), 103(F)
 - bottoming, 34(F), 36(F)
 - B-pillar
 - FEM of hot stamping, 143–145(F,T), 146(F)
 - hot stamping, 140
 - hot stamping simulation, 62–65(F,T)
 - inner forming results, 334(F)
 - tool materials, 334(F)
 - brass
 - roll forming, 211
 - THF, 181
 - UHS, 12
 - brazing, 215
 - breakthrough, 1(F)
 - brick-type elements, 26
 - bronze, 10, 12, 214
 - BTM Corporation, 294–295(F)
 - buckling, 140, 202
 - FRF, 222
 - roll forming, 219
 - bulge (biaxial) test, 84–85, 87(T), 89(F)
 - bulge tests. *See also* bulging
 - elliptical bulge test, 56
 - hydraulic bulge test (*see* hydraulic bulge test)
 - online material property evaluation, 311
 - setup, 184(F)
 - state of stress, 184(F)
 - 3003-H alloy, 85
 - 3003-H111, 87(T)
 - true stress versus true strain curves, 88
 - tube, 182, 183, 185(F)
 - VBT, 27(F), 53, 58(T), 59, 65
 - bulges, 261
 - bulging. *See also* bulge (biaxial) test
 - cracks, 263(F)
 - electrohydraulic bulging of tubes, 231, 232(F)
 - flow forming, 262(F)
 - hydraulic, 91
 - sheet bulging, 165
 - SHF-D, 158
 - SHF-P, 167, 168, 169
 - tube bulging simulation, 203
 - bullet (crimping), 299
 - burr
 - blanking, 4–5, 6(F)
 - HER, 39
 - high-speed tools steels, 11
 - burr heights, 12
 - burr length, 4–5(F), 6(F)
 - burr zone, 4
 - business card holder, 103–104(F)
- C**
- Calmax, 333
 - cartridge heaters, 93–94(F), 102(F)
 - case (surface) hardening, 322–324
 - flame hardening, 322–323(F,T)
 - induction hardening, 323
 - laser beam hardening, 323(F,T)
 - methods, 323(T)
 - quenching, 322–323
 - case-hardened carbon steel, 220
 - casing (crimping), 299
 - cast iron, 319
 - blanking, 11
 - definition of, 319
 - FCD700, 326(F)
 - galling, 319
 - grades, 319
 - wear, 319
 - cast iron dies, 122(F), 319
 - cast steels, 319–320(F)
 - cast steels, specific steels
 - Caldie, 319
 - Carmo (1.2333), 319
 - GP4M, 319
 - SKD12, 319
 - 0030, 319
 - 0050A, 319
 - cavitation, 228
 - ceramics, 242, 318
 - C-frame, 195, 303
 - C-frame press
 - force sensors, 302
 - frame mounting, 303
 - channel forming test, 333
 - charge-coupled device (CCD) cameras, 44(F)
 - Charpy test, 322(F)
 - chemical vapor deposition (CVD), 11, 121, 326(F), 327–329(F,T)
 - chipping, 153, 317(T), 320
 - chrome, 135(T)
 - chrome plating, 319, 323(T), 324, 325(F), 326(F)
 - chromic acid (CrO₃), 326(F)
 - chromium, 220
 - roll forming, 212
 - Cincinnati Machine Tools, 160
 - circular viscous pressure bulge test, 53
 - clamp die, 187
 - clamping
 - automatic, 45
 - bulge test, 84
 - die clamping force, 194
 - dieless clinching, 297
 - elastic clamping, 257
 - elastic tool clampings, 257
 - hydraulic quick clamping, 221
 - hydraulic system, 45
 - mechanical system, 45
 - overview, 45
 - process-machine interactions, 282
 - rotary draw bending, 187
 - SHF-P, 162
 - THF, 187, 192, 193, 194, 195, 197
 - clamping dies, 187
 - clamping force, 84, 85, 187, 194, 197, 282
 - clinched joints, 298–299
 - fatigue tests, 298–299
 - longitudinal and transverse clinching indentations, 298(F)
 - stress-number of cycles curves, 299(F)

- clinchling
 - advantages of, 293–294
 - applications, 293
 - BTM Corporation, 294–295(F)
 - conventional clinching dies, 296(F)
 - dieless clinching
 - FEA, 297
 - process, 296–297
 - schematic, 296(F)
 - dieless clinching at elevated temperatures, 297
 - dieless rivet clinching, 297
 - disadvantages of, 294
 - Eckold GmbH, 295–296(F)
 - FEA, 299, 300
 - with fixed die, 293(F)
 - flat anvil for dieless clinching, 296(F)
 - future trends
 - dieless joining, 296–297(F)
 - overview, 296
 - hydroclinching
 - operational sequence, 298(F)
 - process principle, 297–298
 - overview, 293–294
 - process
 - with fixed die, 293(F)
 - four steps, 293
 - techniques, 294
 - Tog-L-Loc, 294–295(F)
 - die used, 294–295(F)
 - process, 295(F)
 - stages, 294
 - TOX Pressotechnik GmbH, 294(F)
- closed-die system, 197, 199(F)
- clutch hub, 79–81(F)
- coatings. *See* plating and coating
- cobalt-molybdenum high-speed steels, 220
- Cockcroft-Latham fracture model, 34
- coefficient of friction (COF)
 - FEM simulations, 53
 - hot stamping, 138
- coin, 80, 81(F)
- coining
 - bottoming, 37(F)
 - fine blanking, 13
 - high-velocity forming, 239
 - mechanical press brake, 42
 - transfer die forming, 80, 81(F)
 - V-die bending, 34(F)
- commercial software, 52(T)
- complex-phase (CP) steels, 107, 133–134(F)
- compound dies, 13
- compression bending, 187, 188(F)
- computer numerical-controlled (CNC) machines, 254–255, 256, 273, 274, 276, 283
- computer-aided design (CAD), 52, 220–221, 276, 277(F), 281
- computer-aided manufacturing (CAM) system, 254, 255
- cone expansion test, 183(F)
- contact pressure
 - AHSS, 108, 119, 120
 - B-pillar simulation, 144
 - COF, 53
 - contact pressure, 317–318
 - FEA of warm forming of 5754-O, 100–101
 - forming tests, 332
 - galling, 317–318(T)
 - heat-transfer coefficients, 139, 141(F)
 - hot stamping, 63, 64
 - hot stamping dies, 149
 - large tools, 126
 - lubrication, 318
 - plastic deformation, 317
 - scratching tests, 330
 - SPR, 291
 - THF, 199
 - tool coatings, 317
 - tool wear, 317–318(T)
 - warm sheet hydroforming/issues in process simulation, 173
- continuous time-temperature transformation curve, 134–135(F)
- continuum theory, 191
- contour flanging, 37–39
 - defects, 38(F)
 - types, 38(F)
- convex and concave dies, 7(T)
- cooling ducts, 150–151, 152(F), 153(F)
- coordinate measuring machine (CMM), 61, 62(F)
- copper
 - high-velocity forming, 227
 - roll forming, 211
- copper alloys
 - blanking, 6(F), 8–9(F)
 - THF, 181
- copper-beryllium alloys, 238
- COPRA LaserCheck, 44(F)
- Coulomb friction coefficient, 77
- counterpressure pot, 162
- counterpunches, 167(F), 199(T)
- countersink, 201, 202(T)
- Cowper-Symonds coefficients, 143, 144(T)
- cracking
 - bending, 20
 - tool materials, 317
- cracks
 - acoustic emission sensors, 307
 - AHSS, 116, 118(F)
 - eddy current sensors, 308
 - failure modes, 268(F)
 - radial cracks, 253
 - SPR, 291
 - ultrasonic sensors, 308
- crank angle, 301
- crash forming, 128
- crash performance (hot-stamped components), 154
- creep, 41, 42(F)
- creep and grow, 41
- crimping, 299–300(F)
 - crimp quality, 300
 - FEM, 299
- critical damage value (CDV), 54

crosswise split dies, 197, 199(F)
 crowning system, 46
 cup drawing test, 332(F)
 Curie temperature, 148
 current pulsed power generators, 237(T)
 cut-off machines, 215

D

D2 steel, 220
 damping systems, 10–11(F)
 DC04, 115
 decoiler, 213(F)
 deep drawing
 AHSSs, 115–116(F)
 aluminum alloys, 98–99(F)
 process window for aluminum 5754-O, 99(F)
 business card holder, 103–104(F)
 Chevrolet Malibu Maxx lift gate, 102(F)
 experimental investigations, 99
 FEA Al 5754-O
 geometric data and input parameters, 100(T)
 punch load predictions, 100(F)
 General Motors lift gate, 102–103
 heated tool used in QPF, 102(F)
 industrial components, 101–102
 industrial processes, 101–102
 laptop cover, 104(F)
 LDR, 171
 magnesium forming production line, 103(F)
 Mercedes inner door panel, 104
 overview, 98–99
 pneumatic forming tooling, 102(F)
 process window for AZ31-O, 99(F)
 defense industry, 242
 DEFORM
 FEA of warm forming of 5754-O, 99–101(F,T)
 hot stamping simulation, 62, 64–65
 HSPR, 292
 springback and bending, 65–67(F,T)
 DEFORM-2D
 AHSS, 116
 progressive die design, 74
 springback and bending, AHSS, 66(T)
 stretch bending tests, 34
 V-die bending, 27, 28(F)
 warm sheet hydroforming, 172
 DEFORM-3D, 27, 28(F), 172
 deformation
 bulge test, 84(F)
 cyclic deformation, 280
 ISF, 280
 mechanics of (warm forming), 91–92(F)
 roll design, 215–216(F)
 shear spinning, 267
 dent resistance, 159
 destructive methods, 311
 detonation, 228–229
 diaphragm hydroforming press, 160
 die crashes, 304
 die inserts, 121, 197, 198–199, 201(T), 335(T)

dies. *See also* individual dies
 AHSS, 116
 air bending, 27
 blanking presses, 125
 bulge test, 84
 cast iron, 319
 conductive heating, 147
 die plug installation, 304
 double-action, 125
 fine blanking, 13
 heating techniques, 93, 94, 95(F)
 hot stamping, 64, 65, 149–150, 151–152, 154
 in-die mounting, 303
 ISF, 274, 276
 joining, 242
 mechanics of deformation, 91
 monoblock design, 125
 open/closed, 197
 press forces, effect of, 10
 press frame designs (THF), 194, 195
 progressive die design, 74, 81
 progressive die forming, 73
 proximity sensors, 305
 roll forming, 214
 rotary draw bending, 187
 SHF-D, 166
 springback, 126
 tandem press lines, 125
 THF, 179, 199, 203
 transfer presses, 124
 warm sheet hydroforming, 173
 X-Tec, 154
 DIN 8584, 249
 discretization, 51, 52
 discretizes, 69, 191, 283
 double bending, 36(F), 37
 double-action dies, 125
 double-pancake flat tool coil, 243
 draw bead test, 119
 draw bending, 187
 draw bending machine, 189(F)
 drawability
 AHSS, 115(F)
 DC04, 115
 DP 590, 115
 DP 980, 115
 LDR, 115–116
 nonisothermal warm forming, 92(F)
 TRIP 800, 115
 X-IP steel, 115–116
 drawbead simulator, 332(F)
 dual-phase (DP) steels
 flow stress, 108–109
 K-B equation, 119
 stretchability, 115(F)
 dual-phase (DP) steels, specific steels
 DP 440, 128–129
 DP 590
 blanking, 5(F), 56(T)
 blanking simulation, 54
 drawability, 115

dual-phase (DP) steels, specific steels, DP 590 (continued)
 forming velocity modification, 128
 ranking of, 332(T)
 springback, 128
 warm forming, 128–129
 DP 600, 117(F), 118(F)
 flow-stress curves, 122
 friction, 119
 galling, 119
 inconsistency of materials, 113
 tool material for forming, 121(T)
 true stress (flow stress), 123(F)
 DP 600-HDGI, 119
 DP 699, 122, 123(F)
 DP 780, 27(F,T), 66(T), 67, 110, 111, 115, 128–129
 DP 800, 121, 122(T), 125(T)
 DP 980
 B-pillar, 334(F)
 drawability, 115
 galling, 122
 tensile strength, 112–113
 warm forming, 128–129
 DP 980-GI, 121
 DP 1000, 121(T), 122(T), 335(T)
 ductile iron, 319
 ductility
 AHSS, 107, 108(T)
 bending, 19
 minimum bending radius, 31, 32
 part edge quality, 5
 roll forming, 212
 SPR, 291
 tool failures, 317(T)
 duplex coating, 325–326, 327(F)
 dwell time
 aluminum-silicon-base coatings, 154
 springback, 128, 129(F)
 springback, AHSS, 129(F)
 dwelling stage, 96
 DYNAMore GmbH, 143

E

Eckold GmbH, 295–296(F)
 edge cracking, 38, 39, 116
 edge stretchability, 38
 elastic blank holder, 166–167(F)
 elastic cushions, 165
 elastic modulus
 AHSS, 109–110(F), 111(F)
 ERC/NSM, 110
 FEM simulations, 68
 springback issues, 68
 TRIP steels, 109–110
 elastic springback, 19
 elastic-plastic deformation, 126
 electrical industry, 242
 electrohydraulic forming
 applications, 232(F)
 equipment, 230–231

overview, 228
 PPG, 230
 setups, 229(F)
 shock wave focusing, 232(F)
 spark gap arrangement, 231(F)
 electromagnetic forming (EMF)
 advantages of, 234
 applications, 239
 blanking, 242, 243(F)
 composite winding, 238
 conventional and electromagnetic processing, combined,
 242–245
 bending and electromagnetic calibration steps, 245
 deep drawing and electromagnetic sheet metal
 forming, 243(F)
 electromagnetic compression and hydroforming,
 244(F)
 extrusion and electromagnetic compression, 244(F)
 disadvantages of, 234
 environmental factors, 234
 equipment, 237–239
 current pulsed power generators, 237(T)
 electromagnetic compression using a fieldshaper, 239(F)
 separable tool coil, 238(F)
 forming, 242
 joining, 239–242
 examples, 240(F)
 force-fit joining, 240(F)
 metallic connection, 241(F)
 piercing, 242, 243(F)
 process principle, 234–235
 electrical conductivities of materials, 235(T)
 process variations
 pressure distribution and die cavity, 236(F)
 process principle, 236(F)
 process variants, 235–237(F)
 tube material, 235
 electromagnetic presses, 12
 electronics industry, 96–97
 elevated-temperature sheet hydroforming. *See* warm sheet
 hydroforming
 embossing, 213
 enabled plasma-assisted CVD, 328
 Engineering Research Center for Net Shape Manufacturing
 (ERC/NSM)
 circular viscous pressure bulge test, 53
 elastic modulus, 110
 evaluation of tool materials using different lubricants,
 121
 FEA of springback, 26–27(F,T)
 galling properties, DP 980-GI, 121
 progressive die sequence, 58
 room-temperature sheet hydroforming, 169
 stretch bending tests, 34
 V-die bending tests, 26
 warm sheet hydroforming, 172
 engineering strain, 21, 86(F), 109(F)
 Enutron, 45
 EP additives, 120
 ETG-100 steel, 314(F)

evolutionary algorithm (EA), 150–151(F)

explosive forming

applications, 232–233

contact operation, 229(F)

detonation velocities, 230

equipment, 231

explosive gases, 230

gas forming technique, 230

locations for, 231

overview, 228–230

propellant forming, 230(F)

stand-off operation, 229(F)

techniques, 229(F)

explosive gases, 230

extrados, 185, 187, 189

F

fabrication industry, 42

fatigue tests, 298–299(F)

ferrite

AHSS, 108(T), 109, 113

B-pillar simulation, 143

coupled thermomechanical and microstructure evolution,
141

through hardening, 321

22MnB5, 135(T)

ferrous materials, 319

fieldshaper, 234, 239(F)

final hemming (flattening), 40, 41(F)

fine blanking, 12–14(F)

blanking force (F_s), 12

counterforce (F_c), 12

flatness, 13

forces, 12–13(F)

moving and fixed punch systems, 14(F)

process, 13(F)

punch systems, 14(F)

stages, 13(F)

standard blanking, difference between, 12

V-ring force (F_R), 12

fine stamping. *See* fine blanking

finite element (FE) simulations, 15–16

blanking a circular part, 16(F)

part edge, 16(F)

part fracture, 16(F)

elastic stresses in punch, 16(F)

warm sheet hydroforming, 172–173(T)

finite element method (FEM)

bending and springback, 26–27(F,T), 28(F)

blanking/piercing (case study), 56(T)

crimping, 299

forming simulations, 51

ISF, 283–284

process design, 74

process sequence design, 76(F)

punch corner radii, 80(F)

punch diameters, 79(F)

punch riveting, 290

THF, 189, 192

finite element modeling (FEM)

interface friction coefficient, 173

interface heat-transfer coefficients, 173

finite-element (FE) programs, 221

finite-element analysis (FEA)

AHSS, 27

bending, 26–27(F,T)

clinch, 299, 300

forming force and energy, 123, 124(T)

progressive die design, 81–82

progressive die forming, 73–79(F,T), 80(F)

progressive die sequence, 58–59

springback, 26–27(F,T)

steps, 51–52

THF, 202

V-die bending, 26–27(F,T)

finite-element method (FEM) simulations

accuracy, factors affecting

comparison of reality and the simulation model, 68(T)

comparison of thickness profile, 68(F)

nonisothermal simulations (heat transfer coefficients),
69

overview, 67–68

shell elements, 69

springback issues—*influence of elastic modulus*, 68

thickness variations of the incoming material, 68–69

case studies (*see* finite-element simulations, case studies)

FEA, 51–52

FLCs, 54(F)

input to simulations

COF, 53

geometry (CAD model) for tooling, 52

material properties, 53

overview, 52

temperature, *influence of*, 53

output/predictions, 53

stamping defects, 53–54

thinning, 54(F)

Timoshenko's buckling theory, 54

finite-element simulations, case studies

blank holder force optimization

aluminum alloy A6111-T4, 60(F)

input parameters, 60(T)

objective, 59–60

optimized BHF variable in space and constant in time,
60(F)

output, 60

blanking/piercing

blanking process and experimental and simulation *see*,
55(T)

blanking simulation of DP590, 55(F)

objective, 54

obtained length of shear zone, 56(F)

output, 55–56

sheared edge, 57(F)

deep drawing of round and rectangular cups

input parameters, 58(T)

objective, 56–57

one-fourth finite-element model of round cup drawing,
58(F)

- finite-element simulations, case studies, deep drawing of
 - round and rectangular cups (continued)
 - output, 57–58
 - tool geometry, 57(F)
- hot stamping
 - B-pillar using PAMSTAMP, 65(F)
 - heat-transfer coefficient as a function of pressure, 64(F)
 - input parameters, 64(T)
 - objective, 62–64
 - output, 64–65
 - process parameters, 64(T)
 - section 3 of a B-pillar, 63(F)
 - temperature distribution at end of ten forming cycles, 65(F)
 - temperature distribution in the die, 65(F)
 - temperature distribution in the punch, 65(F)
 - thickness distribution along the curvilinear length, 64(F)
 - two-dimensional plane-strain simulation, 63(F)
- progressive die sequence
 - input parameters, 58(T)
 - objective, 58–59
 - progressive die sequence, 58(F)
 - thinning distribution, 59(F)
- sheet hydroforming with punch (SHF-P)
 - finite-element model, 61(F)
 - input parameters, 61(T)
 - objective, 60
 - output, 60–61
 - part profile comparison, 62(F)
 - predicted thinning percentage, 62(F)
 - thickness profile, 63(F)
- springback and bending of AHSS
 - inner bending angles under load obtained by DEFORM 2D, 66(F)
 - input parameters, DEFORM 2D, 66(T)
 - input parameters, PAMSTAMP, 66(T)
 - objective, 65–66
 - output, 66–67
 - springback angles obtained by PAMSTAMP, 67(F)
 - tool geometry of V-die bending, 66(F)
 - variation of loading and unloading apparent modulus for DP780 sheet material, 67(F)
- stretch bending, 33–34
- flame hardening, 322–323(F,T)
- flange arm, 22
- flange wrinkling, 168
- flanges, 38(F), 222, 223
- flanging
 - with counterpressure, 37(F)
 - overview, 19
 - springback-compensating methods, 36(F)
 - straight flanging, 35–37(F)
- flare-form deviation, 219–220
- flat anvil, 296(F)
- flatness, 13
- flexform fluid cell process, 160, 164(F)
- flexible roll forming (FRF)
 - buckling, 222
 - CAD system, 221
 - FEA, 222
 - flange, 222, 223
 - geometric parameters for profile definition, 222(F)
 - laser-assisted, 223
 - overview, 221
 - prototype profiles, 221(F)
 - tooling, 221–222
 - kinematics of flexible roll forming, 222(F)
 - mill prototype, 222(F)
 - products, 222(F)
 - TRB, 223, 224(F)
 - wrinkling, 222
- flow forming
 - applications, 265–266
 - aluminum automotive wheel, 266(F)
 - clutch housing, 266(F)
 - gas bottle neck, 266(F)
 - gas liner, 266(F)
 - ball shaped tools, 263, 265(F)
 - bulging, 261, 262(F,T), 263(F)
 - cracks, 263(F)
 - failure modes, 260–261(F)
 - flow-formed cylinder tolerances, 266(T)
 - forming forces, 260–261(F)
 - internal gear tooth form, 265(F)
 - machines, 262
 - counter rolls, 264(F)
 - necking-in machine, 264(F)
 - three forming tools, 263(F)
 - overview, 259
 - part properties, 265, 266(T)
 - process description, 259–261
 - backward flow forming, 260(F)
 - forward flow forming, 260(F)
 - process variations, 262
 - roller tools, 262–263, 265(F)
 - specialized tools, 262, 263(F)
 - split forming of flat disks, 264(F)
 - stress state, 260–261(F)
- flower diagram, 217–218(F)
- flywheel rotation, 42
- force signatures, 301
- formability
 - AHSS, 107, 108
 - aluminum alloys, 83
 - AZ31, 171
 - AZ31B, 86, 88(F)
 - EMF, 234, 235, 244
 - fracture, 3
 - high-velocity forming, 227
 - hole flanging, 37
 - hot stamping, 133, 134
 - lubrication, 312
 - magnesium alloys, 83, 89(F), 293
 - mechanical joining, 289, 290
 - mechanics of deformation, 91–92(F)
 - multipoint blank holder control, 166
 - online material property evaluation, 311
 - PAMSTAMP-2G, 56
 - QPF, 173
 - room/elevated temperatures, 90(F)

SHF-P, 158
 spinning, 257, 258
 SPR, 293
 stamping, 83–84
 temperature, effect of, 114
 tensile (uniaxial) test, 84
 THF, 181–207(F,T)
 TRIP steels, 113
 TWIP steels, 113
 warm deep drawing, 98, 102
 warm forming process, 91, 92, 93
 warm SHF-P, 171
 forming coil, 237–238
 forming limit curves (FLCs)
 AHSS, 117–119
 edge cracking, 38
 stamping (AHSS), 117–119
 forming limit diagram (FLD), 54
 forming tests, 331–332(F)
 forming velocity, 99, 128, 228(T)
 fracture
 blanking, 1
 hemming, 41, 42(F)
 ISF, 280
 laser-assisted ISF, 285
 SHF-P, 168
 stretch bending, 33
 stretch flanging, 38(F)
 free bending. *See* air bending
 free bulging, 158, 203, 204(T)
 fretting wear, 291
 fretting wear phenomenon, 291
 friction coefficient, 77, 136–138(F), 139(F), 173
 friction zones, 193, 194(F)

G

galling
 acoustic emission sensors, 307
 AHSS, 119
 aluminum alloys, 84
 benchmark studies, 333, 334
 DP 980, 122
 DP 980-GI, 121
 dry film lubricants, 120
 effect of temperature, 113
 factors affecting, 317–318(T)
 forming tests, 332(F)
 lubrication, 92, 215
 magnesium alloys, 84
 pin-on-disk test, 330
 roll material selection, 220
 strip reduction test, 331
 TCT, 330
 tool coatings, 121–122
 tool materials, 121, 317–318
 galling/wear tests
 forming tests, 331–332
 cup drawing test, 332(F)
 drawbead simulator, 332(F)
 part forming test, 332(F)

SDT test, 332(F)
 overview, 329–330
 scratching tests, 330(F)
 pin-on-disk test, 330(F)
 slider-on-sheet test, 330(F)
 strip reduction test, 331(F)
 TCT, 330–331(F)
 galvaannealing, 119
 German patent DE 1806283, 229(F)
 gibs, 10
 GOM GmbH, 310
 gooseneck punch, 45, 46(F)
 gray cast iron, 220, 319
 growing (grow), 42(F)

H

hard chrome plating, 324, 325(F), 326(F)
 hardening treatments. *See* tool hardening treatments
 heat transfer. *See also* heat-transfer coefficients
 air gaps, 151
 Behrens model, 142
 blank and die, between, 140
 conduction, 69
 convection and radiation, 144
 drawn part and die, between, 150
 FE simulations, 172
 FEM simulations, 69
 friction coefficient, 136, 137
 hot stamping, 62, 145(F)
 lubrication, 92, 93(F), 120
 press selection, 95
 preventing, 94
 sheet and the tools, between, 173
 tool dies, 149
 warm forming, 92
 warm SHF-D, 171
 heating methods
 conductive heating, 147–148
 induction coils, 148(F)
 induction heating, 148–149
 overview, 147
 resistance heating, 148(F)
 two-step induction heating device, 149(F)
 heat-transfer coefficients
 B-pillar simulation, 143, 144(T)
 FEA of warm forming of Al 57-54-O, 99–101(F,T)
 FEM simulations, 69
 hot stamping, 138–139, 140(F), 141(F)
 nonisothermal simulations, 69
 process simulation, 53
 simulation of B-Pillar using LS-DYNA, 143–144(T)
 warm forming Al 5754-O, 99–101
 warm sheet hydroforming/issues in process simulation,
 173
 hemming
 defects, 40–42(F)
 final hemming (flattening), 40, 41(F)
 geometric configurations, 41(F)
 hems, 39–40(F)
 overview, 19, 39–40

- hemming (continued)
 - prehemming operation, 40(F)
 - stages, 40(F)
 - types, 39(F)
- hemming steel (or upper die), 40(F)
- hem-out, 41, 42(F)
- hems, 39–40(F)
- high-strain-rate forming. *See* high-velocity forming
- high-carbon, high-chromium tool steel, 220
- high-energy-rate forming. *See* high-velocity forming
- high-pressure sheet hydroforming, 157
- high-rate forming. *See* high-velocity forming
- high-strength low-alloy (HSLA) steels, 109(F), 112, 122, 123(F)
 - HSLA 450, 122, 123(F)
- high-strength steel (HSS), 127(F), 223–224, 328(F)
- high-strength steels
 - automotive industry, 53
 - sheet hydroforming, 173
 - springback, 25(F)
- high-thermal-conductivity tool steels (HTCS)
 - HTCS-117, 151
 - HTCS-130, 151
 - HTCS-150, 151
 - HTCS-170, 151
 - HTCS-RE, 152
 - HTCS-Rod, 152
- high-thermal-conductivity welding alloys, 152
- high-velocity forming
 - advantages of, 227–228
 - approximate forming velocities/strain rates, 228(T)
 - classification of technologies, 227(F)
 - disadvantages of, 228
 - electromagnetic forming (*see* electromagnetic forming (EMF))
 - hydroforming (*see* high-velocity hydroforming)
 - mechanical forming (*see* high-velocity mechanical forming)
 - overview, 227–228
 - springback, 227
 - strain rates, 227
 - wrinkling, 227
- high-velocity hydroforming
 - electrohydraulic forming
 - applications, 232(F)
 - equipment, 230–231
 - overview, 228
 - setups, 229(F)
 - shock wave focusing, 232(F)
 - spark gap arrangement, 231(F)
- explosive forming
 - applications, 232–233
 - equipment, 231
 - overview, 228–230
 - propellant forming, 230(F)
 - techniques, 229(F)
- high-velocity hydropunching
 - applications, 233
 - equipment, 231(F)
 - hydropunch process, 231(F)
 - overview, 230
- high-velocity mechanical forming
 - electromagnetic compression process, 233(F)
 - electromagnetically-driven blanking press, 233(F)
 - equipment, 233–234
 - process principle, 233
 - process variations, 233–234
- Hill's yield index, 22
- hole expansion ratio (HER), 38–39
- hole expansion test, 38, 39(F), 116, 118(F)
 - AHSS, 118(F)
- hole flanging, 37–39(F)
- hole size, 1
- hoop test, 182, 183(F)
- hot dip galvanized (HDGI), 119
- hot dip galvanized (HDGA) coating, 119
- hot forming (HF) steels, 107
- hot stamping
 - case study, 61–65(F,T)
 - coatings (oxidation prevention)
 - aluminum-silicon-base, 154
 - effects of, 153–154
 - iron-zinc-base, 154
 - overview, 153
 - X-Tec—nanotechnology-based coating, 154
 - components manufactured using, 133(F)
 - constitutive model by Akerstrom, 142
 - constitutive model by Behrens, 142
 - coupled thermomechanical and microstructure evolution,
 - simulation of, 140–141
 - interactions, 141(T)
 - mechanical field, thermal field, and microstructure evolution, 141(F)
 - crash performance, 154
 - DEFORM, 62, 64–65
 - developed by, 133
 - direct method, 133–134(F)
 - finite-element simulations (*see* hot stamping, FE simulations)
 - heating methods
 - conductive heating, 147–148
 - induction coils, 148(F)
 - induction heating, 148–149
 - overview, 147
 - resistance heating, 148(F)
 - two-step induction heating device, 149(F)
 - high-temperature forming simulation, 142
 - hot stamping simulation, 62–65(F,T)
 - indirect method, 134(F)
 - material flow and process simulation, 139–140
 - nonisothermal simulations, 69
 - overview, 133
 - PAMSTAMP, 62, 65

- process variables
 - continuous cooling transformation diagram, 135(F)
 - cooling rate, 136, 137(F)
 - effect of temperature on mean friction coefficients, 138(F)
 - effect of temperature on mean friction coefficients, SPHC steel, 138(F)
 - flow-stress data, 136(F)
 - friction coefficient, 136–138
 - friction coefficient, μ , 139(F)
 - heat-transfer coefficient, 138–139, 140(F), 141(F)
 - modified cup drawing test, 138(F)
 - modified Gleeble 1500 system, 135, 136(F)
 - strain rate, 136(F), 137(F)
 - temperature transformation curve, 134–135
 - 22MnB5, 135–136(F,T)
 - USIBOR 1500, chemical composition of, 135(T)
 - tailor-welded blanks, 154
 - tool dies (*see* hot stamping dies)
 - 22MnB5
 - continuous cooling transformation diagram, 135(F)
 - overview, 133
 - process variables, 135–136(F,T)
 - warm forming, 129
 - weight reduction, 154
 - hot stamping dies, 149, 150, 151–152
 - with cast cooling channels, 151
 - characterization tests, 152–153
 - cooling channels, 150
 - drawn part, 150(F)
 - test geometry, 150(F)
 - cooling ducts, 151, 153(F)
 - cooling system, 150–151
 - cooling ducts, 152(F)
 - flow chart of the evolutionary algorithm, 151(F)
 - tool surface, 151(F)
 - die design, 149
 - die steels, 149–150
 - hard trimming of quenched parts, 152–153
 - tailor-made die materials, 151–152
 - hot stamping, FE simulations
 - B-Pillar using LS-DYNA
 - blank thickness and temperature results, 145(T)
 - contact heat transfer from the blank to the tool, 145(F)
 - contact heat-transfer coefficient as a function of interface pressure, 145(T)
 - convection, radiation, and effective heat-transfer coefficients, 144(T)
 - forming process, 144
 - heating the blank, 143
 - overview, 143
 - quenching process, 144–145
 - quenching temperature history, 146(F)
 - tools and FE model, 143(F)
 - transport from oven to press, 143–144
 - 22MnB5 (AUDI), 143(T)
 - 22MnB5 (DYNAmore GmbH), 144(T)
 - hat shape using DEFORM, 145–147
 - die geometry for hat shape, 146(F)
 - experimental and calculated forming force versus time, 147(F)
 - experimental and calculated temperature versus, 147(F)
 - simulation setup, 146(F)
 - steel strip, 146(F)
 - temperature measurement point, 146(F)
 - HWS steels, 152–153
 - hydraulic bulge test
 - AHSS, 114
 - aluminum alloys, 85, 88(F)
 - AZ31-O flow-stress curve, 90(F)
 - heating the sheet, 85
 - initial/pressurized sheet, 85(F)
 - magnesium sheets, 87
 - THF, 182–185(T)
 - hydraulic clamping cylinders, 162, 163
 - hydraulic cushions, 124
 - hydraulic presses
 - tool design, 96(F)
 - tooling design for warm forming magnesium, 96(F)
 - hydraulic shock dampers, 11
 - hydromechanical deep drawing, 157
 - Hydropulsor, 12
 - hydro-self-pierce riveting (HSPR), 291–293(F)
- I**
- impulse forming. *See* high-velocity forming
 - incremental sheet forming (ISF)
 - definition of, 274
 - forming limits, 278–280
 - cyclic deformation, 280
 - feed rate, 280
 - FLCs, 280(F)
 - friction, 280
 - localized deformation, 280
 - punch curvature, 280
 - side wall of a pyramidal test shape, 279(F)
 - strain rate, 280
 - stress state, 280
 - temperature, 280
 - through-thickness shear, 280
 - tool movements, 280
 - tool pressure, 280
 - triaxiality, 280
 - forming parameters
 - CAD/computer-aided manufacturing process chain, 277(F)
 - parameters, 278(F)
 - tool path, 277(F)
 - tool pitch, 277(F)
 - forming tools, 275, 276(F)
 - geometrical accuracy
 - adapted multistage forming strategies, 282
 - elastic effects, 281(F)
 - localized springback, 281(F)
 - orbital motions, 281(F)
 - overview, 281
 - process-machine interactions, 281(F), 282

incremental sheet forming (ISF), geometrical accuracy
 (continued)
 residual stresses, 282
 springback, 281(F)
 springback on removal of forming tool, 281–282
 springback on trimming, 281(F), 282
 springback on unclamping, 282
 hybrid process variations
 laser-assisted ISF, 285, 286(F)
 overview, 285
 stretch forming and ISF, 285(F), 286(F)
 KISF, 274–275(F)
 limit strains, 279–280
 machines, 275–276(F)
 multistage forming strategies, 282–283(F)
 pyramidal frustum with vertical walls, 283(F)
 single and multistage forming, 284(F)
 stiffening brace, 283(F)
 overview, 273
 parts manufactured, 273(F)
 plastic deformation, 277
 process mechanics, 277
 process modeling, 283–285
 process variations, 274
 sheet thinning, 277–278(F), 279(F)
 SPIF, 274(F)
 TPIF, 274(F)
 work flow, 277(F)
 induction hardening, 323(T)
 inserts
 cast iron dies, 319
 cast steels, 126, 319(F)
 die design, 201(T)
 DP 600, 335(T)
 DP 800, 335(T)
 DP 1000, 335(T)
 large tools, 126
 polymeric materials, 318
 prototyping dies, 198–199
 PVD coatings, 327
 THF, 197
 tool materials, 121(T), 122(F,T)
 tool steel selection, 335(T)
 instantaneous shock, 8(F)
 Institute for Metal Forming Technology, 102(F)
 Institute of Metal Forming and Casting, 150
 Institute of Tools and Forming, 151
 integration points, 69, 127
 intrados, 185, 186, 187, 189
 IRMCO 136-292, 120
 IRMCO 146-492, 120
 ISO PUNCH, 52(T)

J

Jektole punch, 8(F)
 Johnson-Mehl-Avrami equation, 142
 joining, 239–242
 applications, 242
 examples, 240(F)

force-fit joining, 240(F)
 impact velocity, 242
 mandrels, 240
 metallic connection, 241(F)

K

Keeler-Breizer (K-B) equation, 118
 kinematic incremental sheet forming (KISF), 274–275(F)
 Koistinen-Marburger equation, 141, 142

L

laptop cover, 104(F)
 laser beam hardening, 323, 323(F,T)
 leakage, 158, 165, 166, 167, 170
 leaking, 167, 168–169
 lengthwise split dies, 197–198, 199(F)
 Lenz's law, 239
 liftgate tooling, 59(F), 60(F,T), 174(F)
 light-emitting diode (LED), 305
 limiting dome height (LDH) test, 114–115
 limiting draw ratio (LDR)
 drawability, 115–116
 warm deep drawing, 99
 warm SHF-P, 171
 linear flow splitting, 223
 linear variable differential transformers (LVDTs), 89(F),
 304–305(F), 309
 lithium sulfate, 302
 LMC Inc., 12
 LMC SIP-15B, 12
 localized necking, 280
 lockbeads, 84, 102(F)
 Lorentz forces, 234, 237
 low-alloy tool steel, 220
 low-carbon steels (LCS)
 AHSS, 112
 bake hardening, 111
 BEND, 30
 bending, 19
 expansion percentage limits, 207(T)
 forces and stresses, 2
 material flow stress, 185(T)
 1006, 83
 roll forming, 220
 roll material selection, 220
 warm forming, 83
 LS-DYNA, 53
 Behrens model for hot stamping, 142
 B-pillar simulation, 143–145(F,T), 146
 ISF, 284
 loading paths, 202
 progressive die design, 81–82
 simulation of B-Pillar, 143–144(T)
 LS-DYNA version 971, 142
 lubricants
 dry film, 120
 EP additives, 120
 graphite, 92

- IRMC0 136-292, 120
- IRMC0 146-492, 120
- molybdenum disulfide, 92
- polytetrafluoroethylene (PTFE), 92
- urethane resin-containing silanol, 120
- wet, 120
- lubrication
 - acoustic emission sensors, 307
 - AHSS, 119-120
 - galling, 318
 - roll forming lines, 215
 - sensors, 312
 - tool wear, 318
 - warm forming, 92
- M**
- machine vision systems, 309-311(F)
- magnesium
 - density, 83
 - dieless clinching, 297
 - roll forming, 212, 223
 - tooling design for warm forming in a hydraulic, 96(F)
- magnesium alloys
 - applications, 101-102(F)
 - business card holder, 103-104(F)
 - deep drawing (*see* deep drawing)
 - formability, 83, 293
 - forming production line, 103(F)
 - laptop cover, 104(F)
 - Mercedes inner door panel, 104
 - roll forming, 212
 - warm sheet hydroforming, 172
 - warm SHF-P, 171
- magnesium alloys, specific types
 - AZ31, 285
 - AZ31B, 86, 88(F), 89
 - AZ31B-O, 85
 - AZ31-O, 87, 90(F), 99(F), 103-104(F)
 - AZ61, 85
 - AZ80, 85-86
 - HK31A-H24, 89
 - HM21A-T8, 89
 - HM31A-T5, 89
 - Mg-Al-Zn, 85
 - Z31B, 83
- magnesium alloys, warm forming
 - bulge (biaxial) test, 87, 89
 - AZ31-O flow-stress curve, 89(F)
 - formability at room and elevated temperatures, 89(F)
 - geometrical/process-related parameters, 85(F)
 - hoop, transverse and dome radii, 85(F)
 - initial and pressurized sheet, 85(F)
 - LVDT, 89(F)
 - overview, 84-85
 - submerged bulge test tooling, 89(F)
 - E*-modulus and yield stress comparison, 83(F)
 - mechanical behavior, 83-84
 - overview, 83
 - specific strength and specific stiffness comparison, 84(F)
 - strength asymmetry, magnesium alloy sheet, 89-90
 - tensile (uniaxial) test, 85-86
 - effect of strain rate on flow stress, 89(F)
 - overview, 84
 - temperature-dependent flow stress of AZ31B, 88(F)
 - test specimen, 84(F)
- magnesium wrought alloys, 227
- mandrels
 - flow forming, 259, 265(F)
 - joining, 240
 - shear spinning, 266-267, 269
 - spinning, 249, 251(F), 256
- MARC, 52(T)
- martensite
 - flow stress, 109
 - hole flange stretchability, 39
 - through hardening, 321-322
- martensitic steels (MS), 107
 - stretchability, 115(F)
- martensitic transformation, 64, 69, 134, 149
- MAT-244, 142, 144(T), 145
- MBW-K 1500, 153
- mechanical disk sensors, 44-45(F)
- mechanical joining
 - advantages of, 289
 - clinching (*see* clinching)
 - crimping, 299-300(F)
 - disadvantages of, 289
 - overview, 289
 - riveting (*see* riveting)
- mechanical presses, 95, 97(F), 125, 301
- membrane theory, 84, 184, 190, 191
- Mercedes inner door panel, 104
- Merklein data, 144
- mesh, 52, 54, 56, 127, 283, 292
- meshing, 52, 292
- Metal Forming Machine Tools (IFUM), 309
- Microsoft Excel-based calculator. *See* SHEETCOST
- minimum bending radius, 19, 32, 93(T), 115, 218
- modified cup drawing test, 138(F)
- modified Gleeble 1500 system, 135, 136(F)
- monoblock design, 125(F), 126, 198
- multiple-point control, 124
- multi-point cushion (MPC) systems, 162, 169
- N**
- Nakajima test, 280
- nanocasting technology, 151
- nanotechnology-based coating, 153
- nanotechnology-based painting, 154
- natural axial feed, 203
- necking
 - ISF, 280
 - spinning, 257-258
- Netronic, 12
- Newton's cooling law, 138-139
- nickel
 - roll forming, 212
 - UHS, 12

Nihon Kohsakuyu Co., Ltd., 153
 NIKE3D, 52(T)
 nitriding
 D2 tool steel, 324(F)
 DP 600, 122(T), 335(T)
 DP 800, 122(T), 335(T)
 DP 1000, 122(T), 335(T)
 duplex coating, 327(F)
 gas nitriding, 324
 ion (plasma) nitriding, 324, 326(F)
 ion-nitrided forming tool, 325(F)
 liquid (salt bath) nitriding, 324
 plasma, 121
 PVD coatings, 326
 ranking of, 332(T)
 tool hardening treatments, 324(F,T), 325(F)
 tool steel materials selection, 121(T)
 tool steel selection, 335(T)
 nitrogen cylinder cushions, 10–11
 nondestructive methods, 311
 nonferrous metals, 318
 nonmetallic materials, 318
 NUMIFORM, 68
 NUMISHEET, 68

O

off-center loads, 124
 oil canning, 218, 219
 Opel Astra, 199
 Opel Vectra, 173
 open-die system, 197, 199(F)
 optical/laser sensors, 44(F)
 OPTRIS, 52(T)
 organic coatings, 120
 oval spinning, 256, 257(F)
 overbending, 36(F), 37
 oxidation prevention
 aluminum-silicon-base, 154
 effects of, 153–154
 iron-zinc-base, 154
 overview, 153
 X-Tec—nanotechnology-based coating, 154

P

pad holder, 162
 PAMSTAMP, 52(T)
 hot stamping simulation, 62, 65
 ISF, 284
 loading paths, 202
 progressive die design, 81–82
 springback and bending, AHSS, 66(T)
 V-die bending, 27, 28(F)
 PAMSTAMP (2000), 59(F), 169–170
 PAMSTAMP-2G (2011), 53, 56
 pancake coils, 243
 pancake tool coils, 236
 percentage thinning, 54
 photodiodes, 305

phototransistors, 305
 physical vapor deposition (PVD), 121
 plating and coating, 324–327(F,T), 328(F)
 piercing, 1(F). *See also* blanking
 blanking, difference between, 1
 description of, 1
 electromagnetic forming, 242, 243(F)
 joining, 242
 load-stroke-curve, 3(F)
 theoretical load-stroke curve, 3(F)
 pilots, 9–10(F)
 pin-on-disk test, 120, 330(F)
 plasma-enhanced CVD, 328
 plastic deformation
 AHSS, 109
 air bending, 29
 bending under tension, 25
 blanking clearance, effect of, 4
 blanking process, 1
 burr zone, 4
 deep drawing, 331
 of the die, 199
 galling/wear tests, 330
 high-velocity forming, 227
 ISF, 273, 277, 280, 285
 roll forming, 215
 scratching tests, 330
 shearing force, 15
 through hardening, 320
 tool design considerations, 199, 201(T)
 tool failure, 317
 tool materials, 317
 transformation-induced plasticity, 142
 V-die bending, 34
 plating and coating
 AHSS, 334(T)
 CVD, 326(F), 327–329(F,T)
 coating thicknesses and process temperature, 326(F)
 defined, 327–328
 materials and properties, 329(T)
 enabled plasma-assisted CVD, 328
 hard chrome plating, 324
 Carmo die after 50,000 stampings, 325(F)
 cast iron FCD700, 326(F)
 organic coatings, 120
 PVD
 applications, 327(F)
 coating thicknesses and process temperature, 326(F)
 crack in PVD Layer, 327(F)
 materials and properties, 326(T)
 residual stresses, 327(F)
 PVD coatings, 324–327(F,T), 328(F)
 selection guidelines
 benchmark studies, 332–334(F,T)
 comparative studies, 332(T)
 ranking (ten coatings), 333(T)
 TD coating, 326(F), 329, 330(T)
 platings. *See* plating and coating
 pneumatic bulge tooling, 102(F)
 Poisson's ratio, 142, 143, 144(T)

- polytetrafluoroethylene (PTFE), 92
- Porsche Engineering, 175–176
- portable infrared analyzer, 315(F)
- pot pressure
 - room-temperature sheet hydroforming, 158
 - sheet bulging, 165
 - SHF-D, 158, 160
 - SHF-P, 60, 160, 162, 168, 170, 171(F)
- prebulging, 160–161, 162
- precision blanking. *See* fine blanking
- pre-coated materials, 220
- prepainted sheets, 220
- press bending, 187, 188(F)
- press brake bending
 - clamping, 45
 - crowning system, 46
 - fabrication industry, 42
 - press bakes, 42
 - tonnage, 42, 44
 - tooling, 45, 46(F)
- press brake drive types
 - alternating current (ac)-servo press brake, 44
 - drive types, 43–44
 - hydraulic press, 42–43(F), 44(F)
 - hydromechanical-servo drive, 43–44
 - mechanical press brake, 42
 - press brakes, 42
- press joining. *See* clinching
- pressure die, 187, 189
- pressure pot, 158, 165
- pressure vessels/containers, 37
- process simulation
 - advantages, 51
 - commercial codes, forming simulations
 - FEA steps, 51–52
 - FEM, 51
 - overview, 51
 - commercial software, 52(T)
 - commercial software, code features
 - dynamic explicit, 52
 - inverse (one-step) approach, 52
 - quasi-static implicit approach, 52
 - FEM simulations (*see* finite-element method (FEM) simulations)
 - objectives, 51
 - overview, 51
- process window, 167–168(F)
- production dies, 200(F)
- profile roll forming, 217
- progressive die design, 74, 77, 81–82. *See also* progressive die forming
- progressive die forming
 - case study I: progressive die design
 - BHF for first stage, 77
 - design parameters, flow chart, 76(F)
 - die corner radii, 78(T)
 - die diameter, 77–78(T)
 - drawing depth, 77–78(T)
 - existing automotive part, 74(F)
 - FEA predicted geometry, 75(F)
 - FEM and experienced-based methods, comparison
 - between, 78–79(F), 80(F)
 - final sequence, 78(F)
 - maximum thinning at first stage, 77(F)
 - new part geometry, 75(F)
 - overview, 74–75
 - process sequence design, 75–77
 - punch corner, 78(T)
 - punch diameter, 77–78(T)
 - punch diameter and wall thinning in progressive forming stages, 76(F)
 - simulation model, 77(F)
- case study II: transfer die forming of clutch hub, 79–81
 - clutch hub, 81(F)
 - coin the inside corner after flanging, 81(F)
 - coin the plate before flanging, 81(F)
 - current process—flanging and upsetting, 81(F)
 - three defects, 80(F)
 - three stages, 80(F)
- knowledge-based systems, 74
- overview, 73
- process design using FEA, 73–79(F,T)
- progressive die strip, 73(F)
- progressive die sequence, 58–59(F,T), 75, 78(F)
- progressive dies
 - FE simulation of stamping, 58
 - fine blanking, 13
 - fixed punch system, 13
 - progressive die design, 74
 - proximity sensors, 305
- prototyping, 164, 256, 273, 318, 319(F)
- prototyping dies, 198–199
- Pryer Machine Co., 160
- pullout test, 300
- pulsating pressure, 194(F)
- pulsed power generator (PPG), 230, 233(F), 237, 239
- punch
 - finite element (FE) simulations, 15–16(F)
 - mechanics of deformation, 91–92(F)
 - shearing, 14(F)
 - SHF-P, 165
 - systems (fine blanking), 13, 14(F)
 - warm SHF-P, 171
- punch (blanking)
 - blanking force, 2, 3
 - blanking presses, 10
 - compressive stress, calculating, 2
 - contact of, 1(F)
 - elastic deformation, 1(F)
 - high-speed stamping, 8
 - Jektole punch, 8(F)
 - lubrication, effect on punch wear, 8–9(F)
 - misalignment, 8
 - plastic deformation, 1(F)
 - punch geometries, 4(F), 6
 - punch life
 - clearance, 8
 - punch coatings, 7
 - punch materials, 7
 - punch point geometry, 8

- punch (blanking) (continued)
 - punch profiles, 3(F)
 - punch shapes, 7(T)
 - punch stagger, 7, 8(F)
 - rigidity during impact, 8
 - shearing, 1(F)
 - stripper plate, 9(F)
 - stripping, 1(F), 2
 - UHS, 12
- punch corner radius, 4, 61, 75, 78, 158
- punch point geometry, 8
- punch stagger, 7, 8(F)
- punch velocity
 - Al 5754-O, 99(F)
 - AZ31-O, 99(F)
 - blanking/piercing, 55(T)
 - deep drawing, 98
 - high-velocity mechanical forming, 233
 - magnesium alloy sheet, 99
 - magnesium AZ31-O, 99(F)
 - progressive die design, 77
 - SHF-P, 61(T)
 - springback, 129(F)
 - UHS, 12
- punch wear, 8–9(F), 10
- punch-die clearance, 4, 5(F), 8(F), 9, 22, 125(T)

Q

- quartz, 302
- quenching
 - B-pillar simulation, 144–145, 146(F)
 - case (surface) hardening, 322–323
 - case hardening, 322–323
 - induction hardening, 323
 - laser beam hardening, 323
 - self-quenching, 322–323
- quick die-change mechanism, 173
- quick plastic forming (QPF), 102–103(F), 173, 174(F)
- Quintus fluid cell presses, 164(F)

R

- radial cracks, 253
- ram bending, 187, 188(F)
- recoil, 41, 42(F)
- relief valve, 158
- residual stresses
 - bending, 19
 - flare defect, 220
 - ISF, 282, 283
 - progressive die forming, 73
 - PVD, 327(F)
 - PVD coatings, 326–327(F), 328(F)
 - roll forming, 220
 - springback, 126
- retained austenite
 - AHSS, 107, 108(T), 113
 - through hardening, 320–322
 - TRIP steels, 109

- reverse tonnage. *See* snap-through forces
- riveting
 - HSPR, 291–293
 - damage value distribution, 293(F)
 - DEFORM, 292
 - effective stress distributions, 292(F)
 - operational sequence, 292(F)
 - SPR, difference between, 293
 - overview, 289
 - punch riveting, 289–290(F)
 - rivets, 289
 - self-piercing riveting at elevated temperatures, 293
 - SPR, 290–291(F), 293
- rivets, 289
- robots, 275(F), 276
- rocker die, 35
- Rockwell B (HRB) scale, 320
- Rockwell C (HRC) scale, 320
- Rockwell hardness, 320, 321(F), 322(F)
- roll bending
 - bending of the ends, 37
 - overview, 37(F)
 - three-roll bending, 37(F)
- roll forming
 - AHSS, 223–224
 - applications, 212
 - branched profiles, 223, 224(F)
 - CAD roll form design, 220–221
 - ceramic coating, 220
 - defects in parts, 218–220(F)
 - future of, 224
 - HSS, 223–224
 - line speed, 211
 - linear flow splitting, 223
 - longitudinal bow, 219
 - longitudinal strain, 219
 - materials processed, 211
 - metal-nonmetal composites, 212
 - mill configurations, 214(F)
 - nitriding, 220
 - overview, 211–212
 - prefinished materials, 212
 - product classification, 211
 - product examples, 212(F)
 - recent developments
 - branched profiles, 224(F)
 - flexible roll forming, 221–223(F)
 - new materials, 223–224
 - overview, 221
 - tailored rolled blank, 224(F)
 - variable strip geometries, 223
- roll design
 - longitudinal bending, 216(F)
 - overview, 215
 - principles of, 215–216
 - real behavior of bending zone, 216(F)
 - strip width calculation, 216–217
 - theoretical approach, 216(F)
- roll forming lines, 212–215
- roll forming machine, 213(F)

- roll forming process, 211(F)
 - roll material selection, 220
 - split rolls, 220
 - springback, 220
 - strategies, 217–218
 - bending sequences, 217, 218(F)
 - constant arc length bending methods, 217(F)
 - constant arc length method, 217(F)
 - constant radius bending, 217(F)
 - constant radius method, 217(F)
 - flower diagram, 217–218(F)
 - vertical leveling strategies, 218(F)
 - Young's modulus, 220
 - roll forming lines, 212–215(F)
 - brazing, 215
 - cut-off machines, 215
 - defined, 212
 - double-head machines, 213–214(F)
 - drive units, 214
 - embossing, 213
 - forming closed profiles, 215
 - inboard-type machines, 213, 214
 - lubrication, 215
 - main control unit, 215
 - outboard machine, 213, 214
 - parts of, 212–213
 - peripheral units, 215
 - raft-type machines, 214(F)
 - roll forming machine, 213(F)
 - roll stands, 212–213
 - side roll stands, 214
 - soldering, 215
 - welding, 215
 - roll stands, 212–213, 214
 - roll wear, 220
 - roller dies, 213, 214
 - rotary bending, 35–37(F)
 - rotary draw bending, 187–189(F), 190(F,T)
 - bend die, 187
 - bending methods, 188(F)
 - clamp die, 187
 - draw bending machine, 189(F)
 - pressure die, 187–189
 - thickness distribution, 189, 190(F)
 - tube dimensions/material properties, 190(T)
 - wiper die, 189
 - rotating die, 35
 - rubber-pad forming, 160, 162(F)
- S**
- Saab Automobile AB, 133
 - salt baths, 321, 324, 329
 - sandblasted, 153–154
 - Saturn V moon rocket, 237
 - scaling, 150, 153, 284, 285
 - Schnupp hydromechanical press, 173
 - Schuler SMG, 175–176
 - scratching tests, 120, 330(F)
 - seamless tubes, 181
 - self-feeding (SF) approach, 202–204(F,T)
 - pressure curve and axial feed curves, 204(F)
 - simulations, 204(T)
 - self-feeding axial feed, 203
 - self-piercing riveting (SPR), 290–291(F)
 - sensors, 309
 - acoustic emission sensors, 307(F), 308(F)
 - contactless optical sensor, 309
 - displacement sensors, 304–307(F)
 - draw-in sensor, 309, 310(F)
 - eddy current sensors, 308
 - eddy-current-based material properties evaluation, 311
 - eddy current material testing, 312(F)
 - ETG-100 steel, 311, 313(F)
 - silver, 314(F)
 - flatpack proximity sensor, 306(F)
 - force sensors installation
 - die plug installation, 304(F)
 - frame mounting, 303(F)
 - in-die mounting, 303–304
 - normal and an incorrect tool setup, 304(F)
 - overview, 303
 - force-monitoring devices, 301
 - inductive proximity sensor, 305(F)
 - LED, 305
 - load cells, 302(F)
 - for lubrication, 312, 315(F)
 - LVDTs, 304–305(F), 309
 - machine vision systems, 309–311(F)
 - material flow measurement, 308–309(F), 310(F)
 - online material property evaluation, 311
 - overview, 301
 - photoelectric sensors
 - direct reflective, 306(F)
 - example application, 307(F)
 - opposed-mode, 305–306(F)
 - optical convergent, 306–307(F)
 - overview, 305
 - piezoelectric force sensors, 302
 - portable infrared analyzer, 315(F)
 - proximity sensors, 305(F)
 - reflex sensors, 306(F)
 - retroreflective sensors, 306(F)
 - roller ball sensor, 309(F)
 - strain gages
 - strain gage, 302(F)
 - strain gage load cell, 302(F)
 - Wheatstone bridge circuit, 302(F)
 - 3-D images, 310–311
 - through-beam or transmitted beam sensors, 305–306
 - tool breakage and flaws in parts, 307–308(F)
 - ultrasonic sensors, 307–308(F)
 - wrinkle sensor, 309, 310(F)
 - servo-driven presses
 - slide motion, 98(F)
 - springback in stamping, 128
 - servo-motor-driven presses, 95–96, 97(F), 98(F), 128
 - Seventh European LS-DYNA Conference, 143
 - shape roll forming, 217

- shear spinning
 - accuracy, 269(T)
 - applications, 269–270(F)
 - of a cone, 267(F)
 - of convex shapes, 267(F)
 - failure modes, 267–268
 - circular flaring, 268(F)
 - circumferential cracks, 268(F)
 - sufficient part, 268(F)
 - wrinkling, 267, 268(F)
 - machines, 268–269
 - dieless shear spinning, 269(F)
 - with two symmetric roller tool-heads, 269
 - overview, 266
 - part properties, 269
 - maximum angles, 270(T)
 - tolerances, 269(T)
 - preforms of the blank, 268(F)
 - process description, 266–267
 - process design, 268
 - conventional and shear spinning combination, 268(F)
 - preforms of the blank, 268(F)
 - process kinematic, 267(F)
 - tools, 269
 - wrinkling, 267
- sheared dies, 7(F)
- shearing, 14(F)
 - blade clearance, 15
 - hold-down force, 15
 - material properties, 15
 - overview, 14–15
 - penetration during, 15(F)
 - rake, 15
 - ram incline, 14(F), 15
 - shearing velocity, 15
- shearing stresses, 125
- sheet bending, 19(F), 20(F)
- sheet bulging
 - bulge height control techniques, 165(F)
 - die assembly with segmented elastic blank holder, 167(F)
 - elastic blank holder, 166–167
 - elastic cushion to form sharp corners, 165
 - multi-point blank holder control, 165–166
 - overview, 165
 - pressure pot with mechanical/elastic cushions, 165(F)
 - SHF-D, 166(F)
- sheet hydroforming
 - advantages, 158–160
 - components, 158(F)
 - counterpunches, 167(F)
 - elevated temperature application
 - heated tool, 174(F)
 - production forming cell, 174(F)
 - production parts, 174(F)
 - QPF at General motors, 173
 - QPF process, 174(F)
 - industrial applications, 173
 - limitations, 160
 - using liquid media, 157(F)
 - overview, 157
- presses
 - flexform fluid cell press, 164(F)
 - horizontal SHF-D press, 164(F)
 - Schuler active hydromechanical process, 163(F)
 - sheet hydroforming with punch short-stroke press, 163(F)
 - SHF-D, 162–164
 - SHF-P, 162
- process economics (*see* sheet hydroforming process economics)
- process simulation—room-temperature sheet hydroforming
 - application with die, 169(F)
 - application with punch, 169–170(F)
 - FE model of trunk lid-outer, 170(F)
 - optimization of SHF-P process, 170, 171(F)
 - overview, 169
 - results, 170(F)
 - validation, 170
- process variations
 - combination SHF-P process with regular stamping, 160–161(F)
 - double-blank hydroforming/parallel-plate hydroforming, 162
 - flexform fluid cell/rubber pad forming, 160, 161(F)
 - rubber forming, 162(F)
 - with punch (SHF-P), 159(F)
- room temperature applications
 - flexible multiforming system, 173
 - high-strength steels, 173
- room-temperature system, 157–158
- sheet bulging, avoiding (*see* sheet bulging)
- SHF-D, 158, 159(F)
- SHF-P
 - bulge formation, 168(F)
 - defects, 167
 - fracture, 168(F)
 - leaking, 168–169(F)
 - process limits, 167
 - process window, 167–169(F)
- tool design, 164–165
- warm sheet (*see* warm sheet hydroforming)
- sheet hydroforming process economics
 - case study I: rear door panel, 175–176(F)
 - case study II: fifteen body panel parts, 176–177(F)
 - outputs from calculator, 175(F)
 - overview, 173–174
 - SHEETCOST calculator inputs
 - general inputs, 174
 - process-related inputs, 174
- sheet hydroforming with die (SHF-D)
 - advantages of, 158–160
 - blank holder, 158
 - dent resistance, 159
 - description of, 157, 158
 - double-blank hydroforming/parallel-plate hydroforming, 162
 - free bulging, 158
 - limitations, 160
 - multi-point blank holder control, 165–166(F)

- pot pressure, 160
- presses, 162–164(F)
- room-temperature sheet hydroforming, 169(F)
- schematic, 159(F)
- strain hardening, 159
- sheet hydroforming with punch (SHF-P)
 - advantages of, 158–160
 - blank holder, 165
 - bulge formation, 168(F)
 - bulging, 167
 - case study, 60–61(F,T), 62(F)
 - counterpunches, 167(F)
 - defects, 167
 - description of, 158
 - economical, 160
 - elastic blank holder, 166–167(F)
 - fracture, 168(F)
 - leaking, 168–169(F)
 - limitations, 160
 - overview, 157
 - presses, 162, 163(F)
 - process, 159(F)
 - process economics (*see* sheet hydroforming process economics)
 - process limits, 167
 - process window, 167–169(F)
 - punch, 165
 - regular stamping operations, combining, 160–161(F)
 - room-temperature sheet hydroforming, 169–170(F)
- sheet metal spinning. *See* spinning
- SHEETCOST
 - calculator inputs
 - general inputs, 174
 - process-related inputs, 174
 - case study I: rear door panel, 175–176(F)
 - case study II: fifteen body panel parts, 176–177(F)
 - outputs from calculator, 175(F)
 - overview, 173–174
- shell elements, 69
- shell theory, 190
- shock wave
 - contact of the punch, 1
 - electrohydraulic forming, 228, 230–231, 232(F)
 - explosive forming, 228, 229
 - focusing, 323(F)
 - high-velocity forming, 228
 - high-velocity hydroforming, 228
 - punch rigidity during impact, 8
- shock wave hardening, 229
- shotblasting, 153–154
- Siebenwurst GmbH, 173
- Siempelkamp Pressen Systeme, 162
- SIMEX2, 52(T)
- simplified bending theory, 20
- simplified modeling approach (SMA), 278
- single-point incremental forming (SPIF), 274(F), 276, 277
- skin effect, 234–235, 238, 239
- slab, 84, 85(F)
- Sleipner, 333
- slide displacement, 301
- slider-on-sheet test, 330(F)
- slug ejection, 304, 305, 306(F), 307
- slugs, 6–7, 8
- snap-through forces, 10–11(F), 125
- soldering, 215
- sound waves, 307
- spark gap, 228, 230, 231(F)
- SPHC steel, 138(F)
- spinning. *See also* flow forming; shear spinning
 - accuracy, 259(T)
 - applications, 258, 259(F)
 - characterization of, 250(F)
 - DIN 8584, 249
 - failure modes, 250, 252–253(F)
 - radial cracks, 252(F), 253
 - tangential cracks, 252–253(F)
 - wrinkling, 252(F)
 - machine setup for spinning, 250(F)
 - machines, 254–256
 - hydraulic or electric drives, 256(F)
 - spinning by hand, 256(F)
 - teach-in, 257(F)
 - overview, 249
 - part properties, 258
 - process variations, 249(F)
 - spinning ratio in single-cycle spinning, 251(F)
 - stress states, 249–250
 - tool path planning, 253–254
 - involute tool path, 254(F)
 - parametrized tool path, 253(F)
 - process variables, a round cup, 255(T)
 - recommended feed rate, 255(T)
 - recommended spindle speed, 255(T)
 - spinning cycles, cup geometry, 255(F)
 - tool paths, composition of, 253(F)
- tooling
 - assisting tool devices, 258(F)
 - big parts, 257(F)
 - oval spinning, 256, 257(F)
 - roller-type tool designs, 257, 258(F)
 - teach-in, 256–258(F)
 - tool designs, 258(F)
- split rolls, 220
- splitting, 42(F)
- springback
 - AHSS (*see* springback in AHSS)
 - angle, 22–23
 - backing pads, 34, 35(F)
 - BEND, 31
 - bending, 20
 - bending (angle change), 126
 - bending angle, 44
 - blanking, 2
 - elastic recovery, 127(F)
 - EMF, 245
 - high-strength steels, 25(F)
 - high-velocity forming, 227
 - hybrid, 126
 - ISF, 281–282
 - membrane (wall curl), 126

- springback (continued)
 - overview, 126
 - roll forming, 220
 - straight flanging, 35–37(F)
 - tractrix die bending, 31(F)
 - tube bending, 186
 - twisting, 126
 - types, 126
 - wipe die bending, 22, 35–37(F)
 - Young's modulus, 23
- springback in AHSS
 - bottoming, 127–128
 - compensation for, 127
 - crash forming, 128
 - geometry-based compensation, 127
 - mechanics-based compensation, 127
 - forming velocity modification, 128
 - DP 590, 128
 - dwelt time, 129(F)
 - punch velocity, 129(F)
 - sheet thickness reduction, 129(F)
 - overbending/overforming, 127
 - channel cross-sectional design, 129(F)
 - overbending, 128(F)
 - overforming, 128(F)
 - part design, 129(F)
 - overview, 126, 127(F)
 - part or process modification
 - crash drawing process, 129(F)
 - drawing process, 129(F)
 - form drawing process, 129(F)
 - predicting, 126–127
 - warm forming, 128–129
- stainless steels
 - bend allowance, prediction of, 30
 - roll forming, 211, 220
 - SS 304, 185(F,T)
 - UHS, 12
- stamping
 - defects, 53–54
 - formability, 83–84
 - tool coatings, AHSS, 123(T)
 - wrinkling, 54
- stamping presses, 10, 215
- stamping tools, 317. *See also* plating and coating; tool
 - hardening treatments; tool materials
 - cast steel materials, 126(T)
 - cooling ducts, 151
 - cooling system, 150
 - failure mechanisms, 149
 - hardening, 320, 323(T)
 - heating system, 94(F)
 - ion-nitrided, 324, 325(F)
 - monoblock design, 125
 - overview, 317
 - PVD-coat inserts, 327
 - tool failure mechanisms, 317
 - ISF, 280
 - schematic, 184(F)
 - sheet hydroforming, 160
 - SHF-P, 167
 - tensile test, 84
 - THF, 189, 191, 193
- steel alloys
 - explosive forming, 233
 - THF, 182(T)
- steels
 - ETG-100 steel, 311, 313(F)
 - high-velocity forming, 227
 - roll forming, 211
- stick-slip phenomenon, 307
- straight-side press, 302
- strain
 - AHSS, 108–128(F,T)
 - aluminum alloys, 85(F,T), 86(F), 87(F,T), 88(F)
 - bending, 21–37(F,T)
 - dieless clinching, 297
 - flanging, 37–39(F)
 - flow forming, 262
 - force sensors, 303, 304
 - hemming, 39–42(F)
 - high-velocity forming, 227–244(F,T)
 - hot stamping, 135–143(F,T)
 - HSPR, 292
 - ISF, 280
 - machine vision systems, 309
 - magnesium alloy sheet, 90
 - prediction of, 20–21(F)
 - process simulation, 51–69(F,T)
 - progressive die design, 74, 75
 - roll forming, 218–222(F)
 - sheet hydroforming, 158–173(F,T)
 - sheet thinning, 277, 278
 - THF, 179–206(F,T)
 - tool/process design, 93
 - TRIP, 109
- strain hardening
 - AHSS, 108–126(F,T)
 - aluminum alloys, 85, 87(F)
 - bending, 22–30(F,T)
 - blanking, 2, 3
 - hot stamping, 136
 - magnesium alloys, 86
 - progressive die design, 74
 - roll forming, 220
 - SHF-D, 159
 - SHF-P, 159
 - THF, 185(T), 190(T), 206
- strain rate
 - AHSS, 112, 114
 - aluminum alloys, 85(T), 86(T), 87(F,T)
 - coupled thermomechanical and microstructure evolution, 140
 - flow stress, 89(F), 136(F), 142
 - high-velocity forming, 227, 228(T)
 - ISF, 280
 - magnesium alloys, 86–87(F)
 - process simulation, 53, 54

- THF, 191
 - TRIP, 112
 - 22MnB5, 135–136, 137(F), 143
 - TWIP, 112
 - warm forming, 90
 - warm sheet hydroforming, 172(T), 173
 - strain rates
 - aluminum alloys, 86(F), 87(F)
 - effect of, 112
 - EMF, 234, 235
 - high-velocity forming, 227, 228(T)
 - hot stamping, 63
 - magnesium alloys, 86
 - QPF, 102
 - sheet hydroforming process, 172
 - 22MnB5, 135, 143
 - stress
 - aluminum alloys, 86(F), 87(F), 88(F)
 - bending, 21(F), 22(F)
 - blanking, 2–3
 - LCS, 2
 - in punch, 16(F)
 - punch (blanking), 2
 - tensile (uniaxial) test, 87(F)
 - Young's modulus, 22
 - stretch bending
 - AHSS, 33
 - automotive parts, 32
 - FE simulations, 33–34
 - fracture, 33
 - tests, 33(F)
 - stretch bending tests, 33(F), 34
 - stretchability
 - AHSS, 114–115
 - DP steels, 115(F)
 - MS, 115(F)
 - stretching
 - AHSS, 114–115(F)
 - bending, 19
 - bending, combined, 116, 117(F)
 - BHF optimization, 59
 - flanging/edge stretching, 116–117, 118(F)
 - FLC, 38
 - ISF, 278, 282, 283
 - process mechanics, 277
 - shell elements, 69
 - SHF-D, 159
 - SHF-P, 158, 161(F)
 - springback, 127
 - tandem press lines, 125
 - transfer presses, 124
 - strip drawing (SDT) test, 332(F)
 - strip reduction test, 331(F)
 - stripper plate, 9(F)
 - strippers
 - fixed, 9
 - spring, 9(F)
 - stripping force, 9
 - urethane, 9
 - stripping, 2
 - stripping force, 9
 - submerged testing method, 87, 89(F)
 - surface decarburization, 153
 - surface quality
 - EMF, 234
 - flow forming, 259
 - hydropunch process, 233
 - manual spinning, 255
 - roller tools, 263
 - sheet hydroforming, 159
 - SHF-P, 160
 - spinning, 258
 - stamping tools, 317, 318
 - THF, 202
 - tool path planning, 254
 - Sverker 21, 333
 - Swift's law, 22
- ## T
- tailored rolled blanks (TRB), 223
 - taylor-welded blanks, 154
 - tandem press, 198(F)
 - tandem press lines, 124–125
 - tangential stresses, 250, 252–253(F)
 - tapers, 7(F)
 - teach-in panel, 256, 257(F)
 - tearing, 37, 53–54, 249, 312
 - temperature transformation curve, 134–135(F)
 - tempering, 320, 322(F)
 - tensile (uniaxial) test, 84–86(F,T), 87(F,T), 88(F), 89(F)
 - tensile test
 - AHSS, 110, 114
 - air bending, 32
 - aluminum alloys, 85(T), 86(T), 89
 - DP780, 67(F)
 - hot stamping, 142
 - magnesium alloys, 88(F)
 - online material property evaluation, 311
 - process simulation, 53
 - SHF-P, 170
 - THF, 182, 183(F)
 - warm sheet hydroforming, 172
 - tension, bending under, 25–26(F)
 - thermal conductivity
 - aluminum alloys, 93, 99
 - die steels, 149
 - as a function of temperature, 142
 - magnesium alloys, 93
 - nanocasting technology, 152
 - 22MnB5, 143(T), 145
 - thermal diffusion (TD) coating, 326(F), 329, 330(T)
 - thinning
 - FEM simulations, 54
 - percentage thinning, 54
 - SHF-P, 69
 - three-dimensional (3-D) simulations, 26, 27
 - three-point bending. *See* air bending
 - through hardening, 317(T), 320–323(F)
 - through-thickness shear, 280
 - ThyssenKrupp Steel, 153, 154, 173
 - TiCN, 121, 123(F), 325, 326(T), 327(F), 332(T), 334(T)

- Timoshenko's buckling theory, 54
- titanium
 - density, 83
 - roll forming, 212, 223
- titanium alloys
 - explosive forming, 233
 - high-velocity forming, 227
 - Ti-6Al-4V, 285
- Tog-L-Loc, 294–295(F)
 - die used, 294–295(F)
 - process, 295(F)
 - stages, 294
- tonnage signatures, 301
- tool coatings
 - AHSS, 119, 121–122, 123(T), 334(T)
 - blanking, 11
 - boronizing, 11
 - chemical vapor deposition (CVD) coating, 11
 - hard facing (nickel-base alloys), 11
 - hard-chromium coating, 11
 - nitriding, 11
 - physical vapor deposition, 11
 - TiC, 11
 - vapor deposition, 11
- tool dies. *See* hot stamping dies
- tool hardening treatments
 - case (surface) hardening, 322–324
 - flame hardening, 322–323(F)
 - induction hardening, 323
 - laser beam hardening, 323(F)
 - methods, 323(T)
 - quenching, 322–323
 - HRB scale, 320
 - HRC scale, 320
 - HV, 320
 - nitriding, 324(F,T), 325(F)
 - overview, 317(T), 320
 - Rockwell hardness, 320, 321(F), 322(F)
 - selection guidelines
 - benchmark studies, 332–334(F,T)
 - comparative studies, 332(T)
 - ranking (ten treatments), 333(T)
 - through hardening, 317(T), 320–321, 322(F)
 - Vickers hardness, 320, 321(F)
- tool materials, 319–320(F)
 - A2, 11
 - D2, 11
 - M2, 11
 - AHSS, 120–121(T)
 - background
 - dry sand/rubber wheel abrasion, 318(F)
 - galling, 317–318
 - tool failure mechanisms, 317
 - tool failures, 317(T)
 - tool life, prolonging, 317(T)
 - tool wear, 317–318
 - wear coefficient of several tool materials, 318(F)
 - burr, 11
 - carbides, 11
 - cast iron, 319
 - cast steels, 319–320(F)
 - cemented tungsten carbide, 11
 - classification of
 - ferrous materials, 319
 - nonferrous metals, 318
 - nonmetallic materials, 318
 - cobalt, 11
 - CPM 10V, 11
 - high-vanadium carbide powder metallurgy tools, 11
 - polymeric materials, 318, 319(F)
 - recommendations for forming
 - DP 600, 335(T)
 - DP 800, 335(T)
 - DP 1000, 335(T)
 - selection guidelines
 - benchmark studies, 332–334(F,T)
 - comparative studies, 332(T)
 - ranking (ten materials), 333(T)
 - tool steel selection, 335(T)
 - tool steels, 320(T)
 - tungsten, 11
 - tool steels, 319
 - AHSS, 126
 - as classified by AISI, 320(T)
 - D2, 324(F)
 - overview, 320
 - recommendations, 335(T)
 - selection guidelines, 335(T)
 - tool wear
 - AHSS, 108
 - die design, 201(T)
 - dieless joining, 297
 - dry film lubricants, 120
 - estimation of, 318(F)
 - factors affecting, 317–318(T)
 - FEA, 16
 - force sensors, 301
 - part edge quality, 4–5(F), 6(F)
 - scratching tests, 330
 - tool materials, 120(F)
 - tooling construction, 122(F), 125–126(F,T)
 - total elongation (EL), 108(F), 109, 112–113
 - TOX Pressotechnik GmbH, 294(F)
 - tractrix die bending, 31(F)
 - transfer die forming
 - overview, 73
 - transfer die set, 74(F)
 - transfer dies, 13, 73, 74(T), 79–81(F), 82, 83
 - transfer presses, 124(F)
 - transformation-induced plasticity, 142
 - transformation-induced plasticity (TRIP) steels, 107
 - at elevated temperature, 113
 - flow stress, 109
 - K-B equation, 119
 - strain rate, 112
 - TRIP 780, 109
 - TRIP 800, 113, 115
 - Tribology in forming AHSS
 - lubrication
 - dry film lubricants, 120

- overview, 119–120
 - wet lubricants, 120
- overview, 119
- tooling
 - surface treatment effects on tool wear, 120(F)
 - tool coatings, 121–122
 - tool coatings for stamping, 123(T)
 - tool material for forming DP 600, 121(T)
 - tool material for forming DP 800, 121(T)
 - tool material for forming DP 1000, 121(T)
 - tool materials, 120–121
 - tool steel materials selection, 121(T)
 - tool steels as inserts in cast iron die, 122(F)
 - U-channel drawing of dual-phase steels, 120(F)
- workpiece—sheet metal, 119
 - failures in forming AHSS/ultrahigh-strength steel, (F)
- tube bending
 - bending methods, 187, 188(F)
 - defects, 187
 - overview, 185
 - parts that require preforming, 186(F)
 - process characteristics, 185–186
 - rotary draw bending, 187–189(F), 190(F,T)
 - springback, 186
 - thickness distribution, 186(F)
- tube hydroforming presses
 - optimization of the integrated forming process, 197(F)
 - overview, 193
 - press frame designs, 194–197
 - production line, 194, 195(F)
 - productivity enhancement, 197(F)
 - tandem press, 198(F)
 - tube hydroforming press concepts, 196(F)
- tube hydroforming (THF). *See also* tube bending
 - advantages, 179–180
 - applications, 179
 - automotive industry, 179, 180(F)
 - characteristics, 193
 - classification of, 180–181(F)
 - design guidelines, 202, 205–206
 - classification of formability of tubes, 207(T)
 - expansion percentage limits, 206(T)
 - formulae for tube hydroforming, 206(T)
 - general guidelines, 206(T)
 - drawbacks, 180
 - examples, 180(F)
 - failures, 202, 203(F)
 - flow stress, 183–185
 - formability, 182–183
 - formability tests
 - biaxial tube bulge test, 183–184(F), 185(F)
 - cone expansion test, 183(F)
 - hoop test, 182, 183(F)
 - hydraulic bulge test, 182–183(F)
 - tensile test, 182, 183(F)
 - friction and lubrication
 - die-workpiece interface variables, 192(F)
 - overview, 192
 - friction and lubrication, parameters
 - increased interface pressure, 193(F)
 - increased sliding velocity, 194(F)
 - interface pressure, 192
 - parameters that influence, 193(F)
 - sliding velocity, 193
 - surface expansion/contraction, 192
 - friction zones, 193, 194(F)
 - materials for
 - aluminum alloys, 182(T)
 - overview, 181–182
 - steel alloys, 182(T)
 - mechanics, 189–192
 - process control limits, 190(F)
 - punch force components, 191(F)
 - simple part, 190(F)
 - state of strain on the bulge shape, 191(F)
 - overview, 179
 - presses (*see* tube hydroforming presses)
 - process sequence, 179(F)
 - seamless tubes, 181
 - as a system, 181
 - system components, 182(F)
 - tube bending (*see* tube bending)
 - welded tubing, 181–182
- tube hydroforming (THF) process design
 - AS approach, 204–205
 - adaptive simulation procedure, 205(F)
 - flow chart, 205(F)
 - failures, 203(T)
 - loading paths, 202
 - overview, 202
 - SF approach, 202–204(F)
 - pressure curve and axial feed curves, 204(F)
 - simulations, 204(T)
- tube hydroforming tooling
 - classification of
 - closed die, 197, 199(F)
 - crosswise split dies, 197, 199(F)d
 - lengthwise split dies, 197–198, 199(F)d
 - open die, 197, 199(F)
 - production dies, 198–199, 200(F)
 - prototyping dies, 198, 200(F)
 - optimization of the integrated forming process, 197(F)
 - overview, 193
 - production line, 194, 195(F)
 - productivity enhancement, 197(F)
 - tool design consideration, 199
 - factors to be considered, 201(T)
 - pressures generated in the guiding zone, 200(F)
 - T-shape tube hydroforming die, 200(F)
 - tooling composition, 198(F)
 - tooling parts, 199(T)
- tube hydroforming, 199, 201–202
 - design considerations, 202(T)
 - engine cradle ready for installation, 201(F)
 - engine cradle with multiple holes, 201(F)
 - inward hydropierced holes, 201(F)
 - outward hydropiercing, 202(F)
 - tungsten inert gas wire (HTCS-Rod), 152
 - twelve-node shell element, 144

twinning-induced plasticity (TWIP) steels, 107
 at elevated temperature, 113
 strain rate, 112
 twist compression test (TCT), 119, 330–331(F)
 two-dimensional (2-D) simulations, 26, 27
 two-point incremental forming (TPIF), 274(F), 276, 277, 283

U

U-bend tests, 119
 U-channel drawing of dual-phase steels, 120–121(F)
 U-channels, 120, 121
 warm forming, 128–129
 U-die bending
 punch force/punch displacement curve, 35(F)
 with/without pressure pad, 35(F)
 ultimate tensile strength (UTS), 108
 ultra-high-speed (UHS) blanking
 adiabatic phenomenon, 12
 advantages of, 12
 applications, 12
 punching operations, 12
 ultra-high-speed (UHS) blanking presses, 12
 ultrahigh-strength steels (UHSS), 133, 143
 Ultralight Steel Auto Body Programme, 112
 unclamping, 281(F), 282
 University of Dortmund (IUL), 162, 169
 University of Stuttgart (IFU), 165, 166
 USIBOR 1500P, 154

V

Vanadis 6, 333
 vanadium carbide (VC), 328
 Vancron 40, 333
 V-die bending
 bottoming, 34(F)
 coining, 34(F)
 FEA analysis, 26–27(F,T), 28(F)
 finite-element analysis (FEA), 26–27(F,T)
 overview, 28(F), 34
 punch force/punch displacement curve, 35(F)
 vibrations
 acoustic emission sensors, 307
 cushion systems, 125
 horizontal, 10
 press, 124
 punch, 8
 reducing, 10
 vertical, 10
 Vickers hardness, 320, 321(F)
 Vickers hardness number (HV), 320
 viscous pressure bulge test (VBT), 27(F), 53, 58(T), 59, 65
 viscous pressure forming, 158, 160(F)
 Voestalpine, 154
 Volkswagen Passat, 153
 von Mises yield criterion, 22, 142, 184

W

wall curl, 126
 warm forming, 96(F)
 AHSS, 128–129
 aluminum alloys (*see* aluminum alloys, warm forming)
 applications, 96, 98
 die heating techniques, 93–94
 heating system for round cup tooling, 94(F)
 heating systems for industrial stamping tooling, 94(F)
 open warm forming tooling, 96(F)
 tooling in which dies and punch are heated, 95(F)
 view/dimensions of the round tool, 95(F)
 heat transfer, 92
 heating methods, 91
 isothermal warm forming, 90–91
 lubrication, 92
 magnesium alloys (*see* magnesium alloys, warm forming)
 magnesium sheets, minimum bending radii, 93(T)
 mechanics of deformation, 91–92(F)
 nonisothermal warm forming, 90–91
 drawability, 92(F)
 LDR, 92(F)
 polytetrafluoroethylene film, 92, 93(F)
 press selection, 94–96
 servo motor drive system, 97(F)
 slide motion of the servo press, 98(F)
 tool design, hydraulic press, 96(F)
 tool design, mechanical press, 97(F)
 process design, 92–93
 springback, AHSS, 128–129
 as a system, 90
 tool design, 92–93
 warm sheet hydroforming
 challenges/issues in process simulation
 data required as input, 172(T)
 heat-transfer, 173
 interface friction coefficient, 173
 interface heat-transfer coefficients, 173
 overview, 172
 sheet material flow-stress data, 172–173
 overview, 170–171
 warm SHF-D, 171–172(F)
 warm SHF-P, 171, 172(F)
 warp, 41, 42(F)
 wear. *See also* plating and coating
 AHSS, 113, 118
 Archard wear equation, 318
 cast iron dies, 319
 cast steels, 319
 die inserts, 199
 die wear, 125, 153, 296, 320
 feeding inserts, 197
 inserts, 319
 lubrication, 215
 overentry of the punch, 8
 press cushion, 124

proximity sensors, 305
 punch point geometry, 8
 stamping tools, 317
 tests, 330–334(F,T)
 THF, 192–193, 194(F)
 tool coatings, 121
 tool materials, 11, 149, 317
 tool steels, 126
 warm forming, 96
 Weartec, 333
 weight reduction (hot-stamped components), 154
 welded tubing, 181–182
 welding
 arc welding, 215
 high-frequency welding, 215
 induction, 215
 laser, 215
 plasma, 215
 roll forming lines, 215
 THF, 181–182
 W-forming strategy, 218
 Wheatstone bridge circuit, 302(F)
 wheelon process, 160
 Wila USA, 45
 wind, 41, 42(F)
 WinSets Technologies, LLC, 12
 wipe die bending, 22, 25(F), 35–37(F)
 wiper die, 187, 189
 wire bridge, 228
 wrinkle indicators, 204–205
 wrinkles
 room-temperature sheet hydroforming, 170(F)
 sidewall, 168
 wrinkling
 AS, 204–205(F)

contour flanging, 37, 38(F)
 FRF, 222
 hemming, 41, 42(F)
 high-velocity forming, 227
 shear spinning, 267
 shrink flanging, 38(F)
 spinning, 252(F)
 stamping, 54
 THF, 202
 wrinkle sensor, 309

X

X-IP steel, 115–116
 X-Tec, 153, 154

Y

Young's modulus
 AHSS, 110
 B-pillar simulation, 143, 144(T)
 as a function of temperature, 142
 roll forming, 220
 springback, 22, 23
 stress, prediction of, 22

Z

zinc alloys
 AHSS, 121
 hard chrome plating, 324
 iron-zinc-base coating, 154
 magnesium alloys, 85
 tool materials, 318
 zirconate titanate, 302

